An Experimental Investigation of the Relationship between Flow Turbulence and Temperature Fields in Turbulent Non-premixed Jet Flames

Dissertation

Presented in Partial Fulfillment of the Requirements for the Degree Doctor of Philosophy in the Graduate School of The Ohio State University

By

Thomas Andrew McManus

Graduate Program in Mechanical Engineering

The Ohio State University

2019

Dissertation Committee

Jeffrey Sutton, Advisor

Mohammad Samimy

Seung Hyun Kim

Jeffrey Bons

Abstract

In this dissertation, two sets of experiments were performed to improve the understanding of the relationship between flow turbulence and the temperature field in turbulent non-premixed flames. Independent high-speed temperature and velocity measurements were carried out to examine flow and flame dynamics with a focus on spatio-temporal statistical analysis. Subsequently, simultaneous three-component velocity and high-resolution temperature measurements were performed to examine the interaction between fluid kinematics properties and the temperature field. The research presented within this dissertation focused on four overarching thrusts: (1) development and application of high-repetition rate (10 kHz) two-dimensional temperature measurements in turbulent non-premixed flames, (2) spatio-temporal analysis of temperature and velocity data to determine characteristic length and time scales, examine isotropy, and elucidate fundamental mechanisms governing decorrelation of the fluctuations, (3) development of a novel laser-based thermometry approach that can be performed simultaneously with particle image velocimetry in turbulent non-premixed flames, and (4) application of simultaneous temperature and velocity measurements to examine the kinematic mechanisms governing the topology of the scalar (thermal) field.

Temperature field dynamics were first examined using high-repetition-rate (10 kHz) planar Rayleigh scattering in a series of turbulent non-premixed $CH_4/H_2/N_2$ flames at two different Reynolds numbers, Re = 15,200 and 22,800. The high-speed temperature measurements were facilitated using a custom high-energy pulse burst laser system (HEPBLS) developed at Ohio State. The unique combination of ultra-high energy output (> 1 Joule/pulse at 10 kHz) and an optimized optical collection system allowed for previously unavailable high-resolution multi-dimensional temperature measurements with excellent signal-to-noise ratios (SNR > 60).

Additional high-speed particle image velocimetry (PIV) measurements were acquired in the same series of flames in order to facilitate a statistical comparison between the turbulent flow and a reactive scalar. Since the temperature and velocity data were resolved in both space and time, temporal auto-correlations, two-point spatial correlations, and two-point space-time correlation functions were derived as a function of spatial position and Reynolds number. Integral length and time scales were calculated from the correlation functions and it was observed that the velocity fluctuations exhibited larger integral length scales and slower integral time scales compared to those calculated for the temperature fluctuations for both Reynolds numbers and at all spatial locations. Differences by as much as a factor of three were noted showing that temperature fluctuations de-correlate much faster than velocity fluctuations. The faster de-correlation times are indicative of the effects of chemical reaction increasing the rate at which the reactive scalar fluctuations are destroyed.

The two-point space-time correlation maps for both the velocity and temperature fluctuations were used to show that the recently proposed "elliptical" model provides an improved transformation of correlation functions from space to time as compared to Taylor's hypothesis. The current work presents the first results showing the accuracy of the elliptical model in turbulent reacting, free-shear flows. The elliptical model also was used to better understand the mechanisms governing decorrelation for temperature and velocity fluctuations in turbulent non-premixed flames. Results show that the decorrelation of both temperature and velocity fluctuations is largely governed by both convection and turbulent velocity fluctuations, although reaction also appears to play a role, especially in the case of the temperature fluctuations.

In order to examine the direct interaction between flow turbulence and temperature fluctuations, simultaneous velocity and temperature measurements are required. A critical part of the current dissertation research involved the development of a novel implementation of filtered Rayleigh scattering (FRS) as a thermometry approach that can be performed simultaneously with PIV in a turbulent non-premixed flame. Quantitative temperature measurements using the FRS-based temperature measurement require detailed understanding of the temperature- and species-dependent Rayleigh-Brillouin scattering (RBS) spectra, which are commonly modeled. A detailed assessment of the most common RBS model, the Tenti S6 model, was performed for a number of gas species and gas mixtures at combustion-relevant temperatures. Overall, the results show that the Tenti S6 model produces accurate predictions of the RBS spectra for a wide range of combustion-

relevant conditions and is suitable for use in FRS applications. Subsequently, a series of $CH_4/H_2/Ar$ turbulent non-premixed flames were designed that facilitate quantitative temperature imaging using only a single FRS measurement. A detailed characterization of the accuracy and SNR of the FRS-based temperature measurements was performed.

Simultaneous planar temperature and three-component velocity measurements were performed using FRS and stereo PIV in a series of piloted, turbulent non-premixed flames at Reynolds numbers of 10,000, 20,000, and 30,000. The joint temperature and velocity measurements were used to visualize relevant interactions of the velocity and temperature fields and to generate detailed statistics characterizing their coupled relationship. From visualization, large-magnitude values of strain rate appear to be spatially coincident with regions of large thermal gradients or large-magnitude thermal dissipation, especially near the primary reaction zone. Statistical results show that both the extensional and compressional principal strain rates play a significant role in generating large-magnitude thermal dissipation. However, for the higher Reynolds number cases, the most compressive principal strain rate plays a larger role. The thermal scalar flux was calculated for both the axial and radial directions. It was observed that the gradient transport hypothesis appears to be satisfactory for describing transport in the radial direction; however, in the axial direction, clear indications of counter gradient transport are present.

Dedication

This is dedicated to all of my family and friends who have always believed in me, even when I sometimes do not. This is also dedicated to my father, John, who pushed me to always do my best. This is also dedicated to my late mother, Jacqueline, who I would like to think would be proud of me. This is especially dedicated to my lovely and supportive wife, Sarah, who makes me a better and happier human being.

Acknowledgments

I would like to acknowledge the support of my advisor, Dr. Jeffrey Sutton. The long (sometimes very long) discussions of various experimental details as well as discussions of underlying physics of turbulence and turbulent reacting flows has been invaluable to my growth as a student and practitioner of turbulent combustion studies. I would also like to acknowledge the many colleagues and friends that I have interacted with over the course of my time at Ohio State University. The camaraderie and discussions have been a great boon to my time here.

Vita

2011..... B.Sc. Aerospace Engineering
Illinois Institute of Technology
Summa Cum Laude

2011.....B.Sc. Physics with Mathematics Minor
DePaul University
Summa Cum Laude

2011 – 2018..... Ph.D. Candidate
Mechanical Engineering
Ohio State University

Publications

McManus, T. A., & Sutton, J. A. (2019). Quantitative planar temperature imaging in turbulent non-premixed flames using filtered Rayleigh scattering. *Applied Optics*, *58*(11), 2936-2947.

McManus, T. A., Monje, I. T., & Sutton, J. A. (2019). Experimental assessment of the Tenti S6 model for combustion-relevant gases and filtered Rayleigh scattering applications. *Applied Physics B*, *125*(1), 13.

Allison, P. M., McManus, T. A., & Sutton, J. A. (2016). Quantitative fuel vapor/air mixing imaging in droplet/gas regions of an evaporating spray flow using filtered Rayleigh scattering. *Optics letters*, *41*(6), 1074-1077.

McManus, T. A., Papageorge, M. J., Fuest, F., & Sutton, J. A. (2015). Spatio-temporal characteristics of temperature fluctuations in turbulent non-premixed jet flames. *Proceedings of the Combustion Institute*, *35*(2), 1191-1198.

Papageorge, M. J., McManus, T. A., Fuest, F., & Sutton, J. A. (2014). Recent advances in high-speed planar Rayleigh scattering in turbulent jets and flames: increased record lengths, acquisition rates, and image quality. *Applied Physics B*, *115*(2), 197-213.

Fields of Study

Major Field: Mechanical Engineering

Table of Contents

List of Tables

List of Figures

Chapter 1. Introduction

1.1 Motivation

According to analysis by Lawrence Livermore National Laboratory, combustion processes comprised over 85% percent of all energy production in the US (in 2018) and over 94% of all energy production in Ohio (in 2014) [1]. This demand for power production using combustion-related technology has changed very little over the past seven years [1] and will likely remain a significant source for energy production for the foreseeable future. Applications of energy-conversion devices utilizing turbulent combustion processes range from transportation to power production and affect the majority of the population in some manner. Therefore, reducing emissions and increasing efficiency of these technologies (through increased control) are critical research goals that can offer strong positive impacts for society at large.

At a scientific level, there is a need for improved fundamental understanding of various aspects underpinning turbulent combustion processes, including reactant mixing, ignition, and turbulence-chemistry interaction, where the last topic is a broad-sweeping area representing the direct and indirect effects of flow turbulence on reaction, heat release, and species formation (and vice versa). The means of gaining improved fundamental

knowledge of these process will come through advanced experimental and computational research. In terms of experimentation, laser diagnostic-based measurements provide a way to probe turbulent reacting flows in a non-intrusive manner with excellent spatial and temporal resolution. Such laser-based measurements can provide data characterizing a variety of important flow/reaction parameters including velocity, temperature, chemical species concentrations, reaction rates, and pollutant output (i.e., CO, SOx, NOx, soot) [2-4]. In general, the over-arching goals for experimental research in the area of turbulent combustion can be categorized into two distinct, but complementary areas: (1) measurements and analysis that lead to improved fundamental understanding of the underlying physics and chemistry governing the dynamics of turbulent reacting flows, and (2) measurements that aid in the assessment, validation, and/or improvements of turbulent combustion computational models.

During his Hottell Plenary Lecture during the 26th International Symposium on Combustion in 1996, K.N.C. Bray stated "the problem of turbulence still represents the most serious bottleneck between combustion science and its application" [5]. These challenges manifest themselves due to complex interplay between chemistry and flow turbulence over a wide range of spatial and temporal scales. This "turbulence-chemistry interaction" influences flame structure, governs flame stability, modulates reaction rates, and leads to intermittent species production/destruction that is difficult to predict. During the past two decades there have been many advancements in experimental and numerical approaches that have proven invaluable in identifying important and rate-controlling

physical and chemical mechanisms within turbulent combustion systems [2, 4]. In addition, many targeted workshops have been established, such as the International Workshop on the Measurement and Computation of Turbulent Non-premixed Flames [6] (also referred to as the "TNF workshop") that combine efforts from various researchers to generate joint experimental and numerical results from various well-documented target flames. These detailed data sets are used to improve the fundamental understanding of turbulent reacting flows and further develop modeling capabilities. However, in spite of these efforts, the extreme complexity of turbulent reacting flows still pose significant challenges such that the ultimate goal of turbulent combustion research – the development of robust, predictive, and physically based models - remains elusive.

In non-reacting turbulent flows, the interaction between the turbulent flow and scalar fields has been widely studied in the context of scalar mixing (e.g., [7-9]). Statistical moments, including $\langle u_i^n \theta \rangle$, where u_i represents the i^{th} velocity component, n is the moment order, and θ is the targeted scalar, have been used to define parameters such as the turbulent Prandtl number and directly examine terms appearing in turbulent transport models ([10-14]). Such measurements are not as readily available in turbulent reacting flows as one of the biggest challenges in turbulent combustion environments is simultaneous velocity and *quantitative* scalar measurements. Therefore, there is a significant need for the development of experiments that can provide details on the coupling between velocity and scalars in reacting flows, including multi-parameter laser diagnostic approaches with good spatial and temporal resolution. Such measurements are

critical to examine the interaction between the turbulent flow field, flow scalars, and the underlying chemical processes. In this manner, the current research focuses on the interaction and foundational relationship between the flow velocity and the temperature field in turbulent non-premixed jet flames. The temperature field is targeted because (i) it is an active scalar that is closely linked to both mixing and chemistry and (ii) measurements with high signal-to-noise and excellent resolution are possible.

1.2 General Characteristics of Turbulent Flows

Turbulence is characterized by seemingly random spatial and temporal fluctuations in both velocity and scalar fields that lead to rapid momentum exchange and mixing of scalar quantities in the flow. The conservation equations describing the fluid motion and the scalar transport are highly non-linear and thus extremely sensitive to initial and boundary conditions. This facet creates two difficulties: (1) no general closed form solution of the conservation equations exists and (2) any instantaneous realization cannot be used to predict the behavior of the flow at another realization. In addition, the non-linear processes that lead to the observed fluctuations generate a broad range of length and time scales such that direct numerical solutions of the governing equations is impractical for a majority of realistic or even laboratory-scale flows. This is especially true in reacting flows, where the number of conservation equations increases from 5 (continuity, momentum, passive scalar) to 5+N (continuity, momentum, energy, and N species). In this manner, a statistical or probabilistic approach to analyzing turbulent flows typically is employed since many of the statistical properties within turbulent flows are repeatable and quasi-universal.

1.2.1 General Statistical Concepts

In statistical analysis of turbulent flows, the variables within a turbulent field are treated as random variables such that any variable can be completely described by its probability density function (pdf), $P(u)$, where $P(u)du$ is the probability of variable u having a value bound by u and $u + du$ and subject to

$$\int_{-\infty}^{\infty} P(u)du = 1 \qquad \text{Eq. (1.1)}$$

From the pdf, the statistical moments can be derived, where the n^{th} statistical moment is defined as

$$\langle u^n \rangle = \int_{-\infty}^{\infty} u^n P(u)du \qquad \text{Eq. (1.2)}$$

Relevant moments include the mean ($n = 1$), variance ($n = 2$), skewness ($n = 3$), and kurtosis ($n = 4$). The statistical moments are used in an attempt to gather characteristic details about flow. For example, the variance describes the inherent variability of the fluctuations from the mean in flow; the skewness describes the asymmetry of the pdf which describes where the mass of the distribution (the majority of the samples) is concentrated; and the kurtosis characterizes the "flatness" of the pdf and gives an indication of how extreme intermittent events affect the overall process.

Often in turbulent flows it is desirable to determine if two variables have some dependence on one another other. To explore whether any two random variables, u and v,

are correlated, the joint probability distribution function (jpdf), $P(u, v)$, can be determined as

$$\int_{-\infty}^{\infty}\int_{-\infty}^{\infty} P(u,v)dudv = 1 \qquad \text{Eq. (1.3)}$$

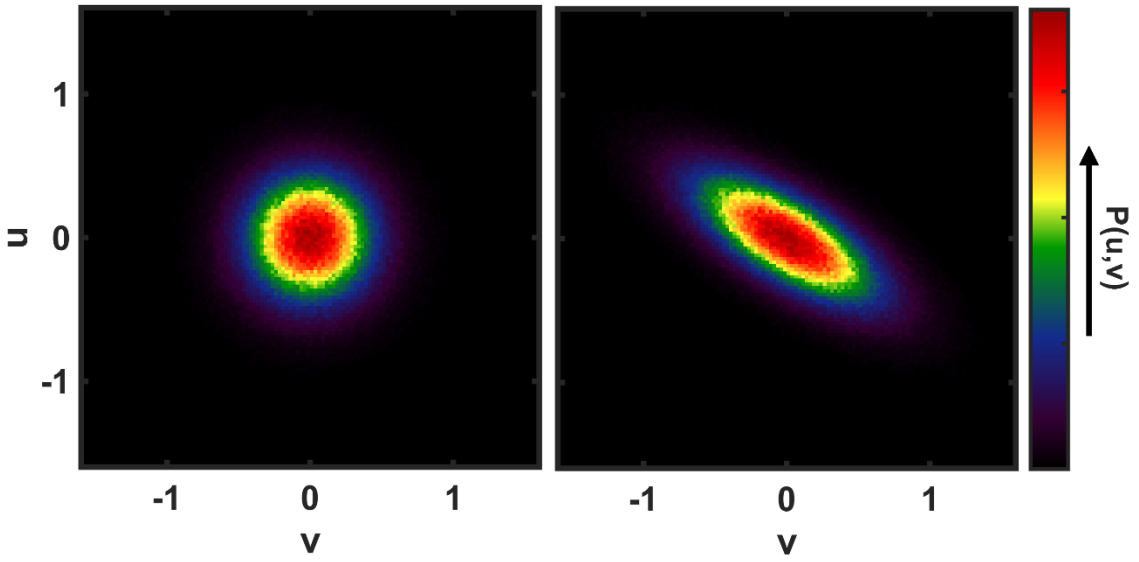

Figure 1.1: Example joint probabilty density functions (jpdf) for synthetically generated random variables u and v. (Left) jpdf in the case u and v are not correlated. (Right) jpdf for the case where u and v are linearly correlated.

Figure 1.1 shows two different jpdfs, shown as false colormaps, of random variables u and v. For the simulated data in the left plot the two variables appear to be unrelated or "uncorrelated", while the two variables shown in the right plot appear to be dependent on

one another and are characterized as linearly (negatively) correlated. Joint moments of the jpdf, $P(u,v)$ or the "$(m+n)^{th}$-order correlations" are defined as

$$\langle u^n v^m \rangle = \int_{-\infty}^{\infty} \int_{-\infty}^{\infty} u^n v^m P(u,v) du dv \qquad \text{Eq. (1.4)}$$

For $n = m = 1$, the correlation coefficient between u and v is defined as

$$R_{uv} = \frac{\langle uv \rangle}{\sqrt{\langle u^2 \rangle}\sqrt{\langle v^2 \rangle}} \qquad \text{Eq. (1.5)}$$

If $R_{uv} = 0$, then u and v are said to be uncorrelated; if $R_{uv} = \pm 1$, u and v are said to be perfectly correlated; if $R_{uv} < 0$, u and v are said to be negatively correlated; and if $R_{uv} > 0$, u and v are said to be positively correlated. Uncorrelated variables may also be statistically independent. Statistical independence is achieved only if

$$P(u,v) = P_u(u) \times P_v(v) \qquad \text{Eq. (1.6)}$$

where P_u and P_v are the marginal pdfs extracted from the jpdfs. Within turbulent flows, it may also be useful to consider the probability density function of a variable, u, conditioned on a particular value of another variable, v. This is termed the conditional pdf and denoted as $cpdf(u|v)$. The conditional pdf is simply a "slice" of the jpdf at the desired value of v, but re-normalized such that the area is unity. Conditional moments may then be calculated from the $cpdf(u|v)$ in a similar manner as presented in Eq. (1.2).

In turbulent flows the random variables are often decomposed into their mean and fluctuating component as $u = \langle u \rangle + u'$ (often termed Reynolds decomposition) and the

governing transport equations are often examined statistically; that is, transport equations are written for each statistical moment. Derivation of these transport equations can be found in several reference texts (e.g., [15, 16]). A challenge with solution of these equations arises in the fact there are unknown terms related to higher-order moments and thus, the transport equations are said to be unclosed. For example, in the mean flow equations, additional "turbulent flux" terms appear that relate the energy exchange between the mean and fluctuating fields. For the momentum equation, this term is the Reynolds stress $\langle u_i' u_j' \rangle$ and for the scalar transport, there appears the scalar flux term $\langle u_i' \psi' \rangle$. To solve this "closure problem", a model for the flux parameters must be provided. In the case of the scalar flux, models commonly employ the gradient transport assumption that assumes that the scalar flux term is proportional to the negative gradient of the average of the scalar field ($\langle u_i' \psi' \rangle \propto -\nabla \langle \psi \rangle$). While these terms have been measured in non-reacting flows, measurements in turbulent reacting flows are much sparser and are needed to assess its validity.

1.2.2 Length and Time Scales in Turbulent Flows

Turbulent flows are characterized by a wide range of length scales (and corresponding time scales). The largest scale is the "outer scale" (δ) which is related to the flow geometry and supplies the energy to the flow. In jet flows, the outer length scale is the width of the jet, which is defined as the width of the mean velocity profile [15,16]. The outer-scale velocity is given by the mean centerline axial velocity $\langle u_{cl}(x) \rangle$ and the outer time scale is determined as

$$\tau_\delta(x) = \frac{\delta(x)}{\langle u_{cl}(x) \rangle} \qquad \text{Eq. (1.7)}$$

Using outer-scale variables, the outer-scale Reynolds number is defined as $Re_\delta = u_{cl}(x)\delta(x)/\nu$, where ν is the kinematic viscosity. The outer-scale Reynolds number properly scales turbulence properties across all turbulent shear flows.

The energy generated at the largest outer scales is transferred continuously from the "integral scales" to subsequently smaller and smaller scales until the energy is finally dissipated. The integral length scales, $\ell(x)$, are the largest scales that appear due to the turbulent nature of the flow (often considered as the size of the largest possible eddies in the flow). They contain most of the kinetic energy [17] and are responsible for the majority of momentum and energy transport. The corresponding time scale is the integral time scale. Through eddy interaction at multiple scales, energy is transferred through a range of scales referred to as the "inertial subrange". Finally, the eddies become sufficiently small such that viscosity becomes important and the energy is dissipated into heat. These scales are referred to as the "dissipative scales". Figure 1.2 shows a turbulent kinetic energy spectrum illustrating the energy cascade process in turbulence.

The integral scales can be determined by using the correlation coefficient defined in Eq. (1.5) and setting the random variables to $u = u'(x,t)$ and $v = u'(x + \Delta x, t + \Delta t)$. When $\Delta t = 0$, the two-point spatial correlation function is determined and when $\Delta x = 0$, the temporal autocorrelation function is determined. Integration of these two correlation functions yield the integral length and time scales, respectively. The smallest length scale,

termed the Kolmogorov scale (denoted as η in Fig. 1.2, but as λ_k throughout this dissertation) is defined from dimensional analysis as

$$\lambda_k = (\nu^3/\epsilon)^{1/4} \qquad \text{Eq. (1.8)}$$

where ϵ is the kinetic energy dissipation rate. The smallest length scale over which scalar fluctuations occur is the Batchelor scale, λ_B, defined using dimensional arguments as:

$$\lambda_B = \left(\frac{\nu D}{\epsilon}\right)^{1/4} = \lambda_k Sc^{-1/2} \qquad \text{Eq. (1.9)}$$

where Sc is the Schmidt number and is defined as the ratio of viscosity to scalar diffusivity.

In order to estimate the range of scales present in a turbulent flow, it is assumed that the energy generated at the largest scales is balanced with the energy dissipated at the smallest scales. In this manner, the energy dissipation rate at the smallest scales is equal to the rate of energy input at the outer scales such that $\epsilon \sim (\langle u_{cl} \rangle^3/\delta)$. Substitution into Eq. (1.8) yields an estimate of the ratio of the outer scale to the Kolmogorov scale as

$$\frac{\delta}{\lambda_k} \sim \frac{\delta}{(\nu^3/\epsilon)^{1/4}} \sim \frac{\langle u_{cl} \rangle^{3/4}}{\nu^{3/4}\delta^{3/4}} \sim Re_\delta^{3/4} \qquad \text{Eq. (1.10)}$$

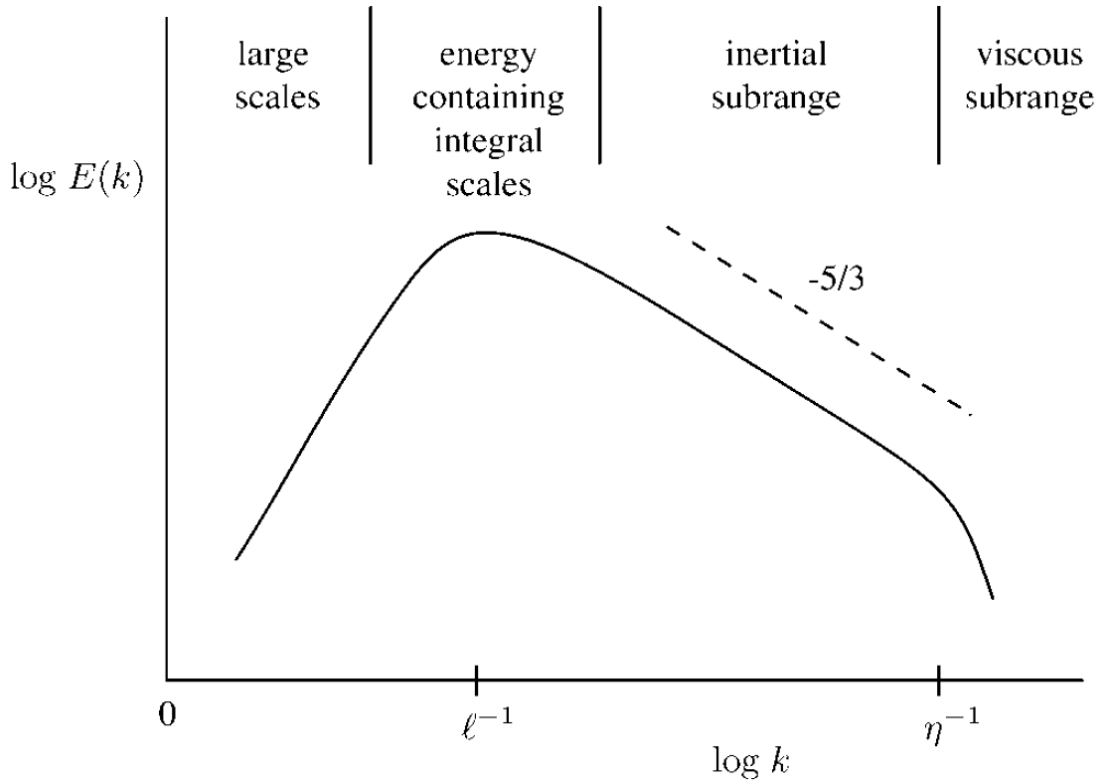

Figure 1.2: Representive schematic of turbulent kinetic energy spectrum as a function of wavenumber, k. Reproduced from [17]. This spectrum represents the eneergy cascade process.

This illustrates the wide range of length scales possible in turbulent flows and shows that even for moderate values of Re_δ of 10^4, the ratio of scales is ~10^3. A similar argument can be made for time scales such that the ratio of the outer time scale (τ_δ) to the Kolmogorov time scale (τ_k) is

$$\frac{\tau_\delta}{\tau_k} \sim Re_\delta^{1/2} \qquad \text{Eq. (1.11)}$$

1.3 General Concepts of Turbulent Flames

In general, combustion can be divided into two distinct categories, premixed and non-premixed, that show markedly different behavior and interaction with turbulent flow fields. For premixed combustion, the fuel and oxidizer are mixed homogeneously prior to ignition, whereas for non-premixed combustion the fuel and oxidizer originate from separate streams and must be mixed at the molecular level prior to reacting locally. Since chemical time scales are, in general, much faster than turbulent mixing timescales, the mixing processes control the overall combustion process for non-premixed flames. However, for high levels of turbulence the mixing time scales can approach the times scales of the slowest chemical reactions and lead to local flame extinction [17].

1.3.1 Mixture Fraction Concepts

A particularly useful concept in non-premixed flames is the mixture fraction variable, ξ, which describes the state of molecular mixing for a two stream (fuel and oxidizer) flow. The mixture fraction is a conserved scalar that is defined as the ratio of the mass flux issuing from the fuel stream to the total mass flux in a mixture

$$\xi = \frac{\dot{m}_{fuel}}{\dot{m}_{fuel}+\dot{m}_{ox}} \qquad \text{Eq. (1.12)}$$

Equivalently, it is the ratio of the mass of any material originating in the fuel stream to the mass of a mixture. This allows the mixture fraction to be written in terms of other elemental conserved scalars, Z_i

$$\xi = \frac{Z - Z_{ox}}{Z_{fuel} - Z_{ox}} \qquad \text{Eq. (1.13)}$$

where Z is the value of the conserved scalar at any point in the flow, Z_{fuel} is the value of the conserved scalar in the fuel stream, and Z_{ox} is the value of the conserved scalar in the oxidizer stream. In combustion systems, Z is typically chosen as elemental species mass fractions (Y_C, Y_H, or Y_O) and ξ is bound between 0 and 1, where it is 1 for pure fuel and 0 for pure oxidizer. Bilger [18] defined a mixture fraction based on the combination of atomic mass fractions of carbon, hydrogen and oxygen that shows decreased sensitivity to preferential molecular diffusion, where $Z = 2Y_C/W_C + 0.5\ Y_H/W_H - Y_O W_O$ yielding

$$\xi = \frac{\frac{2}{W_C}(Y_C - Y_{C,ox}) + \frac{1}{2W_H}(Y_H - Y_{H,ox}) - \frac{1}{W_O}(Y_O - Y_{O,ox})}{\frac{2}{W_C}(Y_{C,fuel} - Y_{C,ox}) + \frac{1}{2W_H}(Y_{H,fuel} - Y_{H,ox}) - \frac{1}{W_O}(Y_{O,fuel} - Y_{O,ox})} \qquad \text{Eq. (1.14)}$$

where W_C, W_H, and W_O are the atomic weights of carbon, hydrogen, and oxygen, respectively. In addition to describing the state of mixing, the utility of ξ lies in the fact that for many combustion modeling approaches the complete thermo-chemical state can be parameterized as a function of ξ [17].

The scalar dissipation rate, χ, describes the rate of mixing in a system and is defined as

$$\chi = 2D(\nabla\xi \cdot \nabla\xi) \qquad \text{Eq. (1.15)}$$

where D is the molecular diffusivity. The scalar dissipation rate is a critical parameter for non-premixed turbulent combustion as it describes the dissipation of scalar energy or

equivalently the destruction of scalar variance in an analogous manner to the kinetic energy dissipation rate. In this manner, the rate of molecular mixing governs chemical reaction in non-premixed combustion systems. The scalar dissipation rate also underpins several combustion models including "flamelet-based" [19-22] and "conditional moment closure" [23-25] models.

1.3.2 Mixture Fraction and Temperature Measurements

Because of the importance of ξ and χ in turbulent combustion modeling, there have been sustained efforts for measuring these quantities in both turbulent non-reacting and reacting flows for several decades. Within reacting flows, the combined approach of spontaneous Raman and Rayleigh scattering is the most accurate method for measuring ξ (and deducing χ) through instantaneous, spatially-resolved distributions of the temperature and all major species concentrations such as CH_4, O_2, CO, CO_2, H_2O, H_2 (see Eq. 1.14). This approach has been successfully applied in turbulent jet flames (e.g., [26-29]), opposed-flow flames (e.g., [30]), bluff body and stratified flames (e.g., [31-34]), and laboratory-scale gas-turbine burners (e.g., [35]). While the measurement of the major species (and temperature) allows an accurate determination of ξ, the measurements are limited to single point or 1D configurations yielding a 1D surrogate of the true scalar dissipation rate. There has been much work on developing methodologies for two-dimensional imaging of the mixture fraction and scalar dissipation rate fields (e.g., [36-44] to examine mixing topology, all with different levels of accuracy and signal-to-noise ratio (SNR). However, it is noted that scalar dissipation occurs at the finest scales of turbulence

and makes measurements in flames quite challenging due to the need to simultaneously have good spatial resolution and precision (SNR).

As an alternative, many researchers have proposed measuring the temperature field and deducing the thermal dissipation rate defined as

$$\chi_T = 2\alpha(\nabla T \cdot \nabla T) \qquad \text{Eq. (1.16)}$$

where T is temperature and α is the thermal diffusivity [45-54]. For example, Frank and co-workers have used high-fidelity 2D temperature measurements (obtained with planar Rayleigh scattering) to derive the thermal dissipation rate in a series of non-premixed jet flames [51-54]. From these measurements they have determined dissipation energy spectra, layer thicknesses, layer orientations, and dissipative length scales. The thermal dissipation is of interest because (1) of the importance of understanding how thermal mixing effects chemical reaction processes, (2) temperature can be measured with significantly higher SNR and spatial resolution compared to mixture fraction measurements, and (3) there is the belief that χ_T is related to χ and that measurements of the fluctuating T and χ_T fields may reveal information about the turbulence and mixture fraction fluctuations [50]. For example, Everest et al. [48] argued that if the state relationship $T = T(\xi)$ holds, then $\chi_T = Le(\frac{dT}{d\xi})^2 \chi$, where $Le = \alpha/D$ is the Lewis number, shows the direct relationship between χ_T and χ. With the assumption of infinitely fast chemistry, the "flame" exists as an infinitely thin layer where the fuel and oxidizer have mixed in stoichiometric proportions at $\xi = \xi_S$, and the relationship between the temperature and mixture fraction is given by the Burke-

Schumann solution [55] shown schematically in Figure 1.3. For realistic non-premixed flames, the situation is more complicated, but the schematic shown in Figure 1.3 illustrates the close link between the temperature and mixture fraction and is a reasonable representation for flames far away from extinction.

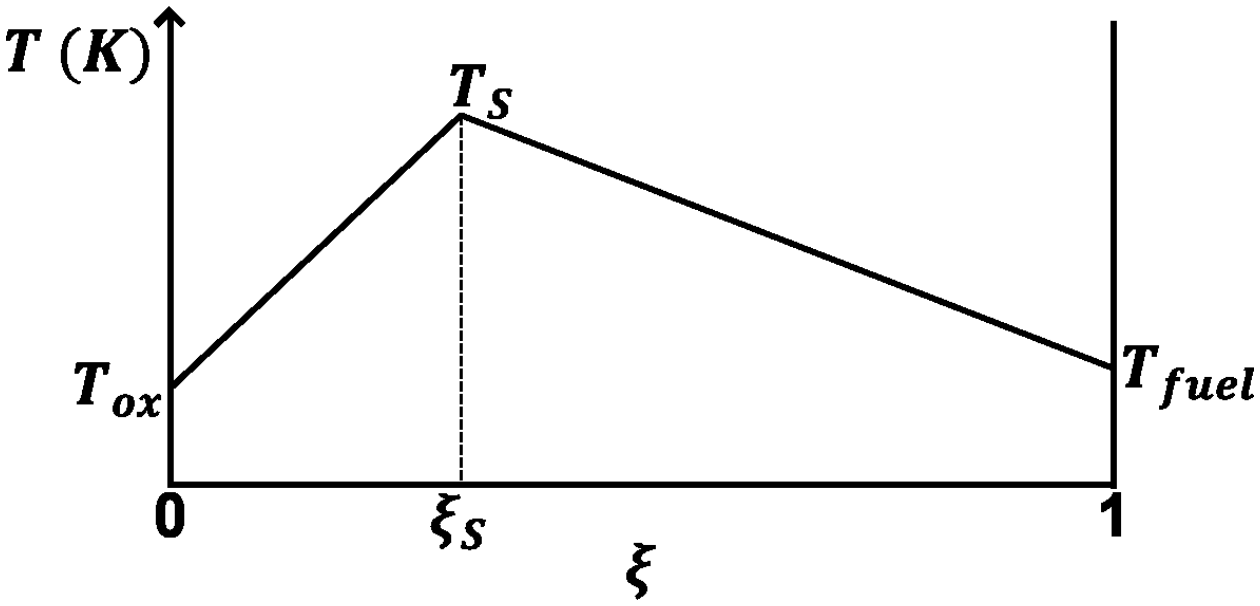

Figure 1.3: Schematic of temperature versus mixture fraction from the Burke-Schumann solution [17, 55].

1.4 Laser Diagnostics in Turbulent Combustion Studies

Laser-based diagnostics play an important role in experimental research in turbulent, reacting flows. Compared to physical probes, laser-based measurements do not

interfere or disturb the flow and/or chemistry, may offer improved spatial resolution compared to physical probes such as hot-wires or thermocouples [2], and can survive the "harsh" measurement environment. Many laser-based measurements also offer the opportunity to generate "instantaneous" realizations (and "snapshots" in 2D) as the duration of laser pulses can be nanoseconds or shorter and thus, the flow is "frozen" over this time scale. A wide range of laser diagnostic techniques exist to measure relevant flow and thermodynamic parameters and the reader is referred to a number of excellent texts discussing these approaches and their application in combustion environments [2-4, 56, 57].

Relevant to the work presented in this dissertation are measurements of temperature and velocity in turbulent reacting flows. Prominent laser-based thermometry approaches utilized in reacting flows include spontaneous Rayleigh or Raman scattering [2, 58-61], laser-induced fluorescence [62], coherent anti-Stokes Raman scattering (CARS) [2, 58, 63] thermographic phosphorescence [64], and absorption based methodologies [2, 58]. Due to the complex topology of turbulence, multi-dimensional measurements or "imaging" are desired in order to characterize the turbulent flame structure. The most common approach for multi-dimensional temperature imaging in turbulent flames has been through the use of planar Rayleigh scattering (described in detail in Chs. 2 and 3). This approach has been used successfully by many research groups for detailed measurements of temperature and thermal dissipation rate as discussed above in Sec. 1.3.2. Temperature measurements using Rayleigh scattering also have been performed in non-premixed flames at high-repetition

rates using modern kHz-rate pulsed lasers [47, 65, 66] although those measurements were limited to 0D and 1D measurements. In order to simultaneously examine spatial structure and dynamic behavior, it is desired to measure the temperature fields at high data repetition rates. This dissertation presents the first high-repetition-rate 2D temperature imaging in turbulent flames and therefore, previously unavailable spatio-temporal analysis of temperature fluctuations.

The most common method for measuring velocity in turbulent flows is particle image velocimetry (PIV), a robust and proven approach that involves seeding small tracer particles into the flow field to track the fluid motion [67] (see Ch. 2 for a discussion). As PIV is a field measurement, it allows greater insight into flow field structure (and the calculation of derivative-based quantities) as compared to traditional single-point techniques such as laser Doppler velocimetry (LDV). While the basic principles underlying the implementation and execution of PIV in flames is the same as in non-reacting flows, the localized heat release (and the associated gas expansion effects) characteristic of reacting flows does provide additional demands and sources of uncertainty. Issues include uniform particle seeding (especially in non-premixed flames), particle lag due to thermophoresis, and interference from flame luminosity. Even with these additional challenges, PIV has been utilized in turbulent flames for nearly three decades and has become a critical tool for characterizing reacting flow fields. In the current work, both high-repetition-rate planar PIV and high-resolution stereo PIV measurements are performed in a series of turbulent non-premixed flames.

1.4.1 Relevant Temporally Resolved Measurements

In turbulent flows there is a rich history of time-resolved measurements of the velocity and flow scalars with a specific intent on examining spectra, space-time correlations, and the coupled spatial and temporal relationship between velocity and scalar fluctuations. The majority of these studies are non-laser based (utilizing hot wires and thermocouples), but they still detail the coupled spatio-temporal behavior in a number of challenging environments including near-wall and natural convection boundary layers and in shear flows. For a detailed and historic review on the subject, the reader is referred to articles by Favre [68] and by Wallace [69]. Recently, high-speed imaging in turbulent flow (reacting and non-reacting) environments has been made possible by several technological advances in laser and camera technology as reviewed by Böhm et al [57], Thurow et al. [70], and Sick [71]. In non-reacting flows, the majority of the studies have examined velocity fluctuations using time-resolved PIV with passive scalar measurements to a lesser degree [72]. Notable work in turbulent, non-reacting flows includes the work of Wernet [73] who performed temporally resolved PIV at 25 kHz in order to measure space-time correlations in incompressible and compressible cold and heated jet flows; Buxton and Ganapathisubramani [74] who performed PIV measurements acquired at 7.25kHz to estimate convection velocities in a turbulent mixing layer; and Wang, Guan, and Jiang [75] who performed time resolved tomographic PIV to measure space-time correlations in turbulent boundary layers.

In combustion studies, the predominate applications have been high-speed particle imaging velocimetry (PIV) and OH planar laser-induced fluorescence (PLIF) in reacting flows (see Refs. [57] and [70] for a detailed listing of recent studies). Other examples of high-speed imaging related to combustion environments using commercial technology includes tracer LIF measurements to image fuel-air ratios in non-firing engines (e.g., [76-80]) and mixture fraction in unsteady, non-reacting jets [81], respectively; laser-induced incandescence (LII) measurements for time-resolved soot distributions in flames [82]; toluene LIF-based thermometry near surfaces [83]; NO distributions in a plasma torch [84]; high-speed phosphor-based thermometry [85]; and high-speed imaging of the CH radical to monitor the temporal evolution of the primary reaction zone [86, 87]. Numerous other examples of high-speed imaging in combustion environments are found within the previously cited review papers [57, 70, 71].

Most relevant to the current work are quantitative high-repetition-rate temperature measurements and space-time correlations in turbulent flames. This includes the 1D temperature measurements by Bork et al. [66] in a turbulent non-premixed jet flame. Using 10-kHz thermometry, they were able to determine integral time scales as a function of spatial position. Also relevant is the work by Wang and co-workers who reported single- and two-point temperature measurements using Rayleigh scattering at 10-kHz acquisition using Rayleigh scattering. With these measurements they were able to examine temperature fluctuations, temperature power spectra, time scales, thermal gradients, and thermal dissipation rate characteristics in a turbulent non-premixed jet flame that appears

as part of the TNF workshop and which is also considered in part of the current dissertation (DLR flame A). In a series of turbulent hydrogen and hydrocarbon flames, single and two-point time series measurements of the hydroxyl (OH) radical, were performed using laser-induced fluorescence (LIF) to determine power spectra, space-time correlations and integral scales (e.g., [88-91]). Temporal statistics were reported to exhibit self-similar behavior and thus indicated that the integral time scale is a good measure of macroscale fluctuations of OH [92]. Estimates of the integral time scale for the mixture fraction in a turbulent H_2/N_2 flame were reported by using OH time-series measurements with an assumed strained, laminar flamelet state relation [92]. The space-time correlation maps of the OH radical are reported in Refs. [89] and [88] obtained from two-point LIF measurements. Based on the shape of the space-time correlation maps they conclude that Taylor's hypothesis is reasonable at the location of peak OH concentration but do not discuss the elliptical nature of the correlation maps. This aspect will be discussed in the current dissertation. While there have been measurements and analysis that have provided new insight regarding space-time statistics in flames, there has not been, to the author's knowledge, previous direct comparisons between spatial, temporal, or coupled spatio-temporal statistics between velocity and scalar fluctuations in turbulent reacting flows.

1.4.2 Relevant Simultaneous Velocity and Scalar Measurements

Many theoretical models (i.e., [19] and [93]) indicate a strong coupling between the strain-rate field and the scalar dissipation rate field as well as proportionality between the scalar dissipation rate and the gradients of reactive scalars. These model assumptions are

at least partially supported by DNS and experimental work. For example, a DNS study by Nomura et al. [94] examined the turbulent mixing characteristics of an inhomogeneous scalar field in an isothermal reacting environment. They observed that the gradient of the mixture fraction field aligned parallel to the axis of the most compressive strain rate and orthogonally to the vorticity. They also observed that the magnitude of the mixture fraction gradient was directly influenced by the local strain rate.

In non-reacting turbulent flows, Kothnur et al. [95] used simultaneous PIV and tracer PLIF measurements to examine the effects of the strain rate field on the scalar dissipation structures in planar jets and verified that the scalar gradients tended to align parallel to the axis of principal compressive strain. Within premixed flames, there has been work examining the relationship between strain, scalars, and flame structure. For example, Steinberg et al. [96] observed that the most extensive principle strain aligned preferentially in a perpendicular orientation with the flame normal whereas Sponfeldner et al. [97] observed that the most extensive strain aligned preferentially parallel to the flame normal. More recently, Coriton and Frank [98] performed simultaneous measurements of the three-dimensional velocity (using tomographic PIV) and the 2D OH field to explore the effect of heat release on the strain rate field in turbulent premixed Bunsen flames. They also found that the extensive strain rate preferentially aligned with the flame normal in the reaction zone and found this alignment to increase with increasing heat release.

There also has been work performed in non-premixed flame studies exploring the interaction between the velocity and scalar fields. Driscoll et al. [99] performed

simultaneous point measurements of density (Rayleigh scattering) and velocity (LDV) in a high Reynolds number turbulent non-premixed flame and determined the axial and radial scalar flux terms. They found examples of counter gradient diffusion, which is inconsistent with the gradient transport hypothesis (see Sec. 1.2.1). Similarly, Dibble et al. [100] used simultaneous LDV and Raman scattering for velocity, major species, and mixture fraction measurements. They also examined the scalar flux and found examples of counter gradient diffusion, which is inconsistent with the gradient transport hypothesis (see Sec. 1.2.1). Rehm et al. [101] examined the relationship between the strain rate, vorticity, and the reaction zone (as marked by OH-PLIF measurements) and observed that the thinnest reaction zones aligned orthogonally to the principal compressive strain. More recently, work by Gamba et al. [102] performed simultaneous measurement of the three-dimensional velocity and OH radical fields in lower Reynolds number turbulent flame and observed sheet-like layers of strain and vorticity aligned with the OH layer.

1.4.3 Simultaneous Temperature and Velocity Measurements in Flames

As discussed in the previous section, there are a number of simultaneous velocity and scalar measurements performed in turbulent flames; however, the scalar is predominantly the OH radical due to its ease of measurement. The OH radical is destroyed by slow three-body reactions and thus is useful for representing high-temperature product gases, but does not give any information on the state of mixing in non-premixed flames. As discussed in Secs. 1.1 and 1.3, temperature is an important scalar as it is linked to both mixing and reaction chemistry. In general, there is a scarcity of simultaneous temperature

and velocity in turbulent flames with even fewer laser-based measurements and even fewer planar measurements. Heitor et al. [103] reported simultaneous measurements of temperature and velocity in premixed flames using laser Doppler velocimetry and a small-diameter thermocouple. Also in a premixed flame, Goss and coworkers [104, 105] used coherent anti-Stokes Raman spectroscopy (CARS) with LDV to measure temperature and velocity. Li and Gupta [106] made use of a technique called photo-thermal deflection spectroscopy to simultaneously measure temperature, velocity, and OH concentration in a premixed H_2/air flame. In a diffusion flame, Hu et al. [107] used hydrogen tagging velocimetry and spontaneous Raman spectroscopy to measure temperature, velocity and concentration. Within premixed flames, Most and Leipertz [108] and Most et al. [109] have demonstrated the use of filtered Rayleigh scattering (FRS), a modification of Rayleigh scattering, for temperature measurements, along with PIV in laminar and turbulent premixed flames to measure the heat flux and examine several common transport models. For laminar and turbulent non-premixed flames there are no previous planar laser-based measurements of simultaneous temperature and velocity.

1.5 Scope and Overview of Dissertation

The major objectives for the current dissertation are as follows: (1) to improve the understanding of the spatial and temporal dynamics of temperature and velocity fluctuations in turbulent non-premixed flames using high-repetition rate measurements and spatio-temporal statistical analysis, (2) the development of a novel laser-based measurement approach to enable simultaneous temperature and velocity measurements in

turbulent non-premixed flames, and (3) to directly investigate the interaction of temperature and velocity fields in turbulent non-premixed flames, targeting the coupled kinematic-thermal mechanisms governing thermal mixing and dissipation.

Chapter 2 gives a brief overview of the theory underlying the measurement techniques utilized in the current dissertation research. Chapter 3 describes the experimental methodology and data processing for high-repetition-rate (10 kHz) temperature and velocity imaging performed in a series of turbulent non-premixed jet flames. Chapter 4 discusses the results of applying spatio-temporal statistical analysis to the temporally correlated temperature and velocity measurements over a broad range of spatial positions and Reynolds number. Chapter 5 describes the development and careful assessment of a new Filtered Rayleigh scattering (FRS)-based thermometry technique for turbulent non-premixed flames. The FRS-based approach allows temperature measurements simultaneously with particle image velocimetry (PIV) measurements. Chapter 6 discusses the experimental methodology and data processing for the simultaneous FRS temperature and stereo PIV (sPIV) measurements in turbulent non-premixed flames. Chapter 7 presents results from the simultaneous sPIV/FRS measurements focusing on the interplay between various kinematic properties such as vorticity and strain rate and thermal fluctuations and dissipation. Finally, Chapter 8 summarizes the main research contributions of the current dissertation work and makes recommendations for future work and additional analysis of the simultaneous temperature and velocity data.

Chapter 2. Theoretical Aspects Related to Current Measurement Techniques

For experimental work in turbulent reacting flows, laser diagnostics have played an integral role in pushing forward fundamental understanding of important chemical and physical processes. Laser diagnostics have proven critical for obtaining measurements of flow or scalar properties without directly interfering in the flow and chemistry as would occur in the case of a physical measurement probes such as hot-wire anemometry. A wide variety of laser diagnostic approaches exist for the measurement of such quantities as velocity, temperature, pressure, species concentrations, and reaction rates. This chapter gives an overview of some of the more pertinent theoretical and experimental considerations underpinning the measurements performed in this dissertation. The targeted flow properties include temperature measurements (laser Rayleigh scattering thermometry and filtered Rayleigh scattering thermometry) and velocity measurements (planar and stereo particle image velocimetry). Section 2.1 discusses the general features of measurement tools used in laser diagnostic experiments including lasers, optics, and cameras. Section 2.2 discusses the general features of light scattering which underpins the measurement approaches used in the dissertation. This includes a discussion of Rayleigh-

Brillouin scattering (RBS), which is used in multiple ways to measure temperature in various turbulent non-premixed flames. Finally, Sec. 2.3 will briefly discuss particle image velocimetry (PIV) and its implementation in turbulent reacting flows.

2.1 General Features of Measurement Tools Used in Laser Diagnostics Experiments

All laser diagnostic experiments have a common set of tools which include a laser light source, optics to focus and/or redirect the light to a probe volume of interest, and a detector(s) with associated optics to collect light from the experiment. For multi-dimensional flow measurements or "imaging", the detector is generally a "camera", where the sensor consists of an array of photosensitive pixel arrays. There are two common types of cameras which include a charge coupled device (CCD) or a complementary metal oxide semiconductor (CMOS).

In addition, for measurements in turbulent flows, the laser light typically is focused at the measurement volume using optics in order to maximize spatial resolution. For imaging experiments, the laser beam is commonly re-shaped and focused in one dimension to form a laser sheet (unless a volumetric measurement approach is targeted, which is outside the scope of this dissertation). For high quality and quantitative measurements it is important to have an understanding of these facets of laser diagnostic experiments and how they can affect the results.

2.1.1 Lasers and Optics

Lasers are used by many experimentalists over other light sources because of high levels of incident power or intensity and because they are coherent, nearly monochromatic, and can be focused well to achieve satisfactory measurement spatial resolution. There are many different types of lasers and applications in turbulent reacting flows. The interested reader is referred to any number of review texts (e.g., [2, 58, 110]). In the current work the primary laser system used is a flashlamp-pumped, Q-switched, Neodymium:Yttrium Aluminum Garnet (Nd:YAG) laser. The Nd:YAG laser has a fundamental output wavelength near 1.06 μm and can be used to generate 532-nm, 355-nm, or 266-nm output through 2^{nd}, 3^{rd}, or 4^{th}-harmonic generation using non-linear crystals [111]. The most common wavelength used in light scattering experiments is the frequency-doubled, 532-nm output, where pulse energies up to O(1) J/pulse [112] can be generated at common repetition rates of 10-30 Hz. For a laser using Q-switch operation, buildup of energy within the laser cavity occurs until the medium becomes gain saturated and at which point an electro-optical device is activated and the energy is released in the form of a high intensity pulse over a short time period [112]. Thus, the output of an Nd:YAG laser can be characterized by laser intensities; that is a high-energy laser pulse that tens of nanoseconds long in duration.

As described in Ch. 3, a different type of laser system also is used that is based on Nd:YAG laser technology. The high-energy pulse burst laser system (HEPBLS) [113] is a unique system that allows the same high output energies described above for conventional

10-Hz systems, but at repetition rates exceeding 10's of kHz. Such a system allows many conventional laser-based combustion diagnostics approaches to be extended to time-resolved measurements to track dynamics and determine new space-time statistics. Details of this system and its application are given in Ch. 3.

Another type of laser system used in the research presented in this dissertation is a tunable Nd:YAG-pumped dye laser. A dye laser uses an organic dye in liquid solution as the gain medium [112]. Dye lasers are used to extend the wavelength range of "fixed" output lasers such as Nd:YAG system or other comparable high-energy laser systems. The dye laser output is "red shifted" from the pump source and is characterized by its output bandwidth which can be up to 20-40 nm. Wavelength tuning and selection within this bandwidth is achieved using a grating or prism, which allows a narrowband laser pulse at a user-selected output wavelength that is offset from the pump source. Typically the output of a dye laser is used in conjunction with non-linear optics to generate specific wavelengths in the ultraviolet to infrared regions that can be used to access specific energy bands of chemical species for techniques such as laser-induce fluorescence [2, 114]. Within the current dissertation, the dye laser output is used in a different capacity; that is, it is used only to generate light with a different wavelength compared to that of the 532-nm output from the Nd:YAG laser for simultaneous measurements that require wavelength discrimination as described in Chs. 6 and 7.

The ability for a laser beam to be focused is related to its mode structure and, in particular, the number of transverse electromagnetic modes (TEM) present within the beam

[111]. In general, a beam with fewer transverse modes will have better focusing characteristics as compared to a beam with more transverse modes. A single parameter M^2 (also known as the beam quality factor) is used to describe the multi-mode nature of a particular beam. Specifically, the M^2 represents the variation of any beam from an ideal Gaussian beam and is calculated by taking the ratio of the product of a laser beam's divergence angle and the beam waist to that same product from a Gaussian beam at the same wavelength. For a single-transverse mode (TEM_{00}) the M^2 value is unity and the beam has an intensity distribution that is Gaussian. For many scientific lasers, M^2 is near unity, but for laser beams with more transverse modes that are used in industrial settings, the M^2 value can reach as high as tens to hundreds [111].

The diffraction-limited focal spot size, d_0, (or waist) of a laser beam with initial diameter, d, and wavelength, λ, that is focused by a spherical lens with focal length, f, is given by

$$d_0 = \frac{4f\lambda M^2}{\pi d} \qquad \text{Eq. (2.1)}$$

Thus, beams with higher transverse modes have spot sizes which would be M^2 times the spot size for a TEM_{00} Gaussian beam. In general, the diffraction-limited spot size is never achieved because laser beams have divergence, leading to an effective value of $M^2 > 1$, even for TEM_{00} beams. The actual beam diameter measured at a distance f from the focusing lens is given by

$$d_f = \tan(\Theta) f \qquad \text{Eq. (2.2)}$$

where Θ is the divergence angle of the beam. With the small angle approximation, $d_f = \Theta f$.

Almost as important for laser diagnostic experiments as the focal spot size is the Rayleigh range for the laser. The Rayleigh range is the distance over which the laser remains "focused" and is defined as the distance along the beam from the focus to the point where the beam diameter is $\sqrt{2}$ times the beam waist:

$$x_R = \frac{\pi d_0^2}{4\lambda M^2} \qquad \text{Eq. (2.2)}$$

Again, the impact of increased M^2 factors is observed in the fact that as M^2 increases, the Rayleigh range decreases compared to a Gaussian single transverse mode beam. For many quantitative laser diagnostic experiments it is important to have a small focus spot over a long range as this directly relates to the spatial resolution of the measurement. Therefore, in general, it is desired to have a beam that is as near to "Gaussian" as possible. While the preceding discussion related to focusing a circular beam to a circular focal spot via a spherical lens, the same factors impact the ability to focus a beam in one dimension; that is forming a narrow, focused laser sheet for imaging applications.

For some laser techniques, such as filtered Rayleigh scattering (FRS) discussed below, it is important to have a laser source with a very narrow spectral linewidth. For Q-switched lasers, this is achieved using "injection seeding", which consists of introducing a single longitudinal mode (SLM) continuous wavelength (CW) laser into the pulsed laser's cavity. This results in preferential buildup in the cavity for the particular longitudinal mode

supported by the cavity that is closest to the frequency of the CW laser. The output of an injection-seeded laser system is a high-energy, pulsed laser with a linewidth comparable to a single supported cavity mode.

2.1.2 Cameras

2.1.2.1 CCD and CMOS Sensors

Camera sensor technologies are fast evolving but at present the most common camera sensor technologies used for laser-based imaging based experiments are CCD or CMOS cameras. Both sensors collect light and convert the light to electrons (photons to photoelectrons), but the major difference between the two sensor technologies lies in how the accumulated charge from each pixel is read out from a sensor. For common CCD sensors utilizing what is known as interline transfer, the accumulated charge is performed by a non-photo-sensitive region of the pixel that lies adjacent to the photo-sensitive portion. The charge from the pixels is then serially transferred from one pixel storage site to another, all ultimately routed to a single analog-to-digital (A/D) converter where each pixel's analog signal is converted to a digital signal. There are other methods to transfer charge such as full frame transfer or frame transfer CCD arrays, but the readout is performed on a much slower timescale. Because of the relative speed of interline transfer CCD arrays, they can be operated in a frame straddling manner whereby two images can be acquired in quick succession [111]. This is useful for imaging two successive particle scattering images as is done for particle image velocimetry (PIV). A consequence of having the charge storage

sites adjacent to the photo-sensitive regions of the pixel is a reduction of the fill-factor for the pixel, or the area of the pixel taken up by the photo sensor.

CMOS sensors have A/D converters for each pixel which consist of several transistors at each pixel that amplify and move the signal using traditional wires. The benefit this architecture is that it provides a much faster method to read information due to the parallel A/D conversion versus the serial A/D conversion for the CCD sensor arrays. Thus CMOS cameras can operate at very high framing rates, which is important for high-speed laser diagnostic measurements. Because each pixel has its own A/D converter, CMOS sensors are subject to higher levels of noise and sensor non-uniformities as compared to CCD cameras [115]. Thus, care must be taken when using CMOS cameras, especially for quantitative measurements. The application of the various camera technologies are discussed in the subsequent chapters.

2.1.2.2 Magnification, f-number, and Collection

The following discussion follows the work of Clemens [111]. As mentioned previously, it is common for laser-based experiments to utilize a laser source that has been formed into a sheet with height, s_h, and thickness, s_t. The camera imaging the scattered light will have a lens with a numerical aperture, or $f\#$, that is defined by the ratio of the camera lens back focal length, f, to the diameter of the lens aperture, D ($f\# = \frac{f}{D}$). A higher $f\#$ means a smaller aperture and leads to less light collection, but with a greater depth of focus (DOF). The camera system, imaging the area of the illuminated laser sheet will have a magnification, m, defined by the ratio of object height to image height (m = O/I). This

means that each pixel on the image plane of size $x_i \times x_i$, images a region in the object plane of size $x_o \times x_o = x_i/M \times x_i/M$. All of the scattered light generated within the sheet is imaged by the pixels such that the light comes from the full sheet thickness, s_t. For the current work presented in this dissertation, the laser source is pulsed with fluence, $F_I = E/A$ (E= laser energy; A= laser sheet area defined as $s_h \times s_t$) and the scattered light is imaged with an un-intensified camera (i.e. gain = 1). In this case, the number of photoelectrons generated for each pixel can be written as

$$S_{e^{-1}} = \eta\eta_c \times \frac{F_I}{h\nu} \times s_t x_o^2 \times \frac{\partial\sigma}{\partial\Omega}\Delta\Omega \times N \qquad \text{Eq. (2.3)}$$

The products making up Eq. (2.3) have been separated out for clarity. The first term is comprised of the quantum efficiency of the sensor, η and the efficiency of the collection optics, η_c. The second term, which is the local fluence divided by Planck's constant, h, and laser frequency, ν, describes the number of photons generated in the laser sheet and incident on the camera. The third term in Eq. (2.3) is the product of the laser sheet thickness, s_t, and the imaged area, x_o^2, which represents the volume imaged by each pixel. The fourth term is the product of the differential scattering cross section, which is different depending on the scattering process, and the solid angle subtended by the camera lens. Finally, the last term is the number density of the scattering medium. The solid angle, $\Delta\Omega$, can be related to the magnification and $f\#$, as [111]:

$$\Delta\Omega = \frac{\pi}{4}\frac{M^2}{f\#^2(M+1)^2} \qquad \text{Eq. (2.4)}$$

If the laser fluence is assumed to be constant over the entire sheet height, the fluence is replaced with pulse energy, $E_I = F_I/(s_h s_t)$, and x_o is replaced with x_i/M such that Eq. (2.3) is re-written as

$$S_{e^{-1}} = \eta\eta_c \times \frac{\mathrm{E_I}/s_h}{h\nu} \times x_i^2 \times \frac{\partial\sigma}{\partial\Omega}\frac{\pi}{4}\frac{1}{f\#^2(M+1)^2} \times N \qquad \text{Eq. (2.5)}$$

From Eq. (2.5) it is observed that the number of photoelectrons, and thus the measurement signal, is proportional to the number density and the differential scattering cross section of the scattering medium and inversely proportional to the $f\#$ for a system. In addition, the number of photoelectrons increases with decreasing magnification (i.e. moving the camera away from the experiment and imaging a larger FOV). This is due to the fact that the number of scattered photons hitting a single pixel come from a larger physical volume, i.e., there are more photons per pixel. It is noted that the increased signal (from the decreased magnification) comes at the cost of decreased spatial resolution.

Another important consideration regarding signal collection is the noise or uncertainty in the generated signal. Common sources of noise for both CCD and CMOS sensors include read noise and shot noise. Read noise is the noise generated in converting photoelectrons into an analog voltage which is subsequently converted into a digital signal. Read noise is generally less for CCD cameras as compared to CMOS cameras due to the fact that the CCD cameras have one A/D converter for the entire sensor whereas a CMOS camera has an A/D converter for every pixel. Shot noise is a result of statistical fluctuations in "counting" the number of generated photoelectrons and is described by a Poisson

statistical distribution where the variance is equal to the mean [111]. As the number of photoelectrons increase, the Poisson distribution approaches that resembling a Gaussian distribution. The noise, or uncertainty, in the number of photoelectrons generated (and thus uncertainty in the signal) can be written for an un-intensified camera as the square root of the variance of the distribution:

$$N_{e^{-1}} = \sqrt{S_{e^{-1}}} \qquad \text{Eq. (2.6)}$$

In Eq. (2.6) it is assumed that read noise is small compared to shot noise, which is typically the case for most common laser-based measurements.

2.2 General Features of "Elastic" Light Scattering

Light and matter can interact in a number of ways. For example, light can be absorbed by the medium (with possible re-emission) or it can be scattered. For the work presented in the current dissertation, light scattering is the most relevant process underpinning the laser diagnostic methods. Scattering processes can be described as incoherent or coherent. For an incoherent scattering process the scattered light (arriving at a point) has a random collection of phases; that is, the light scattered from each scatterer has random relative phases in the direction of interest (i.e., light scatters in all directions). For a coherent scattering process, the scattered light arriving at a point maintains its coherence; that is, the scatterers have non-random relative phases in the direction of interest. There are laser diagnostic techniques that utilize either incoherent or coherent scattering process, with each process containing its own advantages and disadvantages. For

example, incoherent light scattering techniques depend linearly on the number of scatterers and do not have a built in dependence on the laser intensity allowing for a straightforward calibration [2]. However, the collected light from incoherent scattering is only a fraction of the total scattered light, depending on the solid angle of collection, $\Delta\Omega$ and leads to lower measured signals. In contrast, coherent scattering techniques allow collection of the total amount of scattered light, resulting in much higher signal collection. However, the coherent signal can be more difficult to calibrate due to the fact that coherent scattering processes are non-linear.

Scattering processes also can be designated elastic or inelastic. For inelastic scattering processes, which includes spontaneous Raman scattering and laser-induced fluorescence, the scattering process involves energy exchange between the incident photons and molecules within the scattering medium, such that the scattered light is shifted in frequency relative to the incident light [2]. Elastic scattering processes, which include Rayleigh scattering and Mie scattering, are scattering processes in which there is no net energy exchange between the incident photons and molecules of the scattering medium. In the current dissertation work the laser diagnostic techniques used are Rayleigh (and filtered Rayleigh) scattering and particle image velocimetry (PIV) which is underpinned by Mie scattering from particles. In the current work, the nomenclature of 'Mie' is used loosely to describe scattering from particles with size comparable to the wavelength of light and not strictly spherical particles as in Mie's solution to Maxwell's equations. Both of these approaches are incoherent, elastic scattering processes.

2.2.1 Rayleigh-Brillouin Scattering

2.2.1.1 Rayleigh Scattering Intensity

Laser Rayleigh scattering is a quasi-elastic scattering process from molecules or particles whose diameter is much smaller than the wavelength of light (i.e. $d \ll \lambda$). The following discussion of Rayleigh scattering follows closely the work of Miles et a. [116] and the reader is referred there for more details. One common approach used to describe Rayleigh scattering is that of an "induced dipole". More specifically, the electrons in the constituent atoms are driven to oscillate in the presence of an applied oscillating electric field (such as from an electro-magnetic wave). This oscillating electron acts as an electron dipole antennae causing radiation with the same frequency as the applied electric field [116]. The dipole induced by the electric field is established a short time relative to the incidence of the electric field such that Rayleigh scattering can be considered "instantaneous", especially compared to longer lifetime scattering processes such as laser-induced fluorescence. In the case of scattering in a solid, where the scattering sources are largely stationary, the scattering is in the forward direction only and is coherent. In the case of a continuum of scattering sources where the scattering sources can move (as in a gas or liquid), the phase of the scattering from each scattering source is randomized and the scattering is incoherent in all directions except for the forward direction where it is still coherent [116]. In a gas, there is a large number of molecules and it is the molecular motion that leads to microscopic density fluctuations (non-uniform distribution of scatter sources) where the interference between each scattering source removes coherence effects. The total

scattered intensity from the incoherent portion of the scattering is proportional to the number of scattering sources. If there were not density fluctuations then the scattering from each isolated oscillator cancels out in all but the forward direction (i.e., solid). Thus, density fluctuations are responsible for Rayleigh scattering.

The goal for the following section is to derive the differential Rayleigh scattering cross section and describe the collected scattering power (signal) for an observer (i.e., detector). First the analysis will be performed for the case of a spherically symmetric molecule (i.e. noble gases) and subsequently modifications for realistic molecules will be described. Figure 2.1 shows a schematic of general laser Rayleigh scattering geometry for a spherical scattering source and its observation. The laser beam path and observer direction (in this case observed by a camera) is indicated in Fig. 2.1. The incident laser, aligned with the y-axis, has an associated electric field with amplitude, E_I, and polarization indicated by an arrow. In Fig. 2.1, the laser polarization is shown with a general orientation (i.e., angled relative to the vertical (x-axis) for clarity), while in an actual experiment the laser polarization would be aligned vertically with the x-axis for the observation orientation shown. The dipole moment, $\vec{p}$, induced by the electric field, forms an angle relative to the vertical direction given by β, and forms an angle relative to the observer given by ϕ. The dipole moment vector in Fig. 2.1 also is shown in a general orientation. For a spherically symmetric molecule the dipole moment aligns coincident with the incident laser polarization and for the case where the observer is aligned parallel to the z-axis (in a typical Rayleigh scattering experiment) the angle between the dipole moment and the observer is

90°. However for non-spherical molecules (anisotropic), the scattered light can experience a small amount of depolarization such that the 'average' dipole vector would have a major component in the vertical direction (i.e. vertically polarized light with β = 90°) and have a minor component which has been depolarized in the horizontal direction (i.e. horizontally polarized light with β = 0°.

For a spherically symmetric molecule the expression for the amplitude, E_s, of the scattered electric field from an infinitesimally small oscillating dipole is written as [9]

$$E_s = \left|\overrightarrow{E_s}(r,\phi)\right| = \frac{\omega^2 p \sin\phi}{4\pi r \epsilon_0 c^2} \qquad \text{Eq. (2.7)}$$

and the corresponding intensity, I_s, is given by

$$I_s(r,\phi) = \frac{\epsilon_0 c \left|\overrightarrow{E_s}(r,\phi)\right|^2}{2} \qquad \text{Eq. (2.8)}$$

where ω is the oscillation frequency, p is the magnitude of the oscillating dipole moment, c is the speed of light in a vacuum, r is the distance from the scattering source and the observer, and ϵ_0 is

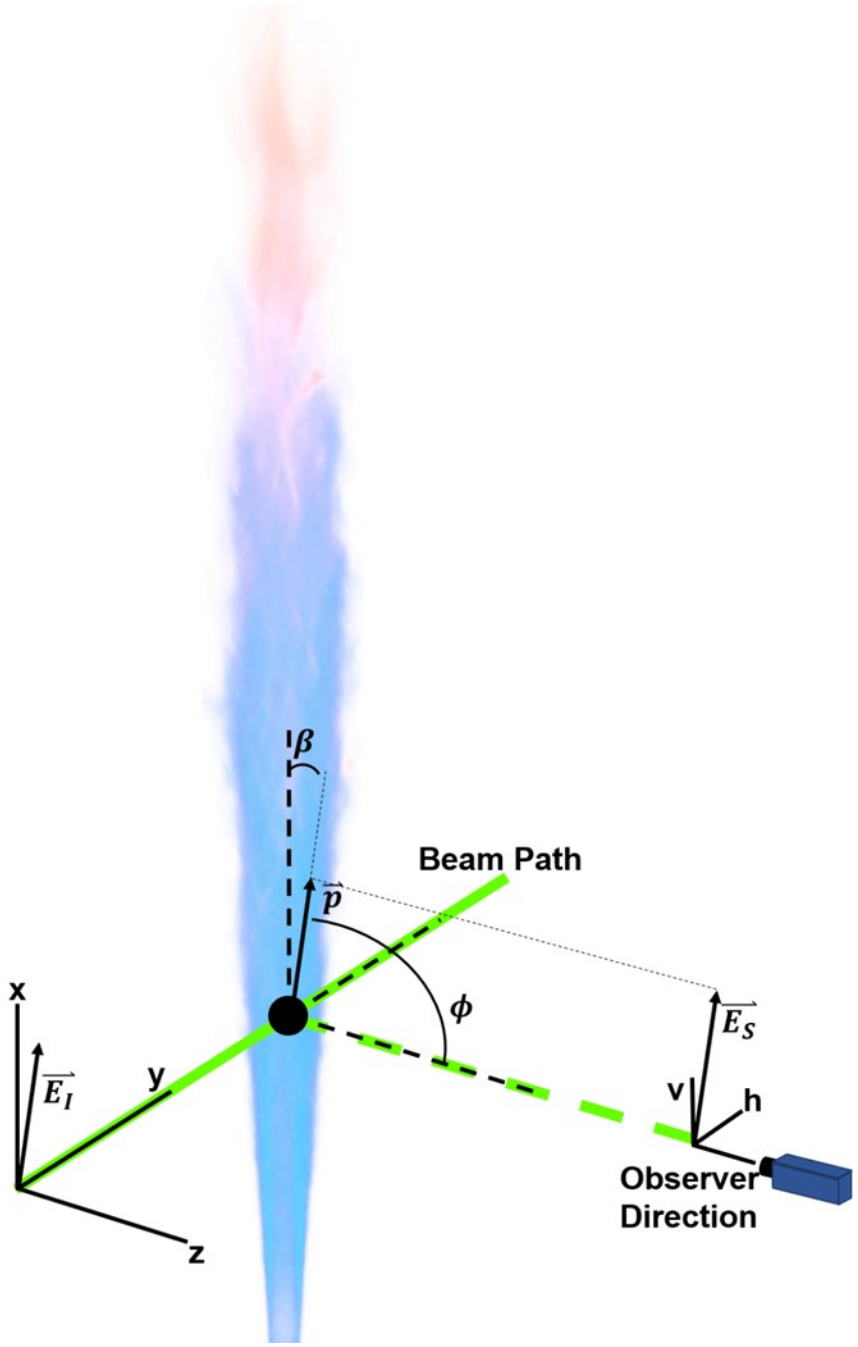

Figure 2.1: Diagram of Rayleigh scattering geometry for spherical scattering sources and its observation. Inspired by the established Rayleigh scattering coordinate system in Miles et al. [116].

the permittivity of free space. Combining Eqs. (2.7) and (2.8) ($\omega = 2\pi c/\lambda$) the scattered intensity is written as

$$I_s = \frac{\pi^2 c p^2 \sin^2 \phi}{2\epsilon_0 \lambda^4 r^2} \qquad \text{Eq. (2.9)}$$

where the expression $\omega = 2\pi c/\lambda$ has been substituted to remove the dependence on the oscillation frequency. The dipole moment, $\vec{p}$, for a symmetric molecule is aligned with the incident electric field, $\overrightarrow{E_I}$, and the magnitude of $\vec{p}$ is linearly proportional to E_I, where the proportionality constant is the polarizability of the scattering source, α. The polarizability describes the willingness of a scattering source to oscillate with the incident electric field. Since $p^2 = \alpha^2 |E_I|^2$ and the incident intensity $I_I = (\epsilon_0 c/2)|E_I|^2$, Eq. (2.9) is re-written as

$$I_s = \frac{\pi^2 \alpha^2}{\epsilon_0^2 \lambda^4 r^2} I_I \sin^2 \phi \qquad \text{Eq. (2.10)}$$

From Eq. (2.10) it is observed that for the case where the incident electric field propagates in the y-direction and is vertically polarized (meaning $\overrightarrow{E_I}$ is aligned with the x-axis), the maximum scattering will be achieved with the observer oriented at ϕ= 90° relative to the x-axis. An observer situated at ϕ = 0° (meaning the observation would be directly above or below the experiment) would not see any scattering.

The time-averaged power scattered from one oscillating dipole can be obtained by integrating the scattered intensity over a spherical surface containing the dipole. Subsequently, it is common to define a scattering cross section, σ_{ss}, as the time-averaged power divided by the incident intensity ($\langle P \rangle / I_I$). Once the scattering cross section is

obtained, a differential scattering cross section is determined to remove geometric dependence and is defined as

$$I_s = \frac{\partial \sigma_{ss}}{\partial \Omega} = \frac{1}{r^2} I_I \qquad \text{Eq. (2.11)}$$

Thus, a differential scattering cross-section is defined as

$$\frac{\partial \sigma_{ss}}{\partial \Omega} = \frac{\pi^2 \alpha^2}{\epsilon_0^2 \lambda^4} \sin^2 \phi \qquad \text{Eq. (2.12)}$$

The polarizability is related to the index of refraction by the Lorentz-Lorenz equation [116, 117] as

$$\alpha = \frac{3\epsilon_0}{N} \frac{n^2 - 1}{n^2 + 1} \qquad \text{Eq. (2.13)}$$

where N is the gas number density (molecules/m^3) and n is the index of refraction. For gases at atmospheric conditions $n \approx 1$ so the differential scattering cross-section is approximated as

$$\frac{\partial \sigma_{ss}}{\partial \Omega} \cong \frac{4\pi^2}{\lambda^4} \left(\frac{n-1}{N} \right)^2 \sin^2 \phi \qquad \text{Eq. (2.14)}$$

which gives the differential scattering cross section for a single species (assuming a symmetric molecule).

Real molecules are not symmetric so the induced dipole does not lie in the same direction as the applied electric field. The random orientation of the molecule with respect to the electric field (with respect to the observer) required that the scattering model be

extended and averaged over all molecular orientations. For this case the polarizability is described by a 3×3 symmetric tensor and the average polarizability, a, and anisotropy, γ, for the case where the observer is oriented at ϕ = 90° are given by

$$a^2 = (1/9)\left(\alpha_{xx} + \alpha_{yy} + \alpha_{zz}\right)^2$$
$$\gamma^2 = (1/2)\left[\left(\alpha_{xx} - \alpha_{yy}\right)^2 + \left(\alpha_{yy} - \alpha_{zz}\right)^2 + (\alpha_{xx} - \alpha_{zz})^2 + 6\left(\alpha_{xy}^2 + \alpha_{yz}^2 + \alpha_{zx}^2\right)\right]$$

Eq. (2.15)

In this case, scattering intensities and therefore, differential scattering cross sections, are written for each polarization; that is, the portions of light scattered both vertically and horizontally with respect to the incident electric field. Each component is a function of the mean polarizability and anisotropy. The effect of the polarization on the scattering cross section is usually written in terms of a depolarization ratio, ρ, which is the ratio of the intensities scattered perpendicular and parallel to the polarized light source. For linear and diatomic molecules the depolarization ratio is given by

$$\rho_p = \frac{3\gamma^2}{45a^2+4\gamma^2}$$ Eq. (2.16)

Using this result, the differential scattering cross-section for light polarized in the vertical direction (based on the orientation shown in Fig. 2.1) is written

$$\frac{d\sigma_V}{d\Omega} \cong \frac{4\pi^2}{\lambda^4}\left(\frac{n-1}{N}\right)^2 \sin^2\phi\left(\frac{3}{3-4\rho_p}\right)$$ Eq. (2.17)

Equation 2.17 shows that the differential scattering cross section for a linear or diatomic molecule is the same as that of a spherically symmetric molecule with an extra depolarization correction term factor. Indeed, in the case of a spherically symmetric molecule, where ρ_p = 0, Eq. (2.17) and Eq. (2.14) are the same.

For a laser diagnostic experiment the scattered light will be collected over a solid angle, $\Delta\Omega$ (see Eq. (2.4)). The power collected from a single molecule over that solid angle is given by

$$\Delta P = I_I \frac{\partial \sigma_V}{\partial \Omega} \Delta\Omega \qquad \text{Eq. (2.18)}$$

For a gas flow, the molecular motion of the molecules randomizes the phase of the scattered light from each scattering source such that on aggregate the total scattered light is incoherent and proportional to the number of scatterers as discussed previously. If a probe volume, V, is considered, then the total number of scatterers in the volume is NV and the detected laser Rayleigh scattering (LRS) signal, $S_{LRS,i}$, from a single gas species, i, is related to the detected power through the relation

$$S_{LRS,i} = \eta_T I_I NV \left(\frac{\partial \sigma_V}{\partial \Omega}\right)_i \Delta\Omega \qquad \text{Eq. (2.19)}$$

where η_T is the total efficiency which encompasses the optical efficiency and quantum efficiency of the system and $\left(\frac{\partial \sigma_V}{\partial \Omega}\right)_i$ is the differential scattering cross section for a particular species. For a mixture of gases the differential Rayleigh scattering cross section is written as a mole fraction-weighted average of all of the individual differential scattering

cross sections of the molecules in the probe volume (i.e. $(\partial\sigma/\partial\Omega)_{mix} = \sum_i X_i(\partial\sigma/\partial\Omega)_i$, where X_i is the mole fraction for species, i). Thus, the LRS signal from a mixture of gases is written as

$$S_{LRS,mix} = CI_I N \left(\frac{\partial\sigma_V}{\partial\Omega}\right)_{mix} \quad \text{Eq. (2.20)}$$

where the constant C encompasses the effects of the particular experimental setup and includes the total collection efficiency, the volume, and the solid angle.

2.2.1.2 Spectroscopic Description of Rayleigh Scattering

The aforementioned discussion was presented in the context that the dipole only oscillates at the frequency of the incident electric field. However, there can be internal motion within a molecule (i.e., rotational or vibrational) that modulates the induced oscillating dipole and causes additional frequencies to appear. Thus, scattered light consists of both elastic scattering (Rayleigh scattering) and inelastic scattering processes involving vibrational and rotational modes of energy transfer in the molecule. For example, if the induced polarization couples to a vibrational state, this corresponds to "vibrational excitation" and photons are scattered at a different frequency as the original photon; that is there is a scattering signal that is spectrally shifted relative to the laser frequency. The same process can occur if the induced polarization couples to a rotational state. These inelastic processes are referred to as vibration and rotational Raman scattering, respectively. In the context of Rayleigh scattering measurements, the relative signals from Raman scattering processes are small compared to the elastic scattering. Vibrational Raman scattering signals

are approximately 10^{-2} to 10^{-3} times that of the Rayleigh scattering and spectrally shifted by hundreds to thousands of wavenumbers so that they can be easily isolated during Rayleigh scattering measurements. The inelastic scattering due to the modulation of the induced dipole by the rotation of the molecule ("rotational Raman") generates rotational transitions that are in close proximity to the central elastic band ($O(1\ cm^{-1})$). In fact the anisotropy factor (γ) introduced in Eqs. (2.14) and (2.15) arises from the emergence of the rotational Raman components. Thus, the differential Rayleigh scattering cross section derived in Eq. (2.16) contains a rotational Raman contribution. The signal of the rotational Raman typically is approximately 1-2% of total "elastic" scattering signal for most molecules and can generally be neglected with some notable exceptions in larger more complex molecules such as CO_2 [118].

In general, light scattering occurs due to fluctuations in the optical properties of the medium, mainly the dielectric tensor. For gases, the coupling between the temperature and the dielectric constant is weak such that fluctuations in the dielectric properties can be considered to come from microscale fluctuations in the gas density (and hence refractive index) alone. The fluctuations in the gas density arises from both (isobaric) entropy fluctuations and (isentropic) pressure fluctuations. The former are due to random, thermal motion in the gas and gives rise to a Doppler-broadened, Gaussian-shaped central elastic Gross or Landau-Placzek line [118]. The pressure fluctuations (due to molecular collisions) manifest as acoustic waves within the medium and the interaction between light and the sound waves results in a set of Brillouin doublets which are Doppler shifted from the

central peak due to the motion of the scattering acoustic wave. This is commonly referred to as 'Brillouin-Mandel'shtam scattering' [116]. The collective process, along with the rotational Raman Q-branch (see [116] for a discussion on the generation of the Q-branch), yields the Cabannes line and is commonly referred to as "Rayleigh-Brillouin scattering" (RBS). In general, "Rayleigh scattering" is the summation of the Cabannes line and the additional spectrally shifted rotational Raman lines.

For gases at low density (Knudsen regime; high temperature and/ or low pressure), the thermal broadening of the Gross line is dominant and the spectral lineshape of the Cabannes line resembles a Gaussian profile given by

$$g(T,\nu) = \frac{2\sqrt{\ln 2/\pi}}{\Delta\nu_T}\exp\left[-4\ln 2\left(\frac{\nu}{\Delta\nu_T}\right)^2\right] \qquad \text{Eq. (2.21)}$$

where, ν, is frequency, and $\Delta\nu_T$ is the full width at half max of the Gaussian profile and varies with temperature and observation angle, θ as

$$\Delta\nu_T = \frac{2}{\lambda}\sqrt{\frac{8kT\ln 2}{m}}\sin\left(\frac{\theta}{2}\right) \qquad \text{Eq. (2.22)}$$

The Brillouin sidebands are likely present in the Knudsen regime, although they would have a small contribution compared to the central lineshape such that they would not be detectable.

When the density of the gas increases, the mean free path between the gas molecules decreases and the acoustic side bands (Brillouin doublets) become more pronounced with frequency shifts that are related to the speed of sound in the medium

[116]. For higher density gases where collisions dominate, the gas is said to be in the hydrodynamic limit and the spectral lineshape resembles three Lorentzian functions. Gases at elevated densities are said to be in the hydrodynamic regime.

Several researchers have developed spectroscopic models in order to treat the cases of spectra that are not clearly within the Knudsen (or kinetic) nor the hydrodynamic regime. While the discussion of spectroscopic models is outside the scope of this dissertation, the most commonly used model for single species is the S6 (or S7) model developed by Tenti et al. [119]. This model is used in the dissertation and is discussed in more detail in Chapter 5. In order to compare the relative importance of the random thermal motion as compared to the correlated acoustic motion, a common property termed the y-parameter is defined as the ratio of the characteristic scattering wavelength to the mean free path:

$$y \equiv \frac{\lambda_s}{2\pi\ell_m} \qquad \text{Eq. (2.23)}$$

where ℓ_m is the mean free path and λ_s is the spatial frequency of an interference pattern formed from the incident and scattered light given by

$$\lambda_s = \frac{\lambda_I}{2}\frac{1}{\sin\theta/2} \qquad \text{Eq. (2.24)}$$

where λ_I is the incident wavelength. Substituting Eq. (2.24) and the definition of the mean free path from kinetic theory into Eq. (2.23) yields

$$y \cong \frac{NkT}{\sqrt{2}|K|v_0\mu} \qquad \text{Eq. (2.25)}$$

where N is the number density, k is the Boltzmann constant, $|K|$ is the magnitude of the scattering wave vector ($|K| = (4\pi/\lambda_s)\sin(\theta/2)$), v_0 is the thermal velocity ($v_0 = \sqrt{kT/m}$), and μ is the dynamic or shear viscosity of the gas. When $y \gg 1$ the mean free path is much smaller than the interference pattern and the gas is said to be in the hydrodynamic regime. For this case, the RBS profile is dominated by sharp acoustic sidebands. When $y \ll 1$ the mean free path is large relative to the interference pattern and

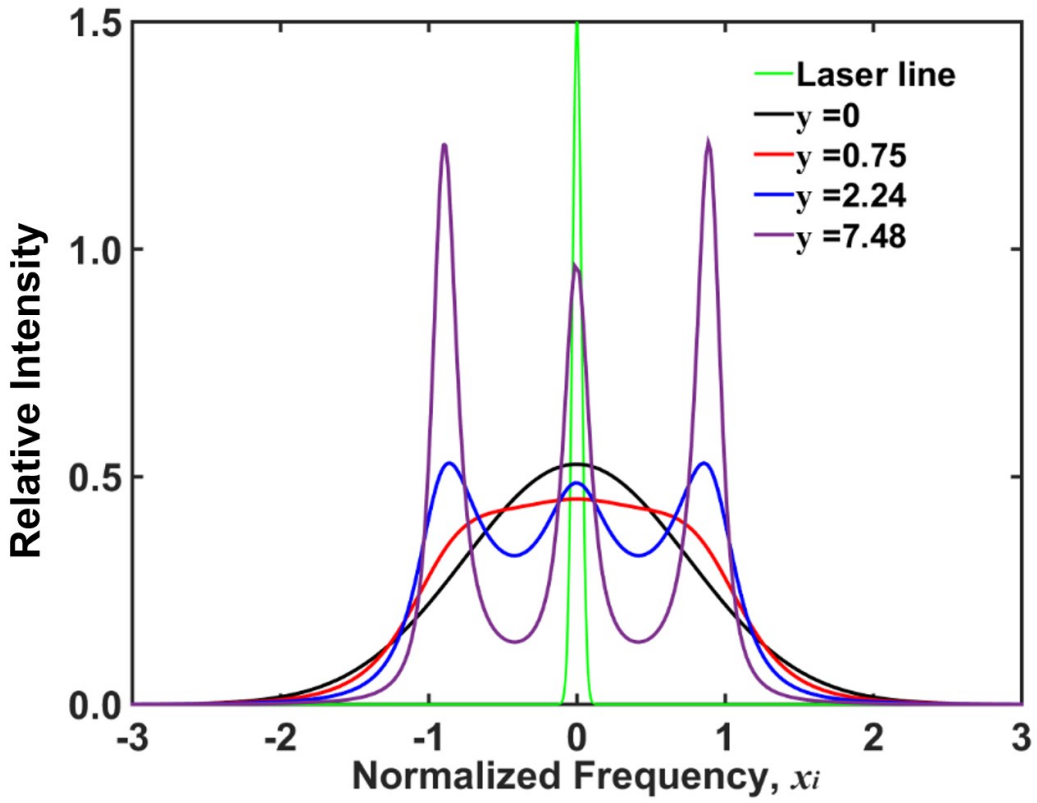

Figure 2.2: Example normalized RBS profiles for different values of y, compared with a narrow laser line.

the gas is said to be in the Knudsen or kinetic regime and the lineshape can be satisfactorily represented by Eq. (2.21). Figure 2.2 shows a series of normalized RBS spectra at various values of the y-parameter, compared to a narrow laser linewidth. It is clear that for y = 0, the profile is Gaussian and with increasing values of y, the importance of properly accounting for the Brillouin sidebands increases. As one example, at T = 300 K and p = 1 atm, the y-parameter for air is 0.75 (as shown in Fig. 2.2).

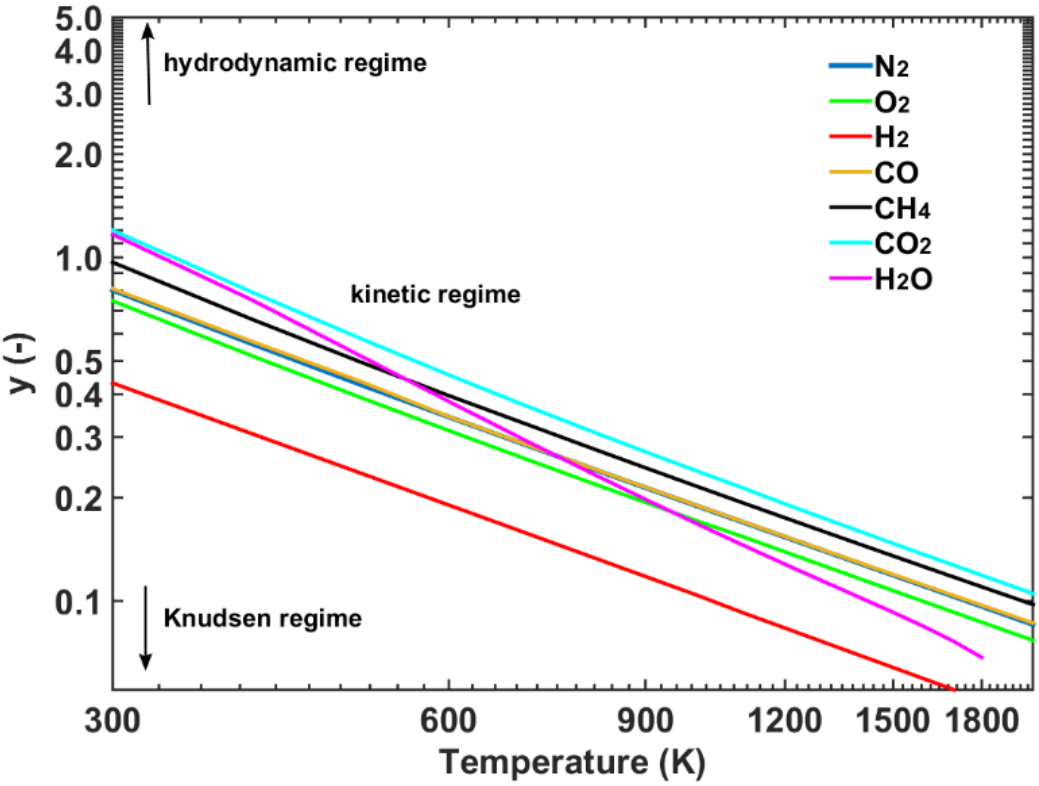

Figure 2.3: Calculated y parameter for several combustion-relevant species as a function of temperature at P = 1 atm.

The gas flows considered in the current turbulent flames have a large span of temperatures ranging from room temperature (296 K) to >2000 K and consequently span a range of y-parameter values. Figure 2.3 shows examples of calculated y-parameters as a function of temperature for several combustion-relevant gases. At the higher temperatures, the scattering approaches the kinetic regime (low values of y), but the RBS spectra are still not fully Gaussian profiles. Closer to room temperature the y-parameter approaches 1 such that Brillouin scattering effects have to be included. Figure 2.4 shows example RBS lineshapes as calculated using the Tenti S6 model [119] for several different gas species and at two different temperatures. Overlaid on both plots is the absorption (or transmission) spectra of molecular iodine, I_2, which will be discussed in section 2.2.1.3. The top plot in Fig. 2.4 shows the RBS lineshapes of nitrogen, methane, hydrogen, and argon at 300 K and the bottom plot of Fig. 2.4 shows the RBS lineshapes of nitrogen, methane, carbon dioxide, and water at 1600 K. Fig. 2.4 shows the wide variation in possible lineshapes that can be encountered under combustion conditions.

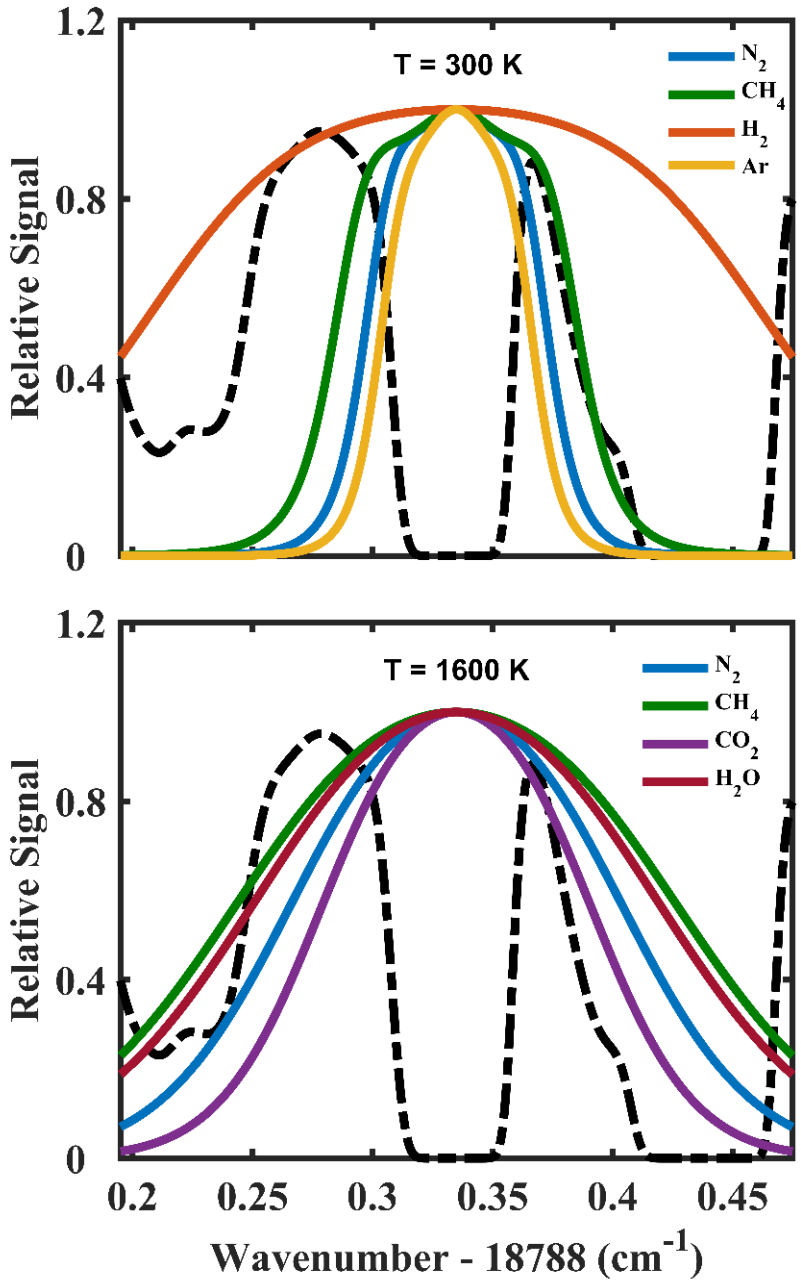

Figure 2.4: Example RBS lineshapes (solid) calculated using Tenti S6 model [119] overlaid with I_2 spectra (dashed) in the spectral neighborhood of 532 nm. (Top) T = 300 K with N_2, CH_4, H_2, Ar. (Bottom) T = 1600 K with N_2, CH_4, CO_2, and H_2O. Both sets are at atmospheric pressure.

2.2.1.3 Filtered Rayleigh Scattering

Having an understanding and ability to model RBS lineshapes is important for many different measurement techniques including recent advancements in LIDAR-based measurements for wind speed and temperature distributions in the Earth's atmosphere [120, 121]. For fluid dynamics and combustion measurements, knowledge of the RBS spectrum is a key component in a diagnostic referred to as filtered Rayleigh scattering (FRS) as first put forth by Miles et al. [122]. In FRS, a spectrally narrow laser is used in conjunction with an atomic or molecular vapor filter placed in front of a camera. The filter suppresses the unwanted background interference scattering that is resonant with the laser (i.e., surface and/or particulate) and allows collection of scattering from gas-phase species that is broadened due to the RBS process. Figure 2.5 shows a graphical representation of the FRS approach when using a narrowband Nd:YAG laser and a molecular iodine filter. The intent is that surface and/or particle scattering occurs at the same frequency as the laser and is absorbed by the iodine filter when the laser is tuned to the center of the iodine absorption feature. In contrast, the RBS profile is broad compared to the iodine absorption line and a portion of the gas-phase RBS light transmits (to the detector). As shown in Fig. 2.5, iodine makes an excellent filter in conjunction with a narrowband Nd:YAG laser, where the I_2 absorption spectrum acts as a suitable medium for absorbing unwanted surface/particle scattering, while transmitting a portion of the broadened RBS spectrum. This allows the possibility of FRS facilitating gas-phase measurements in the presence of

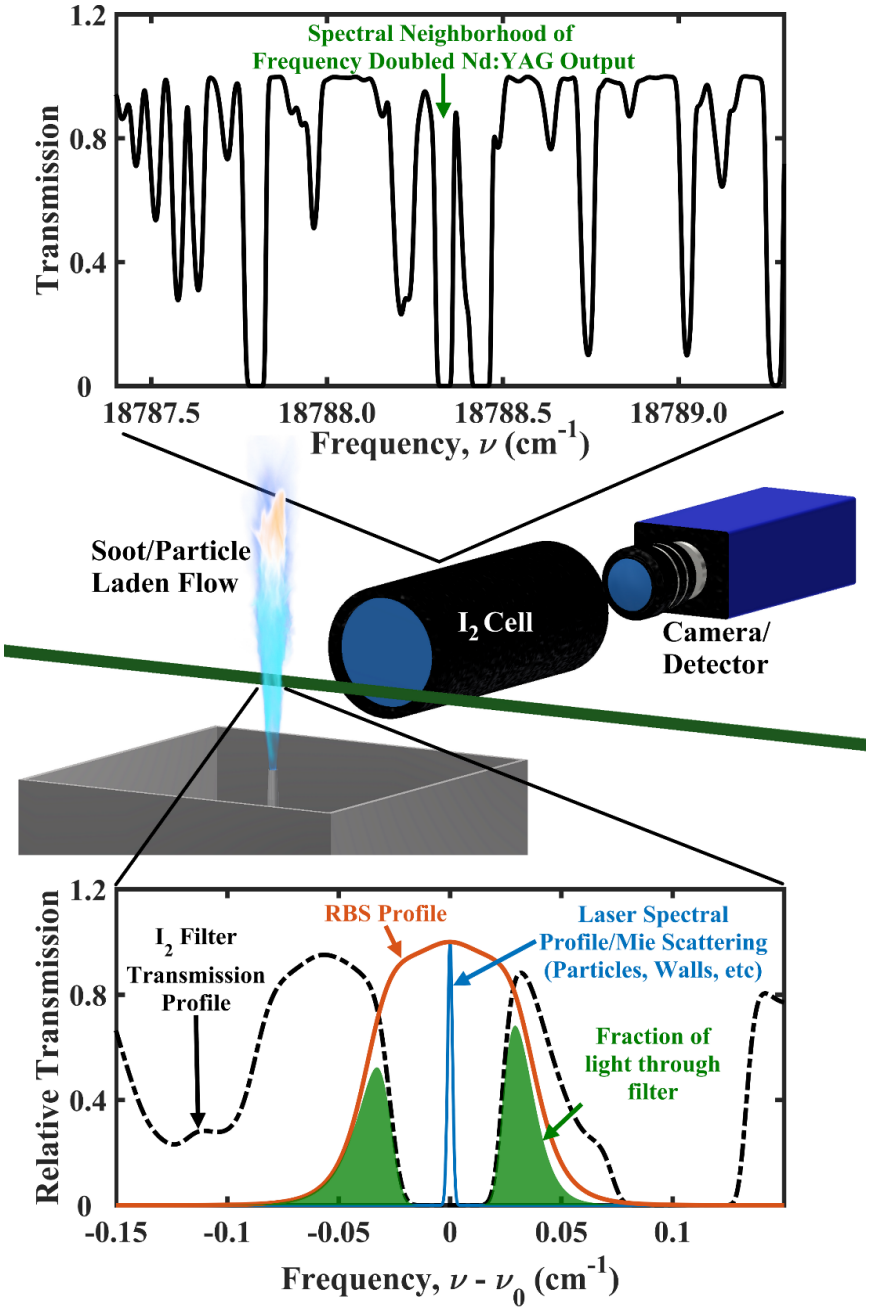

Figure 2.5: Graphical representation of FRS approach using an Nd:YAG laser and molecular I_2 filter cell. (Top) Modeled I_2 spectra. The feature marked with an arrow is used in the present work for FRS measurements. (Middle) Application of FRS imaging within a particle laden flow. (Bottom) Overlap of the I_2 filter profile with particle scattering, and an example RBS profile from gas-phase molecules.

interfering scattering media. For example, FRS has been used previously in non-reacting fluid environments to measure average velocity, pressure, and temperature in compressible flows [123], turbulent jets [124], and ducted gas flows [125]; trajectory and mixing properties in buoyant jets [126]; temperatures in boundary layers near surfaces [127] and fuel vapor/air mixing in droplet/gas regions of an evaporating spray flow [128]. The most common application of FRS in combustion and plasma systems is the deduction of temperature in environments with high levels of interference (e.g. [108, 109, 129-132]) and this will be discussed in detail in Ch. 6.

The measured FRS signal from a single gas species can be written as

$$S_{FRS,i} = CI_I N\psi_i \qquad \text{Eq. (2.26)}$$

where C, I_I, and N are the same as in Eq. (2.20) and ψ_i is a FRS specific variable given by

$$\psi_i = \left(\frac{\partial\sigma_V}{\partial\Omega}\right)_i \int_\nu \mathcal{R}_i\left(P, T, \vec{V}, \theta, \nu - \nu_0\right)\tau(\nu)d\nu \qquad \text{Eq. (2.27)}$$

where $(\partial\sigma_V/\partial\Omega)_i$ is the differential Rayleigh scattering cross section e, $\mathcal{R}_i\left(P, T, \vec{V}, \theta, \nu - \nu_0\right)$ is the RBS lineshape for species i, $\tau(\nu)$ is the frequency-dependent transmission of the molecular I_2 filter, and ν is the spectral frequency over which the RBS light and I_2 transmission bands are distributed. It is noted that in addition to being a function of gas composition, the RBS lineshape is a function of the flow velocity (V), the laser frequency (ν_0), observation angle (θ), temperature (T), and pressure (P). Equations (2.26) and (2.27) show that quantitative interpretation of the measured FRS signal requires knowledge of the

RBS lineshape of each species such as those shown in Fig. 2.5. The measured FRS signal from a mixture is generally written in an analogous manner to Eq. (2.20) as

$$S_{FRS,mix} = CI_I N \sum_i X_i \psi_i \qquad \text{Eq. (2.28)}$$

It should be noted that it is an assumption that the net effect of the FRS signal from each individual component can be written as the mole weighted sum from all components. Chapter 6 discusses this assumption and presents results demonstrating the validity of this assumption for combustion relevant gas species.

2.2.2 Mie (Particle) Scattering

When the size of the scattering source has the same order of magnitude of wavelength of incident light this is often referred to as "Mie scattering". For fluid mechanics studies, Mie scattering often is considered in the context of multi-phase flows or from seeded flow tracer particles with typical diameters in the range of ~0.5 – 1 μm [133]. Generally speaking, Mie scattering is much more effective at scattering the incident light as compared to Rayleigh scattering. For example, for a 0.5-μm-diameter particle, the number of photons per pixels collected is more than three orders-of magnitude greater than the number of photons per pixels collected via Rayleigh scattering with the same incident laser energy [2]. Figure 2.6 shows a polar plot of the light (λ = 532 nm) scattering intensity from oil particles in air. The angle of the polar plot represents the scattering direction such that 0° indicates complete backward scattering and 180° is complete forward scattering. The polar plot radius represents the intensity shown on a log scale where the subsequent

lines are separated by 100. It is clear from Fig. 2.6 that for larger particles the scattering intensity increases significantly and the scattering direction develops a preferential direction in the forward direction (i.e. scattering in the angles between 90° and 180°). At 90° observation, the ratio of light scattering from a $10-\mu$m particle to that from a $1-\mu$m particle is approximately four orders of magnitude. In the current dissertation work, "Mie scattering" is considered in the context of particle image velocimetry, which is discussed below in section 2.3.

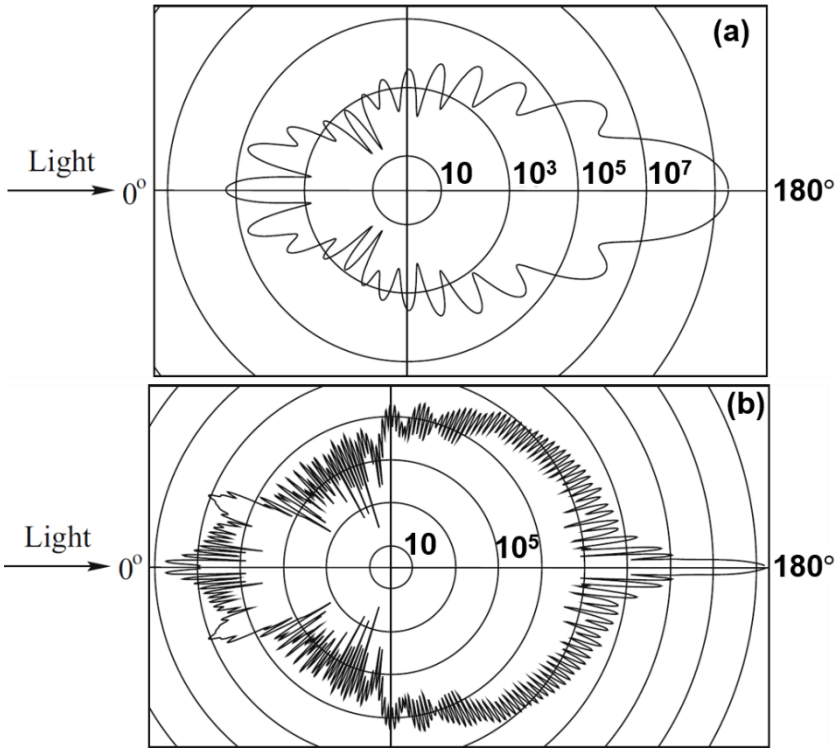

Figure 2.6: Light scattering from oil particles in air shown as polar plots from [133]. The angle shown on the polar plot represents the scattering direction while the polar plot radius represents the intensity shown on a log scale where the subsequent lines are separated by 100. (a) $1-\mu$m oil particle. (b) $10-\mu$m oil particle.

2.3 Particle Image Velocimetry

2.3.1 PIV Basics

Particle image velocimetry (PIV) is a laser diagnostic technique that enables velocity field measurements. There are several excellent reference texts (e.g., [67, 133-135]) concerning PIV and the reader is referred to them for a thorough discussion. In this section, only a very brief description of PIV, including measurement approaches and processing are given, as to orient the reader. Specifics pertaining to the particular experimental setup and approach used in the work presented in this dissertation is described in Chs. 3 and 6. Following the work presented in Ref. [133], the basic premise behind PIV is that the flow is seeded with tracer particles which are assumed to faithfully follow the flow and are illuminated by two successive laser pulses (formed into laser sheets) separated by Δt_{PIV}. The particle ("Mie") scattering from the two successive laser pulses is imaged onto a detector. For a CCD camera, an interline transfer CCD array is commonly used to capture the particle scattering images from both pulses while high-frame-rate CMOS cameras are used to capture many pairs of successive particle images in rapid succession for kHz-rate measurements. Once the particle images are acquired, they are divided into smaller sub images called interrogation windows and the displacement of the particle images between the two laser pulses (and thus velocity) is determined for each interrogation window using cross correlation algorithms. Post-processing is then applied to remove potential spurious velocity measurements [133].

The temporal spacing, Δt, between the two successive laser pulses should be chosen based on the particular flow velocities expected in the flow and the magnification and field of view of the cameras. Keane and Adrian [136] presents a number of commonly accepted PIV "design rules", including protocol for maximum in-plane particle displacements, maximum flow gradients, maximum out-of-plane motion, and seeding density. A commonly applied rule of thumb for Δt_{PIV} is that the particles should be allowed to displace 1/4 times the size of the largest interrogation window. For example, if the largest interrogation window is 16×16 pixels then Δt_{PIV} should be set such that the particles move approximately 4 pixels from the first laser pulse to the second.

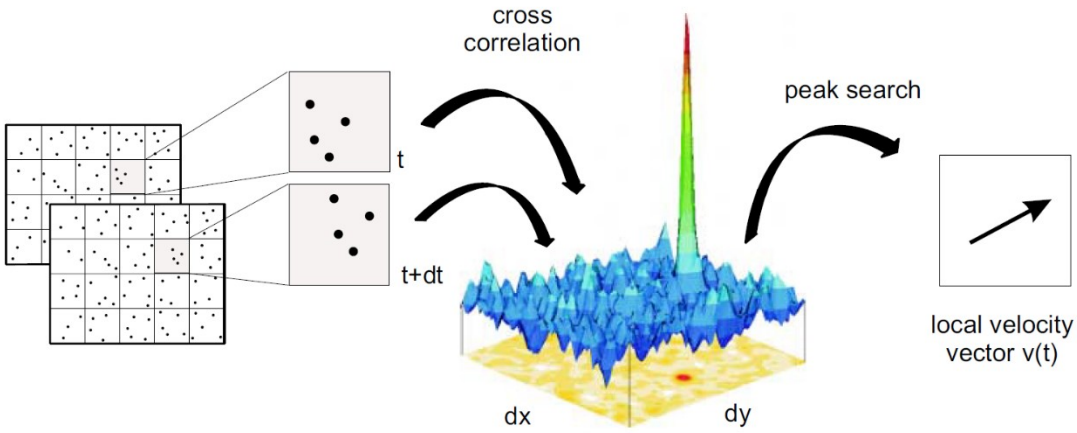

Figure 2.7: Schematic illustrating the cross-correlation of particle images for the estimation for the local velocity vector for the given interrogation window. Reprinted from [137].

Figure 2.7 shows an example schematic of the cross-correlation technique applied to a single interrogation window. When applied to particle images within an interrogation window, the cross correlation forms a peak which corresponds to the shift in both pixel directions that maximizes the correlation between the two successive images. Based on this correlation peak, an average particle displacement during Δt_{PIV} is determined. An assumption that underpins the correlation-based analysis is that the velocity of the particles in the interrogation window all move with the same local velocity. The average displacement of the particles in the interrogation window in pixels is then converted to displacement in the real world coordinates and using the known value of Δt_{PIV}, the average velocity for the interrogation window is estimated. For PIV, the in-plane resolution is determined by the interrogation window size and the out-of-plane resolution is determined by the thickness of the laser sheet. Often the interrogation windows are overlapped by 50% or even 75% to increase the number of vectors for improved gradient determination [133]. A more advanced PIV processing algorithm used in the current dissertation performs multiple passes, performing the cross-correlation on decreasing, optimally deforming interrogation window sizes with a shift to the interrogation window for the second image based on the result from the previous interrogation window size result [138].

A single camera observing particle scattering from a laser sheet at 90° is often referred to as "planar PIV" and can determine two components of the velocity field. This allows 4/9 components of the velocity gradient tensor to be calculated. Adding a second camera and orienting the two cameras to image the same object plane of interest at distinct

off-axis views is known as “stereo PIV”. Stereo PIV allows the determination of all three components of velocity in a single plane and 6/9 components of the velocity gradient tensor. An additional benefit of stereo PIV aside from the measurement of the third velocity component is the improvement in the accuracy of the two in-plane velocity components by eliminating perspective error that can arise from using a single camera [134]. Finally, three or more cameras observing particle scattering from volumetric illumination facilitates tomographic PIV, which allows the determination of the full velocity gradient tensor. Tomographic PIV is not used in the current dissertation, but the reader is referred to [135] for a thorough discussion of its implementation. Specific details of implementing planar and stereo PIV are discussed in Ch. 3 and 6, respectively.

2.3.2 Uncertainty and Dynamic Range Estimates for PIV

Two important aspects for PIV measurements is the consideration of the measurement uncertainty and dynamic range. The following analysis follows the work of Adrian [139] assuming diffraction-limited imaging and an estimation of the measurement noise as Gaussian in nature. The uncertainty of the velocity measurement (assuming minimal uncertainty in Δt_{PIV}) can be written as

$$\sigma_u = \frac{\sigma_{\Delta x}}{\Delta t_{PIV}} \qquad \text{Eq. (2.29)}$$

where $\sigma_{\Delta x}$ is the uncertainty in the particle displacement in the fluid plane (Δx), which is related to the uncertainty in the particle displacement in the camera image plane (ΔX) by

$$\sigma_{\Delta x} = \frac{\sigma_{\Delta X}}{m} \quad \text{Eq. (2.30)}$$

where m is the magnification of the system. Adrian et al. [139] argue that $\sigma_{\Delta X} = c_\tau d_\tau$ where d_τ is recorded image diameter and c_τ is a constant that is particular to a given PIV algorithm characterizing the ability to determine the displacement between images (typically 1 – 10%) [139]. The recorded image diameter d_τ is determined from $d_\tau^2 = d_e^2 + d_r^2$, where d_e is the diameter of the optical image and d_r is the resolution of the camera. The optical image diameter is given by

$$d_e^2 = d_s^2 + M d_p^2 \quad \text{Eq. (2.31)}$$

where d_p is the particle size and d_s is the diffraction-limited spot size given by $d_s = 2.44(1 + M)f\#\lambda$, where, λ is the light wavelength, and $f\#$ is the camera lens f-number. From these expressions, an uncertainty in the particle displacement and the velocity measurements can be determined. If the uncertainty of the velocity measurement is considered as the smallest resolvable velocity fluctuation (i.e., fluctuations occurring below this threshold would be below the noise floor of the measurement), then the dynamic velocity range (DVR) for the measurement can be considered as the ratio of the largest possible velocity (u_{max}) to the velocity uncertainty:

$$DVR = \frac{u_{max}}{\sigma_u} = \frac{\Delta x_{p,Max}/\Delta t_{PIV}}{c_\tau d_\tau/\Delta t_{PIV}} = \frac{\Delta x_{p,Max}}{c_\tau d_\tau} \quad \text{Eq. (2.32)}$$

In Eq (2.32), u_{max} is equal to the maximum particle displacement, $\Delta x_{p,Max}/\Delta t_{PIV}$. The maximum particle displacement is estimated as the 1/4th of the largest interrogation box

per the one-quarter rule discussed above. Specific values of the uncertainty and DVR are given in Chs. 3 and 6 for the specific experimental configurations employed.

2.3.3 Particle Tracking for Flames

An important consideration for any PIV measurement is the ability of the particles to faithfully follow the flow. For reacting flows the relevant forces acting on a particle in the flow include the particle's inertial force, F_{IF}, the fluid viscous force (sometimes referred to as the Stokes force), F_S, and the thermophoretic force, F_T, due to thermal gradients [140]. The treatment of the particle tracking characteristics used within the current PIV measurements follows that of Ref. [140]. It is well known that particles clump to larger diameters so for ease of calculation, it will be assumed that a particle cluster is 1 μm in diameter. First, no thermophoretic forces (i.e. an isothermal region) are considered. Following [140] the particle inertial force and the Stokes force are written as

$$F_{IF} = \frac{\pi d_p^3}{6}\,\rho_p\,\frac{dV_p}{dt} \qquad \text{Eq. (2.33)}$$

and

$$F_S = -\frac{3\pi\mu d_p\left(V_p - V_f\right)}{C(Kn)} \qquad \text{Eq. (2.34)}$$

In Eqs. (2.33) and (2.34), d_p is the particle diameter, ρ_p, is the particle density, μ is the fluid viscosity, and V_p and V_f are the particle and fluid velocity, respectively. In Eq. (2.34), is the Knudsen number is defined as $Kn = L_{mfp}/2d_p$, where L_{mfp} is the mean free path

length of the molecules within the gas medium, which can be taken as air values at atmospheric pressure of L_{mfp} = 72 nm at 300 K and L_{mfp} = 480 nm at 2000 K [140]. Also shown in Eq. 4.4 is $C(Kn)$, which is a coefficient that is a function of Kn given as [141]

$$C(Kn) = 1 + Kn(\alpha + \beta \exp(-\gamma/Kn)) \quad \text{Eq. (2.35)}$$

where α = 1.142, β = 0.558, and γ = 0.999. Performing a force balance, it can shown that the particle response to a sharp acceleration of the fluid is given by

$$\frac{V_f - V_p}{V_f} = \exp\left(-\frac{t}{\tau_S}\right) \quad \text{Eq. (2.36)}$$

where τ_S is the response time for the particle and is given by

$$\tau_S = \frac{d_p^2 \rho_p C(Kn)}{18\mu} \quad \text{Eq. (2.37)}$$

Considering two temperature values of 300 K and 2000 K and assuming the fluid viscosity to be that of air at those respective temperatures (1.85×10^{-5} Pa s at 300 K, and 6.81×10^{-5} Pa s at 2000 K), the particle response frequency is ~74 kHz for 300 K and ~222 kHz for 2000 K for a 1-μm TiO_2 particle and is ~121 kHz for 300 K and ~363 kHz for 2000 K for a 1-μm SiO_2 particle.

Of course the flame is not isothermal and thus the thermophoretic forces acting on the particle should be considered [140]. Stella et al. [140] estimates the velocity lag for an Al_2O_3 particle experiencing a temperature gradient in a laminar atmospheric stoichiometric methane/air flame and showed that thermophoresis can cause maximum velocity lag values

of ~0.3 m/s for 0.3 μm size particles, and ~1 m/s for 3 μm size particles. These values are considered maximum possible lags since the temperature gradient in the laminar flame are sharper than what would be encountered in a turbulent flame [140]. While the lags due to thermophoresis are not negligible, Stella et al. [140] argues that the consequence of this lag is a physical shift in the particle velocity relative to the fluid velocity, which does not exceed 300 μm for d_p < 3μm. For PIV measurements, this shift is small compared to the size of the interrogation window and thus the net effect of the lag on several particles tends to be reduced, placing the actual uncertainty due to the thermophoretic force in the cm/s range [140].

Chapter 3. Experimental Considerations for High-speed Temperature and Velocity Measurements

High-speed (10 kHz), two-dimensional planar laser Rayleigh scattering (LRS) and planar particle image velocimetry (PIV) are used to acquire temporally correlated, quantitative temperature and velocity measurements in a series of axisymmetric turbulent non-premixed jet flames issuing into a low-speed coflowing stream of air. The interaction of the velocity field with scalar fields is important in the context of understanding the underlying relationship between flow turbulence, chemistry, and transport as the local turbulence largely govern how scalars fluctuate and de-correlate under turbulent combustion conditions. The time-varying temperature field is of particular importance as it plays a key role in the majority of chemical and physical processes occurring within turbulent combusting environments. For example, finite-rate chemical kinetic processes such as soot and NOx formation are strongly dependent on local temperature fluctuations. In addition, it can be argued that the turbulent temperature field is closely linked and correlated with the mixture fraction field for flame cases far from extinction ([45, 47]). The mixture faction (ξ) and the scalar dissipation rate ($\chi = 2D\nabla\xi \cdot \nabla\xi$) describe the state and rate of molecular mixing within the flame, respectively, and can be considered as the most critical parameters for describing non-premixed and partially premixed combustion. For flames operating far from extinction the state relationship $T = T(\xi)$ exists, implying a proportionality between the rate of thermal mixing and the rate of molecular mixing (i.e., scalar dissipation rate). Thus, measurements

of the temperature field and its gradient may be important in yielding information on the underlying molecular mixing processes when mixture fraction measurements are not available.

While time-resolved PIV measurements are common within turbulent combustion experiments, previous multi-dimensional temperature measurements using Rayleigh scattering have been limited in temporal resolution, meaning that any two consecutive images are not correlated in time. The current high-repetition temperature measurements are acquired at 10 kHz in order to resolved the typical time scales of turbulent processes within laboratory-scale flows (>> 1 kHz). In this chapter, measurements are described from a series of turbulent non-premixed flames that examine the effect of Reynolds number and spatial location on the dynamics of the time-varying temperature field.

This chapter describes the experimental methods and data processing techniques for the high-repetition rate temperature and velocity measurements (acquired separately), while Ch. 4 discusses the results of these experimental campaigns. The experimental methodology is discussed in Sec. 3.1 and the data processing is discussed in Sec. 3.2. Finally, precision and accuracy of the PIV and LRS thermometry measurements are discussed in Sec. 3.3.

3.1 Experimental Methodology

3.1.1 Flow Configuration

The series of turbulent non-premixed flames introduced in this chapter and analyzed in Ch. 4 are axisymmetric turbulent jet flames stabilized above a 7.75-mm diameter (d) circular tube. The fuel jets issue into a 30×30 cm^2 co-flowing stream of low-speed room-temperature air that was filtered to remove particulates. A top down schematic of the test section is shown in Fig. 3.1. The fuel tube is 63.5 cm in length (x_{EL}), which is sufficient to ensure that fully developed flow is

established at the jet exit based on previous empirical analyses, $x_{EL}/d > 4.4(Re)^{1/6}$ [142], where *Re* is the Reynolds number based on tube diameter. The air enters the coflow section at the bottom of the 48-cm-tall coflow section through two 25-mm-diameter inlet ports and encounters flow elements designed to filter and straighten the coflow stream. The first flow element is a perforated plate that simultaneously reduces large-scale structures and creates a uniform flow through the pressure drop induced by the plate. The second flow element is a HEPA filter (removed for the PIV measurements) which primarily filters the air to remove dust and other small particulates, but also acts as another pressure drop element to further increase the uniformity of the air. The third flow element is a 25-mm-tall aluminum honeycomb structure with 5.35 mm openings to "straighten" and "laminarize" the flow. Extension walls of various heights can be placed at the exit of the coflow section in order to extend the region of straightened and filtered air, which reduces entrainment of the ambient laboratory air (which contains particles) at the measurement location of interest. The various precautions to remove dust and flow particulate only is important for the LRS measurements and are not needed for the independent PIV measurements. The complete jet-in-coflow assembly is mounted on two high-resolution translation stages with a precision of 76 μm that allows for fine axial and radial displacement.

The turbulent flames described in this chapter and analyzed in Ch. 4 are the well-characterized "DLR" flames [28, 143] that serve as benchmark flames within the International Workshop for the Measurement and Computation of Turbulent Nonpremixed Flame (TNF Workshop) [6]. The fuel consists of 22.1% CH_4, 33.2% H_2, and 44.7% N_2 by volume and issues from the 7.75-mm-diameter tube at 43.2 m/s for DLR flame A (Re = 15,200) and 63.2 m/s for DLR flame B (Re = 22,800). The CH_4 (99.0% purity), H_2 (99.995 % purity), and N_2 (99.998 % purity) are each controlled using user-calibrated Alicat mass flow controllers and are mixed in a

long tube downstream of the flow controllers and sufficiently upstream of the jet tube. The accuracy and repeatability of the flow controllers is important to achieve consistent operational Reynolds numbers over multiple test days; therefore, the flow controllers are calibrated on a consistent basis using a laminar flow element (LFE; Meriam Technologies). The flow rates of each of the gases is given for both DLR A and B in Table 3.1.

Gas	Flow Rate, DLR A, (SLPM)	Flow Rate, DLR B, (SLPM)
H2	39.3	59.0
CH4	26.2	39.3
N2	52.9	79.4

Table 3.1: Flow rates, in SLPM, of each of the gasses used for DLR A and DLR B.

The co-flowing air is supplied from a triple-filtered high pressure facility line to ensure particulate-free operation. The filtered co-flowing air stream is controlled using a needle valve and rotameter and is targeted to achieve a flow rate of 1620 LPM yielding an average coflow velocity of 0.3 m/s. The stoichiometric mixture fraction for the DLR fuel mixture and air is 0.167. The particular fuel mixture is chosen such that the differential Rayleigh scattering cross-section throughout the flame (reactant to products) and in the co-flowing air is constant to within +/- 3% [28, 143]. This implies that temperature measurements can be acquired in a straightforward manner using Rayleigh scattering alone. The ideal gas law ($p = NkT$; k is the Boltzmann constant, T is temperature) can be substituted into Eq. (2.20) and the constant C, in Eq. (2.20) can be accounted for by normalizing the in-flame Rayleigh scattering signal by a signal of known temperature and composition. For the current LRS temperature measurements those constants are accounted for

through normalization from air at room temperature. In this manner, the temperature is determined from

$$T = T_{ref}\left(S_{ref}/S_{LRS,mix}\right) \quad \text{Eq. (3.1)}$$

where S_{ref} is the reference Rayleigh scattering signal from air at room temperature (T_{ref}).

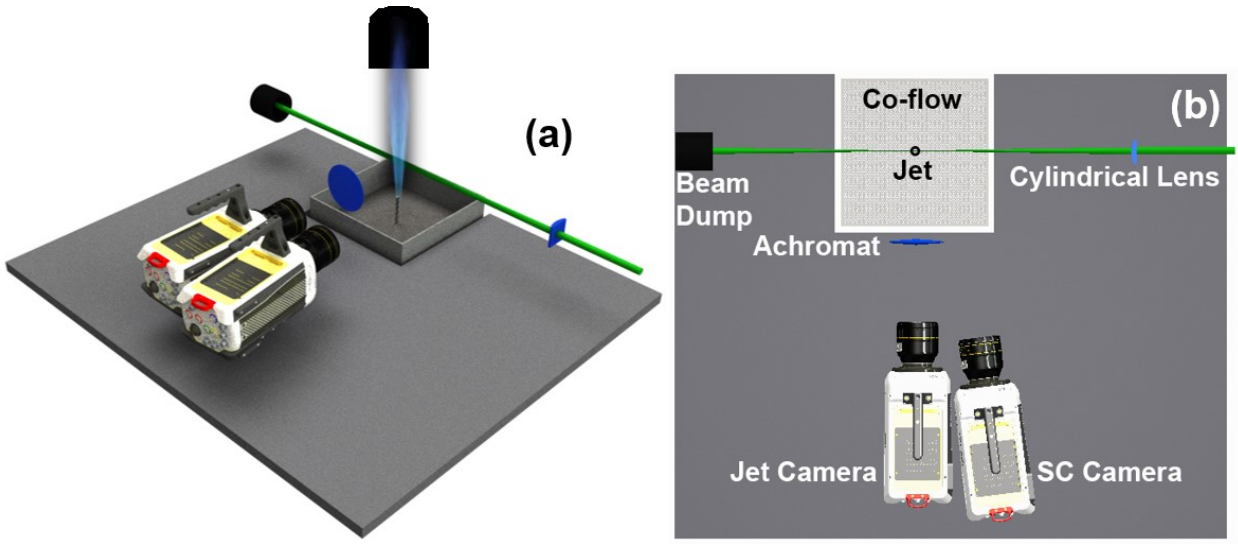

Figure 3.1: (a) Perspective view of experimental setup for LRS measurements. (b) Top-down schematic of experimental setup for the high-speed temperature measurements. The "Jet Camera" coupled to an achromat images Rayleigh scattering from the flame, while the "SC Camera" is used to perform sheet correction and energy fluctuation corrections. The frequency doubled output from an Nd:YAG laser (532 nm) is focused over the center of the jet tube (surronded by the coflow).

3.1.2 Particle Seeding for PIV Measurements

Both the fuel and air streams are seeded with titanium dioxide (TiO_2) particles, which is a common flow tracer particle for PIV, especially within reacting flows [140, 144]. The nominal particle size is 0.5 μm, although it is well known that the particles can cluster together to form

larger agglomerates. The co-flow particle seeder is a simple fluidized bed seeder while the jet seeder is a fluidized bed/cyclonic seeder. For a general fluidized bed seeder design, the seeding particles rest on the surface of a porous material (i.e. a fine mesh screen or sintered metal plate) suspended above the bottom of the seeder. The gas enters through the bottom and passes through the fine mesh screen or sintered metal plate creating a fluidized "bubbling" bed of particles. Small particles are carried by the gas flow and out of the seeder towards the experiment, presumably following the flow of interest faithfully. While both seeders utilized in the PIV experiments are fluidized bed seeders, the main jet seeder has an additional cyclonic feature designed to improve seeding stability [144]. The schematic for the coflow seeder is shown in Fig. 4.1a while the schematic for the main jet seeder is shown in Fig. 3.2b.

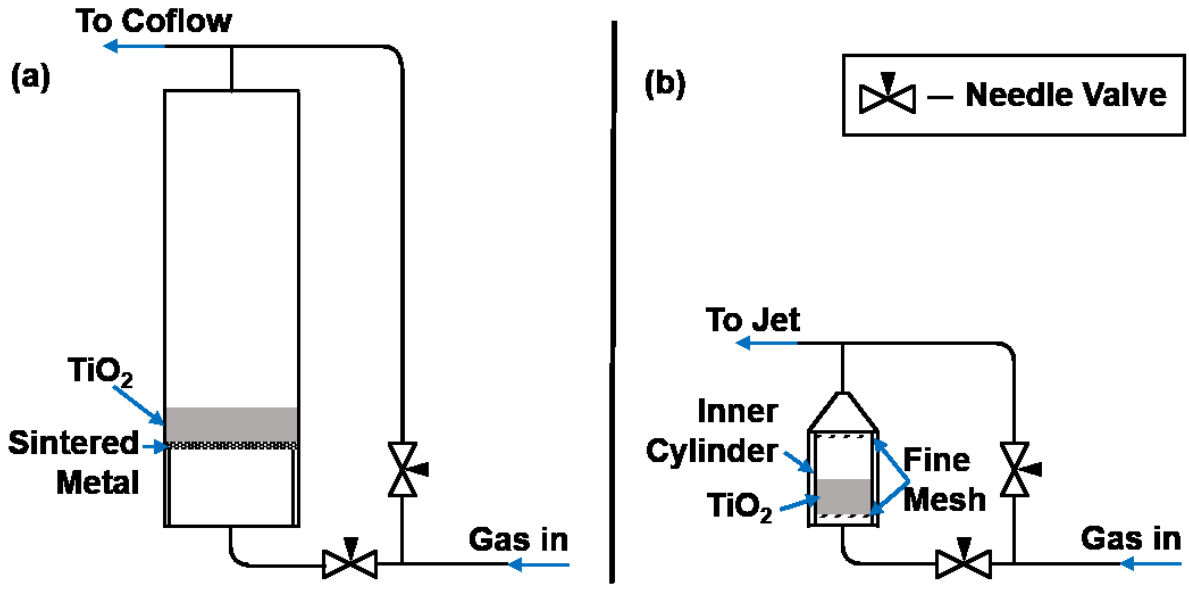

Figure 3.2: Schematic of particle seeders used in high-speed (10 kHz) velocity measurements. (a) Schematic of seeder used for coflow stream. (b) Schematic of seeder used for main jet stream.

For the coflow seeder, the air enters at the bottom plate. The TiO_2 powder rests on a sintered metal plate that is offset from the bottom of the seeder using spacers. The air passes through the sintered metal plate and fluidizes the TiO_2 powder and the particle-laden air flows to the exit of the seeder. The height of the seeder is 0.9 m tall to ensure that only the smallest particles reach the exit. A small orifice is put in-line at the exit of the seeder to help break up any agglomerated particles. For the main jet seeder the flow also enters at a bottom plate, but through two entrance ports that are at angles with respect to the seeder walls and in opposite directions with respect to one another such that a cyclonic motion of the incoming gases is created. The seeder has an inner cylinder with mesh screens on the top and bottom and is vertically offset from the bottom plate of the seeder by approximately 5 mm. The TiO_2 powder rests on the bottom fine mesh screen where the incoming cyclonic gas stream fluidizes the TiO_2 power and carries the small particles to the exit of the seeder. The main jet seeder also has an air-powered vibrating plate attached to the bottom of the seeder to help break up any agglomeration or channeling of the TiO_2 powder. For the PIV measurements, the particle-seeded air follows the same flow path as described above, except that the HEPA filter is removed from the coflowing section. For the fuel mixture, the gases CH_4, H_2, and N_2) are mixed prior to entering the jet seeder. A seeding density of 0.08 – 0.1 particles per pixel was targeted such that there are around 20 – 26 particles per final interrogation box (16×16 pixels). This relatively high seed density was used in order to compensate for the variations in flow (and hence seed) density within the flame due to heat release. In the high-temperature regions, the seed density is reduced as compared to low-temperature portions of the flow. Thus, targeting higher seeding density ensures that there is adequate seeding even in the high-temperature regions.

3.1.3 Laser Configuration for High-Speed LRS

The quantitative, high-speed temperature measurements are performed using planar laser Rayleigh scattering (LRS). LRS is a relatively "weak" process that typically requires high levels of laser energy for sufficient signal collection. Commercially available high-speed laser systems have continuous output, but relatively low output energies making 2D LRS imaging difficult. The laser utilized for the current high-speed temperature measurements is the high-energy pulse burst laser system (HEPBLS) (schematic shown in Fig. 3.3a) at Ohio State. The HEPBLS has been described in detail previously in Refs. [113] and [145] and thus only a brief description is given here. The HEPBLS is a master oscillator, power amplifier (MOPA) system that amplifies the output of a continuously operating, narrow-linewidth (2.5 GHz), pulsed oscillator (PO) in a series of custom, long-duration, flashlamp pumped Nd:YAG amplifier stages. As described in [145], the HEPBLS is a flexible, dual-leg system that allows for ultra-high energy output through beam combination or two independent outputs for multi-parameter measurements. A single output leg is used for the planar Rayleigh scattering thermometry measurements.

The PO, which outputs pulse energy of 10 μJ at 1064 nm, is double passed through the first three amplifiers, labeled AMP 1-3 in Fig. 3.3a. The double pass configuration is achieved using a combination of a polarizing beam splitter (PBS), which passes horizontally polarized light and reflects vertically polarized light, a quarter wave-plate (QWP) and a high reflector. More specifically, examining a single amplifier in Fig. 3.3, the laser pulse train first passes through the PBS and is amplified by the flashlamp-pumped amplifier. Subsequently, the pulse train passes through the QWP changing polarization from horizontal to circular and is retro-reflected (using the high reflector) back through the QWP changing the polarization from circular to vertical and

is amplified by the flashlamp-pumped amplifier a second time. Since the pulses now have vertical polarization, they are reflected by the PBS and sent to the next amplifier stage where the process is repeated. While the first three amplifier stages are double-passed, the final three stages are in single-pass configurations. For the current high-speed temperature measurements, a 6^{th} amplifier (not shown in Fig. 3.3) is used after AMP 5A in order to further boost laser pulse energy. After six amplifier stages, the total system gain is > 2 x 10^5 and the final 1064-nm energy output exceeds 1.5 J/pulse at a repetition rate of 10 kHz. Between each successive amplifier stage, spatial filtering and image relay optics are employed in order to mitigate birefringence, diffraction, and thermal lensing effects for high output beam quality. After the final amplifier stage, the 1064-nm pulse train is frequency-doubled using a type-I LBO crystal (12×12×20 mm^3) to generate ~ 1 Joule/pulse at 532 nm at 10 kHz. A sample 10-kHz pulse energy trace (prior to the addition of the 6th amplifier) is shown in Fig. 3.2b. The reported trace is 20 ms in duration with an average pulse energy of 900 mJ. The 6th amplifier increased the 532 nm output to > 1 J/pulse. As reported previously [113, 145] and shown in Fig. 1b, there is low (< 5%) pulse-to-pulse fluctuation within the 532 nm burst enabling temperature measurements with consistent signal-to-noise characteristics.

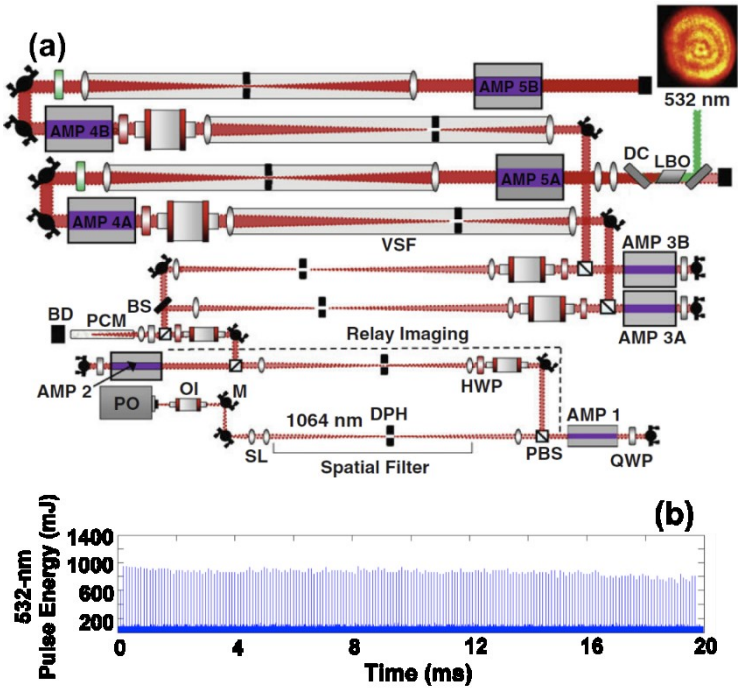

Figure 3.3: (a) Schematic of HEPBLS; (b) example 20 ms, 10 kHz pulse burst trace.

3.1.4 Optical and Imaging Configuration for LRS

A schematic of the imaging system is shown in Fig. 3.1. The vertically polarized 532-nm output of the HEPBLS is formed into a 15-mm tall laser sheet using a 750-mm focal length, plano-convex cylindrical lens, which is shown in Fig. 3.1. The laser sheet thickness has been measured previously to have a $1/e^2$ value of 300 μm [113]. The Rayleigh scattering images within the flame are collected by a high-speed CMOS camera (Vision Research V711) in combination with a 100-mm diameter, 210-mm focal length achromat lens and an 85-mm f/1.4 Nikon camera lens. This optical combination results in a total collection f/# of 2.1 and results in a measured magnification of 0.36 and an imaged area of 55×55 μm^2/pixel. The high collection efficiency in conjunction with the high pulse energies of the HEPBLS allow for the planar Rayleigh images to be collected

without the use of an image intensifier while still allowing for high signal-to-noise and high spatial resolution, which is discussed further below.

A second high-speed CMOS camera (Vision Research, Phantom 711), which is shown in Fig. 3.1 and is labeled as "SC", images a uniform region of air adjacent to the flame to correct for shot-to-shot energy fluctuations as well as to correct for variations in laser sheet intensity. The camera is aligned with a slight angle relative to the laser normal (due to space limitations) thus only a portion of the SC camera field of view (FOV) is in focus. The in-focus region is carefully mapped out and used for the laser energy/sheet intensity corrections. The SC camera uses an 85-mm, f/1.4 lens. Both cameras are synchronized from a TTL signal from the HEBPLS and are triggered at 10 kHz.

3.1.5 Laser and Optical Configuration for PIV

The laser utilized to obtain the high-speed TR-PIV measurements is an 80-W diode-pumped solid state (DPSS) laser (EdgeWave IS80-2) which outputs two 532-nm laser pulses in quick succession. The system is capable of 2 mJ/pulse for each laser head for a repetition rate of 10 or 20 kHz with pulse-to-pulse energy fluctuations of < 2.5%. Two independent laser heads within the DPSS allow for a range of temporal separation (Δt_{PIV}) between laser pulses ranging from Δt_{PIV} = 0.1 μs to 98 μs in 0.1 μs increments. The laser pulses are combined within the DPSS using polarization optics such that the two pulses have orthogonal polarization (i.e., one vertically polarized and one horizontally polarized).

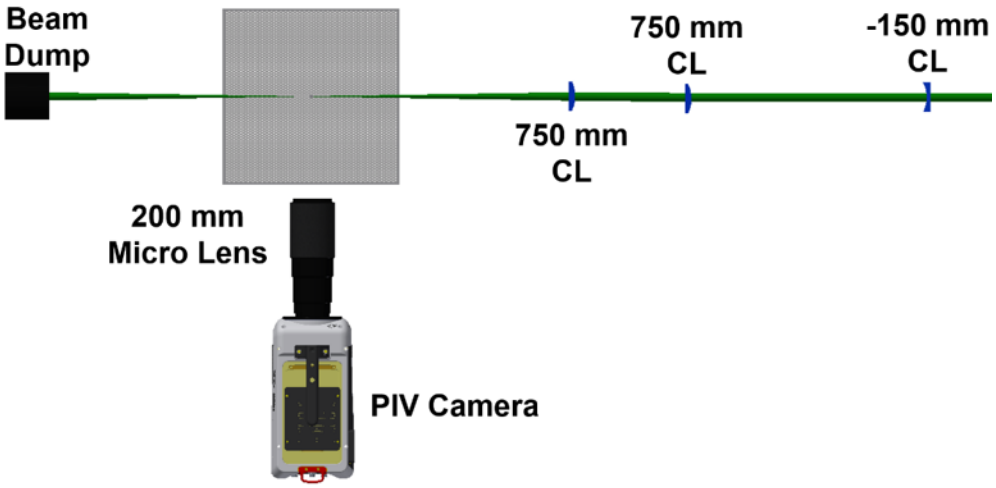

Figure 3.4: Top-down schematic of the TR-PIV measurements.

The pulse output is rectangular is shape with a width of 8 mm and a thickness of 1.6 mm. The laser pulses are subsequently shaped by first reflecting from a periscope to rotate the laser pulses 90 degrees such that beam is 8 mm tall by 1.6 mm wide. The pulses are then expanded vertically via a concave f = -150-mm focal length cylindrical lenses lens and then collimated by a concave f = +750-mm focal length cylindrical lens such that the beam is ~ 40 mm tall by ~1.6 mm wide. Finally, the beam is focused via another f = +750-mm focal length cylindrical lens oriented vertically to focus the width of the beam such that the final laser sheet is 40 mm × 0.35 mm at the measurement location. A simple schematic of the laser and the cylindrical lenses are shown in Fig. 3.4. Additional mirrors, which are not shown in Fig. 3.4, are used to ensure the focused sheet is aligned directly over the center of the fuel tube.

The particle scattering from the TiO_2 is imaged using a Vision Research Phantom v711 high-speed CMOS camera with a 200-mm micro Nikkor lens with the aperture set to f/16 and the camera and lens arranged to achieve a magnification of M = 1. This magnification dictates that

each pixel of the CMOS sensor images 20 μm in physical space. Further discussion of the camera resolution and its impact on the overall spatial resolution of the temperature can be found in section 3.4. The CMOS camera is operated in frame-straddling mode (FSM) which means that the CMOS camera is operated at twice the desired acquisition frequency such that the first laser pulse (A) is timed to arrive in the first frame and the second laser pulse (B) is timed to arrive within the second frame, delayed by Δt_{PIV}. For the current 10-kHz measurements, the camera operates at 20 kHz, which necessitates a reduction in the overall field of view FOV from the original sensor size of 1280 pixels × 800 pixels to 775 pixels × 380 pixels (15.5 mm tall × 7.5 mm wide). The particular FOV of 775 × 380 was chosen to cover a large spatial range in the axial (or streamwise) direction.

3.2 Data Collection and Processing

Planar laser Rayleigh scattering (LRS) and particle image velocimetry (PIV) measurements are performed in both flame A (Re = 15,200) and flame B (Re = 22,800). The measurements are conducted separately, where LRS measurements are acquired at axial locations of x/d = 10, 20 and 40 and PIV measurements are acquired at x/d = 10, 20, 30, 40, 50 and 60; d is the jet tube diameter of 7.75 mm. For the LRS measurements, only a single field-of-view (FOV) is needed at the axial locations of x/d = 10 and 20 to capture the entire radial extent of the flame (i.e., centerline to coflow). Two FOVs (in the radial direction) are needed at x/d = 40 in order to capture the full radial profile. With the HEPBLS operating at a repetition rate of 10 kHz and outputting burst lengths of 20 ms, each burst contains 200 images each separated in time by 100 μs. For each flame and spatial location, 200 separate bursts (40,000 total images) are obtained in order to produce converged statistics. In addition to obtaining image sequences for the non-premixed flame conditions, a series of reference image bursts are acquired in room-temperature (296 K) air before

and after the set of 200 flame image bursts. These reference images are used to normalize the Rayleigh scattering images obtained in the flame to determine temperature as described below.

For the PIV measurements, the reduced FOV necessary for the desired data acquisition rate made it such that a single FOV did not cover the full radial profile for any axial location. Multiple FOVs (moving radially outward from centerline) are used at x/d = 20 and 40 in order to obtain full radial profiles for those axial locations, while a single FOV is used at x/d = 10, 30, 50 and 60 for "near-centerline" data. Specifically, at x/d = 20, four FOVs are acquired, while at x/d = 40, imaging at seven adjacent FOVs is needed. The multiple FOVs and thus, the full radial extent was measured at x/d = 20 and x/d = 40 to compare spatio-temporal statistics with the high-speed temperature data. For the high-speed velocity measurements the limiting factor for the number of consecutive image pairs acquired consecutively is the memory capacity of the CMOS camera system. For the current reduced FOV, approximately 9000 consecutive images could be acquired before transferring to a computer. In Ref. [146] it was shown that for measurements in statistically stationary turbulent flows it takes approximately 300 integral timescales for the estimator of the mean of variable ϕ to converge to within 2% of the expected value of the mean of ϕ and approximately 5000 integral timescales for the estimator of the variance to converge to within 2% of the expected variance of ϕ. In order to balance well-converged statistics with data storage and facility limitations, data were acquired such the PIV measurement duration targeted at least 2000 integral time scales. For any given FOV, an estimate of the slowest local integral timescale within the FOV for the lowest Reynolds number condition (flame A) was used to determine the number of images to acquire. For the axial locations of x/d = 10, 20 and 40, estimates for the velocity

integral time scales were determined from the temperature integral time scales[1]. For axial positions of x/d = 30, 50 and 60, estimates of the slowest velocity integral time scales were determined from the estimates at x/d = 10, 20 and 40 and adjusted accordingly based on known turbulent jet scaling laws [147].

It should be noted that after analysis, the results showed that the velocity integral time scales were slower than that of the temperature (see results below) and thus, the actual duration of the velocity data (in terms of integral time scales) is less than estimated. Table 4.1 shows a data log of the amount of PIV data and the corresponding duration in terms of integral time scales obtained at each measurement location for x/d = 20 and 40. The same number of images are taken for both flame A and flame B for a given FOV.

Setting a proper temporal separation, Δt_{PIV}, between consecutive laser pulses from the PIV laser is important for accurate velocity estimations. If Δt_{PIV} is too long then particles displace too far and particle matching (via correlation) becomes difficult as particles have moved too far in frame 2 relative to their position in frame 1. If Δt_{PIV} is too short then the dynamic range of the velocity measurement is limited. For simple single-pass algorithm, a commonly used metric to determine Δt_{PIV} is to allow the particles to move one-quarter of the interrogation window [133, 136]. In the case of a multi-pass PIV algorithm, where the interrogation volume reduces in size in successive passes, the "one-quarter rule" is applied to the largest interrogation volume [133]. For the current velocity measurements, the values of Δt_{PIV} were determined using the known field-of-view (with known magnification), the largest interrogation box (64 pixels, discussed more below in Sec. 4.2.2), and previous velocity measurements performed in flame A [148] according to

[1] The high-speed temperature measurements preceded the high-speed PIV measurements by approximately one year.

x/d	FOV number	Radial range (r/d)	Slowest I_t in FOV (ms)	Number of images (total)	Amount of data in seconds	Number of integral timescales
20	1	-0.10 – 0.89	0.32	3828	0.38	1187
	2	0.79 – 1.79	1.24	12793	1.28	1032
	3	1.68 – 2.67	3.22	55509	5.55	1723
	4	2.57 – 3.56	5.90	137490	13.37	2266
40	1	-0.10 – 0.89	1.07	8638	0.86	803
	2	0.79 – 1.79	1.42	10022	1.00	704
	3	1.68 – 2.67	2.54	22739	2.27	894
	4	2.57 – 3.56	4.11	47209	4.72	1148
	5	3.46 – 4.45	5.27	58304	5.83	1106
	6	4.35 – 5.35	7.35	76924	7.69	1046
	7	5.25 – 6.24	9.71	156000	15.60	1606

Table 3.2: Number of images taken for selected FOVs for both x/d = 20 and x/d = 40 relative to slowest integral timescales. The same number of images are obtained for both flame A and flame B. The slowest integral timescales come from high-speed velocity measurements.

$\Delta t_{PIV} = dx/\langle u_{max} \rangle$, where dx is the actual spatial scale of 64 pixels and $\langle u_{max} \rangle$ is the highest estimated mean velocity in a given FOV. Since there no published velocity measurement for flame B, $\langle u_{max} \rangle$ is estimated by multiplying the value of $\langle u_{max} \rangle$ from flame A by 1.5, which is the ratio of exit velocities between flame B and flame A. The values of Δt_{PIV} varied from as low as 4 μs for flame B at x/d = 10 to as high as 48 μs for flame A at x/d = 40 for the farthest radial FOV (FOV #7).

3.2.1 LRS Temperature Data Processing

This section describes the steps to convert the measured Rayleigh scattering signal into temperature. For each image sequence, 50 extra images are acquired on the camera prior to the first laser pulse arriving at the measurement volume in order to obtain a measurement of the camera darkfield signal level. These 50 images are averaged (hence referred to as the "darkfield") and

subtracted from the acquired LRS images. Ideally, after subtraction of the darkfield, the regions in the camera above and below the location of the laser sheet should have zero signal level. However, there can be additional sources of background signal that need to be removed. Stray light from surrounding surfaces and optics are all possible sources of background laser scattering that can be detected and in some cases, are spatially non-uniform. Because unwanted scattering signals can lead to erroneous temperature measurements, there are significant efforts made to mitigate all sources of background scattering. For example, the experiment is contained within a set of laser curtains and the beam propagates through a series of laser tubes to reduce the background scattering to levels that are small and approximately constant throughout the measurement volume. For the high-speed temperature measurements the additional level of unwanted background scattering is estimated to be approximately 10 counts, which represents less than 1% of the acquired Rayleigh scattering signal in air. This background scattering is then removed from the Rayleigh scattering images.

The process for subtracting the darkfield and additional background signal can be written as

$$S^*_{Ray} = S^*_{Ray,Raw} - S_{Darkfield} - S_{Background} \qquad \text{Eq. (3.2)}$$

where S^*_{Ray} is the darkfield- and background-subtracted Rayleigh scattering signal (with the star denoting that it has not been corrected for shot-to-shot energy fluctuations (energy corrected) nor has it been corrected for non-uniform laser sheet intensity (sheet corrected). This processing is performed for both the reference air and flame Rayleigh scattering images acquired with the "Jet Camera" (Fig. 3.1) and the sheet-correction measurements performed with the "SC camera".

Subsequently, the individual air reference images are averaged to yield a single air reference image, denoted S_{Ref}.

The next step is to normalize the single shot Rayleigh images in the flame by the average reference image, S_{Ref}. This step has two purposes which include placing the flame Rayleigh image onto a scale relative to the reference condition and correcting for sensor non-uniformities. In practice, scientific CCD sensors generally are fairly uniform, but high-speed CMOS sensors generally display a certain level of non-uniformity [115]. While this non-uniformity can be corrected through calibration by imaging a uniform field of light, it is challenging to produce a perfectly uniform light field source in the lab. Instead, the normalization of the in-flame Rayleigh scattering images by the reference image (acquired with the same camera sensor and optics) cancels out any sensor non-uniformities.

Figure 3.5 shows a series of images highlighting the aforementioned data processing steps. Fig. 3.5a shows an example of a single shot Rayleigh scattering image taken from flame B for x/d = 10 processed using Eq. (3.2). The flame is located on the left side of the image in the horizontal pixel range of around 1 to 600 and is characterized fluctuations in signal level due to the turbulent and reacting nature of the flow. The right side of the image shows the Rayleigh scattering from the air coflow and the Rayleigh signal fluctuations seen as horizontal stripes are due to laser sheet intensity non-uniformities. Fig. 3.5b shows the corresponding average reference air image and the signal levels are similar to that of the coflow (right side of the sample Rayleigh image) in Fig. 3.5a, although the laser sheet "striping" is not as evident in the reference Rayleigh image due to smoothing that comes from the averaging effect over many images. Fig. 3.5c shows the normalized Rayleigh signal S^*_{Ray}/S_{Ref} where the sample Rayleigh image shown in Fig. 3.5a is normalized by the average reference air Rayleigh image shown in Fig. 3.5b. The normalized Rayleigh image in

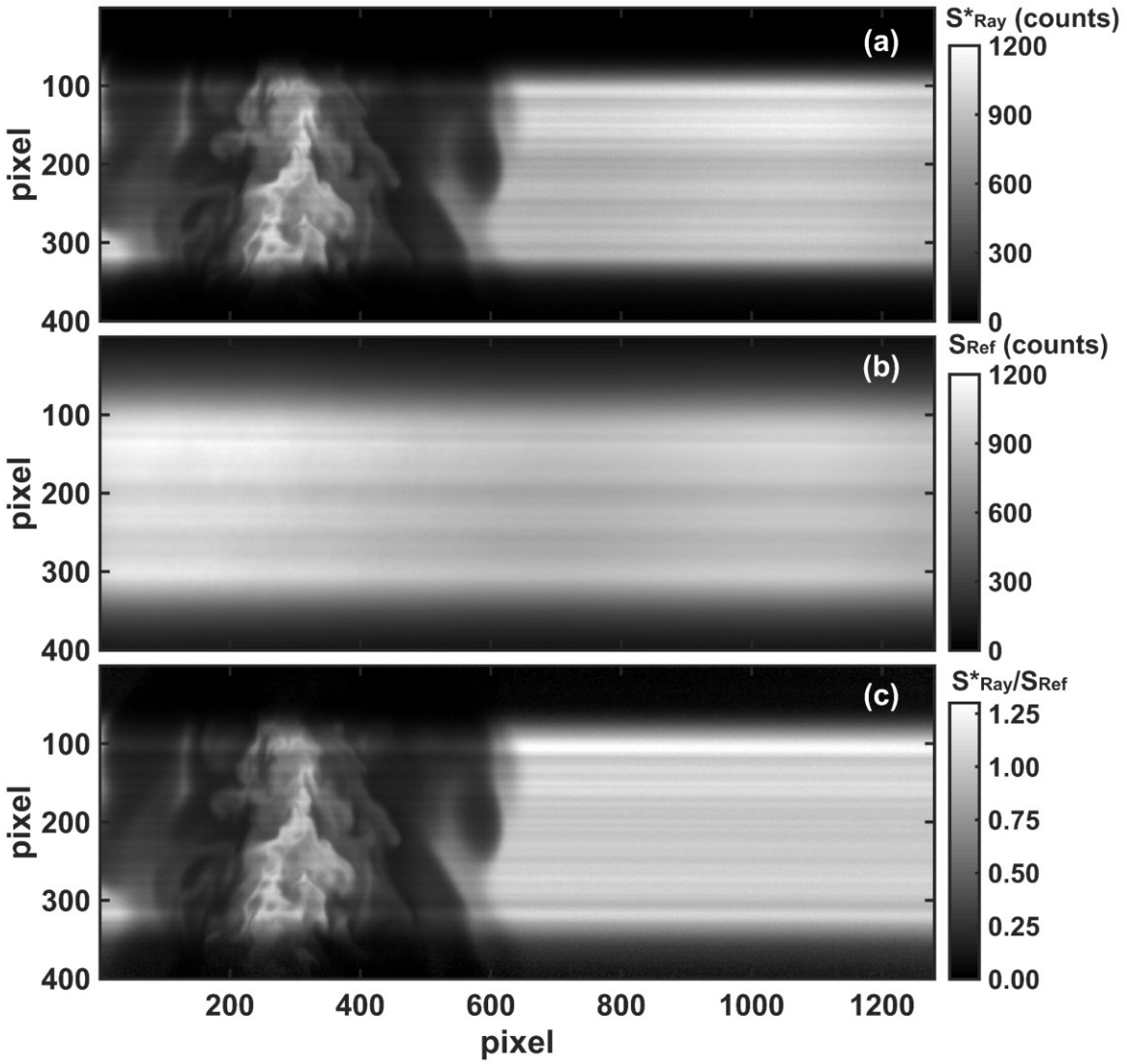

Figure 3.5: (a) Raw Rayleigh image from flame B, from x/d = 10, which has been darkfield and background subtracted. (b) Average reference air Rayleigh image, averaged over individual reference air images that have also been darkfield and background subtracted. (c) Normalized single shot Rayleigh image in which the Rayleigh image from (a) is normalized by the average reference air Rayleigh image in (b).

Fig. 3.5c looks qualitatively similar to the original sample Rayleigh image of Fig. 3.5a; however, non-uniformities (across pixels) have been removed and the image is now on a relative signal scale that can be converted to temperature as shown below.

Fig. 3.5c shows why it is necessary to correct for the laser sheet intensity non-uniformities. If Eq. (3.1) is used to convert the normalized signal shown in Fig. 3.5c to temperature, it is clear that there would be variations in temperature perpendicular to the beam path that are not actually present (i.e., in the spatially uniform coflow). Therefore, a laser sheet intensity fluctuation correction (or "sheet correction"), is needed to correct for the non-uniformities in the laser sheet. Additionally, accounting for the shot-to-shot variations in laser energy is needed to place the Rayleigh scattering images on a common scale relative to each other and relative to the reference air condition. For the current temperature measurements, sheet corrections are performed in two manners: (1) "single camera correction" from the jet camera at lower axial positions where the uniform coflow is present in the flame images or (2) a "two camera correction" using the secondary SC Camera at further downstream locations, if a region of uniform air is not present in the field-of-view of the 'Jet Camera'. For both strategies the laser sheet intensity fluctuations are estimated from an average across 50 pixels in the uniform coflow in order to reduce image noise in the laser sheet fluctuation corrections. Performing the laser sheet intensity correction using the single camera approach is ideal and leads to the most effective method because it is less prone to error as compared to using a second camera to perform the sheet correction. In the latter case, the SC camera image needs to mapped to the image from the Jet Camera before the profile is extracted. While this sheet correction strategy can be done with good precision, it requires a great deal of care in order to not introduce additional errors that negate the implementation of the laser sheet correction. Performing the sheet correction from the coflow region using the single camera correction is utilized for both flames at both x/d = 10 and 20 whereas the two camera correction (SC camera) is used for both radial FOVs for both flame conditions at x/d = 40.

Figure 3.4 highlights some of the key steps during the final processing steps including sheet/energy correction and converting the normalized signal into temperature. Due to the fact that the horizontal axis of the sensor is not perfectly parallel to the laser beam direction, the Jet Camera image is rotated prior to the sheet correction step, although the angle is very small. The built-in MATLAB function 'imrotate' with a bicubic interpolation method is used to rotate the images. The optimal rotation angle for the Jet Camera images has been determined by performing sheet corrections on reference air cases with varying angles while monitoring the signal-to-noise ratio in a 30×30 pixel region in the air. The optimal angle is determined when the SNR is maximized. Using this method the optimal angle was determined to be 0.17°.

Figure 3.6a shows the normalized Rayleigh scattering signal which is the same as Fig. 3.5c with the additional image rotation. Overlaid on Fig. 3.6a is a red line indicating the center of the 50-pixel wide region from which the laser sheet intensity fluctuations are extracted. Figure. 3.6b shows the 50-pixel average intensity profile extracted from Fig. 3.6a. A matrix is then constructed from the intensity profile that is the same size as the normalized Rayleigh signal ratio image/matrix whose columns consist of the extracted intensity profile and is used to normalize the Rayleigh signal ratio image. The intensity profile captures the intensity fluctuations within an individual laser sheet and also embeds the relative pulse-to-pulse laser energy correction. If a particular laser shot is lower (or higher) in energy than the average laser energy for a burst then the sheet correction matrix will be less than (or greater than) unity and the corrected Rayleigh signal ratio will be increased (or decreased) relative to the average.

In the case of the "two camera" sheet correction involving the SC Camera, the image from the SC Camera is resized using the built-in MATLAB function 'imresize' using a bicubic interpolation and then an intensity sheet is extracted from the resized image. The vertical position

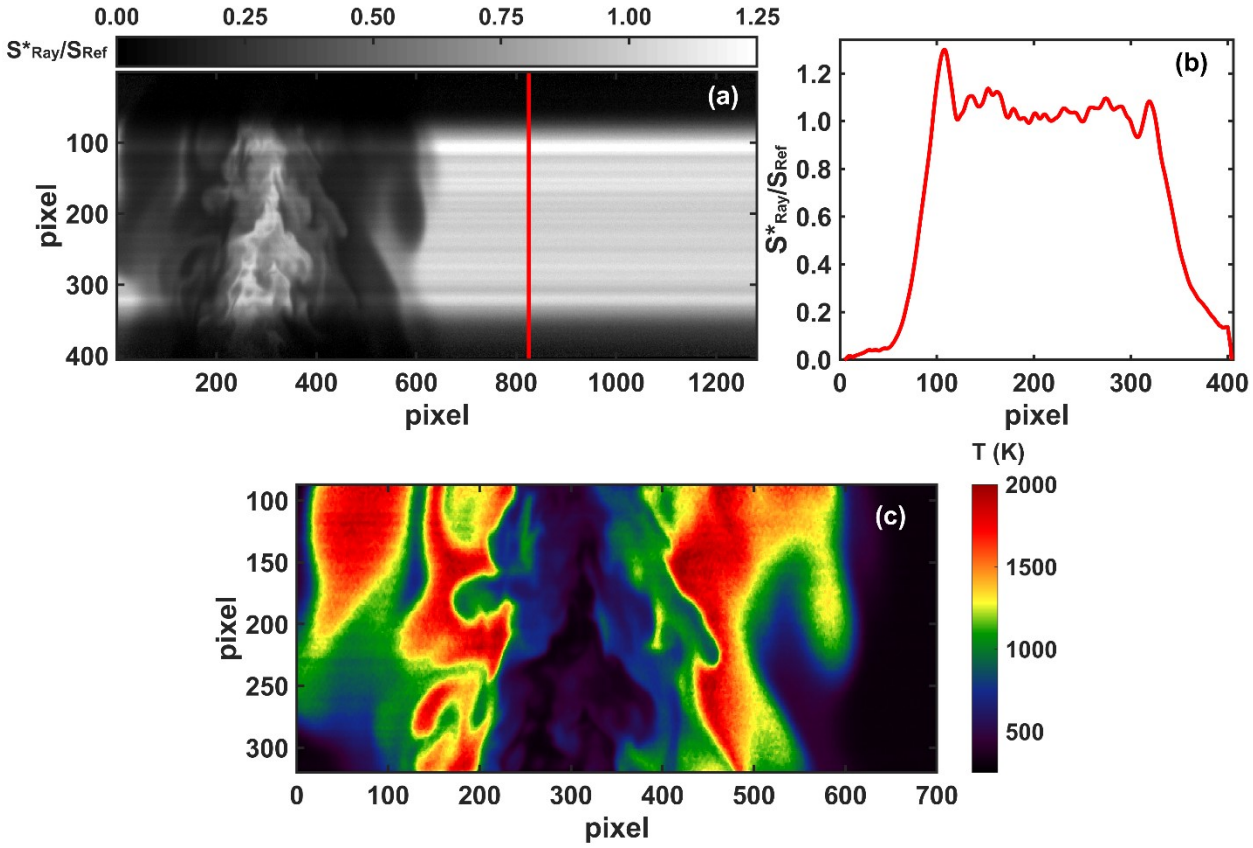

Figure 3.6: (a) Example normalized Rayleigh scattering signal image that has had the darkfield and background signals subtracted and has been properly rotated. The red line indicates center of the 50-pixel region where the laser sheet intensity variations are determined. (b) The 50-pixel average intensity profile used to correct the image shown in (a). (c) Sheet-corrected Rayleigh image converted to temperature and median filtered using a 3×3 kernel.

of the extracted intensity profile is then aligned with the vertical position of the laser sheet in the Jet Camera image by zero padding the sheet intensity vector with a number of pixels, termed the offset factor. The optimal resize offset factors are determined through iteration and performing test sheet correction on the reference air images until the spatial signal-to-noise in the corrected jet camera image is maximized. The magnification of the SC Camera is set such that the resize factor is always less than 1, meaning that the extracted sheet intensity profile from the SC Camera is not

under sampled relative to the Jet Camera image. For the current high-speed temperature measurements the optimal resize factor was determined to be 0.828 and the optimal offset factor was determined to be 34 pixels. After the laser-sheet intensity fluctuations are extracted from the SC Camera, the sheet correction protocol follows the same steps outlined above for the single-camera sheet correction approach. The laser-sheet intensity-corrected Rayleigh scattering signal ratios, denoted S_{Ray} are then converted to temperature using Eq. (3.1). The converted temperature field is subsequently filtered using a median filter with a 3×3 filter kernel to improve SNR. Figure 3.6c shows an example of these final two steps applied to the sample Rayleigh image in Fig. 3.6a. While the full FOV covers ~22 mm vertically, only a vertical span of ~11 mm (~200 pixels) of the image is used for extracting temperature.

As an example of the measurement capabilities, Fig. 3.7 shows a partial sequence of temporally correlated temperature images obtained from flame B (Re = 22,800) at an axial position x/d = 20. The size of the images in Fig. 3.7 are approximately 11×55 mm^2 and the sequence highlights the time-dependent nature of the turbulent flames under consideration. For example, in images 11 – 14 there appears to be a large low-temperature hole forming on the left side of the image that could be a local extinction event occurring due to the highly turbulent nature of the flame. Images 15 – 18 appear to show the re-healing of the layer, possibly due to the convection of higher temperature gases (frame 17, 18). 10-kHz temperature measurements similar to those shown in Fig. 3.7 are obtained at x/d = 10, 20, and 40 for both flame A and flame B. As described above, 200 bursts of 200 sequential images have been obtained for each position/flame combination corresponding to 40,000 individual samples at each spatial position. The statistics that be determined from the data set of temperature images include mean and RMS temperature values, spatial correlations and the corresponding estimates of the integral length scales. The kHz-

rate acquisition of the current measurements means that additional temporal and spatio-temporal statistics can be determined from the data set.

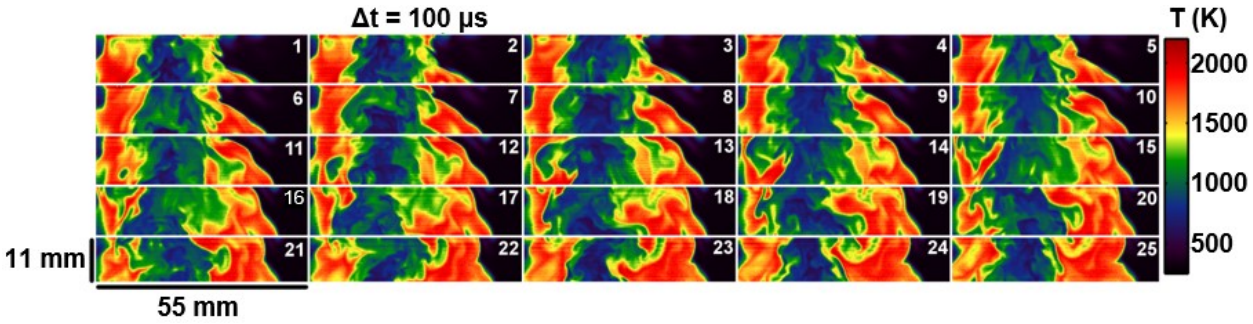

Figure 3.7: 25-frame (out of 200), 10-kHz image sequence of the temperature field in flame B (Re = 22,800) from axial location x/d = 20.

3.2.2 PIV Data Processing

The acquired particle image pairs are converted to velocity fields using LaVision Davis 8 software and a planar PIV algorithm. A multi-pass algorithm is used to increase the dynamic range and resolution of the velocity measurement [138]. The initial size of the interrogation boxes is set to 64 × 64 pixels with 50% overlap between adjacent interrogation boxes and two iterations at this size. The interrogation box size is then iteratively reduced until it reaches the final interrogation box size of 16 × 16 pixels with 50% overlap. At the final interrogation box size, two iterations of the velocity estimate is performed. With a magnification of unity (m = 1), the 16 × 16 interrogation box with 50% overlap leads to a vector spatial resolution of 320 μm and a velocity vector separation of 160 μm.

The largest interrogation box (64 × 64 pixels) determines the initial vector field for the multi-pass approach. Then for the subsequent, smaller interrogation boxes, the multi-pass algorithm allows the interrogation window of frame 2 to shift relative to frame a using the velocity information from the larger interrogation box. This process continues until the smallest interrogation box is reached. Vector post-processing is performed within the multi-pass algorithm at each interrogation box size to remove vectors if the peak ratio (ratio of the highest correlation peak to that of the next highest correlation peak) is less than 1.5 or if the difference from the average of its neighbors greater than 1.3× the standard deviation of its neighbors. Vectors can be iteratively reinserted if the difference to the neighborhood average is less than 1.5× the standard deviation of the neighborhood. These steps help reduce spurious vectors from being computed during the PIV algorithm and passed to the subsequent iteration of smaller interrogation window size. This same vector-post processing also applied after the velocity field is computed on the final interrogation box size. No interpolation is performed at this point and any velocity vectors that had a peak ratio < 1.5 were removed and not reinserted during the final post processing step show up as being equal to 0 when the velocity data is exported from DaVis. Any "0 values" are replaced with NaNs for subsequent data processing in Matlab. It should be noted that the occurrence of NaNs in the high-speed velocity data is rare such that they do not significantly impact the statistical analysis in Ch. 4. After the velocity field is computed from Davis it is exported and further post processed to reduce the impact of noise on the results. A Gaussian filter with $\sigma = 0.5$, is applied to the velocity field with a 3×3 grid kernel where each grid point corresponds to a single 16×16 pixel interrogation box with 50% overlap.

As an example of the measurement capabilities, Fig. 3.8 shows a partial sequence of temporally correlated velocity vectors (mean subtracted) overlaid upon images of the velocity

fluctuation magnitude obtained from flame B (Re = 22,800) at an axial position x/d = 20 and centered around r/d = 2. The size of the images are ~15.7 mm × ~7.7 mm and each image is separated in time by 100 μs with the vectors sub-sampled by a factor of two for visual clarity. The temporally correlated nature of the images showcase the ability to track the velocity field dynamics within the turbulent flame. The velocity fields shown in Fig. 3.8 have been processed in the manner described above with an additional step of interpolation (zero or NaN values) for visual clarity. It should be noted that any statistics derived from the velocity field do not use the locations with interpolated vectors.

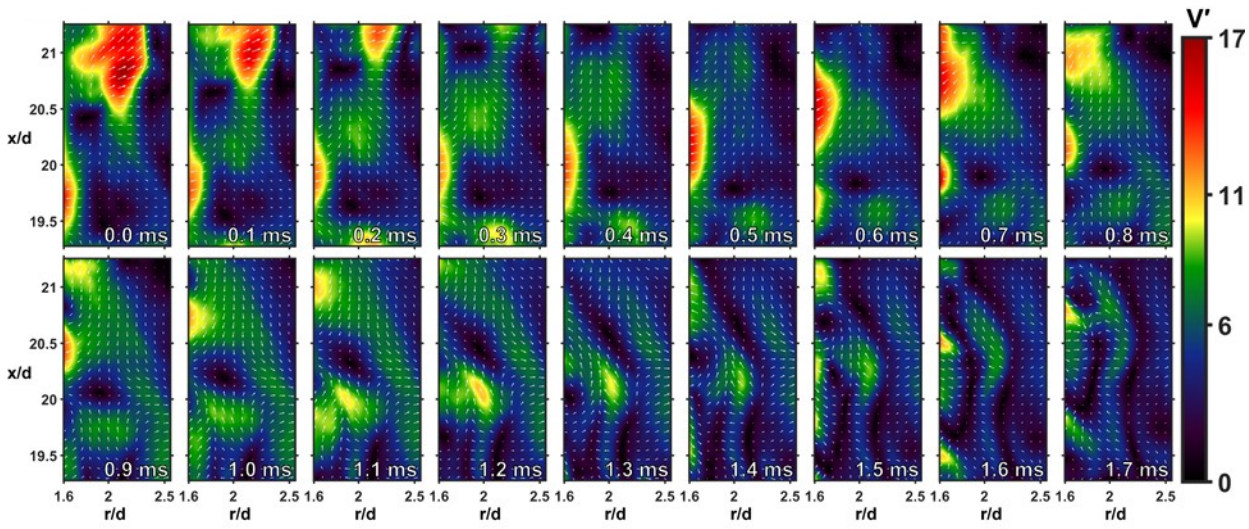

Figure 3.8: Partial image sequence from flame B, x/d = 20, radial FOV#3 (1.68 ≤ r/d ≤ 2.67).

3.3 Measurement Accuracy and Precision

In this section, the accuracy of the measurements as well as the resolution of the measurements will be discussed. The accuracy is assessed by comparing the first two statistical moments (mean and RMS) extracted from the current high-repetition-rate measurements with existing data which is available through the TNF database [6]. The spatial resolution for the temperature measurements is assessed through a series of calibration targets with known size features, while the temporal resolution is assessed through power spectral density (PSD) measurements. More sophisticated and accurate spatial resolution tests are performed for the measurements discussed in Chs. 6 and 7.

3.3.1 Comparison with Previous Results from Literature

To assess the accuracy of the current high-speed measurements, radial profiles of the mean and the root-mean square (RMS) fluctuation of the temperature and velocity fields are extracted from the high-speed image sequences at axial positions of x/d = 10, 20, 40, and 60. The temperature results are compared to point-based data taken at Sandia National Laboratories and the PIV measurements are compared to single-point laser Doppler velocimetry (LDV) measurements acquired at Darmstadt [148] for DLR flame A, both of which appear as part of the TNF data base for the DLR flames [6]. The mean and RMS values from the current high-speed temperature data are determined using the full set of images (200 image/bursts × 200 bursts = 40,000 images). The TNF data were acquired with approximately 1000 uncorrelated simultaneous Raman/Rayleigh/LIF measurements of T, N_2, O_2, CO_2, H_2O, H_2, CO, OH, and NO at low-repetition rates and a spatial resolution of 750 μm. The temperature measurements reported in Ref. [6] are assumed to be an accurate benchmark since the simultaneous Raman/Rayleigh/LIF diagnostics allow measurements

of the species concentrations that can be used to directly calculate the local differential Rayleigh scattering cross section as opposed to the assumption of a constant Rayleigh scattering cross section. The statistics of the current high-speed PIV data are determined from the full set of images (see Table 3.2). The TNF data were acquired with a probe volume of 1 mm long and 0.075 mm diameter.

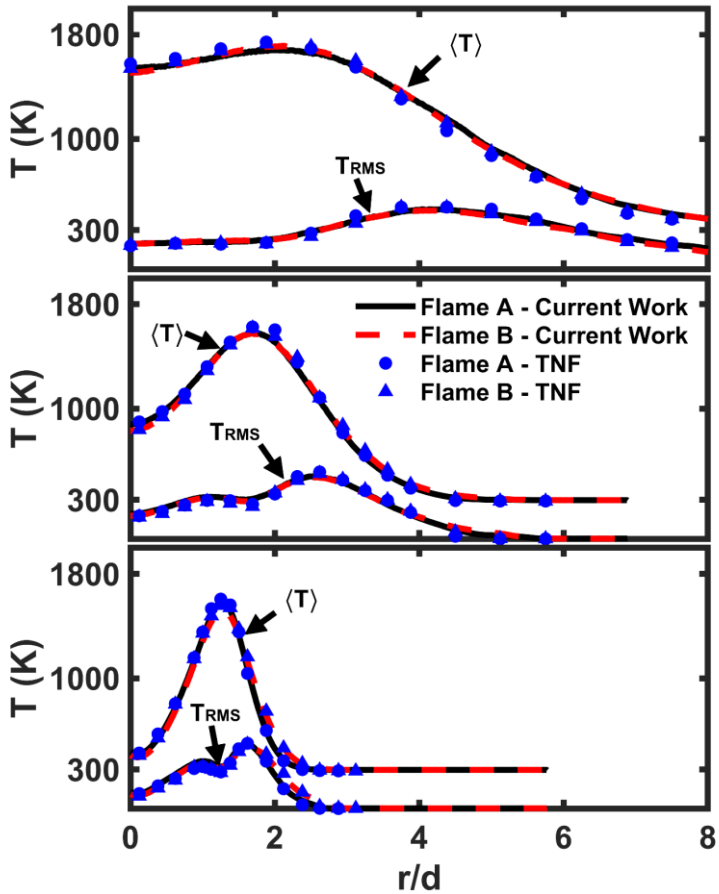

Figure 3.9: Comparison of mean and RMS radial temperautre profiles from the current high-speed imaging results (solid black line for flame A and dashed red line for flame B) and the TNF reference point data (solid blue circles for flame A and solid blue triangles for flame B) from Sandia National Laboratories [6]. (Top) Profile from x/d = 40. (Middle) Profile from x/d = 20. (Bottom) Profile from x/d = 10.

Figure 3.9 shows the comparison of the mean and RMS fluctuations from the current kHz-rate imaging results (shown as lines) and the TNF reference data (shown as solid blue symbols) as a function of normalized radial position for all three axial locations. Figure 3.9 shows that there is very good agreement between the statistics derived from the current high-speed imaging data and the Sandia reference data, both in profile shape and magnitude. In addition, Fig. 3.10 shows a comparison of the derived PDFs of the temperature fluctuation T' from the two data sets at several locations within the flame. These locations include discrete points at x/d = 10, 20, and 40 and at the radial location of mean stoichiometric mixture fraction (as determined from the reference TNF data), which is approximately r/d ~ 1.5 for x/d = 10, r/d ~ 2 for x/d = 20, and r/d ~ 2.5 for x/d = 40. In Fig. 3.10 the results from flame A are shown in the left column and results from flame B are shown in the right column with the current high-speed imaging data shown as a solid red line and the reference TNF data shown as black bars. Each position shows a positive skewness and additionally there is excellent agreement in the shape and mode of the PDFs between the current results and the reference TNF results. Overall, the high level of agreement in all derived statistical quantities from the current high-speed Rayleigh temperature imaging and the results from the simultaneous Raman/Rayleigh/CO-LIF measurements performed at Sandia National Laboratories yields a high degree of confidence in the accuracy of the current temperature results.

Figure 3.11 shows radial profiles of the average axial velocity field and the root-mean square (RMS) of the axial velocity field at axial positions of x/d = 10, 20, 40, and 60 extracted from the current high-speed measurements for both flame A (black symbols) and flame B (red symbols). Also shown in Fig. 3.11 are the results from the two-component LDV measurements for flame A taken from Ref. [148] (blue symbols). While only axial velocity results are shown here, similar comparisons could be made for the radial (v) component. As discussed previously, full

radial profiles have been obtained for the axial locations of x/d = 20 and 40 while at x/d = 10 and 60, only a single FOV was obtained and thus the current measurements are limited to a small radial span. For all axial and radial locations where direct comparisons can be made, there is excellent agreement between the current velocity measurements and the reference velocity measurements for the first two statistical moments of the axial velocity for DLR flame A. This gives confidence in the quantitative nature of the current high-speed PIV measurements for DLR flame A and also gives a high degree of confidence in the results for DLR flame B, which do not appear within the literature, since they were acquired using the same protocol as in the DLR A flames.

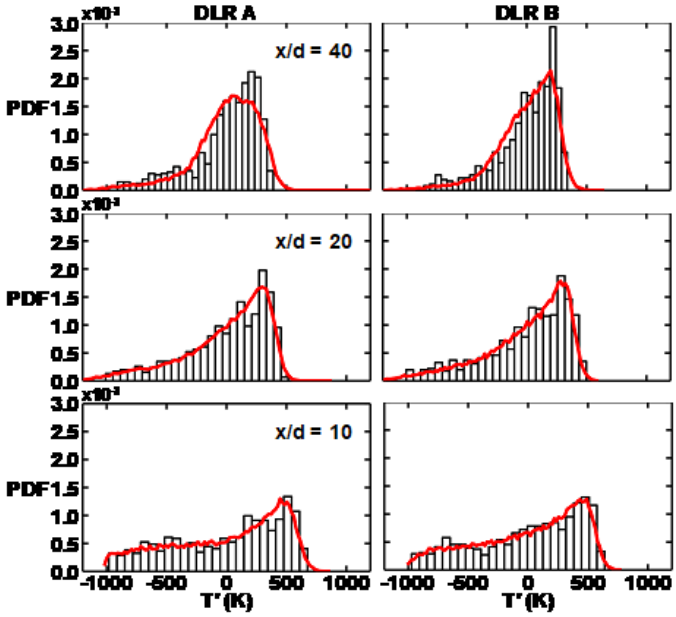

Figure 3.10: Representative pdf estimates of the temperature fluctuations at a single point for x/d = 10 (bottom), 20 (middle), and 40 (top) at the location of mean stoichiometric mixture fraction which is approximately r/d ~ 2.5 for x/d = 40, r/d ~ 2 for x/d = 20, and r/d ~ 1.5 for x/d = 10. Flame A is on the left and flame B is on the right. Current data is shown as a solid red line and the reference data from Sandia [6] is shown as black bars.

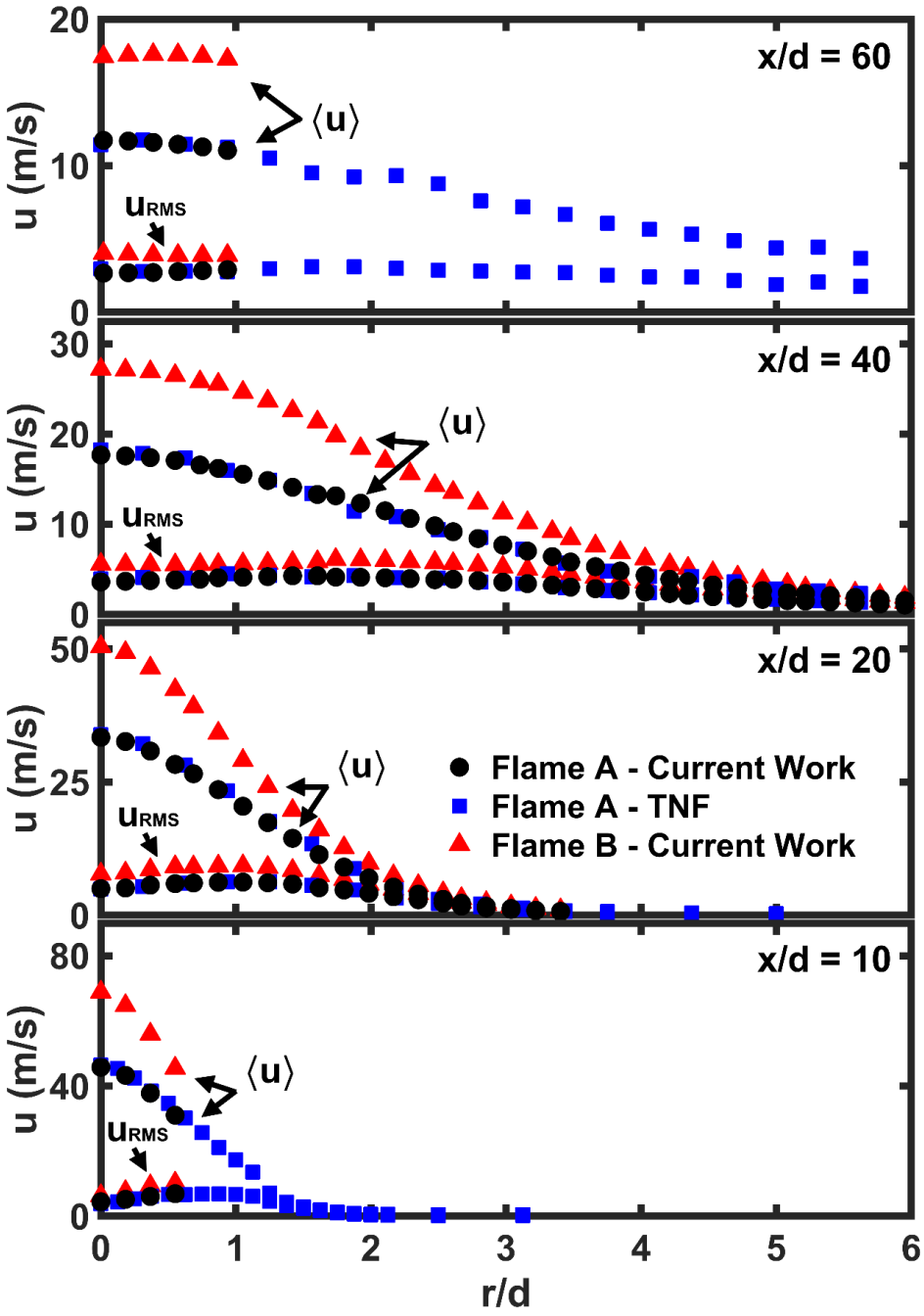

Figure 3.11: Comparison of mean and RMS radial axial velocity profiles for the current high-speed PIV measurements (black circles for flame A, red triangles for flame B) alongside TNF reference data (blue squares) from [148].

3.3.2 Signal-to-Noise Ratio Estimation for LRS Measurements

In addition to accuracy, a high-quality measurement should also exhibit high precision that can be quantified in terms of the signal-to-noise ratio (SNR). Potential sources of noise for the current Rayleigh scattering measurements include sensor "read-noise", which is a result of the conversion of analog voltage to digital signal in the analog-to-digital converter (ADC), and "shot-noise", which is described by a Poisson distribution and is a function of the number of photoelectrons generated by the pixels. The "read noise" does not change with variations in signal levels whereas the "shot-noise" is a function of the number of incident photons. For measurements involving a high levels of incident photons (i.e., high signal levels) the "shot-noise" is much greater than the "read-noise" and the measurement is said to be "shot-noise-limited" [111]. The current high-speed temperature measurements fall into the "shot-noise-limited" category. For an un-intensified camera the shot noise is proportional to the square root of the signal as $N \sim \sqrt{S}$, where N is noise and S is signal [111]. Thus, the signal-to-noise ratio for a "shot-noise limited" measurement is estimated as

$$SNR \sim \frac{S}{N} = \frac{S}{\sqrt{S}} = \sqrt{S} \qquad \text{Eq. (3.3)}$$

indicating that the SNR is proportional to the square root of the signal. In terms of Rayleigh scattering thermometry measurements within a flame, Eq, (3.3) implies that the highest SNR values occur in the cold fuel or coflowing air stream and the lowest SNR values occur in the highest temperature regions in the flame.

In order to estimate the SNR for the current high-speed temperature results, Rayleigh thermometry measurements were obtained in a laminar (Re = 1500) $CH_4/H_2/N_2$ non-premixed

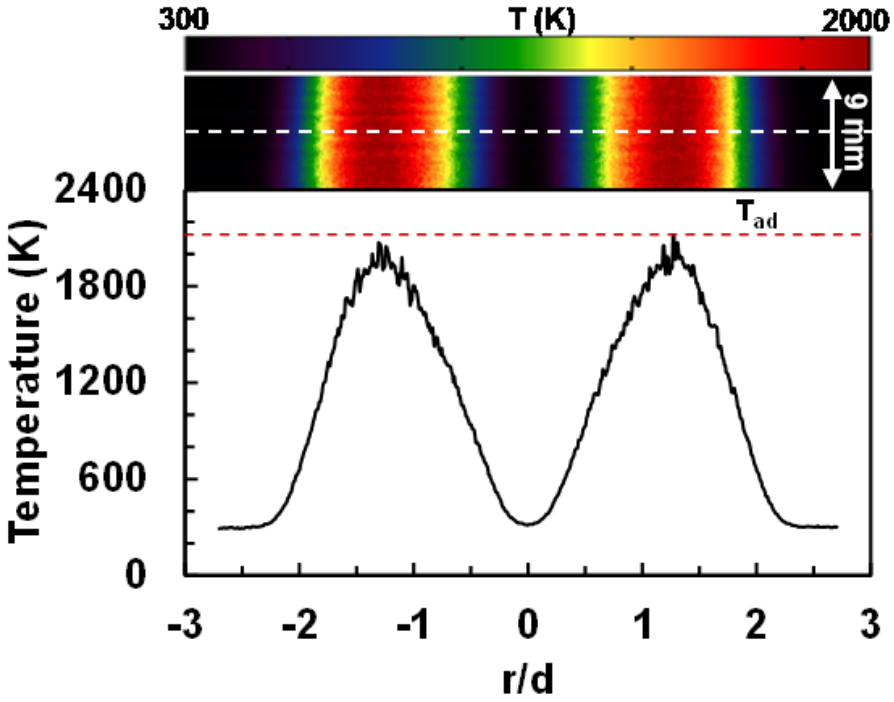

Figure 3.12: (Top) Instantaneous temperature image in a Re = 1500, laminar non-premixed flame with a fuel comprised of the same fuel ratio as DLR flame A and B. Image is acquired at an axial position of x/d = 7. (Bottom) The radial temperature profile corresponding to the axial position indicated by the white dashed line in the top image. The adiabatic flame temperature (T_{ad}) for the current fuel/oxidizer combination is also shown as a red dashed line.

flame with the same fuel composition as that for flame A and B. Figure 3.12 presents an instantaneous temperature image acquired within this flame at an axial location of x/d = 7. The temperature image has been median filtered with a 3×3 kernel to be consistent with the high-speed temperature measurements in the turbulent flames. Shown below the 2D temperature image in Fig. 3.12 is a plot of the radial temperature profile extracted from the 2D temperature image at an axial position indicated by the white dashed line. Also shown on the same radial plot is a red dashed line, which indicates the adiabatic flame temperature (T_{ad}) for the current fuel/oxidizer combination. The utility of acquiring instantaneous temperature images in a laminar flame is the

fact that there are uniform regions at low temperatures (i.e., the coflow) as well as in the high-temperature regions. The SNR can be estimated from these uniform regions, where the SNR is defined as the mean temperature divided by the RMS temperature fluctuations in a uniform region. From the uniform air regions (r/d > 2.5) the SNR is determined to be approximately 90. In a similar manner, a 9-mm axial profile can be extracted from r/d ~ 1.3 and this profile represents a nearly uniform high-temperature region. For this location, the SNR is determined to be ~35 at an average temperature of T = 1900 K. These are significant improvements in SNR as compared to previous high-speed Rayleigh temperature that use high-speed intensified relay optics (IRO) to boost signal levels [149].

3.3.3 Uncertainty and Dynamic Range Estimates for PIV

Following the discussion in section 2.3.2, Table 3.3 lists some of the relevant parameters used in determining the velocity uncertainty, σ_u, and the velocity dynamic range, *DVR*. For the analysis, it is assumed that the nominal clustered particle diameter is d_p = 1 μm and c_τ is 5%. Table 4.5 shows that for the current measurements there is not a significant difference between the diffraction spot size, the optical image diameter, and the recorded image diameter due to the f/16 camera setting. Using c_τ = 5%, the particle displacement uncertainty in the camera image plane is estimated as 0.12 pixels, highlighting the fact that PIV algorithms often have subpixel accuracy in determining the pixel displacement. The uncertainty in the velocity measurement (σ_u) depends on Δt_{PIV} and varies from 0.05 m/s for the largest value of Δt_{PIV} (slow velocities) to 0.58 m/s for the smallest values of Δt_{PIV} (highest velocities). For the two extrema cases, this corresponds to uncertainties of 0.8% at x/d = 10 (u_{max} = 68.9 m/s) and 1.7% at x/d = 40 (u_{max} = 2.9 m/s). Finally, Table 3.3 shows that the dynamic velocity range is estimated as 139.

d_p (μm)	1		d_s (μm)	41.54		$\sigma_{\Delta X}$ (μm)	2.31
M	1		d_e (μm)	41.55		$\sigma_{\Delta X}$ (pixels)	0.12
$f\#$	16		d_r (μm)	20		$\Delta x_{p,Max}$ (μm)	320
λ (nm)	532		d_t (μm)	46.11		DVR	139

Table 3.3: Parameters used to estimate PIV uncertainty and dynamic velocity range (DVR).

3.4 Spatial and Temporal Resolution

An important consideration for any measurement in turbulent flows is the spatial and temporal resolution and how the resolution compares to the smallest expected scales in the flow. As discussed in Chapter 1, the smallest expected length scale within the flow field is the Kolmogorov length scale (λ_κ) which is associated with a corresponding Kolmogorov frequency (f_K). For turbulent scalar fields the smallest expected scales are the Batchelor length scale (λ_B) and the Batchelor frequency (f_B), which are related to λ_κ and f_K as discussed below. Based on non-reacting jet studies, an estimate for determining the local Kolmogorov scale is

$$\lambda_\kappa = 2.3\delta Re_\delta^{-3/4} \qquad \text{Eq. (3.4)}$$

where δ is the local outer scale, which is the half width of the jet; Re_δ is the local outer-scale Reynolds number defined by $Re_\delta = \langle U_c \rangle \delta/\nu$; $\langle U_c \rangle$ is the average centerline velocity; and ν is the kinematic viscosity. The corresponding smallest frequency is a *convective* Kolmogorov frequency estimated as

$$f_\kappa = \frac{\langle U_C \rangle}{2\pi\lambda_\kappa} \qquad \text{Eq. (3.5)}$$

The Batchelor length scale is related to the Kolmogorov length scale through the relation [50]

$$\lambda_B = 2.3\delta Re_\delta^{-3/4} Sc^{-1/2} \quad \text{Eq. (3.6)}$$

where Sc is the Schmidt number. The corresponding smallest frequency associated with scalar fluctuations is a convective Batchelor frequency, estimated as

$$f_B = \frac{\langle U_C \rangle}{2\pi\lambda_B} \quad \text{Eq. (3.7)}$$

For the current scale estimations the kinematic viscosity is determined using $\nu = \nu_0(T/T_0)^{1.7}$, where ν_0 is the kinematic viscosity of air at room temperature, T_0. Using the average temperature results and the average centerline velocity values from measurements acquired in the same flame (discussed below), an estimate of the Kolmogorov length scales and frequencies for the current flames and measurement positions are shown below in Table 3.4. The corresponding Batchelor scales and frequencies can be calculated by assuming a value of the Schmidt number, which is near unity for gas-phase species (e.g., Sc ≈ 0.7 for air at T ≈ 296 K).

	x/d = 10		x/d = 20		x/d = 40	
	λ_κ (μm)	f_κ (kHz)	λ_κ (μm)	f_κ (kHz)	λ_κ (μm)	f_κ (kHz)
Flame A	17.7	402.6	62.2	94.8	243.5	11.4
Flame B	12.0	897.4	41.9	187.9	170.0	25.6

Table 3.4: Estimates of centerline Kolmogorov scales based on Eqs. 3.4 and 3.5.

Table 3.4 shows that resolving the smallest length scales and highest frequencies can be very challenging even in these laboratory-scale flames. However, Wang et. al [50] used time-resolved temperature measurements in flames to show that the resolution requirements for scalars

are not as stringent as resolving the Batchelor length scale and frequency. Specifically, Wang et al. [50] determined that the temporal resolution requirements corresponding to measuring 90% of the scalar variance and scalar dissipation rate are approximately $0.17f_B$ and $0.7f_B$, respectively. From Eq. 3.7 this translates into spatial resolution requirements of $37\lambda_B$ and $9\lambda_B$ for measuring 90% of the scalar variance and scalar dissipation, respectively. Because Sc = O(1) for gas-phase species, the same arguments can be extended to flow field measurements. Based on this rationale, it is expected that in order to resolve 90% of the variance in the velocity fluctuations and 90% of the kinetic energy (or viscous) dissipation, spatial resolution requirements are $37\lambda_K$ and $9\lambda_K$,

	$37\lambda_K$ (μm)	$9\lambda_K$ (μm)
Flame A – x/d = 10	784.4	190.8
Flame B – x/d = 10	532.8	129.6
Flame A – x/d = 20	2749.1	668.7
Flame B – x/d = 20	1853.7	450.9
Flame A – x/d = 40	10767	2619
Flame B – x/d = 40	7518	1828

Table 3.5: Estimates of spatial requirements to measure 90% of the variance of the velocity fluctuation (2nd column) and to measure 90% of the viscous dissipation rate (3rd column) according to work by Wang et al. [50]. Since Sc = O(1), the same guidelines can be applied to the scalar variance and dissipation as well.

respectively. Within the literature, there are a number of additional resolution guidelines for accurately estimating derived quantities such as turbulent kinetic energy [150], Reynolds stresses, [151], and velocity derivatives and vorticity [152, 153]. These recommendations range from $2\lambda_K$ to $10\lambda_K$, which are consistent with the recommendation of $9\lambda_K$ for resolving 90% of the dissipation. Table 3.5 shows estimations of the spatial resolution requirements for measuring the variance and

dissipation rate for the current kHz-rate temperature measurements. From Table 3.5 it is observed that the resolution requirements decrease significantly with increasing axial location. This is due to the fact that with increasing axial location velocities decrease and temperatures increase. The higher temperatures (due to heat release) cause the local kinematic viscosity to increase, which leads to a reduction in the outer-scale Reynolds number and a "laminarization" of the flow field.

3.4.1 Estimation of LRS Measurement Spatial Resolution

As described above, the high output laser energy of the HEPBLS and the use of an improved optical collection system allow the use of a non-intensified CMOS camera for signal collection, meaning that an IRO is not required as in previous studies [149]. In addition to improving SNR, the use of an un-intensified camera leads to improved measurement spatial resolution. An IRO is typically used to boost collected signals in cases where signal levels are low,

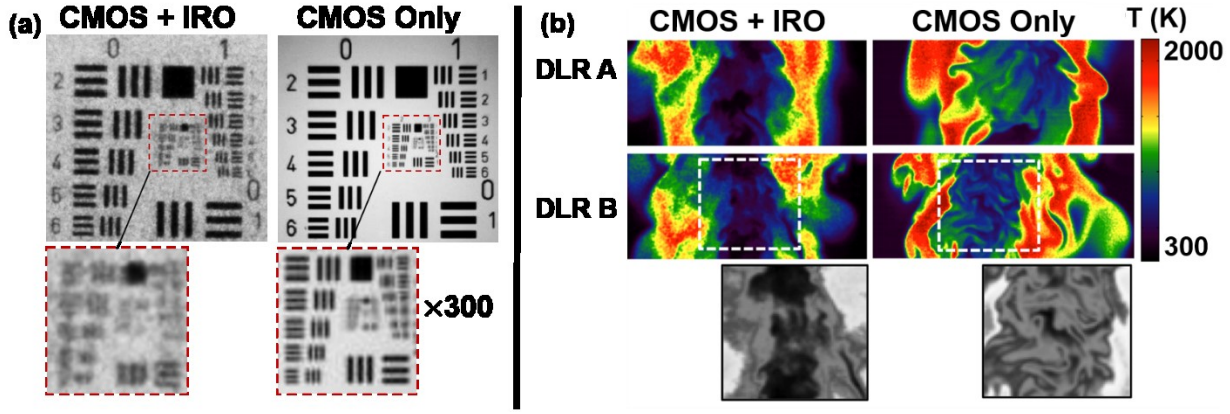

Figure 3.13: (a) Sample images of USAF 1951 resolution target with and without the use of a high-speed image intensifier (IRO). (b) Comparison of turbulent flame images from 10-kHz sample image sequences from a previous study utilizing an IRO (left, [149]) and from the current study with high-energy laser pulses and an unintensified CMOS camera.

but it is known that a two-stage intensifier degrades the spatial resolution of the measurements due to gradient blurring and can also introduce additional sources of spurious noise [115]. Figure 3.13 shows a comparison of images acquired by the combination of a CMOS + IRO and a CMOS camera only.

Figure 3.13a shows a pair of images of a USAF 1951 resolution target acquired with and without the use of an IRO. The IRO gain and exposure time are set to that used previously in turbulent non-premixed studies [149]. The exposure time for the CMOS-only images has been adjusted to have comparable signal levels to those for the current Rayleigh scattering temperature measurements. The FOV for both target images is 41 mm × 61 mm before cropping. Both images are shown with the same dynamic range, meaning the ratio of "light" and "dark" signal from the images are equal. It is clear from Fig. 3.13a that the CMOS-only images show much higher spatial resolution as compared to the CMOS+IRO images. This point is further emphasized by comparing the section of the USAF 1951 target displaying the smallest features as shown in Fig. 3.13a. This section is extracted and magnified by 300% for ease of viewing by the reader. For the CMOS + IRO images, almost all of the individual line-pairs in this magnified region are unable to be distinguished from one another, whereas the same line pairs are distinct in the CMOS-only image. Figure 3.13b shows sample turbulent flame images from flames A and B. The images on the left are from a previous high-speed temperature imaging study using an intensified CMOS camera [149] and the images on the right are from the current measurements an un-intensified CMOS camera. The center portions from both DLR flame B images are enlarged and shown in grey-scale with a 30% increase in contrast ratio to highlight the small scale structures present in the flow. Again, the CMOS-only images show a significant improvement in spatial resolution (and SNR). For the CMOS+IRO images the small scale structure is not discernable, whereas a broad range of

small-scale structures can be discerned with the CMOS-only images. Again, it is noted that the ability to use an un-intensified CMOS camera is due to the use of the HEPBLS and improved optical setup for increased Rayleigh scattering signal collection.

In order to get a quantitative estimate of the in-plane spatial resolution and improvement in spatial resolution from previous work, the USAF 1951 resolution target images shown in Fig. 3.13a are used. It is well known that there are a number ways to estimate the resolution of an optical-based measurement as discussed in Clemens [111]. For the current set of results, the contrast ratio (CR) and modulation transfer function (MTF) are used as metrics of resolution. Figure 3.14 shows a series of normalized signal profiles taken through various bar patterns from the USAF 1951 target image. The profiles acquired with the CMOS-only image are shown as solid red lines and the profiles taken from the CMOS+IRO image are shown as solid blue lines. As observed in Fig. 3.13a, there are a number of sets of bar patterns on the USAF 1951 target which have varying thicknesses and spatial frequencies (units: pairs/mm). The profiles shown in Fig. 3.14a are plotted as normalized signal versus $\Delta x/L$, where Δx is the pixel spacing and L is the local bar thickness. The profiles are taken from regions in the target image where the line thicknesses are L = 446 μm, L = 280 μm, L = 198 μm, and L = 111 μm. The dashed line represents the ideal signal distribution for the bar pattern, i.e. what an ideal sensor would achieve. The profiles from the actual camera setups (CMOS+IRO and CMOS only) reveal the achievable contrast or modulation between the highest and lowest signal that can be obtained for the given optical setup and imaged spatial frequencies.

The profiles in Fig. 3.14 highlight the superior resolving power of CMOS camera system vs the CMOS+IRO camera system. For example, the profiles extracted from the series of 111-μm-

thick bars, show no contrast for the CMOS+IRO system while the CMOS-only profile shows a resolved contrast ratio greater than 0.6 between the highest and lowest signals in the profile. From

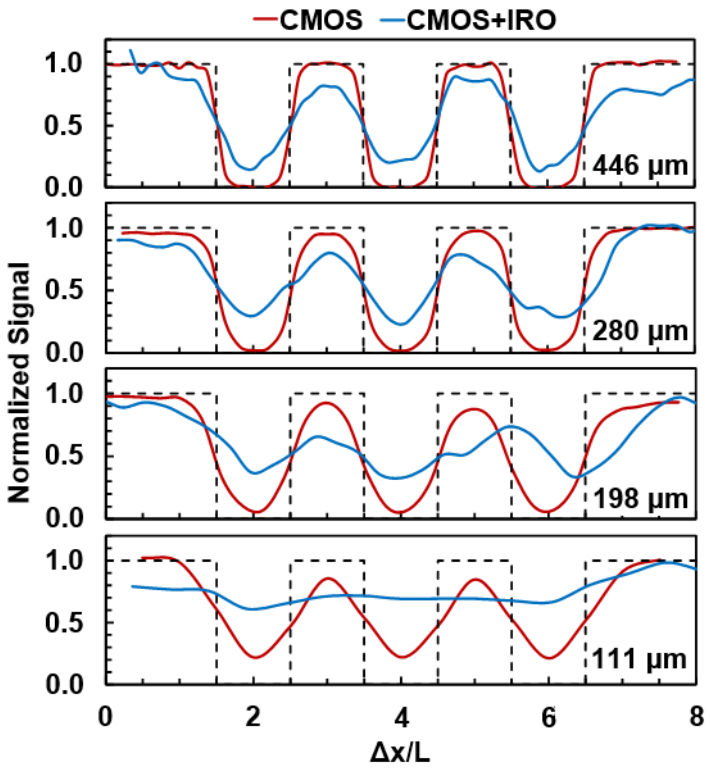

Figure 3.14: Normalized intensity profiles at various spatial positions from images of a USAF 1951 resolution target (Fig. 3.9a) taken with a CMOS+IRO (solid blue lines) and a CMOS only (solid red lines). The bar thicknesses and spatial frequencies are deteremined from the group numbers listed on the USAF 1951 target.

the extracted profiles an estimation of the modulation transfer functions (MTF) for both imaging systems can be made. The MTF is defined as the ratio of the modulation of the image of interest, M_{image}, to the modulation of an ideal image, M_{ideal} where modulation, M, is defined as

$$M = \frac{S_{max} - S_{min}}{S_{max} + S_{min}} \quad \text{Eq. (3.8)}$$

and S_{max} and S_{min} are the maximum and minimum signals in the repeating pattern, respectively. For a normalized signal M_{ideal} is unity and $MTF = M_{image}$ and is described by Eq. 3.8. The MTF for each camera system as a function of spatial frequency is shown in Fig. 3.15. If the 20% MTF value is used as a cutoff defining the resolution of an optical system, then the smallest resolvable scale is approximately 270 µm for the CMOS + IRO system and approximately 120 µm for the CMOS system. These estimates of the in-plane spatial resolution can be compared to the laser thickness of 250 µm, which defines the out-of-plane spatial resolution.

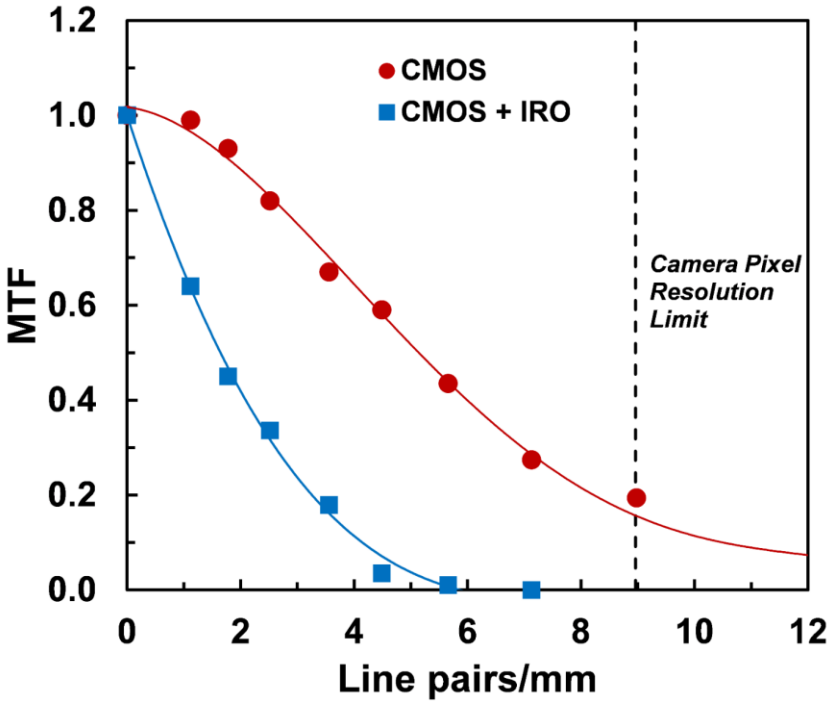

Figure 3.15: Estimated modulation transfer functions (MTF) of a CMOS (red) imaging setup and CMOS+IRO camera imaging setup with the same field of view as that of the current high-speed temperature measurements.

In summary, the estimated smallest resolvable spatial feature is between 120 and 250 μm, depending on which way the temperature gradient is aligned. These values can be compared with the resolution requirements listed in Table 3.5. From an examination of Table 3.5 it is observed that the current measurements satisfy the spatial resolution requirement to resolve 90% of the scalar variance ($37\lambda_B$) for all axial locations examined. The current high-speed temperature measurements also resolve 90% of the dissipation ($9\lambda_B$) for axial locations of x/d = 20 and higher. At x/d = 10, the estimated in-plane spatial resolution is not sufficient to resolve 90% of the scalar dissipation rate.

3.4.2 PIV Measurement Spatial Resolution

The spatial resolution for the velocity measurement is determined by the size of the smallest interrogation box used in the correlation analysis. For the current work, the smallest interrogation window is 16×16 pixels, which corresponds to a spatial resolution of 320 μm. Comparing the PIV spatial resolution with the resolution guidelines shown in Table 3.2 it is observed that the current high-speed PIV measurements sufficiently resolve the variance of the velocity fluctuation at all measurement locations. In addition, the viscous dissipation is well resolved for axial positions for x/d ≥ 20. At x/d = 10, the estimated in-plane spatial resolution is not sufficient to resolve 90% of the viscous dissipation rate.

3.4.3 Estimation of LRS Measurement Temporal Resolution

A useful way to characterize the temporal resolution is to determine the highest resolvable temporal frequency, denoted as f_{res}. While the sample rate (or frequency, f_s) for the measurements, is 10 kHz, f_{res} is less than f_s. In fact, Nyquist-Shannon sampling theory determines that the highest resolvable temporal frequency would be $1/2 f_s$. In order to estimate f_{res}, the

temporal power spectral density (PSD) of the temperature fluctuations is used. Figure 3.16 shows two PSD curves determined from flame A at a spatial position of r/d = 1.5 and x/d = 20 (solid black line) and r/d = 1.5 and x/d = 40 (dashed black line). As expected, both PSDs demonstrate the existence of an inertial subrange. This is due to the fact that for scalars where Sc~1, the PSD follows the same qualitative behavior as that for velocity fluctuations (i.e., "energy spectra") [154]. At higher frequencies, the PSD should continue to decrease into the dissipative range and ultimately fall off. However, due to the presence of measurement noise, the slope of the PSDs will actually level off or increase with increasing frequency. This is due to the added energy content at high frequencies from noise. Using this feature allows an estimation of f_{res}. From Fig. 3.16 and from examination of PSDs determined at other spatial locations, it is estimated that the f_{res} is the current temperature measurements is approximately 4.5 kHz.

Comparing the temporal frequencies in Table 3.4 it is observed that the temporal resolution of the current measurement is not as adequate as the spatial resolution. The Kolmogorov frequencies are not resolved on centerline even at the further downstream axial locations. However, it is noted that Batchelor scale increases and the Batchelor frequency decreases with increasing radial position at all axial locations. An estimation of the Batchelor scale and Batchelor frequency can be extended to other radial locations by calculating an estimate for ν using the local average temperature as opposed to the centerline temperature, while keeping the other parameters needed to calculate $Re_\delta, \lambda_B, f_B, f_{res}$ constant. This analysis shows that the Kolmogorov frequency is resolved for many radial positions at x/d ≥ 20. However, it should be emphasized that the

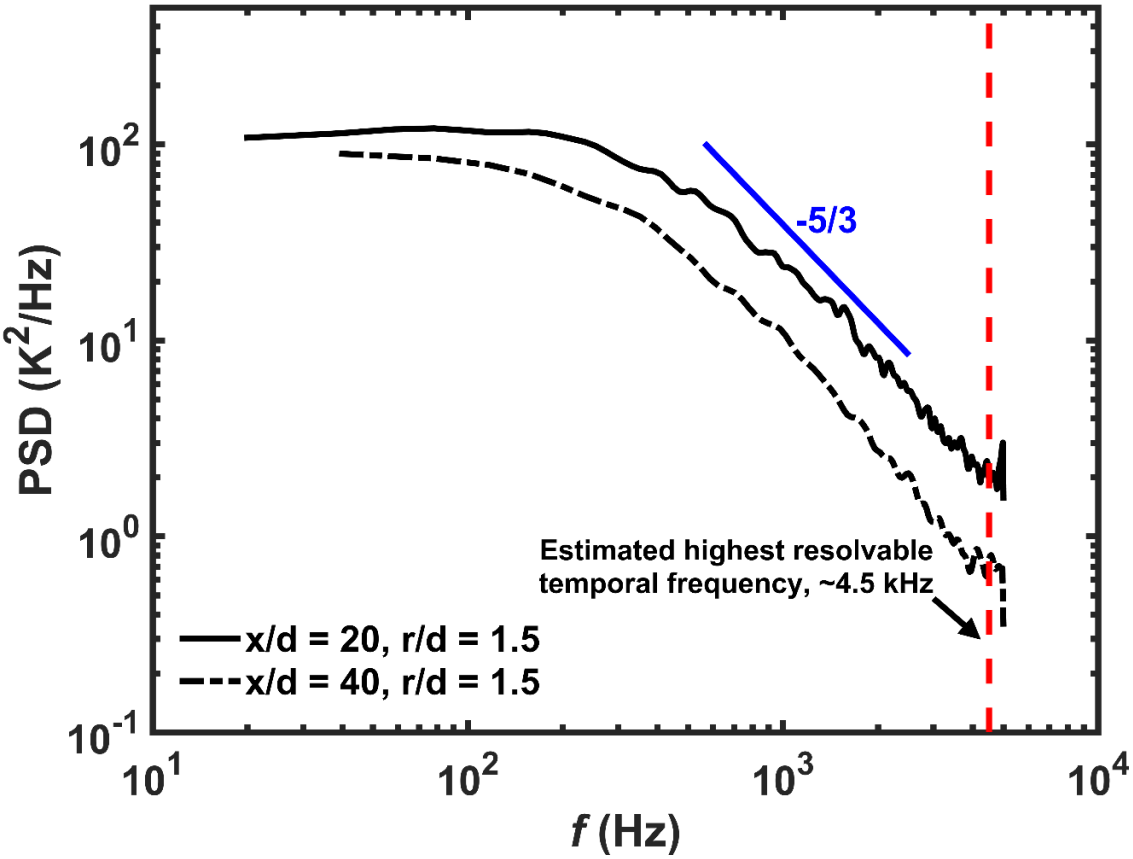

Figure 3.16: Estimates of the power spectral density (PSD) of the temperature fluctuations for flame A from axial locations of x/d = 20 (solid) and x/d = 40 (dashed). The blue solid line shows a -5/3rd slope in log-space. The dashed red line represents the estimate of the highest resolvable temporal frequency.

primary utility of the "temporal aspect" of the current high-speed temperature measurements is to determine large-scale dynamics and derive statistics such as the integral time scales (see Ch. 4). For the current value of f_{res} = 4.5 kHz, processes occurring on time scales of 220 μs or longer can be resolved.

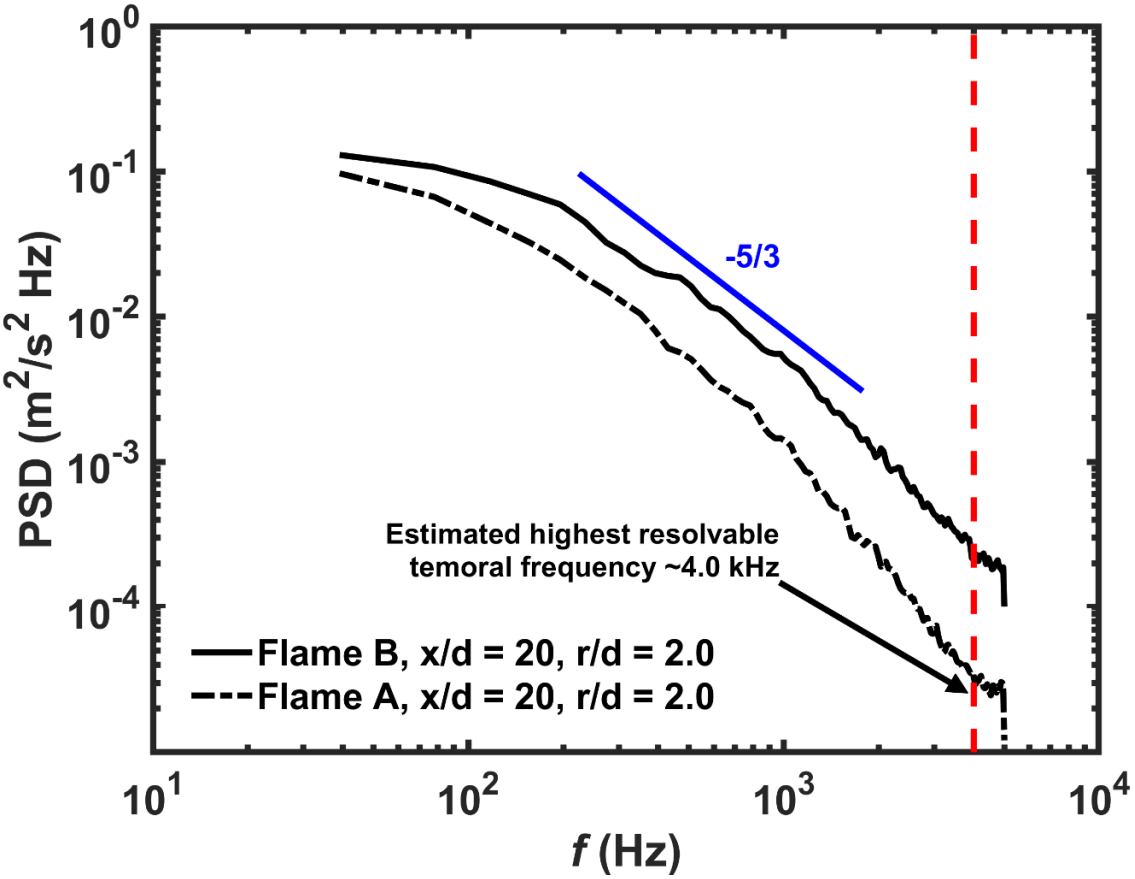

Figure 3.17: Estimates of the power spectral density (PSD) of the velocity fluctuations for flame B (solid black line) and flame A (dashed black line) from the axial location of x/d = 20, and radial location of r/d = 2.0. The dashed red line represents the estimate of the highest resolvable temporal frequency.

3.4.4 Estimation of PIV Measurement Temporal Resolution

The temporal resolution of the high-speed PIV measurements is analyzed in a similar manner as the temperature measurements discussed in Sec. 3.4.3; that is, the power spectral density (PSD) of the velocity fluctuations is calculated. Figure 3.17 shows two PSD curves determined from flame A and flame B at a spatial position of r/d = 2.0 and x/d = 20. The PSD computed from flame A is represented by the dashed black line and the PSD computed from flame B is the solid,

black line. Similar to the temperature fluctuation PSD, the position at which the slope of the PSDs level off or increase with increasing frequency can be used to estimate the highest resolvable frequencies (f_{res}) of the measurement. From Fig. 3.17 and from examination of PSDs determined at other spatial locations, it is estimated that the f_{res} for the current PIV measurements is approximately 4 kHz. For the current value of f_{res} = 4.0 kHz, processes occurring on time scales of 250 μs or longer can be resolved.

Chapter 4. Spatio-temporal Statistical Analysis of Temperature and Velocity Fluctuations in Turbulent Non-premixed Flames

The temporally correlated temperature and velocity imaging described in Chapter 3 enables a spatial and temporal statistical description of the DLR flames. Statistics including probability density functions, joint probability density functions, correlations and corresponding integral scales provide characterization of the flames with a focus on the effects of Reynolds number. While measured separately, the statistics can be used to gather an initial understanding of relationship between the temperature and velocity fluctuations under turbulent non-premixed flame conditions. In addition, new joint spatial and temporal statistics that have not been available previously are used to better understand the mechanisms for how temperature and velocity fluctuations decorrelate within a turbulent reacting flow field. Before proceeding any further, a coordinate system is given in Fig. 4.1. While, the jet is axisymmetric, all calculations are performed on a Cartesian grid and thus "r" represents a Cartesian coordinate. The symbol "r" is used over "y" due to literature convention of reporting the one-dimensional distance from the center of an axisymmetric source in terms of the source's radius (r), diameter (d), or normalized "radial distance" (i.e., r/d)

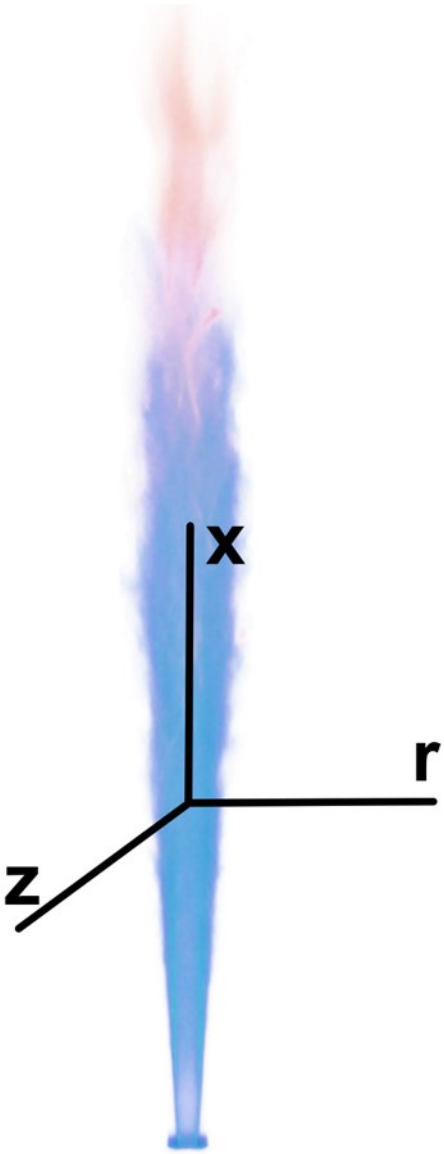

Figure 4.1: Schematic of coordinate system for current work.

4.1 Statistical Characterization of Temperature Fluctuations

Figure 4.2 shows a composite plot of individual probability density functions (*pdf*s) of the temporal derivative, dT/dt (K/μs), as a function of normalized radial position, r/d. For the current results, dT/dt was determined with a first-order forward finite difference scheme. For each radial

position, a “vertical slice” through dT/dt would yield the conventional single-variate *pdf*, where the intensity, shown as a false color scale, represents the probability density of dT/dt, denoted pdf(dT/dt). In Fig. 4.2, pdf(dT/dt) is displayed as its natural logarithm for viewing clarity. As

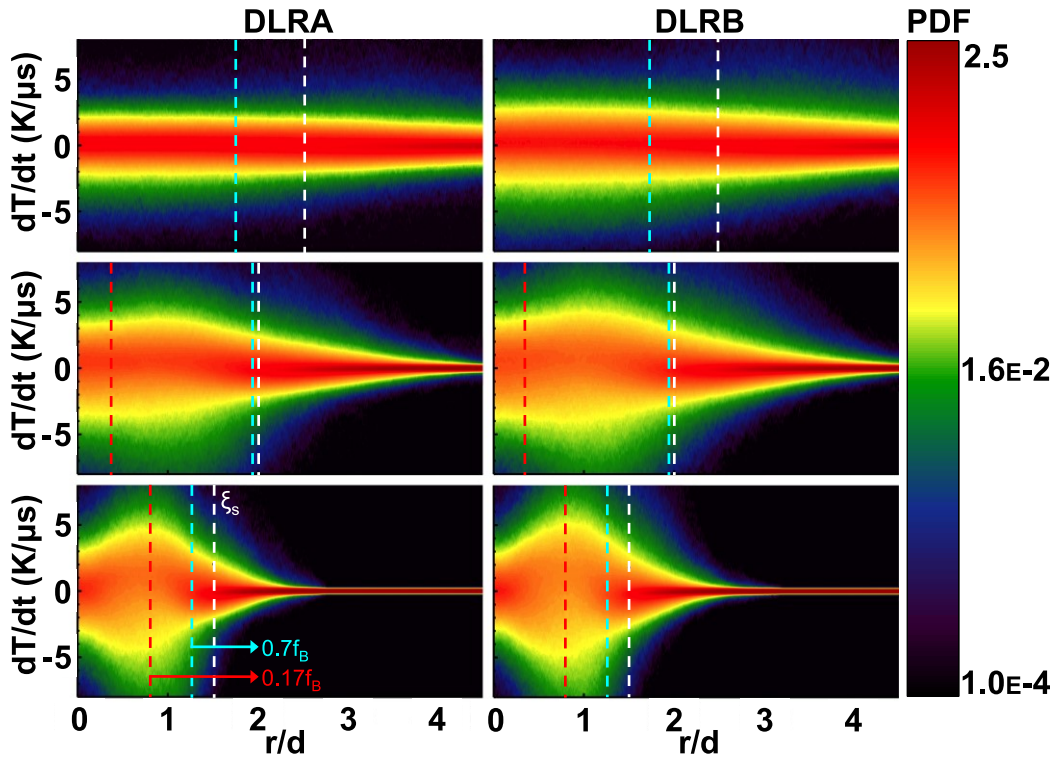

Figure 4.2: Probability density function (pdf) of dT/dt as a function of radial position. (Left) Flame A. (Right) Flame B. (Top) x/d = 40. (Middle) x/d = 20. (Bottom) x/d = 10. The intensity is displayed as the natural logarithm of the pdf. Dashed lines indicate points of note. (Red) where $0.17f_B$ is estimated to be resolved. (Cyan) where $0.7f_B$ is estimated to be resolved. (White) location of mean stoichiometric mixture fraction.

noted in Chapter 3, meaningful statistics require that dT/dt should be sampled such that the smallest temporal fluctuations (or highest temporal frequencies) are resolved. Since the temporal

derivatives are essentially "single point" quantities, the sampling requirements for a scalar correspond to $0.17f_B$ and $0.7f_B$ to properly resolve the scalar variance and scalar dissipation, respectively , according to analysis from Ref. [155]. Shown on Fig. 4.2 are dashed lines indicating where the current measurements are estimated to resolve frequencies of $0.17f_B$ (cyan) and $0.7f_B$ (red). Also shown on Fig. 4.2 is a line (white) indicating the location of mean stoichiometric mixture fraction. The left column of Fig. 4.2 show results from flame A and the right column shows results from flame B. The top two images are from x/d = 40, the middle two images are from x/d = 20, and the bottom two images are from x/d = 10.

It is noted in Fig. 4.2 that for all radial and axial positions, pdf(dT/dt) has a lower peak value and is broader in its distribution for DLR B as compared to DLR B. While this is somewhat expected for a higher-Reynolds number flame closer to the nozzle, the magnitude of the differences is surprising, especially considering that the *ln*[pdf (dT/dt)] is plotted. Furthermore, there is some expectation that the level of temporal fluctuation should be damped out further downstream and the PDFs between DLR A and DLR B would converge to some degree. This is not observed in the current results. In addition to the higher flow velocity, the broad distribution of pdf(dT/dt) for DLR B is likely due to significantly increased levels of local extinction (large negative dT/dt) and the subsequent re-ignition (large positive dT/dt). Noise contributions from the measurements were examined by calculating dT/dt in uniform regions of ambient air (T = 300 K) and in the product gases of a steady, lean premixed H_2/air flame near 1500 K. The mean value of dT/dt in ambient air was -9.5×10^{-7} K/μs and the standard deviation of dT/dt was 2.9×10^{-2} K/μs, while the mean value of dT/dt in the 1500 K product gases was -4×10^{-4} K/μs and the standard deviation of dT/dt was 3.1×10^{-1} K/μs. The standard deviation of dT/dt from the product gases of the premixed H_2/air flame (1500 K) is approximately an order of magnitude smaller than the reported standard

deviation of the pdfs shown in Fig. 4.2 and thus it is concluded that noise effects do not influence the results in the turbulent flame significantly, especially in the context of the comparison between flames DLR A and DLR B.

Figure 4.3 displays the joint probability density function (jpdf) between the temperature fluctuation, $T' = T - \langle T \rangle$ and $ln\left[\left(\frac{dT}{dt}\right)^2\right]$, denoted as β, at a radial position corresponding to the location of the mean stoichiometric mixture fraction. For x/d = 10, 20, and 40, this corresponds to approximately r/d = 1.5, 2.0, and 2.5, respectively. It is noted that this radial location occurs between the mean location of peak temperature and the highest RMS fluctuation. For conditions in which Taylor's hypothesis [156] is valid, $(dT/dt)^2$ is proportional to the axial component of the thermal dissipation rate and thus is used as a surrogate of the axial component of the thermal dissipation rate in this section. However, even for conditions where Taylor's hypothesis is not valid, $(dT/dt)^2$ is still a meaningful quantity in the fact that it contains temporal dissipative information; that is, the rate at which thermal fluctuations are destroyed in time.

For both flame A and flame B, the jpdf is centered at positive values for T' (T' = 100 to 300 K depending on flame condition and spatial position) and is centered around small negative values for β. The jpdf centroid approaches T' = 0 with increasing axial position for flame A, but at a somewhat higher value ($T' \sim$ 200K) for flame B. The non-zero mode and negative skewness of the jpdfs (in terms of T') is a physical phenomenon and not an artifact of the measurements. For both flames at x/d = 10 the jpdf has a negative slope, indicating the negative correlation between T' and $(dT/dt)^2$. However, with increasing axial position, DLR A approaches log-normality; that is T' and $(dT/dt)^2$ exhibit a high level of statistical independence at x/d = 40. The same trend is not observed for DLR B, where at x/d = 40, the negative correlation between T' and $(dT/dt)^2$ still exists.

The apparent Reynolds-number dependence on the convergence to statistical independence between the temperature fluctuations and its surrogate dissipation value may have implications for model formulations wishing to apply statistical independence assumptions over a broad range of conditions.

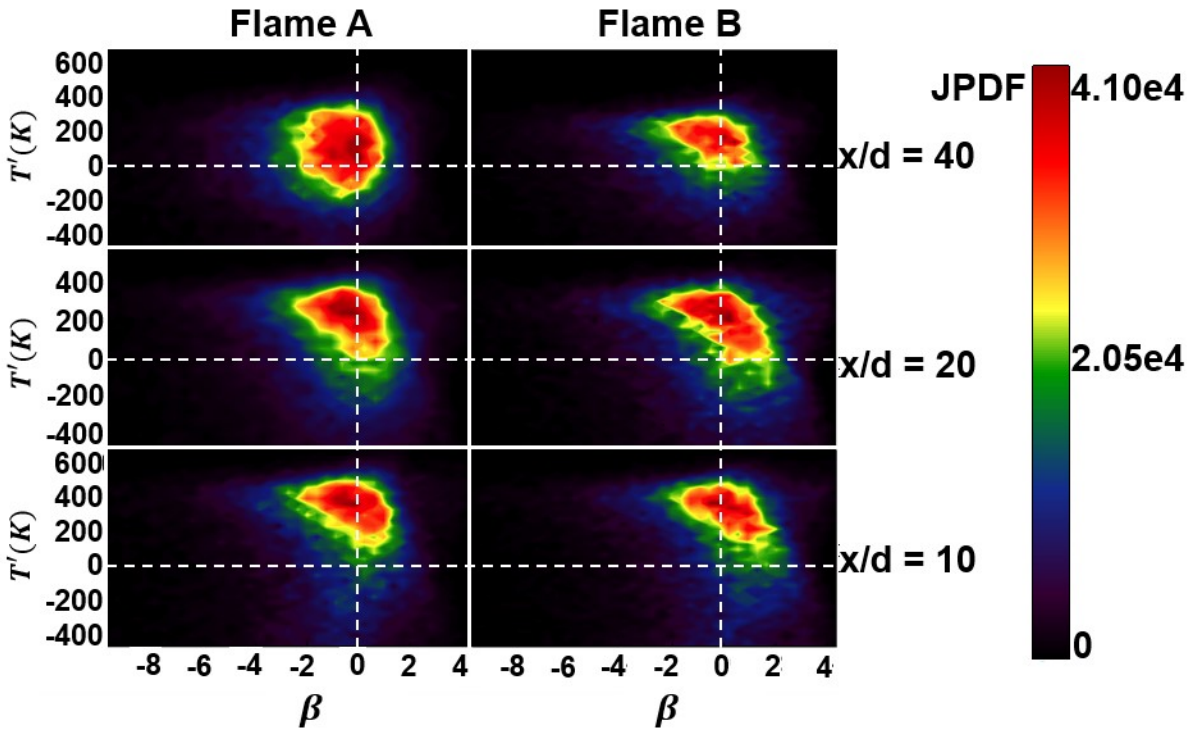

Figure 4.3: Joint probability density function between T' and $[(dT/dt)^2]$ at r/d corresponding to mean position of stoichiometric contour. x/d = 10 (bottom); x/d = 20 (middle); x/d = 40 (top). Intensity is displayed as the natural logarithm of the probability density; red values indicate high probability; black values indicate low probability.

4.2 Correlation and Integral Scales

4.2.1 Determination of Integral Scales from High-speed Measurements

The two-dimensional, temporally correlated measurements from both the temperature and velocity data allow for the computation of both spatial and temporal autocorrelation functions at various spatial locations. The term 'autocorrelation' refers to the measurement of the correlation of one variable with itself, whether the coordinate is time or space. Since the temperature and velocity data were not obtained simultaneously, cross-correlation analysis is not possible. The temporal autocorrelation for a given flow variable, ϕ' (where ϕ' could be either T' or u') for any given spatial position of interest is determined by

$$R(x_0, r_0, \Delta t) = \langle \phi'(x_0, r_0, t) \cdot \phi'(x_0, r_0, t + \Delta t) \rangle / \phi'^2_{rms}(x_0, r_0) \qquad \text{Eq. (4.1)}$$

where x_0 is the axial point of interest, r_0, is the "transverse" or radial point of interest, and Δt is the temporal lag between successive measurements. The autocorrelation is often considered a measure of the temporal "memory" of a given signal and is frequently applied in turbulent flow analysis. For example, in a region of the flow where the velocity is high or where the turbulent fluctuations are large, one would only expect the signal to exhibit similarity with itself for only a short time period. This would correspond to a low correlation value after a reasonably short temporal lag. On the other hand in a region of flow where the flow moves slowly with low turbulence levels, one might expect that the signal will have similarities with itself over a much longer time period. This would correspond to a higher correlation value over longer temporal lags. Since the data were resolved in both time and space, spatial autocorrelation functions can be computed as well, which also can be referred to as the "two-point" spatial correlation. For two-

point spatial correlation functions where the spatial lag is in the axial (or streamwise) direction, the correlation function is referred to as the longitudinal correlation function and is written as

$$R(x_0, r_0, \Delta x) = \frac{\langle \phi'(x_0,r_0,t) \cdot \phi'(x_0+\Delta x,r_0,t) \rangle}{\phi_{rms}(x_0,r_0) \cdot \phi_{rms}(x_0+\Delta x,r_0)} \quad \text{Eq. (4.2)}$$

where x_0 and r_0 are the spatial point of interest (similar to above for the temporal autocorrelation) and Δx is the longitudinal (or axial) spatial lag. For the case where the spatial lag is in the radial (i.e., lateral or transverse) direction, the correlation is referred to as the transverse correlation function and is calculated in a similar manner to Eq. (4.2) using

$$R(x_0, r_0, \Delta r) = \frac{\langle \phi'(x_0,r_0,t) \cdot \phi'(x_0,r_0+\Delta r,t) \rangle}{\phi_{rms}(x_0,r_0) \cdot \phi_{rms}(x_0,r_0+\Delta r)} \quad \text{Eq. (4.3)}$$

where Δr is the spatial lag in the radial direction. The spatial correlations given in Eqs. (4.2) and (4.3) represents the spatial "memory" of a given signal in a similar manner to the time memory of the temporal autocorrelation function. Of course the physical mechanisms for how a given signal decorrelates both in space and time depends on the nature of the signal itself (i.e., temperature or velocity fluctuation) the particular turbulence characteristics of the flow, and the effects of reaction for combustion environments.

The decorrelation of the temperature or velocity fluctuations and their dependence on spatial location and Reynolds number are described in a more quantitative manner by computing the integral time and length scales from the calculated temporal autocorrelation and spatial correlation functions. The integral scales provide a concise method for measuring the spatial or temporal "memory" of the flow. The integral scales are defined as

$$I_s(x_0, r_0) = \int_0^\infty R(x_0, r_0, \Delta s) d\Delta s \quad \text{Eq. (4.4)}$$

where s in Eq. (4.4) represents either time, the axial dimension, or the radial dimension and I_s is the integral time/axial length/radial length scale. For turbulent flows, the integral scales can be thought of as representing the scales of the largest eddies in the flow which transfer energy to smaller scales until the eddies are small enough such that their energy is dissipated through viscous processes at the smallest scales present in the flow (Kolmogorov scale for velocity and Batchelor scale for scalars). In principle, if a given data set (i.e., velocity or scalar) extends axially, radially or temporally to infinity, then the integral scales are determined through direct integration using Eq. (4.4). In practice, data record lengths are finite due to finite measurement domains and recording memory. In addition, for longer lags where the correlation values are small, noise may become a problem. In this manner, direct integration of the correlation functions using Eq. (4.4) may not be preferred. For the current set of measurements, a two-part approach was adopted to compute the integral length and time scales. Briefly, the correlation curves are first fit using an exponential function of the form $a\exp(bs)$ (where s represents either Δx_i or Δt) from the lag where the correlation equals 0.8 to the lag at which the correlation has decreased to $\exp(-2)$, denoted s_1. This exponential function represents the high Reynolds number functional form of the correlation function and is denoted as HRC [157]. Since this fit is smooth and continuous, it can be integrated to infinity without adverse effects of noise. Subsequently, the integral scales are determined by adding the integration of the actual, measured correlation curve from lag 0 to s_1 with the integration of the HRC with limits of s_1 to ∞ as written in Eq. (4.5)

$$I_s(x_0, r_0) = \int_0^{s_1} R(x_0, r_0, s)ds + \int_{s_1}^{\infty} a\exp(bs)\,ds \qquad \text{Eq. (4.5)}$$

Directly integrating the correlation from lag 0 to s_1 accounts for any Gaussian-like behavior of the correlation which may be present at short lags. Integrating the fits after the lag at which the correlation equals $\exp(-2)$ mitigates noise which is non-negligible for large lags.

4.2.2 Comparison of Temperature and Velocity Integral Scales

The temporal autocorrelations have been computed using Eq. (4.1) for the temperature and axial velocity fluctuations. Subsequently, the integral time scales were computed as a function of radial location (normalized by the jet diameter, d) for axial locations of x/d = 20 and 40. It should be noted that the integral time scale is computed only at locations where there is sufficient temporal resolution. This criteria is satisfied when the temporal lag is greater than twice the temporal spacing (100 μs) when the autocorrelation reaches the value of $1/e^2$. This satisfies the Nyquist-Shannon sampling requirements. As a result, integral time scales of the temperature fluctuations are not presented for r/d < 0.2 and r/d < 0.7 for flame A and B, respectively. Figure 4.4 shows the integral time scales as a function of radial position for axial velocity fluctuations for flame A (solid blue) and flame B (dashed green) and for temperature fluctuations for flame A (solid black) and for flame B (dashed red). The gaps in the integral time scales for the axial velocity fluctuations are due the finite size of the FOV for the PIV measurements. Figure 4.4 shows that for a given Reynolds number, the integral time scale is larger for the axial velocity fluctuations as compared to the temperature velocity fluctuations at all axial and radial positions. Thus, it takes a longer time for the axial velocity fluctuations to de-correlate than the temperature fluctuations. This shows that the temperature fluctuations are destroyed faster than the axial velocity fluctuations and can imply that the effective 'mixing time' for temperature is shorter than that of the axial velocity fluctuations due to increased thermal diffusion and dissipation as compared to that of the kinetic energy. It is

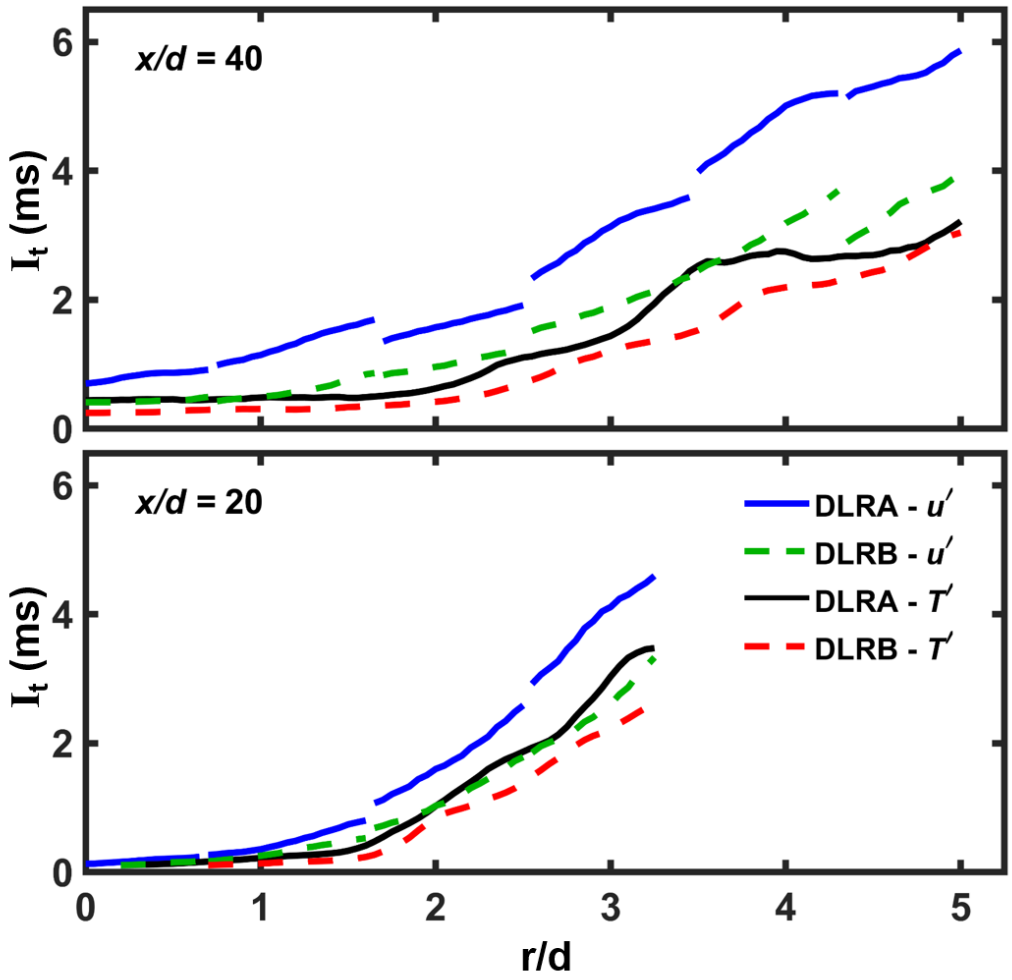

Figure 4.4: Integral time scale for flame A axial velocity fluctuations (solid blue) and temperature fluctuations (solid black) and flame B axial velocity fluctuations (dashed green) and temperature fluctuations (dashed red) versus radial position for $x/d = 40$ (top) and $x/d = 20$ (bottom).

noted that for the higher-Reynolds number case (flame B) the integral time scales for the velocity and temperature fluctuations are closer relative to one another compared to flame A. This implies that the increase in axial kinetic energy dissipation (relative to the thermal dissipation) is greater for flame B compared to flame A.

The spatial integral length scales I_x and I_r, which are derived from the longitudinal and transverse spatial cross-correlations using Eqs. (4.2) and (4.3), are shown as a function of normalized radial position (r/d) in Fig. 4.5. Results are shown for both flames and for both temperature and axial velocity fluctuations at x/d = 20 and x/d = 40. Shown in the left column are plots for the longitudinal integral scales and the center column shows the results for the transverse integral scales. Also shown in Fig. 4.5 in the right column are results displaying the ratio of the longitudinal to transverse length scales (I_x/I_r) as a function of radial position for the different data sets. The ratio of I_x/I_r can be used to characterize the degree of isotropy present in the flow. For turbulent velocity fluctuations in an isotropic flow it can be shown the ratio of longitudinal to lateral integral length scales should be 2 [158]. In contrast, for turbulent scalar fluctuations it can be shown that the ratio of longitudinal to lateral integral length scales should be 1 for an isotropic flow. Any deviation from those values imply non-isotropy in a flow which can arise from a number of reasons, including shear effects and/or heat related effects.

It should be noted that the spatial resolution of the measurements is sufficient to resolve the shape of the spatial correlation functions, but due to the finite FOV size for the velocity measurements it was not possible to capture the full spatial decorrelation of u'. Previous work in our lab has shown that it is necessary to capture the decorrelation of the correlation functions down to at least 0.5 in order to recover an accurate integral length scale estimation [159]. For spatial locations where this is not satisfied the integral length scale is not computed. This constraint did not allow the computation of the longitudinal integral length scales of the axial velocity fluctuations for r/d > 2.5 at x/d = 40 for flame A and for r/d > 2.8 at x/d = 40 for flame B. In addition, the transverse integral length scales of the axial velocity fluctuations are limited to regions closer to centerline at x/d = 20 due to the relatively narrow width of the PIV FOV.

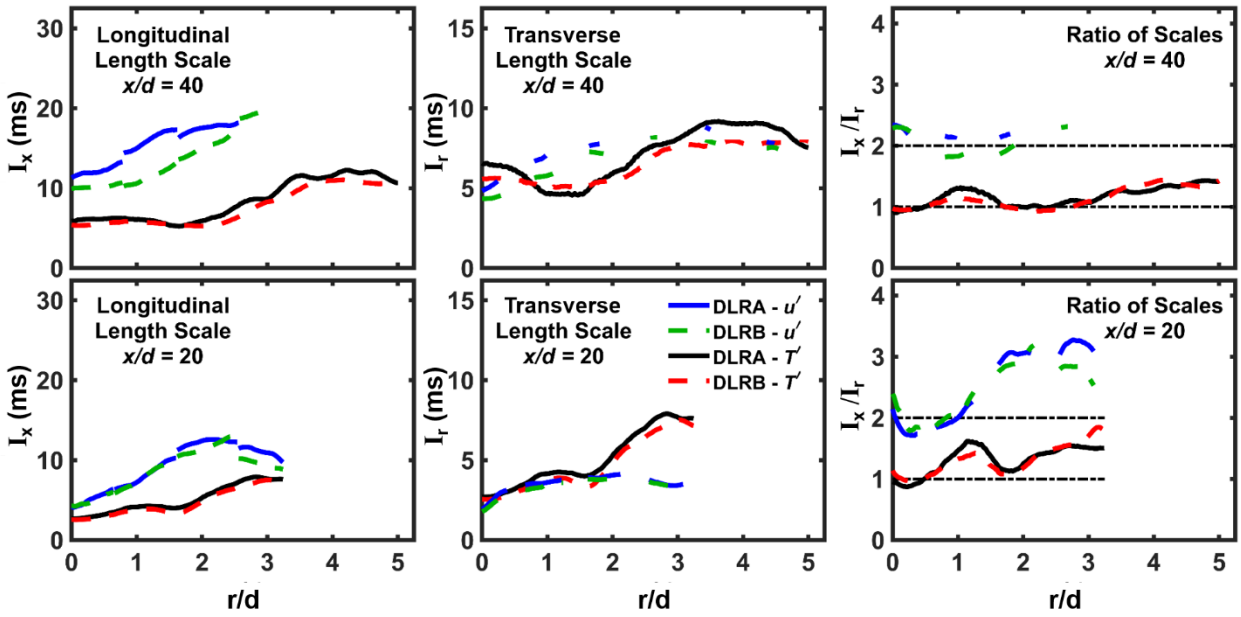

Figure 4.5: Longitudinal integral length scale, I_x (left), transverse integral length scale, I_r (center), and the ratio of I_x/I_r (right) versus normalized radial position for flame A axial velocity fluctuations (solid blue), flame B temperature fluctuations (solid black), flame B axial velocity fluctuations (dashed green), and flame B temperature fluctuations (dashed red). Results are shown for x/d = 40 (top) and x/d = 20 (bottom).

Examining the longitudinal integral length scales for the temperature fluctuations ($I_{x,T}$), it is observed that the integral length scales are approximately the same for both Reynolds number flames and at all radial locations for both axial locations. The same trends are observed for the longitudinal integral length scale of the axial velocity fluctuations ($I_{x,u}$) at x/d = 20. However, there are differences between $I_{x,u}$ for the two Reynolds number flames at x/d = 40. For that case, the higher Reynolds number flow (flame B) has a smaller $I_{x,u}$ as compared to flame A. This is possibly due to the higher levels of heat release at x/d = 40, leading to a more of "laminarization" of the lower Reynolds number flame. The increased occurrence of local extinction for flame B compared to flame A may also play a role as there would be more samples at lower temperatures

and relatively higher local Reynolds numbers. The same result is observed for the transverse integral scales of the velocity fluctuations ($I_{r,u}$) for both Reynolds numbers at x/d = 20. However, at x/d = 40, there are some small discrepancies between the lateral integral scales (temperature and velocity fluctuations) for the two Reynolds number flames. Again, since Reynolds number dependencies typically are not observed in integral length scales for non-reacting flows, this affect is likely due to heat release effects and/or extinction effects.

Similar to the integral time scale results shown in Fig. 4.4, the longitudinal integral length scales are larger for u' as compared to those for T'. The difference between the longitudinal integral length scales of $u'$and T' is more pronounced near centerline compared to the differences observed between the integral time scales. For instance, for both flames at x/d = 40 $I_{t,u}/I_{t,T} \approx 1.6$ and $I_{x,u}/I_{x,T} \approx 1.9$ while at x/d = 20 $I_{t,u}/I_{t,T} \approx 1.5$ and $I_{x,u}/I_{x,T} \approx 1.7$. Additionally, at x/d = 20, Fig. 4.5 shows that $I_{x,u}$ increases with increasing radial distance until r/d = 2 and then decreases, while $I_{x,T}$ actually decreases from r/d = 1 to r/d = 2. At x/d = 20 the mean peak temperature is located at approximately r/d = 1.7. This indicates that the values of $I_{x,u}$ are likely increasing due to increases in temperature which increase the kinematic viscosity and effectively lowers the local Reynolds number (i.e., "laminarization"). In contrast, with increasing temperature there is increased reactivity, which leads to more rapid destruction of temperature fluctuations and thus, smaller integral scales. Similar trends are observed at x/d = 40.

A comparison of the lateral integral length scales shows that at x/d = 20, $I_{r,u}$ and $I_{r,T}$ closely track one another from centerline to approximately r/d = 1.8. For radial positions r/d > 1.8, the two lateral length scales diverge as $I_{r,T}$ rapidly increases while $I_{r,u}$ remains constant or slightly decreases. At x/d = 40, there are distinct differences between $I_{r,u}$ and $I_{r,T}$ across the radial

locations. Near centerline $I_{r,u}$ increases while $I_{r,T}$ decreases slightly. $I_{r,u}$ continues to increase and peaks at approximately r/d = 2.6 where it then starts to decrease. In contrast, $I_{r,T}$ decreases near centerline until it reaches a minimum near r/d = 1.5 and then increases until r/d = 4. The results at x/d = 20 and 40 show the competing effects of axial velocity and temperature profiles (on $I_{r,u}$ and $I_{r,T}$) as a function of radial position. The reader is referred to Figs. 3.9 and 3.11 for the mean temperature and velocity profiles. For $I_{r,u}$ the decrease in axial velocity and increase in temperature (until r/d = 1.7 at x/d = 20 and r/d = 2.4 at x/d = 40) both lead to lower values of the local Reynolds number and thus an increase in the transverse integral scale. For larger radial positions, the velocity continues to decrease, but the temperature also decreases and thus the two effects offset one another leading to the near constant values of $I_{r,u}$. For $I_{r,T}$ at x/d = 20, the initial decrease in velocity and the increase in temperature leads to lower values of the local Reynolds number and hence an increase in $I_{r,T}$. However, near r/d = 1.7, the highest temperatures lead to peak reactivity, which lead to a decrease in $I_{r,T}$. For larger radial positions, the higher temperatures and lower velocities lead to large increases in $I_{r,T}$. A similar analysis can be performed at x/d = 40 by examining the mean velocity and temperature profiles.

The ratio of the integral length scales (I_x/I_r) as a function of radial position for both axial velocity and temperature fluctuations for both Reynolds number flames are shown in the right column of Fig. 4.5. For a given quantity (u' or T') the radial variation is largely independent of Reynolds number. For the axial velocity fluctuations $I_{x,u}/I_{r,u}$ is approximately two near centerline for x/d = 20 and x/d = 40 implying isotropy for both flame A and B. At x/d = 20, $I_{x,u}/I_{r,u}$ remains near two for radial positions < r/d = 1.1, but increases to approximately a value of three for radial locations further way from centerline. It appears that in terms of the axial velocity

fluctuations, there is a degree of isotropy near centerline under the colder, more turbulent conditions, but the isotropy is destroyed in the high-temperature, high-reactivity regions of the flow. The ratio of integral scales for the temperature fluctuations ($I_{x,T}/I_{r,T}$) is approximately one for the majority of radial locations measured at x/d = 40 except for r/d > 3.3. At x/d = 20 $I_{x,T}/I_{r,T}$ is approximately one from centerline to approximately r/d = 0.55, at which the ratio of integral length scales increases to a local peak near r/d = 1.25, decreases to near one again near r/d = 1.8 and then increases to a value of approximately 1.7 near r/d = 3.2. From these results it appears that the velocity and temperature fluctuations follow similar trends in terms of I_x/I_r; that is, the flow appears isotropic near centerline, but the isotropy is destroyed in regions of high temperature or more specifically, regions corresponding to large temperature gradients. In addition, the flow appears to become more isotropic with increasing axial locations. However, it should be noted that that at x/d = 40, the limited FOV leads measurements at much smaller r/δ, where δ is the outer scale and r/δ represents a similarity coordinate. When the I_x/I_r results are plotted against r/δ (not shown), the results collapse and thus measurements at further radial positions would be needed at x/d = 40 to see the departures from isotropy.

4.3 Multi-Point Spatial Correlations

The two-dimensional spatial information allows for the computation of multi-point spatial correlation maps. A multi-point spatial correlation is defined in this work as the correlation of any point of interest (x_0, r_0) with another point offset axially or radially. The multi-point spatial correlation is given by

$$R(x_0, r_0, \Delta x, \Delta r) = \frac{\langle \phi\prime(x_0,r_0,t)\cdot\phi\prime\,(x_0+\Delta x,r_0+\Delta r,t)\rangle}{\phi_{rms}(x_0,r_0)\cdot\phi_{rms}(x_0+\Delta x,r_0+\Delta r)} \qquad \text{Eq. (4.6)}$$

where Δr is the radial (transverse or lateral) spatial lag. This is similar to Eqs. (4.2) and (4.3) with the added complexity of being a function of both the radial and axial spatial lag. From inspection it is noted that the longitudinal and transverse spatial correlation curves are simplifications of the multi-point spatial correlation and thus the longitudinal and transverse integral length scales can be determined from Eq. (4.6). For example, for a given spatial correlation map, vertical movement along a line of fixed radial lag yields the two-point spatial longitudinal correlation and longitudinal integral length scale as discussed above. Similarly, horizontal movement along a line of fixed axial lag yields the two-point transverse correlation function and the transverse integral length scale. The utility of the multi-point spatial correlation map is that it highlights directionality associated with the spatial decorrelation of a particular quantity of interest, ϕ. It can show the preferred direction in which ϕ stays correlated longest or the direction that leads to the fastest decorrelation. These maps are especially useful in terms of comparing the spatial decorrelation of temperature and velocity. For example, by observing the preferred direction of correlation, (i.e. the direction of shallowest decorrelation descent), the direction with strongest transport can be determined.

Sample multi-point spatial correlation maps are shown below in Fig. 4.6 for flame A axial velocity fluctuations (solid blue), flame A temperature fluctuations (solid black), flame A axial velocity fluctuations (dashed green), and flame B temperature fluctuations (dashed red). Various spatial correlation maps are shown which are centered on individual points of interest (x_0, r_0) in the flame as shown with red x's. The spatial correlation maps in Fig. 4.5 are shown as contour maps with two isocontours for each variable (T and u) and for each Reynolds number flame (A and B). The isocontours include the correlation values of 0.9 and 0.7. At $x_0/d = 40$, correlation maps are centered on centerline, near the location of peak $\langle T \rangle$ ($r_0/d = 2.2$), and near the location of

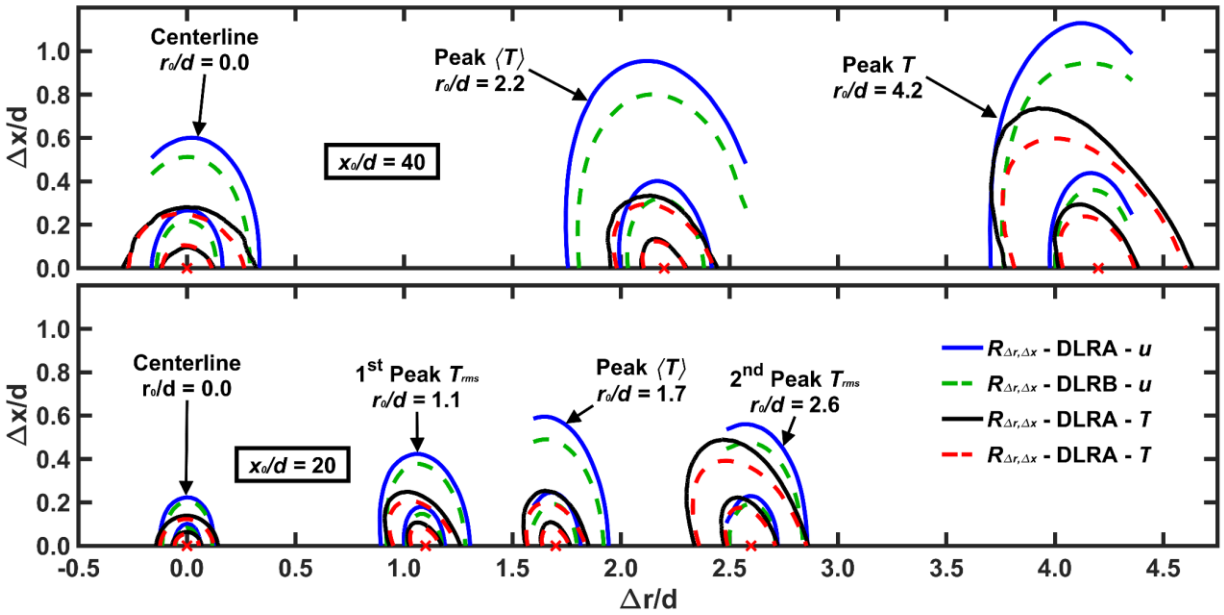

Figure 4.6: Sample spatial correlation maps showing two correlation isocontours (0.7 and 0.9) for flame A axial velocity fluctuations (solid blue), flame A temperature fluctuations (solid black), flame B axial velocity fluctuations (dashed green), and flame B temperature fluctuations (dashed red). Results are shown for x/d = 40 (top) and x/d = 20 (bottom). The correlation maps are centered on various origin points shown as red x's.

peak T_{rms} ($r_0/d = 4.2$). At $x_0/d = 20$, correlation maps are centered on centerline, near the locations of peak T_{rms} ($r_0/d = 1.1$; $r_0/d = 2.6$), and near the location of peak $\langle T \rangle$ ($r_0/d = 1.7$). While the limited FOV for both data sets are not able to capture the full spatial decorrelation of T or u in all directions, important information concerning the decorrelation of T' and u' is gleaned from these spatial correlation maps.

An important feature of the multi-point spatial correlation maps is the directionality of the contours. For x/d = 20 and 40 at centerline, the correlation maps for both u' and T' are preferably aligned in the vertical direction; that is, the correlation maps exhibit symmetry about a vertical line at $\Delta x_0/d = 0$. With increasing radial distance from centerline the spatial correlation maps begin to

differ between u' and T'. For both u' and T', the orientation of the correlation maps are aligned towards centerline, although the alignment away from vertical is slight for u'. At the locations of peak $\langle T \rangle$, the orientation of the axial velocity and temperature fluctuation correlation maps are the closest, while at the locations of peak T_{rms}, the temperature fluctuation correlation maps are aligned much more steeply towards centerline than the axial velocity fluctuations.

An angle can be defined for the alignment directions in terms of the shallowest descent in correlation relative to vertical direction; that is a negative angle would imply a direction pointing towards centerline. The angle for each correlation map is determined by fitting a line to the set of points originating at $(r_0/d, x_0/d)$ and passing through $(r_m/d, x_m/d)$, where $(r_m/d, x_m/d)$ is the normalized radial and axial positions at peak correlation. The arctan of the slope yields the angle of the orientation of the spatial correlation maps. For the sample spatial correlation maps shown in Fig. (4.6), the orientation angle for the temperature fluctuations for both flames A and B at x/d = 40 is approximately -14° for r/d = 2.2 (location of peak $\langle T \rangle$) and -18° for r/d = 4.2 (location of peak T_{rms}). This can be compared to the orientation angle of the axial velocity fluctuations for both flames at x/d = 40 of approximately -5° at r/d = 2.2 and -3° at r/d = 4.2. At x/d = 20 the orientation angle of the temperature fluctuations for both flames A and B is approximately -19° for r/d = 1.1 (location of the first peak T_{rms}), -11° for r/d = 1.7 (location of peak $\langle T \rangle$), and -15° for r/d = 2.6 (location of the second and highest peak T_{rms}). Again, these can be compared to the orientation angles for the velocity fluctuations for both flames of approximately -5° for r/d = 1.1, -5° for r/d = 1.7, and -3° for r/d = 2.6. Overall, it appears that the correlation maps for u' are largely aligned in the vertical direction for all radial positions with slight inclinations toward centerline, while at regions of intense turbulence and shear (as denoted by the local peaks in T_{rms}) the temperature fluctuation contours are aligned away from the velocity fluctuation contours.

Probability density functions (PDFs) of the orientation angles of thermal dissipation structures were estimated from the $|\nabla T'|^2$ field in the same DLR flames at x/d = 20 in Ref. [52]. The results showed that the angle of the normal vector from the dissipative structure (pointing from the cold side of the structure to the hot side of the structures) is negative with respect to the x-axis. It was observed that for samples in rich portions of the flame (conditioned via simultaneous OH imaging) that both flame A and B had a range angles between around -91° and -120°. This implies that there are lines (in a 2D measurement plane) of similar values of $|\nabla T'|^2$ that lie along these dissipative structures and would be perpendicular to the alignment directions discussed above. Lines perpendicular to the normal of these dissipative structures would point to the left at an angle ranging between -1° to -30°. This range of angles agree well with the -21° angle observed at approximately the same radial position at x/d = 20 for both flames in the current work. Given that the largest changes in temperature fluctuations would occur normal to dissipative structures it seems reasonable that the alignment directions of T' would closely correlate with the direction of the dissipative structures.

4.4 Space-Time Correlations, Elliptical Model and Decorrelation Mechanisms

4.4.1 Determination of Space-time Correlations

A unique aspect of the data having both spatial and temporal information allows for the computation of two-point, two-time space-time correlations, which is a fundamental quantity in turbulent flow research. The space-time correlation can be computed using

$$R(x_0, r_0, \Delta x, \Delta t) = \frac{\langle \phi'(x_0,r_0,t) \cdot \phi'(x_0+\Delta x,r_0,t+\Delta t) \rangle}{\phi_{rms}(x_0,r_0) \cdot \phi_{rms}(x_0+\Delta x,r_0)} \quad \text{Eq. (4.7)}$$

Equation (4.7) is closely related to Eqs. (4.1) and (4.2). For $\Delta x = 0$ Eq. (4.7) reduces to Eq. (4.1) and for $\Delta t = 0$ Eq. (4.7) reduces to Eq. (4.2). The usefulness of the space-time correlation is that it can provide a higher-order statistical metric for the assessment of computational models. Traditionally, the only experimentally derived statistical metrics that are used to assess the accuracy of models are the first two statistical moments, i.e., the mean and RMS. From a physical understanding aspect, the space-time correlation provides a statistical metric which captures the dynamics of the de-correlation, including both the spatial and temporal contributions. Specifically, in this work, the space-time correlation and subsequent analysis is used to understand the physical mechanisms governing de-correlation.

4.4.2 Sample Space-time Correlation Maps

A set of sample space-time correlation maps are shown in Fig. 4.7 corresponding to the location of peak $\langle T \rangle$. The location of peak $\langle T \rangle$ for is approximately r/d = 1.7 at x/d = 20 and r/d = 2.2 at x/d = 40. The space-time correlation maps for the axial velocity and temperature fluctuations are shown in Fig. 4.7 as contour maps with two isocontour levels for each data set. More isocontours can be shown but are left out for clarity. The isocontour levels display the correlation between the fluctuations at points (r_0, x_0) and $(r_0, x_0 + \Delta x)$ for different temporal lags (Δt). The abscissa of the space-time correlation maps is the temporal lag, Δt, and the ordinate is the normalized axial spatial lag, $\Delta x/d$. The axial velocity fluctuation contours are shown as solid blue lines for flame A and dashed green lines for flame B. The temperature velocity fluctuation contours are shown as solid black lines for flame A and dashed red lines for flame B. Figure 4.7 shows that the temperature fluctuations decorrelate faster both in space and time as compared to the axial

velocity fluctuations, which was observed from the integral length and time scale analysis discussed above.

Previous work in turbulent shear flows [160] has suggested that the convection speed for a variable ϕ can be determined from the space-time correlation map as the slope of the line given by $\Delta x^* = f(\Delta t^*)$, where Δx^* is the axial lag corresponding to the maximum correlation for any given

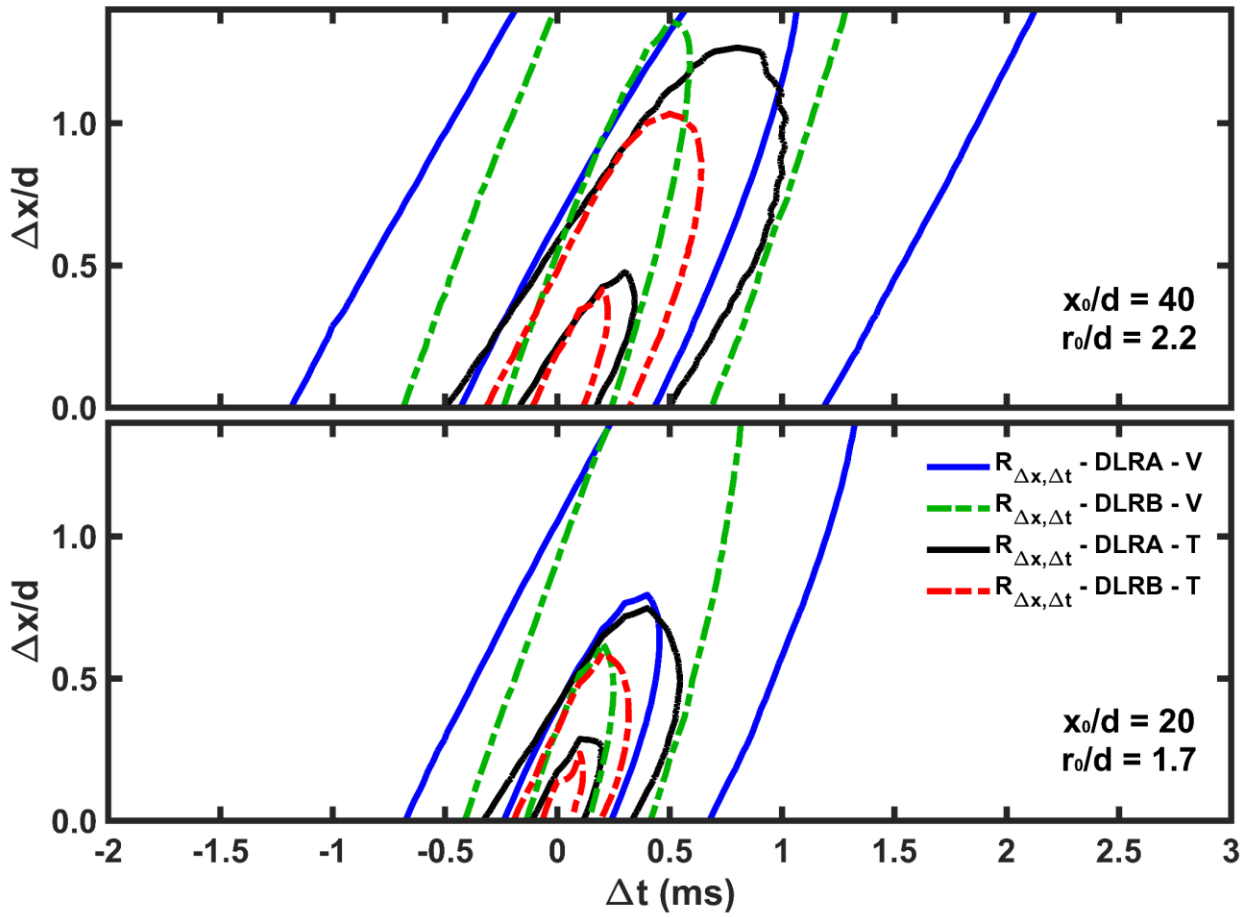

Figure 4.7: Sample space-time correlation maps at the location of peak $\langle T \rangle$ for $x_0/d = 40$ (top) and $x_0/d = 20$ (bottom). Space-time isocontours of 0.5 and 0.8 (closest to (Δt, $\Delta x/d$) = (0 ,0)) are shown as solid blue lines for axial velocity for flame A, dashed green lines for axial velocity for flame B, solid black lines for temperature for flame A, dashed red lines for temperature for flame B.

temporal lag Δt^*. Using this approach, the estimated convection speed for the axial velocity fluctuations (11.2 m/s for flame A and 15.8 m/s for flame B) is 40 – 50% faster than that of the temperature fluctuations (8.1 m/s for flame A and 10 m/s for flame B). Similar results are observed at $x_0/d = 20$ where the estimated convection velocities for the axial velocity fluctuations at this location are 10.6 m/s and 15.3 m/s for flame A and B, respectively and the convection velocities for the temperature fluctuations are 6.5 m/s and 9 m/s for flame A and B, respectively.

Another sample set of space-time correlation maps is shown in Fig. 4.8 for all sets of data at the location corresponding to the peak T_{rms}. The isocontour levels, as well as line coloring scheme shown in Fig. 4.8 are the same as in Fig. 4.7. Examining the contour maps at both axial locations, it is observed that the individual isocontours for the axial velocity fluctuation stretch farther downstream (axially) as compared to the isocontours for the temperature fluctuations, just as in Fig. 4.7. However, the u' and T' contour maps are much closer in appearance at this location (corresponding to the location of peak T_{rms}) as compared to the spatial locations shown in Fig. 4.7. For $x_0/d = 20$ the individual contour levels appear to occur at similar temporal lags for both u' and T', although the orientation of the contour maps are different for u' and T'. The estimated convection velocities derived from the space-time correlation maps at the location of peak T_{rms} are more comparable between u' and T' as compared to the results shown at the radial locations corresponding to peak $\langle T \rangle$ (Fig. 4.7). At $x_0/d = 40$ the estimated convection velocities for the axial velocity fluctuations are 4 m/s and 5.9 m/s for flames A and B, respectively, while the convection velocities for temperature fluctuations are 3.6 m/s and 4.1 m/s for flames A and B respectively. The comparison is even closer at $x_0/d = 20$ where the convection velocities for the axial velocity fluctuations are 2.6 m/s and 3.5 m/s for flames A and B, respectively, while the convection velocities for temperature fluctuations are 2.8 m/s and 3.4 m/s, respectively.

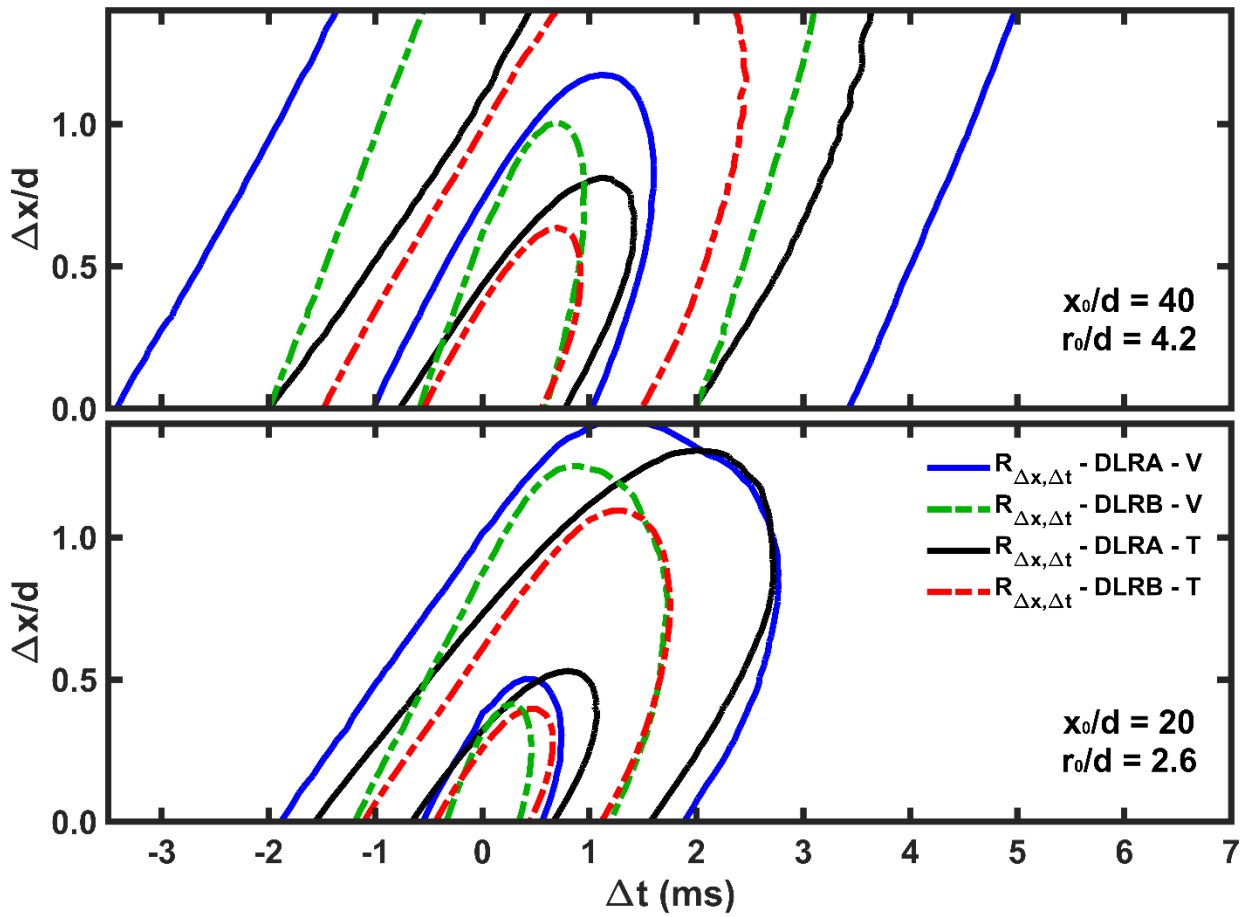

Figure 4.8: Sample space-time correlation maps at the location of peak T_{rms} at $x_0/d = 40$ (top) and $x_0/d = 20$ (bottom). Space-time isocontours of 0.5 and 0.8 (closest to (Δt, $\Delta x/d$) = (0, 0)) are shown as solid blue lines for axial velocity for flame A, dashed green lines for axial velocity for flame B, solid black lines for temperature for flame A, dashed red lines for temperature for flame B.

This convergence of the convection velocities between the axial velocity and temperature fluctuations when moving from the spatial location corresponding to peak $\langle T \rangle$ to peak T_{rms} also is marked by an increase in turbulence intensity ($u_{rms}/\langle u \rangle$). For x_0/d = 40 and r/d = 2.2, $\langle u \rangle$ is approximately 11.0 m/s and 16.2 m/s for flames A and B, respectively, while u_{rms} is approximately 4.0 m/s and 5.9 m/s for flames A and B, respectively. For x_0/d = 40 and r/d = 4.2,

$\langle u \rangle$ is approximately 3.9 m/s and 5.5 m/s for flames A and B, respectively, while u_{rms} is approximately 2.3 m/s and 3.3 m/s for flames A and B, respectively. This leads to a turbulence intensity increase from 36% at $r_0/d = 2.2$ to 60% at $r_0/d = 4.2$. Thus it appears that at the highest temperature regions, there is a discrepancy between the convection speeds of the axial velocity and temperature fluctuations, where the convection speed of the velocity fluctuations is very similar to the measured mean axial velocity. At the regions of the peak T_{rms} (which also corresponds to regions of high u_{rms} and $u_{rms}/\langle u \rangle$) the convection speeds of the axial velocity and temperature fluctuations are more similar and both are close to the measured values of $\langle u \rangle$. Similar observations are made for the measurements at x/d = 20. It is likely that the apparent lower convective velocities of the temperature fluctuations at the highest temperatures represent faster de-correlation due to increased chemical reactivity and diffusion that play an important role in addition to flow convective/turbulence effects. As will be discussed below, there are competing thermodynamic and kinematic effects that govern how various flow properties de-correlate. At the regions with higher values of T_{rms} and $u_{rms}/\langle u \rangle$, it is likely that "flow effects" dominate , such that the apparent convective velocities derived from the space-time correlation maps for both the velocity and temperature fluctuations correspond with the local mean axial velocity and the primary de-correlation mechanism is through convection and flow turbulence (discussed more below).

4.4.3 Elliptic Approximation

A striking feature of the space-time correlation maps of Fig. 4.7 and 4.8 is the apparent elliptic-like nature of the correlation isocontours. In turbulent flows, Taylor's hypothesis and approximation [156], which is often used to relate spatial and temporal gradients, is a simple linear

transformation between space and time or equivalently a linear transformation of two-point space-time correlations into two-point spatial correlations only. The linear transformation is given by

$$R(\Delta x, \Delta t) = R(\Delta x - U\Delta t, 0) \qquad \text{Eq. (4.8)}$$

where U is the mean convective velocity (discussed above) in the principal flow direction. In a strict sense this transformation would imply that the isocontours levels of the space-time correlation maps are described by a series of parallel straight lines of the form $x_0 + \Delta x - U\Delta t = C$,

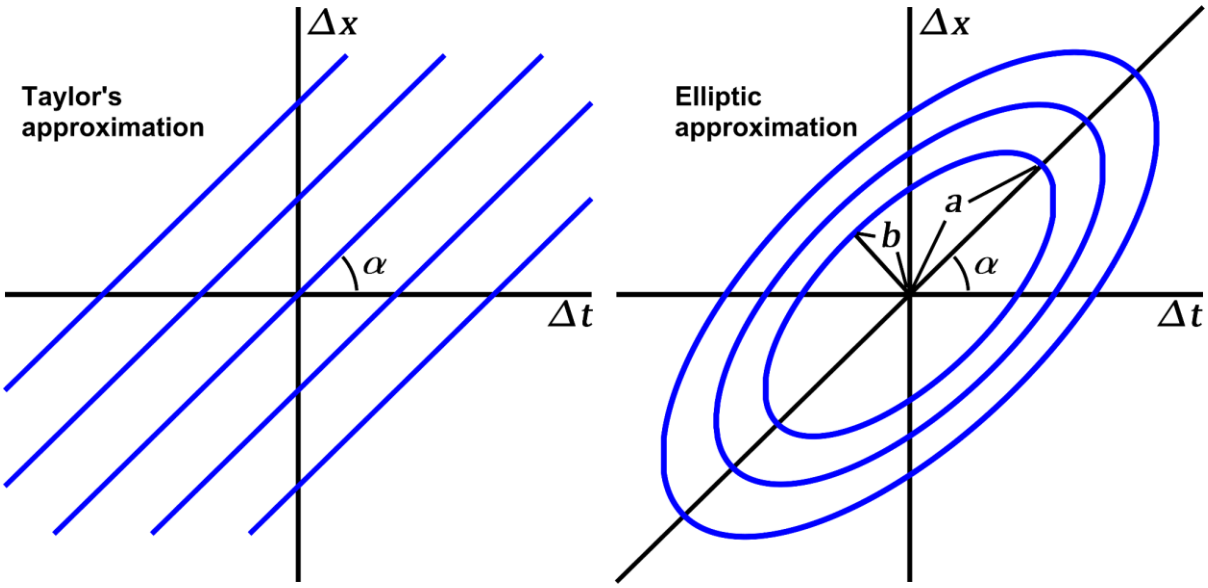

Figure 4.9: Schematic showing space-time correlations isocontours for Taylor's approximation (left) and for the elliptic approximation (right).

where C is a given contour level. Such a scenario can be seen in the left side of Fig. 4.9 which shows a theoretical space-time map with parallel isocontours. This feature is not observed in the

sample space-time maps shown in Fig. 4.7 and 4.8; instead the isocontours levels are highly elliptical and appear to resemble the angled elliptical curves shown on the right side of Fig. 4.9. Zhao and He [161] used similar observations from DNS studies of the velocity field within non-reacting, homogenous shear flows to develop what they refer to as an "elliptic approximation" that sought to provide a better transformation of the space-time correlations to spatial correlations, or more generally, a better transformation between space and time within the context of a turbulent system where the decorrelation of any variable ϕ may be governed by additional processes other than the mean convection velocity. The elliptic approximation described by Zhao and He [161] is derived from a second-order Taylor power-series expansion of the correlation function at the origin ($\Delta x = 0$, $\Delta t = 0$). The form of the expansion is given by

$$R(\Delta x, \Delta t) = \begin{matrix} R(0,0) + \Delta x \cdot \Delta t \cdot \partial^2 R(\Delta x, \Delta t)/\partial x \partial t \\ + 1/2\,[\Delta x^2 \cdot \partial^2 R(0,0)/\partial x^2 + \Delta t^2 \cdot \partial^2 R(0,0)/\partial t^2] \end{matrix} \qquad \text{Eq. (4.9)}$$

The first derivatives of R are assumed to be 0 and are thus left out of Eq. (4.9) due to the flow being statistically stationary ($\partial R/\partial t = 0$) and homogeneous ($\partial R/\partial x = 0$). A transformed spatial lag Δx_E is then sought such that for a specific contour C, $R(\Delta x, \Delta t) = R(\Delta x_E, 0)$. From Eq. (4.9) Δx_E is given as

$$\Delta x_E^2 = (\Delta x - \beta \Delta t)^2 + \eta \Delta t^2 \qquad \text{Eq. (4.10)}$$

where

$$\begin{aligned} \beta &= -\left. \partial^2 R(\Delta x, \Delta t)/\partial x \partial t \right/ \partial^2 R(0,0)/\partial x^2 \\ \eta &= \left. \partial^2 R(\Delta x, \Delta t)/\partial t^2 \right/ \partial^2 R(0,0)/\partial x^2 - \beta \end{aligned} \qquad \text{Eq. (4.11)}$$

For the velocity field in non-reacting, homogenous shear flows, Zhao and He [161] showed that β (referred to as 'u' in their paper) was equivalent to the mean convective velocity ($\beta = \langle u \rangle$) and η was the net effect of the RMS velocity fluctuation and the shear-induced velocity. The physical meaning of β and η in the context of a free-shear reacting flow will be discussed below.

Equation (4.10) describes the functional form of an ellipse (hence the name elliptic approximation) and the transformation from a space-time correlation to a purely spatial correlation is given by

$$R(\Delta x, \Delta t) = R(\sqrt{(\Delta x - \beta \Delta t)^2 + \eta \Delta t^2}, 0) = R(\Delta x_E, 0) \qquad \text{Eq. (4.12)}$$

While a Taylor power series expansion is strictly applicable only for small displacements near the origin, Zhao and He [161] made two assumptions that allowed the applicability of the elliptical model to extend to larger spatial and temporal lags. The first assumption is that the isocontours can be approximated by algebraic elliptical curves and the second assumption is that the different isocontours share a preferential direction, $\tan[\alpha]$ and aspect ratio, $\gamma = b/a$ (see Fig. 4.9), where b is the length of the semi-minor axis of the elliptical isocontour and a is the length of the semi-major axis of the elliptical isocontour (both shown in the right side of Fig. 4.9). The relationship between the preferential direction, $\tan(\alpha)$, the aspect ratio $\gamma = b/a$, and the elliptical parameters β and η is given by

$$\begin{aligned} \beta(x_0, r_0) &= \tan[\alpha(x_0, r_0)] \cdot (1 - \gamma(x_0, r_0)^2) / \{1 + \tan^2[\alpha(x_0, r_0)] \cdot \gamma(x_0, r_0)^2\} \\ \eta(x_0, r_0) &= \lambda(x_0, r_0) \cdot \{1 + \tan^2[\alpha(x_0, r_0)]\} / \{1 + \tan^2[\alpha(x_0, r_0)] \cdot \gamma(x_0, r_0)^2\} \end{aligned} \qquad \text{Eq. (4.13)}$$

For more detailed information on the elliptical model and its justification see [161]. The goal of the current work is to apply the elliptical mode developed by Zhao and He [161] to the space-time correlations of the axial velocity and temperature fluctuations for the current turbulent non-

premixed jet flames. Specifically, the model will be used to gain better insight into the mechanisms by which the axial velocity fluctuations and temperature fluctuations de-correlate and to understand the differences in the physical mechanisms governing the decorrelation of the two quantities.

The process to determine the β and η parameters involve fitting the isocontours (such as shown in Fig. 4.7 and 4.8) with algebraic elliptical curves at various spatial locations of interest. Independent ellipses were fit for the u' and T' contours. For a given variable and spatial position, 30 isocontours ranging in value from $\exp(-1)$ to 0.9 were extracted from the measured space-time correlations and an algebraic elliptic curve was fit yielding an angle α, a semi-major axis, a, and a semi-minor axis, b, for each isocontour. Assessing whether a fit for any given isocontour is "good" is performed by finding the distance from the origin to each point on the measured isocontour and comparing that to the distance from the origin for a corresponding points on the elliptical fit. A fit is then deemed "good" if the average value of the absolute difference of the distance between the measured and fit isocontour points, normalized by the distance of the data points, is $\leq 4\%$. For the cases where the number of "good" elliptical fits is ≥ 12, $\tan(\alpha)$ and γ are determined and used to compute the β and η for that given spatial location. These parameters are then used in conjunction with Eq. (4.12) to transform the space-time correlations to purely two-point spatial correlations. As an example of this approach, the spacetime transformation using the elliptic approximation is applied to the example space-time correlation maps shown in Fig. 4.8. Figure 4.10 shows several two-point, space-time correlation curves as a function of temporal lag, Δt, for flame A at $x_0/d = 40$ and $r_0/d = 4.2$. Results are shown for the axial velocity fluctuations in the top row and for the temperature fluctuations in the bottom row. The spatial lag values of the various curves are shown in the figure legend. As expected, for a given temporal lag, Δt, the

correlation value for the five different spatial lags vary significantly for both the axial velocity and the temperature fluctuations (left column of Fig. 4.10). The right column of Fig. 4.10 shows the result of applying the elliptic approximation transformation of the two-point space-time correlations with the transformed spatial lag Δx_E given in Eq. (4.10) where the β and η parameters are determined using the methods described above. Also shown in the plots on the right column of Fig. 4.10 is the longitudinal spatial correlation function determined at the same spatial location. A

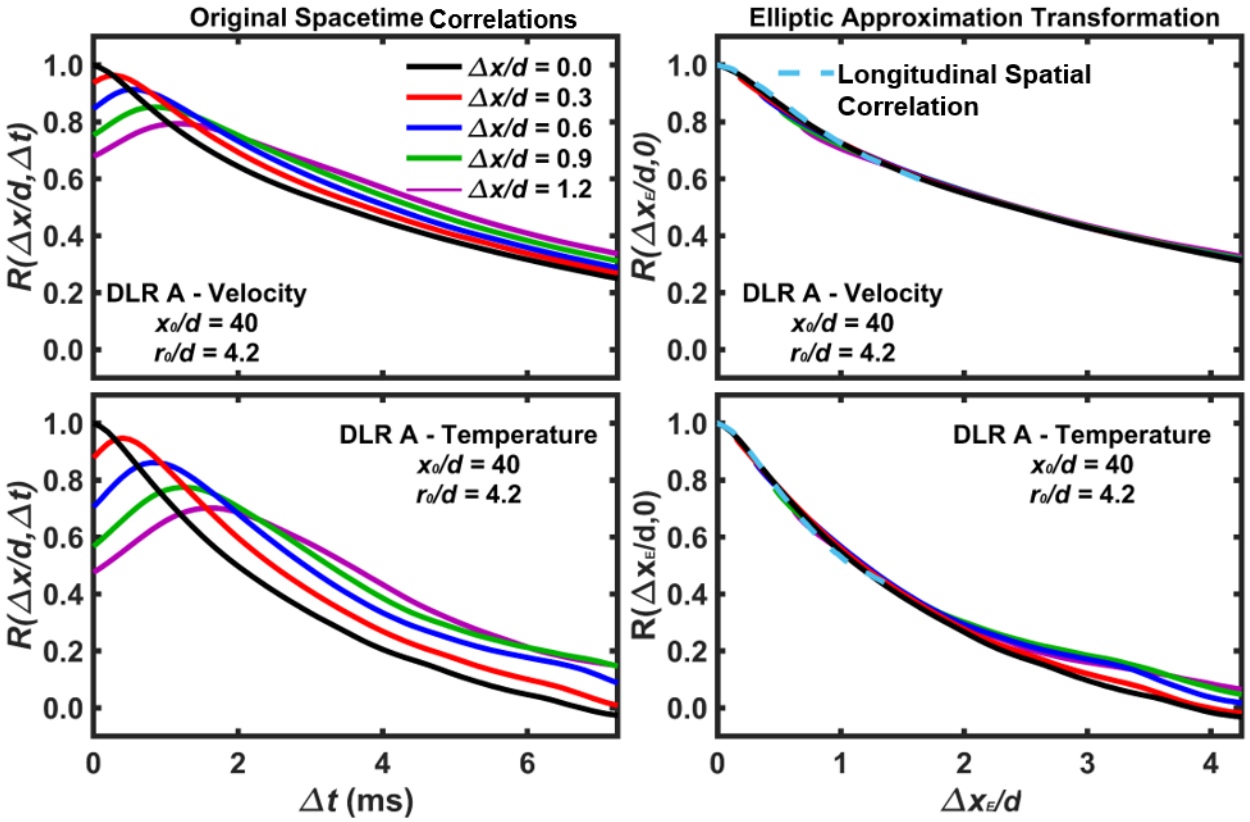

Figure 4.10: Space-time correlation curves for flame A at $x_0/d = 40$ and $r_0/d = 4.2$ for axial velocity fluctuations (top) and temperature fluctuations (bottom). Results are shown for various spatial lag values (Δx/d) as a function of temporal lag (left) and as a function of the transformed spatial lag using the elliptic model (right). The longitudinal spatial correlation also is shown with the elliptic transformed curves (dashed cyan line) for comparison.

key observation from Fig. 4.10 is that the elliptic transform shows a near-complete collapse of all the two-point space-time correlations when plotted as a function of Δx_E.

Figure 4.11 shows several two-point space-time correlation curves as a function of temporal lag, Δt for flame B at $x_0/d = 40$ and $r_0/d = 4.2$. Similar to the results shown in Fig. 4.10 for flame A, Fig. 4.11 (right column) shows that the spatial transformation given by the elliptical model accurately collapses the various two-point, space-time correlations for all temporal lags (or

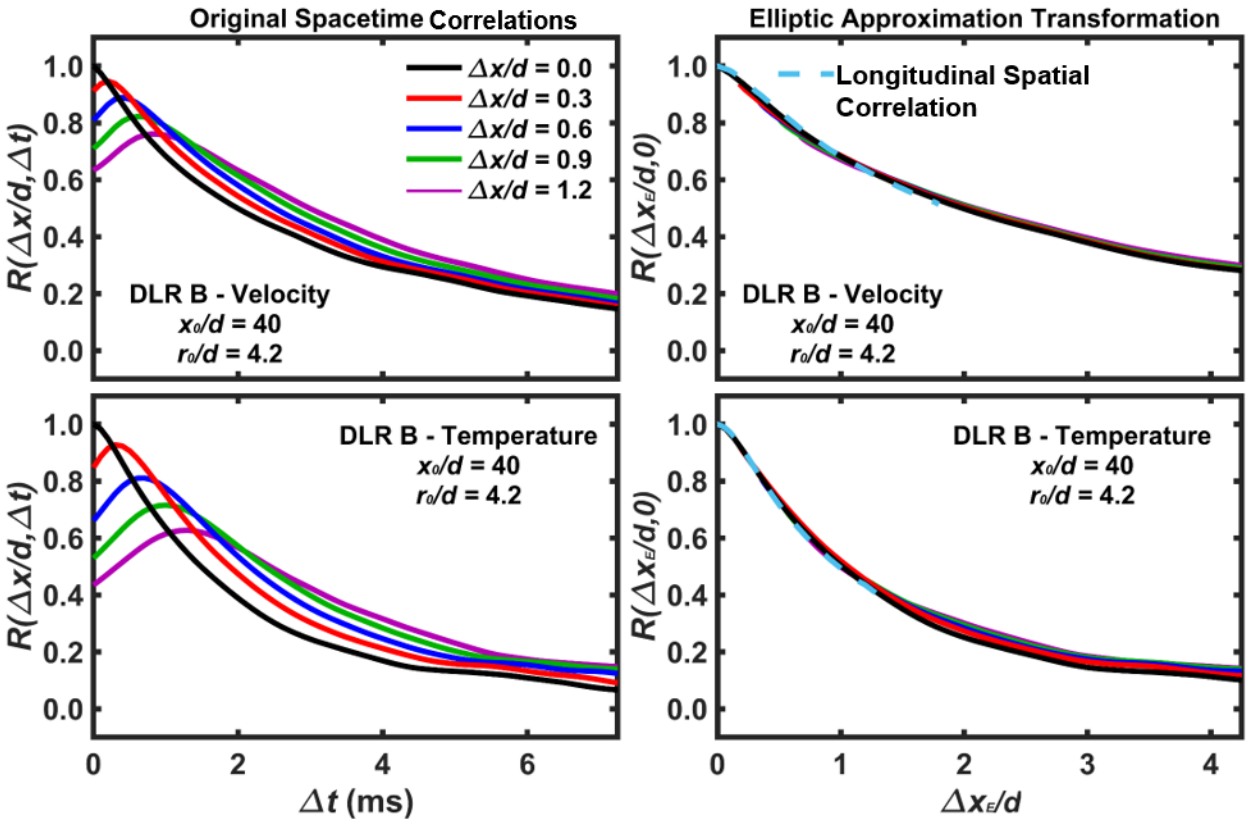

Figure 4.11: Space-time correlation curves for flame B at $x_0/d = 40$ and $r_0/d = 4.2$ for axial velocity fluctuations (top) and temperature fluctuations (bottom). Results are shown for various spatial lag values (Δx/d) as a function of temporal lag (left) and as a function of the transformed spatial lag using the elliptic model (right). The longitudinal spatial correlation also is shown with the elliptic transformed curves (dashed cyan line) for comparison.

transformed spatial lags, Δx_E) and accurately matches the two-point longitudinal spatial correlation function (dashed line). This is particularly notable because it appears that the elliptical model works very well for both velocity and temperature fluctuations, independent of the degree of spatial and temporal lag and Reynolds number at this location.

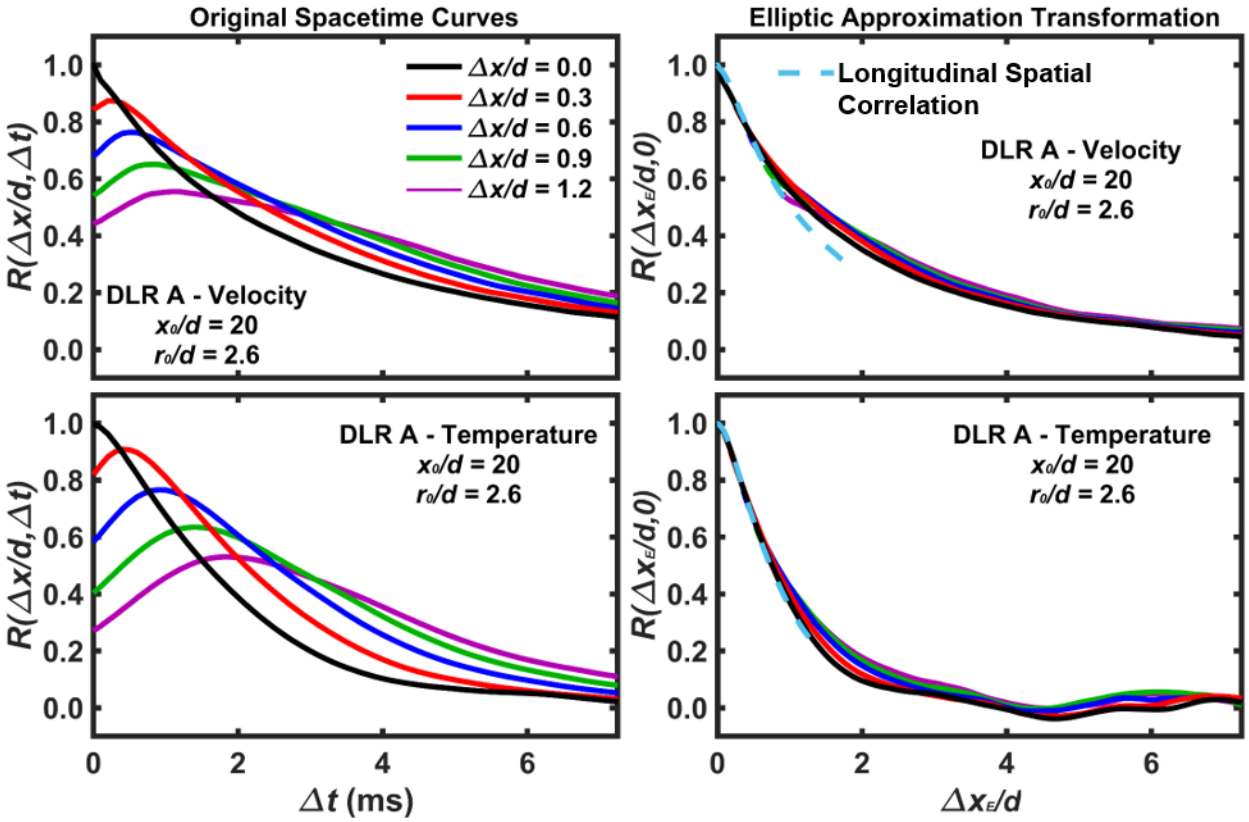

Figure 4.12: Space-time correlation curves for flame A for $x_0/d = 20$ and $r_0/d = 2.6$ for axial velocity fluctuations (top) and temperature fluctuations (bottom). Results are shown for various spatial lag values (Δx/d) as a function of temporal lag (left) and as a function of the transformed spatial lag using the elliptic model (right). The longitudinal spatial correlation also is shown with the elliptic transformed curves (dashed cyan line) for comparison.

Figure 4.12 and Fig. 4.13 show the original and transformed space-time correlations for flame A flame B, respectively, acquired at $x_0/d = 20$ and $r_0/d = 2.6$. Similar to the previous results shown at x/d =40, the results at x/d = 20 show a good collapse of the space-time correlations into a single transformed spatial correlation function for both flames and for both u' and T'. Overall, for all conditions shown (Figs. 4.10 – 4.11), there has been a strong collapse of the different space-time correlation functions onto a single spatial correlation curve and the collapsed (transformed) curve follows closely (within uncertainty) with the measured longitudinal spatial correlation function. This provides strong evidence that the elliptic approximation yields an appropriate transformation from time to space in the context of the axial velocity and temperature fluctuations within the current turbulent non-premixed jet flames.

In an effort to assess the effectiveness of the elliptic model transformation, the overall collapse of the space-time correlations into a single spatial correlation is examined. For each space-time correlation shown in Figs. 4.10 – 4.13, five different spatial lags were considered. If the standard deviation of the five points at each transformed axial lag is determined and averaged over all conditions (referred to as σ_{EM}), this provides a rigorous metric to assess the transformation at a given spatial location. The values for σ_{EM} at x/d = 40 at the location of peak RMS temperature (shown in Fig. 4.10 and Fig. 4.11) for the axial velocity fluctuations are 0.01 for flames A and B, while the values of σ_{EM} for the temperature fluctuations are 0.02 and 0.01 for flames A and B, respectively. The values for σ_{EM} at x/d = 20 at the location of peak RMS temperature (shown in Fig. 4.12 and 4.13) for the axial velocity fluctuations are 0.02 for flames A and B and σ_{EM} for the temperature fluctuations are 0.03 and 0.01 for flames A and B, respectively. For the majority of other spatial locations at x/d = 20 and 40, σ_{EM} is less than 0.03 indicating that the elliptical model

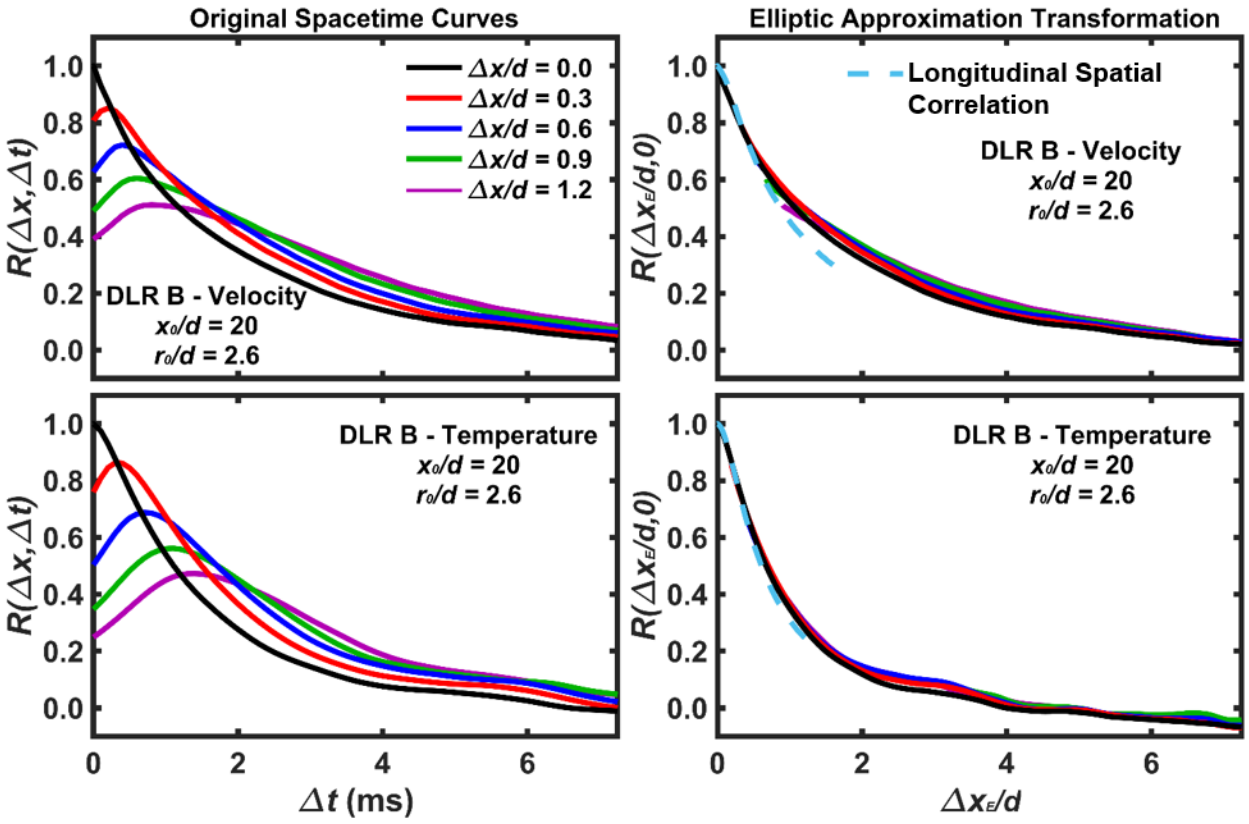

Figure 4.13: Space-time correlation curves for flame B at $x_0/d = 20$ and $r_0/d = 2.6$ for axial velocity fluctuations (top) and temperature fluctuations (bottom). Results are shown for various spatial lag values (Δx/d) as a function of temporal lag (left) and as a function of the transformed spatial lag using the elliptic model (right). The longitudinal spatial correlation also is shown with the elliptic transformed curves (dashed cyan line) for comparison.

is able to adequately transform the two-point space-time correlations to a single two-point spatial correlation for both axial velocity and temperature fluctuations at all positions and flame conditions. As the applicability of the elliptic approximation has been assessed only in non-reacting flows previously [161-164] (and predominately only for velocity fluctuations), the suitability of the elliptic approximation for both axial velocity fluctuations and temperature fluctuations (a reactive scalar) in turbulent non-premixed flames is a notable outcome.

One goal of the current work is to use the elliptic approximation, and more specifically, the observation of the collapse of the space-time correlations as a function of Δx_E to better understand the physical mechanisms governing the decorrelation of both the axial velocity and temperature fluctuations in the context of a turbulent non-premixed flame. The two elliptical model parameters β and η are key to understanding the decorrelation process as they are linked to the mechanisms that govern decorrelation. Previous results in non-reacting, homogenous shear flows showed that β corresponds to the mean velocity, and η corresponds to the net effect of the RMS velocity fluctuation and the shear-induced velocity [161].

Based on these previous results the β parameter is compared with the mean axial velocity $\langle u \rangle$ and η is compared with the RMS velocity fluctuation u_{rms} in the current work. Figure 4.14 shows comparisons of the β parameter from the axial velocity fluctuations (β_u; solid red) and the β parameter from the temperature fluctuations (β_T; solid black) with the mean axial velocity, $\langle u \rangle$, (solid blue) as a function of normalized radial position at x/d = 40 for flame A in the top left and flame B in the top right. Also shown in Fig. 4.14 is the comparison of the η parameter for the axial velocity fluctuations (η_u; solid red) and the temperature fluctuations (η_T; solid black) with RMS axial velocity fluctuations, u_{rms}, (solid blue) at x/d = 40 for flame A in the bottom left and flame B in the bottom right. From the results in the top row of Fig. 4.14 it is observed that the β parameters for axial velocity and temperature qualitatively follow the mean axial velocity radial profile. Close to centerline for flames A and B, β_u is a bit smaller than the mean axial velocity. This also is observed for the temperature fluctuations in flame A. For flame B no β (nor η) values were computed near centerline because it was not possible to generate a sufficient number of "good" elliptic fits of the contours.

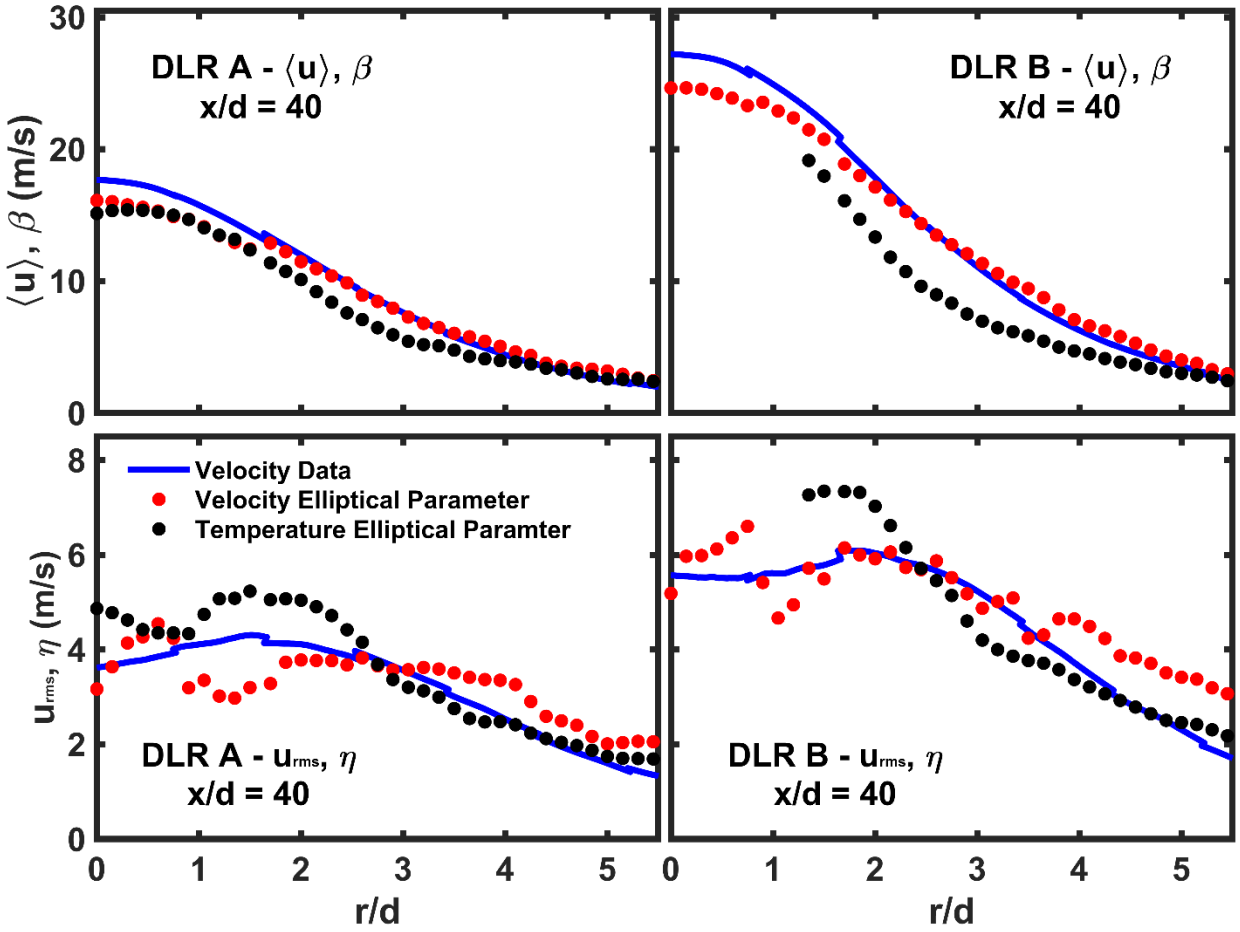

Figure 4.14: Comparison of the β parameter for axial velocity fluctuations (solid red) and temperature fluctuations (solid black) with mean axial velocity (solid blue) for flame A (top left) and flame B (top right). Comparison of the η parameter for axial velocity fluctuations (solid red) and temperature fluctuations (solid black) with the axial RMS velocity fluctuations for flame A (bottom left) and flame B (bottom right). Results are for x/d = 40.

For increasing radial position, β_u tracks the mean axial velocity for both flame A and B very well. For both flames, β_T is less than the mean axial velocity and the difference between β_T and $\langle u \rangle$ is much more pronounced for flame B compared to flame A. For example, at r/d = 2.5 the difference between β_T and $\langle u \rangle$ for flame A is approximately 2.4 m/s and 4.9 m/s for flame A and B, respectively. This corresponds to $\beta_T/\langle u \rangle$ of approximately 0.76 and 0.66 for flame A and B,

respectively. In the bottom row of Fig. 4.14 it is observed that the η parameter for both the axial velocity and temperature fluctuations qualitatively follow the u_{rms} values for both flame A and flame B. Within the uncertainty of deriving η, it appears that η_u is approximately the same as u_{rms} for r/d < 4. Near r/d = 4, η_u increases relative to u_{rms} for both flames. Near centerline, η_T is larger than u_{rms} but tracks u_{rms} very well for r/d ≥ 2.

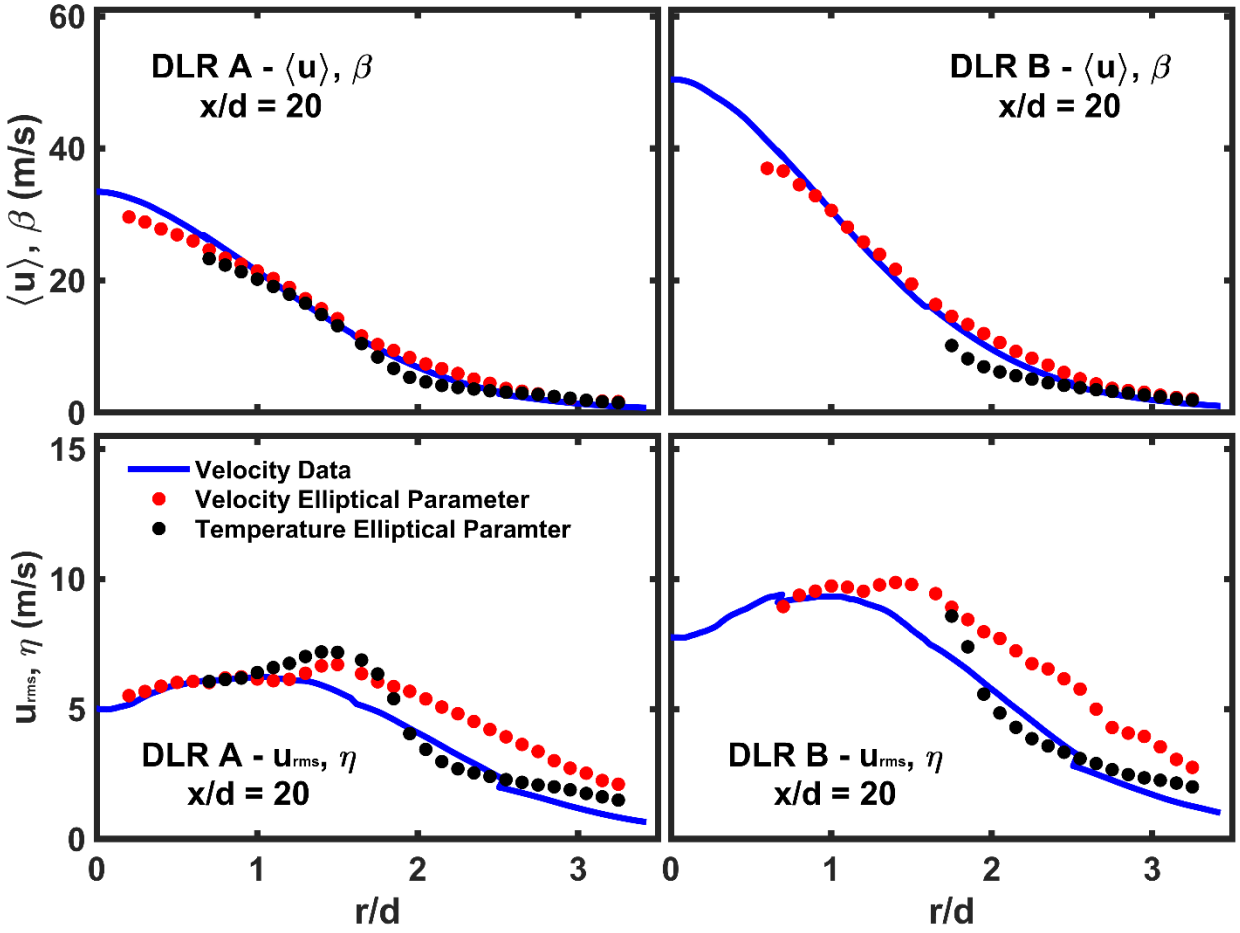

Figure 4.15: Comparison of the β parameter for axial velocity fluctuations (solid red) and temperature fluctuations (solid black) with mean axial velocity (solid blue) for flame A (top left) and flame B (top right). Comparison of the η parameter for axial velocity fluctuations (solid red) and temperature fluctuations (solid black) with the axial RMS velocity fluctuations for flame A (bottom left) and flame B (bottom right). Results are for x/d = 20.

Figure 4.15 shows the comparison of β_u and β_T with $\langle u \rangle$ and η_u and η_T with u_{rms} at x/d = 20. The same plotting scheme as in Fig. 4.14 is used. Compared to the results shown in Fig. 4.14 at $x/d = 40$ the comparison between compared β and $\langle u \rangle$ at x/d = 20 for both flames is stronger for both the axial velocity and temperature fluctuations. As observed in Fig. 4.15, the β_u profile (solid red) almost lies on top of the $\langle u \rangle$ profile and the β_T profile closely follows $\langle u \rangle$ for both flames A For flame B, there is not enough information to make a definitive comparison. The results in Fig. 4.15 also show that both η_u and η_T qualitatively follow u_{rms} at x/d = 20. For flame A near centerline, both η_u and η_T are nearly identical with u_{rms}. For both flame A and B near r/d = 1, the η parameter for both u' and T' increases to relative to u_{rms} and reaches the same peak value (~7.2 m/s for flame A and ~9.8 for flame B) near r/d = 1.6, which corresponds to the radial position of peak $\langle T \rangle$ at x/d = 20. For further increases in r/d, both η_u and η_T decrease. η_T decreases rapidly compared to η_u for both flames and tracks the u_{rms} profile, while the η_u remains higher than u_{rms} with a steady offset for both flames.

In general, the fact that the two elliptical parameters β and η agree with $\langle u \rangle$ and u_{rms} at least qualitatively (and in some locations quantitatively) for both flames and all spatial locations implies that the β parameter is proportional to $\langle u \rangle$ and the η parameter is likely proportional to or a function of u_{rms}. This argument is particularly strong for the decorrelation of the velocity fluctuations in the current flames. Taylor's hypothesis implies that decorrelation is governed by convective effects alone, but previous results in homogenous shear flows (e.g., [161, 164, 165]) have shown that in addition to $\langle u \rangle$, u_{rms}, plays a major role in the decorrelation of u'. The current results support that the turbulence-induced RMS fluctuation of the velocity field plays a significant role in turbulent reacting flows as well.

There are, of course, deviations of either β or η relative to $\langle u \rangle$ and u_{rms}, respectively (especially for β_T and η_T) in certain locations in the current non-premixed flames and these differences are important to consider. In fact, the location of the deviations may provide insight into additional processes contributing to decorrelation for turbulent non-premixed flames. Important deviations occur for β_T at x/d = 40, where β_T was markedly lower than $\langle u \rangle$ for the majority of the radial location until β converges to $\langle u \rangle$ at approximately r/d = 4.5. At x/d = 40, the region where β_T approaches $\langle u \rangle$ corresponds to the peak of T_{RMS}. Since the temperatures are all relatively high for the radial extent shown in Fig. 4.13, the fact that $\beta_T < \langle u \rangle$ may imply that in regions of high temperature or heat release, purely convective effects on temperature fluctuation decorrelation may be reduced. Since $\beta_u \approx \langle u \rangle$ at the same spatial locations, the decorrelation of u' due to convective effects may not be as sensitive to heat release effects as for T'.

There also are some interesting deviations of η_u and η_T from u_{rms} at x/d = 20 near r/d = 1.6, where both η_u and η_T increase substantially compared to u_{rms}. This location is near the location of peak $\langle T \rangle$. It is likely that in locations of high temperatures (and hence reactivity) the η parameter characterizes the combination of local turbulence effects (i.e., RMS) and additional chemical reactivity or gas expansion effects. For lower temperature regions (i.e., near centerline) η largely represents the effects of turbulent velocity fluctuations on the decorrelation of u' or T'.

Previous work within our laboratory measured space-time correlations and applied the elliptical model to conserved scalar mixing results in non-reacting jets [162]. A similar analysis as used in this dissertation showed that the β closely tracked $\langle u \rangle$ and that η closely tracked u_{rms}, with some deviations. The results implied that (1) $\beta \propto \langle u \rangle$ and $\eta \propto u_{rms}$ as in homogenous shear flows and (2) the decorrelation of the conserved scalar fluctuation under non-reacting flow conditions is governed strongly by the combined mechanisms of mean convection along with the

turbulent velocity fluctuations. Comparing those previous results to the current results highlights the potential effects of chemical reactivity and heat release on the decorrelation of both u' and T'. It is apparent from the current results that the de-correlation of u' is largely governed by the combined mechanisms of convection and local flow turbulence as in previous non-reacting homogeneous [161, 164, 165] and free shear [162] flows, with some minor differences due to chemical reaction and/or heat release. The decorrelation of T' appears to be governed by the same processes in lower-temperature regions, but additional effects appear prominent in high-temperature regions.

The preceding analysis gave a partial statistical viewpoint on the relationship between the fluid kinematics and the dynamics of the temperature field, a reactive scalar, in turbulent non-premixed jet flames. However, simultaneous temperature and velocity measurements can provide a more in-depth look at how these two quantities are topologically coupled in turbulent non-premixed flames. For example, how are various flow kinematic parameters (i.e., vorticity, strain rate, etc.) and thermal properties correlated? What leads to the formation of thermal gradients and how do regions of high dissipation align with vorticity and strain fields? The subsequent chapters discuss the development and application of a new laser diagnostic approach to enable simultaneous temperature and velocity measurements in turbulent non-premixed jet flames.

Chapter 5. Methodology for Filtered Rayleigh Scattering Thermometry in Turbulent Non-premixed Flames

Chapter 4 presented a series of results that implicitly showed the relationship between the temperature and velocity fields within turbulent non-premixed flames. However, the temperature and velocity measurements were performed independently which inhibits a direct evaluation of the role of flow kinematics on the scalar field. In particular, the influence of the local turbulence (manifested through vorticity and strain) on properties such as scalar transport (i.e., heat flux), mixing, gradient formation, and scalar dissipation is needed and can be achieved only through simultaneous velocity and temperature measurements. Simultaneous velocity and scalar measurements have a rich history in combustion research (e.g., [3, 4, 58]), but they are largely confined to qualitative scalar measurements (typically using planar laser-induced fluorescence of minor species [2]). Quantitative scalar measurements are needed, but as discussed below, many approaches for measuring scalars are not possible when combined with particle image velocimetry (PIV), which is the *de facto* standard for velocity measurements in turbulent flows. The current chapter discusses the efforts towards developing a novel thermometry approach to enable accurate temperature measurements simultaneously with velocity measurements (using PIV) in turbulent non-premixed flames.

5.1 Experimental Motivation and Approach

As has been discussed previously, temperature is of particular importance in turbulent combustion environments. Laser-based diagnostic techniques are often preferred because they are non-intrusive and allow for "instantaneous" measurements with good spatial and temporal resolution. Over the last four decades, a number laser-based thermometry techniques have been developed and applied in high-temperature, reacting-flows. Some of the more common approaches include spontaneous Rayleigh and/or Raman scattering [2, 58-61], laser induced fluorescence [2, 58, 62], coherent anti-Stokes Raman scattering (CARS) [2, 58, 63], thermographic phosphorescence [64], and absorption based approaches [166, 167]. Details for these techniques, excluding Rayleigh-based approaches, are outside the scope of this dissertation and the reader is referred to the aforementioned references for more information.

Planar laser Rayleigh scattering (LRS) thermometry is the most commonly applied technique for multi-dimensional temperature measurements or "imaging" under turbulent combustion conditions. As detailed in Chapter 2, the dependence of the scattered light on the mixture-averaged differential Rayleigh scattering cross section $(d\sigma/d\Omega)_{mix}$, requires that one must either (a) have knowledge of the local species concentrations, or (b) use a specific fuel mixture such that $(d\sigma/d\Omega)_{mix}$ is constant throughout the mixture composition space in order to obtain temperature from the LRS signal only. The second approach is commonly employed in isobaric conditions such that the temperature is inversely proportional to signal and examples of this approach can be found in Refs. [28, 47, 52, 113, 143, 168, 169] and the results in Chs. 3 and 4.

Even more challenging in turbulent flame environments is the simultaneous measurement of velocity and temperature. Obtaining simultaneous temperature and velocity measurements in turbulent non-premixed flames would allow for a detailed understanding of turbulence-scalar interaction both qualitatively through visualization but also quantitatively through correlation statistics. Furthermore, simultaneous measurements of temperature and velocity would provide measurements of the turbulent scalar flux term, an unclosed term which has to be modeled in turbulent combustion simulations. Such measurements would prove extremely beneficial for new physical insights and provide previously unavailable information for assessing different approaches for model closure in turbulent non-premixed flames. The predominate method for measuring velocity in turbulent reacting flows is particle image velocimetry (PIV), which has been described in detail in Chs. 2 – 4. PIV is a robust and proven approach that involves seeding small tracer particles into the flow field to track the fluid motion by acquiring particle scattering images from two sequential laser pulses closely spaced in time. The light scattering from the PIV particles occurs at the same wavelength as the incident laser and would therefore mask and overwhelm any gas-phase Rayleigh scattering which also occurs at the same wavelength as the incident laser. Consequently, simultaneous PIV and LRS-based measurements are not possible.

One potential solution for obtaining gas-phase information via Rayleigh scattering processes in the presence of high levels of particulate or background scattering is filtered Rayleigh scattering (FRS), first introduced by Miles et al. [122]. As described in Ch. 2, FRS is a variant of the traditional LRS approach in which Rayleigh scattering from a spectrally narrow laser source is imaged by a camera through an atomic or molecular vapor filter. A graphical representation of the FRS approach when using a narrowband Nd:YAG laser in conjunction with a molecular iodine filter is shown in Fig. 2.5 (reprinted from Sec. 2.2.1.3). The general features of light scattering was

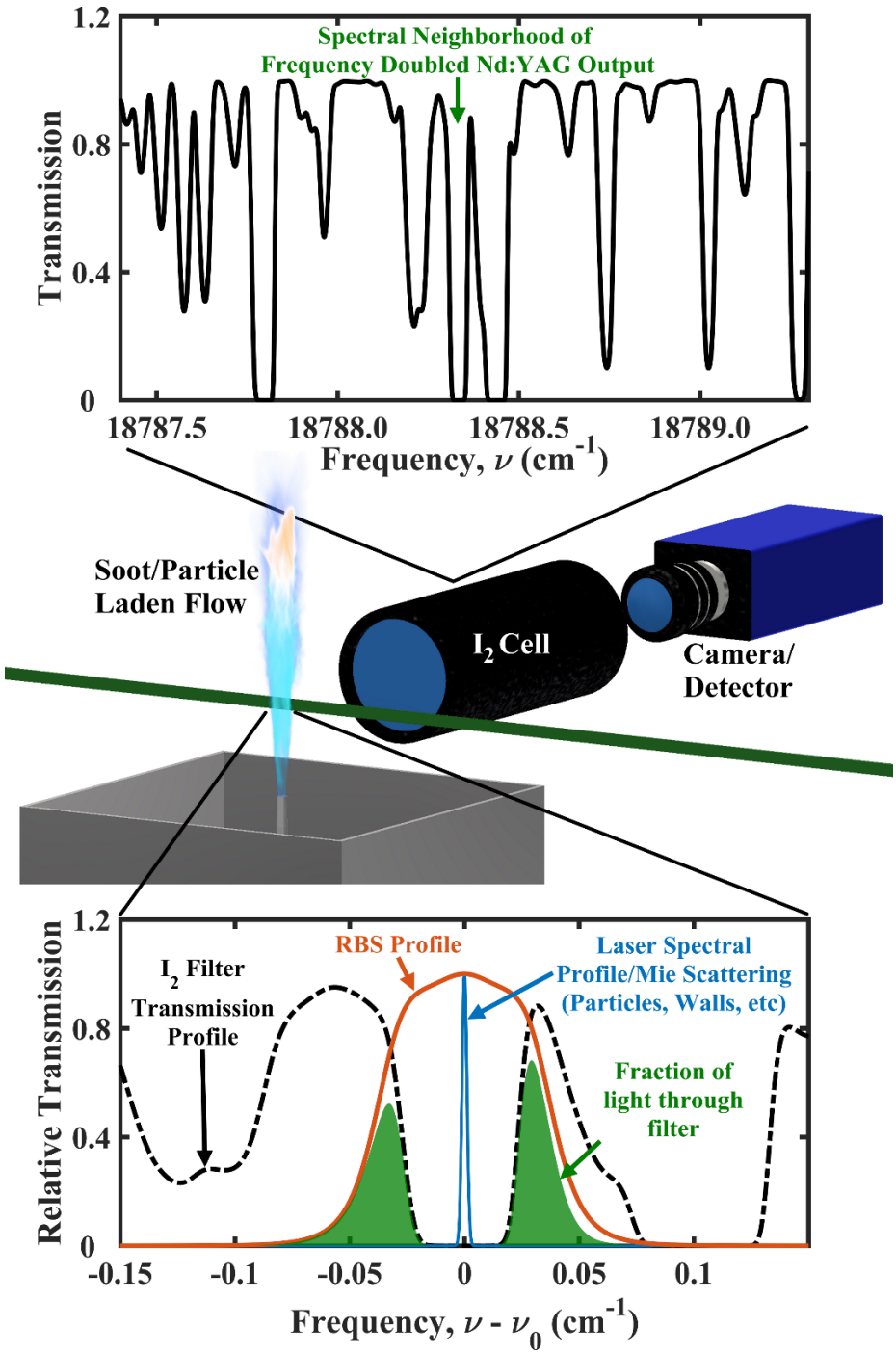

Figure 2.5: Graphical representation of FRS approach using an Nd:YAG laser and molecular I_2 filter cell. (Top) Modeled I_2 spectra. The feature marked with an arrow is used in the present work for FRS measurements. (Middle) Application of FRS imaging within a particle laden flow. (Bottom) Overlap of the I_2 filter profile with particle scattering, and an example RBS profile from gas-phase molecules.

discussed in Ch. 2. From this discussion, it can be inferred that the scattered light from the solid, tracer particles has effectively the same spectral distribution as the incoming laser beam. This is because the constituent atoms within a solid cannot move past one another, but only gain kinetic energy through vibration. Hence their movement is very slow and generates a very narrow Doppler-broadened profile that is much narrower than the laser linewidth (which is itself spectrally narrow).

In contrast, the gas-phase Rayleigh-Brillouin scattering (RBS) is broadened due to the random thermal motion of the molecules (Doppler broadening) and Brillouin scattering effects (see Ch. 2). For a spectrally narrow laser source (meaning much narrower than the absorption linewidth of the filter species), laser light scattering from the particles and surfaces will be absorbed by the vapor filter (cell filled with an absorbing species such as molecular iodine, I_2) which is placed in front of a camera, while the spectral wings of the broadened gas-phase scattering signal (discussed in more detail in Sec. 2.2.1.3) falls outside of the I_2 absorption band and will be transmitted to the camera. Assuming all the light scattered from the particles is properly suppressed by the I_2 filter, the collected light represents only gas-phase information.

5.2 Conceptual Approach of FRS Thermometry in Non-Premixed Flames

From the discussion in Sec. 2.2.1.3 an FRS measurement in a mixture can be written as

$$S_{FRS}(T,\vec{V}) = CI_0 n \sum X_i \psi_i(T,\vec{V}) \qquad \text{Eq. (5.1)}$$

where C is a constant encompassing the setup of the optical setup, I_0 is the incident laser intensity, n is the number density. When Eq. 5.1 is normalized by an FRS measurement from a known reference condition, the ratio of signals can be written as

$$\frac{S_{FRS}(T,\vec{V})}{S_{FRS,ref}(T_{ref},\vec{V}=0)} = \frac{T_{ref}}{T} \times \frac{\sum X_i \psi_i(T,\vec{V})}{\psi_{ref}(T_{ref},\vec{V}=0)} \quad \text{Eq. (5.2)}$$

where T is the temperature of the mixture of interest, X_i, is the mole fraction of species i, $\vec{V}$ is the flow velocity, and ψ_i and ψ_{ref} are FRS specific parameters for the species i and the reference condition, respectively. The FRS-specific parameters are written as

$$\psi_i = (d\sigma/d\Omega)_i \int_\nu \mathcal{R}_i(P,T,\vec{V},\theta,\nu_r)\tau_{I2}(\nu)d\nu \quad \text{Eq. (5.3)}$$

where $(d\sigma/d\Omega)_i$ is the differential Rayleigh scattering cross section for species i, $\mathcal{R}_i$ is the Rayleigh-Brillouin scattering (RBS) lineshape for species i, τ_{I2} is the frequency-dependent transmission of the molecular I_2 filter cell, ν is the spectral frequency over which the RBS light and I_2 absorption bands are distributed, and $\nu_r = \nu - \nu_o$ is a frequency referenced to the center laser frequency. It is clear from Eqs. (5.1) – (5.3) that the FRS signal from a mixture is dependent on the species-specific lineshapes, $\mathcal{R}_i$ which typically are modeled. There are several models that exist within the literature, but perhaps the most utilized is the Tenti S6 lineshape model [119], which is used in the current work and has been discussed in Chapter 2 and more below. An example RBS lineshape for nitrogen at 300 K calculated using the Tenti S6 model is shown as an orange curve in the bottom plot in Fig. 2.5. Equations. (5.1) – (5.3) also show that the normalized FRS signal also is dependent on the I_2 filter transmission profile which can be measured directly or can be modeled using the I_2 transmission model from Forkey et al. [170]. An example I_2 transmission profile also is shown (and overlaid with the RBS profile) in the bottom panel of Fig. 2.5.

A complication with FRS measurements in flames (and especially within non-premixed flames) is that at any spatial location there is a local mixture of species such that the collected FRS

signal comes from the net effect of the contribution from each individual species in the mixture. It will be shown in section 5.3 that the assumption that the net effect n can be written as a mole fraction-weighted sum of each species individual contribution (see Eq. (5.1)) is an accurate assumption. Another challenge with FRS measurements in non-premixed flames is the dependence of Eq. (5.1) and (5.2) on the local species composition which appears as part of the mixture-averaged differential scattering cross section as well as the species-dependent RBS lineshapes. For premixed flames with simple hydrocarbon fuels such as methane, an assumption is typically made that the local mixture-averaged scattering cross section changes little in either physical or composition space. In those cases FRS has been used to determine temperature by assuming a constant differential scattering cross section and calculating the temperature-dependent RBS lineshape based on N_2 alone (e.g. [108, 109, 129, 130]). For example, Hoffmann et al. demonstrated FRS in lightly sooting premixed flames [129] and Elliott et al. [130], Most and Leipertz [108], and Most et al. [109] demonstrated the ability to acquire simultaneous velocity and temperature in laminar and turbulent premixed flames using simultaneous PIV and FRS [108, 109, 130]. While this approach may be somewhat valid for premixed flames using small hydrocarbon fuels, the assumption of the N_2 scattering cross section and RBS lineshape describing the entire compositional space is not appropriate for premixed flames using hydrogen or longer-chained hydrocarbon fuels and certainly is not generally applicable for non-premixed flames. For non-premixed flames, the RBS profiles vary significantly for different species as well as for variations in temperature. Given that there are large variations in both local species and temperature within non-premixed flames (especially turbulent non-premixed flames) the collected FRS signal will change significantly as well. Figure 2.4 (reprinted from Chapter 2) shows the variation of RBS profiles for various combustion-relevant species for both room temperature and elevated

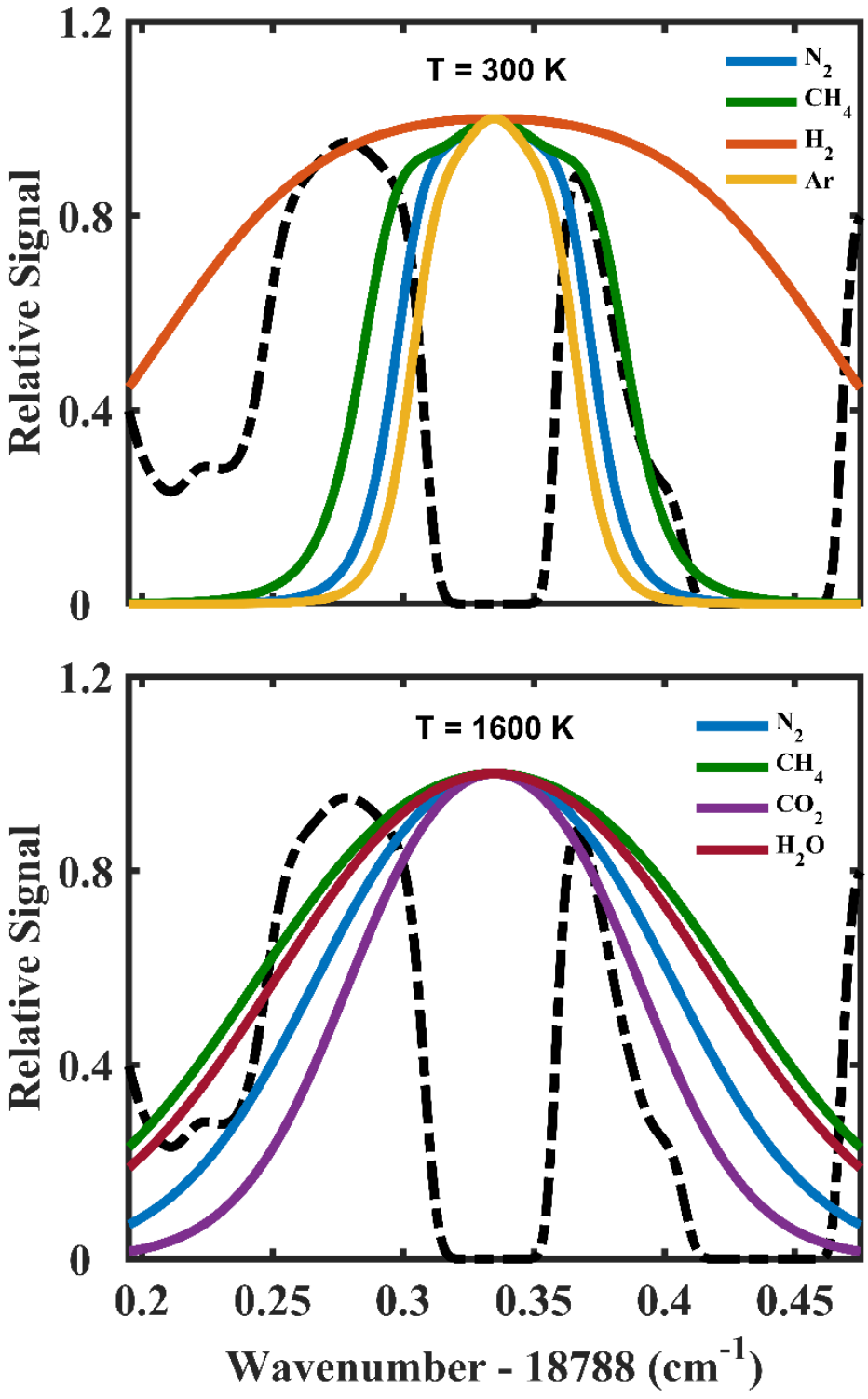

Figure 2.4: Example linshapes (solid) overlaid with I_2 spectra (dashed) in the spectral neighborhood of 532 nm. (Top) T = 300 K with N_2, CH_4, H_2, Ar. (Bottom) T = 1600 K with N_2, CH_4, CO_2, and H_2O. Both sets are at atmosheric pressure.

temperatures. The top part of Fig. 2.4 shows spectra (solid lines) from N_2, CH_4, H_2, Ar at T = 300 K while the bottom part of Fig. 2.4 shows spectra (solid lines) from N_2, CH_4, CO_2, and H_2O. The dashed black line shows a calculation of the I_2 transmission profile. These profiles have discussed previously in Sec. 2.2.1.2 but are reprinted in this section to highlight the wide variation in RBS profiles across species and temperatures.

A limited number of attempts at FRS-based thermometry have been performed within non-premixed combustion environments. Kearny et al. [132] made FRS-based measurements in laminar non-premixed flames using a joint FRS/spontaneous Raman scattering approach that measured both FRS and CH_4 Raman signals. A laminar flamelet model was used in conjunction with the measured FRS and CH_4 signals in order to estimate the scattering cross sections using an assumed state relationship. Whether or not this approach is valid under turbulent conditions is unknown due to the large spatial and temporal variation of species concentrations as well as the dependence of local species concentrations on the local flow field strain. It should be noted that this approach also requires an additional spontaneous Raman scattering measurement in conjunction with the FRS measurement, which is not trivial.

The current FRS-based approach used to obtain temperature measurements in non-premixed flames is based on "fuel tailoring" where a fuel mixture is generated that allows quantitative single shot temperature measurements in turbulent non-premixed flames using a single FRS measurement. For traditional LRS thermometry, the concept of fuel tailoring is commonly used for quantitative temperature measurements. It is best represented by the well-known and characterized DLR series of $CH_4/H_2/N_2$ jet flames [28, 113, 143, 169] which have become a standard test case within the TNF workshop [6] and were the focus of Chs. 3 and 4. As previously discussed for the DLR flames, the relative proportions of CH_4, H_2, and N_2 are chosen such that the

local mixture-averaged differential scattering cross section is reportedly constant to within $\pm 3\%$ across mixture fraction space. Thus, the local temperature is inversely proportional to the measured Rayleigh scattering signal only. Determining a viable fuel composition for FRS is much more challenging due to the fact that the measured signal depends not only on the local mixture-averaged differential scattering cross section but also on the species- and temperature-dependent Rayleigh-Brillouin lineshapes as indicated in Eq. (5.1) and Eq. (5.2) (see Fig. 2.4 for illustrations). For example, following the formulation of Eq. (5.2), a fuel mixture should be selected such that the mixture-averaged product of the scattering cross section and the transmitted RBS light over all composition and temperature is equal to the product of the scattering cross section and the transmitted RBS light of air at T_{ref}. While it is possible to match the mixture-averaged scattering cross section within the flame to the air reference condition, it is nearly impossible to match the transmitted RBS light (of the mixture) at varying temperatures to that of a single gas (air) at a single reference temperature.

Alternatively Eq. (5.2) can be reformulated as

$$\frac{S_{FRS}(T,\vec{V})}{S_{FRS,air}(T_{ref},\vec{V}=0)} = \frac{T_{ref}}{T} \times \boxed{\frac{\sum X_i \psi_i(T,\vec{V})}{\psi_{air}(T,\vec{V})}} \times \frac{\psi_{air}(T,\vec{V})}{\psi_{air}(T_{ref},\vec{V}=0)} \qquad \text{Eq. (5.4)}$$

which is simply Eq. (5.2) multiplied by $\psi_{air}(T,\vec{V})/\psi_{air}(T,\vec{V})$ and re-arranged. The normalized FRS signal in Eq. (5.4) is equal to the product of three terms. The first term is the ratio of the known reference temperature divided by the local gas temperature. The second term is the ratio of the mixture-averaged FRS parameter for the local gas composition to the FRS parameter for the reference gas, air, at the same temperature and velocity as the gas mixture of interest. The third term is the ratio of the FRS parameter for air at the local temperature T to the FRS parameter for

air at the reference temperature, T_{ref}. The temperature-dependent third term is easily computed using the Tenti S6 lineshape model [119] for air. By arranging Eq. (5.2) in the formulation presented in Eq. (5.4), the goal for the fuel tailoring becomes the generation of a fuel mixture such that the boxed term, termed the "figure of merit" ($\mathcal{F}$) for the experiment, is unity across the entire mixture fraction space. Assuming $\mathcal{F}$ = 1, the temperature can then be determined via

$$T = T_{ref} \times \left[\frac{S_{FRS}(T,\vec{V})}{S_{FRS}(T_{ref},\vec{V}=0)}\right]^{-1} \times \frac{\psi_{air}(T,\vec{V})}{\psi_{air}(T_{ref},\vec{V}=0)} \qquad \text{Eq. (5.5)}$$

where the temperature dependence is embedded within the measured FRS signal and the temperature-dependent response curve for air (second ratio in Eq. (5.5)), which is calculated from the Tenti S6 model [119]. For the work described in this chapter (and Chs. 6 and 7), a fuel mixture has been designed such that $\mathcal{F} = 1 \pm \epsilon$ across all mixture fraction space, where $\epsilon \leq 0.015$ based on laminar flame calculations. The fuel selection (discussed in more detail in section 5.4) process is based on a series of opposed-flow non-premixed flame calculations where all important parameters have been modeled and thus are subject to experimental verification. More specifically, the fuels are designed with the assumptions that (a) Eq. (5.1) accurately describe normalized FRS signal from a gas mixture at varying temperatures normalized by some reference condition, (b) that the Tenti S6 model accurately describes the RBS spectral profiles and that the transport properties (dynamic viscosity, heat conduction, and bulk viscosity which are used in the Tenti S6 model) of each species i are accurately known over all relevant temperatures, (c) that the I_2 absorption (transmission) spectra is accurately modeled, and (d) the chemical kinetic mechanism used within the non-premixed flame simulations accurately describes the combustion chemistry. Work from Refs. [170-172] have explored (c) and have verified the modeled I_2 spectra to some

extent. The accuracy of the assumptions of (a) and (b) have been tested as part of the current dissertation and are discussed below in Sec. 5.3.

5.3 Assessment of Tenti S6 Model for Combustion Species

This section details measurements targeted to test the Tenti S6 model [119] for several combustion-relevant species over a broad range of combustion-relevant temperatures. As discussed in Ch. 2, the most common models for describing the RBS spectra of individual molecules are the Tenti S6 and S7 models [119, 173]. Due to the importance of these models in many fields (i.e., atmospheric sensing), researchers have measured the RBS spectra for various species to test the accuracy of these models. For example, Vieitez et al. [174] measured both coherent and spontaneous RBS profiles of N_2 and O_2 at room temperature and at pressures ranging from 1 to 3 bar. RBS profiles of N_2 and air at temperatures ranging from 250 to 340 K and pressures ranging from 1 to 3 bar were performed by Ma et al. [175]. Witschas et al. [176] measured RBS spectra for N_2, dry air, and humid air for temperatures of 295 K to 301 K and for pressures of 0.3 to 3 bar. Gu et al. [177] examined the RBS spectra of CO_2 at pressures of 2 – 4 bar at room temperature conditions. Additionally, Gu and Ubachs and Gu et al. [178, 179] measured RBS spectra of N_2, O_2, and air at pressures ranging from 0.6 – 3 bar and at temperatures ranging from 250 K – 340 K. For the conditions covered by these efforts, it was observed that the Tenti S6 model performs very well with deviations between the modeled RBS spectra and measurements at the few percent level. It was also observed that the S6 model generally outperformed the S7 model in terms of accuracy and so the S6 model is utilized in the current work. It should be noted that previous RBS measurements are largely confined to air constituents (i.e., O_2, N_2, or CO_2) and over

a relatively limited range of temperatures and thus there is a need to extend measurements to more combustion relevant conditions.

Whereas in Refs. [174-179] the RBS profiles are directly measured for single species, the current work takes a different approach to assess the Tenti S6 model. Specifically, indirect testing of the Tenti model is performed by comparing measured FRS signals from various combustion relevant conditions to synthetic FRS signals generated from the combination of the Tenti RBS model and the experimentally verified I_2 transmission model from Forkey et al. [170] (see Eqns. (5.1) and (5.3)). As shown from Eqns. (5.1) and (5.3), if the Rayleigh scattering cross section and I_2 transmission are known accurately, then the agreement between measured and synthetic FRS signals would imply that the Tenti S6 model accurately reproduces RBS lineshapes for combustion relevant species. In this way, comparing the measured and synthetic FRS signals provides a high-level assessment of the accuracy of the Tenti S6 model over a broad range of species and temperatures. For a large number of species and mixtures and a broad range of temperatures, the current approach is a more practical and holistic approach to assess the Tenti S6 model within combustion environments.

In Sec. 5.2.1 the experimental methodologies used to perform the different specific model RBS assessment is discussed. Second, in Sec. 5.2.2 comparisons between measured and synthetic FRS signals from various species as a function of temperature are examined. In Sec. 5.2.2, results are discussed from measurements in gas mixtures at atmospheric conditions to assess the assumption that the FRS signal from a gas mixture is simply a mole fraction-weighted average of the individual species contributions. Finally, in Sec. 5.2.3 a comparison between measured and synthetic FRS signals from near-adiabatic H_2/air and CH_4/air flames over a broad range

equivalence ratios, corresponding to several mixture compositions and temperatures, is discussed. The work discussed in the following sections has been published in Applied Physics B [118].

5.3.1 Experiments for Model Assessment

The RBS/FRS model assessment measurements are performed using a common experimental setup, where particular changes to the test apparatus for the various assessments are discussed individually. A schematic of the general experimental setup is shown in Fig. 5.1 with

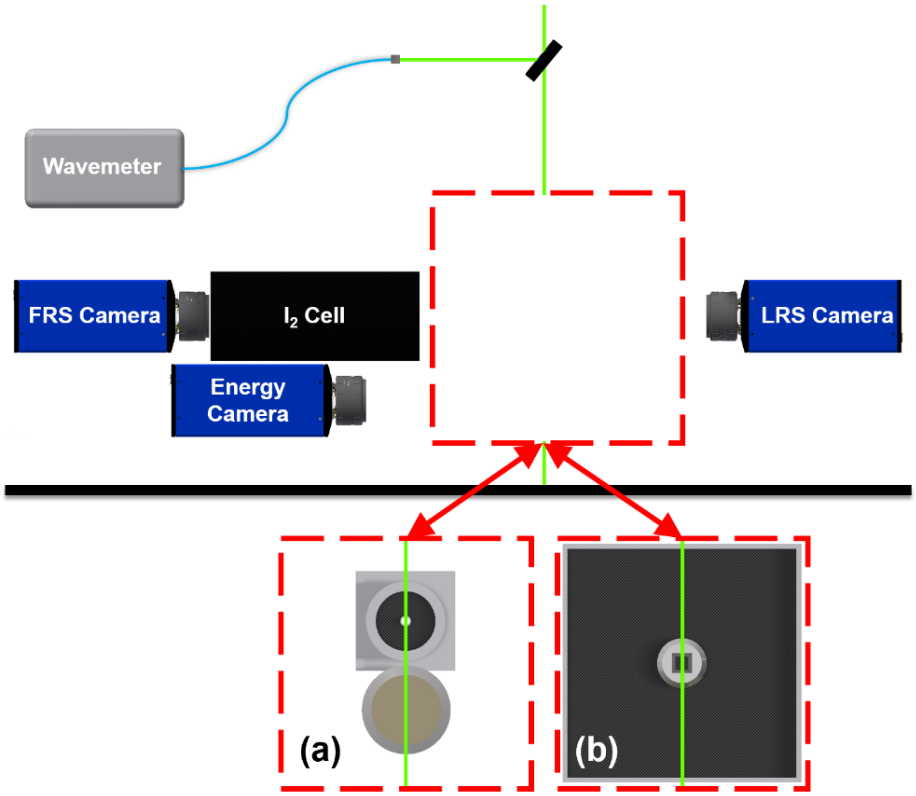

Figure 5.1: Schematic of experimental setup for FRS measurements to assess the accuracy Tenti S6 RBS spectral lineshape model and assumptions in current FRS thermometry approach. (a) Setup for temperature dependent single species FRS measurements and room temperature binary mixture FRS measurements. (b) Setup for FRS measurements in near adiabatic H2/air and CH4/air flames.

insets depicting the different flow configurations used for various assessments as described below. The laser source is an injection-seeded, frequency doubled, Q-switched, Nd:YAG laser operating at a repetition rate of 10 Hz. The nominal pulse energy for the measurements is ~160 mJ/pulse. Prior to entering the measurement volume, a small portion of the laser beam is sent to a high-resolution wavemeter (High Finesse WSU30) with an accuracy of 30 MHz in order to monitor the wavenumber for each laser pulse. The wavemeter is automatically calibrated every half-hour by a fiber-optic-coupled, frequency-stabilized, He-Ne laser operating at 632.9918 nm. The 532-nm output from the Nd:YAG laser is then directed towards the test section and focused down to a small spot using a 750-mm focal length spherical lens.

Three actively cooled, scientific-grade charge couple device (CCD) cameras are used in the model assessment experiments. The first camera (labeled the "FRS Camera" in Fig. 5.1) is placed behind an I_2 cell to collect the temperature- and species-dependent FRS signals. A high transmission, 532-nm bandpass filter is placed between the FRS Camera and the I_2 cell to minimize any extraneous light signals generated in the cell. The I_2 cell is 248 mm long and 76 mm in diameter. It is a starved cell design filled with a sidearm temperature of approximately 37 °C, corresponding to an I_2 partial pressure of 0.75 Torr. This type of cell design is a permanently sealed starved (or super-heated) vapor cell. The cell is made by evacuating a glass cell and heating a sidearm filled with iodine crystal to a desired temperature that sets the desired I_2 vapor pressure. Once the desired vapor pressure is achieved, the cell is sealed off from the side arm fixing the amount of iodine within the cell [180]. The main body of the cell is surrounded by electrical resistance heating tape and operated at a super-heated temperature of 341 K to ensure no I_2 vapor recrystallizes to the solid phase within the filter cell during operation. The cell is maintained at the specified temperature by a digital temperature controller (Cole-Parmer DigiSense) which has a

quoted accuracy of 0.1K. The second camera is used to capture traditional laser Rayleigh scattering (LRS) from the flow of interest (labeled the "LRS Camera" in Fig. 5.1). For the heated single-species FRS response measurements and for the near-adiabatic flame measurements, the LRS measurements are used to determine the local gas temperature, which is used in the analysis of the FRS signals and the corresponding comparison to modeled FRS predictions. For the binary mixture measurements, the LRS measurements are used to determine the component mole fractions with high accuracy. The LRS camera is focused over the same field-of-view as the FRS camera. A third CCD camera (labeled the "Energy Correction" camera in Fig. 6.1) is focused over a uniform air flow issuing from either a matrix burner (as is the case for the temperature and mixture response measurements, shown in Fig. 5.1a) or over a region of coflowing air (as is the case for the near-adiabatic flame measurements, shown in Fig. 5.1b) to monitor and correct for shot-to-shot laser energy fluctuations.

For each of the following FRS signal measurements, the wavenumber measurements are acquired synchronously with the camera images and are used to establish the average wavenumber, $\langle \nu \rangle$ for the particular case. A wavenumber filtering technique is employed, which was first detailed in Ref. [128], that discards instantaneous measurements that have a wavenumber fluctuation greater than ± 0.001 cm^{-1} from $\langle \nu \rangle$. An example signal trace of wavenumbers measured using the wavemeter is shown in Fig. 5.2. In Fig. 5.2 the wavenumber measurements, plotted as a solid blue line, are shown as fluctuations from the mean and the wavenumber filter bounds of ± 0.001 cm^{-1} away from $\langle \nu \rangle$ also are shown. Wavenumber measurements that fall outside the bounds are flagged with a red x and represent samples that are discarded and not used. The corresponding FRS and LRS images also are discarded. In this manner, wavenumber (wavelength) variations do not have to be considered in the interpretation of the results. The average wavenumber values are then used

to determine the relative spectral position between the RBS lineshapes and the I_2 transmission spectra for the calculation of the synthetic FRS signal ratios that are compared with the measured FRS signal ratios.

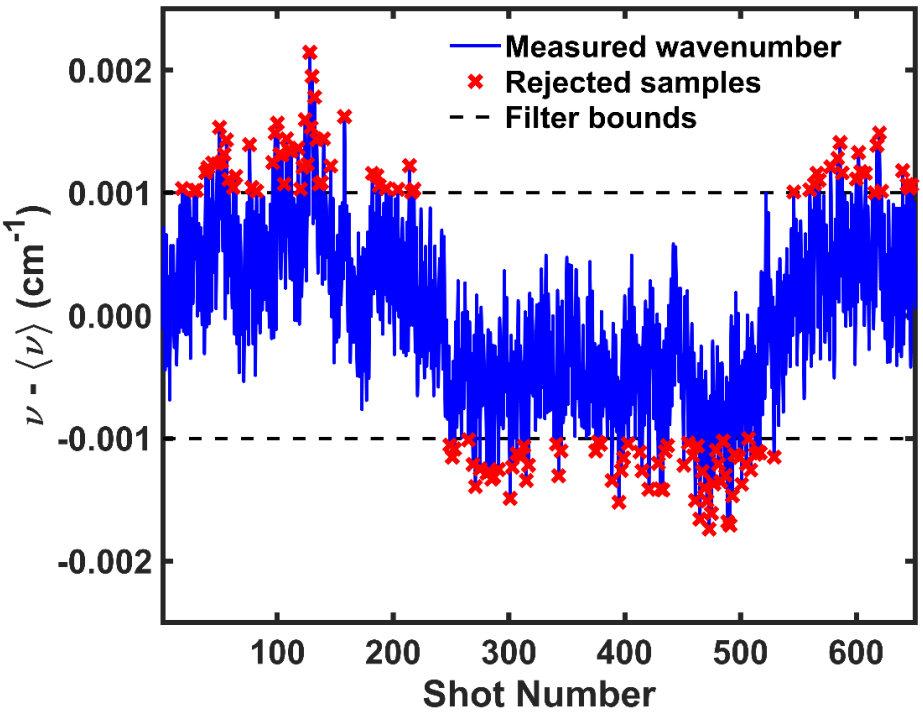

Figure 5.2: Sample wavenumber signal trace. The blue line shows the fluctuations from mean. The dashed black lines represent the wavenumber filter bounds while the red x's represent samples which are discarded.

5.3.1.1 Temperature-dependent, Single Species FRS Measurements

A straightforward experimental configuration is implemented to generate the conditions necessary for the temperature-dependent FRS measurements of each gaseous species. An electrically heated jet surrounded by an inert N_2 coflow is used, where the laser measurements are

performed within the potential core of the jet to ensure that the scattered light originates only from the single species of interest (i.e., no mixing of multiple streams). A schematic of this flow configuration is shown in Fig. 5.1a. This approach avoids challenges associated with using typical optical test cells for high-temperature test conditions, such as non-uniform heating, low heat-transfer-limited peak temperatures, and interference/background scattering from windows and other surfaces within and around the cell. Measurements within the potential core also allow for an additional straightforward temperature measurement of each single species via traditional LRS. Two inline heaters are used separately to achieve the desired temperature range. The first heater is a Tutco HT050 rated for a maximum wattage of 450 W and is used to access the low to mid-range temperatures of 300 K to 900K. The second heater is an Osram-Sylvania Series III air heater rated for a maximum wattage of 2050 W and is used to reach the upper temperature ranges for the current work (~ 900 K to ~1400 K). The inline heaters are oriented in a vertical orientation and placed directly into the inert N_2 coflow, such that the circular outlet of the inline heater acts as the jet exit. The gases examined include N_2, Ar, air, CO_2, H_2, CH_4, and CO. The coflow of N_2 not only provides isolation from the surroundings (i.e., prevention of dust for LRS), but also helps prevent autoignition from occurring when measuring the FRS signals for the fuels at high temperatures. For the current measurements, the flow rates entering the inline heater range from 26 to 37 standard liters per minute (SLPM), depending on the particular gas. For each particular gas, the flow rates are fixed for the full range of temperatures, corresponding to Reynolds numbers (Re) based on jet exit diameter ranging from 310 to 5700, covering both laminar and turbulent jet conditions. With the exception of H_2, all operating conditions correspond to $Re > 1200$ and all cases are turbulent for $T < 400$ K.

Because it is important to ensure the scattering originates from a single species in this configuration, the measurements must be performed within the potential core of the jet. The potential core of a jet does not experience any momentum nor mass transfer and thus does not mix with the surroundings such that the species composition remains constant within the potential core. In general, the potential core length is a non-monotonic function of Re for laminar flow conditions with no analytical solution for variable-density flows. However, previous works have shown for Re $\gtrsim$ 300, the potential core of the laminar jet is greater than that of the turbulent jet (e.g., [181, 182]) which is not dependent on Re. Thus, for any given temperature, the potential core of a turbulent jet case can be considered as the shortest possible potential core length that could be encountered during testing and can be used to determine the appropriate measurement location. The length of the potential core (x_{pc}) of turbulent jets can be estimated from known turbulent jet scaling laws [147, 183] as

$$x_{pc}/d \leq 5.4^2(\rho_i/\rho_\infty)(x/d)^{-1} \qquad \text{Eq. (5.6)}$$

where d is the jet exit diameter, ρ_i is the jet gas density, and ρ_∞ is the coflow gas density, which for the current measurement is nitrogen with an assumed temperature of 296 K.

Using Eq. (5.6) the potential core is estimated across the range of temperatures targeted for each gas species, assuming it remains turbulent for all cases (which again is the conservative guideline on the necessary measurement location). Figure 5.3 shows the estimated potential core length normalized by the tube diameter for turbulent jets of each gas species as a function of temperature. For all gases, the calculated potential core length decreases with increasing gas temperature due to the change in the jet density, ρ_i. Based on these estimates, a measurement location of x/d = 0.5 was targeted, which should ensure than the LRS/FRS measurements are

performed within the jet potential core regardless of operating condition. The measurement location is indicated in Fig. 5.3 as a dashed line. For all test cases the temperature within the potential core is determined via LRS using

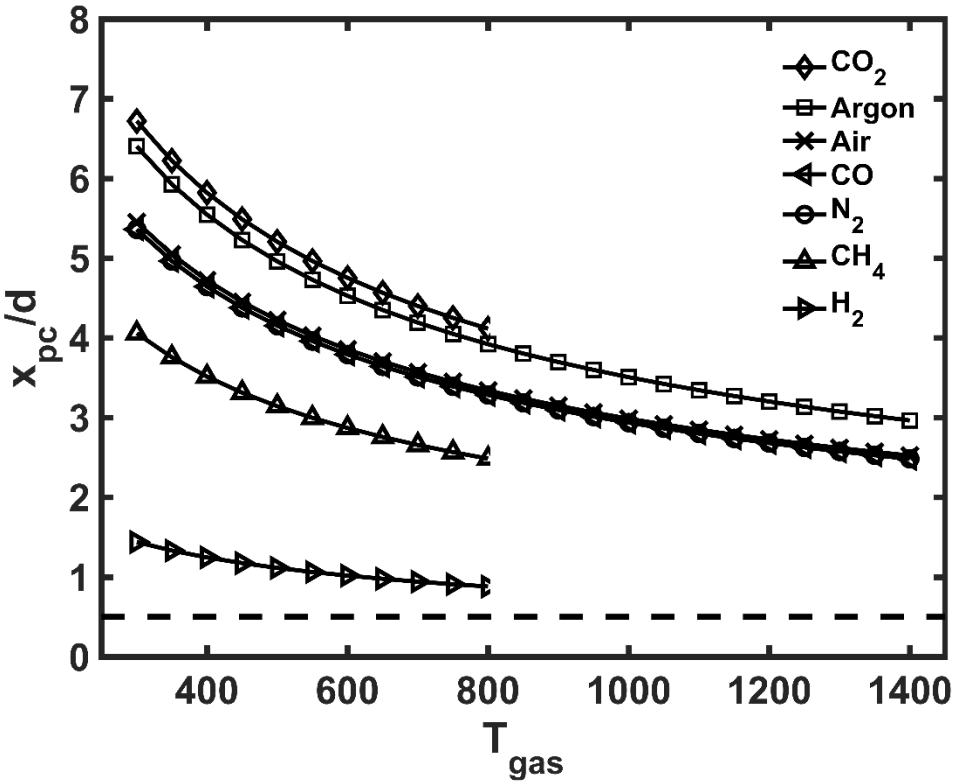

Figure 5.3: Estimated potential core lengths assuming turbulent flow (which have shorter potential lengths then laminar flows) using Eq. (6.6) and assuming the nitrogen coflow has a temperature of 296 K.

$$T_{LRS} = T_{ref} \times S_{LRS,i}(T_{ref})/S_{LRS,i}(T) \qquad \text{Eq. (5.7)}$$

where $S_{LRS,i}(T)$ is the measured LRS signal of species i at temperature T, T_{ref} is a reference temperature, which is 296 K for all cases considered in this work, and S_{ref} is the measured LRS signal at T_{ref}.

Given that the internal structure of the inline heaters is more complex geometrically than a simple circular tube, the jet flow structure occasionally experienced perturbations such that small amounts of fluid from the coflow entered into the measurement region and thus contaminated the measurement. In order to mitigate the effects of these rare occurrences, a post processing algorithm was applied to the FRS and LRS signal profiles to flag "contaminated" signal profiles. These particular measurements are then discarded such that the analysis and statistics are applied only to acceptable samples. The algorithm to filter out contaminated samples involves examining the FRS and LRS profiles within a central region in the jet and rejecting the samples with a percent difference between the maximum and minimum value within that region that exceeded a user-defined threshold. For all of the gases and temperature conditions examined, the majority of the samples were considered "acceptable" and thereby provided large sample sizes for determining the mean FRS signal ratio and gas temperature via LRS.

Figure 5.4 shows examples of two "acceptable" instantaneous FRS signal profiles and the corresponding average FRS signal profiles from measurements in N_2 and H_2. The normalized FRS signal, $S_{FRS,i}/S_{FRS,ref}$ is shown, where $S_{FRS,i}$ represents the measured FRS signal for a particular species and $S_{FRS,ref}$ is the reference condition for the measurements, which is pure N_2 at T = 296 K. The two conditions shown are at elevated temperatures and, in particular, the H_2 jet at T = 801 K is the most challenging case across all the species and temperatures accessed due to it having

the shortest potential core (Re ≈ 300) as well as due to potential buoyancy effects. The example relative FRS signal profiles show some distinct features that give confidence in the measurement

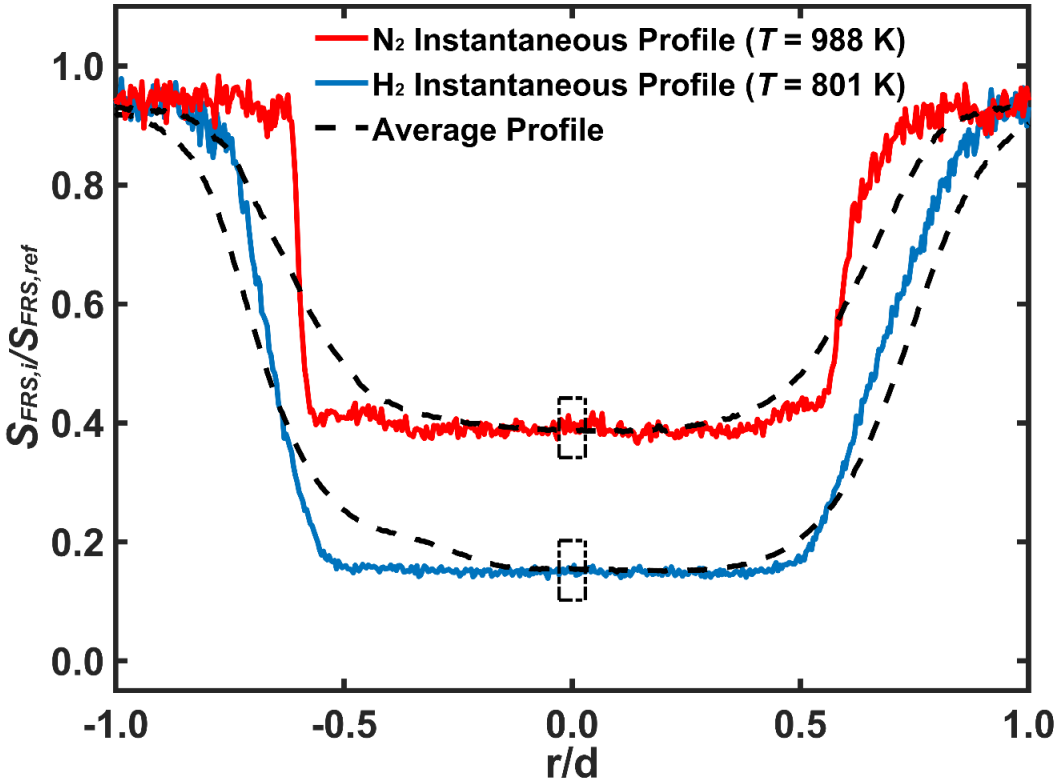

Figure 5.4: Example FRS signal profiles from N_2 and H_2 at elevated temperatures, normalized by a reference conditions of N_2 at T = 300 K. Instantaneous profiles shown as red for N_2 and blue for H_2 while the dashed black lines are the average profiles for the two cases.

approach. First, it is observed that the instantaneous signal profiles show distinct flat regions that span a radial distance of one jet diameter, which is the expected result when in the potential core near the jet exit. Second, it is observed that the FRS profiles approach a value of unity near the coflow region, which is to be expected given the fact that the coflow and the reference case are

both N_2 at T = 300 K. While the instantaneous profiles show a large flat region of minimum signal, the average profiles display more curvature and a smaller flat region of minimum signal. This is due to some spanwise motion of the heated jets during operation. The focus of the post processing algorithm is to flag coflow contamination near the center measurement region and is effective at doing so. However, it does not identify samples that exhibit an intact potential core that were simply displaced some small distance in the radial direction. Thus, the average signal profiles in Fig. 5.4 show the effect of this small "side-to-side" movement of the jet potential core. However, it is noted that the average value in the analysis region (small dashed black box) is identical to that of the instantaneous samples. This implies that the average FRS signal in the analysis region, which is used to assess the results below, is not affected by the small radial drifts of the jet potential core. The results shown in Fig. 5.4 give confidence that all reported measurements were performed in the jet potential core and thus the measured FRS signal is from a single species for all conditions tested.

5.3.1.2 Binary Mixture Experimental Setup

The binary mixture measurements were performed within the same test section as the temperature–dependent single-species measurements, with the exception that a long circular tube replaced the in-line heater since the measurements were performed at room temperature. The circular tube has a smooth interior profile that facilitated fully developed pipe flow at the exit of the tube. This ensured a stable jet potential core such that no samples that were contaminated with the coflow species had to be discarded. The FRS signals of four pairs of binary mixtures (containing combustion-relevant species) were examined as a function of mole fraction. The specific mixture pairs were chosen to test the assumption that the measured FRS signal from a

mixture can be described by the mole fraction-weighted average of the FRS signals from each constituent. The mixtures are described by a molecular weight ratio, R_{MW}, and a ratio of the differential Rayleigh scattering cross sections, R_σ. First, binary mixtures of fuels (CH_4 and H_2) with N_2 (the major component of air) were examined. For the N_2/CH_4 mixture the ratio of molecular weights is R_{MW} = 1.75 while the ratio of differential Rayleigh scattering cross-sections is R_σ = 0.47. For the N_2:H_2 mixture the molecular weight ratio and differential scattering cross ratio are much higher with R_{MW} = 14.3 and R_σ = 4.7. A mixture of two fuels (CH_4 and H_2) also is examined, with a molecular weight ratio of R_{MW} = 7.96 and a differential scattering cross section ratio of R_σ = 10. A final mixture of CO_2 and H_2 was chosen to explore the difference between gases with large difference in both molecular weight and scattering where the ratio of molecular weights of R_{MW} = 21.8 and a ratio of differential scattering cross-sections of R_σ = 11.2.

For each of the four binary mixtures, the FRS signal is measured at six different mixture ratios covering the entire range of possible mixtures. The mass flow rate for each gas is controlled using a calibrated mass flow controller (Alicat) and the target mixture ratio is set by adjusting the flow rates for each species accordingly. The actual mixing state is determined on a shot-by-shot basis using the LRS measurements. The mole fraction for species 1 is determined from

$$X_1 = \frac{S_{LRS,mix} - S_{LRS,2}}{S_{LRS,1} - S_{LRS,2}} \qquad \text{Eq. (5.8)}$$

where $S_{LRS,mix}$ is the LRS signal from any mixture with $0 \leq X_1 \leq 1$, $S_{LRS,1}$ is the LRS signal when the gas mixture is made up entirely of component 1, and $S_{LRS,2}$ is the LRS signal when the gas mixture is made up entirely of component 2.

5.3.1.3 Near-adiabatic Flame Measurements

A burner that is used often in combustion research is the well characterized, near-adiabatic, flat-flame "Hencken" burner [184]. This burner produces a physically flat-flame that stabilizes just above the burner surface (and is not touching the burner) thereby drastically reducing the heat-loss from the flame to the burner surface. Since the configuration results in near-adiabatic conditions, chemical equilibrium software can be used in conjunction with the LRS measurements to estimate the mole-fractions of the species and temperature within the post-flame region with a high degree of accuracy. The burner has three separate gas inputs for fuel, oxidizer, and an inert gas. The fuel and oxidizer streams exit the burner surface separately in a series of small nozzle arrays and mix before igniting above the burner surface. This small mixing region provides a buffer zone between the burner surface and flame. The inert gas (nitrogen in this case) exits in a coflowing region surrounding the main burner matrix and is used to provide momentum balance for the fuel/oxidizer streams such that the flame is flat and not affected by shear. More information about the design and operation of the burner can be found in Ref. [184].

The flow rate for each gas was controlled by mass flow controllers (Alicat), which were calibrated against a laminar flow element (LFE; Meriam Process Technologies) to ensure accurate equivalence ratios for the flames. FRS and LRS measurements of H_2/air and CH_4/air flames at various equivalence ratios, ϕ, were performed. For the H_2/air flames the equivalence ratio ranged from 0.2 to 2.4 while for the CH_4/air flames the equivalence ratio spanned from 0.7 to 1.3. For the H_2/air flames, measurements were performed at 30 mm above the burner surface, while for the CH_4/air flames, the measurements were performed at 18 mm above the burner surface. Similar to the temperature-dependent, single species measurements, the FRS and LRS signals in the post-flame region are normalized by reference measurements in pure N_2 at T = 296 K. Example

normalized profiles from a $\phi = 0.95$ H_2/air flame are shown in Fig. 5.5. The example profiles shown in Fig. 5.5 are consistent with profiles from all other fuel and ϕ cases. The fact that there is a large flat region in the center of the profiles indicates that the measurements provide unambiguous LRS and FRS signals representing the high temperature gas mixture found within the post-flame region of these flames. Furthermore, it is clear from the agreement between the

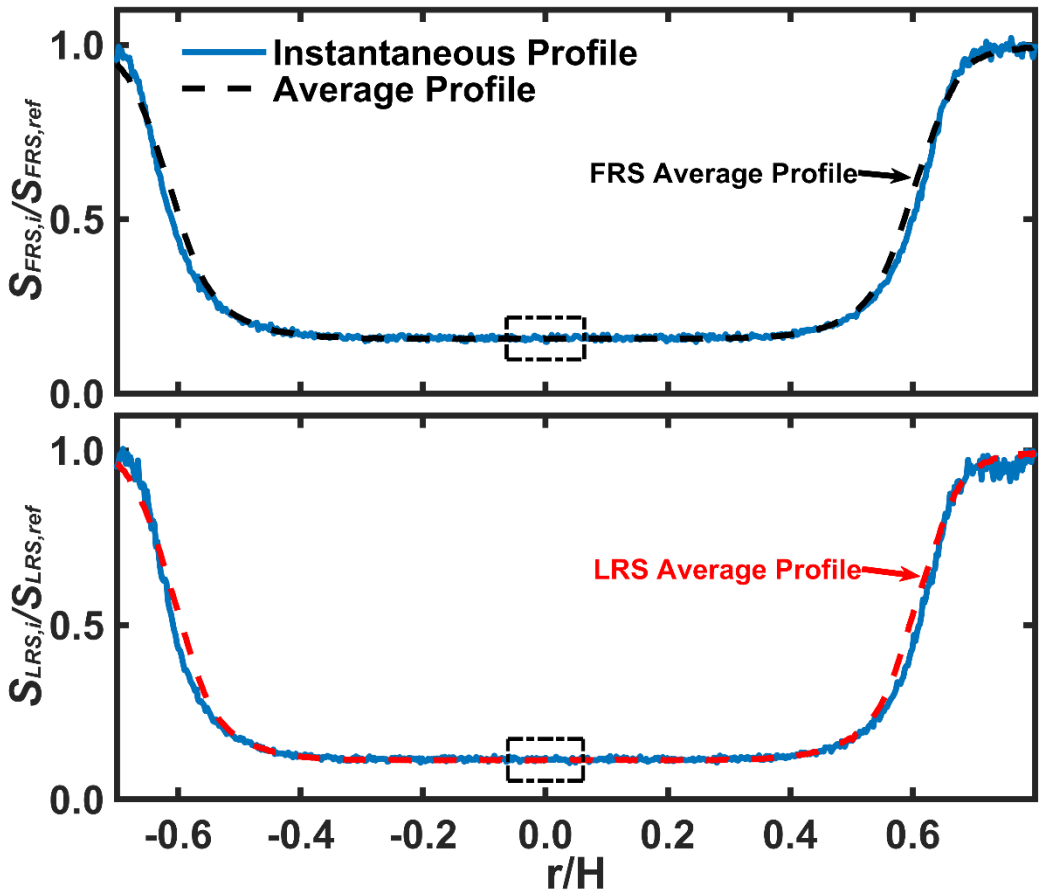

Figure 5.5: (Top) Example normalized FRS signal profiles and (bottom) example normalized LRS signal profiles from measurements from a ϕ = 0.95 H_2/air flame stabilized above the Hencken burner surface. The reference condition is N_2 at T = 296 K. Single shot profiles are shown as solid blue lines and the dashed lines are the average profiles. The dashed black lined boxes represent the region where the signal ratios are obtained for analysis.

single-shot and average profiles that the flame is stable and the measurements are obtained with low signal noise.

For a given ϕ, equilibrium calculations are performed using the NASA chemical equilibrium analysis program (CEA), in conjunction with the signal measurements, to determine both the gas temperature as well as the mole fractions of species including N_2, O_2, CH_4, H_2, CO_2, H_2O, CO, and OH. The process of determining the temperature and species concentration is the same strategy presented in [185] to determine the coflow temperature of jet-in-hot-coflow auto-ignition experiments. The first step is to assume adiabatic equilibrium and calculate the product species using CEA. Using the adiabatic flame temperature (T_{ad}) and the associated mole fractions generated from that assumption, a synthetic LRS signal ratio is calculated and compared to the measured LRS signal ratio. In the case where the measured LRS signal ratio exceeds the theoretical signal ratio (implying that there is some heat lost, either to the burner or through some other means), CEA is then run again with a temperature $T < T_{ad}$, yielding new mole fraction values. Using the new temperature guess and the updated mole fraction values, a new synthetic LRS signal is determined and compared with the measured LRS signal. This process is repeated until the measured and synthetic LRS values converge. In this way, the LRS measurements accounts for heat loss and provides an accurate estimate of both the post-flame temperature and the species composition in the post-flame region. Once the temperature and species mole fractions are determined, a synthetic FRS signal is calculated in order to compare with the measured FRS signal. This comparison of the FRS measurements with a synthetic FRS signal generated using the Tenti S6 model provides an indirect method to assess both (a) the Tenti S6 RBS model at high temperatures and (b) the mixture-averaged FRS signal assumption outlined in Eqs. 5.1 and 5.2. In addition, these measurements provide an indirect test of the FRS signals for gas-phase H_2O, which

is an important major species within combustion environments which is not able to be assessed within the temperature-dependent, single-species measurements.

5.3.2 Results of Tenti S6 model assessment

Since the basis for evaluating the Tenti S6 model is a comparison between measured and synthetic FRS signals, a few comments on the generation of the synthetic FRS signals are warranted. The Tenti S6 model only considers Placzek trace scattering in the calculation of the Cabannes line, while measurements of scattered light will consist of three different components: (i) Placzek trace scattering, (ii) Q-branch rotational Raman scattering, and (iii) Stokes and anti-Stokes rotational Raman scattering. For a more complete comparison between measured and calculated FRS signals, Q-branch and S/AS Raman scattering effects are added into the synthetic signal calculations as described in [118]. For a single species, Eq (5.2) is modified to

$$S_{FRS,i} = CI_0 n_i \psi_i' \qquad \text{Eq. (5.9)}$$

where ψ_i' is a modified FRS specific variable which can be expressed as

$$\psi_i' = \begin{matrix} \sigma_i^t \int_\nu \mathcal{R}_i(\nu_r)\tau_{I2}(\nu)\tau_{BPF}(\nu)d\nu \; + \sigma_i^Q \int_\nu \mathcal{R}_i^Q(\nu_r)\tau_{I2}(\nu)\tau_{BPF}(\nu)d\nu \\ + \sum_{J=0}^{\infty} \sigma_i^{J\to J'} F_J \int_\nu \mathcal{R}_i^{J\to J'}\left(\nu_r, \Delta\nu_{J\to J'}\right)\tau_{I2}(\nu)\tau_{BPF}(\nu)d\nu \end{matrix} \qquad \text{Eq. (5.10)}$$

In Eq. (5.10) the last two terms represent the Q-branch and Stokes/anti-Stokes Raman scattering contributions to the total scattering signal, respectively. σ_i^t, σ_i^Q, and $\sigma_i^{J\to J'}$ are the Placzek trace[2], Q-branch rotational Raman, and Stokes/anti-Stokes rotational Raman scattering components of the

[2] The trace scattering cross section, σ_i^t is calculated as $\sigma_i - (4\rho_i/3 - 4\rho_i)$, where ρ_i is the depolarization ratio of species *i*.

differential Rayleigh scattering cross section, respectively; J is the initial rotational-angular-momentum quantum number; F_J is the fraction of molecules in state J; $\Delta\nu_{J\rightarrow J'}$ are the rotational Raman shifts; $\mathcal{R}_i(\nu_r)$, $\mathcal{R}_i^Q(\nu_r)$, and $\mathcal{R}_i^{J\rightarrow J'}\left(\nu_r, \Delta\nu_{J\rightarrow J'}\right)$ are the spectral lineshapes for the Placzek trace, Q-branch rotational Raman, and Stokes/anti-Stokes rotational Raman scattering, respectively; and $\tau_{\mathrm{BPF}}(\nu)$ is the transmission of the bandpass filter centered around 532 nm. Details concerning the generation of the Q-branch and Stokes and anti-Stokes rotational Raman spectra are discussed in [118]. As discussed below, with the exception of CO_2, the rotational Raman scattering contributions are small and thus the comparison of the measured and synthetic FRS signals is an evaluation of the Tenti S6 RBS model.

For the temperature-dependent single species measurements, the reference condition is pure N_2 at T_{ref} = 296 K such that the normalized synthetic FRS signals are written as

$$\left.\frac{S_{FRS,i}(T)}{S_{FRS,N_2}(T_{ref})}\right|_{syn} = \frac{T_{ref}}{T} \times \frac{\psi'_i(T)}{\psi'_{N_2}(T_{ref})} \qquad \text{Eq. (5.11)}$$

For the near-adiabatic flame measurements the reference condition also is N_2 at room temperature, such that the normalized synthetic FRS signals are written as

$$\left.\frac{S_{FRS,mix}(T)}{S_{FRS,N_2}(T_{ref})}\right|_{syn} = \frac{T_{ref}}{T} \times \frac{\sum_i^N X_i\psi_i}{\psi_{N_2}(T_{ref})} \qquad \text{Eq. (5.12)}$$

where the mole-fractions, X_i, are determined from the combination of CEA and the LRS measurements as described above. For the flame temperatures considered, the total rotational Raman effects were < 1% and thus were not considered in the analysis. Average wavenumbers from the experiment (discussed above in section 5.3.1) are used to determine where the incident laser is centered relative to the I_2 spectra. The Rayleigh scattering cross sections used in the

calculation of synthetic signals are obtained from Refs. [186, 187] and the I_2 spectral transmission ($\tau(\nu)$) profile is determined using a code originally developed by Forkey et al. [34] that calculates the absorption spectra of the $B({}^3_0\Pi_{0^+u}) \leftarrow X({}^1_0\Sigma_g{}^+)$ electronic transition of iodine. The I_2 model has been validated experimentally to a certain extent [170, 172, 188] and has been modified to account for non-resonant background effects [189]. Therefore, for the following tests to evaluate the Tenti S6 model, the calculated I_2 absorption spectrum is treated as accurate. Finally, it should be noted that as described in Ch. 2 the S6 model from Tenti et al. [119] is based on solving a linearized Boltzmann equation, where the intermolecular forces are treated semi-classically. To calculate the scattering profiles of each species, values for shear viscosity (μ), thermal conductivity (κ), bulk viscosity (μ_B), and the internal specific heat capacity per molecule (c_{int}) are needed as inputs. Ref. [118] describes in detail how these values are determined and utilized.

5.3.2.1 Temperature-dependent FRS Signals for Single Species

As a first assessment of the measurements, the relative LRS signal ratio of each gas, $S_{LRS,i}/S_{LRS,N_2}$ at T = 296 K is compared to known relative Rayleigh scattering cross-sections as shown in Table 5.1. Those measurements show good agreement with scattering cross sections measured from Ref. [186], with a maximum difference of < 2.2%, which is less than the uncertainty in the Rayleigh scattering cross section measurements. This close agreement gives confidence in the LRS measurement technique which will be used to determine the gas-phase temperature and in the ability to provide a reliable uncontaminated FRS/LRS signal from the species of interest in the heated jet configuration.

The measured relative FRS signals, $S_{FRS,i}/S_{FRS,ref}$, for each individual gas species are compared to synthetic FRS signals calculated using Eq. (5.11). Table 5.1 shows the results of

Gas	$\left.\frac{S_{LRS,i}}{S_{LRS,N_2}}\right\|_{Exp}$	$\frac{\sigma_i}{\sigma_{N_2}}$ [186]	$\left.\frac{S_{FRS,i}}{S_{FRS,N_2}}\right\|_{Exp}$	$\left.\frac{S_{FRS,i}}{S_{FRS,N_2}}\right\|_{Syn}$
Ar	0.866	0.865	0.649	0.647
air	0.970	0.969	0.952	0.979
H2	0.216	0.213	0.325	0.318
CO2	2.394	2.390	1.881	1.888
CH4	2.188	2.140	2.929	2.801
CO	1.254	1.250	1.258	1.252

Table 5.1: Measured LRS and FRS signal ratios at T = 296 K compared to published values of Rayleigh scattering differential scattering cross section ratios (here shown as σ instead of $d\sigma/d\Omega$ for clarity), and synthetic calculated FRS signals.

$S_{FRS,i}/S_{FRS,ref}$ at T = 296 K and P = 1 atm. Comparisons between the measured FRS signal ratios and the synthetic FRS signal ratios show excellent agreement with < 2% error between the measurements and the synthetic signal ratios for Ar, air, H_2, CO_2, and CO and 4% error for CH_4. It is noted that the inclusion of the Q-branch and Stokes/anti-Stokes rotational Raman scattering contributions in the synthetic signals have negligible effects on the results with the exception of CO_2. For N_2, O_2, CO, and H_2, the estimated combined contribution of the Q-branch, Stokes, and anti-Stokes rotational Raman scattering to the total scattering signal is < 2.5% at 296 K and decreases with increasing temperature (see [118]). In this manner, the accuracy of the synthetic FRS signals implies accurate RBS lineshape predictions at 296 K using the Tenti S6 model. For CO_2, rotational Raman scattering is approximately 16% of the total scattering signal at 296 K. As shown in Table 1, the exclusion of rotational Raman scattering leads to a discrepancy of approximately 10.3% between the measured and synthetic FRS signals. When including rotational Raman effects, the measured and synthetic CO_2 FRS signals are within 0.3% of one another. This likely implies that the Placzek-trace portion of the RBS lineshape is accurately predicted using the

Tenti S6 model, which would be consistent with the reasonable agreements observed between measured and modeled CO_2 RBS spectra presented by Gu and Ubachs [178]. In their work, there are small, but noticeable differences between measured and modeled spectra near the center frequency that may be due to the exclusion of Q-branch rotational Raman scattering contributions (~ 4%).

Figure 5.6 shows the measured and calculated synthetic FRS signal ratios as a function of temperature for seven gaseous species. The black circles are the direct measurements of the temperature-dependent FRS signal ratios of the various gases normalized by FRS signal obtained in pure N_2 at 296 K. The experimental results are average values computed from approximately 350 samples per data point. The red squares are the synthetic FRS signal ratios calculated using Eq. (5.11) in conjunction with the Tenti S6, the Forkey I_2 transmission model, and additional rotational Raman scattering calculations. While not shown here, the exclusion of rotational Raman scattering contributions for CO_2 led to notable discrepancies between the synthetic and experimental results for lower temperatures (< 600 K). However, as temperature increases the difference between the synthetic results and measurements reduces as expected based on the results shown Ref. [118] which shows that the contribution of the rotational Raman scattering signal to the total signal decreases with increasing temperature. Since the formation of CO_2 only becomes important at elevated temperatures and peak CO_2 mole fractions are typically less than 0.15 under combustion conditions, it is expected that the total contribution of rotational Raman scattering will be less than 1.5% of the total FRS signal. Thus, the exclusion of rotational Raman scattering contributions is not a major concern for the accuracy of the FRS thermometry techniques used in reacting flows.

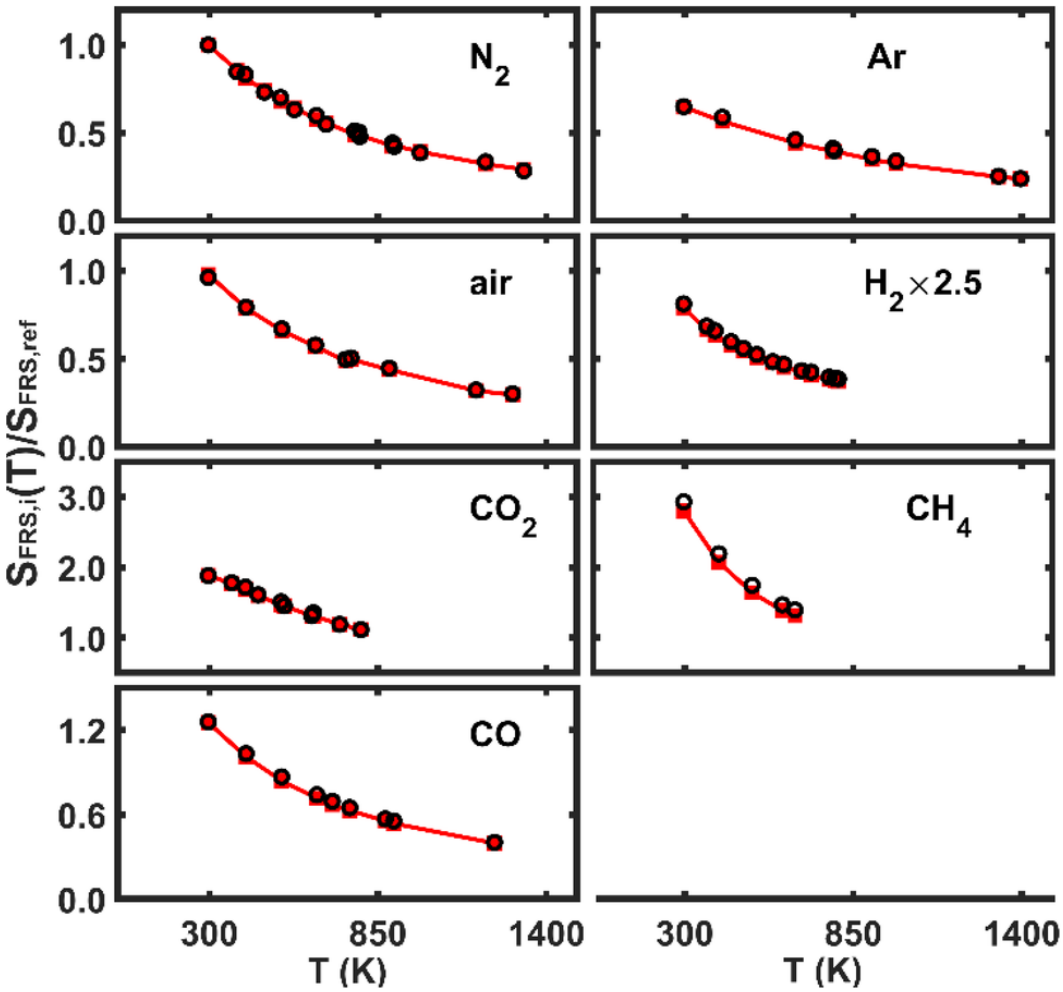

Figure 5.6: Temperature-dependent FRS signals for various gases. All FRS signal ratios are normalized by results from pure N_2 at T = 296 K. Results are show for N_2, Ar, air, H_2, CO_2, CH_4, and CO with experimental values shown as black circles and synthetic data shown as red squares. For H_2, the experimental and synthetic FRS signal ratios have been multiplied by 2.5 for clarity.

In terms of the fuels, both H_2 and CH_4 show good agreement between the modeled results and measurements throughout the range of temperatures tested. The peak temperatures achieved for these cases is due to limitations in the heaters. It should be noted, however, that this is not a significant issue for FRS flame-based measurements since the contribution from fuels to the total FRS signal in the majority of reacting flows will be small at higher temperatures due to reaction.

Since the fuels will be consumed at lower temperatures, the assessment of the accuracy of the RBS spectral modeling only is critical at lower temperatures. From these results it is clear that the synthetic FRS signals, and therefore the predicted RBS lineshapes computed using the Tenti S6 model are sufficiently accurate over a broad range of temperature considered for several combustion-related species.

5.3.2.2 Binary-gas Mixture Results

In order to assess the assumption that the FRS signal from a gas mixture in the kinetic regime can be treated as the mole fraction-weighted average of the FRS signal from each component, FRS measurements were performed in binary mixtures at atmospheric pressure and temperature. For a binary mixture, validation of this assumption implies that the relationship between the FRS signal and the mole fraction of one of the components is linear. In this manner, a normalized FRS signal is defined as

$$S_{1:2}^{*}(X_1) = \frac{S_{FRS,mix} - S_{FRS,2}}{S_{FRS,1} - S_{FRS,2}} \qquad \text{Eq. (5.13)}$$

where X_1 is the mole fraction of component 1 (where the corresponding mole fraction of component 2 given by $X_2 = 1 - X_1$), $S_{FRS,mix}$ is the FRS signal from a mixture of components 1 and 2, $S_{FRS,1}$ is the FRS signal from a gas consisting of component 1 only and $S_{FRS,2}$ is the FRS signal from a gas consisting of component 2 only. It is noted that $S_{1:2}^{*}$ is bound between 0 and 1, when X_1 varies from 0 to 1.

Shown in Fig. 5.7 are plots of the normalized FRS signal $S_{1:2}^{*}$ as a function of mole fraction of the mixture components. While only the mole fraction value of one component is shown, the

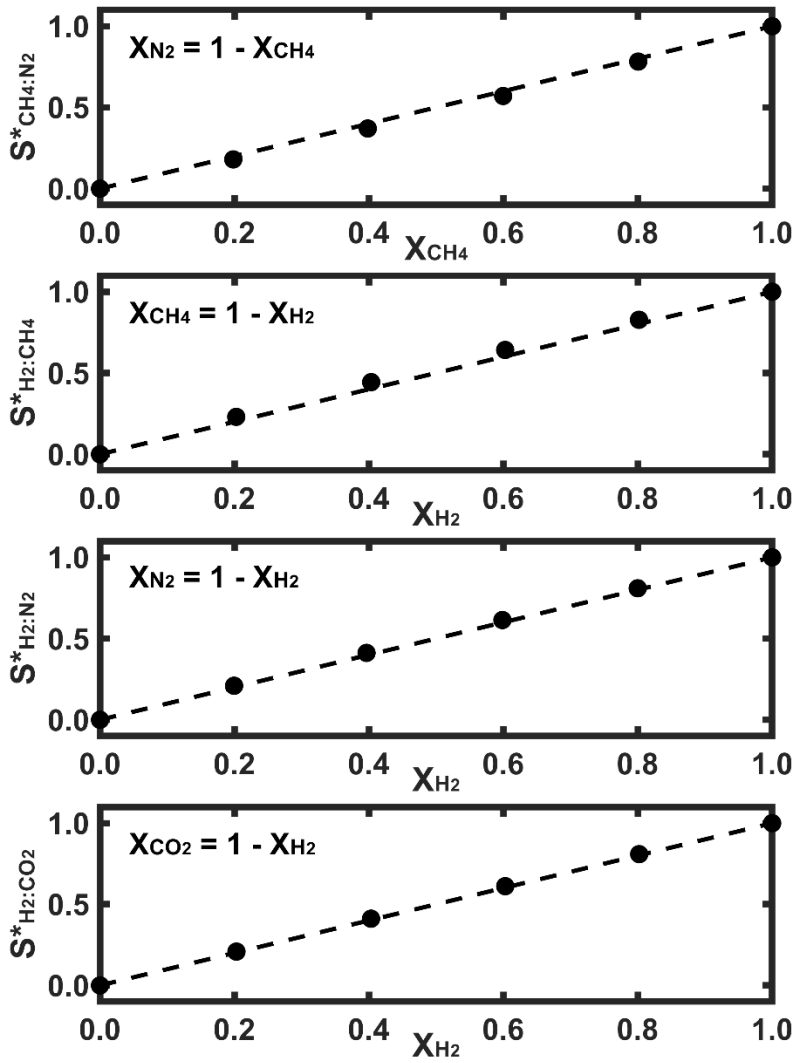

Figure 5.7: Normalized FRS signal (S^*) versus mole fraction for binary gas mixtures at room temperature and pressure. Experimental results are shown as black symbols and the dashed black line represents the ideal linear behavior.

other can be determined via the expression in the inset. For each of the four mixtures, the measured normalized FRS signal, $S^*_{1:2}$ (shown as solid symbols), closely follows the ideal linear curve (shown as a solid black line). Least-squares linear fits applied to the data yield an R-squared value of > 0.997 for all four binary mixtures indicating a high degree of linearity for the measured

response curves. These results imply that for the current set of conditions, the assumption that total FRS signal can be represented as the mole fraction-weighted average of the components of the mixtures is valid. Given that the mole fraction-weighted assumption is valid for atmospheric temperature and pressure conditions ($y \approx 1$), then it would be expected to hold for higher temperature conditions in combustion environments at atmospheric pressure as this means lower density and thus decreased y-parameter; conditions that can be characterized as being in the 'kinetic' regime.

5.3.2.3 Near-adiabatic Flame FRS Signal Response Results

Simultaneous FRS and LRS measurements were made within the post-flame region of near-adiabatic flames produced by the Hencken burner as described above. A full range of equivalence ratios of H_2/air ($0.2 < \phi < 2.4$) and CH_4/air ($0.7 < \phi < 1.3$) have been tested, resulting in a large range of temperature and mixture fractions. Figure 5.8 shows the comparison between the measured FRS signals and the synthetic FRS signals calculated using measured temperatures, estimated species mole fractions (described above), and the combination of I_2 absorption and Tenti S6 RBS models via Eq. 5.12. Figure 5.8a shows the results from the set of CH_4/air flames and Fig. 5.8b shows the results from the set of H_2/air flames. For both sets of the flames, the measured FRS signals are represented by the black, circular symbols and the synthetic FRS signals are represented by the red, square symbols.

The results show that there is excellent agreement between measured and synthetic FRS signals for both the CH_4/air and H_2/air flames across the wide range of equivalence ratios examined. This can be seen clearly in Fig. 8(c), which plots the measured FRS signals as a function of the synthetic FRS signals for all CH_4/air and H_2/air flame cases. For the CH_4/air flames, there

is less than 1.2% difference between the measured and synthetic FRS signals, while there is less than 2% difference between measured and synthetic FRS signals for the H_2/air flames for $0.2 <$

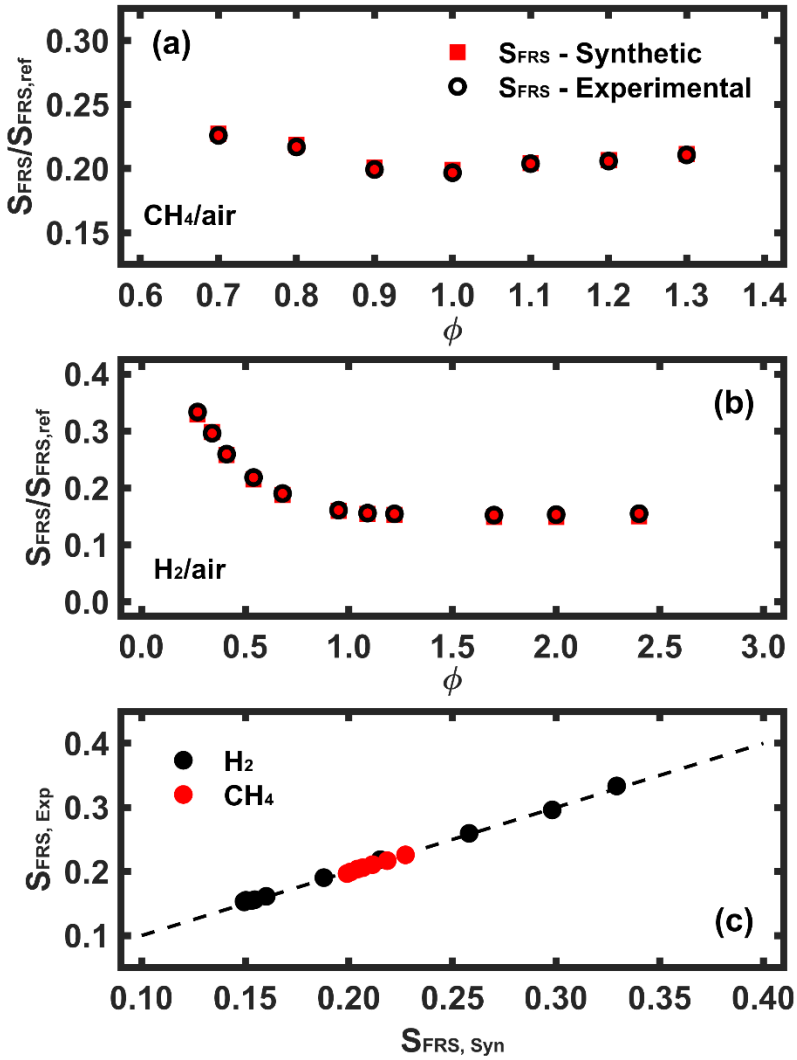

Figure 5.8: (a) Normalized FRS signal versus equivalence ratio for a CH_4/air near-adiabatic Hencken flame and (b) normalized FRS signal versus equivalence ratio for an H_2/air near-adiabatic Hencken flame. Experimental results are shown as black circles while the estimated synthetic symbols are shown as red squares. (c) Comparison of experimental normalized FRS signal versus synthetic normalized for the CH_4/air (red circles) and H_2/air (black circles) Hencken flames. The dashed line represents the ideal case where $S_{FRS,Exp} = S_{FRS,Syn}$.

$\phi < 1.7$. For $\phi = 2.0$ and 2.4, the difference between measured and synthetic FRS signals is ~ 3%. The agreement between measured and synthetic FRS signals over the broad range of equivalence ratios is notable since (a) the calculation of the synthetic FRS signal assumes the mixture-weighted formulation shown in Eqs. (5.1) and (5.2) and (b) the various species mole fractions change considerably over the full range of equivalence ratios considered. Table 5.2 shows the span of various species mole fractions for the range of equivalence ratios considered.

From the good agreement between the measured and synthetic FRS signals, it can be inferred that the assumed mixture-weighted formulation of Eq. 5.1 is justified within the kinetic regime, further corroborating the binary mixture results discussed above. In addition, from these results it can be argued that the RBS spectra of the relevant combustion species, including H_2O, are calculated accurately, at least over the range of temperatures represented by the current atmospheric-pressure flame conditions.

H_2/Air - $0.2 \leq \phi \leq 2.4$			CH_4/Air - $0.7 \leq \phi \leq 1.3$		
Species	X_{Low}	X_{High}	Species	X_{Low}	X_{High}
H_2	0	0.33	N_2	0.66	0.74
N_2	0.44	0.75	O_2	0	0.06
O_2	0	0.75	H_2O	0.14	0.19
H_2O	0.11	0.33	CO	0	0.06
			CO_2	0.05	0.09

Table 5.2: Estimated species mole-fractions for H_2/air (left) and CH_4/air (right) near-adiabatic Hencken flames for a range of equivalence ratios.

The combined results from Secs. 5.3.2.1 – 5.3.2.3 show excellent agreement between the experimentally measured FRS signals and synthetically calculated FRS signals, which utilize RBS

lineshapes calculated using the Tenti S6 model [119] in conjunction with modeled I_2 transmission, originally developed by Forkey et al. [170]. This gives a high-degree of confidence that these models will be sufficient to allow for quantitative FRS-based measurements in reacting flows.

5.4 Application of FRS Thermometry Approach in Turbulent Nonpremixed Flames

As discussed previously, once the Tenti S6 RBS model was validated, a fuel comprised of $CH_4/H_2/Ar$ was designed to enable FRS measurements using Eq. (5.5). In addition to having an FRS figure of merit ($\mathcal{F}$) near unity, the fuel also has the property of having nearly constant mixture-averaged Rayleigh scattering across mixture fraction space, thereby allowing traditional laser Rayleigh scattering (LRS) to be used to determine temperature as a "standard" with which to compare and assess the accuracy of the FRS-based results. Section 5.4.1 will discuss the fuel mixture as it pertains to the thermometry approach. Section 5.4.2 will discuss the experimental methodologies of a simultaneous LRS/FRS thermometry measurement in order to test the FRS thermometry approach. Finally, Sec. 5.4.3 will discuss the results of those efforts. The work in the following sections have been published in Applied Optics [190].

5.4.1 Fuel selection for FRS thermometry

In order to determine specific fuel mixtures that produce $\mathcal{F} = 1$ across mixture fraction space, a comprehensive FRS simulation tool has been developed consisting of several sub-modules. First is the calculation of the I_2 transmission spectra for given cell temperatures, absorption path length, and I_2 partial pressures using the I_2 absorption code from Forkey et al. [170] described above. The Rayleigh-Brillouin scattering of each species is calculated using the S6 model from Tenti et al. [119] as described above. In order to calculate the RBS spectral profiles of each species, temperature-dependent transport coefficients (dynamic viscosity, heat conduction,

and bulk viscosity) are required. The temperature dependent transport properties of N_2, O_2, H_2, CH_4, Ar, CO_2, H_2O, CO, and OH are calculated based on published data and temperature-dependent empirical fits as described and reported in Ref. [118]. All calculated RBS spectra are then convolved with a model of the current laser system as described in Refs. [172] and [188]. The differential Rayleigh scattering cross sections are taken from [186] and the predicted species-specific FRS parameter ψ_i is then coupled to laminar counterflow flame simulations using the OPPDIF code [191] with GRI-mech 3.0 [192] chemistry. Using this FRS simulation tool, a series of "trial and error" calculations are performed until a fuel mixture is found that satisfies $\mathcal{F} \approx 1$.

Figure 5.9 shows the results of applying Eq. 5.5 to the laminar counterflow flame simulations results for a fuel comprised of 16% CH_4, 16% H_2, and 68% Ar issuing into room temperature air. The I_2 spectra are simulated using a path length of 25.4 cm, a cell temperature of 341 K, and cell pressure of 146.65 Pa. The central frequency of both the laser and RBS profiles for both the flame case as well as the reference air case are set to 18788.335 cm^{-1} which is in the center of a particular I_2 absorption feature (marked in Fig. 2.5 above). These I_2 and laser properties are chosen so as to match the current experimental conditions. The top part of Fig. 5.9 shows the calculated temperatures as a function of mixture fraction, ξ, which can be calculated using Eq. 1.14, where ξ = 1 corresponds to pure fuel and ξ = 0 corresponds to pure air. The solid black line represents the "actual" temperature from the counterflow flame simulation which has been calculated using detailed chemistry. The dashed, red line represents the temperature which would be inferred from a single FRS measurement using Eq. 5.5. The simulated FRS signals are calculated using the local composition from the OPPDIF simulation under the aforementioned fueling conditions. A fortuitous outcome of choosing the particular fuel combination is that the

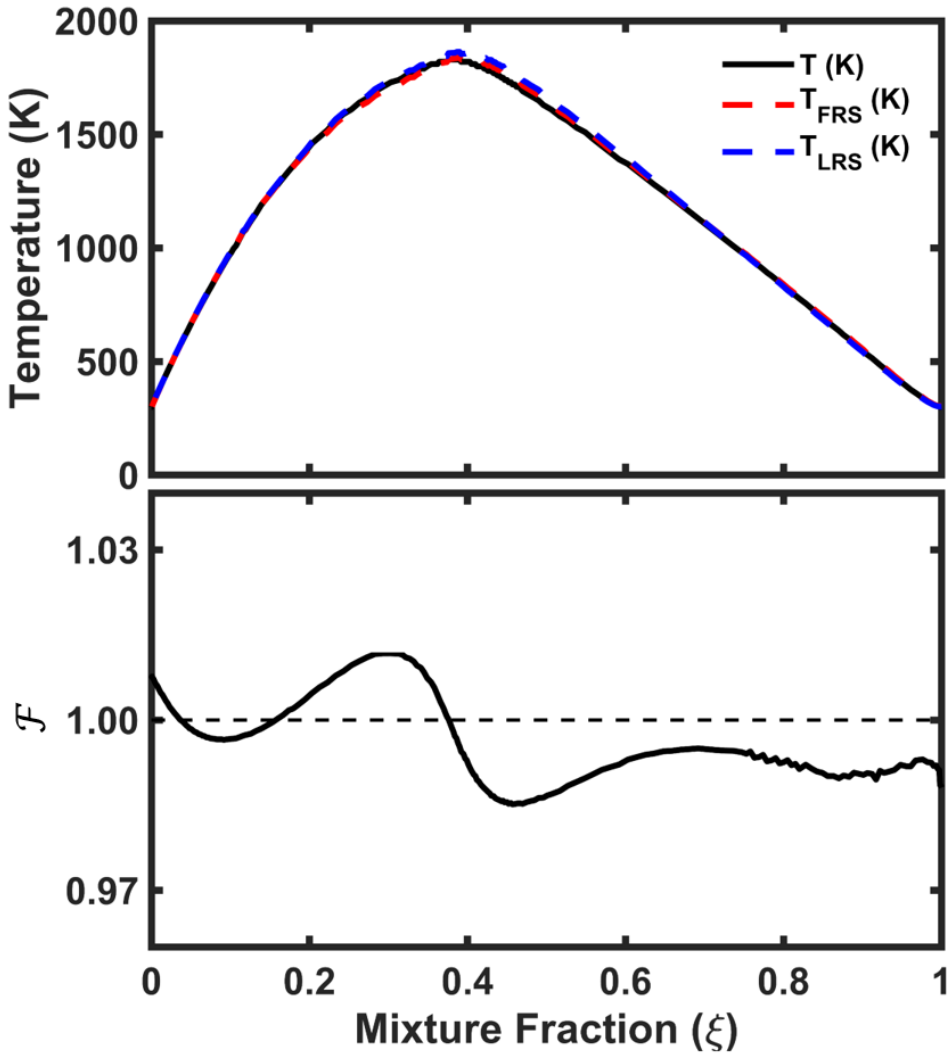

Figure 5.9: (Top) Simulated temperature versus mixture fraction using an LRS thermometry approach (blue dashed, via Eq. 5.7), and using the FRS thermometry approach (red dashed, via Eq. 5.5), compared with the "actual" temperature output from the OPPDIF simulation of 16% CH_4, 16% H_2, and 68% Ar reacting with air. (Bottom) Variation of figure of merit ($\mathcal{F}$, from boxed term in Eq. 5.4) as a function of mixture fraction.

mixture-averaged Rayleigh scattering cross section is nearly constant (±1.5%) across all composition space. This allows for an LRS-based temperature measurement to be utilized as an independent standard against which the accuracy of the FRS thermometry approach can be

assessed. The dashed, blue line in Fig. 5.9 represents the temperature that would be inferred from an LRS thermometry approach. The predicted FRS- and LRS-based temperatures agree quite well with the "actual" temperatures from the flame simulations. The bottom part of Fig. 5.9 shows the calculated figure of merit, $\mathcal{F}$, which is determined from the boxed term in Eq. 5.4, also as a function of mixture fraction for the selected fuel mixture reacting with air. It is observed that $\mathcal{F}$ is near unity throughout the mixture fraction space. These results support the proposed methodology of fuel tailoring for enabling accurate temperature measurements in non-premixed flames using a single FRS measurement.

5.4.2 Experimental methodology for simultaneous FRS/LRS thermometry

The schematic for the simultaneous LRS and FRS temperature imaging system is shown in Fig. 5.10a. The laser source is an injection-seeded, frequency doubled, Q-switched, Nd:YAG laser operating at a repetition rate of 10 Hz. The nominal pulse energy for the current LRS/FRS measurements is ~850 mJ/pulse. Prior to passing through the sheet forming optics, a small portion of the laser beam is picked off using a beam splitter and reflects 5% of the light to the same high-resolution wavemeter (High Finesse WSU30) as used in section 5.3, to monitor the wavenumber for each laser pulse. The wavemeter is calibrated every half-hour by a fiber-optic-coupled, frequency-stabilized, He-Ne laser operating at 632.9981 nm. The 532-nm output from the Nd:YAG laser is then directed towards the test section and is focused using a 750-mm focal length cylindrical lens to a two-dimensional (2D) laser sheet approximately 8 mm tall and 0.1 mm thick as determined from the full width at half of maximum (FWHM) of the laser sheet. Three scientific-grade CCD cameras are used in the experiment. One camera is focused over a uniform air flow issuing from a matrix burner (labeled the "Energy Camera" in Fig. 5.10) adjacent to the main

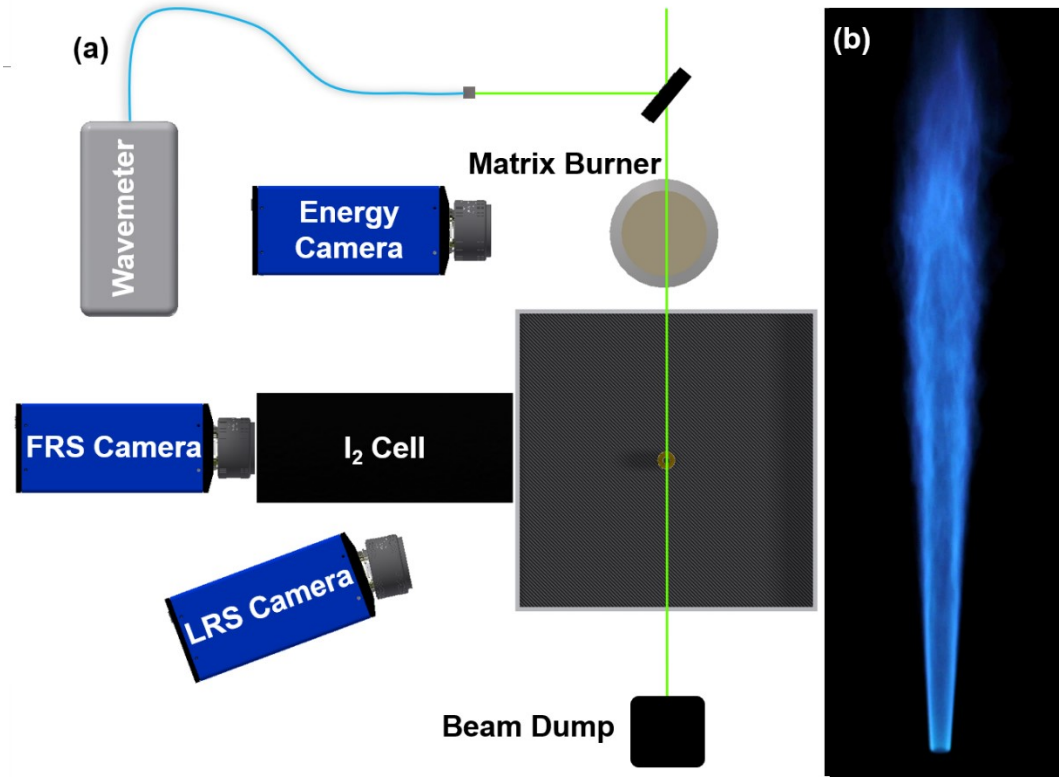

Figure 5.10: (a) Schematic of experimental setup for simultaneous LRS/FRS planar temperature measurements. (b) Photograph of turbulent CH_4/H_2/Ar non-premixed piloted jet flame operating at Re = 10,000.

burner in order to monitor and correct for shot-to-shot laser energy fluctuations as well as to correct for laser sheet intensity variations within each laser sheet. This is similar to the CMOS camera labeled "SC Camera" in Fig. 3.1b. A second camera (labeled "FRS camera" in Fig. 5.10a) is placed behind an I_2 cell and is focused over the test section. The I_2 cell is the same as that used in section 5.3. Just as in the experimental setup described in section 5.3, a high-transmission, 532-nm bandpass filter is placed in between the CCD camera (coupled to an 85-mm *f*/1.4 lens) and the I_2 cell to minimize any extraneous light signals. A third camera (labeled "LRS camera" in Fig. 5.10a) is placed adjacent to the FRS camera at an angle and is focused over the same region as the FRS

camera using a Scheimpflug adapter to ensure sharp focus across the entire field of view (FOV). For both the FRS and LRS measurements, the image magnification is 0.195 and hardware binning of 4 × 4 pixels is used during signal collection. This results in a projected volume onto a single pixel of 132.6 x 132.6 x 100 μm^3 for both cameras, where the first two dimensions represent the effective area imaged by a single pixel due to geometric magnification and the third dimension represents the laser beam thickness according to the FWHM. The FOV for the FRS and LRS images is approximately 8 mm tall as limited by the laser sheet height and is approximately 45 mm wide as limited by the width of the camera sensors.

The turbulent jet flame setup under consideration utilizes the Sandia piloted burner [26] geometry surrounded by a large 30 cm × 30 cm coflowing stream of filtered air to remove dust and other particulate. The fuel issues from a 7.2-mm diameter tube and is surrounded by an 18.2-mm diameter recessed pilot flame stream. A fuel mixture of 16% CH_4, 16% H_2, and 68% Ar, as determined from the laminar flame calculations described above, is used in all flame cases which results in a stoichiometric mixture fraction of $\xi_s = 0.35$. Three turbulent cases are considered including jet Reynolds numbers of 10,000, 20,000 and 30,000. The pilot consists of a mixture of 20% CH_4 and 80% H_2 mixed with air at an equivalence ratio of 0.7 and is operated at a flow rate such that the thermal power is 6% of the that of the main jet. The thermal power of the main jet is estimated by calculating the higher-heating-value (HHV) for the reactive components of the fuel stream and determining a volumetric average. The pilot mixture is chosen such that the post flame gases have a FRS-based figure of merit near unity. For the current reactant mixture, the post-flame yield a value of $\mathcal{F} = 1.013$. The coflow consists of a series of HEPA filters and flow straighteners to provide a stable, particle-free coflow operating at 0.3 m/s, similar to the coflow described in section 3.1.1. Measurements are performed at 20 and 40 diameters downstream (x/d = 20, 40).

The chosen FOV allowed for measurements of the full radial span (i.e. from centerline to the point where the temperature reaches room temperature) in a single image at $x/d = 20$. However, it was necessary to translate the burner radially to measure the full radial span at $x/d = 40$. The complete pilot flame, main jet and coflow assembly were attached to a Velmex VXM stepper motor translation stage with a resolution of 76 μm that allowed for the entire burner system to be translated axially and radially. A photograph of the Re = 10,000 turbulent flame is shown in Fig. 5.10b.

5.4.3 Results of Simultaneous FRS/LRS Thermometry in Turbulent Non-premixed Flames

5.4.3.1 Single Shot and Statistical Comparisons

Approximately 1000 simultaneous 2D FRS and LRS images were collected at each measurement location (1 FOV for $x/d = 20$ and 2 FOVs for $x/d = 40$) and for all Reynolds number cases (Re = 10,000, 20,000 and 30,000). Two hundred FRS and LRS images were collected in room temperature, quiescent air to serve as the reference condition for normalization according to Eqs. 5.5 and 5.7. First, using the wavenumber filtering technique described in section 5.3.1, instantaneous measurements that have a wavenumber fluctuation greater than $\pm 0.001\ cm^{-1}$ from the average wavenumber, $\langle \nu \rangle$, are removed and not considered in the results. In this manner, the effects of laser frequency fluctuations on the results do not have to be considered. In the current work, approximately 95% of the simultaneous FRS and LRS images were retained after the wavenumber filtering strategy. Next, both the FRS and LRS images are processed by removing average dark field images. Typical "background scattering" due to stray laser light is not as much of an issue for the FRS images since the stray light scattering of surfaces, which have the same spectral profile as that of the narrow-line width laser, is blocked by the I_2 filter cell. For the LRS

images where stray light can impact the temperature results, the background scattering is dealt with through the use of blackout curtains and blackout tape to ensure that only the light from the laser sheet passes through the test section. Following these steps, each instantaneous LRS and FRS image is normalized by the average image from the reference air case. The normalized images are then corrected for fluctuations in energy and non-uniform laser sheet intensity distributions using images from the energy correction camera, in a similar manner to that as described in section 3.2.1. The energy- and laser sheet-intensity-corrected FRS signal ratio images are then converted to temperature using Eq. 5.5 with a calculated temperature-dependent response curve for air (third term in Eq. 5.5) using the Tenti S6 RBS model [119]. The average wavenumber measured during the flame measurements is used when determining the numerator of Eq. 5.5 and the average wavenumber measured during the reference air measurements is used when determining the denominator of Eq. 5.5. The energy- and sheet-corrected LRS signal ratios are converted to temperature using Eq. (5.7), which is valid due to the nearly constant Rayleigh scattering cross section for this fuel mixture as discussed above. Finally, both the FRS and LRS temperature images are median filtered using a 3×3 kernel to reduce the effect of measurement noise.

An example 2D single-shot temperature image comparison is shown in Fig. 5.11 which is taken from data acquired at $x/d = 20$ at the highest Reynolds number case (Re = 30,000). The top image is the 2D temperature field determined using LRS and the bottom image is the 2D temperature field determined using FRS. Both images are mapped to the same false colormap which depicts the gas-phase temperature. A white dashed line overlaid on the images show the location where a radial profile is extracted from both the LRS and FRS temperature measurements. The extracted radial profiles are plotted below the two example images with the LRS single shot temperature profile shown as a solid red line and the FRS single shot temperature profile shown

as a solid black line. A qualitative visual comparison of the two images shows strong agreement with almost identical topological features and structure in both low- and high-temperature regions. In addition, the two single shot profiles at the bottom of Fig. 5.11 demonstrate excellent agreement between the two thermometry approaches. The FRS temperature tracks with the LRS temperature well, even across a sharp gradient occuring near $r/d = 2.25$. Furthermore, the LRS and FRS

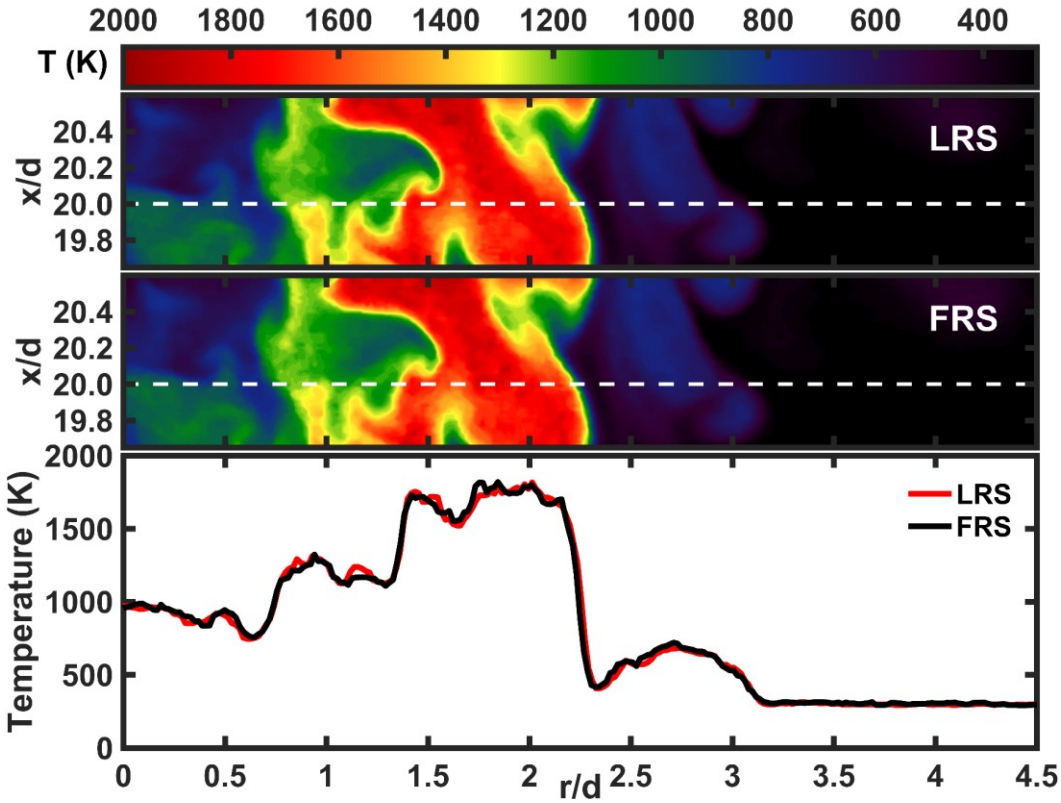

Figure 5.11: Single shot image comparison between the LRS based thermometry approach (top) and the FRS based thermometry approach (middle) for x/d = 20, Re = 30,000. Temperature is shown as the same false colormap for both LRS and FRS. Also shown (bottom) are extracted radial profiles (taken from location highlighted as a white dashed line in the images) for both approaches with LRS shown as a red line and FRS shown as a black line.

images both exhibit low amounts of noise, or high SNR, where the SNR definition used in this dissertation is the ratio of the mean value to the standard deviation in a uniform region. For example, in the uniform co-flow region (T ≈ 296 K), the SNR of the temperature measurements are 111 for the LRS-based temperature approach and 50 for the FRS-based temperature approach. A discussion of the SNR at higher temperatures, and in particular, the unique and favorable temperature dependence of the FRS-based temperature SNR is discussed below in section 5.4.3.2.

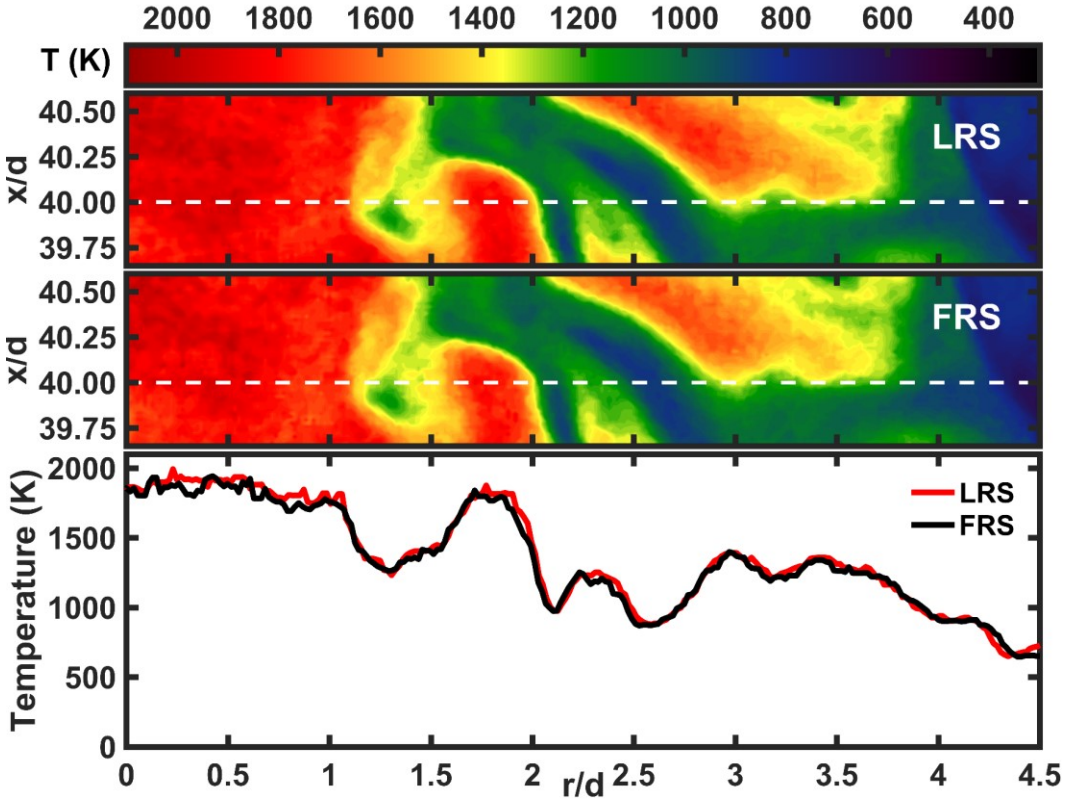

Figure 5.12: Single shot image comparison between the LRS based thermometry approach (top) and the FRS based thermometry approach (middle) for x/d = 40, Re = 30,000. Temperature is shown as the same false colormap for both LRS and FRS (same as in Fig. 6.11). Also shown (bottom) are extracted radial profiles (taken from location highlighted as a white dashed line in the images) for both approaches with LRS shown as a red line and FRS shown as a black line.

Another example 2D single-shot temperature image comparison is shown in Fig. 5.12 from the Re = 30,000 flame, but further downstream at x/d = 40. The same false colormap is used for both images which depicts the gas-phase temperature. Again, a white dashed line is overlaid on the images to show the location where a radial profile is extracted from both the LRS and FRS temperature images. The extracted radial profiles are plotted below the two images, where LRS is plotted as a solid red line and FRS is plotted as a solid black line. This single-shot example shows a good comparison between the two thermometry approaches in the case where the temperature is overall quite high. Again, the two images appear to be almost identical and show the same spatial features overall. The profiles extracted from the single shot images again show excellent agreement throughout the entire radial range. From the comparison of the two sets of single shot image comparisons from x/d = 20 and 40 it is observed that the LRS and FRS thermometry approaches give equivalent temperature information.

Figure 5.13 shows the mean temperature, $\langle T \rangle$, and RMS fluctuation, T_{RMS}, deduced from ~900 simultaneous LRS and FRS thermometry measurements at both axial locations (x/d = 20 and 40) and for all three Reynolds number cases (Re = 10,000, 20,000 and 30,000). The LRS curves are shown as solid red lines and the FRS curves are shown as solid black lines. It should noted, again, that the LRS temperature measurements are being considered as the reference standard and the accuracy FRS measurements are being assessed relative to those LRS measurements. In examining Fig. 5.13, it is observed that there is overall strong quantitative agreement between the two thermometry approaches both in average temperature and in RMS fluctuation. The largest discrepancy is observed near centerline at x/d = 40 for Re = 20,000. At this location, the average LRS based temperature value is 1655 K, while the mean FRS based temperature value is 1607 K. While this is the largest discprepancy detected within the flames, it

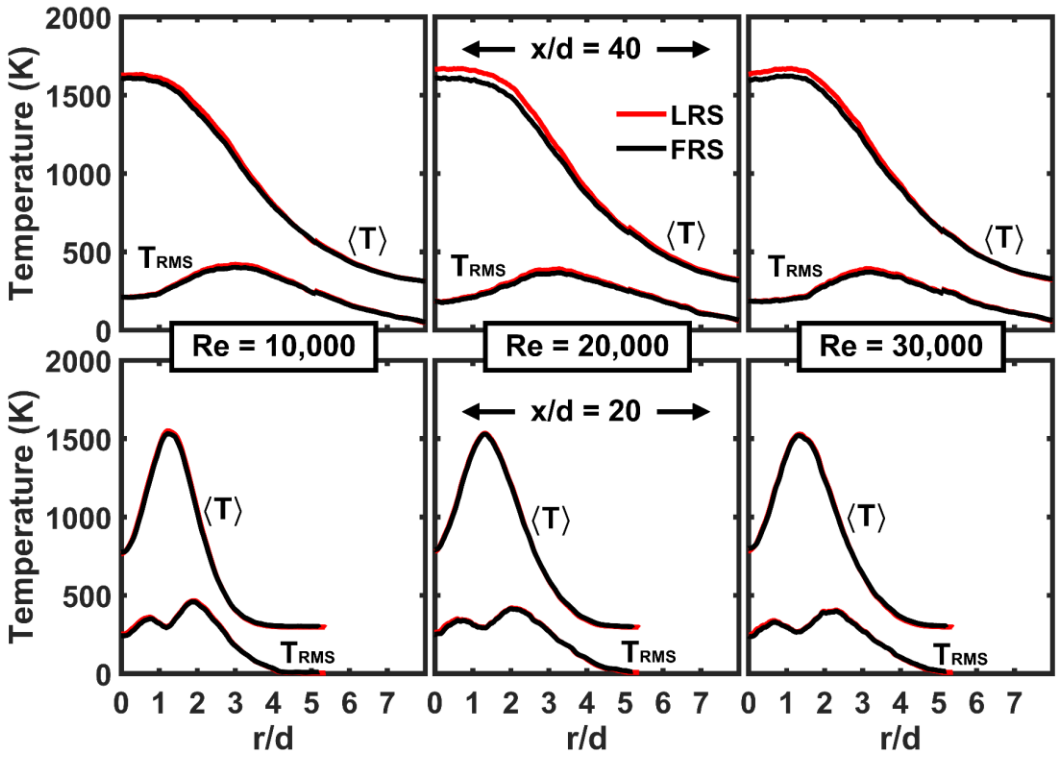

Figure 5.13: Comparison of mean and RMS temperature profiles from all axial locations and Reynolds number conditions for LRS (red) and FRS (black) thermometry approaches. Data from x/d = 40 is shown on top, and data from x/d = 20 is shown on the bottom, with increasing Reynolds number cases going from left to right.

should be noted that the percent difference is only 2.9%. Table 5.3 shows a summary of mean temperatures at various spatial position measured with both the LRS based thermomety appoach and the FRS based thermometry approach. For the flames with Re = 10,000 and 30,000, the difference between the mean LRS- and FRS-based temperature values on centerline at x/d = 40 is 1.2% and 2.6%, respectively. The agreement improves at the lower axial location of x/d = 20 with percent differences in peak mean temperatures of 1.2%, 0.5%, and 0.7% for Re = 10,000, 20,000 and 30,000, respectively. On centerline for x/d = 20, the percentage differences between the mean temperatures for the two thermometry approaches are 1.9%, 1.3%, and 2.2% for Re = 10,000,

20,000 and 30,000, respectively. For all axial and radial locations, there is excellent agreement between the temperature RMS fluctuations between the two thermometry approaches.

		x/d = 20		x/d = 40	
		$\langle T_{LRS} \rangle$	$\langle T_{FRS} \rangle$	$\langle T_{LRS} \rangle$	$\langle T_{FRS} \rangle$
Re = 10,000	Centerline	763	778	1628	1609
	Location of peak $\langle T \rangle$	1549	1530	-	-
Re = 20,000	Centerline	773	790	1655	1607
	Location of peak $\langle T \rangle$	1535	1528	-	-
Re = 30,000	Centerline	783	800	1635	1593
	Location of peak $\langle T \rangle$	1529	1519	-	-

Table 5.3: Comparison of mean LRS and FRS based temperature measurements (in K) for both x/d = 20 and 40 and for Re = 10,000, 20,000, and 30,000 at various radial locations.

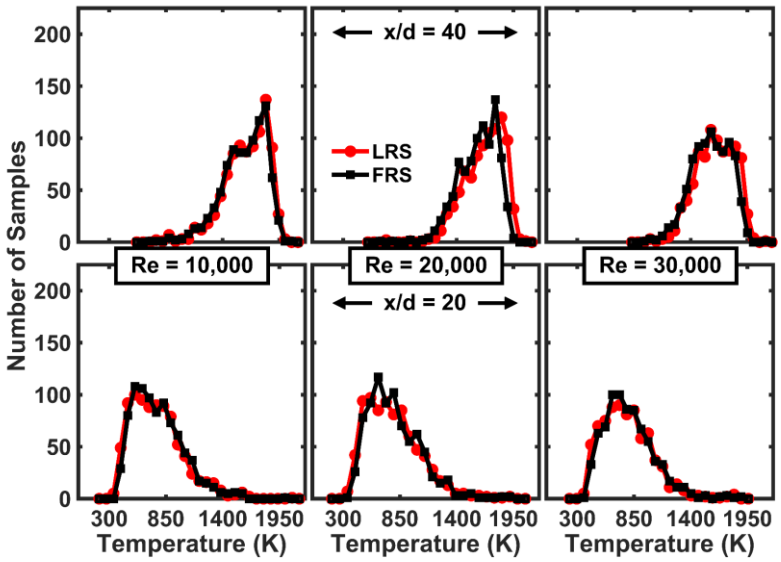

Figure 5.14: Histograms comparing the LRS (red line with circles) and FRS (black line with squares) thermometry approaches from centerline temperature values from both x/d = 40 (top) and x/d = 20 (bottom) for all three Reynolds number flames (increasing from left to right).\

Figure 5.14 shows a comparison of the histograms of the temperature calculated from both the LRS and FRS thermometry approaches at centerline (r/d = 0) for both axial locations and for all three Reynolds number flames. The LRS histograms are plotted as solid red lines with circles and the FRS histograms are plotted as solid black lines with squares. Again, quite strong agreement is observed between the two different temperature results. Some discrepancy is noted at the highest temperature values for the Re = 20,000 case at x/d = 40 where the FRS thermometry approach measures slightly lower temperatures. Based on the fact that the high-temperature values are consistent between the LRS and FRS measurements for both Re = 10,000 and 30,000, it can be concluded that the FRS approach accurately captures the temperature at the highest temperatures and the small differences observed in the results at x/d = 40 for Re = 20,000 are likely anomalous.

Figure 5.15 shows the same histogram comparison but at the location of peak RMS temperature fluctuations for each axial location and Reynolds number; a region with the largest fluctuations relative to the mean. At x/d = 40 the radial locations of peak RMS temperature fluctuations for the current simultaneous LRS/FRS temperature measurements is found to be r/d = 3, 3.25 and 3.15 for Re = 10,000, 20,000 and 30,000, respectively. The radial locations for the peak RMS = temperature at x/d = 20 were found to be r/d = 1.9, 2.0 and 2.3 for Re = 10,000, 20,000 and 30,000, respectively. Figure 5.15 again shows that there is good overall agreement observed between the two temperature approaches over the large range of measured temperature values in the peak RMS region. There are apparent slight discrepancies between the LRS and FRS histograms at the highest temperatures at x/d = 40. It should be noted at this position that there is a limited number of measurements (900 total) and there is a broad range of temperature values occurring at this spatial position. With a histogram bin size of 150K this leads to a lower number of samples per bin (< 50) at the highest temperatures. Given this consideration, the agreement

between LRS and FRS temperatures for these spatial positions are within statistical uncertainty. Again, considering that the histograms agree very well at the same high-temperature values at x/d = 20, it appears there is no limitation with regard to the FRS approach accurately in order to determine the highest temperatures. The comparisons at all locations and Reynolds numbers show overall good agreement between the two techniques indicating a good statistical comparison between the two techniques, and as such, the FRS results can be considered an accurate representation of the true gas temperature (by virtue of its favorable comparison to the LRS results).

Figure 5.15 shows results that directly compare all of the LRS and FRS temperature measurements acquired at x/d = 20 and 40. For each Reynolds number, every single-shot FRS measurement is compared to the simultaneous single-shot LRS measurement acquired at the same axial and radial location. The FRS-based temperature conditioned on the LRS-based temperature is shown as a colormap, where the color represents the logarithm of the number of data points at a particular (T_{LRS},T_{FRS}) value. The data is represented as a logarithm of the number data points in order to account for the larger number of data points at lower temperatures (likely coming from the high number of room temperature data samples) as compared to high-temperature samples. Also, it should be noted that the number of samples for the data acquired at x/d = 20 have been multiplied by 2.5 prior to taking the logarithm in order to show the colormaps for the two axial locations with the same intensity scale. Also overlaid on each colormap is the conditional mean of the FRS-based temperature values conditioned on the LRS-temperature values (solid, red symbols) in 50-K bins. Finally, the white, dashed line shows the (ideal) linear relationship between the FRS-based and LRS-based results (T_{LRS}= T_{FRS}). The colormap-based presentation displayed in Fig. 5.15 is chosen

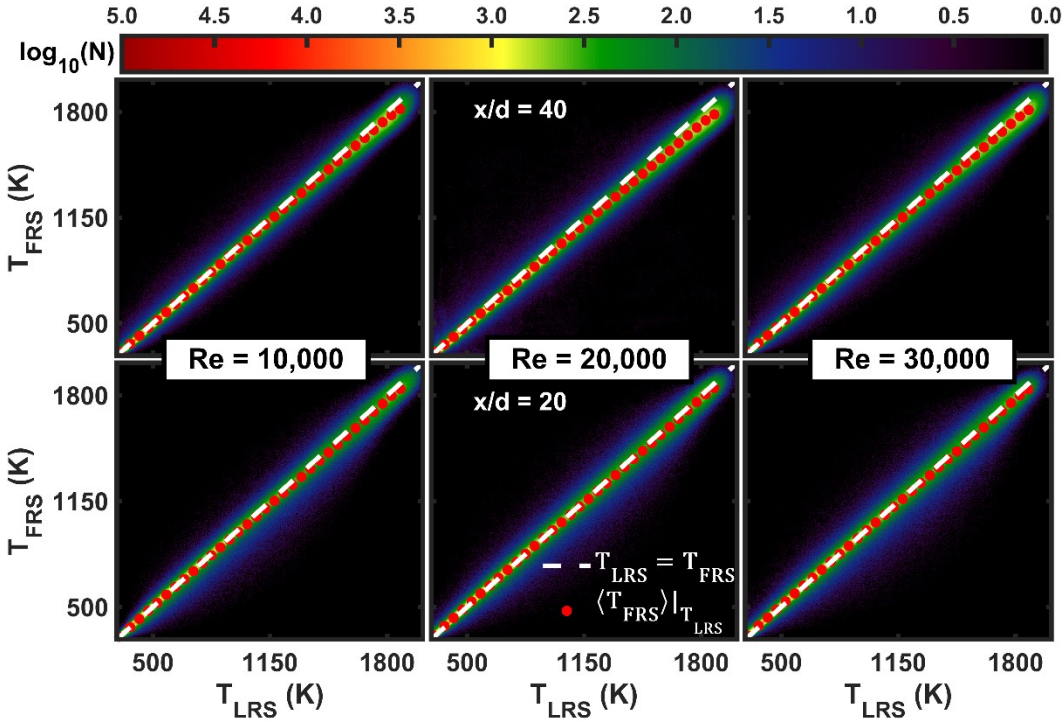

Figure 5.15: A comparison of single shot comparison of LRS and FRS based temperature measurements for x/d = 40 (top) and x/d = 20 (bottom) with increasing Reynolds number going from left to right. The single shot measurements are shown as a colormap depicting the logarithm base 10 of the number of samples. The logarithm is shown for clarity. The LRS values form the ordinate and the FRS values form the abscissa for the plots. Also shown is the ideal case where $T_{LRS} = T_{FRS}$ as a white dashed line. The conditional average of the FRS temperatures, conditioned on LRS temperature measurements is shown as red circles.

over a traditional "scatter plot", so that a small number of outliers do not lead to a misinterpretation of the results.

It is clear from examination of Fig. 5.15 that vast majority of the instantaneous data samples for each axial location and Reynolds number clusters tightly around the conditional mean values (red symbols) indicating a high correlation between the single-shot LRS and FRS measurements. More importantly is the observation that both the instantaneous values and conditional means closely follow the ideal curve where $T_{LRS} = T_{FRS}$, indicating accurate single-shot FRS temperature

measurements relative to the LRS temperature measurements which are taken as the "truth". For x/d = 20, the agreement is excellent for all temperatures and Reynolds numbers, while for x/d = 40, the data closely follows the white, dashed curve for the most of the temperature range, with slightly lower values from the FRS thermometry approach as compared to the LRS thermometry approach at the highest temperatures, especially for the Re = 20,000 case. This observation is similar to observations made in Figs. 5.13 and 5.14 and is likely due to an insufficient number of data samples at the highest temperature ranges under non-premixed flame conditions. One observation from Fig. 5.15 is that the spread of the instantaneous measurements increases with increasing temperature for all conditions. This is to be expected, however, because as the temperature increases, the absolute values of the temperature fluctuations increase and additionally the signal and the single-shot measurement precision decrease. Overall, both the instantaneous results and the conditional means of the FRS temperature (conditioned on the LRS temperature) indicate excellent measurement accuracy for the proposed FRS temperature imaging technique over the full range of temperature values at all spatial locations and across a range of Reynolds numbers.

5.4.3.2 Signal-to-Noise (SNR) Comparison between LRS/FRS Thermometry

An important consideration for any measurement approach is the signal-to-noise ratio (SNR) characteristics. Specifically, it is desired to compare the temperature-dependent SNR characteristics of the traditional LRS thermometry approach with that of the new FRS thermometry approach. For any measured signal, S, the measurement noise, N_S, for shot-noise-limited detection scales as the square root of the measured signal, $N_S \propto \sqrt{S}$ [111]. For scientific-grade CCD cameras, the inherent camera noise (i.e., read noise) is typically quite small in comparison to the

shot noise, and thus the approximation that the measurements discussed in this section are acquired under shot-noise-limited conditions is appropriate. Indeed, at the lowest signal conditions in the current set of LRS and FRS measurements ($T \approx 1900$ K), the read noise-to-signal ratio is 0.007 and 0.009, respectively. Thus, the SNR for any given measured signal, whether it occurs from LRS or FRS, is written as

$$SNR_S = S/N_S = C\,S/\sqrt{S} = C\sqrt{S} \qquad \text{Eq. (5.14)}$$

where C is a proportionality constant accounting for electron gain and associated noise introduced through the gain process. For a scientific CCD, $C = 1$. Assuming that shot noise is the largest source of uncertainty in the collected signal for the current temperature measurements, the relationship between signal uncertainty and temperature uncertainty can be determined. If a constant differential Rayleigh scattering cross section is assumed then the measured LRS signal (or signal ratio) is only a function of temperature for isobaric conditions as indicated above. If Eq. (5.2) is examined, it is observed that the FRS signal is a function of several parameters, but, assuming isobaric conditions, the largest sensitivity is due to temperature. Therefore, the temperature can be approximated as a function of the collected signal (i.e. $T = f(S)$) for both LRS and FRS, where the exact functional form depends on the specific approach.

For a general function of one variable, $y = f(x)$, the uncertainty of y due to the uncertainty of x can be given as $N_y \approx |df/dx| \times N_x$, where N_y and N_x are the uncertainties of y and x, respectively. In terms of both the LRS and FRS temperature approaches this implies that the uncertainty in the temperature measurement, N_T, due to shot noise only, can be estimated as

$$N_T \approx |dT/dS| \times N_S \qquad \text{Eq. (5.15)}$$

Since the temperature measured via LRS is inversely proportional to signal, $T_{LRS} \propto 1/S_{LRS}$, $|dT/dS|$ scales as $1/S_{LRS}^2$. Using Eq. (5.15) the uncertainty of the temperature measurement using the LRS thermometry approach can be written as $N_{T,LRS} \propto 1/S_{LRS}^2 \times \sqrt{S_{LRS}} \propto S_{LRS}^{-3/2}$. This leads to an estimate of the SNR for the temperature measurement using an LRS thermometry approach as

$$SNR_{T,LRS} = T/N_{T,LRS} \propto S_{LRS}^{-1}/S_{LRS}^{-3/2} \propto \sqrt{S_{LRS}} \propto 1/\sqrt{T_{LRS}} \qquad \text{Eq. (5.16)}$$

Equation (5.16) shows that the variation in SNR for the LRS temperature measurement is the same as that for the variation in the SNR for the measured signal itself. Since the LRS signal varies as $S_{LRS} \propto 1/T$, both $SNR_{T,LRS}$ and $SNR_{,S,LRS}$ vary as $1/\sqrt{T}$.

For the FRS thermometry approach, the relationship between temperature and signal is not as straightforward as in the case for the LRS thermometry approach. For FRS measurements, the signal decreases with the same $1/T$ dependence as in LRS due to number density effects, but in addition to that the FRS signal is subject to the temperature-dependent interaction between the RBS profile and the I_2 transmission profile as shown in Eq. (5.5). Using Eq. (5.15) and assuming that the effects of the bulk velocity (i.e. global Doppler shifts) are small, the uncertainty of the temperature measurement using the FRS thermometry approach can be written as

$$N_{T,FRS} \propto S_{FRS}^{1/2}(T)/\left|\frac{S_{FRS}}{\psi_{air}(T)}\left(\frac{d\psi_{air}(T)}{dT} - S_{FRS}\right)\right| \qquad \text{Eq. (5.17)}$$

Since $S_{FRS} \propto \psi_{air}(T)/T$, this leads to an FRS-based temperature SNR that varies as

$$SNR_{T,FRS} = T/N_{T,FRS} \propto T^{3/2}\psi_{air}^{-1/2}(T)\left|\frac{1}{T}\frac{d\psi_{air}(T)}{dT} - \frac{\psi_{air}(T)}{T^2}\right| \qquad \text{Eq. (5.18)}$$

Clearly, the SNR estimation for FRS measurements is more complicated than that for LRS. As an alternative to using Eq. (5.18), the SNR of the FRS-based temperature can be directly calculated using synthetic FRS signal curves.

Figure 5.16a shows synthetically generated temperature-dependent signals for both the FRS (calculated with a central wavenumber of ν_0 = 18788.335 cm^{-1}) and LRS thermometry approaches. Each signal is normalized according to Eq. (5.4) and (5.7) and as expected, the relative FRS signal is higher than for LRS at any given temperature value greater than 300 K. Another observation from Fig. 5.16a is that the magnitude of the slope of the temperature-dependent LRS signal is greater than that of the temperature-dependent FRS signal near 300 K. This implies that $|dT/dS|_{LRS} < |dS/dT|_{FRS}$ and if the same signal is collected for both LRS and FRS then the noise for the LRS measurements is less than the noise for the FRS measurement. That means that $SNR_{T,LRS} > SNR_{T,FRS}$ near 300 K.

Figure 5.16b shows the variation of the estimated SNR as a function of temperature for the LRS signal (dashed red line), derived LRS temperature (solid red line), the FRS signal (black line), and the derived FRS temperature (solid black line). For these results the SNR at T = 300K is assumed to be equivalent for both the LRS and FRS measurements and are set equal to measured signal values in air. As expected, the SNR for the FRS-based temperature measurement is lower than that of the SNR for the LRS-based temperature near 300 K. However, an interesting feature observed in Fig. 6.16b is that the SNR for the FRS temperature ($SNR_{T.FRS}$) actually increases from 300 K to approximately 1000 K, despite the signal decreasing as $\sqrt{T}$. For $T \gtrsim$ 1000 K, $SNR_{T.FRS}$ asymptotes to $SNR_{S.FRS}$ and remains higher than $SNR_{T.LRS}$. The temperature-dependent characteristics of $SNR_{T.FRS}$ are largely guided by the first term within the absolute value in Eq. (5.18). For low temperatures, $\psi_{air}(T)$ is sensitive to changes in temperature and therefore the

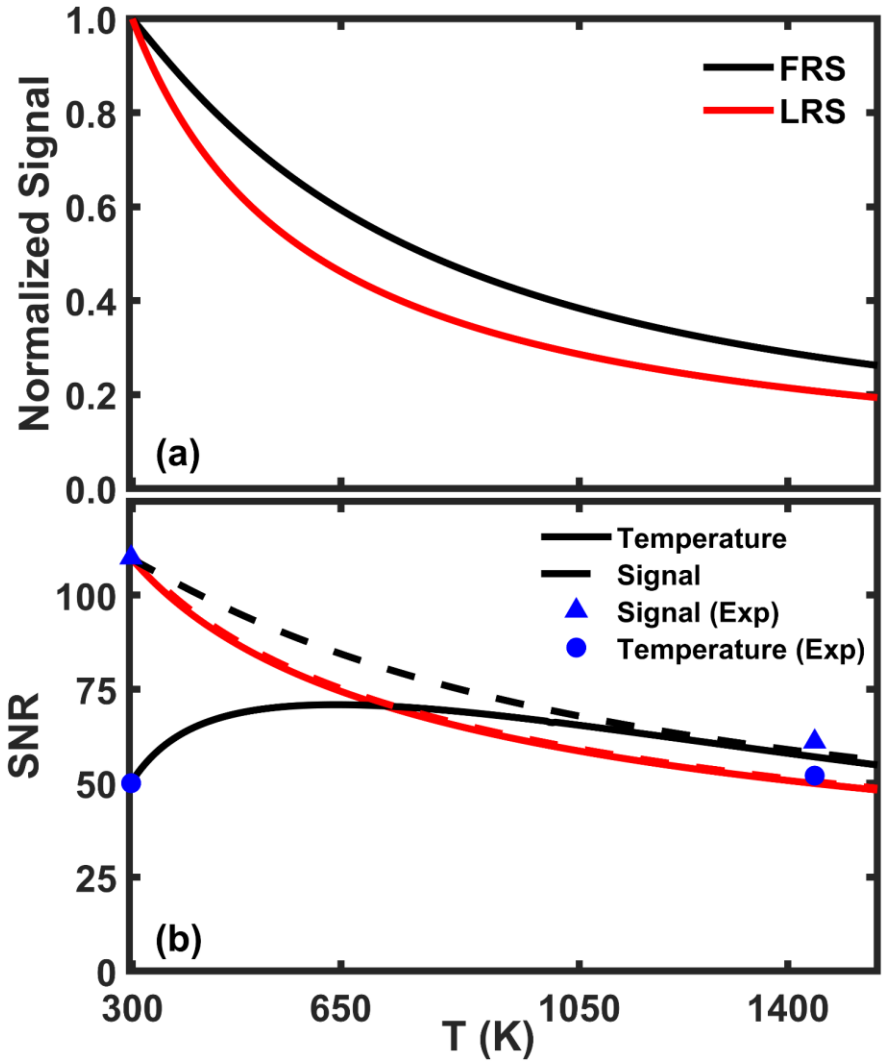

Figure 5.16: (a) Simulated variation of signal in air as a function of temperature for LRS (red) and FRS (black) thermometry approaches. (b) Estimated variation of temperature SNR (solid lines) and signal SNR (dashed lines) as a function of temperature for both LRS (red) and FRS (black). Measured values of SNR from FRS measurements are shown as solid blue symbols.

uncertainty in temperature due to shot noise is magnified through the $d\psi_{air}(T)/dT$ term leading to overall lower values of $SNR_{T.FRS}$ near 300 K. As temperature increases, $d\psi_{air}(T)/dT$ decreases thereby increasing $SNR_{T.FRS}$ as indicated by Eq. (5.18). Furthermore, the increase in $\psi_{air}(T)$ with increasing temperature, leads to an increase in relative signal and a relative decrease in shot noise

as compared with the relative signal and relative shot noise of LRS. At sufficiently high temperatures, $d\psi_{air}(T)/dT$ approaches zero and $SNR_{T.FRS}$ is predominately governed by the behavior of the second term within the absolute value of Eq. (5.18), which represents SNR due to shot noise. Thus, $SNR_{T,FRS} \approx SNR_{S,FRS}$ for $T \gtrsim 1000$ K. For the case where the experimental setup is adjusted such that the SNR values for both the LRS and FRS signals are approximately equal at 300K, $SNR_{T,FRS} > SNR_{T,LRS}$ at higher temperatures. However, it should be noted that since $\psi(T) < 1$, an optical detection system common to both LRS and FRS would lead to $S_{FRS} < S_{LRS}$, and in general, $SNR_{T,FRS} < SNR_{T,LRS}$ for all temperatures. However, the results of Fig. 5.16b show that regardless of the absolute values of $SNR_{T,FRS}$, the lowest SNR for FRS temperature measurements is achieved near T = 300 K and thus the measurements at higher temperatures using the FRS thermometry approach do not suffer from increased uncertainty even though the collected signal levels decrease.

To experimentally assess the SNR predictions for the FRS thermometry, measurements from the uniform co-flow region (T ≈ 296 K) of the turbulent jet flame experiments described above are examined first. For these experiments, the SNR of the collected LRS and FRS signals were set to be equal by using different camera lens settings. $SNR_{S,LRS} \approx SNR_{S,FRS} = 111$ at T ≈ 296 K and this value is used to anchor the SNR predictions shown in Fig. 5.16b. After determining the temperature using Eq. (5.5), the SNR of the temperature in the coflow was determined to be 50 as reported above. This result for $SNR_{T,FRS}$ (shown as solid, blue circle in Fig. 5.16b) matches the SNR prediction (solid, black line in Fig. 5.16b) very well for $T \approx 296$ K. A second, higher-temperature point is examined by performing FRS measurements in the product gas stream from a lean ($\phi = 0.48$), premixed $0.68H_2/0.32CH_4$/air flame. This reactant mixture is chosen such that

the gas composition of the products has a value of $\psi_{prod}(T) \approx \psi_{air}(T)$ at $T \approx 1445$ K. This implies that the collected signal from the flame products is equivalent to that of air at the same temperature, and the experimentally determined SNR can be compared to the predictions shown in Fig. 5.16b. In Fig. 5.16b the experimental results are shown as solid, blue triangles for the FRS signal and solid blue circles for the FRS temperature. It is observed that the measured values of $SNR_{S,FRS}$ and $SNR_{T,FRS}$ closely track the predicted signal and temperature SNR values for the FRS thermometry approach. For example, at T = 1445 K, the predicted value of $SNR_{S,FRS}$ is 57.7 and the measured value of $SNR_{S,FRS}$ is approximately 61. For the temperature SNR, the predicted value of $SNR_{T,FRS}$ is 56.2 while the measured value of $SNR_{T,FRS}$ is approximately 54. While only a single high-temperature data point is examined experimentally, the excellent agreement between the predicted SNR values and the experimentally determined SNR for both FRS signal and derived temperature at T ≈ 296 K and T ≈ 1445 K gives a high level of confidence in the predicted temperature-dependent SNR behavior for the FRS measurements.

Based on the work discussed in the current chapter, it has been conclusively shown in section 5.3 that the Tenti S6 model accurately models the Rayleigh-Brillouin scattering (RBS) lineshapes for combustion-relevant gas species at combustion-relevant temperatures. Also in section 5.3 it has been verified that the FRS signal from mixtures can be written as a mole-weighted sum of each components contribution. Subsequently, using the Tenti S6 model and a laminar opposed-flow diffusion flame calculation section, a fuel was designed such that accurate temperature measurements are possible in turbulent non-premixed flames using only a single FRS measurement. For this same fuel, the differential Rayleigh scattering cross section is constant throughout the composition space meaning an accurate LRS temperature could be used to assess

the accuracy of the proposed FRS thermometry approach (discussed in section 5.2). It was demonstrated both visually and statistically that the FRS thermometry results closely matched the corresponding LRS thermometry results and thus, the FRS thermometry approach yields accurate temperature measurements in turbulent non-premixed flames with a single camera measurement. In the next chapter, the new FRS-based thermometry approach will be combined with particle image velocimetry (PIV) for simultaneous temperature and velocity measurements in turbulent non-premixed flames.

Chapter 6. Simultaneous Filtered Rayleigh Scattering Thermometry and Particle Image Velocimetry Measurements in Turbulent Non-premixed Flames

Chapter 5 demonstrated the ability to acquire quantitative temperature measurements using filtered Rayleigh scattering (FRS) in a series of turbulent non-premixed flames. The current chapter will address the experimental considerations underlying simultaneous temperature and velocity measurements (using particle imaging velocimetry, PIV) in the same series of flames. Section 6.1 focuses on the experimental setup and acquisition methodology for joint FRS and PIV imaging. A key area of work includes choosing appropriate PIV tracer particles that yield good PIV results, but do not interfere with the FRS measurement. The latter issue is largely related to the effectiveness of the particle scattering blocking ability of the FRS channel. Section 6.2 discusses the data processing steps to convert the FRS images and particle images acquired within the turbulent flames into temperature and velocity data, respectively. Section 6.3 discusses the measurement accuracy, signal-to-noise (SNR), and spatial resolution of both the temperature and velocity measurements. The measurements discussed in Sec. 6.1-6.4 will underpin the analysis presented in Chapter 7.

6.1 Experimental Methodology for Simultaneous Filtered Rayleigh Scattering and Particle (Mie) Scattering Imaging

The acquisition of simultaneous filtered Rayleigh scattering (FRS) images with particle (Mie) scattering image pairs is not trivial as there are a number of different subsystems operating needed to perform the measurement. The measurements are performed using two laser systems, four cameras, and multiple *in situ* optical configurations as discussed below.

6.1.1 Experimental Setup

A general schematic of the two laser systems and the corresponding optics used for the current simultaneous experiments is shown in Fig. 6.1. The figure is broken up into sub-components and labeled for clarity. The laser used for the FRS imaging measurements is an injection-seeded, frequency-doubled, Q-switched, Nd:YAG laser operating at a repetition rate of 10 Hz with nominal output energy of ~800 mJ/pulse. As shown in Fig. 6.1 a small portion (< 1%) of the light passes through the top mirror of the periscope and is routed via fiber optic cable to a high-resolution wavemeter (High Finesse WSU30) to monitor the wavenumber for each laser pulse.

After passing through a periscope (for height adjustment), the 532-nm FRS beam is routed through a single-leg pulse stretcher [193] in order to decrease the incident power at the probe volume and prevent possible laser breakdown from occurring when the high-energy FRS laser interacts with the PIV tracer particles in the flow. The schematic of the pulse stretcher used in the current work is shown in Fig. 6.1b and in more detail in the top part of Fig. 6.2. Following three turning mirrors used to properly orient the beam into the pulse stretcher, the laser passes through a 40/60 beam splitter (BS). Forty percent of the incident laser beam is reflected towards the test

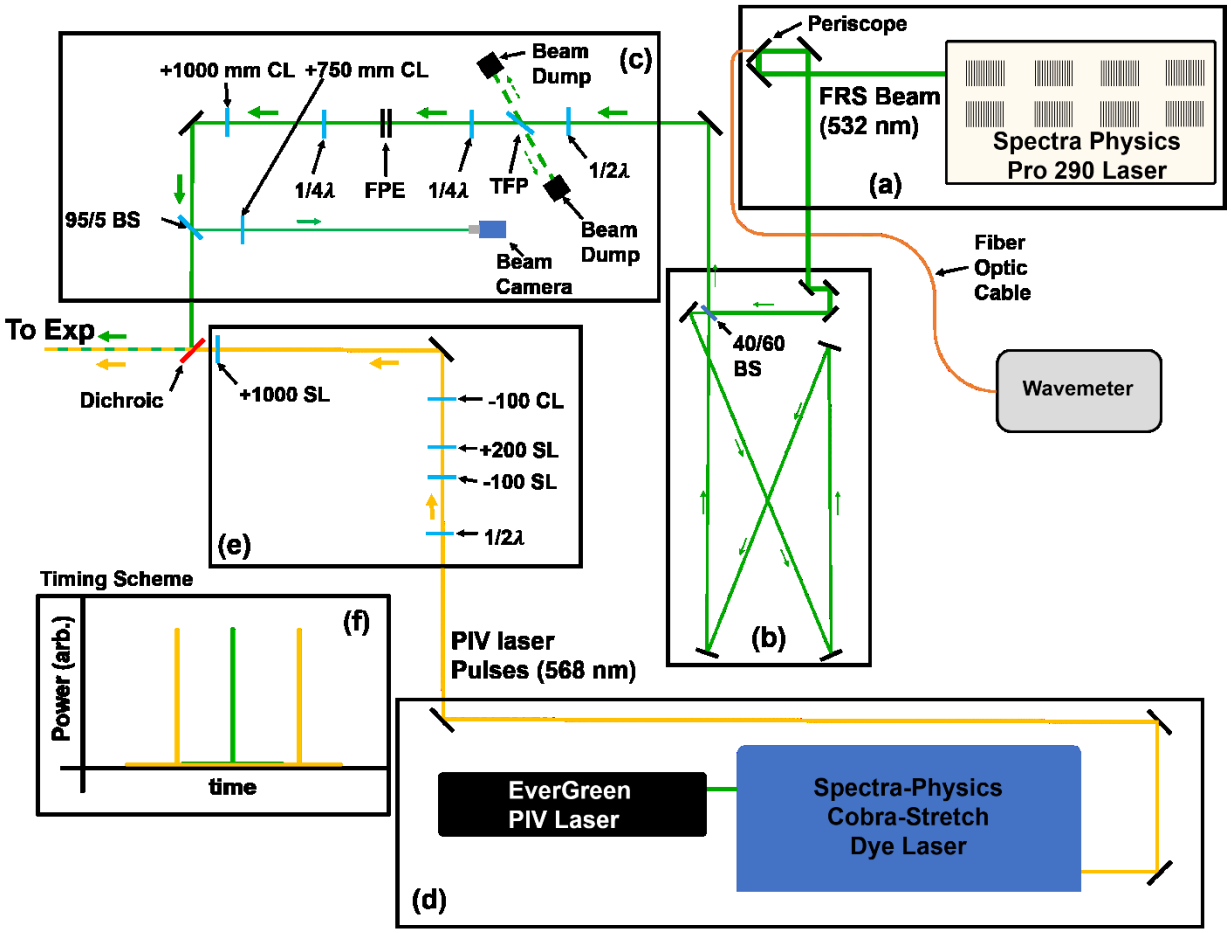

Figure 6.1: Schematic of laser beams and optics used in simultaneous FRS/Mie imaging experiment. (a) FRS laser and initial routing optics. (b) Single-leg pulse stretcher used to temporally stretch the FRS beam in time. (c) FPE-related optics, sheet-forming optics, and pulse stretcher alignment optics for the FRS beam. (d) Dual cavity Nd:YAG-pumped dye laser for generating 568-nm PIV laser pulses. (e) Beam shaping optics for the PIV laser pulses.

section, while 60% of the incident beam continues within the pulse stretcher. This 60% portion of the beam is reflected from four mirrors within the pulse stretcher cavity, where the reflection from the last mirror spatially overlaps the original reflected beam (40% reflected towards the test section). The long distance (3.74 m) traveled by portion of the beam within the cavity, delays it in time relative to the original 40% portion of the beam reflected towards the test section. The inter-

cavity pulse now interacts with the 40/60 BS, where 60% of the original inter-cavity pulse (or 36% of the original pulse energy) transmits through the BS and 40% of the inter-cavity pulse (or 24% of the original pulse energy) is reflected and travels through the pulse stretcher again. This process continues and yields a beam that is stretched in time and results in lower instantaneous power. In the current work, the pulse stretcher increases the pulse width from 8 ns to ~30 ns which is sufficient to avoid dielectric breakdown at the laser focal plane. The bottom of Fig. 6.2 shows sample pulses recorded on an oscilloscope before and after the pulse stretcher. The single-leg pulse stretcher is 3.74 m long and the efficiency of the pulse stretcher is approximately 94%; that is, the laser energy only is reduced by 6% due to optical losses within the pulse stretcher cavity. The longer temporal pulse leaving the pulse stretcher then passes through a final series of optics before being combined with the PIV pulses via long-wave pass dichroic (labeled "Dichroic" in Fig. 6.1). These optics are shown in Fig. 6.1c. First, the 532-nm FRS beam passes through a tunable Fabry-Perot etalon (FPE) and optical isolation optics. The FPE is an air-spaced etalon with two Zerodur-0 mirrors (88% reflectivity) spaced 5 mm apart used to increase the spectral purity of the laser beam [188], which increases the effectiveness of particle scattering blocking on the FRS channel. The FPE is mounted on a rotation stage as the alignment of the beam and the FPE is performed with angle tuning. As described in [188], the output of an injection-seeded Nd:YAG laser contains a spectrally pure single longitudinal mode (~ 0.003 cm^{-1} bandwidth) super-imposed on a low-energy broadband (~3 cm^{-1}) pedestal. While the broadband pedestal is very weak (many orders of magnitude lower than the single mode), its integrated effect is to reduce the blocking capability of the I_2 filter since the broadband pedestal falls outside of the I_2 absorption band and particle scattering is much more intense than Rayleigh scattering. The FPE works by restricting the broadband pedestal to a narrower bandwidth (0.042 cm^{-1}) and thus increases the effective spectral

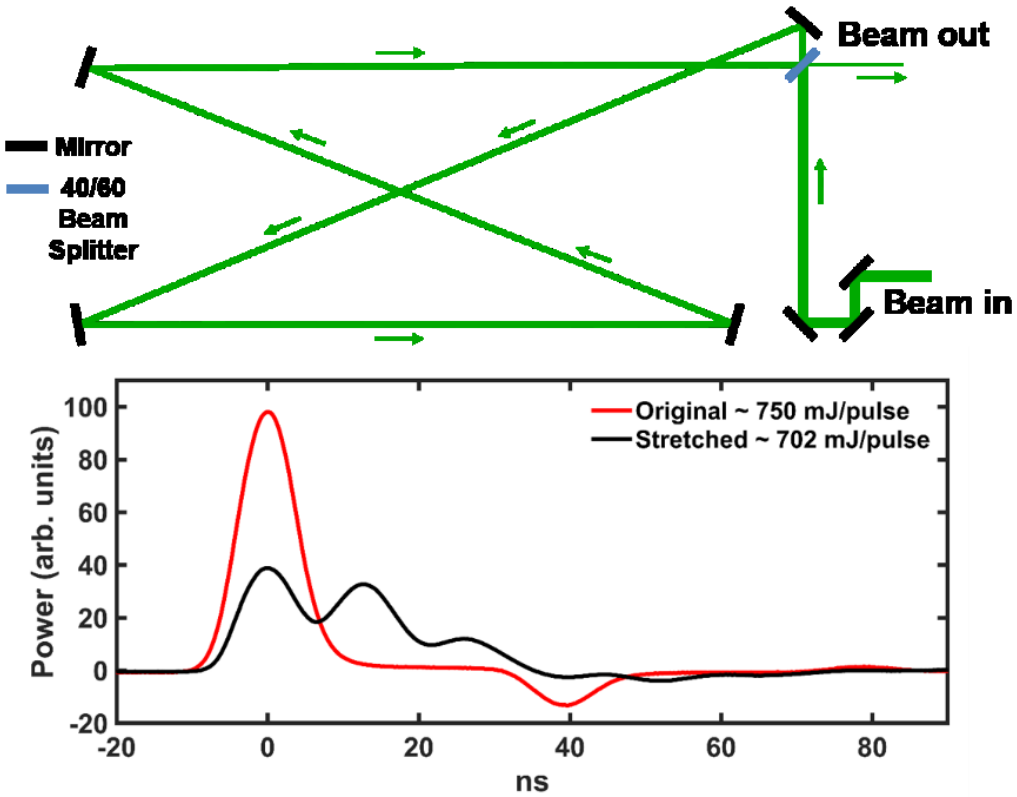

Figure 6.2: (Top) Schematic of pulse stretcher used to temporally stretch the FRS laser pulse from a ~8 ns to ~30 ns (Bottom) Representative trace comparing an original "un-stretched" beam (red) and a beam that has passed through the pulse stretcher.

purity of the laser by at least one order of magnitude and the blocking capabilities by 1.5 to 2 orders of magnitude.

When the FPE is aligned properly, the majority of the light (~ 79%) passes through the FPE and the back reflections are not aligned with the incident beam path (since proper tuning of the FPE requires angle tuning between the 532-nm FRS beam and the FPE). When the FPE is not aligned properly a significant fraction of the light is reflected back through the optical train and towards the Nd:YAG laser. In this manner, precautions must be taken to ensure no damage to the

laser rod occurs. Thus, a set of optics is used to optically "isolate" the FPE from the upstream optics and, in particular, the Nd:YAG laser (primarily the laser rod). To achieve this isolation, the vertically polarized 532-nm FRS beam first passes through a half-waveplate (1/2λ) to rotate the polarization to 'horizontal'. It then passes through a thin film polarizer (TFP) which allows horizontal light to transmit while reflecting any vertically polarized light. It then passes through a quarter-waveplate (1/4λ) which converts it to circular polarization. The circularly polarized beam then passes through the FPE and then transmits through an additional quarter-waveplate (1/4λ) to convert the circularly polarized light back to vertical polarization. For the case where the etalon is not aligned properly, the high-energy circularly polarized back reflections will pass through the first quarter-waveplate rotating to the polarization to 'vertical' and thus is subject to reflection from the TFP into a beam dump. This prevents the back reflections from the FPE from propagating further upstream to sensitive optics or the laser. After passing through the pulse stretcher, FPE and isolation optics, the nominal pulse energy is 550 mJ/pulse.

The 532-nm beam then passes through a 1000-mm focal length cylindrical lens (CL) to form a focused laser sheet at the measurement volume. Immediately following the CL, the beam passes through a 95/5 beam splitter (labeled 95/5 BS in Fig. 6.1a) in order to pick off a small portion of the beam. The reflected (5%) component is focused (vertically) through an additional +750 mm focal length CL such that the picked-off potion is focused in both the vertical and horizontal directions and is imaged on the 'Beam Camera' (Watec WAT-902 B/W Camera). This camera is used to align the pulse stretcher such that for each different pass through the pulse stretcher, the beams are spatially overlapped. The image plane of the beam camera is the same distance from the +1000 mm CL lens as the location of the focus over the test section. In this manner, a good spatial overlap on the beam camera ensures good spatial overlap at the

measurement plane. The 95% portion of the beam that transmits through the 95/5 BS is used for the FRS measurements and is combined with the PIV laser pulses using a long wave pass dichroic mirror ('Dichroic' in Fig. 6.1e) which reflects the vertically polarized 532-nm beam towards the test section. The size of the FRS laser sheet is approximately 8 mm tall and 0.18 mm thick ($1/e^2$) at the measurement volume.

The laser source for the PIV measurement is the 568-nm output from a dual-cavity Nd:YAG-pumped dye laser (Spectra Physics Cobra Stretch) and is shown in Fig. 6.1d. The pump source (also shown in Fig. 6.1d) is a Quantel Evergreen 70 'PIV laser' operating at 532 nm with energy output of 70 mJ/pulse per laser head. The dye laser is a Spectra-Physics Cobra-Stretch dye laser operating with Rhodamine 590 dissolved in methanol. The system produces two sequential 568-nm laser pulses, each with output energy of ~20 mJ/pulse. The use of a dual-pumped dye laser system for PIV is unconventional, but is used in the current work to avoid crosstalk from the FRS laser onto the PIV cameras and crosstalk of the PIV laser onto the FRS camera. Since the FRS and PIV lasers are at different wavelengths, optical filtering assures independent signal collection. The different wavelengths allow the laser pulses to occur "synchronously" so that the FRS and PIV images are captured at the same time – this is not possible if a conventional 532-nm PIV laser source is used as there has to be temporal offsets between the two laser systems to avoid crosstalk. The output of the dye laser is sent through a series of optics to change the shape and size of the beams. The set of two PIV pulse first pass through a $1/2\lambda$ waveplate to rotate the polarization of the PIV beams to 'horizontal' such that it transmits through the dichroic used for overlapping the PIV and FRS laser sheets, The 568-nm laser pulses then pass through a telescope, consisting of a pair of spherical lenses (SL), to expand the beam diameters by a factor of two. The beams then pass through a -100 mm CL followed by a +1000 mm SL to form a pair of 568-nm laser sheets

that are ~30 mm tall by ~0.5 mm thick. The sheets then pass through a narrow slit to remove high-frequency noise from the edges of the beam and block spurious light from transmitting to the test section. The horizontally polarized 568-nm PIV sheets are combined with the vertically polarized 532-nm FRS laser sheet using the dichroic mirror. The overlap of the 568-nm and 532-nm laser sheets is ensured by translating a knife edge into the focal plane and adjusting the beam positions until the locations corresponding to 50% of the incident energy level (of each sheet) were spatially coincident. A schematic depicting the relative timing of the FRS pulse, bracketed by the PIV laser pulses is shown in Fig. 6.1f and a sample time trace from the dye laser output of two sequential PIV pulses is shown in Fig. 6.3 with a temporal separation of 2.5 μs. The example PIV pulses shown in Fig. 6.3 show that double pumping a dye laser with a PIV laser is possible and yields two pulses with nearly equal energy. For example, the sample traces shown in Fig. 6.3 consist of pulse energies of 21 mJ/pulse and ~18 mJ/pulse, respectively.

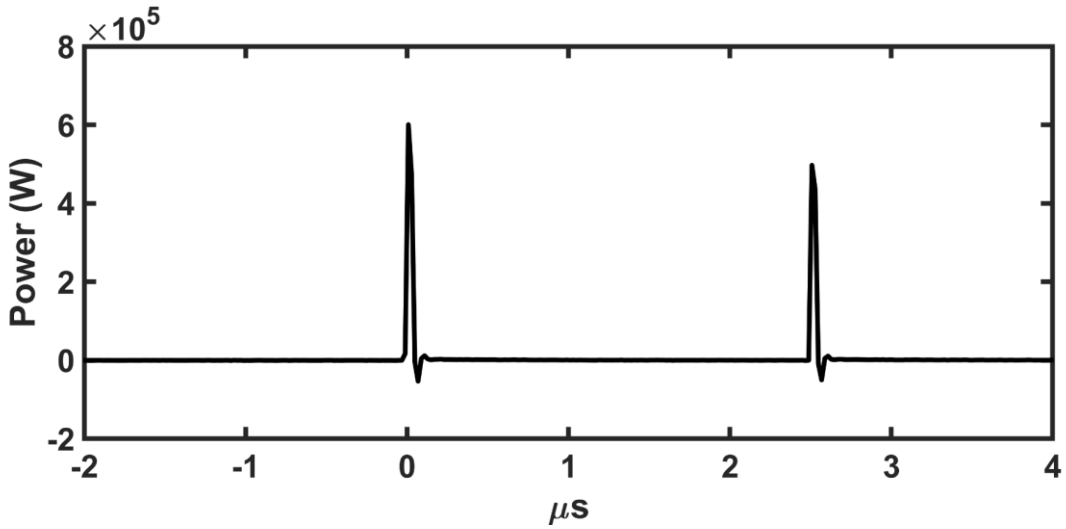

Figure 6.3: Representative time-trace of dye laser output.

A digital delay generator (DG-645, Stanford Digital Systems) acts as the master clock for the experiment. The temporal spacing of the PIV laser pulses (and timing of the cameras) is controlled using TTL timing pulses from a LaVision programmable timing unit (PTU-X) which is synced to the DG-645. The FRS laser operates continuously at 10-Hz, while the repetition rate from the PTU box (and thus the repetition rate for the PIV lasers and cameras) is automatically set to a reduced submultiple integer of 10-Hz due to data-rate limitations stemming from multiple-camera acquisition. With all cameras operating simultaneously, the data rate was reduced to 5 Hz. The temporal spacing between the two PIV laser pulses ranged from 1.5 μs to 7 μs for the test cases.

Fig. 6.4 shows a perspective view of the final beam combination and imaging setup used within the simultaneous FRS and stereo PIV (sPIV) experiment and Fig. 6.5a shows a top down schematic of this imaging system. The simultaneous FRS and sPIV is performed using four scientific CCD cameras (shown in Fig. 6.4 as "FRS/sPIV Camera Setup). As shown in Fig. 6.5a, one camera (PCO Sensicam, labeled "FRS camera") is placed behind the I_2 cell to acquire the FRS images while the two angled cameras adjacent to the FRS camera are used for the stereo particle image velocimetry (sPIV) measurements. The FRS camera is equipped with an 85 mm f/1.4 lens coupled to a 12-mm spacer and a high-transmission 532-nm bandpass filter (95% transmission; 4nm FWHM) to block the 568-nm particle scattering light. The magnification of the FRS camera is 0.2 and a hardware binning of 4×4 pixels is used during signal collection. This results in an in-plane pixel spacing of 128.2 μm for a single 4×4 "super pixel". The details of the I_2 cell are the same as discussed previously in Sec. 5.3.1.

The two PIV cameras (PCO Sensicam) are equipped with 135-mm lenses and are mounted on Scheimpflug mounts to ensure sharp focus throughout the measurement volume. The angular

difference between the two sPIV cameras is 49°, where the angle relative to the axis perpendicular to the laser sheet is -25°and 24° for the camera to the left and right of the FRS camera, respectively. Both PIV cameras are outfitted with a combination of a high-transmission long-pass filter (which cuts on at 550 nm) to block the FRS laser and a 550-nm bandpass filter (50-nm FWHM) to reduce the flame luminosity. Both PIV cameras have an effective magnification of 0.3, resulting in a projected pixel size of 22 μm. Before passing through the test section the laser sheets first passes above the surface of matrix burner (see Fig. 6.5a) which outputs a uniform stream of filtered air. Rayleigh scattering imaging from the 532-nm laser sheet is imaged by a fourth camera (PCO Pixelfly, labeled "Energy Camera" in Fig. 6.5a) for shot-to-shot pulse energy and laser sheet

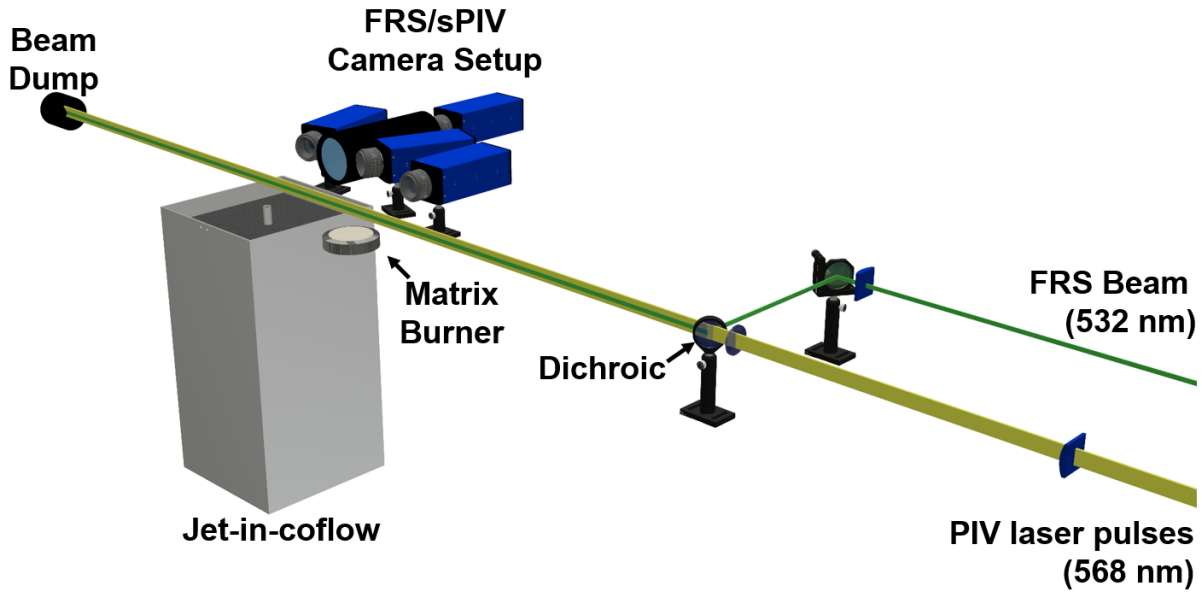

Figure 6.4: Perspective view schematic highlighting the imaging configuration of the simultaneous filtered Rayleigh scattering and particle image velocimetry (PIV) measurements.

intensity corrections for the FRS images (see Sec. 6.3). The energy correction camera is outfitted with an 85-mm f/1.8 lens and all images are acquired with a magnification of 0.55 and 4×4 hardware binning.

The primary focus of this chapter and Ch. 7 are simultaneous FRS and PIV measurements performed in the same series of turbulent, piloted jet flames introduced in Ch.5. Representative images of the flames are shown in Fig. 6.5b for Re = 10,000, 20,000, and 30,000

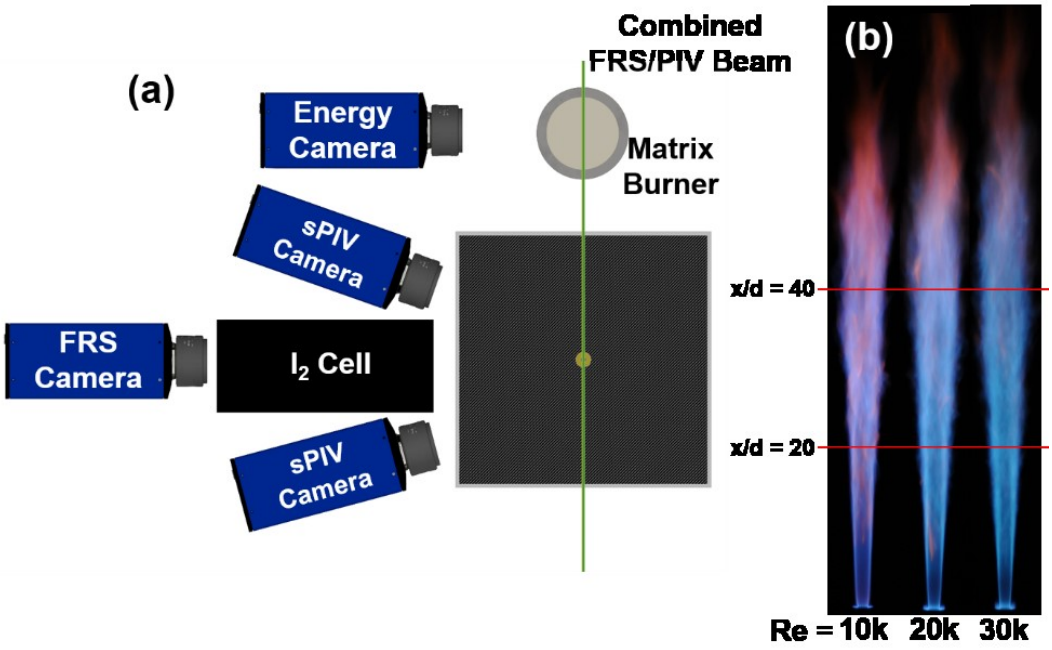

Figure 6.5: (a) Top down schematic of imaging system for simultaneous FRS/Mie scattering imaging. (b) Representative photographs of the series of Ar/CH_4/H_2 turbulent flames studied in the current simultaneous temperature and velocity study.

The 0.16 CH_4/0.16 H_2/0.68 Ar fuel mixture issues from a 7.2-mm-diameter tube from the Sandia piloted burner [26] into a 30×30 cm^2 coflowing stream of air. The central fuel tube is

surrounded by an 18.2 mm-diameter recessed pilot flame which is a premixed 0.2 CH_4/0.8 H_2/air flame operating at an equivalence ratio of 0.7. Measurements are performed at axial locations of x/d = 20 and 40 (as indicated by red lines overlaid on the flame photographs in Fig. 6.5b). The pilot for each Reynolds number operates with a thermal power that is 6% that of the main jet.

For the flame measurements the coflow and central jet are seeded with SiO_2 particles (10-20 nm nominal size prior to any agglomeration) using two individual cyclonic seeders similar to the cyclonic seeder described in Sec. 3.1. An orifice plate is place in line after both seeders to control particle agglomeration by breaking up larger clusters. It is well known that both static electric build up and moisture can induce particles agglomeration, so two distinct protocols are taken: (1) all metal tubing is used prior to and after the seeder to reduce the buildup of static charge on the particles and (2) the SiO_2 particles are baked at 245°C for 12h+ directly before to the measurements to remove moisture in the particles. For the current measurements, the seed density was set to 0.02. While this seed density is within the suggested guidelines from Keane and Adrian [136], it is a bit sparse as compared to "ideal" PIV seeding. This seed level is strictly dictated by the FRS measurements, where increased seeding would lead to increased particle bleed through and interference on the FRS camera (discussed more below in Sec. 6.2.2). Additional details on the particle selection are discussed below in Sec. 6.2.3 and an assessment of the quality of the PIV measurements under the current experimental conditions is discussed in Sec. 6.4.2.

6.2.2 Particle Scattering Blocking on the FRS Camera

Scattering from the PIV tracer particles is much stronger than that from the gas-phase FRS and is strongly dependent on the particle size. For PIV experiments in reacting flows the particles typically are ceramics (i.e., Al_2O_3, TiO_2, SiO_2), which tend to agglomerate. This not only can

reduce the particles ability to faithfully follow the flow, but also decreases the ability of the I_2 filter cell to fully block the particle scattering signal onto the FRS camera. For those reasons the seeding system as described above has been implemented to minimize particle agglomeration. A detailed description of the many experimental issues determining the exact level of FRS particle rejection is beyond the scope of this dissertation, but the work presented in [188] showed the use of an FPE can greatly improve the spectral purity of an injection-seeded Q-switch Nd:YAG laser. Specifically, it was shown that by implementing the FPE, an increase in laser spectral purity of greater than an order of magnitude was achieved which increased the attenuation of unwanted scattering by more than two orders of magnitude [18]. In the current work, the use of an FPE in combination with the seeding system described above is targeted to maximize particle scattering rejection for the current FRS measurements.

To gain a sense of the blocking capabilities/limitations of the FRS system, measurements were performed in a non-reacting H_2/air flow seeded with 0.25-μm oil droplets. The non-reacting flow is chosen as "baseline" of which to compare to the reacting flows (with ceramic particles) since there is little agglomeration of the oil droplets and thus, presents a system with known particle size. Figure 6.6 shows example images of simultaneous FRS and particle scattering images in the droplet-laden non-reacting H_2/air flow. The jet is seeded with the oil droplets using a LaVision Aerosol Generator. Figure 6.6 shows that the particle scattering blocking is strong (OD > 5) as there is no evidence of particle scattering signal leaking onto the FRS image for the O(1 μm) particles.

Figure 6.7 shows example images of simultaneous FRS and particle scattering images corresponding to one of the turbulent non-premixed flame cases (Re = 30,000, x/d = 20), seeded with SiO_2 particles. The SiO_2 particles have individual diameters of 10-20 nm, but it is well known

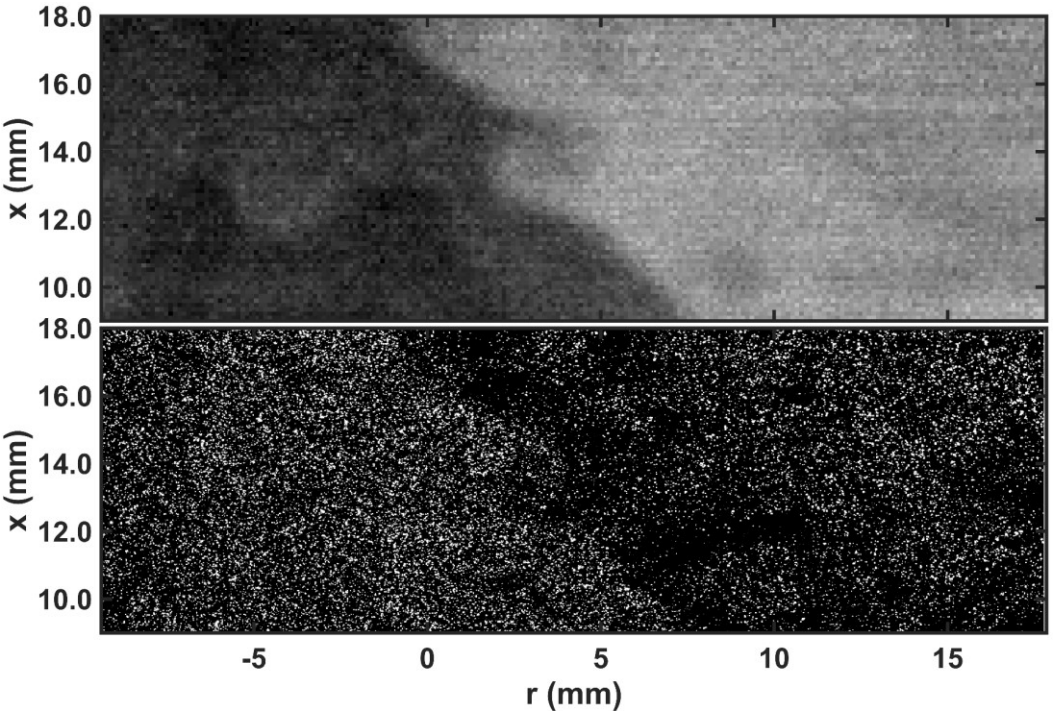

Figure 6.6: (Top) Sample FRS image from non-reacting H_2 flow issuing into air. (Bottom) Sample simultaneous particle scattering image.

that they agglomerate to sizes much larger. The rationale for the selection of these particular seed particles is discussed below. For the reacting flow case seeded with SiO_2 there is an overall good blocking of the particles, although there are examples where particle scattering makes it through the I_2 filter and onto the FRS channel. Based on images such as the one represented by Fig. 6.7, three particle sizes occurring within the FRS images are classified as 'small', 'intermediate', and 'large'. Four examples of 'large' particles are highlighted with red circles in Fig. 6.7. These appear as bright features covering multiple pixels and lead to pixel saturation. The strong scattering signal that is not rejected by the I_2 cell (and saturates the camera) is likely due to significant particle agglomeration.

In addition to the very intense examples of particle bleed through, there also is evidence of

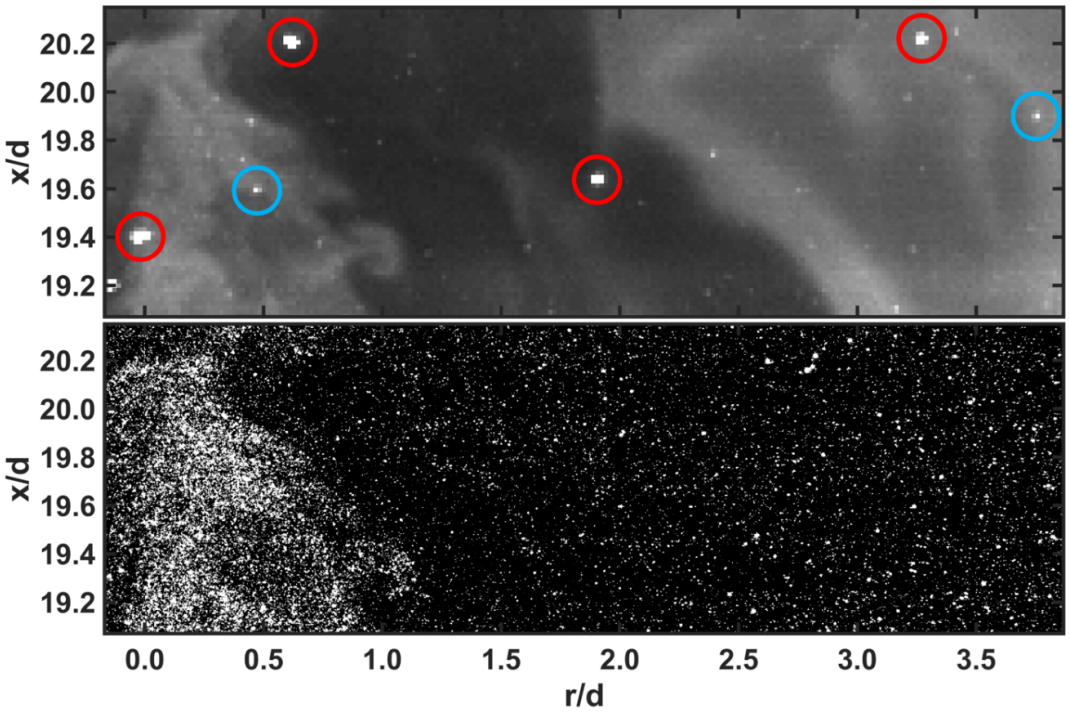

Figure 6.7: (Top) Sample FRS image from a turbulent non-premixed flame (Re = 30,000, x/d = 20) issuing into air. (Bottom) Sample simultaneous particle scattering image

scattering from 'intermediate'-sized particles in Fig. 6.7, which are more readily present, but at a much lower signal level than the 'large' particles. A couple of examples are highlighted in Fig. 6.7 with blue circles for clarity. These particles also likely have experienced a slight degree of particle clumping. These particles may be bright enough to identify above the continuum signal, but are confined to only 1-2 pixels or they may display lower signal levels that are comparable to the gas-phase scattering and appear as subtle "noise sources" in the image. The large particles are straightforward to identify and remove in post processing using simple thresholding techniques as discussed below in Sec. 6.3. However, the intermediate particles can be more problematic since the signal levels fall within the dynamic range of the desired gas phase measurement. If their contribution is not removed, these particular locations could be interpreted incorrectly as low-gas

phase temperatures. Discussion on the image processing used to remove the particle bleed through (for both intermediate and large particles) is dealt is given in Sec. 6.3. Despite the occurrence of a large and intermediate particles that are observed in the FRS images, the majority of the particles present in the flow field (and observed in the particle scattering image shown in the bottom part of Fig. 6.7) are effectively blocked and this permits simultaneous FRS and PIV imaging.

6.2.3 Discussion on Tracer Particle Selection

The choice of using SiO_2 as the PIV tracer particle was made after extensive trials with several different particles commonly used in PIV measurements in reacting flow environments. These included the ceramics, TiO_2, Al_2O_3, and SiO_2. In this work, the particle selection was dictated primarily by the FRS measurement; that is, the ability to minimize the particle signal on the FRS images. Initially, TiO_2 was targeted for use as a tracer because it is known to resist agglomeration the most of the commonly used ceramics. However, it was determined that it was non-viable in the current measurements due to anomalous luminescence (in addition to elastic scattering) from the particles that occurs near 532 nm, but outside of the I_2 absorption profile.

In order to characterize this effect and to examine if the other two particle candidates exhibited more favorable light emission properties, a simple experiment was performed to estimate the blocking ability of the I_2 cell for the different particle types. For all three ceramics, particles were placed between two glass slides and inserted within the beam path at 45°. The laser was unfocused and the laser energy was operated at 20 mJ/pulse. The emitted light was then collected via fiber optic and directed to a spectrometer (Acton). The collected spectra was analyzed for all three ceramic particle cases as well for a scattering from simple ground glass-diffuser to act as a control. For each case data was taken with (a) the I_2 cell and 532-nm bandpass filter in place to

mimic experimental conditions and (b) a series of neutral density (ND) filters only with a total optical density (OD) of 5.1. The measurements using the ND filters were used to place the spectra obtained using the I_2 cell and 532-nm bandpass filter on an absolute optical density scale.

Figure 6.8 shows the estimated peak OD for each particle case for all four cases extracted from acquired spectra. It is clear from Fig. 6.8 that all particle cases perform worse than the baseline glass diffuser case which is known to be pure surface scattering and should emit a spectral distribution identical to that of the laser. Based on these results, the peak OD obtained when using the TiO_2 is less than 3.8 compared with peak OD of approximately 4.8 for SiO_2 and $Al2O_3$ particles. This implies that in addition to pure particle scattering, there is significant luminescence emitted from the TiO_2 particles that is broad enough to transmit through the I_2 filter, but still

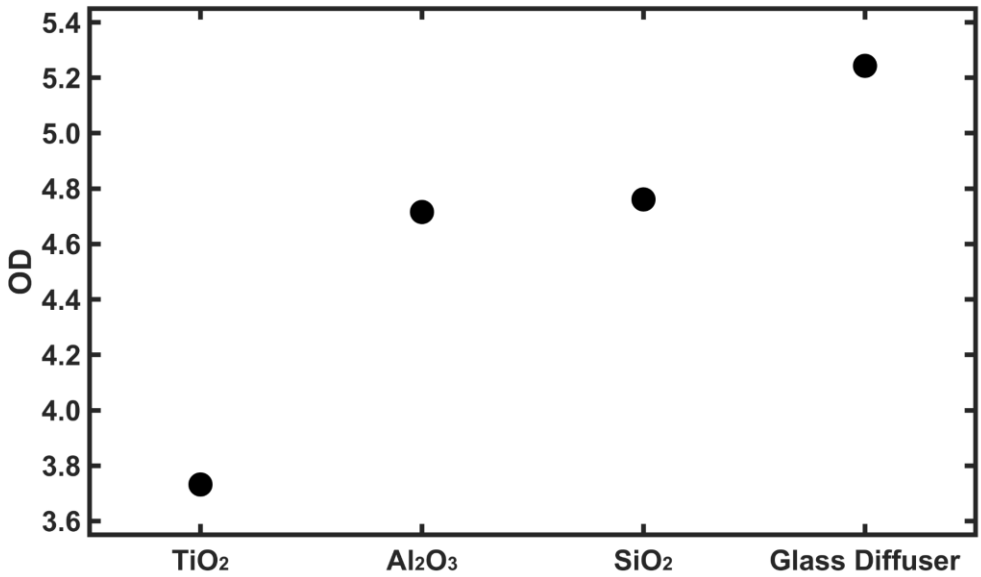

Figure 6.8: Estimated particle scattering blocking capacity (in terms of optical density, OD) obtained using different tracer particles.

sufficiently narrow to fall within the 532-nm bandpass filter (4 nm FWHM). The current spectrometer does not have the spectral resolution to isolate the additional luminescence. As a note, the 5.2 OD for the ground glass diffuser is a bit lower than expected from other laboratory tests and previous work using the FPE [188]. However, even if the current measurement does not yield absolute accuracy in the blocking efficiency, the relative results are correct and shows that TiO_2 particles are not viable candidates for FRS measurements.

Based on the results shown in Fig. 6.8, both Al_2O_3 and SiO_2 were determined to be viable options for the simultaneous FRS/sPIV measurements. It is known anecdotally that Al_2O_3 can be problematic as a tracer for a PIV measurement due to its propensity to agglomerate. This poses a significant issue for FRS measurements where larger particles will lead to increased particle scattering signal transmitting through the I_2 cell and onto the FRS camera. Figure 6.9 shows a representative FRS image from an air jet issuing into air seeded with Al_2O_3 obtained under the same optical and imaging conditions that would be used for the turbulent flame measurements. This image showcases the problems with the potential use of Al_2O_3 for FRS measurements. As observed in Fig. 6.9, there is significant particle bleed through and almost all of the particles imaged saturate the camera and mask out the gas phase information in the image. Subsequently, SiO_2 was added to both the jet and coflow, resulting in images as shown in Fig. 6.7 for both non-reacting and reacting flows. This study highlights the importance of carefully selecting PIV tracer particles when a simultaneous FRS measurement is desired.

Upon adding the SiO_2 to the fuel and coflowing air streams, the flame luminosity displayed a bright yellow-orange luminosity (not present with the other ceramics) that caused notable background levels on the 2nd frame of the sPIV cameras when no optical filters were employed.

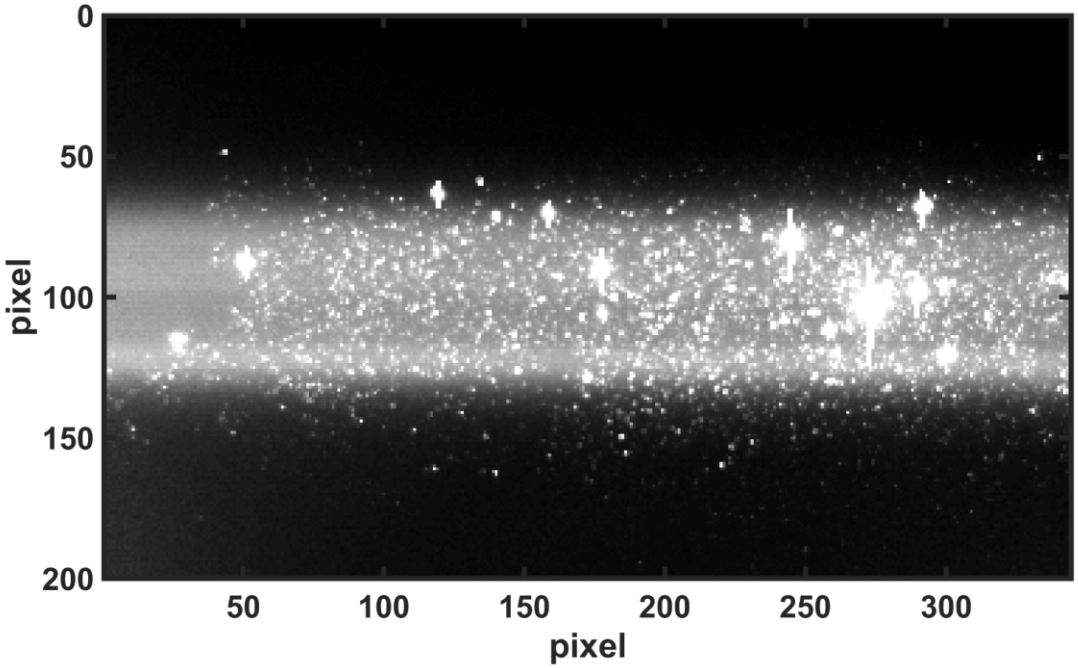

Figure 6.9: Representative FRS image with Al_2O_3 seeded into the flow.

The spectral content of the luminosity was measured using a spectrometer (Ocean Optics USB4000) and was observed to be located primarily near 590 nm. Since the luminosity does not occur near 568 nm (PIV laser pulses) nor 532-nm (FRS laser beam), this content can be optically filtered out. Figure 6.10 shows a plot of the various spectral components of the simultaneous FRS/sPIV measurement, including optical filtering strategies. The SiO_2-induced luminosity is shown in red and the two different laser outputs are shown bracketed by bandpass filters used within the experiment. The 532-nm bandpass filter completely blocks the flame luminosity, the 568-nm dye laser output used for PIV, and any yellow-shifted fluorescence signal generated within the I_2 cell. The 568-nm bandpass filter blocks the flame luminosity and the near-532-nm RBS emission.

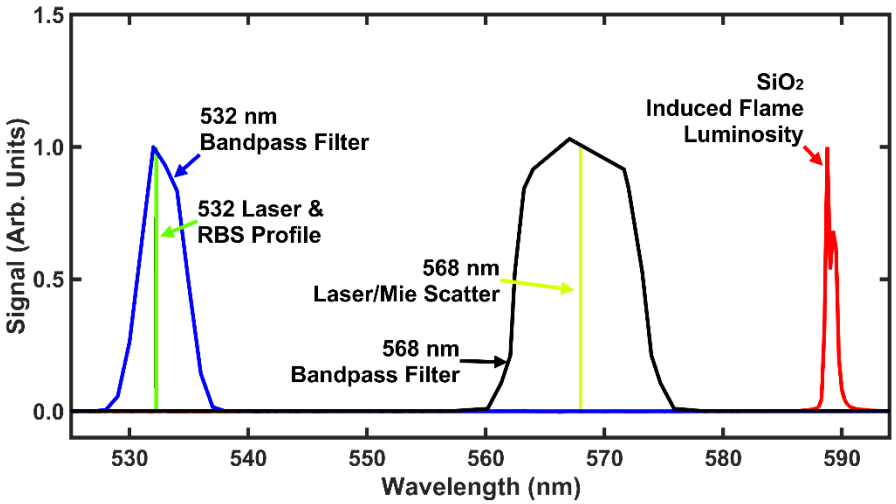

Figure 6.10: Optical filtering scheme for eliminating crosstalk and luminosity interference within the simultaneous FRS and sPIV measurements.

6.3 Data Processing for Simultaneous Temperature and Velocity Measurements

6.3.1 FRS Image Processing

Sixteen hundred simultaneous 2D FRS and stereo PIV images were collected for each axial location and Reynolds number. For each of those cases, 200 FRS image were collected in T = 300 K air to be used as the reference condition. The first processing step for the FRS images uses the wavenumber filtering technique described in chapter 5 and also in Ref. [128]; that is, instantaneous FRS measurements that have laser frequency fluctuations greater than $\pm 0.001\ cm^{-1}$ from the average wavenumber, $\langle \nu \rangle$, are removed and not considered in the results. Next, the FRS images are processed by removing average dark field images to properly set the camera background count levels to zero. The next step involves the application of a simple algorithm to determine the pixel locations where 'large particle' scattering has transmitted through the I_2 filter. This is based on a

signal threshold value that exceeds the known dynamic range of the collected gas-phase FRS signals. Specifically, this corresponds to 120% of the average/peak FRS signal measured in particle-free air. The pixels locations that exceed the threshold as well as nearby pixels within a 4 pixel radius are set to NaN and temperature values are not computed for those pixel locations. An

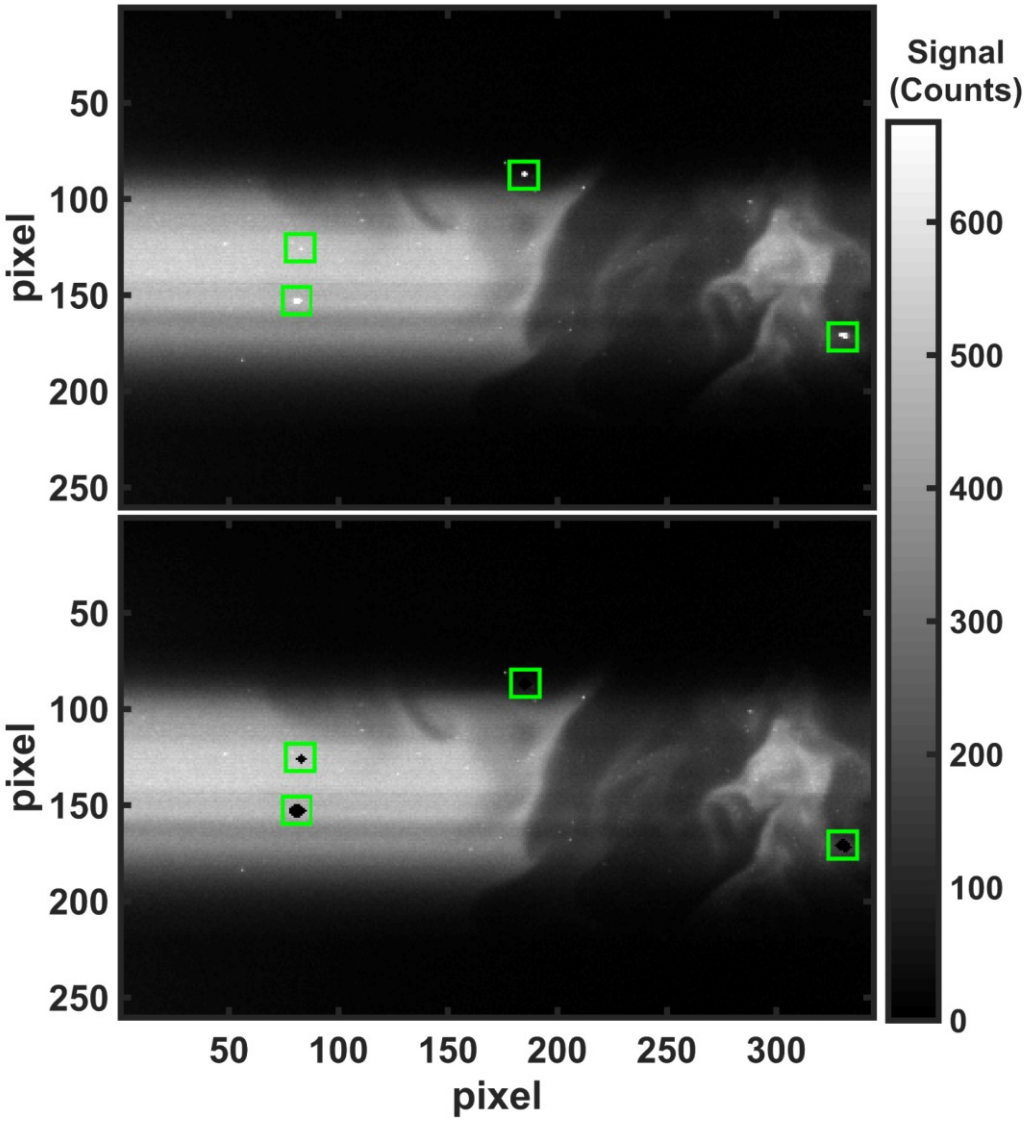

Figure 6.11: Example image processing step to "remove" the large particles from an FRS image. (Top) Example image with large particles highlighted with green rectangles. (Bottom) Same image as in (a) with large particles and nearby pixels set to NaN (shown as black in the image)

example of this algorithm applied to a single FRS image can be seen in Fig. 6.11 where the top image shows large particles present in FRS image (highlighted in green rectangles) and the bottom image shows the same image with the particles removed via the algorithm. It is noted that this step only "flags" large particles that are clearly not gas-phase scattering. The 'intermediate' size particles are still present in the FRS image as observed in the bottom of Fig. 6.11 and the processing to remove their signal contribution will be described below.

The next step is to estimate and remove any spurious background signals. The FRS images obtained with particles present in the flow showed a low-level, diffuse background signal above and below the laser sheet (see the left side of Fig. 6.12a) and it is expected that this background exists within the laser sheet as well. Any extraneous signal needs to be removed as this will falsely lower the estimated temperature and this is could be especially problematic at higher temperatures (lower signals). It is not explicitly known what the source of extra signal is, but it is hypothesized that it is multiple scattering from the gas-phase RBS signal off of the particles or a small level of photoluminescence from the particles (recall the results of Sec. 6.2.3; Fig. 6.8). These are likely candidates based on the fact that (i) any surface scatter (at the laser wavelength) should be effectively blocked by the I_2 cell, (ii) the diffuse background appears to be higher near the coflow region, where there is a higher gas number density and particle seed density, and (iii) the signal should be broader than the I_2 absorption band to appear on the FRS camera. Regardless of the source it should be removed if possible.

Since this diffuse background is non-uniform, the removal process is more involved than a simple average of the signals above and below the laser sheet. An example of this approach is shown in Fig. 6.12 and proceeds as follows. Let the initial FRS image (with darkfield subtraction) be denoted as $I1(x, y)$ (shown in Fig. 6.12a). First, a simple background subtraction is performed

which consists of averaging the pixel intensity values from the top (pixel row 40) and bottom (pixel row 240) of the image and removing this single value, $B1$, from each image, $I2(x,y) = I1(x,y) - B1$. While subtle, this step effectively accounts for shot-to-shot variations in the total background. Next the spatial variation in the background signal is estimated by fitting a fourth-order polynomial through pixels (1:40) and (240:254) of $I2(x,y)$. This is performed for every column, yielding a noisy estimate, $B2(x,y)$, of the spatial variation of background signal for each image. Next, an average is determined from all values of $B2(x,y)$ and that resulting background image is smoothed in the column direction yielding $B2'(x,y)$. Thus, the estimated background signal for image $I1(x,y)$ is $B2'(x,y) + B1$, which is shown in Fig. 6.12b. $B2'(x,y)$ is subtracted from $I2(x,y)$ yielding a proper background-subtracted signal image $I3(x,y)$ that accounts for shot-to-shot differences in background signal and spatial non-uniformities. The final background-removed image is shown in Fig. 6.12c. Figure 6.12d effectively summarizes the effectiveness of the procedure by showing (a) an excellent fit of the non-uniform background estimate (red curve) to the original image (blue curve) and (b) a final profile with background levels properly reduced to zero.

The next processing step involves the normalization of each instantaneous FRS image by the average reference air case. The normalized images are then corrected for fluctuations in energy and non-uniform laser sheet intensity distributions using images from the energy correction camera in a similar procedure to that described in Ch. 3. As discussed previously, the FRS images contain signal from the 'intermediate' particles that are not completely rejected by the I_2 cell. Recall, these signal contributions are comparable to that of the gas-phase signal and cannot be flagged by the signal thresholding used to remove the few instances of 'large' particles. However, since the

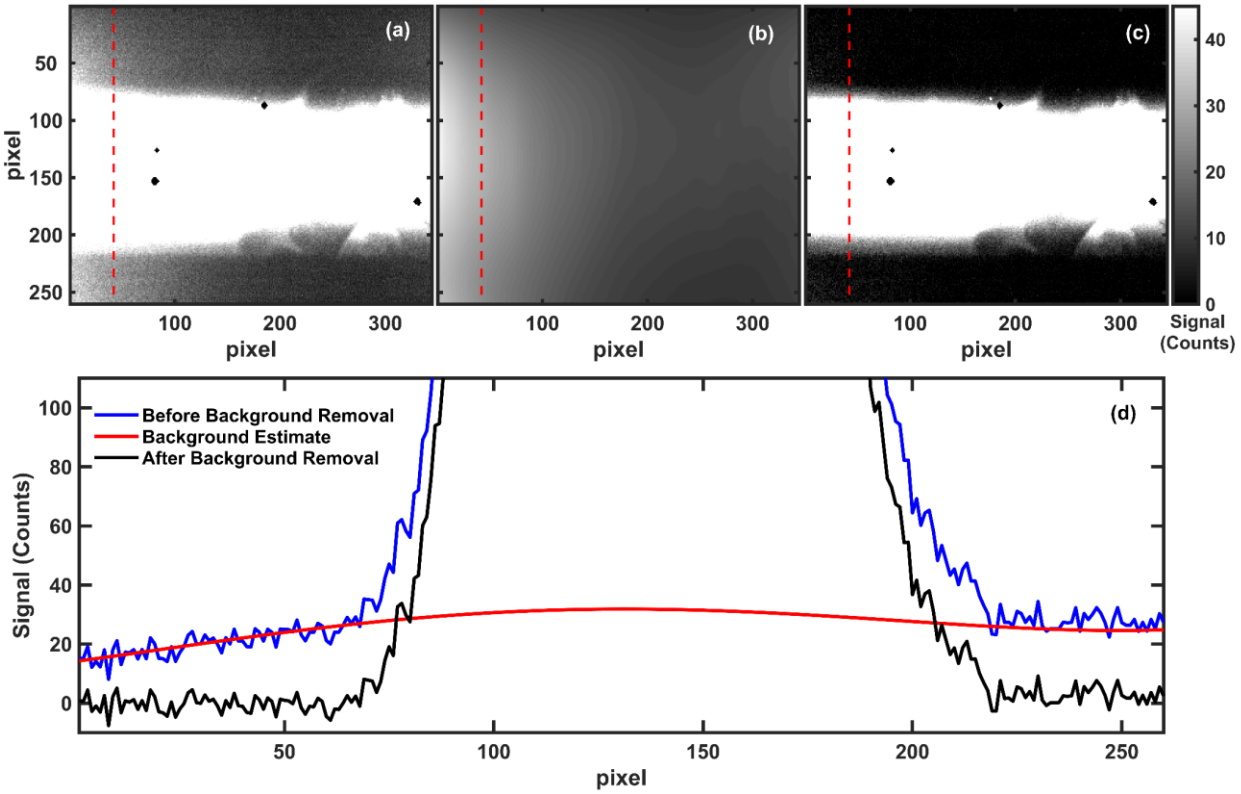

Figure 6.12: Example images showcasing the background scattering estimation and removal in a flame image. (a) Initial image. (b) Estimation of the background signal image. (c) Background-removed image. (d) Profiles taken from the same column (denoted by dashed, red line) for images shown in (a) – (c).

imaged particles comprise only a single pixel and do not saturate the camera, they can be effectively treated as 'noise' and removed with a simple 3×3 median filter.

After median filtering, the images are processed with a wavelet de-noising filter to improve the signal-to-noise ratio (SNR) while preserving the spatial resolution of the measurement (discussed more in Sec. 6.4.3.3). The wavelet denoising filter operates by partial wavelet decomposition and reconstruction across the rows and columns of the image using the lifting method [26]. A wavelet decomposition splits the signal into approximation and detail coefficients.

If the exact approximation and detail coefficients are known, the signal (i.e., image) can be re-constructed perfectly. If an image contains noise, then some of the 'details' of the image are undesired and are targeted for removal. In the lifting method, the approximation coefficients are set as the actual signal values at the even indices of the signal and the detail coefficients are calculated as the difference between the actual values at the odd indices and a value approximated at the even index by a predictor (based on the particular wavelet used). If the predictor is good then the detail coefficients should be small. The signal is then resorted into the approximation coefficients (which is half the length of the original signal), followed by the detail coefficients. This wavelet decomposition can continue across scales (continuing to split the signal and sort into approximation and detail coefficients at each scale) until the estimate of the signal is given as almost all detail coefficients with one approximation coefficient. In the current wavelet de-noising algorithm, this is not necessary.

The next step in the wavelet denoising is to sort all of the coefficients by their absolute value and select the percentage of the largest coefficients to retain. The remaining coefficients are set to 0. This is especially powerful for identifying and removing the noise even if the signal is non-constant as is the case for a turbulent fluctuation. For example, noise is a small fluctuation relative to the main signal and therefore the noise will have a small detail coefficient in the wavelet domain and will be set to zero using the current strategy (which removes it from the image). After keeping a percentage of the coefficients (~40% for the current work), the signal is then reconstructed from the wavelet domain back into the original spatial domain via the inverse process. More information on discrete wavelet transforms can be found in Ref. [194].

An example of this processing is shown in Fig. 6.13a-b as applied to the Re = 20,000 flame at x/d = 20. Figure 6.13 shows a sheet-corrected normalized FRS signal with clear indications of

the presence of intermediate-sized particles. Figure 6.13b shows the same image which has had a 3×3 median filter and wavelet-denoising filter applied. It is clear from the image that the filtering algorithm not only removes the artifacts of the intermediate-sized particles, but greatly increases the SNR without significant loss of spatial features. The significant benefits of the wavelet denoising filter on SNR and spatial resolution are further discussed in Sec. 6.4.3.3 Finally, the corrected and filtered FRS signal images are converted to temperature using Eq. (5.5). It should be noted that for the majority of cases a 3×3 filter kernel was sufficient to remove the signal

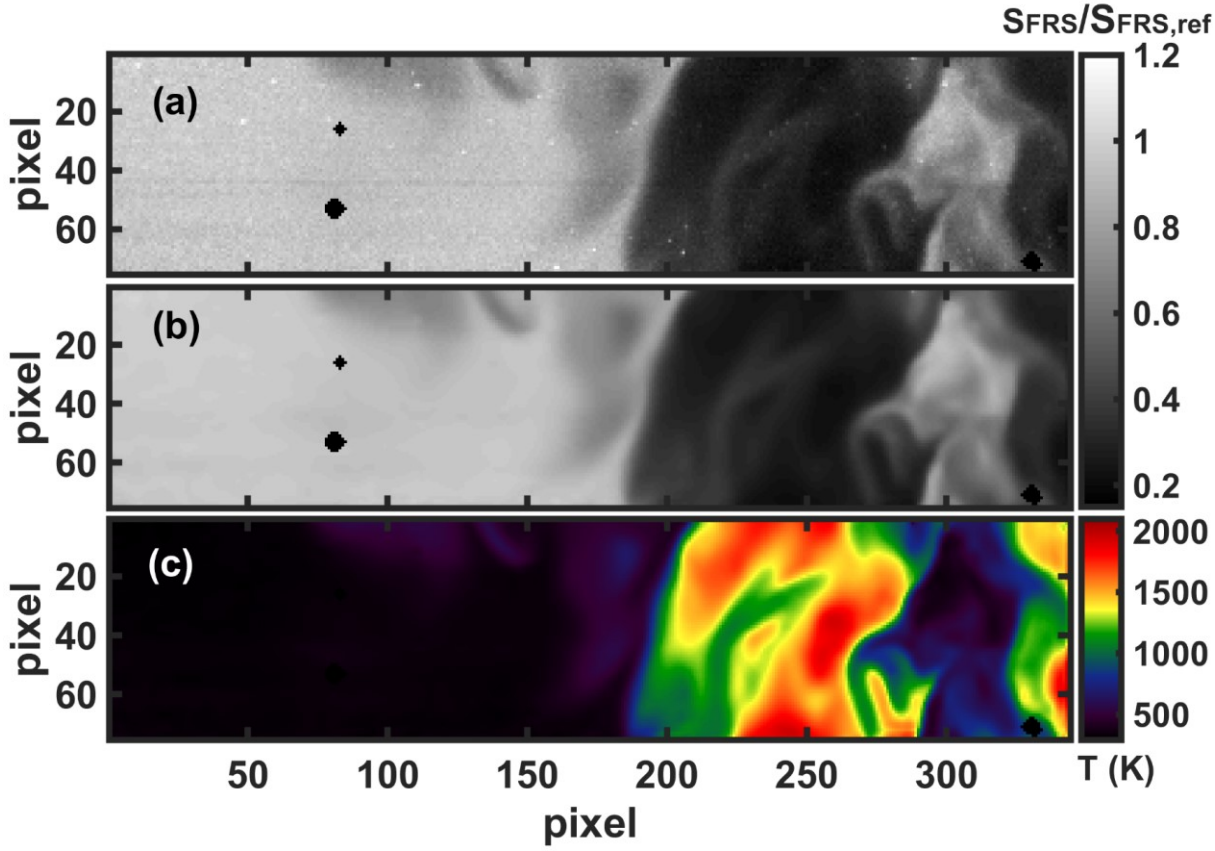

Figure 6.13: Final processing steps for FRS images and the conversion of signal into temperature. (a) Sheet-corrected image with intermediate-sized particles present. (b) Image after a median and wavelet de-noising filter. (c) Temperature image determined from applying Eq. (5.5) to the normalized signal image of (b).

contributions from the intermediate particles, but there were some cases downstream at x/d = 40 that required a 5×5 kernel to effectively remove the particles. This was likely due to increase agglomeration of particles at the downstream locations for these particular cases.

Figure 6.14 shows a series of sample processed temperature images (shown as temperature fluctuations from the mean) for all of the flames/positions for the current measurements. The top two images are from x/d = 40 for Re = 10,000 (a) and Re = 20,000 (b), while the bottom three images are from x/d = 20 for Re = 10,000 (c), Re = 20,000 (d), and Re = 30,000 (e). Any NaN values in the images are interpolated using a robust interpolation operator to fill in the missing values [195] for visual purposes. These locations are not used in any quantitative analysis. All of the images showcase high SNR, where the SNR is determined as 50 in the 300-K coflow and estimated as 61 at an elevated temperature of 1445 K using the method described in Sec. 5.4.3.1. The images shown in Fig. 6.14 also showcase the range of scales and turbulence levels accessed with the current measurements and image processing. As expected, larger scale structures are observed for the temperature images taken at x/d = 40 where the temperature is higher (higher viscosity → lower local Reynolds number) and the velocity is slower. A stringent test to qualitatively assess the spatial resolution of the measurements is to examine the images at x/d = 20 for increasing Reynolds numbers. It is observed that with increasing Reynolds numbers, the size of the images scales decrease (going from Fig. 6.14c to Fig. 6.14d), as expected, implying that even at the highest Reynolds number, the resolution limit of the imaging system (and processing methodology) has not been reached. Overall, the image quality of the current measurements are quite high and similar to the highest quality temperature measurements presented previously within the literature (e.g., [51-54]). However, the current measurements also have a simultaneous velocity component that has not been available previously for turbulent non-premixed flames.

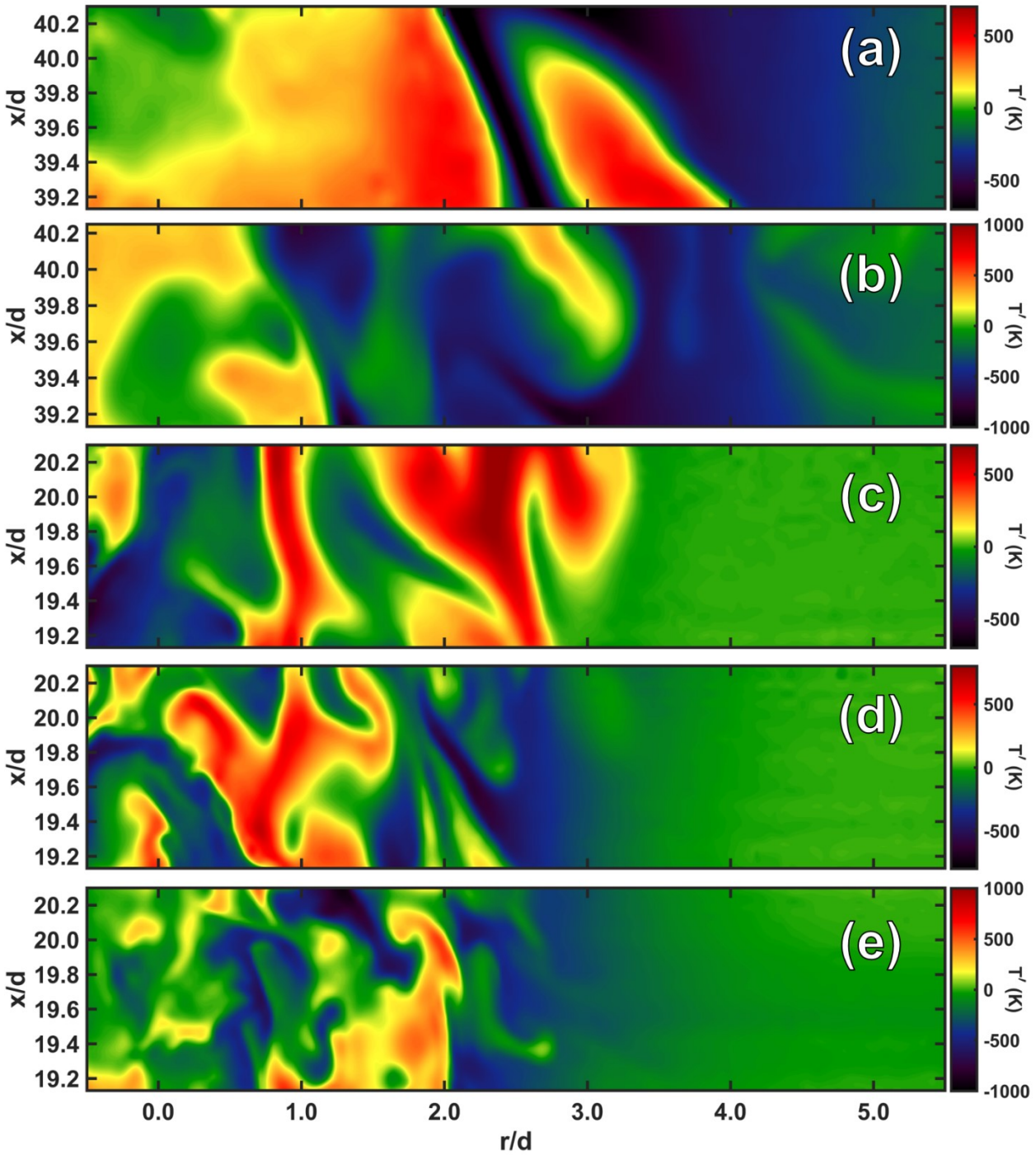

Figure 6.14: Sample processed temperature images from simultaneous temperature and velocity data campaign from x/d = 40 for Re = 10,000 (a), Re = 20,000 (b) and x/d = 20 for Re = 10,000 (c), Re = 20,000 (d), and Re = 30,000 (e).

6.3.2 PIV Processing

Prior to processing the particle images for velocity results, the particle pair images are pre-processed using built-in operations within DaVis 10.0 (LaVision, Inc) in order to (a) reduce the impact of noise and improve the effective particle signal and (b) reduce the impact of laser non-uniformities and relative pulse-to-pulse energy differences. The particle image pairs from each camera are mapped to the real-world coordinate system using a 3D DaVis Calibration target (along with the FRS image). Following the physical calibration, any calibration errors are mitigated by using a built in stereo self-calibration procedure. Following these procedures, the particle images are processed using a multi-pass stereo PIV algorithm with variable interrogation windows ranging from 64×64 pixels to 16×16 pixels, both with 75% overlap. Stringent multi-pass/final vector post-processing is applied to ensure only vectors with a high correlation value are kept. Following the final vector computation, the vector fields are post-processed using an anisotropic de-noising scheme described in detail in Ref. [196] as well as a universal outlier removal scheme developed and discussed in Ref. [197].

A sample image of simultaneous temperature and velocity data are shown in the top of Fig. 6.15. Both the velocity and temperature fields are shown as fluctuations from their respective mean fields with the temperature shown as a false colormap and the in-plane velocity shown as vectors overlaid onto the temperature colormap . Shown in the bottom part of Fig. 6.15 are extracted radial profiles of the temperature fluctuation (black), the axial velocity fluctuations (blue), and the radial velocity fluctuations (red). Both the image and the extracted profiles showcase the quality of both the temperature and velocity measurements as well as highlighting some interesting dynamics present in the flow. For example at $x/d = 19.8$ and $r/d = 0.5$, a clockwise-rotating vortex is observed

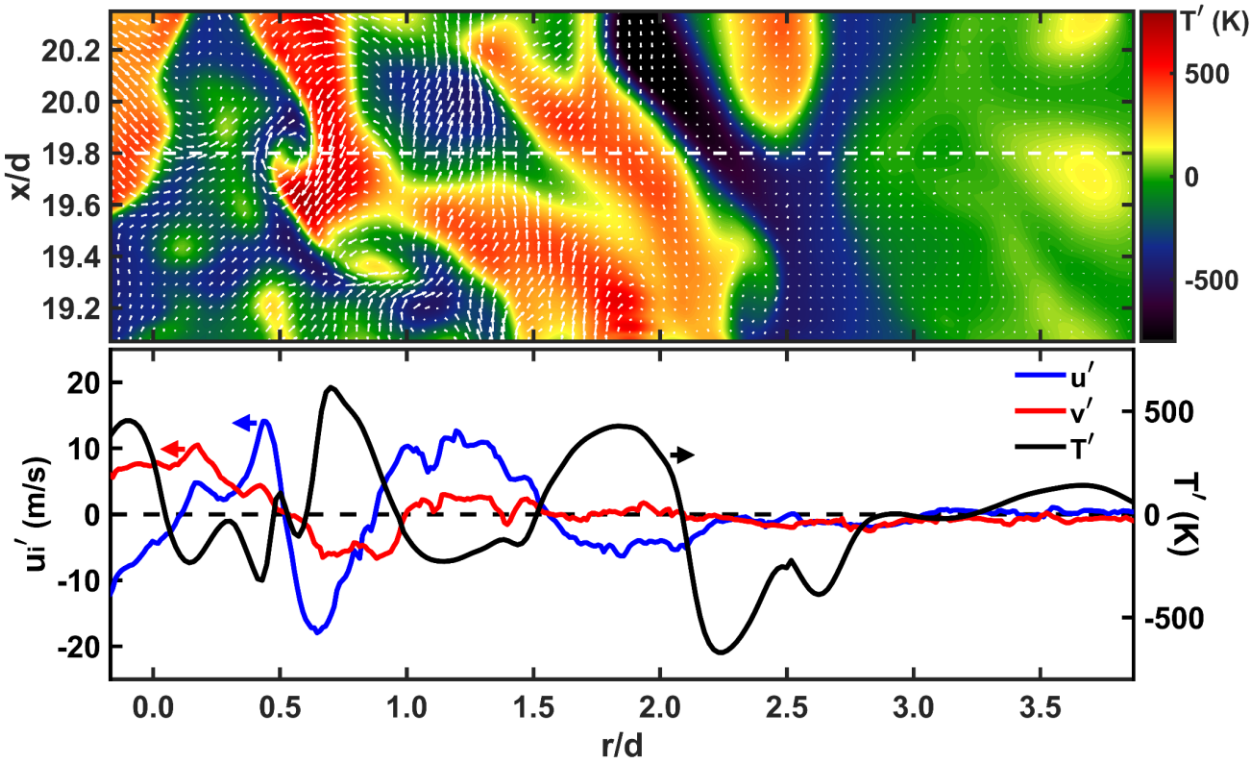

Figure 6.15: (Top) Sample simultaneous temperature and velocity image from the Re = 20,000 case at x/d = 20. Temperature fluctuations are shown as a false colormap with velocity fluctuations overlaid as vectors. (Bottom) Extracted radial profiles of temperature (black), axial velocity (blue) and radial velocity (red) fluctuations taken from the location indicated by the dashed, white line in the image at x/d = 19.8.

in the top part of Fig. 6.15, which appears to lead to a pocket or cusp in the temperature field. In the extracted profiles the axial and radial velocity components display a nearly linear decrease from positive to negative values (0 m/s at the center of the vortex). Near this same location, the temperature decreases and increases again showing the doubled-hump structure which would be expected as a vortex wraps hot fluid around a colder core. This is consistent with the cusp noted in the temperature image.

6.3.2 Considerations for Simultaneous Statistical Analysis and Gradient Analysis

6.3.2.1 Data Mapping

The temperature and velocity fields are mapped to the real world coordinate system using images of a 3D calibration target. As discussed above, the velocity data is properly mapped to the real world coordinate system within the DaVis velocity processing. The temperature field mapping is performed independently using the target image. The pixel centers of circles within the target image are determined with subpixel accuracy using a circular Hough transform [198]. The pixel centers are then matched to real-world coordinate values such that the pixel coordinates (i,j) correspond to real world coordinates (X,Y). Subsequently, an affine transformation mapping is generated in Matlab and applied to each pixel in the FRS image array such that every pixel has a corresponding real-world coordinate value. At this point both the temperature and velocity are mapped to a real-world coordinate system, although the two coordinates systems may not be aligned due to the different number of data points per common field-of-view for the temperature and velocity fields. The temperature field is then mapped to the velocity field using a function built-in to Matlab called 'scatteredInterpolant', which is a interpolation function designed to interpolate data that has no structure between their relative locations (i.e., 'scattered data').

6.3.2.2 Gradient Analysis

The importance of gradient fields in turbulence analysis has been discussed in Chapter 1. Taking gradients of noisy data can pose issues in accuracy as gradients are strongly sensitive to noise. For discrete experimental data there are several finite difference methods used to estimate the derivatives and one common approach is a fourth-order central difference which can be written for a general discrete function $f(x)$ as

$$\left.\frac{df}{dx}\right|_{x_i} \approx \frac{f(x_{i-2})-8f(x_{i-1})+8f(x_{i+1})-f(x_{i+2})}{12\Delta x} \quad \text{Eq. (6.1)}$$

where x_j (j = i, ±1, 2, ...N) is the point at the j^{th} index. This finite difference operation also can be written as a filtering operation whereby a filter kernel, h, with coefficients given by, $h = \frac{1}{12}[1, -8, 0, 8, -1]$, is convolved with the original discrete signal. This discrete convolution process can be applied to an image (or matrix) of quantity ϕ, such that the derivative in the horizontal-direction is given by $d\phi/dy \approx \text{conv}(h, \phi)$ and the derivative in the vertical-direction is given by $d\phi/dx \approx \text{conv}(\text{h}_{rot}, \phi)$, where h_{rot} is the filter, h, rotated by 90°[3]. The fourth-order central differencing scheme only is applied with information from points to the left and right of the point of interest. For the current measurements, the impact of noise on gradient calculations can be reduced using a "noise robust gradient filter", h, that combines a gradient operation with isotropic noise suppression [199]. The filter uses information from the signal not only to the left and right of the point of interest but also above and below the point of interest. The filter kernel used in the noise robust gradient filter scheme is a 5 × 7 kernel and is given by

[3] Convention in work on axis-symmetric turbulent flows refers to the direction in the streamwise direction as 'axial' with abbreviation of 'x, y, or z' and orthogonal to the primary streamwise direction as 'radial' with abbreviation of 'r'. In this work, the x-axis is denoted as that aligned with the jet tube and in the streamwise direction and the orthogonal directions are colloquially referred to as 'r'. However, the coordinate system used in the current dissertation uses a Cartesian grid and thus derivatives are computed in the 'y' and 'z' directions. For clarity, 'r' and 'y' are synonymous.

$$h = \frac{1}{512}\begin{bmatrix} -1 & -4 & -5 & 0 & 5 & 4 & 1 \\ -4 & -16 & -20 & 0 & 20 & 16 & 4 \\ -6 & -24 & -30 & 0 & 30 & 24 & 6 \\ -4 & -16 & -20 & 0 & 20 & 16 & 4 \\ -1 & -4 & -5 & 0 & 5 & 4 & 1 \end{bmatrix} \quad \text{Eq. (6.2)}$$

where the derivative in the horizontal and vertical directions is computed in the same manner as the fourth-order gradient scheme. Figure 6.16 shows a comparison of the fourth-order gradient scheme and the noise robust gradient scheme applied to a sample temperature image taken from the Re = 20,000, x/d = 20 case. Figure 6.17 shows the same comparison for a sample axial velocity image that was obtained simultaneously with the sample temperature data shown in Fig. 6.16. For both figures the top images correspond to the fourth-order gradient scheme while the middle images correspond to the noise robust gradient scheme. The bottom plots are profiles of the respective derivatives (with the 'radial' derivative on the left and the axial derivative on the right) extracted from the location indicated by the dashed white line in the images. The black bars in the axial velocity gradient images are due to damaged pixel columns from the PIV cameras where velocity could not be computed. For the temperature gradient images shown in Fig. 6.16, the differences between the two gradient schemes are very small, likely due to the effective wavelet-based de-noising scheme described above. Visually, the gradient schemes appear to yield the same results; however there are small differences between the two schemes that can be observed in the profile of the radial derivative at the strongest peaks in the gradient field (located near r/d ~ 0.5 and r/d ~ 1.5).

A larger difference in the two gradient schemes can be observed in the axial velocity gradients shown in Fig. 6.17. While the same general topological features are present for both

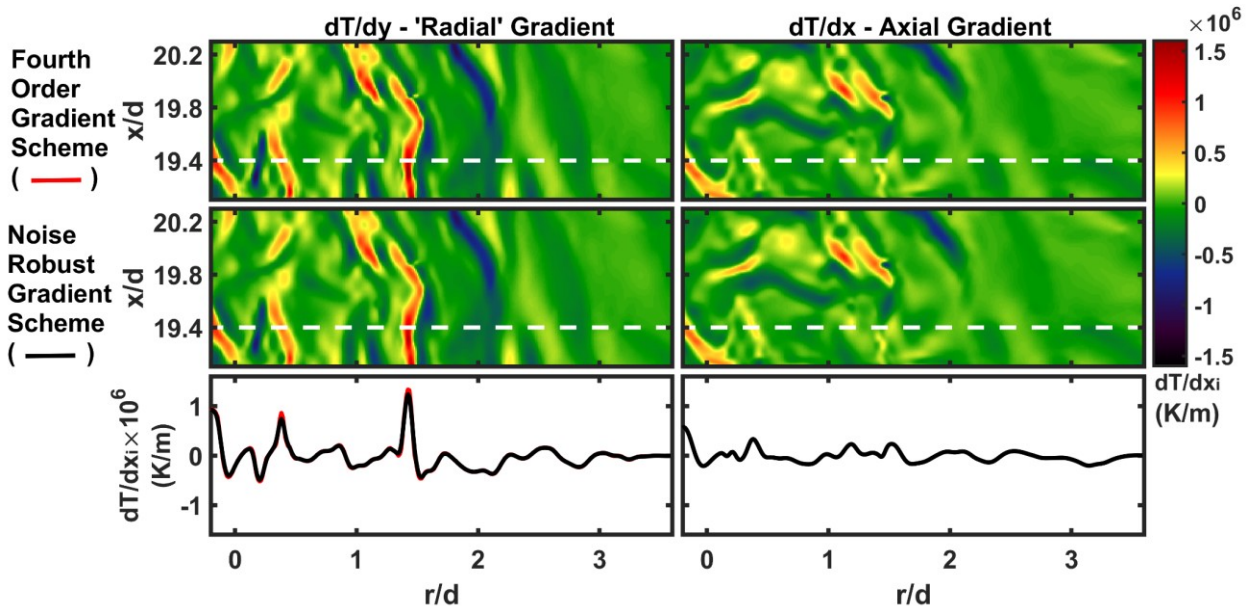

Figure 6.16: (Top) Temperature gradients determined using a fourth-order gradient scheme. (Middle) Temperature gradients determined using the noise robust gradient scheme. (Bottom) Profiles taken from gradient images at the location indicated by white dashed line.

gradient schemes, the images calculated using the fourth-order gradient scheme appear to have higher frequency content as compared to the images computed using the noise robust gradient scheme. This also is clearly observed in the extracted profiles of the derivatives, where the profile generated from the noise robust gradient scheme (black) is much smoother than the profile generated from the fourth-order gradient scheme (red). This is especially true for r/d > 2 where the derivatives are expected to be near zero as those locations are approaching the coflow stream. As shown from these two examples, the noise robust gradient scheme produces gradients with accuracy comparable to a fourth-order finite difference scheme with improved noise suppression. For the gradient analysis presented in this dissertation, the noise robust gradient scheme will be used exclusively.

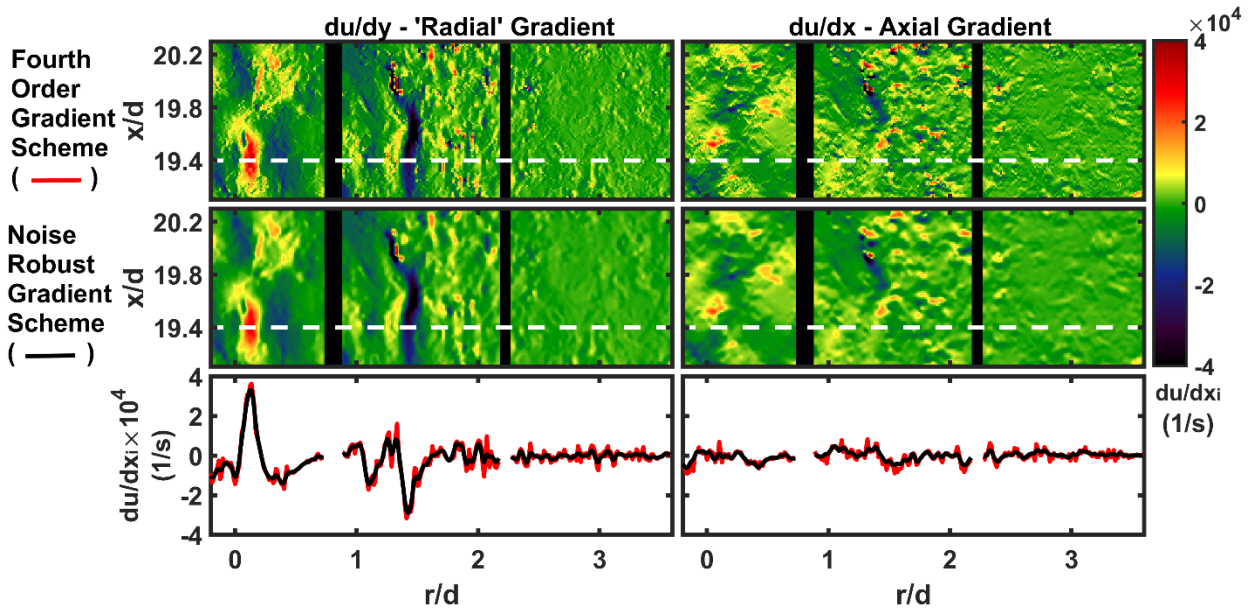

Figure 6.17: (Top) Axial velocity gradients determined using a fourth-order gradient scheme. (Middle) Axial velocity gradients determined using the noise robust gradient scheme. (Bottom) Profiles taken from gradient images at the location indicated by white dashed line. The black bands are from unresponsive pixel columns in the PIV cameras where velocity could not be computed.

6.4 Measurement Precision and Accuracy

6.4.1 Accuracy Assessment of Temperature Measurements

In order to assess the accuracy of the FRS temperature measurements in the presence of the tracer particles, and in particular the efficacy of particle elimination methods, a separate data set of 1600 FRS images was obtained without particles added to the flow. This clean, "unseeded" data set was processed in the same way as the seeded case (but without the protocol for particle removal) and serves as a metric for evaluating the measurements with PIV tracer particles. Figure 6.18 shows comparison of radial profiles of the mean and RMS temperature fluctuations from the

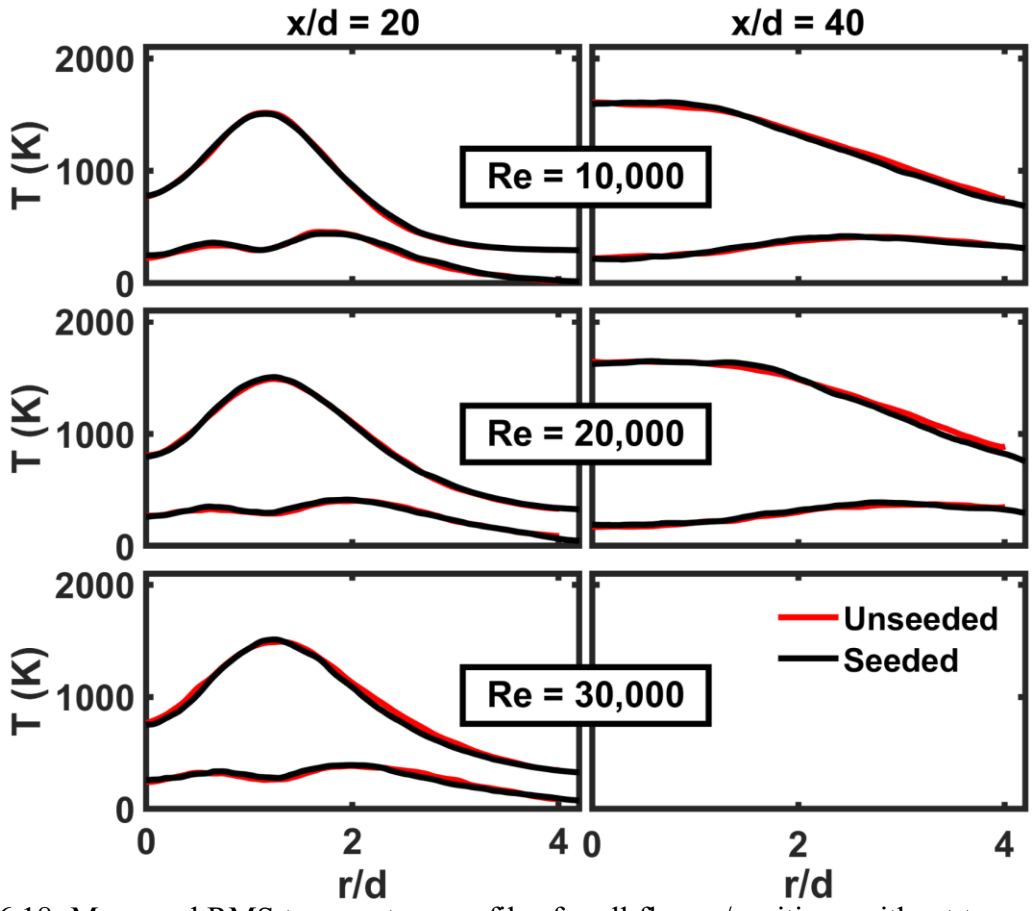

Figure 6.18: Mean and RMS temperature profiles for all flames/positions without tracer particles (red) and with tracer particles (black). (Top) Re = 10,000. (Middle) Re = 20,000. (Bottom) Re = 30,000. (Left plots) x/d = 20. (Right plots) x/d = 40.

two different data sets for all flames/positions. Figure 6.18 shows that the mean and RMS profiles from both data sets are almost identical except for some slight discrepancies at large radial positions. The differences at these locations are small (~ 5%) and it is noted that at these locations the RMS fluctuations are nearly identical. In addition to comparing the first two statistical moments of the temperature field for the seeded and unseeded case, probability density functions (pdfs) are compared at various points in the flow.

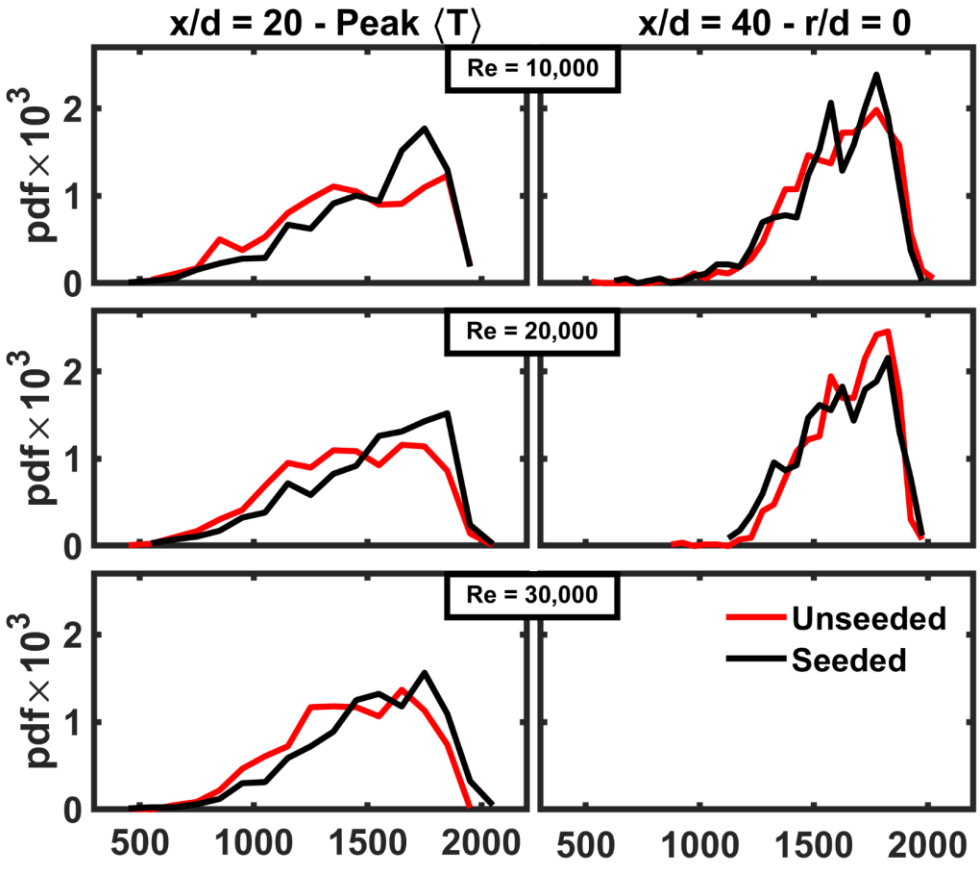

Figure 6.19: Probability density functions (pdfs) of temperature. (Left plots) x/d = 20; location of peak mean temperature. (Right plots) x/d = 40; centerline. (Top) Re = 10,000. (Middle) Re = 20,000. (Bottom) Re = 30,000. Results are shown for flames without tracer particles (red) and with tracer particles (black)

Figure 6.19 shows the pdf of measured temperatures for the seeded and unseeded cases at the location of peak mean temperature for x/d = 20 and on centerline for x/d = 40. Recall, the major source of error in the FRS measurements when flow tracers are present is the particle scattering bleed through and collection of "extra" signal on the FRS channel. The increases signals (due to unwanted particle scattering) would lead to lower deduced temperatures and thus a systematic shift in the measured pdfs towards lower temperatures. However, as observed in Fig. 6.19, the pdfs

from the seeded case are very similar to the pdf of the unseeded cases, where the differences appear to be from noise in the pdfs from an insufficient number of data points. The results in Figs. 6.18 and 6.19 indicate that the combination of particle rejection and processing strategies are highly effective, leading to accurate temperature measurements in the presence of PIV tracer particles.

6.4.2 Velocimetry Measurement Verification

Validation of the velocity measurements in this series of flames is performed using statistical analysis and comparisons to known turbulent scaling laws. Figure 6.20 shows radial profiles of the mean axial velocity, $\langle u \rangle$, the RMS of the axial velocity, u_{RMS}, and the Reynolds stress, $\langle u'v' \rangle$. The mean axial velocity profile is shown in blue, the RMS profile of the axial velocity is shown in red, and the Reynolds stress profile is shown in black. Due to some damaged pixels in the PIV cameras, velocity measurements cannot be obtained in a small radial region near r/d = 1 and r/d = 2.3. These regions are interpolated and plotted (for viewing clarity) as a dashed line in Fig. 6.20. Visually, the results appear consistent with expectation; that is, (1) the centerline velocity increases for increasing Reynolds number and appears to scale linearly with jet-exit Reynolds number, but also decreases for increasing axial position, (2) the mean velocity monotonically decreases from a maximum value along the centerline to a minimum velocity as r/d approaches the coflow and all Reynolds number cases appear to exhibit the same functional form, (3), The RMS fluctuation peaks in the shear layer at x/d = 20 and appears to have a nearly constant peak value of turbulence intensity, $u_{RMS}/\langle u \rangle$, across the different jet flames, and (4) the Reynolds stress term is near zero at centerline, peaks in the shear layer, and scales with Reynolds number.

A semi-quantitative assessment of the velocity measurements is performed by comparing the centerline velocity, $\langle u \rangle_{CL}$ decay with known turbulent (reacting) jet scaling laws. Following

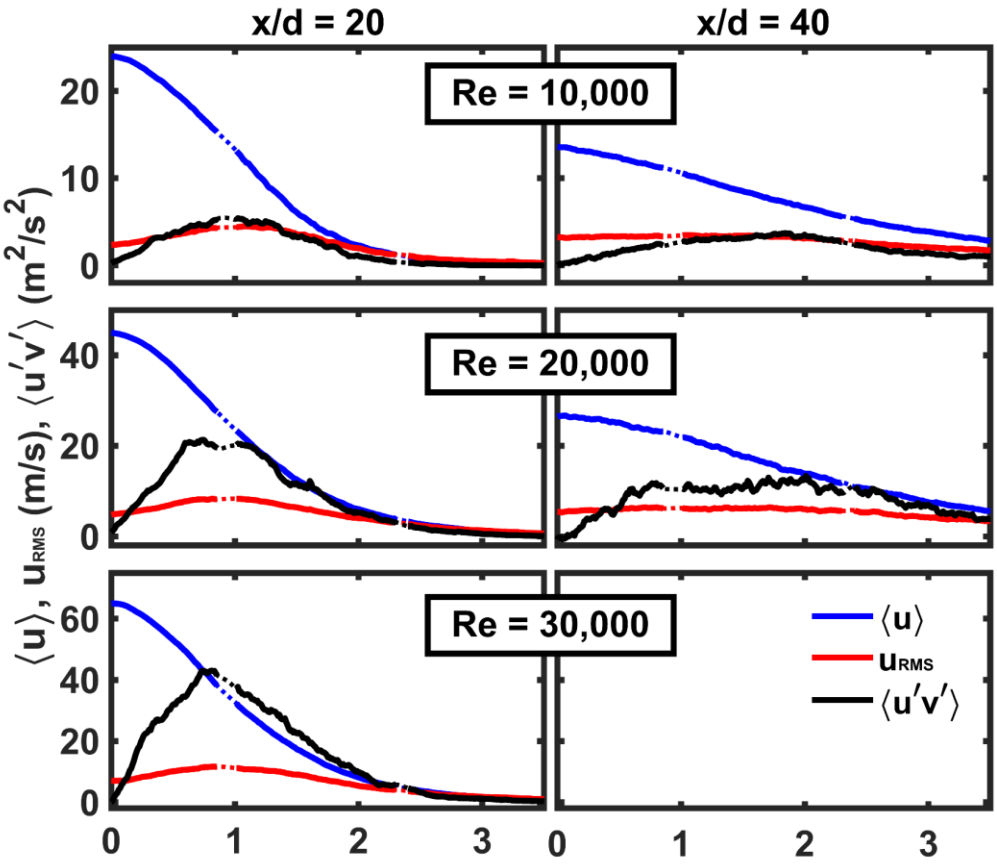

Figure 6.20: Radial profiles of mean axial velocity, $\langle u \rangle$ (blue), the RMS of the axial velocity, u_{RMS} (red), and the Reynolds stress (black). (Top) Re = 10,000. (Middle) Re = 20,000. (Bottom) Re = 30,000. (Left) x/d = 20. (Right) x/d = 40.

the work of Tacina and Dahm [147], the mean centerline velocity is expected to decay as

$$u_{CL}/u_0 = 6.5\left(\frac{x}{a^+}\right)^{-1} \qquad \text{Eq. (6.3)}$$

where u_{CL} is the centerline velocity, u_0 is the jet exit velocity, x is the downstream distance and d^+ is the "extended momentum diameter" which accounts for the density change due to heat release and is given by

$$d^+ = \left(\rho_0/(\rho_\infty)_{eff}\right)^{1/2} d_0 \qquad \text{Eq. (6.4)}$$

In Eq. (6.4) ρ_0 is the density of the jet at T_0, d_0 is the jet exit diameter, and $(\rho_\infty)_{eff}$ is the effective density of the coflow at an effective elevated temperature $(T_\infty)_{eff}$ given by

$$(\rho_\infty)_{eff} = \rho_\infty\left(T_\infty/(T_\infty)_{eff}\right) \qquad \text{Eq. (6.5)}$$

where $(T_\infty)_{eff}$ is calculated using

$$(T_\infty)_{eff} = T_0 + \frac{T_S - T_0}{1 - X_S} \qquad \text{Eq. (6.6)}$$

and T_s and X_s are the stoichiometric temperature and fuel mole fraction, respectively. For the current fuel mixture ρ_0 = 1.229 kg/m^3 and ρ_∞ = 1.177 kg/m^3 for the coflowing air stream. Consistent with Tacina and Dahm [32], the stoichiometric temperature is taken as the adiabatic flame temperature (2068K) and the fuel mole fraction at stoichiometric conditions is 0.35. From these values the extended momentum diameter and the centerline velocity decay are determined. Table 7.2 shows the values of the centerline velocity and centerline Reynolds stress as determined from the current PIV measurements as well as the estimated centerline velocity based on the scaling laws presented in Eqs. 6.3 – 6.6 at x/d = 40. The scaling laws cannot be accurately applied at x/d = 20 as they are only valid for $x/d^+ > 6.5$. For the current flames, $x/d^+ = 6.15$ at x/d = 20. Table 6.1 shows that the measured centerline velocities at x/d = 40 agree very well with the

expectations from the turbulent jet flame scaling laws. In addition, the Reynolds stress measured at centerline are near zero for all cases which is expected.

In addition to comparing the measured velocities with known scaling laws, the velocity data can be assessed by exploring the self-similarity of the average velocity profiles. Figure 6.21 shows results of $\langle u \rangle / \langle u \rangle_{CL}$ as a function of $r/\delta_{50\%}$, where $\delta_{50\%}$ is the jet width based on the FWHM location or more specifically, where velocity has decayed to 50% of the centerline value. Figure 6.21 shows that there is an excellent collapse of data for the Re = 20,000 and 30,000 cases, showing similarity in the velocity profiles for x/d ≥ 20. This is in agreement with classic non-

Flame/Axial Location	$\langle u \rangle_{CL}$, Exp (m/s)	$\langle u'v' \rangle_{CL}$, Exp ($m^2/s^2$)	u_{CL}(m/s)
Re = 10k, x/d = 20	24.0	0.3	-
Re = 20k, x/d = 20	45.0	0.7	-
Re = 30k, x/d = 20	65.1	0.1	-
Re = 10k, x/d = 40	13.5	0.1	14.2
Re = 20k, x/d = 40	26.5	-0.3	26.9

Table 6.1: Average centerline axial velocity and Reynolds stress values determined from the measurements. Also listed are values of centerline velocity based on turbulent jet flame scaling laws.

reacting flow data such as that from Wygnanski and Fiedler [200]. The Re = 10,000 cases show a reasonable collapse, but do not show strict similarity. However, this is expected based on the results of Dimotakis [201, 202] who has discussed the fact that many flows exhibit qualitatively different behavior beyond a transition number. For a number of shear flows including, jets, wakes,

boundary layers, the transition Reynolds number has been found to be $Re_{tr} \approx 10^4$. Overall, the velocity statistics indicate that current PIV measurements are accurate, even with the lower level of seeding density necessary to enable the simultaneous temperature measurements.

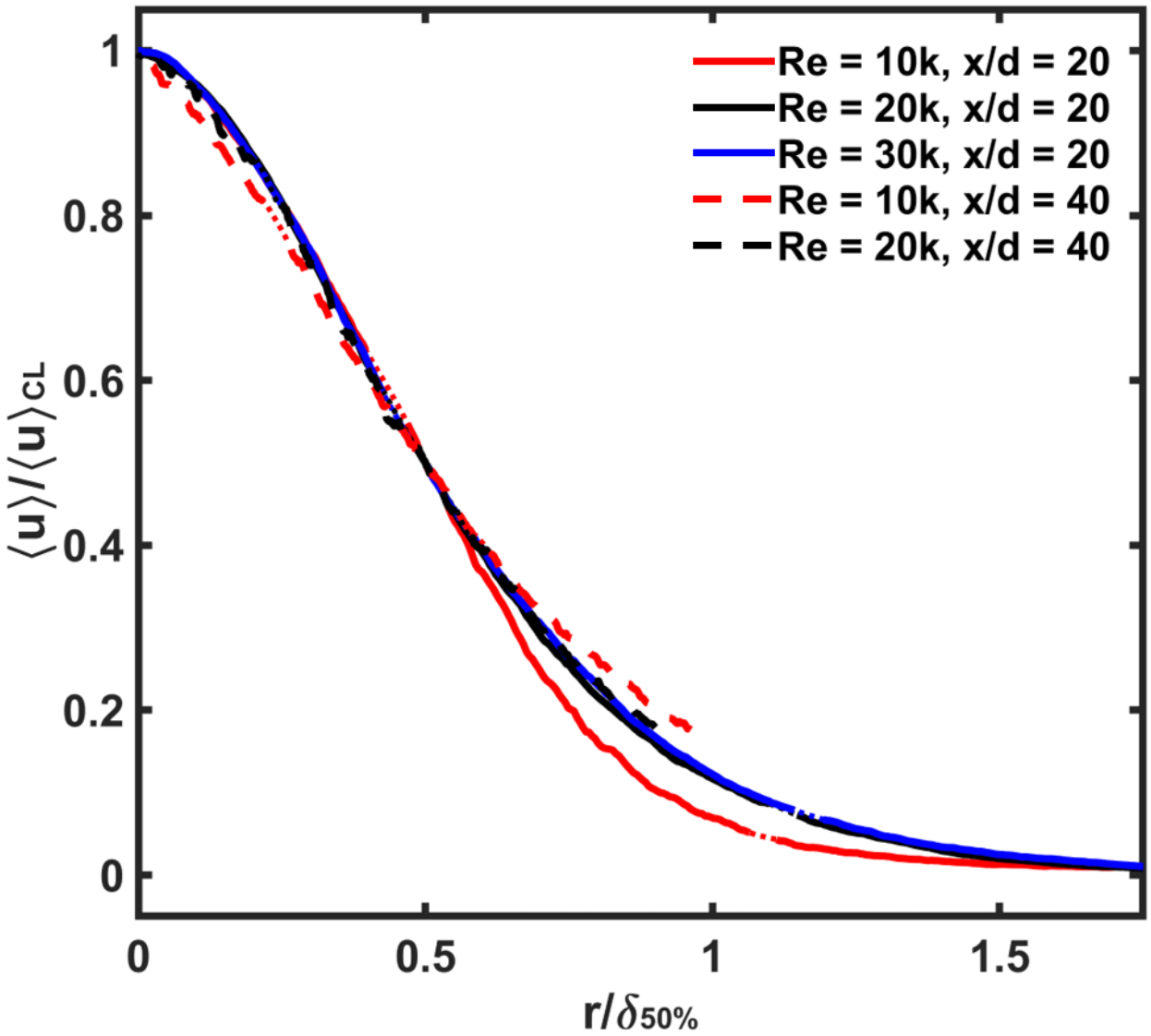

Figure 6.21: Profiles of $\langle u \rangle / \langle u \rangle_{CL}$ versus $r/\delta_{50\%}$ for all flames/positions with x/d = 20 shown as solid lines and x/d = 40 shown as dashed lines for Re = 10,000 (red), Re = 20,000 (black), and Re = 30,000 (blue).

6.4.3 Spatial Resolution Discussion

As discussed previously in Ch. 3, it is important to compare the measurement resolution with that of the smallest expected scales in the flow. As discussed in Ch. 3, the in-plane spatial resolution for a PIV measurement is determined by the interrogation window size and not the optical imaging system. For the sPIV measurements with a final interrogation size of 16×16 pixels, the in-plane spatial resolution is ~344 μm. For the current sPIV measurements, the interrogation windows are overlapped by 75%, which results in vector spacing of ~86 μm. The resolution assessment performed for the temperature measurements discussed in this chapter and in Ch. 7 differs from that previously described in Ch. 3 and represents a more appropriate and accurate approach.

6.4.3.1 FRS Imaging System Resolution

Following the work presented by Clemens [111] a methodology is outlined to estimate the in-plane spatial resolution of the FRS imaging system. The camera resolution is inherently linked to the point spread function (PSF), which is the response of an imaging system to point source of light. Practically, this would be the intensity distribution generated on the camera sensor from an infinitesimally small point source of light [111]. The width of the PSF is effectively the blur spot size, which for a diffraction limited optical arrangement is given by

$$d_{Blur} = 2.44(m + 1)\lambda f_{\#} \qquad \text{Eq. (6.7)}$$

where m is the magnification, λ is the wavelength of light, and $f_{\#}$ is the f-number for the optical arrangement. In practice, the actual PSF of any imaging system is much larger than the diffraction limit. Unfortunately, it is not straightforward to measure the PSF because it is difficult to produce

an infinitesimally small source of light. As an alternative, Clemens recommends a measuring the line spread function (LSF) which is the 1D analog of the PSF [111].

The methodology outlined for measuring the LSF involves scanning a knife edge in the object plane of the imaging system while being back illuminated by a uniform source of light. The signal value for a single pixel is monitored during the knife scan and will from some maximum signal value when the pixel is fully illuminated to some minimum signal (presumably zero counts) when the pixel is fully occluded. This scan represents the step response function (SRF) of the imaging system and the LSF is the derivative of the SRF [111]. For the current work, the FRS

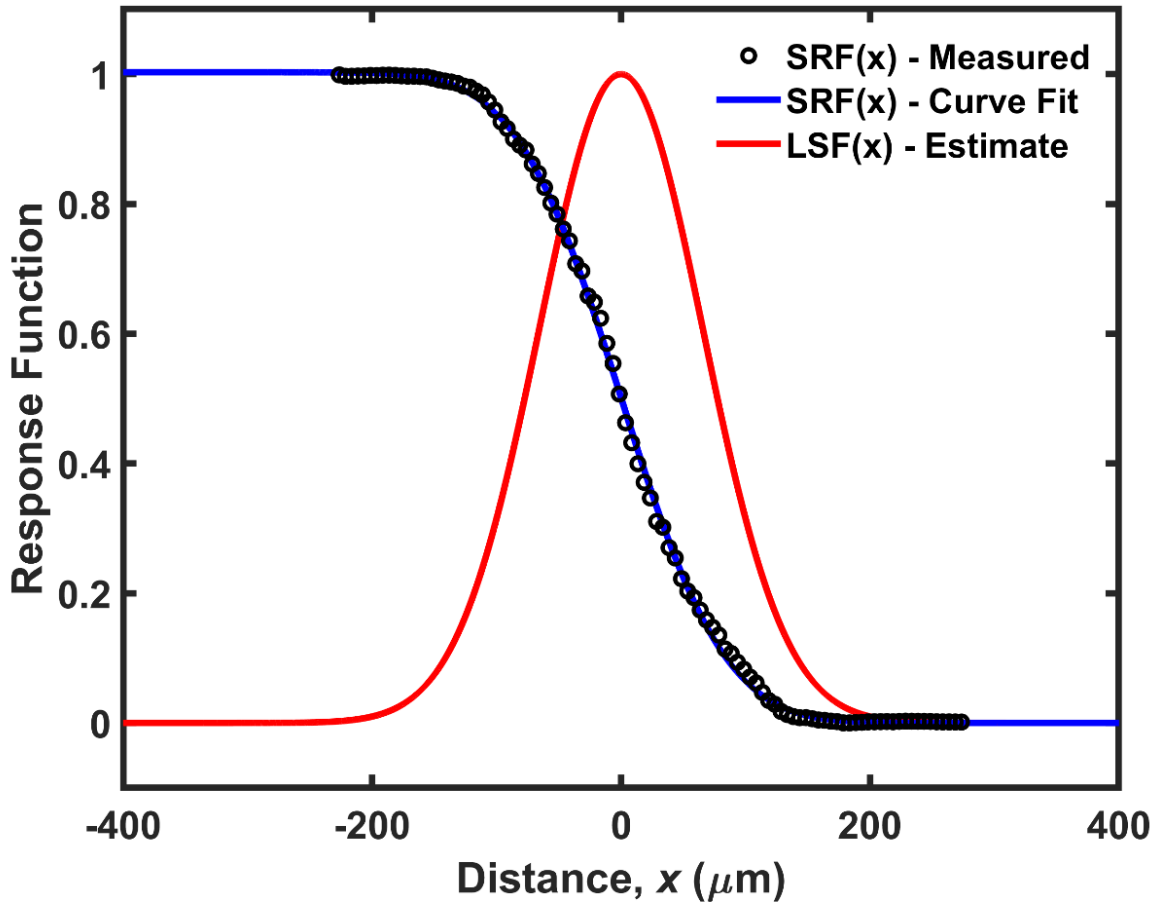

Figure 6.22: Results from knife edge scan to measure the LSF for the FRS imaging experiment.

camera setup remained as shown in Fig. 6.5a with a scanning knife edge placed in the object plane. The knife edge was mounted on two micrometer stages for left/right and forward/backward translation. The uniform light source is a Ulbricht sphere and was placed opposite to the FRS camera, where the scanning knife edge (object plane) is between the FRS camera and the Ulbricht sphere. A 532-nm bandwidth filter is placed at the exit of the Ulbricht sphere such that the emitted light is approximated as a single wavelength. During the scan the camera pixels were binned 4×4 to match the FRS imaging experiment. Figure 6.22 shows the results of the knife edge scan. The measured data, which is shown as the black symbols, is fit with a complementary error function (solid, blue curve). The SRF curve fit matches the measured SRF data very well. The estimate of the LSF is the derivative of the SRF fit (a Gaussian function) and also is shown in Fig. 6.22 as the solid, red curve. The in-plane resolution for the FRS imaging system is estimated at the "width" of the LSF, which if taken as the distance between the $1/e^2$ values is 263 μm or 186 μm for the distance between the 1/e values.

6.4.3.2 Out-of-plane Spatial Resolution

The out-of-plane spatial resolution for both the temperature and velocity measurements is determined by the thickness of the laser sheets at the measurement location. The estimation of the laser sheet width for both the 532-nm FRS and 568-nm sPIV laser sheet is determined in a similar manner as that for determining the in-plane spatial resolution. For each laser a power meter is placed at the location of the beam dump shown in Fig. 6.4. A knife edge, mounted on a micrometer stage, is placed at the focal point the respective laser sheets. The knife edge is scanned across the sheet while the average laser power is monitored and recorded as function of scanning across the laser sheet. That data is normalized 0 to 1 (shown as black symbols in Fig. 6.23) and fit to a

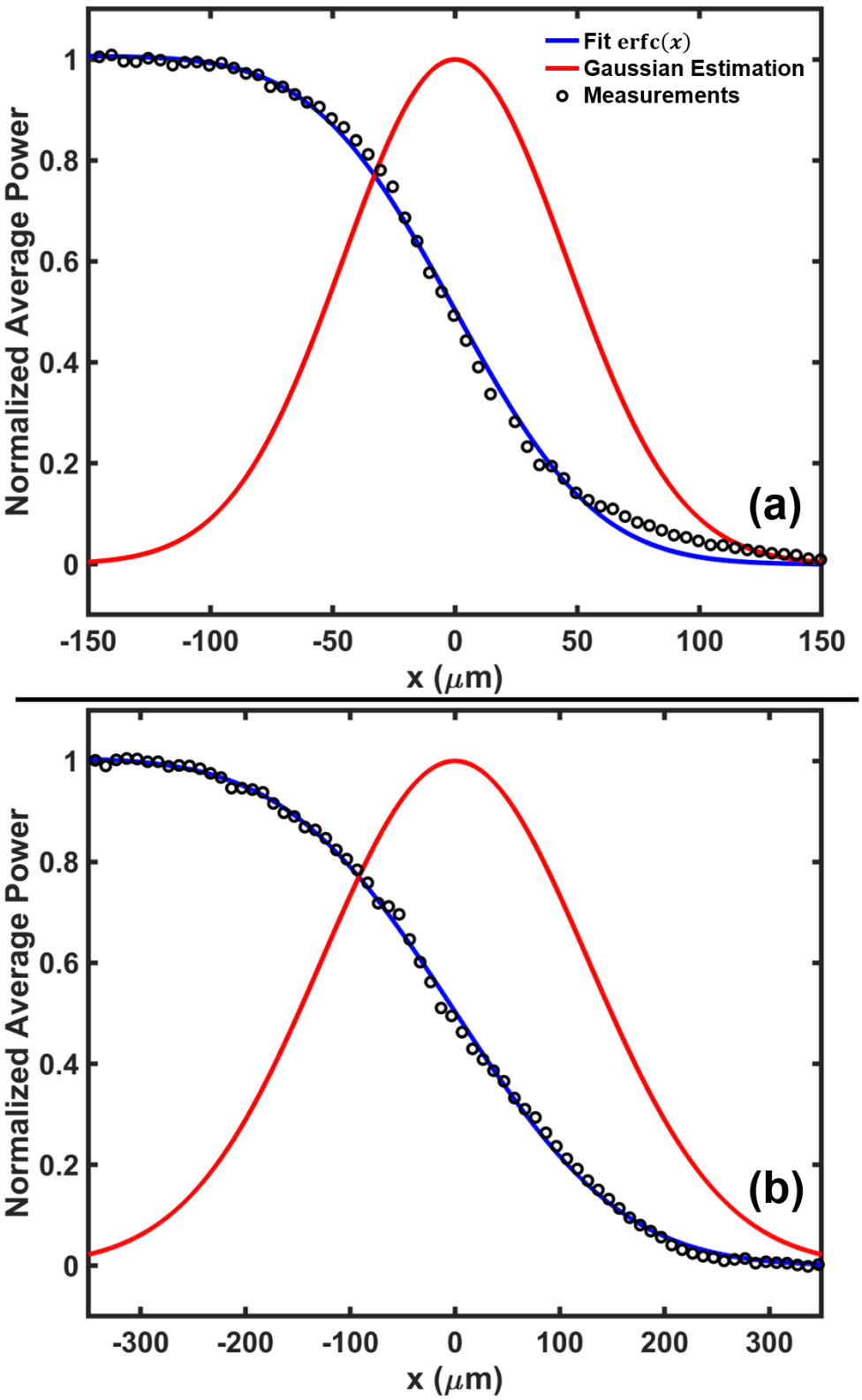

Figure 6.23: Results from knife edge scans to determine both (a) FRS laser sheet thickness and (b) PIV laser sheet thickness.

complementary error function as shown with the solid, blue lines in Fig. 6.23 (a) and (b). The derivative of the fit (solid, red lines) gives an estimate for the laser sheet intensity profile shape from which the sheet thicknesses can be determined. For the FRS laser sheet, the $1/e^2$ value was determined to be ~183 μm while for the sPIV laser sheets, the $1/e^2$ value was determined to be ~508 μm.

6.4.3.3 Impact of Filter Scheme on Temperature Measurement Spatial Resolution

Section 6.4.3.1 discussed the FRS imaging system resolution, but the actual spatial resolution of the temperature measurement is determined by the combination of the imaging system resolution, measurement noise, and image processing. To examine the effect of the proposed filtering scheme on the temperature measurements, the power spectral density (PSD) and dissipation spectra of the temperature fluctuations is calculated for the Re = 20,000 flame case, on centerline at x/d = 20, with and without the combination of the median filter and wavelet de-noising filtering. To obtain the estimate of the temperature PSD, denoted $E(\kappa)$ (where κ is the spatial wavenumber), a discrete, one-sided Fourier transform, $DFT_i(x)$, is calculated for the temperature fluctuations for each image. The PSD for a single image is determined as

$$E_i(\kappa) = (2/N\,\kappa_s)\,|DFT_i(x)|^2 \qquad \text{Eq. (6.8)}$$

where N is the number of samples in the signal, κ_S, is the sample wavenumber, and i is the image number. The PSD estimate, $E(\kappa)$ is then taken as the average of all $E_i(\kappa)$. An estimate of the dissipation spectra, $D(\kappa)$ is then determined from

$$D(\kappa) = 2\kappa^2 E(\kappa) \qquad \text{Eq. (6.9)}$$

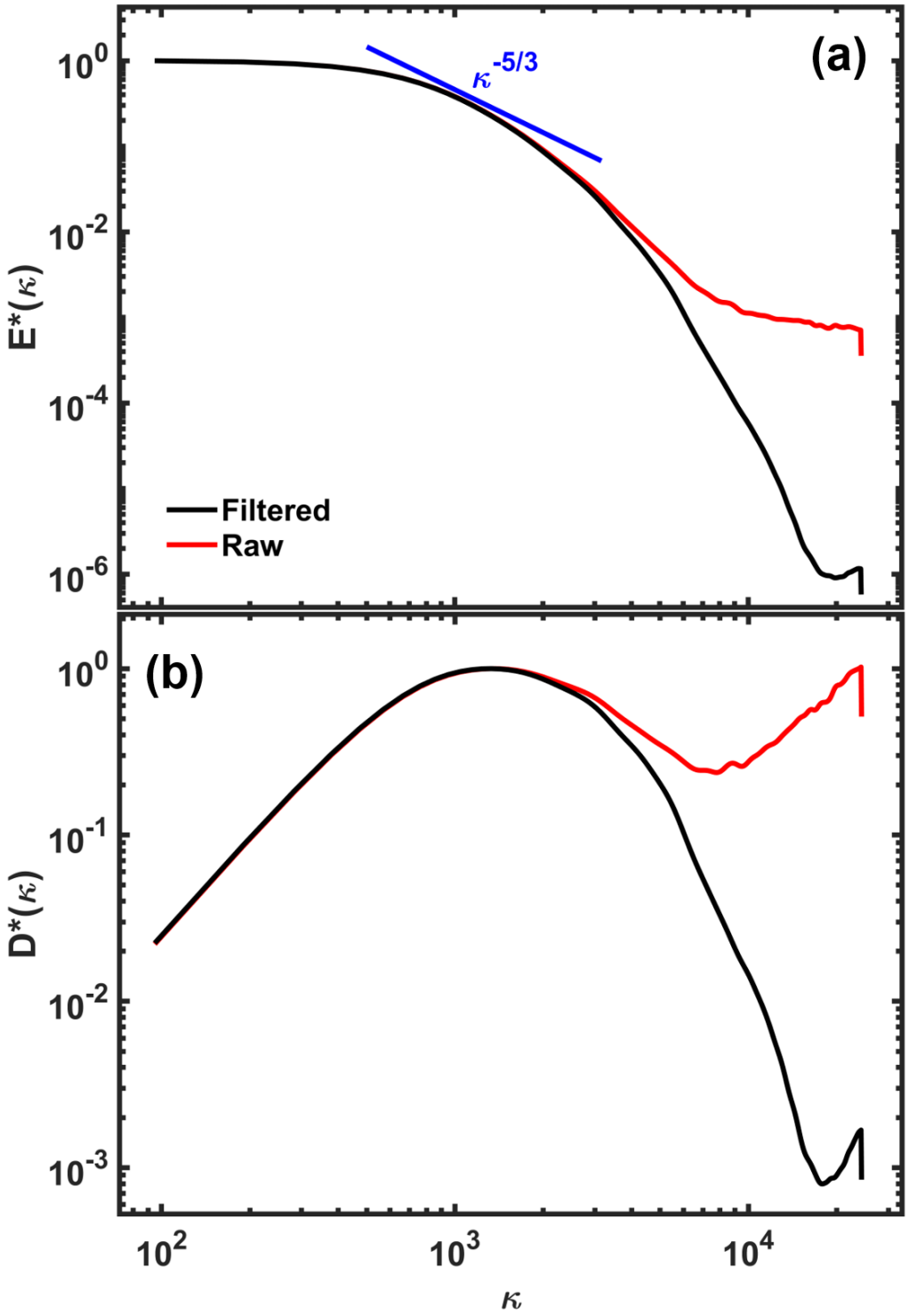

Figure 6.24: (a) Power spectral density (PSD) and (b) dissipation spectra for temperature fluctuations from the Re = 20,000 flame at x/d = 20 and r/d = 0 for the data with PIV tracer particles. (Red) Computed from the data with no processing filters applied. (Black) Computed from the data with a median filter (3×3 kernel) and a wavelet denoising filter applied.

It is noted that the true dissipation spectrum should have a characteristic diffusivity as a multiplicative factor in Eq. (6.9); however, the local diffusivity is difficult to estimate in a turbulent non-premixed flame. As pointed out by Wang and co-workers [155], the exclusion of the diffusivity, while having an impact on the mean dissipation rate, will have a negligible impact on the dissipation spectrum at higher wavenumbers. This region is the most important spectral region for analyzing the effect of the filtering scheme and the determination of the smallest turbulent length scales (discussed below). Figure 6.24a shows the estimated PSD for the temperature fluctuations from the Re = 20,000 flame at x/d = 20 with and without the filtering scheme applied. The PSD shown is the normalized PSD, $E^*(\kappa)$, where the normalization is simply the maximum value of the $E(\kappa)$. Also shown on Fig. 6.24a is a line indicating a -5/3rd slope. The normalized PSD computed from the data without filtering applied is shown in red, while the PSD computed from data utilizing the filtering scheme is shown in black. It is noted that both spectra follow the expected -5/3rd slope in the inertial range for a small range of wavenumbers before starting to roll off. For higher frequencies, the non-filtered data starts to flatten out, which is a result of high-frequency noise falsely contributing energy content. Over the same wavenumber range, the filtered data continues to roll off as expected for approximately three additional decades. Figure 6.24b shows the estimated dissipation spectra, $D^*(\kappa)$ (which is normalized by the maximum value of $D(\kappa)$) for the same flame and position as shown for the PSD Fig. 6.24a. Figure 6.24b shows that the dissipation spectra from both the filtered and unfiltered data follow the expected trends for lower frequencies (slope = 1/3) and then peak in the latter part of the inertial range before rolling off. However, the effect of noise on the unfiltered data (red) is quite apparent in the fact that the normalized dissipation spectra flattens and begins to increase. For the case with the filtering, the dissipation spectrum properly rolls off for an additional two decades. This illustrates the ability of

the current filtering scheme (primarily the wavelet de-noising approach) to mitigate noise in the derived FRS temperatures. The results clearly show that the current filtering scheme allows access to a larger range of scales present in the turbulent flow. In fact, the use of the current filtering scheme allows almost an additional order-of-magnitude increase in the resolvable spatial frequencies. Previously, Pope defined the wavenumber corresponding to 2% of the maximum of the dissipation spectra as the inverse of the Kolmogorov (or Batchelor) scale [33]. If this criterion is used, the current measurements allow a direct determination of the smallest turbulent length scales.

6.4.3.4 Scale and Resolution Estimation from Dissipation Data

In Ch. 3 the spatial scales were estimated using scaling laws via $\lambda_\kappa = 2.3\delta Re_\delta^{-3/4}$ and $\lambda_B = 2.3\delta Re_\delta^{-3/4} Sc^{-1/2}$, where λ_κ and λ_B are the Kolmogorov and Batchelor scales, respectively. For the current FRS temperature measurements, the results in the previous section showed that the data is of sufficient quality to directly determine the smallest length scales using the measured dissipation spectra. Using Pope's criterion [33], a cutoff frequency, κ_B, is determined as the frequency where the dissipation spectrum (of the temperature fluctuations) has fallen to 2% of the peak value of the dissipation spectrum. Wavenumbers $\kappa > \kappa_B$ are expected to contribute less than 2% to the total mean dissipation [155], The Batchelor scale can then defined as $\kappa_B \lambda_B = 1$ (analogous to Pope's definition of $\kappa_K \lambda_K = 1$ for the velocity field) and subsequently the Kolmogorov scale is estimated by $\lambda_\kappa = \lambda_B Sc^{1/2}$. It should be noted, that $\lambda_\kappa$and λ_B are commonly mistaken as the actual length scales corresponding to the cutoff frequency. However, the physical wavelength (which is a length scale) corresponding to the cutoff wavenumber is $2\pi\lambda_B$ (or $2\pi\lambda_\kappa$ for velocity), meaning that scales smaller than this contribute less than 2% to the total mean

dissipation. Figure 6.25 shows example dissipation spectra for all flames measured near centerline with the 2% cutoff point highlighted in each spectrum. The vertical dashed line indicates the estimated cutoff value κ_B. As observed in Fig. 6.25, for all flame conditions and axial locations, the dissipation spectra are resolved for more than three orders of magnitude. In this manner, λ_B

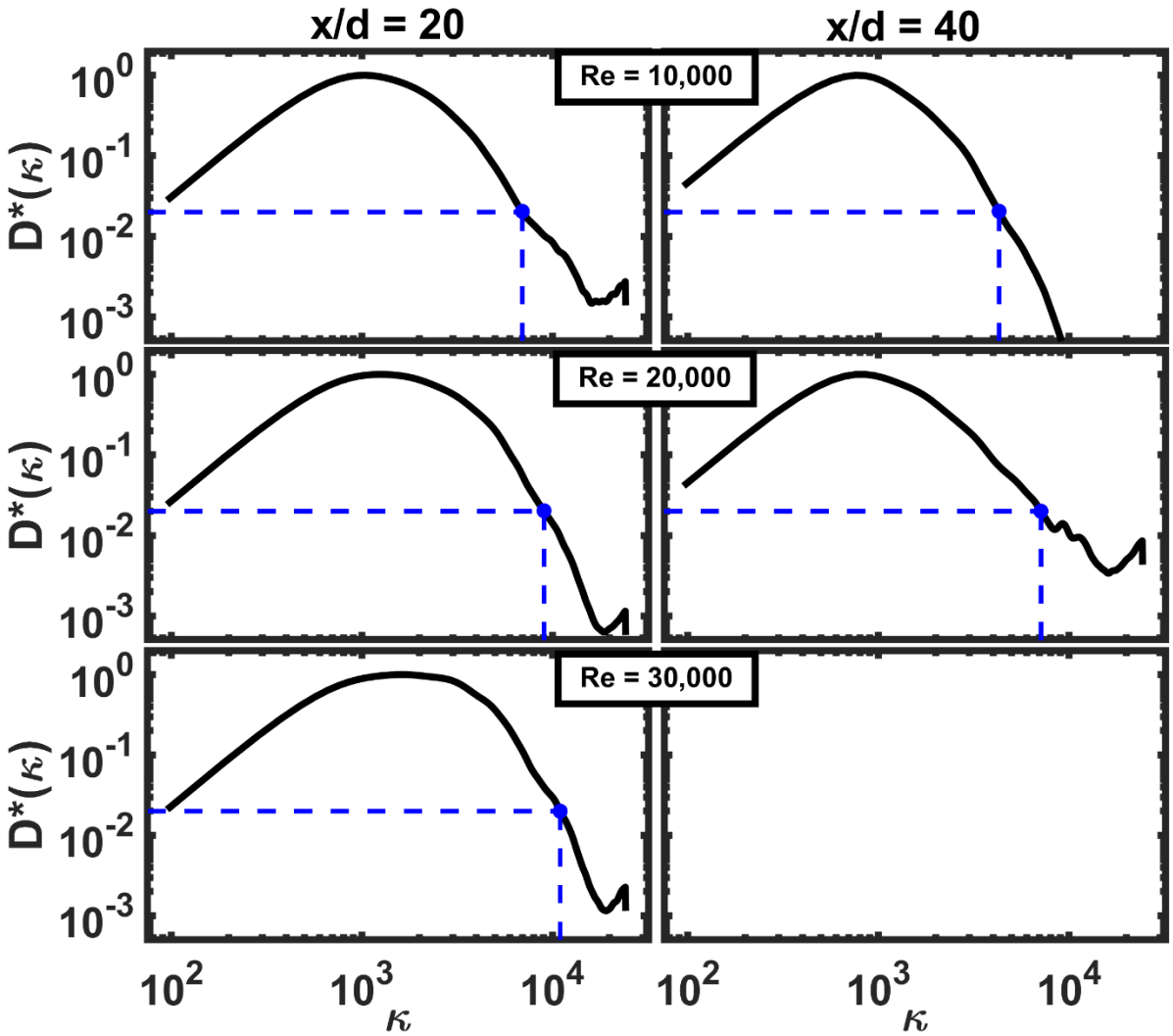

Figure 6.25: Measured dissipation spectra (black) for all flames near centerline. The estimated cutoff wavenumber is indicated in each subplot as a blue square with dashed lines showing its position on the axes. (Top) Re = 10,000. (Middle) Re = 20,000. (Bottom) Re = 30,000. (Left) x/d = 20. (Right) x/d = 40.

(and λ_κ) can be determined for each flame as a function of radial and axial location. These results are shown in Fig. 6.26 as solid, black lines and denoted as $\lambda_{B,D}$, indicating that they have been directly determined from the dissipation spectra.

Since temperature and velocity data are available, the Batchelor scale also can be estimated using the scaling laws as presented in Ch. 3 and compared to the direct determination using the dissipation spectra. Figure 6.26 also the Batchelor scale estimated from scaling laws, $\lambda_{B,SL}$, shown as solid, red lines. For the scaling law estimation Re_δ is determined using the outer-scale variables, $\langle u \rangle_{CL}$ and $\delta_{50\%}$, which are constant for a given axial location, while the local temperature varies, leading to radially dependent value of the kinematic viscosity, ν. Figure 6.26 shows that there is reasonable agreement between $\lambda_{B,D}$ and $\lambda_{B,SL}$ on centerline, especially given the context that the scaling laws are derived from non-reacting flow studies. However, the radial dependence of the Batchelor scale is not captured with the scaling laws, at least when fixing the local outer length and velocity scale for a given axial position. For example, the directly determined values of $\lambda_{B,D}$ increase with increasing radial position, whereas $\lambda_{B,SL}$ simply follow the temperature profiles at x/d = 20 and 40.

Referring back to Fig. 6.25, it is noted that the wavenumber at which noise begins to cause the dissipation spectra to roll off and rise ($D^*(\kappa) < 10^{-3}$) is approximately the same for each flame and measurement position. It is conjectured that this wavenumber corresponds to the minimum resolvable wavenumber for the measurements, which in turn, is a direct determination of the spatial resolution of the measurement. The wavenumber associated with the rise in $D^*(\kappa)$ due to noise is $\kappa_{min} \approx 16700$ rad/m. This corresponds to a physical wavelength of ~ 376 μm. Considering Nyquist criteria, this implies that in order to resolve κ_{min}, the smallest length scale that could be resolved

corresponds to a physical wavelength of 188 µm. This wavelength is consistent with LSF measurement if the width was defined as the distance between the 1/e values. From these results, the estimation of the in-plane resolution for the FRS-based temperature measurements is updated to ~188 µm.

Using $\lambda_{B,D}$ as values for the Batchelor scales (and estimating λ_κ as $\lambda_{B,D}Sc^{1/2}$), Table 6.2 shows a comparison between the smallest length scales (physical wavelengths) present in the flow and the estimated velocity and temperature measurement spatial resolution. The values reported

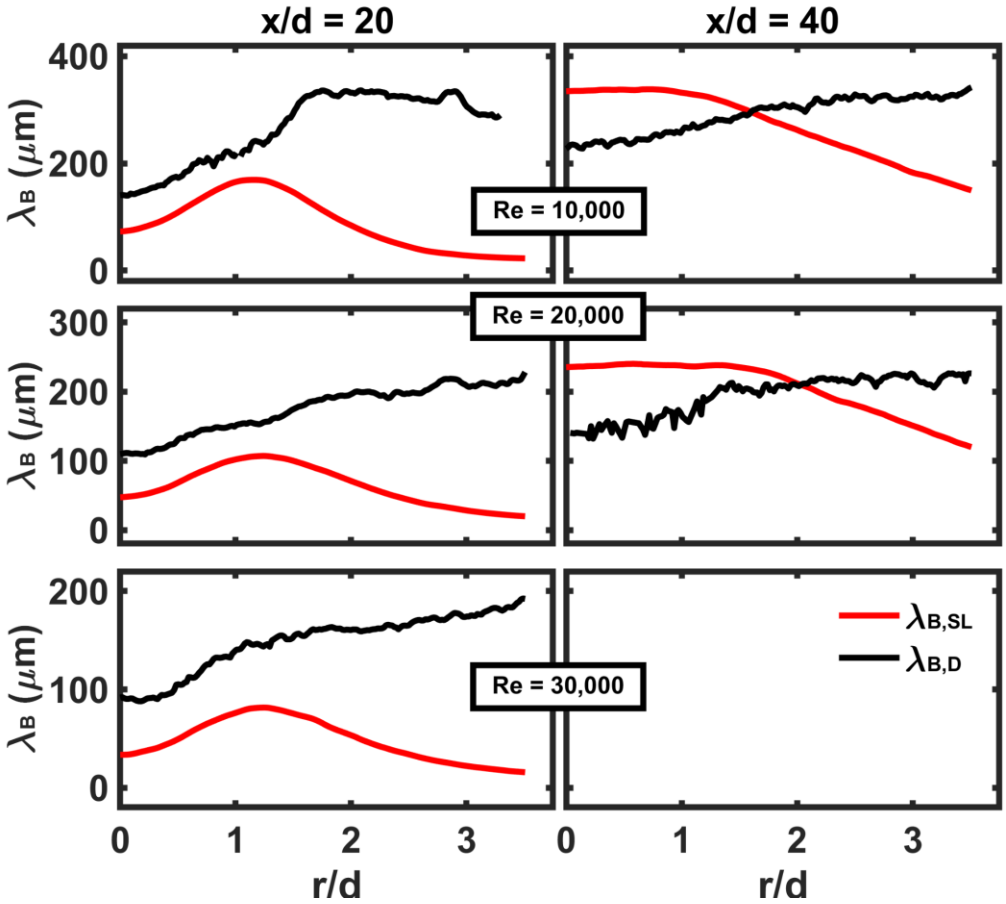

Figure 6.26: Estimation of Batchelor scale based on scaling laws (red) and based on the 2% cutoff in the dissipation spectra (black)\

Flame/Position	$2\pi\lambda_B$ (μm)	$2\pi\lambda_\kappa$ (μm)	Temperature in-plane resolution (μm)	Temperature out-of-plane resolution (μm)	Velocity in-plane resolution (μm)	Velocity out-of-plane resolution (μm)
Re = 10k, x/d = 20	883	738	~188	~183	~360	~508
Re = 20k, x/d = 20	691	578				
Re = 30k, x/d = 20	576	482				
Re = 10k, x/d = 40	1428	1195				
Re = 20k, x/d = 40	882	738				

Table 6.2: Estimated smallest length scales (physical wavelengths) compared with spatial resolution estimates for the temperature and velocity measurements. Results are shown for measurements near centerline.

are at centerline and $\lambda_\kappa$and λ_B have been multiplied by 2π to convert them to physical wavelengths, where scales smaller than this contribute less than 2% to the total mean dissipation. Table 6.2 shows that the temperature measurement is well resolved at centerline (and thus for all radial locations since the spatial scales increase with increasing radial position). In addition, it is observed that the in-plane spatial resolution for velocity is sufficient for all centerline locations (and thus all radial locations), while the out-of-plane spatial resolution for velocity is well resolved for all centerline locations except for the Re = 30,000 flame at x/d = 20, where it is only under-resolved (with reference to the smallest physical wavelength) by less than 6%.

Chapter 7. Analysis of Thermal Fluid Interaction

Using the simultaneous temperature and three-component velocity measurements outlined in Ch. 6, the direct interaction between flow turbulence and thermal properties can be examined in turbulent non-premixed flames. Previously this has been challenging due to a limited amount of data present within the literature. Specific questions of interest include:

- What is the statistical relationship between thermal fluctuations, gradients, and dissipation and various kinematic properties (i.e., vorticity, strain, etc.)?
- How does thermal scalar flux vary with spatial position and Reynolds number? Is there evidence of counter gradient diffusion?
- What are the primary kinematic properties that control the temperature field topology? More specifically, what properties lead to strong thermal gradients and high levels of dissipation?

This chapter provides results using both visualization and detailed statistical analysis to answer these questions.

7.1 Visualization of Thermal Fluid Interaction

7.1.1 Vorticity-Temperature Interaction

Qualitative visualization is a good initial step for gaining an overall sense of the structure of the various field properties as it serves to provide initial insights into the underlying physics and can ground subsequent statistical results. Figure 7.1 shows a comparison of the temperature

fluctuation (T') field with the out-of-plane component of the vorticity field (ω_z) obtained from the same time instance. The out-of-plane vorticity (ω_z) is calculated from the velocity field using

$$\omega_z = \left(\frac{\partial u}{\partial y} - \frac{\partial v}{\partial x}\right) \qquad \text{Eq. (7.1)}$$

where the velocity gradients are determined using the noise-robust gradient operator described in chapter 6. Note that in Eq. (7.1) the positional variables are x and y. As discussed previously, the

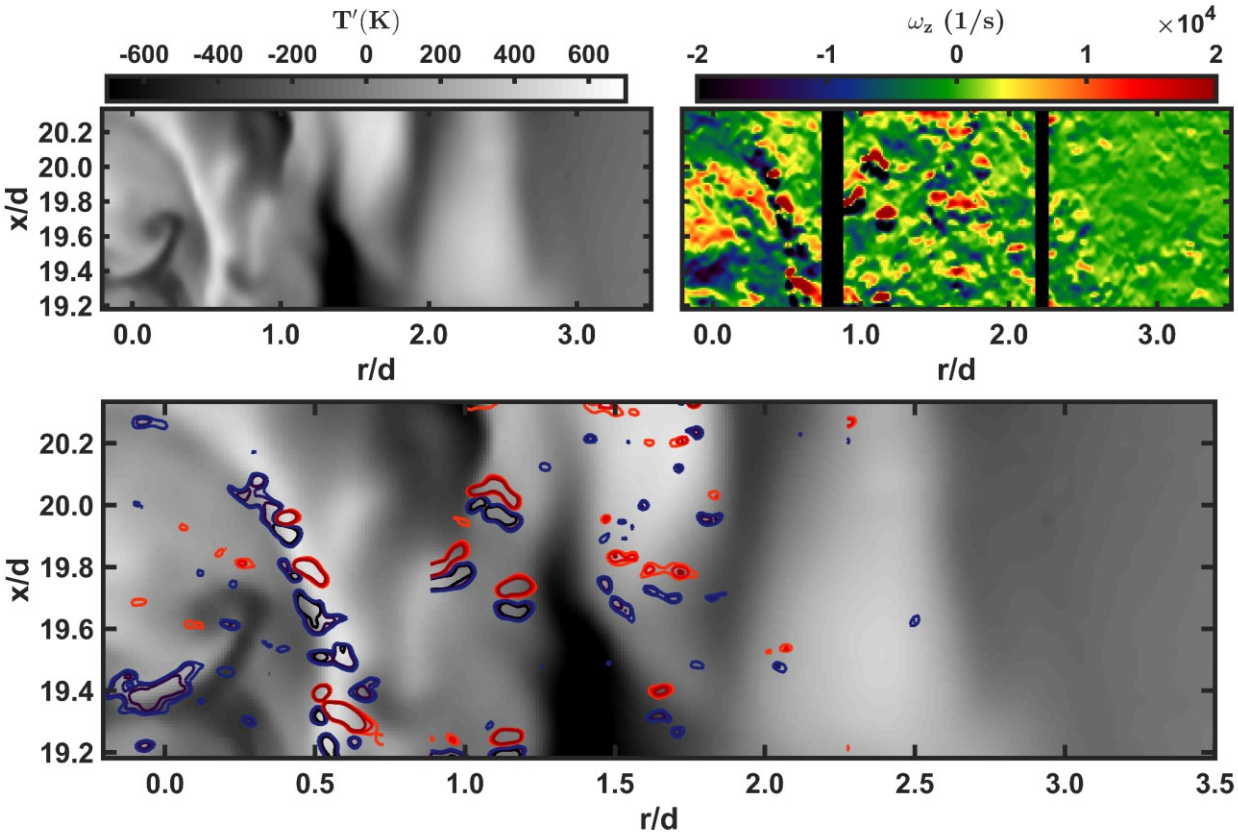

Figure 7.1: Representative comparion of temperature fluctuation field (T') and out-of-plane vorticity field (ω_z) in a Re = 20,000 flame at x/d = 20. (Top-left) Temperature fluctuation image. (Top-right) Vorticity image. (Bottom) Overlay of the two fields.

use of the variable ‘y’ in the derivation of the gradient quantities is to highlight that they are determined from a Cartesian coordinate system and not a cylindrical coordinate system. The y direction is often referenced with r for positional values while y is used when referencing gradient quantities. This is to comport with other researchers in the field who follow the same practice. In Fig. 7.1 the temperature field is shown with a gray scale and the vorticity field is show with a false color map. The top left and right images in Fig. 7.1 show the individual fields while the bottom image shows contours from the vorticity field overlaid upon the temperature fluctuation image. In the bottom image only a few relevant isocontours are shown for clarity. In the temperature field a distinct isolated region of high fluctuation values is observed around r/d = 0.5, highlighting a sharp gradient in the temperature field. Along the same temperature gradient, both large negative and positive values of vorticity appear to be spatially coincident and aligned with the thermal gradient. Also observed in Fig. 7.1 is a region near (r/d, x/d) = (0, 19.4) which shows an additional strong temperature gradient aligned with a region of high negative vorticity.

Given the visual correlation of the regions of high vorticity values with large gradients in T', the overlap of the vorticity field with the thermal dissipation rate field is examined. In chapter 1 the thermal dissipation rate as defined as $\chi_T = 2\alpha(\nabla T' \cdot \nabla T')$, where α is the thermal diffusivity. Due to the large variation in α over the range of temperature in the flame [47] and the potential sensitivity to noise encompassed in an estimation of α, the current work examines $\nabla T' \cdot \nabla T'$ as a surrogate of the thermal dissipation rate. It is noted in Ref. [51] that $\nabla T' \cdot \nabla T'$ contains the majority of the underlying details in the dissipation field and in the majority of situations, the $\nabla T' \cdot \nabla T'$ dominates over the temperature-dependent thermal diffusivity. In this manner, the surrogate thermal dissipation rate, $\widehat{\chi_T} = (\nabla T' \cdot \nabla T')$, will henceforth be referred to as simply the “thermal

dissipation rate" without regards for the calculation of α. Figure 7.2 shows the thermal dissipation rate field calculated from the temperature field shown in the Fig. 7.1. The thermal dissipation rate field is shown in gray scale with the vorticity field shown as a false colormap. The thermal dissipation is shown on a log scale to highlight the wide variation in dissipation rate values across the image. As expected from Fig. 7.1, the same high positive/negative regions of vorticity closely align with along with the regions of high thermal dissipation. In addition, the region of high negative vorticity observed in Fig. 7.1 near (r/d, x/d) = (0, 19.4) is observed to align with a high-

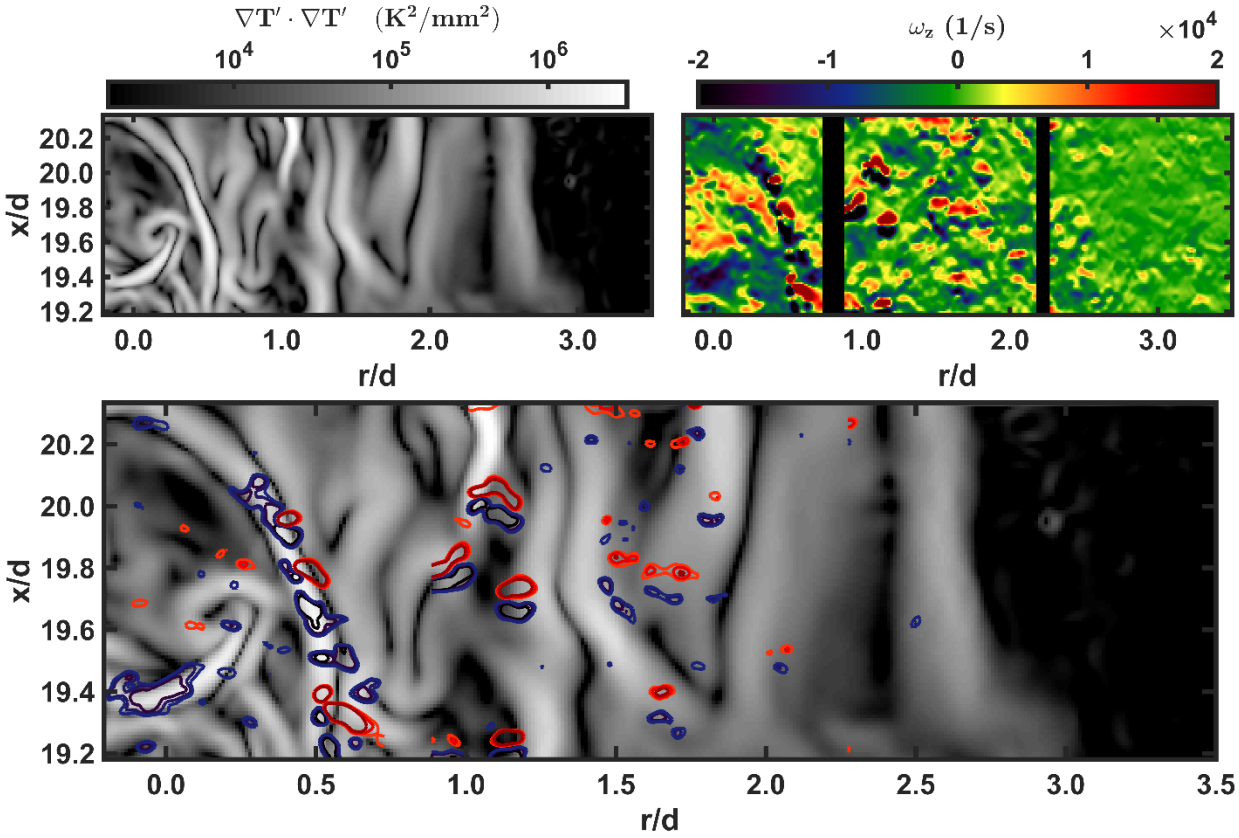

Figure 7.2: Comparison of the thermal dissipation field ($\nabla T' \cdot \nabla T'$) and vorticity field ($\omega_z$) in a Re = 20,000 flame at x/d = 20. (Top-left) $\nabla T' \cdot \nabla T'$. (Top-right) vorticity (Bottom) Overlay of the two fields.

Magnitude thermal dissipation structure. For r/d > 1 there are clear dissipation structures that appear to be less correlated with the vorticity field. However, it is noted that the thermal dissipation rate field is shown on a log scale and the dissipation structures observed at r/d > 1, while clear, are much less intense that the two previously discussed topological features. This may be an indication that large thermal gradients (and hence thermal dissipation) are aligned with large magnitudes of vorticity, but lower levels of thermal dissipation can be due to other mechanisms. Statistical analysis presented below characterizes the relationship between thermal dissipation and vorticity.

While the interaction of the vorticity field with the thermal dissipation field may yield insight into how these dissipative structures are formed or how they align in a flow, it should be noted that vorticity can be a misleading quantity. Large values of vorticity can come from both regions of vortical flow and regions of laminar shear [102]. The latter is especially prominent in regions near reaction zones due to large gradients in both temperatures and velocity. To separate out the true effects of the vortical structures, there are several methods available in the literature (i.e., [203, 204]), which are not discussed in this dissertation. It is interesting that there appears to be a fairly strong overlap between the regions of high-magnitude vorticity and thermal dissipation. In non-reacting flows scalar dissipation and vorticity do not show the same type of spatial correspondence as observed in Fig. 7.2 [7, 205-207] Typically, large values of dissipation appear as sheet-like structures that are observed to “wrap” around vortex tubes (which is where the majority of the high-magnitude vorticity exists). The current results are similar to those observed by Gamba et al [102] downstream in a lower-Reynolds number flame, which showed a strong correlation between the high-magnitude vorticity and sheet-like dissipation structures due to the laminar shear generated across the reaction zone (as visualized with OH radical imaging). As will be shown below, the strong dissipation layer highlighted in Fig. 7.2 occurs in very close proximity

to the primary reaction zone and thus provides consistency with the assertion that for regions near the reaction zone, high-magnitude vorticity (most likely due to laminar shear) and dissipation structures show overlap due to heat-release effects.

7.1.2 Strain Rate-Temperature Interaction

Of particular interest to the turbulent combustion community is the interaction of the dissipation structures with the kinematic strain rate field. The strain field is strongly coupled to turbulent transport and is expected to play a prominent role in reaction processes in addition to governing key fluid properties such as vorticity dynamics. For example, in flamelet models (see Ch. 1 for a discussion), the scalar dissipation rate is the controlling parameter of transport and reaction. Scalar dissipation is generated by the strain rate field, and since the scalar dissipation rate is likely related to the thermal dissipation rate (see Ch. 1), there may be a strong coupling between strain and thermal dissipation rate, especially if the concept of a "flamelet" holds. The strain rate field is determined from the symmetric part of the velocity gradient tensor $\nabla\vec{V}$ as $S_{ij} = \frac{1}{2}\left(\frac{\partial u_i}{\partial x_j} + \frac{\partial u_j}{\partial x_i}\right)$. Written out in its entirety, the strain rate tensor is given by

$$S = \begin{pmatrix} S_{11} & S_{12} & S_{13} \\ S_{21} & S_{22} & S_{23} \\ S_{31} & S_{32} & S_{33} \end{pmatrix} = \begin{pmatrix} \frac{\partial \mathrm{u}}{\partial \mathrm{x}} & \frac{1}{2}\left(\frac{\partial \mathrm{u}}{\partial \mathrm{y}} + \frac{\partial \mathrm{v}}{\partial \mathrm{x}}\right) & \frac{1}{2}\left(\frac{\partial u}{\partial \mathrm{z}} + \frac{\partial \mathrm{w}}{\partial \mathrm{x}}\right) \\ \frac{1}{2}\left(\frac{\partial \mathrm{u}}{\partial \mathrm{y}} + \frac{\partial \mathrm{v}}{\partial \mathrm{x}}\right) & \frac{\partial \mathrm{v}}{\partial \mathrm{y}} & \frac{1}{2}\left(\frac{\partial v}{\partial \mathrm{z}} + \frac{\partial \mathrm{w}}{\partial \mathrm{y}}\right) \\ \frac{1}{2}\left(\frac{\partial u}{\partial \mathrm{z}} + \frac{\partial \mathrm{w}}{\partial \mathrm{x}}\right) & \frac{1}{2}\left(\frac{\partial v}{\partial \mathrm{z}} + \frac{\partial \mathrm{w}}{\partial \mathrm{y}}\right) & \frac{\partial \mathrm{w}}{\partial \mathrm{z}} \end{pmatrix} \qquad \text{Eq. (7.2)}$$

There are a few important notes to consider concerning the current velocity measurements and the determination of S_{ij}. The current stereo PIV measurements enable the direct determination of S_{11}, S_{22}, S_{12} and S_{21}, which are only 4 of the 9 components of the strain rate tensor. The current measurements do not allow for the direct determination of $S_{13} = S_{31}$, $S_{23} = S_{32}$, and S_{33} since the planar-based stereo PIV does not yield the out-of-plane derivatives, $\partial u/\partial z$, $\partial v/\partial z$, and $\partial w/\partial z$.

However the simultaneous temperature measurement, along with the use of the continuity equation allows for an estimation of $\partial w/\partial z$ under certain circumstances. The continuity equation in the Cartesian coordinate system is given by $\frac{\partial \rho}{\partial t} + \nabla \cdot \left(\rho \vec{V}\right) = 0$ which when expanded out is expressed as

$$\frac{\partial \rho}{\partial t} + \rho \frac{\partial u}{\partial x} + \rho \frac{\partial v}{\partial y} + \rho \frac{\partial w}{\partial z} + u \frac{\partial \rho}{\partial x} + v \frac{\partial \rho}{\partial y} + w \frac{\partial \rho}{\partial z} = 0 \qquad \text{Eq. (7.3)}$$

where ρ is the density of the fluid. The CH_4/H_2/Ar fuel mixture reacting in air has the benefit of having a gas constant (R_{mix}) that varies by less than 5% over the entire composition space allowing for an approximation of the gas density via the ideal gas law, $\rho = (P/R_{mix}T)$. The pressure is assumed to be 101.325 kPa, R_{mix} is 283 J/K kg, and the temperature is measured locally. Taylor's hypothesis is utilized to calculate the time derivative of the density

$$\frac{\partial \rho}{\partial t} \approx -\langle u \rangle \frac{\partial \rho}{\partial x} \qquad \text{Eq. (7.4)}$$

where $\langle u \rangle$ is the mean axial velocity. Given that there is no information for the out-of-plane derivative of the density, if only cases where $w \approx 0$ are considered, $\partial w/\partial z$ is estimated using

$$\frac{\partial w}{\partial z} \approx \frac{1}{\rho}\left(\langle u \rangle \frac{\partial \rho}{\partial x} - u \frac{\partial \rho}{\partial x} - v \frac{\partial \rho}{\partial y}\right) - \frac{\partial u}{\partial x} - \frac{\partial v}{\partial y} \ . \qquad \text{Eq. (7.5)}$$

With this estimation, 7/9 of the components of the velocity gradient tensor are now available from the measurements, but there is no direct way to appropriately estimate $\partial u/\partial z$ and $\partial v/\partial z$. Instead, those gradient quantities are assumed to be 0 (the most probable value of $\partial u/\partial z$ and $\partial v/\partial z$) and $S_{13} = S_{31} \approx \frac{1}{2}\frac{\partial w}{\partial z}$ and $S_{23} = S_{32} \approx \frac{1}{2}\frac{\partial w}{\partial y}$. While the assumption of $\partial u/\partial z = \partial v/\partial z = 0$ is undoubtedly incorrect for many instances (even where $w \approx 0$), justification for this assumption is given below that shows the relatively minimal impact of neglecting $\partial u/\partial z$ and $\partial v/\partial z$ within the strain rate calculations.

With the aforementioned assumptions, an estimate for the full 3D strain tensor is possible. This allows an investigation of the strain rate tensor in terms of its principal components. The three principal strain rates are defined as the eigenvalues of the strain rate tensor given in Eq. (7.2), each with principal directions given as the eigenvectors of S_{ij}. The principal strain rates are generally categorized as (α, β, γ) such that $\alpha > \beta > \gamma$. For divergence-free (non-reacting, incompressible) turbulent flows, α is defined as positive and represents the most extensional strain rate; γ is always negative and represents the compressive strain rate; and β can be either negative or positive and represents the intermediate strain rate. As pointed out by Gamba et al. [102], flow divergence due to heat release does not allow an *a priori* conclusion that these results hold for reacting flows, although previous results have shown this is the case [102, 208]. Some researchers have removed the contribution due to gas expansion from the strain rate tensor, examining only the deviatoric portion and calculating the principal strain rates from this tensor [209, 210]. In this manner, $\alpha > 0$ and $\gamma < 0$ explicitly holds. Figure 7.3 shows calculated pdfs for all three principal strain rates for all flames examined in the current study. In Fig. 7.3, α is shown in blue, β is shown in black, and γ is shown in red. The cases from x/d = 20 are shown in Figs. 7.3(a-c) with Re = 10,000, 20,000 and 30,000 corresponding to (a), (b) and (c), respectively. The cases from x/d = 40 are shown in Figs. 7.3(d & e) with Re = 10,000 and 20,000 corresponding to (d) and (e), respectively. From these pdfs in Figure 7.3 it is observed that $\alpha \geq 0$ and $\gamma \leq 0$ for all flames/positions. This is consistent with the results observed in incompressible turbulence [9], in experiments from a lower-Reynolds number non-premixed flame [102], and a DNS study of a turbulent non-premixed flame [208]. It is noted that for increasing Reynolds number and axial position, the width of both α and γ increase indicating that the probability of large-magnitude compressive and extensive strain increases.

The intermediate strain, β, is distributed around 0 with a distribution that is much narrower than that of α and γ. While the width of the pdf of β increases with increasing Reynolds number and axial location, it remains narrower as compared to the width of the pdfs of α and γ for all flames and positions. For all flames and measurement locations, it is more probable that β is positive, which indicates that the strain rate field preferentially forms in a sheet-like manner, which

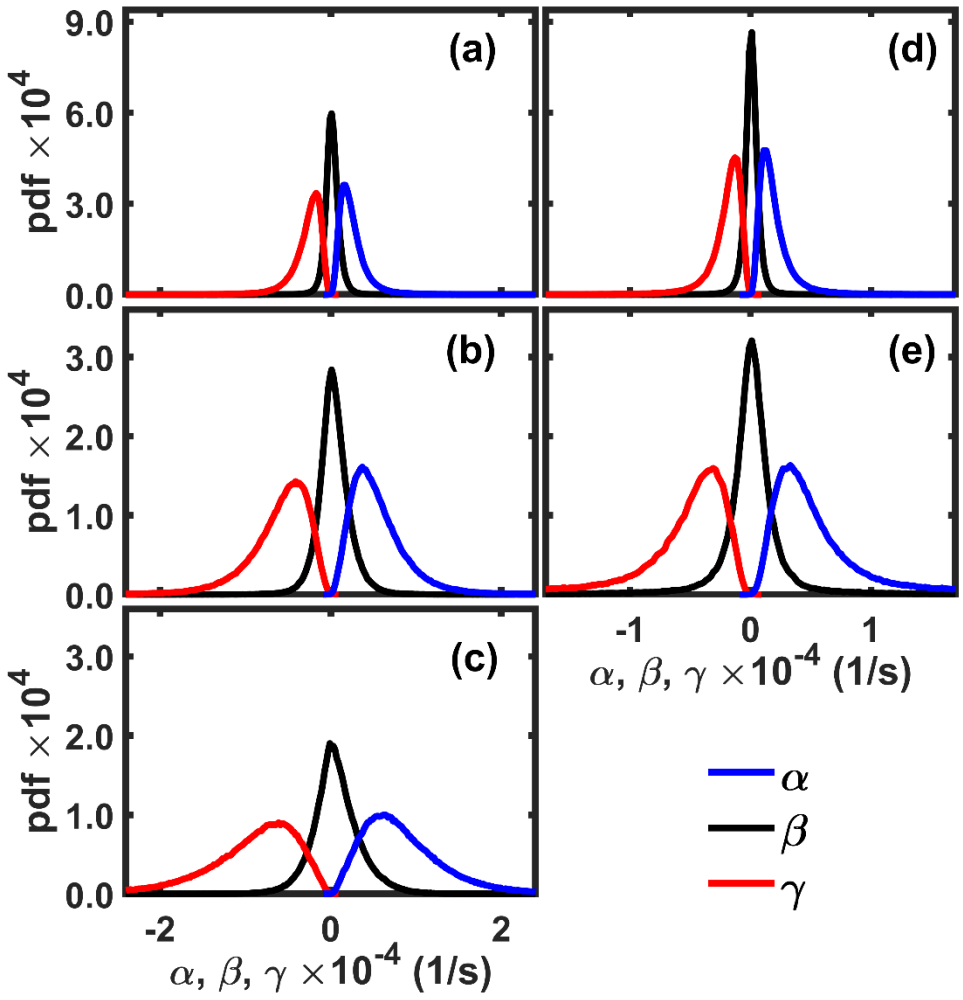

Figure 7.3: Probability density functions of the three principal strain rates γ (red), β (black), and α (blue) for the current set of flames. (a) Re = 10,000, x/d = 20. (b) Re = 20,000, x/d = 20. (c) Re = 30,000, x/d = 20. (d) Re = 10,000, x/d = 40. (e) Re = 20,000, x/d = 40.

Case	$\alpha:\beta:\gamma$ for $\beta > 0$
Re = 10k, x/d = 20	3.77 : 1 : -4.62
Re = 20k, x/d = 20	3.61 : 1 : -4.44
Re = 30k, x/d = 20	3.55 : 1 : -4.38
Re = 10k, x/d = 40	4.15 : 1 : -5.05
Re = 20k, x/d = 40	4.70 : 1 : -5.65

Table 7.1: Ratio of average strain values conditioned on $\beta > 0$ for all flames/positions.

is consistent with previous results in non-reacting flows [7, 9] and reacting flows [102]. For all flames and positions, γ exhibits a broader distribution compared to α which implies that high-magnitude compressive strain is more probable than high-magnitude extensive strain. For a given Reynolds number, the distributions of α and γ at x/d = 40 are more similar to one another than at x/d = 20 implying that with increasing axial distance from the nozzle, the probability of the flow experiencing high-magnitude extensive or compressive strain becomes essentially equal. This trend also seems to hold with increasing Reynolds number at a fixed axial location. As a method for semi-quantitative comparison of the current results with previous research, the averages of the principal strains, conditioned on $\beta > 0$, are calculated. As pointed out by Ashurst et al. [9], this is equivalent to computing the most probable values of the principal strain rates for intense strain values. Table 7.1 shows the results for the strain ratios $\alpha : \beta : \gamma$ for the different flame conditions and axial positions. Previous studies have reported ratios of 3:1:-4 in non-reacting incompressible turbulence [7, 9, 211] and ratios of 6.5:1:-6.5 in the far-field of a lower-Reynolds number turbulent non-premixed jet flame [102]. The current results are consistent with the previous studies in the fact that at x/d = 20, the strain-rate tensor is in the form of 3.8:1:-4.6 at Re = 10,000 and evolves to 3.6:1:-4.4 at Re = 30,000. For a reacting flow, the flow is most similar to that of non-reacting turbulence at the lowest downstream positions and increasing Reynolds number. This facet is

observed in the $\alpha : \beta : \gamma$ ratios, where the values of 3.6:1:-4.4 at Re = 30,000 approach the ratios of 3:1:-4 observed frequently in non-reacting flows. Furthermore, downstream at x/d = 40, the ratios of 4.70:1:-5.65 approach the values determined previously in a lower-Reynolds number flame.

Because the full velocity gradient tensor measurement is not available, the calculated principal strain rates are subject to error and it is necessary to estimate the effect of the assumptions that $\partial u/\partial z = \partial v/\partial z = 0$. Since the jet flames are axisymmetric on average, $\partial u/\partial z$ and $\partial v/\partial z$ have the same statistical relationship with w as $\partial u/\partial y$ and $\partial w/\partial y$ have with v. Thus, the measured statistics of $\partial u/\partial y$ and $\partial w/\partial y$ (conditioned on $v = 0 \pm \epsilon$) can be used to estimate the maximum values of $\partial u/\partial z$ and $\partial v/\partial z$ (conditioned on $w = 0 \pm \epsilon$) that exist within the flow field and thus bound the uncertainty of the strain rate results due to the assumption that $\partial u/\partial z = \partial v/\partial z = 0$. The highest possible deviations in the strain rates (calculated with $\partial u/\partial z = \partial v/\partial z = 0$) will come when $\partial u/\partial z$ and $\partial v/\partial z$ are at their maximum/minimum possible values. For this analysis, the maximum and minimum values for $\partial u/\partial z$ and $\partial v/\partial z$ are set to the 2σ value from the $\partial u/\partial y$ and $\partial w/\partial y$ conditional pdfs ($v = 0 \pm \epsilon$). For the highest Reynolds number case at x/d = 20, the 2σ value for $\partial u/\partial y$ is 12750 1/s and the 2σ for $\partial v/\partial y$ is 7790 1/s. Thus, it is estimated for $w \approx 0$ that $\partial u/\partial z$ is bound by $\pm$ 12750 1/s and $\partial v/\partial z$ is bound by $\pm$ 7790 1/s. The principal strain rates for this flame case were then calculated again, where $S_{23} = S_{32} = \frac{1}{2}\left(\pm 7790\mathrm{s}^{-1} + \frac{\partial \mathrm{w}}{\partial \mathrm{y}}\right)$ and $S_{13} = S_{31} = \frac{1}{2}\left(\pm 12750\mathrm{s}^{-1} + \frac{\partial \mathrm{w}}{\partial \mathrm{x}}\right)$. This involves four additional cases for the possible different variations from the $\pm$ signs. Figure 7.4 shows a comparison of the principal strain rates calculated using $\partial u/\partial z = \partial v/\partial z = 0$ (solid lines; same as in Fig. 7.3) with the principal strain rates from this analysis that yielded the largest difference from the results shown in Fig. 7.3 (shown

as dashed lines). While there are some discrepancies between the two sets of pdfs, the results show qualitatively similar behavior. Again the most probable values of the principal strains are calculated for $\beta > 0$ which resulted in 3.89:1:-4.75 for $\alpha : \beta : \gamma$. Compared to the results presented in Table 7.1, the percent difference for the ratios is 9%. It should be noted that this is a maximum possible error as the values of $\partial u/\partial z$ and $\partial v/\partial z$ will actually fall within a pdf distributed about zero with 2σ bounds equal to the values tested. This also implies that the differences observed in Fig. 7.4 would reduce even further. Therefore it is concluded that although there are certainly

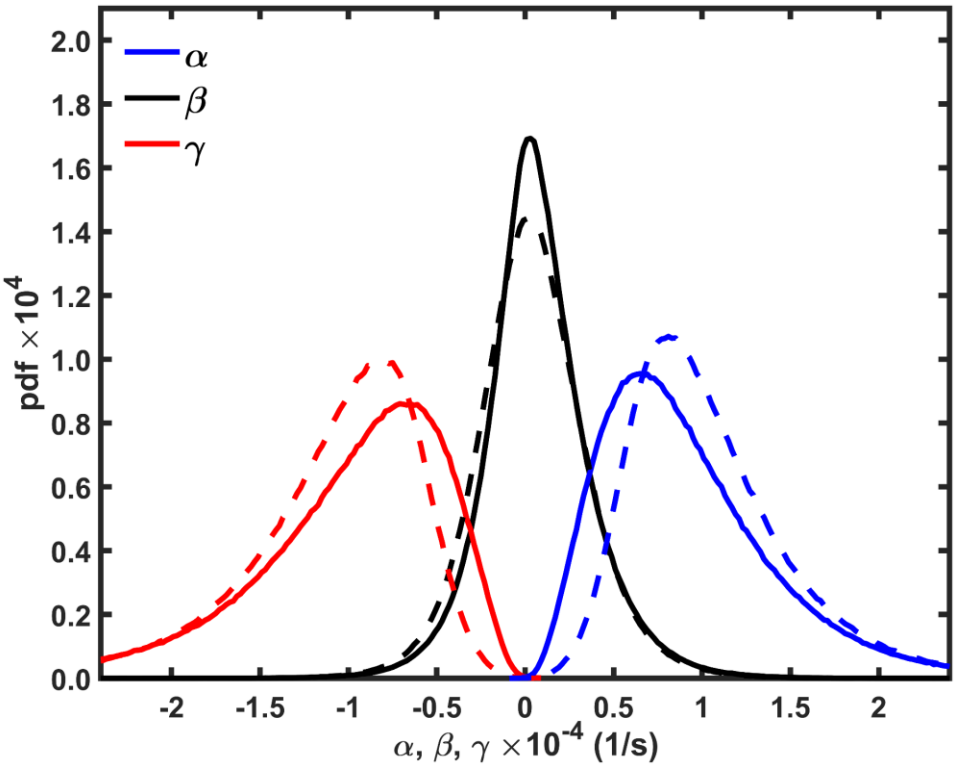

Figure 7.4: Principal strain rate comparisons of α, β, and γ for Re = 30,000, x/d = 20. Solid lines represent principal strain rates calculated with the assumption that $\partial u/\partial z = \partial v/\partial z = 0$ while the dashed lines represent principal strain rates calculated with $\partial u/\partial z = +12750 s^{-1}$ and $\partial v/\partial z = -7790 s^{-1}$.

errors associated with the assumptions that $\partial u/\partial z$ and $\partial v/\partial z$ equal 0, $S_{13} = S_{31}$ and $S_{23} = S_{32}$ is not overly sensitive to the inclusion of the actual values of $\partial u/\partial z$ and $\partial v/\partial z$ and the current approach provides reasonable estimates for the 3D strain rate tensor and the principal strain rates.

Figures 7.5-7.7 show representative interactions of the thermal dissipation field with the three principal strain rate fields for the Re = 20,000 flame at x/d = 20. This image corresponds to the same realization as shown previously in Fig. 7.1 and Fig. 7.2. The interaction of the compressive, intermediate, and extensional principal strain rate fields with the thermal dissipation

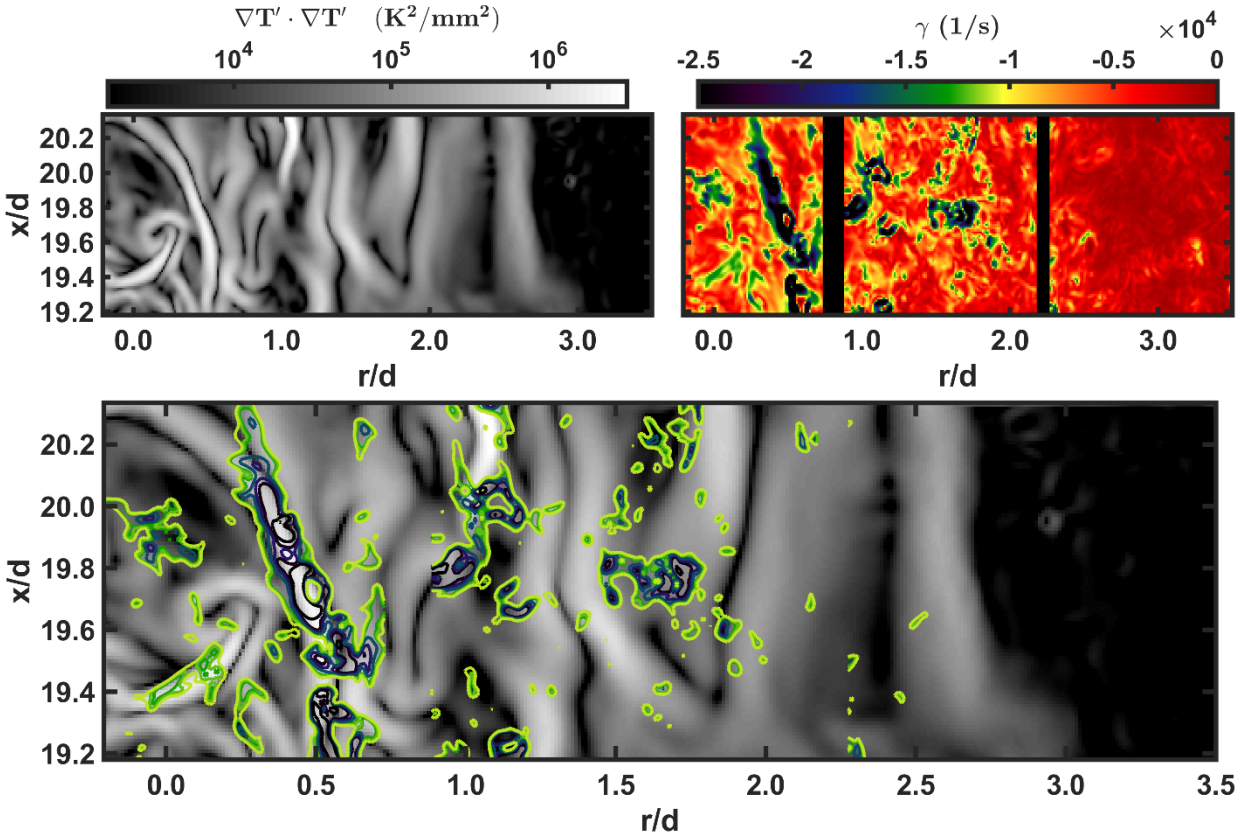

Figure 7.5: Comparison of the thermal dissipation field ($\nabla T' \cdot \nabla T'$) with the compressive principal strain rate field, γ, in a Re = 20,000 flame at x/d = 20. (Top-left) $\nabla T' \cdot \nabla T'$, (Top-right) γ, (Bottom) Overlay of the two fields.

is shown in Figs. 7.4, 7.5, and 7.6, respectively. From all three figures it is observed that the dissipation structure near r/d = 0.5 is aligned with all three principal strain rate components, although there are some notable differences. Figures 7.5 and 7.7 show that the high-magnitude values of strain (α and γ) are oriented along the entire dissipation structure in layer-like structures and appear correlated with one another. Along this same dissipation structure, the results shown in. Fig. 7.6 show positive values of β which is indicative of a sheet-like strain structure which is similar to the results of Gamba and Clemens [102] along an OH contour, but different than line-

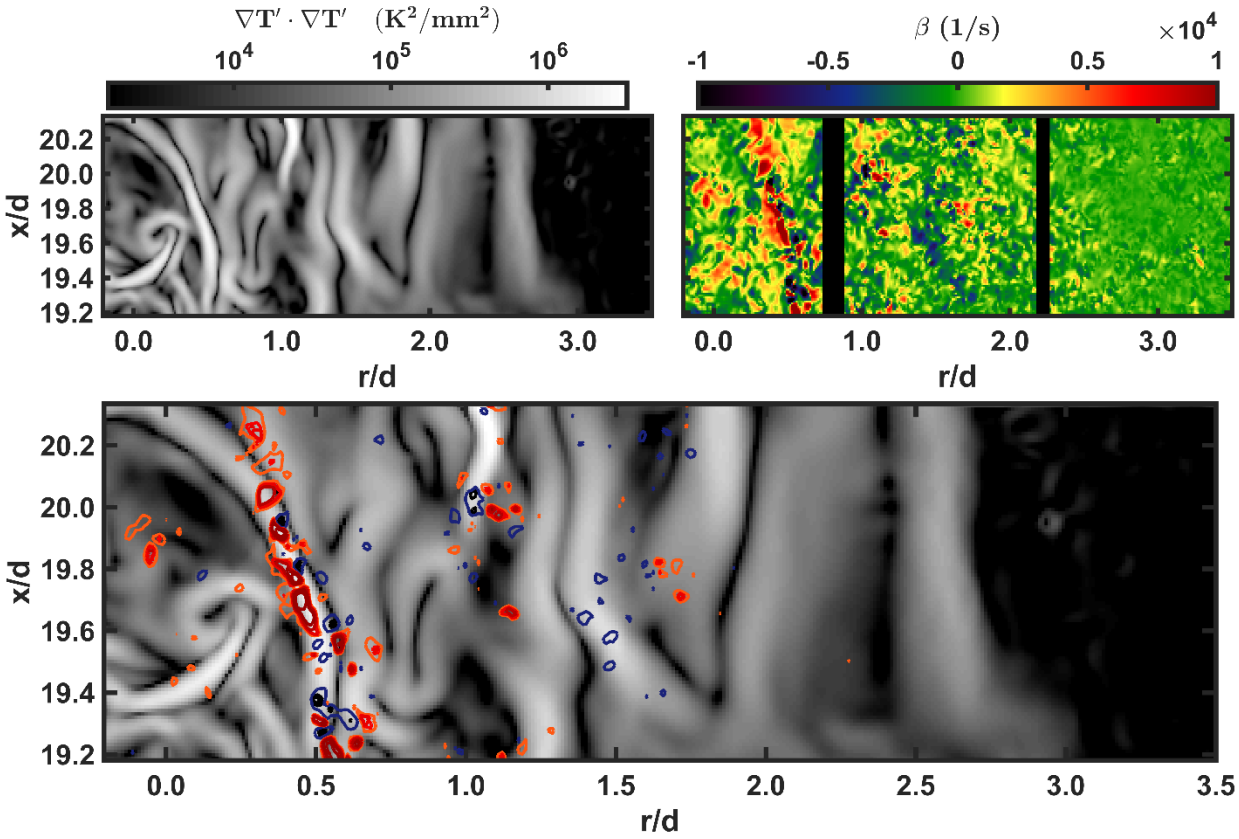

Figure 7.6: Comparison of the thermal dissipation field ($\nabla T' \cdot \nabla T'$) with the intermediate principal strain rate field, β, in a Re = 20,000 flame at x/d = 20. (Top-left) $\nabla T' \cdot \nabla T'$, (Top-right) β, (Bottom) Overlay of the two fields.

singular result is consistent with the statistical results of Fig. 7.3 in that β tends towards more positive values and that the strain rate field is preferentially sheet forming. It is observed in the results of Figs. 7.4 – 7.6 that there are locations of notable thermal dissipation which do not seem to have any corresponding large-magnitude principal strain rate values (negative or positive). This may be due to the fact that the thermal field, being an active scalar, can dissipate in ways other than under the influence of strain or it may be indicative that the high spatial coincidence between the principal strain rate fields and the thermal dissipation rate fields only occurs near the primary

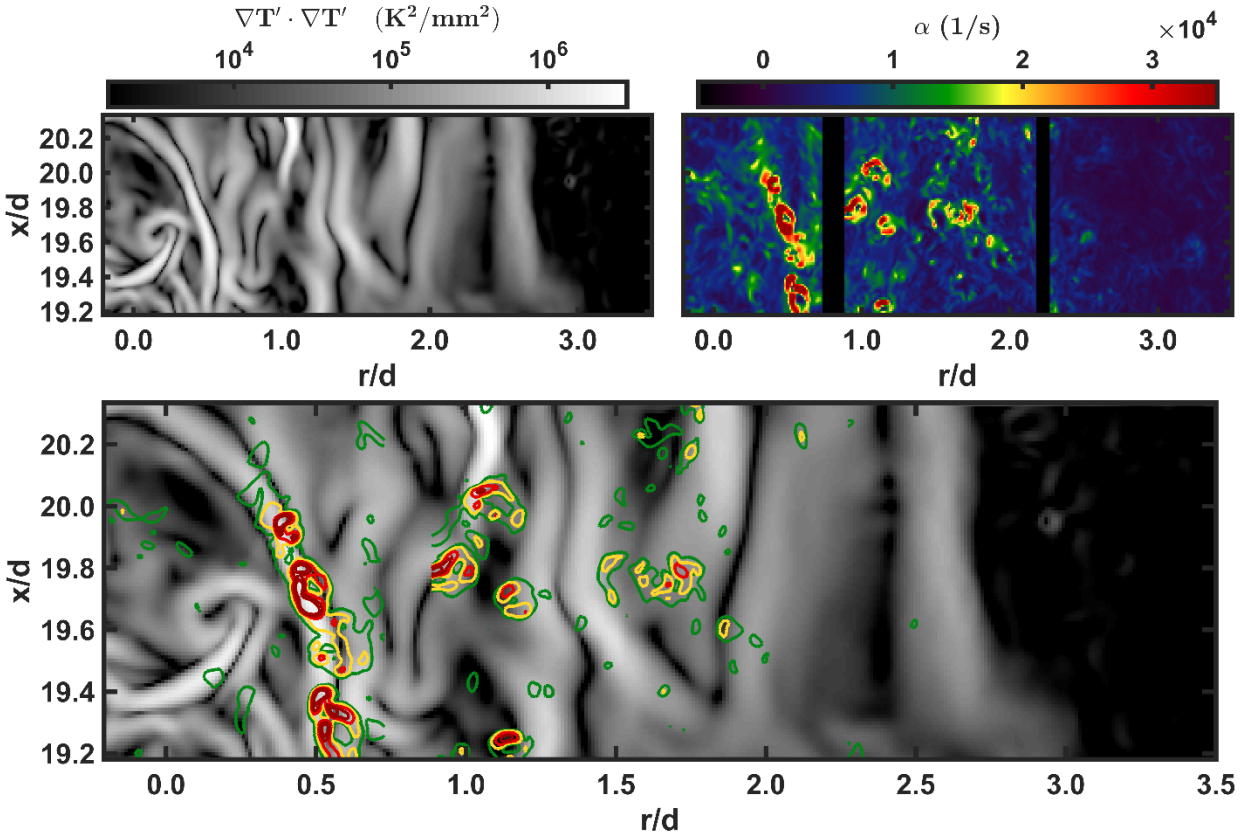

Figure 7.7: Comparion of the thermal dissipation field ($\nabla T' \cdot \nabla T'$) with the extensive principal strain rate field, α, in a Re = 20,000 flame at x/d = 20. (Top-left) $\nabla T' \cdot \nabla T'$, (Top-right) α, (Bottom) Overlay of the two fields.

reaction zones (stoichiometric contour) – it will be shown below that the strong dissipation layer-principal strain interaction is near the stoichiometric contour.

7.2 Thermal Scalar Flux

The joint temperature and velocity measurements allow for the direct evaluation of the turbulent scalar (heat) flux term, which is an unclosed term that is modeled in turbulent combustion simulations. Thus, the determination of the scalar flux provides previously unavailable data assessing model closure methodologies used under turbulent non-premixed flame conditions.

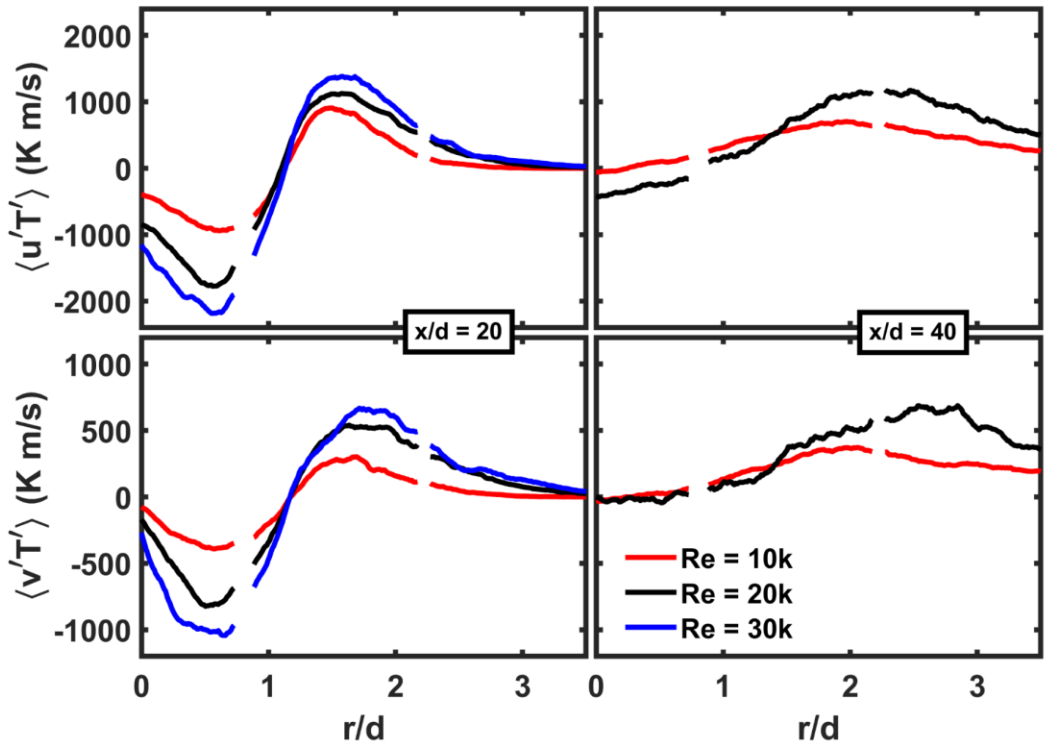

Figure 7.8: Radial profiles of axial (top) and radial (bottom) scalar flux for x/d = 20 on the left and x/d = 40 on the right for Re = 10,000 (red), Re = 20,000 (black) and Re = 30,000 (blue).

Figure 7.8 shows radial profiles of the Reynolds averaged axial thermal flux, $\langle u'T' \rangle$ and radial scalar flux, $\langle v'T' \rangle$, for all flames and measurement positions considered in the present work. Figure 7.8 shows large positive and negative values of thermal flux for x/d = 20 for both the axial and radial flux terms. For x/d = 40 the radial scalar flux is ≥ 0 for all radial positions, while the axial scalar flux is predominately ≥ 0 with some values of $\langle u'T' \rangle < 0$ for Re = 20,000 near centerline. The out-of-plane thermal flux, $\langle w'T' \rangle$ (not shown) is approximately 0 for all flames and positions as expected, confirming the accuracy of the measurement of the w-component of velocity. In general there is a dependence on Reynolds number, where the largest-magnitude values of $\langle u'T' \rangle$ and $\langle v'T' \rangle$ increase (or decrease) with increasing Reynolds number. Since the temperature fluctuations are largely consistent across flames (see the T_{rms} profiles in Ch. 6), the increase in the scalar flux is due to increasing velocity fluctuations with increasing Reynolds number.

The importance of the scalar flux term for turbulent combustion models is derived from the fact the scalar flux term is unclosed and must be modeled. More specifically, it is of interest as to whether or not scalar transport can be described by a simple gradient transport assumption which is sometimes applied for passive as well as reactive scalars [17]. The gradient transport model was derived from studies of passive scalars in constant-density non-reacting flows and is commonly applied in reacting flows as a first-order closure model. With this assumption, the scalar flux is estimated as

$$\widetilde{u_i''\psi_i''} = -D_t \nabla \widetilde{\psi_i} \qquad \text{Eq. (7.6)}$$

where ψ_i is any scalar quantity in the flow, u_i is the i-th velocity component, and D_t is the turbulent diffusivity, modeled analogously to the eddy viscosity as ν_t / Sc_t , where ν_t is the diffusivity for the scalar quantity, and Sc_t is the turbulent Schmidt number. In Eq. (7.6) the double primes indicate

a Favre-fluctuation and the tilde represents a Favre-average. In Favre-averaging the quantity of interest is broken up into a density weighted average $\widetilde{\psi_i}$ and a Favre-fluctuating component via $\psi_i = \widetilde{\psi_i} + \psi_i''$ where $\widetilde{\psi_i} = \langle \rho \psi_i \rangle / \langle \rho \rangle$. The Favre-averaging is preferred over simple Reynolds averaging for flows with varying density fields as it simplifies writing the averaged forms of the Navier-Stokes equations. Given that the density can be accurately determined from the current measurements, the Favre-averaged quantities and Favre-fluctuating quantities can be determined.

Previous results in turbulent premixed flames have clearly shown that the model presented in Eq. (7.6) is violated in regions of heat release (referred to as "counter gradient diffusion), although the effect typically is the greatest for lower turbulence levels [212]. The value of the current simultaneous velocity and temperature measurements allows a determination of whether turbulent non-premixed flames generally follow trends consistent with the gradient transport (GT) assumption (i.e. behaves as described in Eq. (7.6)) or if the flow demonstrates counter gradient transport (CGT). This aspect has not received a great deal of attention in turbulent non-premixed flames due to the lack of simultaneous measurements of velocity and quantitative scalar values. A notable exception includes earlier work of Driscoll and co-workers [99, 100] of which the current results are compared with. In order to assess whether the heat flux for the current turbulent non-premixed flames can be described as exhibiting GT or CGT, both the Favre-averaged flux quantities and the gradient of the Favre-averaged temperature fields must be determined.

Figure 7.9 shows comparisons the gradients of the Favre-averaged temperature fields with the thermal scalar flux term for the axial and radial directions for all flames and locations. Figure 7.9(I) shows the results in the axial direction and Fig. 7.9(II) shows the results in the radial direction. Given that the Favre-averaged temperature field changes very slowly with increasing axial direction, the determination of the axial temperature gradient is challenging and subject to

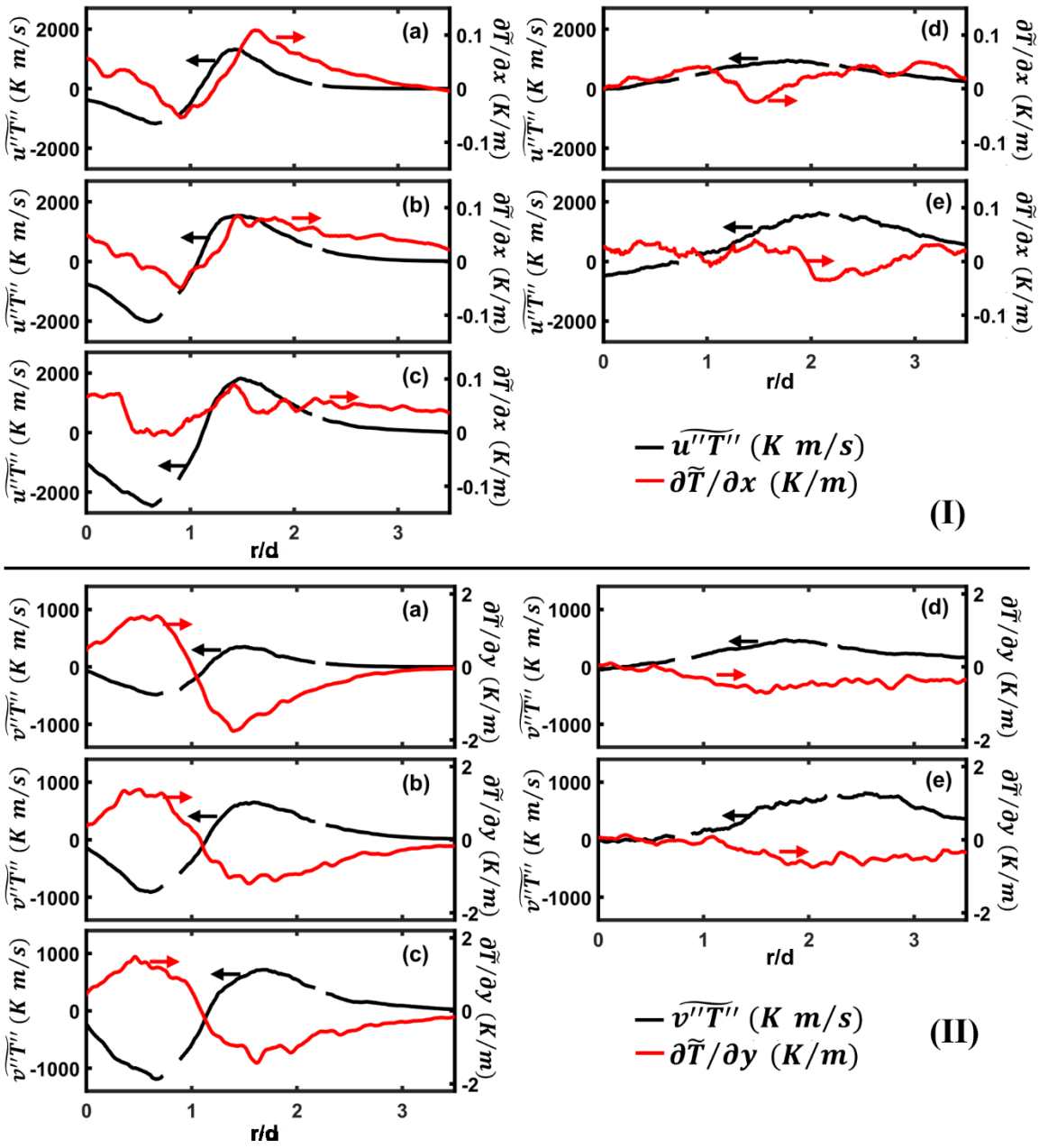

Figure 7.9: Comparison of gradients of the Favre-averaged temperature field with the thermal scalar flux term for the axial direction (I) and the radial direction (II). (a) Re = 10,000, x/d = 20. (b) Re = 20,000, x/d = 20. (c) Re = 30,000, x/d = 20. (d) Re = 10,000, x/d = 40. (e) Re = 20,000, x/d = 40.

more uncertainty than the determination of the radial temperature gradient. Consequently, the axial temperature gradient profile exhibits some effects of noise. For all cases, Fig. 7.9(I) shows that the axial gradient of the Favre-averaged temperature is positive for most radial positions, as expected. There are regions near r/d = 1 (at x/d = 20) that show a small negative gradient. Assuming this is not an artifact of noise, this can be attributed to the combined effects of jet spreading and gas expansion such that strictly in the axial direction, there is a small decrease in average temperature. As expected, the Favre-averaged temperature varies more significantly in the radial-direction (y-direction) allowing for a more accurate estimation of the gradient in the radial direction as compared to the axial direction for x/d = 20. Downstream at x/d = 40 the Favre-averaged temperature field changes very little in the radial direction near centerline so the radial derivative in that region exhibits some noise. Overall, Fig. 7.9(II) appears to show that the radial thermal flux profile follows an inverse relationship with the radial gradient of the Favre-averaged temperature for all flames and at the majority of spatial locations. Figure 7.9(I) does not show a similar trend for the axial gradient; that is in many locations, the radial thermal flux and the radial gradient of the Favre-averaged temperature have the same sign which would imply a negative diffusivity in Eq. (7.6) which is non-physical.

To examine whether GT or CGT is occurring in either the axial or radial direction, the ratio of the thermal flux to the gradient of the Favre-averaged temperature (Ψ_i) is computed using

$$\Psi_x = \frac{\widetilde{u''T''}}{\partial\tilde{T}/\partial x}, \quad \Psi_y = \frac{\widetilde{v''T''}}{\partial\tilde{T}/\partial y} \qquad \text{Eq. (7.7)}$$

Based on Eq. (7.7), if $\Psi_i < 0$ then the scalar transport can be described using the GT assumption but if $\Psi_i > 0$, then the flow exhibits regions of CGT. Figure 7.10 shows the profiles of Ψ_x (in Fig. 7.10(I)) and Ψ_y (in Fig. 7.10(II)). For both Fig. 7.10(I) and Fig. 7.10(II) the data at x/d = 40 is

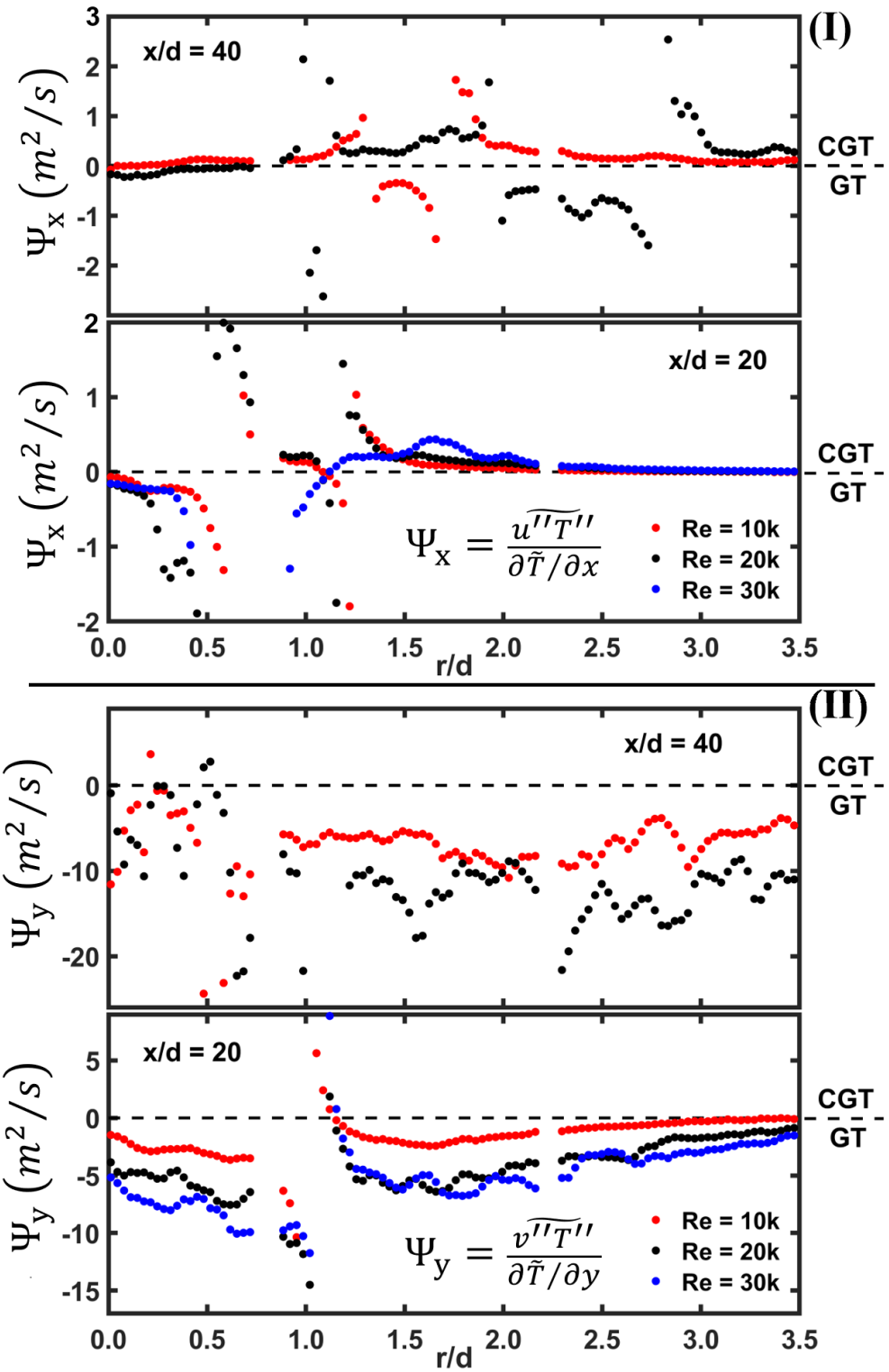

Figure 7.10: Ratios of thermal scalar flux to average temprature gradients - the axial direction (I) and the radial direction (II). (Red) Re = 10,000, (black) Re = 20,000. (Blue) Re = 30,000.

shown in the top panel and the data x/d = 20 is shown in the bottom panel. Data from Re = 10,000 is shown with red symbols, the data from Re = 20,000 is shown with black symbols, and the data from Re = 30,000 is shown with blue symbols. As shown in Fig. 7.10(II) $\widetilde{v''T''}$ appears to display GT at nearly all locations and for all flame conditions. At x/d = 20, there is a sharp discontinuity for Ψ_y near r/d = 1, which is the location at which the radial temperature gradient and the radial thermal flux switch signs. For the measurements at x/d = 40 near centerline, the calculation of Ψ_y exhibits some effects of noise but can be considered to less than 0. Thus $\widetilde{v''T''}$ appears to follow a GT relation in all flames with some small regions of departure in the regions with the sharpest radial gradients of temperature and scalar flux.

Near centerline for the x/d = 20 and x/d = 40 measurements, $\Psi_x < 0$ for all flames implying GT is observed in that region. However, for r/d > 0.5 at x/d = 20, the majority of samples are positive implying some level of CGT for these locations. At x/d = 40 there are both positive and negative values of Ψ_x that may be an effect of uncertainty in the calculation of the axial gradient. However, the results do indicate that there are clear examples of CGT at this location. More refined measurements of the gradient of the Favre-averaged temperature field are needed at x/d = 40 to definitively determined the degree of CGT at this location. Overall the results agree with previous results from Driscoll et al. [99] in turbulent non-premixed flames in that GT appears to be a reasonable approximation for $\widetilde{v''T''}$ but $\widetilde{u''T''}$ demonstrates significant examples of CGT throughout the flame and the simple closure model described by Eq. (7.6) is not consistent with the observed results.

7.3 Conditional Statistics Involving Temperature and Velocity

The simultaneous temperature and velocity data also allows for the determination of conditional statistics. Figure 7.11 shows the average of axial velocity conditioned on temperature, denoted $\langle u|T\rangle$, for all the different flames and spatial positions. Conditional averages are calculated only when the number of samples in a particular temperature bin is greater than 1000. The conditional averages are obtained over a radial span ranging from r/d = -0.1 to r/d 2.7 at x/d =

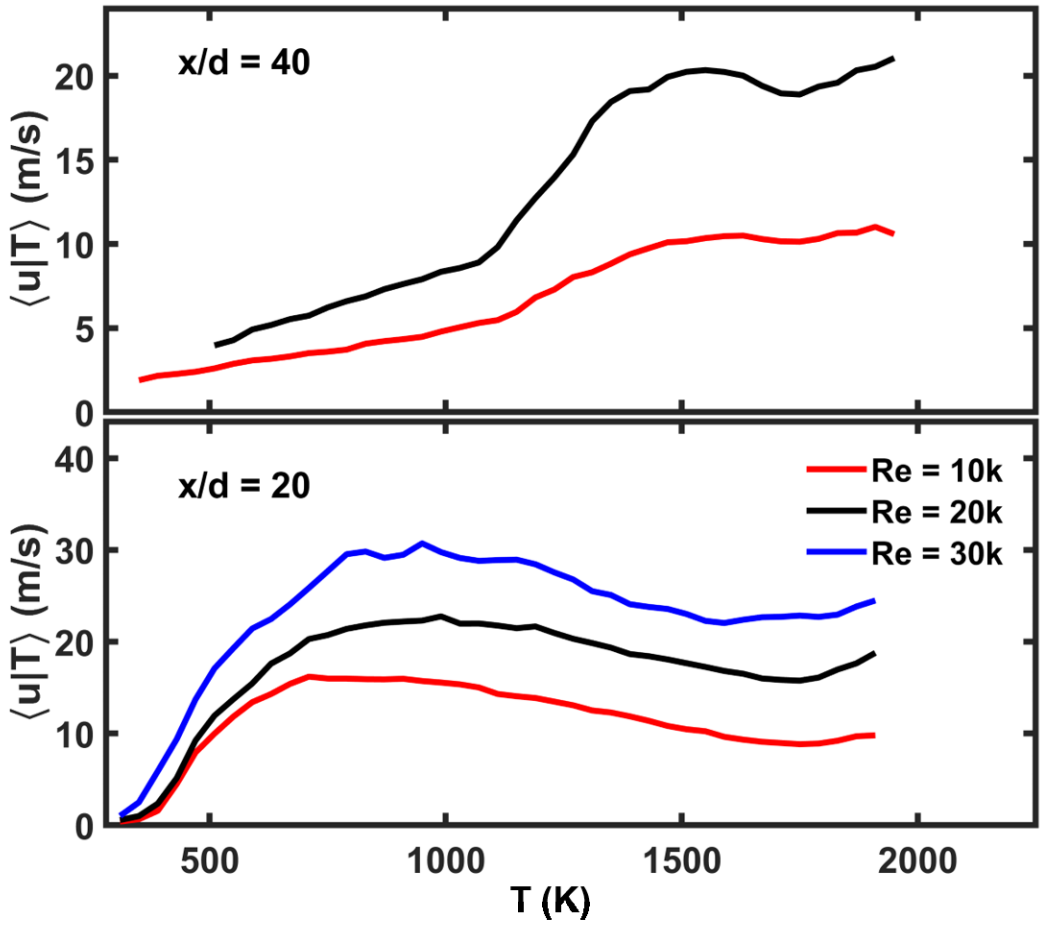

Figure 7.11: Average axial velocities conditioned on temperature at x/d = 20 (bottom) and x/d = 40 (top) for Re = 10,000 (red), 20,000 (black) and 30,000 (blue).

20 and from r/d = -0.1 to r/d = 3.6 at x/d = 40. These radial spans were chosen in an attempt to avoid having samples from the laminar coflow. For the different Reynolds number cases, the conditional average velocity peaks at approximately 710 K for Re = 10,000, 950 K for Re = 20,000, and 950 K for Re = 30,000 at x/d = 20. These likely represent samples from near centerline which are at the highest velocity and heated to the observed temperature values. At x/d = 40, the peak conditional axial velocity averages occur at the highest temperature values of T > 1800 K.

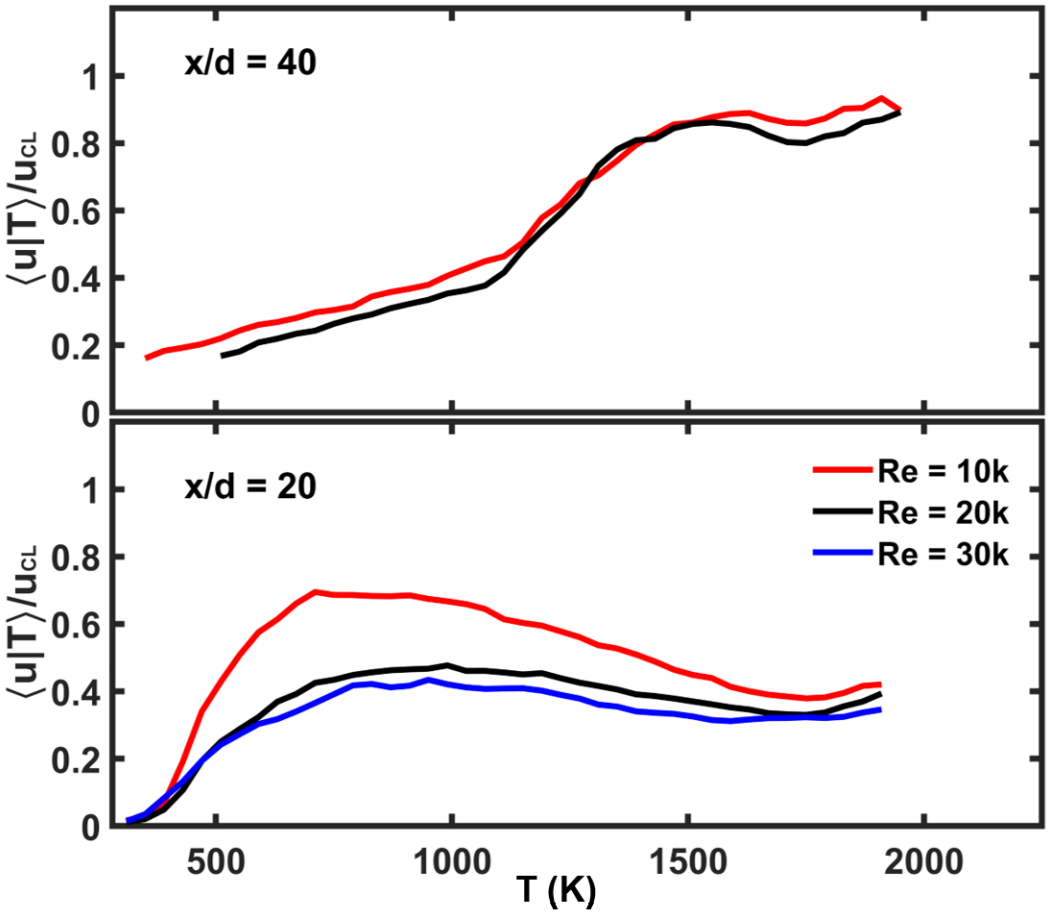

Figure 7.12: Normalized average axial velocity conditioned on temperature at x/d = 20 (bottom) and x/d = 40 (top) for Re = 10,000 (red), 20,000 (black) and 30,000 (blue).

The results from Fig. 7.11 are normalized by the local centerline axial velocity and shown in Fig. 7.12. At x/d = 20 the normalized conditional axial velocity collapses to a single curve for Re = 20,000 and 30,000, but the results from Re = 10,000 are significantly higher for all T as compared to the higher Reynolds number cases. This suggests that the conditional averages of the axial velocity (when properly normalized) becomes independent of Reynolds number for Re ≥ 20,000 at x/d = 20. For the Re = 10,000 flame case, Reynolds number independence has not been achieved, which is consistent with the results of the RMS fluctuation discussed in Ch. 6. Because of heat release and the associated increase in kinematic viscosity, the Re = 10,000 case experiences much lower local Reynolds number throughout the flow field. However, at x/d = 40, both the Re = 10,000 and 20,000 cases collapse to a single curve when normalized demonstrating Reynolds number independence.

The conditioning variable between the axial velocity and temperature can be reversed such that the average of temperature conditioned on axial velocity, denoted $\langle T|u\rangle$, is determined. Figure 7.13 shows the average temperature conditioned on the axial velocity for all of the flames and measurement positions. Figure 7.13 shows that the conditional profiles for both x/d = 20 and x/d = 40 follow similar trends across all Reynolds numbers. At x/d = 20, the lowest temperature values correspond to the extrema of the velocity values for each case, which are presumably the centerline and coflow velocities. The conditional temperatures peak at a particular velocity that is dependent on Reynolds number, but all seem to display a similar peak conditional temperature value; that is the peak conditional temperature is largely independent of Reynolds number. While the temperature peaks at a different velocity for each Reynolds number, the velocity at which the temperature peaks appears to scale with Reynolds number, implying that if the x-axis is properly normalized, then the peaks would correspond to the same location. Furthermore, for a given

Reynolds number condition, the average velocity at which the temperature reaches its maximum is independent of axial position.

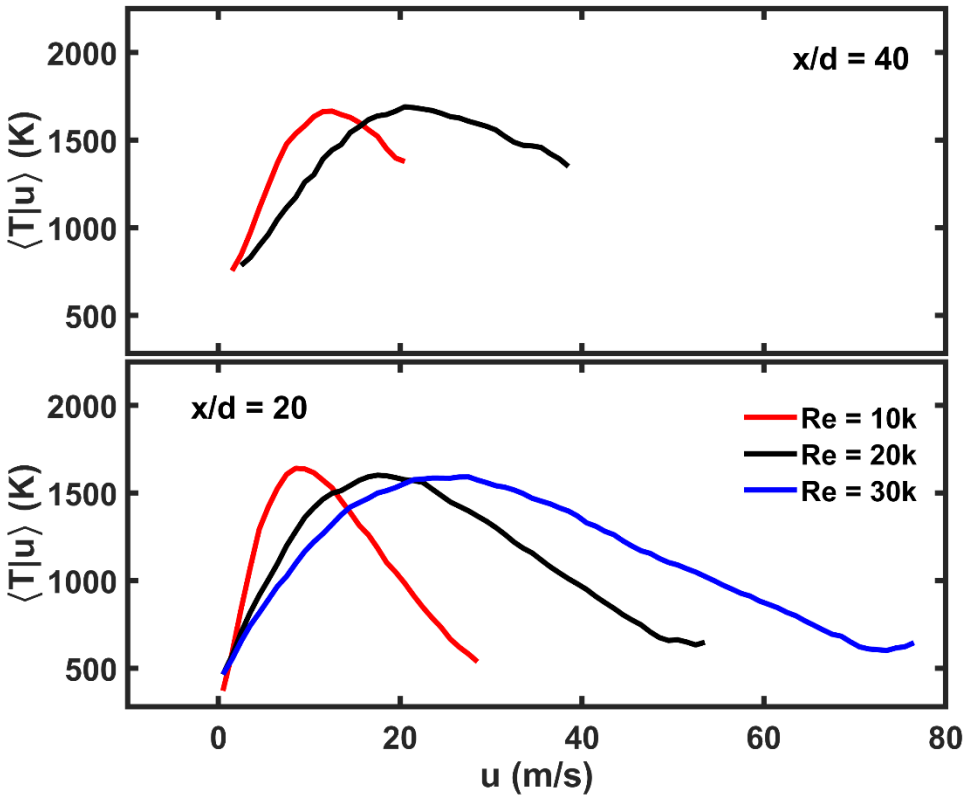

Figure 7.13: Average temperature conditioned on axial velocity for x/d = 20 (bottom) and x/d = 40 (top) for Re = 10,000 (red), 20,000 (black) and 30,000 (blue).

7.4 Estimation of Mixture Fraction

A key observation from Fig. 7.13 is that the conditional profiles of temperature as a function of axial velocity resemble the shape of the well-known state relationship between temperature and mixture fraction for a reacting flow. There is evidence with the literature that there

is a correspondence between the mixture fraction and axial velocity for non-reacting and reacting jet flows. For example, Han and Mungal [213] used simultaneous PIV and CH planar laser-induced fluorescence (PLIF) measurements in a turbulent non-premixed flame to investigate the validity of the so-called stoichiometric velocity, u_s, defined as

$$u_S = \xi_s u_0 + (1 - \xi_s) u_{cf} \qquad \text{Eq. (7.8)}$$

where ξ_s is the stoichiometric mixture fraction, u_0 is the jet exit velocity, and u_{cf} is the coflow velocity. From the velocity measurements, they computed isocontours of u_s and found that they correlated very well with the location of the CH layer, a good marker for the primary reaction zone in non-premixed flames. Similarly, they computed statistics of the measured velocity conditioned on the CH layer and found that it was with a few percent of the calculated values of u_s.

Table 7.2 shows the stoichiometric velocity values calculated using Eq. (7.8) along with the velocity values corresponding to the peak of the conditionally averaged temperatures from Fig. 7.13 for the three Reynolds number flames investigated in the current work. The calculated stoichiometric velocity values are very close to the measured "peak-temperature velocities" or $u_{\max T}$ shown in Fig. 7.13. Given that the stoichiometric mixture fraction occurs near the peak temperature this correspondence further reinforces the relationship amongst mixture fraction and

Case	u_s (m/s)	$u_{\max T}$ (m/s)
Re = 10,000	9.6	10.8
Re = 20,000	18.1	19.0
Re = 30,000	26.5	27.5

Table 7.2: Estimated values of stoichiometic velocity, along with peak-temperature velocities (from Fig. 7.13) for the different Reynolds nubmer cases.

velocity near the stoichiometric contour. In fact, the results in Table 7.2 reveal a subtle clue that the stoichiometric velocity more accurately tracks the stoichiometric mixture fraction beyond the fact that the values are within a few percent of one another. In hydrocarbon flames, it is known that the temperature peaks at slightly rich conditions, $\xi > \xi_s$. This implies that $u_{\max T}$ should be slightly greater than u_s which is shown in Table 7.2. To explore this aspect further the distribution of u conditioned on the highest values of temperature (T > 1900 K) was determined for all flames and spatial positions. Figure 7.14 shows the pdfs of $u|_{T>1900K}$ along with the stoichiometric

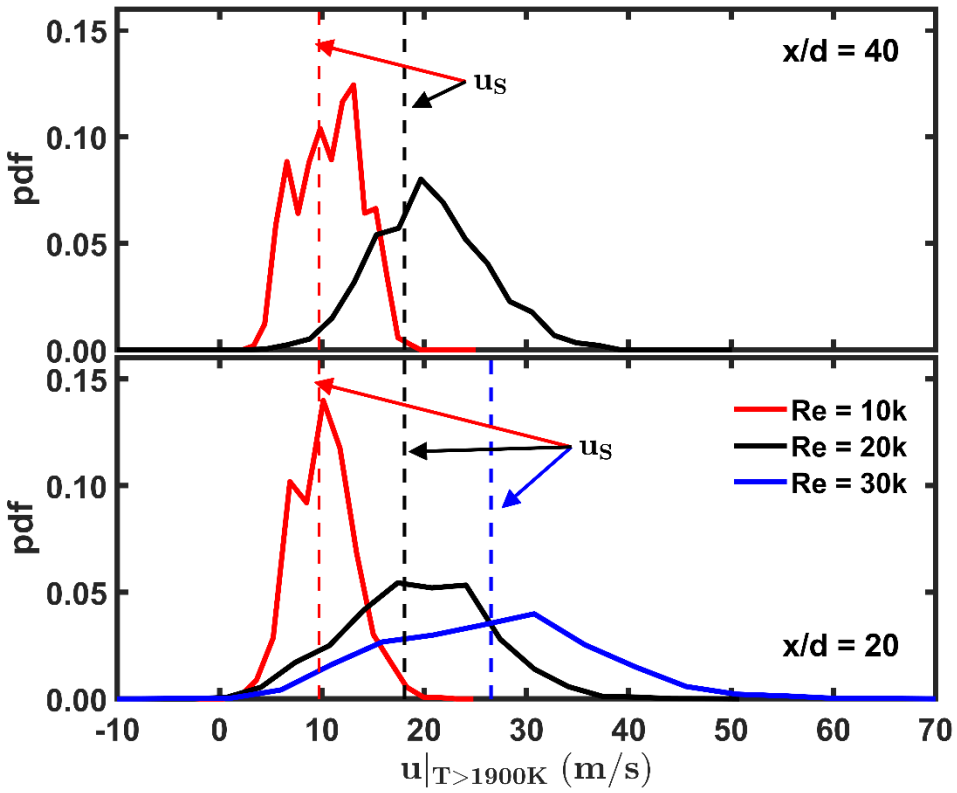

Figure 7.14: PDFs of axial velocity conditioned on the highest temperature values ($T > 1900$) for all flame. Results are shown for x/d = 20 (bottom) and x/d = 40 (top).

velocity value for each Reynolds number (shown as dashed lines). The pdfs and stoichiometric velocity values are color coded such that the Re = 10,000 data is show in red, the Re = 20,000 data is shown in black, and the Re = 30,000 data is shown in blue. The results in Fig. 7.14 show that the calculated stoichiometric velocity values are very close to the centroids and modes of the pdfs of $u|_{T>1900K}$ with the velocity corresponding to the mode of pdf($u|_{T>1900K}$) > u_s which is expected if u_s is a reliable indicator of the location of ξ_s.

Based on the previous work of Han and Mungal [8] and the preceding discussion, it appears that there is a strong correlation between the stoichiometric velocity and the stoichiometric mixture fraction in turbulent non-premixed jet flames. However, it is noted that under the assumptions of no buoyancy and $Sc = 1$, the governing equations for the mixture fraction and axial velocity are the same within a jet or jet flame [214]. Thus, there may be a more general correspondence between mixture fraction and the axial velocity (overall all composition space) within the uncertainties of these assumptions. Using the original concept of a dimensionless axial velocity from [215] and modifying for the existence of a co-flow, an estimated mixture fraction $\hat{\xi}$ can be determined from the axial velocity data using

$$\hat{\xi} = \frac{u - u_{cf}}{u_0 - u_{cf}} \qquad \text{Eq. (7.9)}$$

Figure 7.15 shows scatter plots of temperature versus $\hat{\xi}$ for all flames and positions (black symbols) in addition to the average temperature conditioned on $\hat{\xi}$ (solid green line). Also shown on each subplot of Figure 7.15 is a dashed red line representing the stoichiometric mixture fraction, ξ_s = 0.35. For Fig. 7.15, only a subset of the data is shown in the scatter plot for clarity.

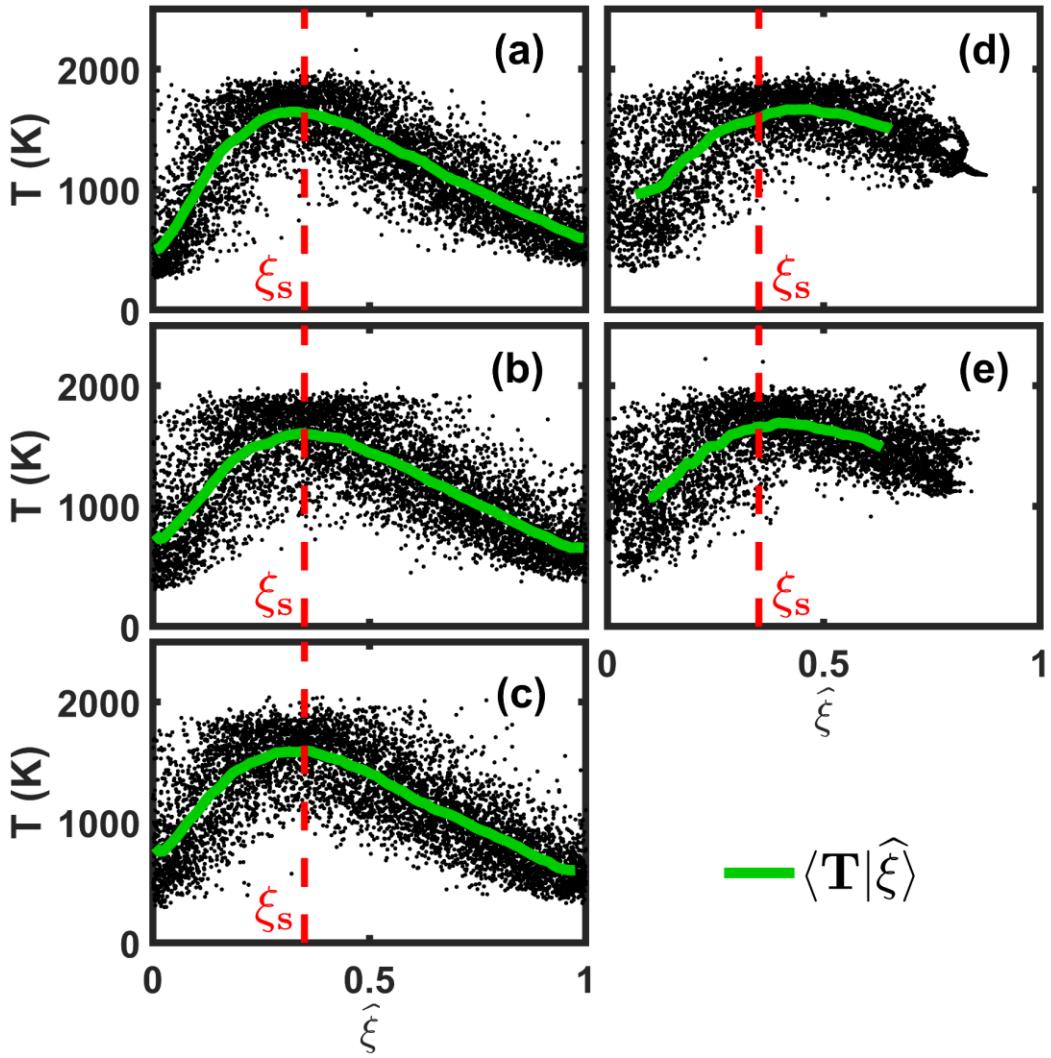

Figure 7.15: Scatter plots of temperature as a function of $\hat{\xi}$ shown as black symbols. The average temperature conditioned on $\hat{\xi}$ is shown in green. The stoichiometric mixture for the flames ($\xi = 0.35$) is shown as a dashed red line. (a) Re = 10,000, x/d = 20. (b) Re = 20,000, x/d = 20. (c) Re = 30,000, x/d = 20. (d) Re = 10,000, x/d = 40. (e) Re = 20,000, x/d = 40.

Figure 7.15 shows that for all flames and axial positions the location of the stoichiometric mixture fraction coincides with the $\hat{\xi}$ value corresponding to the peak of the conditionally averaged temperature. As previously mentioned and hinted by Figure 7.13, the scatter plot and conditional mean of $T = T(\hat{\xi})$ closely resembles the expectation of $T = T(\xi)$. Figure 7.16 shows a comparison of

current temperature measurements conditioned on the estimated mixture fraction ($\hat{\xi}$) from the Re = 20,000 flame at x/d = 20 with published results of temperature conditioned on mixture fraction

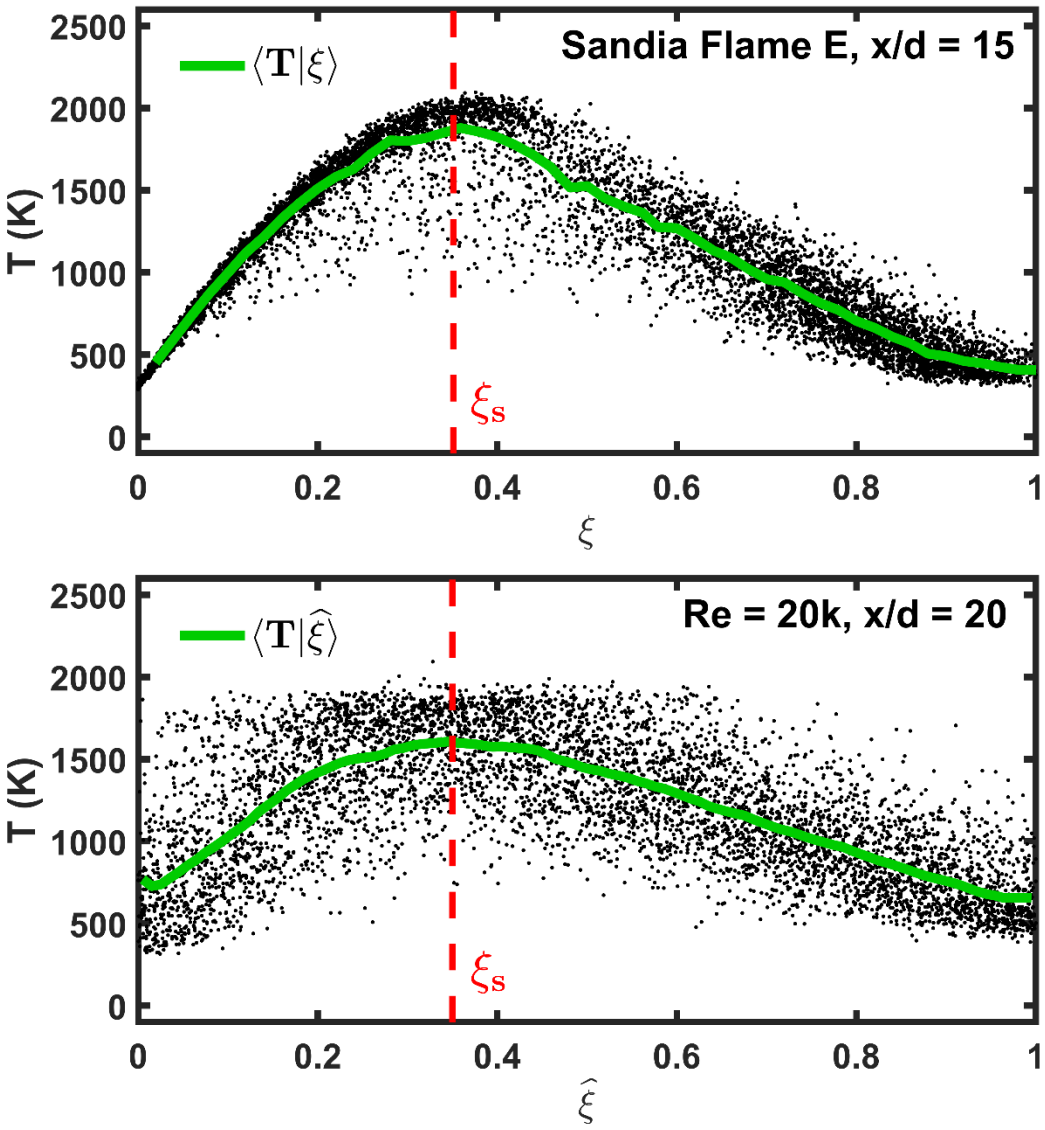

Figure 7.16: Comparison of temperature versus ξ from data from Sandia flame E from x/d = 15 (top) taken fron the TNF workshop [6] and temperature versus $\hat{\xi}$ from the Re = 20,000 flame at x/d = 20 from the current work (bottom). The conditional average of temperature conditioned on ξ and $\hat{\xi}$ are overlaid.

from the piloted, CH_4/air, Sandia flame E (Re = 33,600) at x/d = 15. The Sandia series of piloted flames are benchmark flames which appear as part of the TNF workshop [6]. The piloted jet flame burners used in the current work and the work performed at Sandia are the same design and geometry and the two fuel mixtures reacting in air yield nearly identical stoichiometric mixture fractions, $\xi_s = 0.353$ (current) and 0.351 (Sandia). Six thousand individual data points are shown as solid black symbols, the conditionally averaged temperature value is shown as a solid green line, and the stoichiometric mixture fraction for both flames is shown as a dashed red line. In comparing the two sets of scatter plots, the data from the current work (and using $\hat{\xi}$ as the conditioning variable) shows more spread of the individual data samples compared to the published data from Sandia flame E which uses actual measurements of ξ. However, the overall trend of $T = T(\hat{\xi})$ from the current work closely resembles the measured temperature-mixture fraction relationship, $T = T(\xi)$, determined within the Sandia flame. In fact, the major difference between the two sets of results occurs for the "lean branch", $\hat{\xi} < \xi_s$, where there is significant variance in the current data while the Sandia data is tightly clustered around the conditional average. For $\hat{\xi} \gtrsim \xi_s$ the spread of the individual data points in the current flame is comparable to that observed for actual mixture fraction measurements in the Sandia flame. This indicates the normalized axial velocity, and hence the estimated mixture fraction, behaves quite similarly to the actual mixture fraction in turbulent jet flames.

As one final evaluation of the estimated mixture fraction, the centerline decay of $\hat{\xi}$ from the current work is compared with the centerline axial decay of ξ from a number of piloted Sandia jet flames (C-F) in Fig. 7.17. The axial locations in Fig. 7.17 are normalized by the extended momentum diameter, d^+, given by Eq. (6.14), to account for density differences between the

current flames and the Sandia flames. The Sandia piloted jet flames have Reynolds numbers of 13,400 (flame C), 22,400 (flame D), 33,600 (flame E) and 44800 (flame F) and measurements that span from x/d = 1 to x/d =80 [6, 26]. As observed in Fig. 7.17 the decay of the centerline value of the estimated mixture fraction ($\hat{\xi}$) closely follows the decay of the centerline mixture fraction in the Sandia series of flames. Taken in its entirety, this section shows that, while that there is an underlying uncertainty in the approach, $\hat{\xi} = \frac{u-u_{cf}}{u_0-u_{cf}}$ may act as a reasonable surrogate for ξ under stoichiometric to rich flame conditions. Since mixture fraction measurements are not available in the current work, the calculation of $\hat{\xi}$ allows for conditioning of various kinematic and thermal

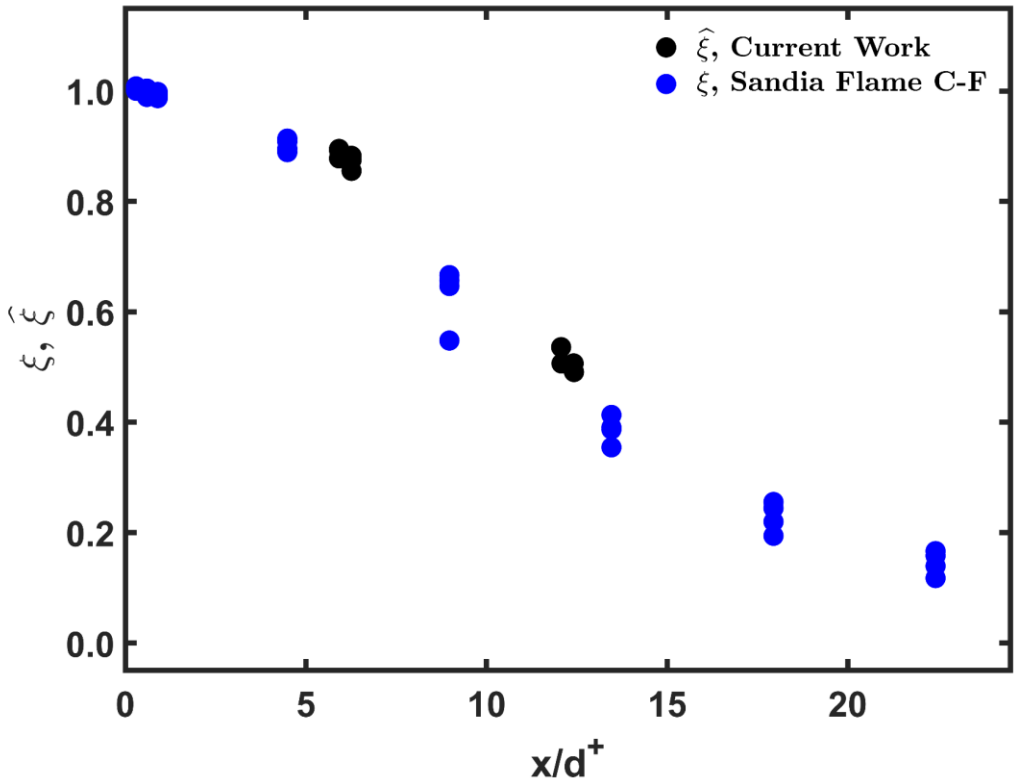

Figure 7.17: Comparison of the centerline decay of $\hat{\xi}$ from the current work to the centerline decay of the mixture fraction from Sandia series of flames (C-F) [6].

properties on the (estimated) mixture fraction with a particular focus on conditioning on $\hat{\xi}_s$ to characterize flow-temperature interactions near the primary reaction zone.

As an example of the utility of using $\hat{\xi}$ as a conditioning variable, Fig. 7.18 shows a pdf of the temperature conditioned on $\hat{\xi}_s$ for all flames and axial locations. Figure 7.18 shows that the pdfs nearly collapse for all flames and both axial locations. The temperature values occur over a range of temperatures from 1000 K – 2000 K with a peak in the pdf for all cases occurring around 1800 K. Although there is a larger spread in the temperature values than expected for a pdf conditioned on the stoichiometric mixture fraction, the collapse of the data for all flames and axial

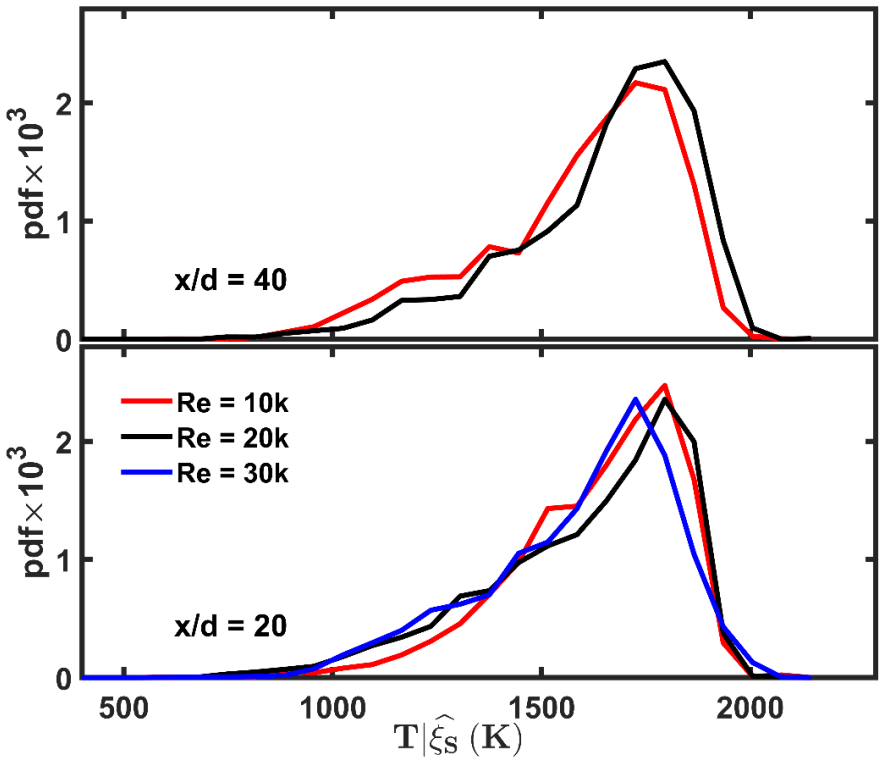

Figure 7.18: Probability density function (pdf) of temperature conditioned on the estiamted stoichiometric mixture fraction, $\hat{\xi}_s$.

locations strengthens the argument that $\hat{\xi}_s$ is a reasonable approximation for ξ_s and is a reasonable conditioning variable to isolate flow-thermal interactions (visually and statistically) near the primary reaction zone.

Figure 7.19 shows the same example interaction shown previously in Figure 7.5 with the addition of the isocontour corresponding to the estimated stoichiometric mixture fraction ($\hat{\xi}_s$) overlaid on the thermal dissipation and compressive principal strain fields. A key observation from

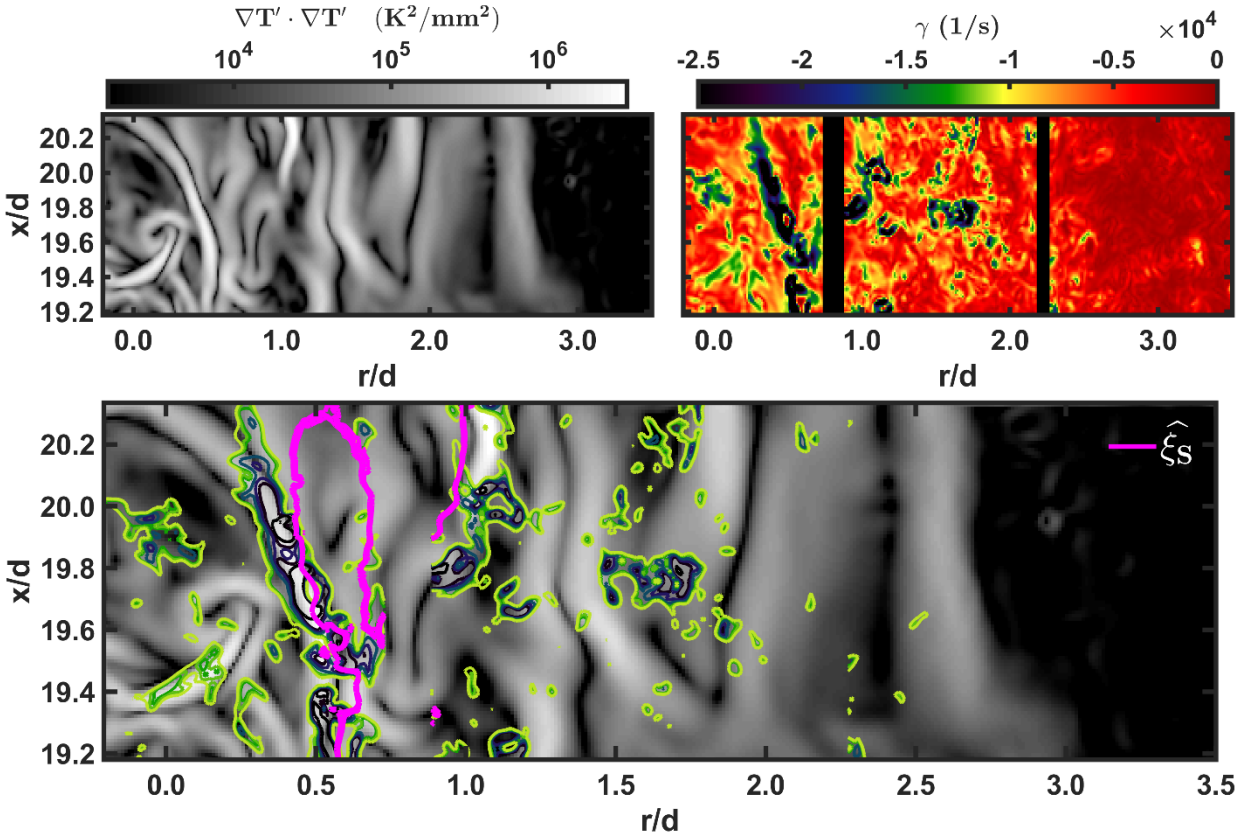

Figure 7.19: Comparison of the thermal dissipation field ($\nabla T' \cdot \nabla T'$) with the compressive principal strain rate field, γ, in a Re = 20,000 flame at x/d = 20. (Top-left) $\nabla T' \cdot \nabla T'$, (Top-right) γ, (Bottom) Overlay of the two fields with the estimated stoichiometric mixture fraction ($\hat{\xi}_s$) overaid in magenta.

Fig. 7.19 is that the strain-dissipation interaction occurs along the stoichiometric mixture fraction contour giving insight to the fact that this particular interaction of large-magnitude strain and dissipation occurs near (presumably the rich side) of a reaction zone.

7.5 Statistical Analysis Involving Gradient Quantities

As discussed previously, flow and scalar gradients control fundamental processes in turbulent reacting flows including mixing and reaction rates. This section presents statistics characterizing the foundational relationship amongst various gradient quantities introduced and discussed in Sec. 7.1. In general, this section follows a hierarchy of analysis, first focusing on characterizing the statistics of the thermal dissipation rate as a function of temperature and spatial position (Sec. 7.5.1). Subsequently, Sec. 7.5.2 examines the alignment of the velocity and temperature gradients and finally Sec. 7.5.3 examines various conditional and joint statistics amongst various key kinematic quantities and thermal dissipation rate.

7.5.1 Statistical Examination of the Thermal Dissipation Rate

Figure 7.20 and 7.21 show pdfs of the thermal dissipation rate conditioned on different radial locations for all flames and axial locations. The thermal dissipation rate is shown on a log scale to highlight the broad range of values present within the flow field and to assess log-normality of the thermal dissipation rate. Figure 7.20 shows the data with a linear y axis, while Fig. 7.21 presents the data with a logarithmic y-axis. The pdfs are is conditioned on centerline ($r/d = 0$), $r/d = 1$, and $r/d = 2$. These correspond to $r/\delta = 0$, $r/\delta = 0.48$, and $r/\delta = 0.96$ for $x/d = 20$ and $r/\delta = 0$, $r/\delta = 0.25$, and $r/\delta = 0.49$ for $x/d = 40$, where δ is the jet-half width. For all flames and axial locations the distributions appear log-normal for large values of dissipation at $r/d = 0$ and 1 and do not show a noticeable difference between the two radial positions (for a given axial position). For

the smaller values of dissipation, the pdf displays an exponential form, which is consistent with previous work (e.g, [216]). There are some differences in the pdfs at r/d = 2 and most notably in the Re = 10,000 case at (x/d, r/d) = (20, 2) which shows a sharp peak in the distribution at lower

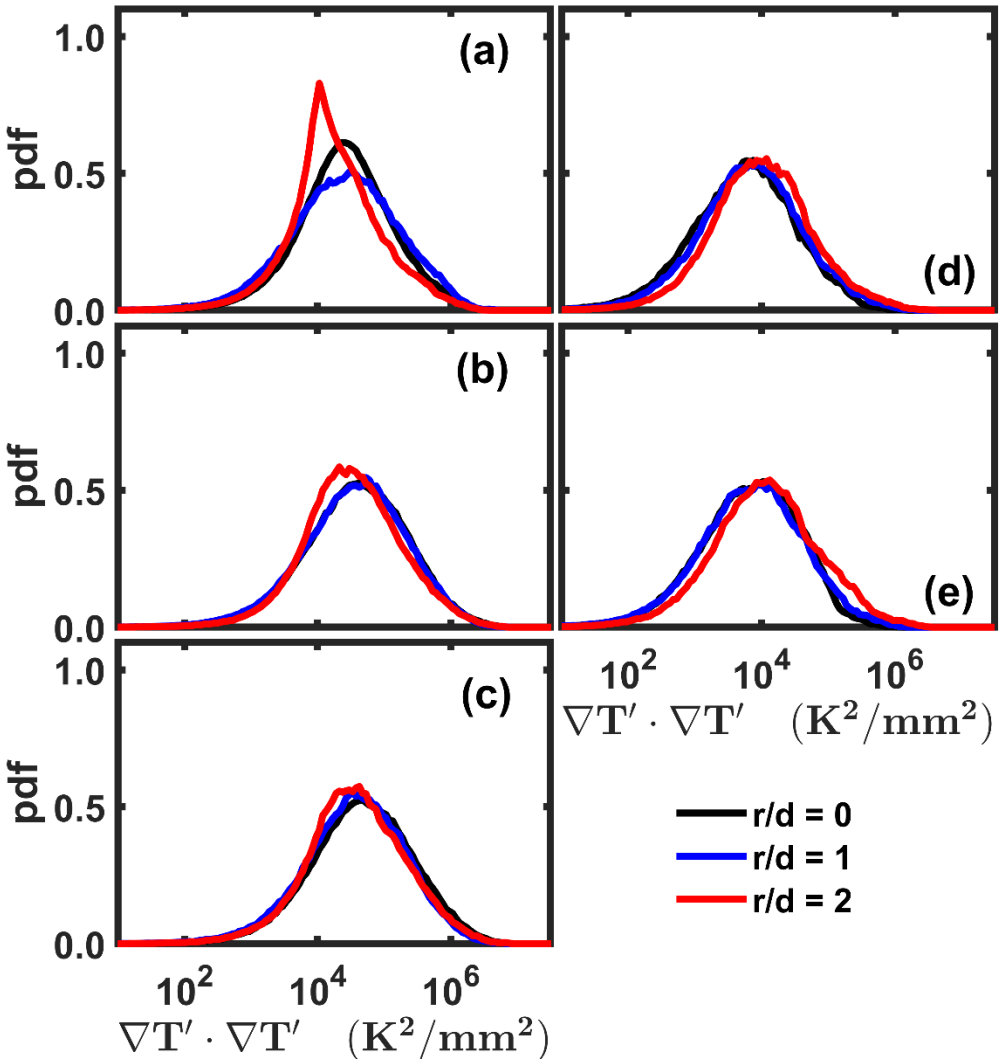

Figure 7.20: Probability density function (pdf) of thermal dissipation rate conditioned on different radial locations with a linear y-axis. (a) Re = 10,000, x/d = 20. (b) Re = 20,000, x/d = 20. (c) Re = 30,000, x/d = 20. (d) Re = 10,000, x/d = 40. (e) Re = 20,000, x/d = 40.

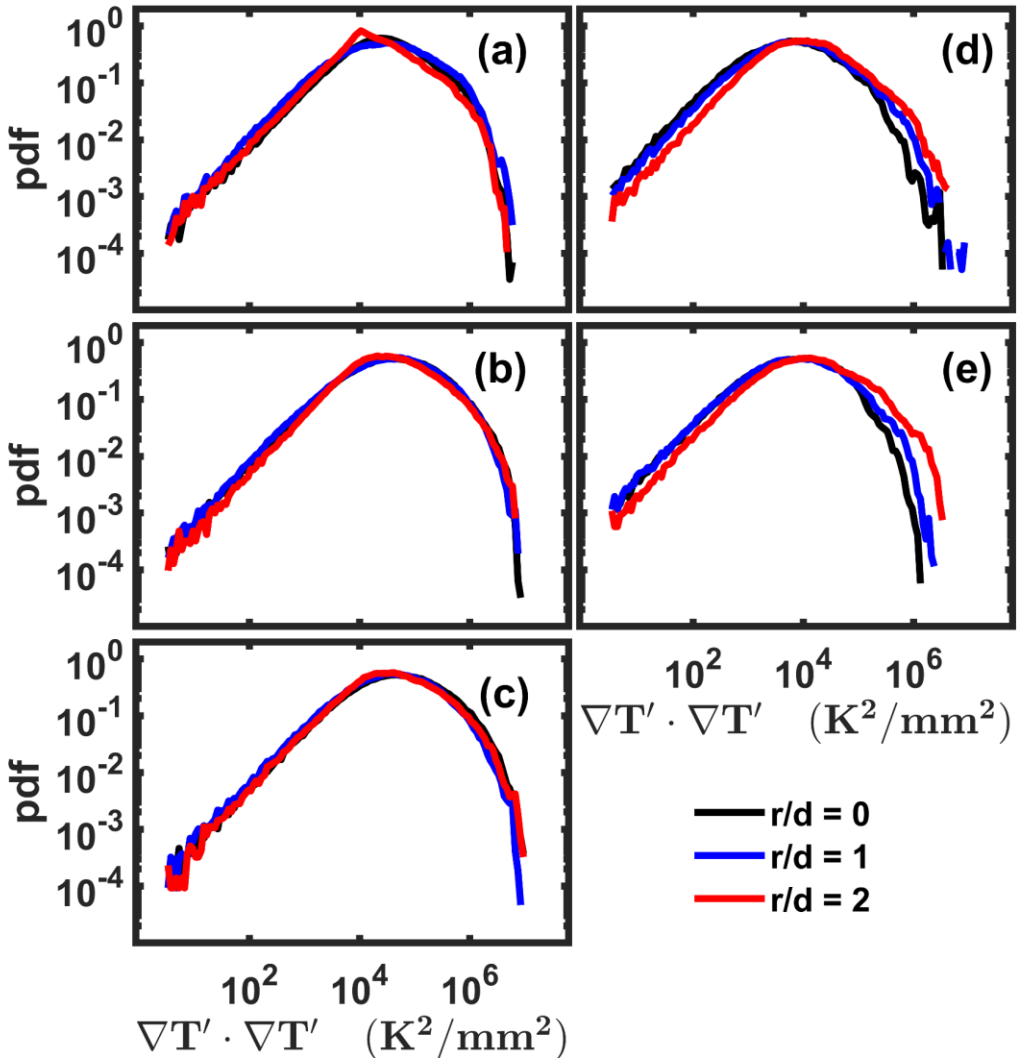

Figure 7.21: Probability density function (pdf) of thermal dissipation rate conditioned on different radial locations with a logarithmic y-axis. (a) Re = 10,000, x/d = 20. (b) Re = 20,000, x/d = 20. (c) Re = 30,000, x/d = 20. (d) Re = 10,000, x/d = 40. (e) Re = 20,000, x/d = 40.

values of thermal dissipation ($\nabla T' \cdot \nabla T' \approx 10^4$ K/mm^2) and exhibits strong positive skewness. It is likely that this is a real artifact and highlights that for the lowest Reynolds number case, the flow is more intermittent with less samples of larger-magnitude dissipation values at that radial location. In fact, the results at x/d = 20 for Re = 10,000 do show a minor progression of pdf shape with

increasing radial position; that is, a decrease in positive skewness as the sampled radial position moves closer to centerline. Aside from the Re = 10,000 case at x/d = 20, the pdfs show that the distribution of the thermal dissipation is largely insensitive to radial location for r/d = 0 to 2 (with the caveat of increased positive skewness at r/d = 2). This is consistent with the results of Wang et al. [216] at x/d = 40 from a Re = 15,200 $CH_4/H_2/N_2$ jet flame who observed that the pdfs of the thermal dissipation rate for radial positions within one jet half width of centerline were very similar. For positions further way from centerline, the pdf became broader and eventually displayed a bimodal shape (high or low values due to intermittency at the jet edge). Again, with exception of the Re = 10,000 case at x/d = 20, the pdfs from the current measurements are largely insensitive to Reynolds number; however there is a dependence on axial position. Based on the results in Fig. 7.20 (or 7.21), the pdfs of the thermal dissipation rate are centered on higher values of dissipation at x/d = 20 as compared to x/d = 40. This is expected due to the fact that the outer-scale strain is proportional to u_c/δ and scales as x^{-2}. The larger global strain yields higher values of local strain, which in turn, induce higher values of local dissipation closer to the nozzle exit.

The dissipation data also can be conditioned on temperature and the estimated value of the stoichiometric mixture fraction, $\widehat{\xi_s}$, which is presumably near the primary reaction zone. Figure 7.22 shows the pdfs of thermal dissipation conditioned on different temperature ranges as well as the pdf conditioned on $\widehat{\xi_s}$. The temperature ranges examined include a range of low-temperatures values (300 K $\leq$ T $\leq$ 500 K), a range of "intermediate" temperatures (1000 K $\leq$ T $\leq$ 1400 K), and a range of high temperatures (T $\geq$ 1800 K). The conditional pdfs, determined for all Reynolds number and axial locations, show distinct distributions for the different temperature ranges as well as the pdf conditioned on the stoichiometric mixture fraction, but display the same general trends across Reynolds numbers and to a lesser extent, across axial positions. For the low-temperature

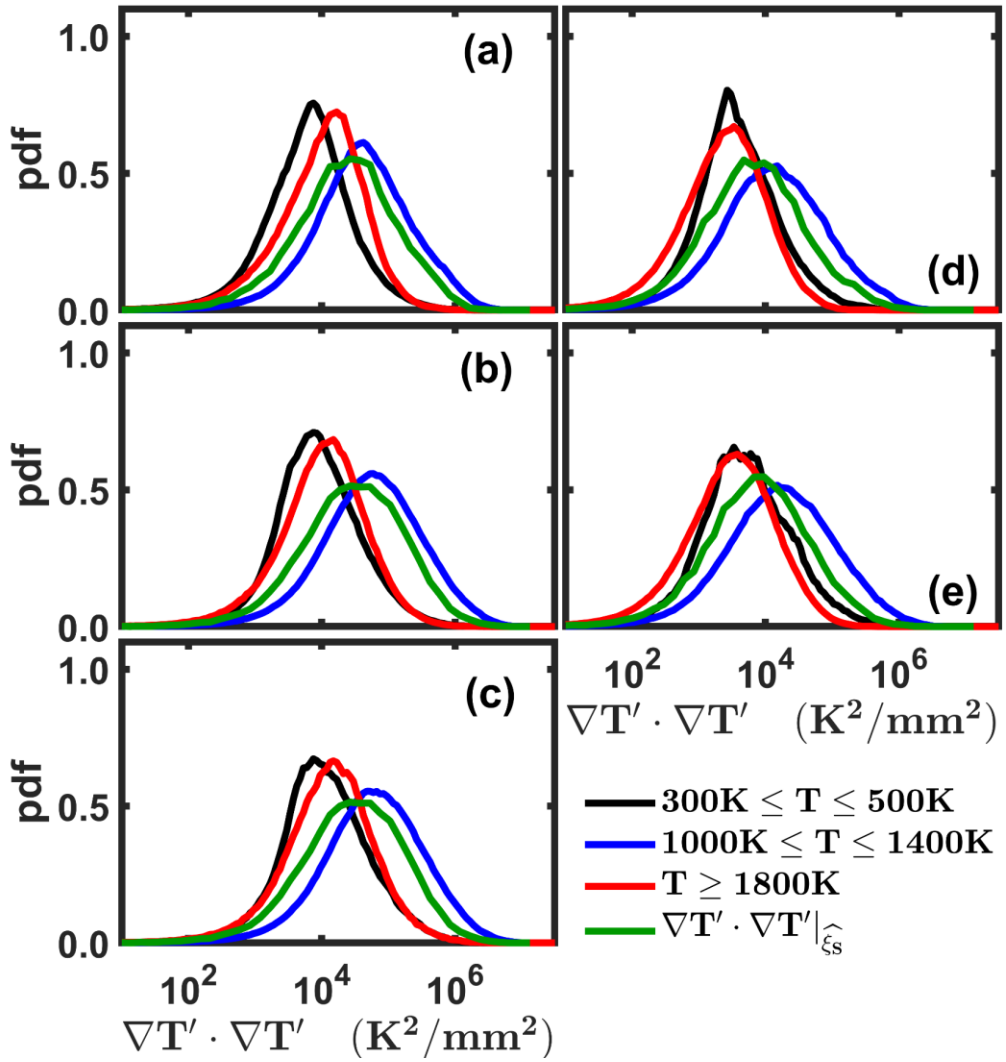

Figure 7.22: Probability density function (pdf) of thermal dissipation condtioned on different temperature ranges. (a) Re = 10,000, x/d = 20. (b) Re = 20,000, x/d = 20. (c) Re = 30,000, x/d = 20. (d) Re = 10,000, x/d = 40. (e) Re = 20,000, x/d = 40.

range (300K to 500K), the mode of the thermal dissipation rate pdf is the lowest of all of the temperature ranges considered, differing by approximately one order-of-magnitude as compared to that of the intermediate temperature range (1000 K $\leq$ T $\leq$ 1400 K). In addition, the pdf displays positive skewness that increases with increasing Reynolds number. The positive skewness means

that intermittent instances of higher dissipation rate occur more often than low-magnitude values of thermal dissipation. These characteristics are observed for both axial positions. The positive skewness of the thermal dissipation rate at low temperatures is quite different from that observed in pdfs of the scalar dissipation rate in turbulent non-reacting flows (e.g., [217, 218]) and reacting flows [38, 219], and thermal dissipation rates presented within the literature [216] (and shown in Fig. 7.22 for other temperatures). The majority of results show that both the scalar and thermal dissipation pdfs are approximately log-normal with minor negative skewness.

For the intermediate temperature range (1000 K $\leq$ T $\leq$ 1400 K) the thermal dissipation rate is distributed amongst the largest magnitudes compared to the other cases and assumes an approximate log-normal distribution. The mode of the pdf and the width of the distribution appear to be independent of Reynolds number at both x/d = 20 and 40. For the highest temperature range considered (T $\geq$ 1800 K), the pdf shifts to lower values of the thermal dissipation rate with a mode that is very similar to that of the lowest temperature range. However, the distributions are approximately log normal, with a degree of negative skewness for Re = 10,000 at x/d = 20. Figure 7.22 also shows the pdf of the thermal dissipation rate conditioned on the estimated stoichiometric mixture fraction. For all Reynolds numbers and axial positions, the mode of the pdf conditioned on $\widehat{\xi_s}$ is slightly less than that of the pdf conditioned on the intermediate temperature range and noticeably higher than the mode of the pdf conditioned on T $\geq$ 1800 K. This bounding is reasonable considering the fact that the mean temperature (conditioned on $\widehat{\xi_s}$) is approximately 1600K (see Figs. 7.15 and 7.16). The highest values of dissipation occurring for the intermediate temperature range is due to the structure of the jet flame. Examining Fig. 6.18, it is noted that the highest average thermal gradients occur from 1000 K $\leq$ T $\leq$ 1400 K for all three flames and both axial positions. The high magnitudes of thermal dissipation occurring for the case of conditioning

on $\widehat{\xi_s}$ suggests that the increased chemical activity, which occurs around the primary reaction zone, leads to strong thermal gradients and hence, higher dissipation rates.

To further characterize the values of thermal dissipation rate observed at each temperature range, the cumulative distribution function (cdf) was determined for all flames and axial locations, and is shown in Fig. 7.23. The cdfs from the data acquired at x/d = 40 are shown as dashed lines while the cdfs for the data acquired x/d = 20 are shown as solid lines. The curves are color coded

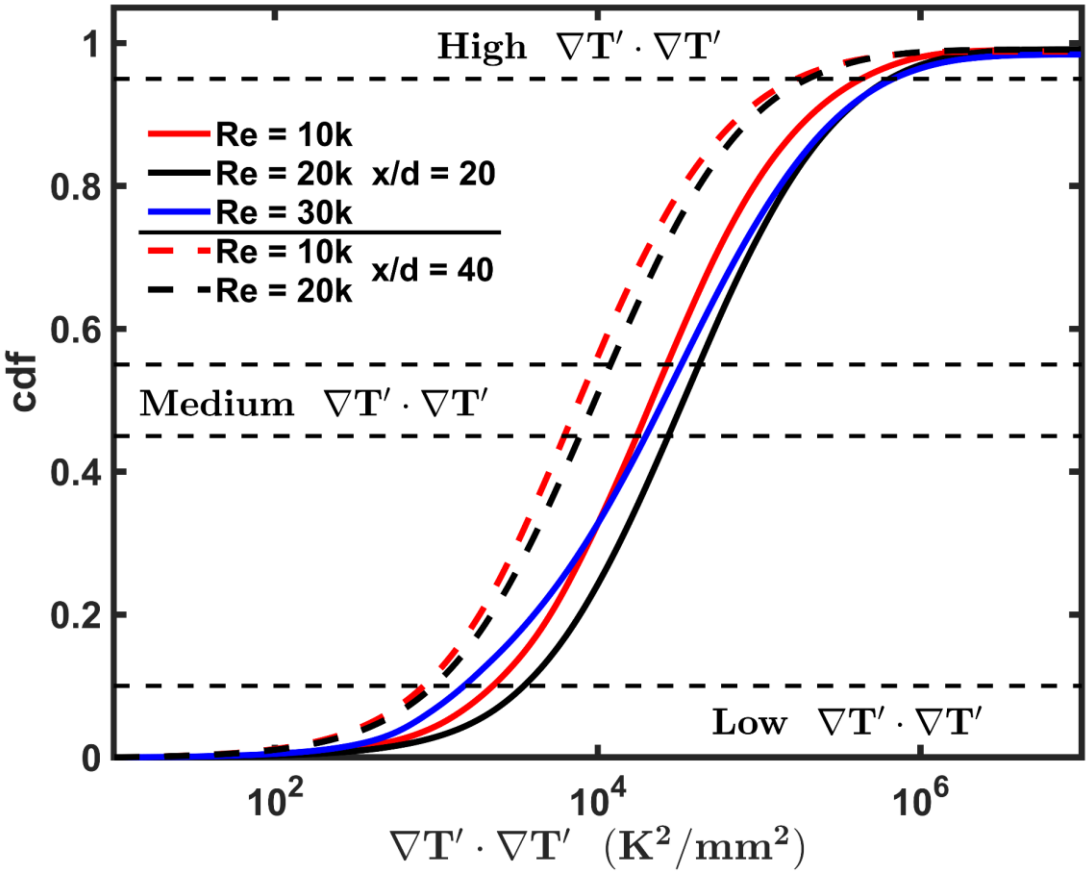

Figure 7.23: Cumulative distribution function (cdf) of the thermal dissipation rate for all flames and poistions. Re = 10,000 shown in red, Re = 20,000 shown in black, and Re = 30,000 shown in blue.

such that Re = 10,000 is shown in red, Re = 20,000 is shown in black, and Re = 30,000 is shown in blue. As one example, at x/d = 20, the most probable value of the thermal dissipation rate within the low-temperature range is < 10^4 K^2/mm^2, which corresponds to the lower 33rd percentile of the thermal dissipation rate pdf for Re = 10,000 and 30,000 and the lower 25th percentile of the thermal dissipation rate pdf for Re = 30,000. In contrast, for the intermediate temperature range, the mode of the pdf is approximately 6 x 10^4 K^2/mm^2, which corresponds to the 72nd percentile of the thermal dissipation rate pdf for Re = 10,000 and the 65th percentile of the thermal dissipation rate pdf for Re = 20,000 and 30,000.

The cdfs also are used to set different ranges of thermal dissipation used in analysis below. More specifically, statistics will be compared for joint kinematic-thermal properties for low-magnitude dissipation ("Low"), intermediate values of dissipation ("Medium"), and high-magnitude dissipation ("High"). The various definitions, based on the cdf values, are indicated in Fig. 7.23 with horizontal dashed lines. "Low" thermal dissipation was defined for each Reynolds number and axial location as cdf values less than or equal to 0.1. "Medium" values of thermal dissipation were defined for each Reynolds number and axial location as cdf values between 0.45 and 0.55 and "High" thermal dissipation was defined for each Reynolds number and axial location as cdf values greater than 0.95.

7.5.2 Alignment between Temperature and Velocity Fields

One method to quantify the alignment (or degree of correlation) between temperature and the axial velocity is to define an alignment index as

$$AI_{uT} = \frac{\nabla T \cdot \nabla u}{|\nabla T||\nabla u|} \qquad \text{Eq. (7.10)}$$

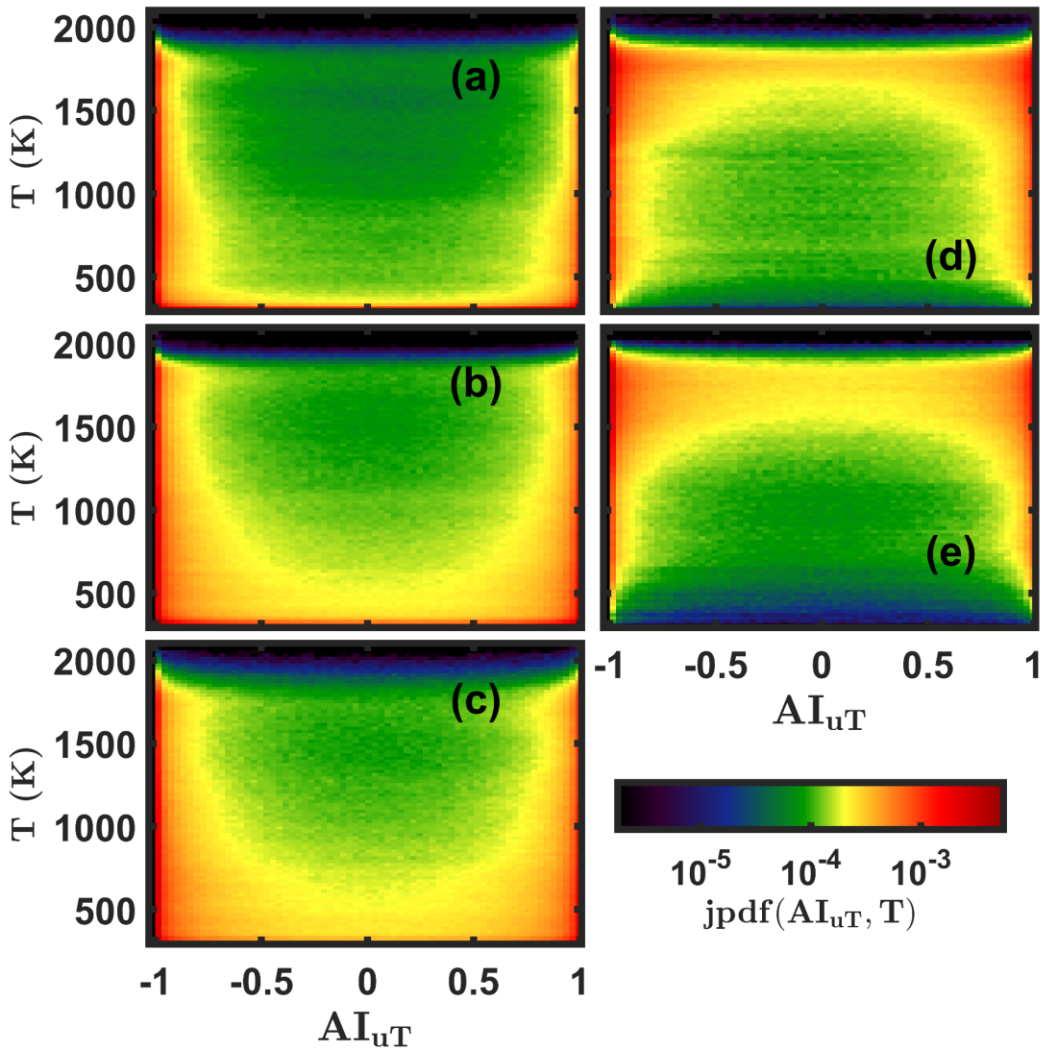

Figure 7.24: Joint pdf (jpdf) of temperature and the alignment index between axial velocity and temperature. (a) Re = 10,000, x/d = 20. (b) Re = 20,000, x/d = 20. (c) Re = 30,000, x/d = 20. (d) Re = 10,000, x/d = 40. (e) Re = 20,000, x/d = 40.

where a value of -1 means the gradients are directly opposed, +1 means the gradients are aligned in the same direction, and a value of 0 means the gradients are aligned orthogonal to one another. Figure 7.24 shows the joint pdf (denoted as jpdf) of the temperature and the alignment index for all flames and axial locations. The jpdf is shown as a color map and in a logarithmic scale to show the variations over a large range of probabilities. For all Reynolds numbers, axial positions, and

temperatures the most probable values of the alignment index values are -1 and 1, indicating that the most probable orientation between the axial velocity and temperature gradients are either direct opposition or alignment. With regards to the most probable values (AI_{uT} = -1 and 1) there appears to be slightly more samples with AI_{uT} = -1 indicating a stronger tendency for the gradients to be opposed. The jpdfs show different trends as a function of temperature for x/d = 20 compared to those at x/d = 40. First, it should be mentioned that for a laminar jet flame, one would expect a purely bimodal distribution with modes at ±1 due to the competing effects of advection, thermal diffusion, and gas expansion. For the cases at x/d = 20, the pdfs are essentially bimodal for high temperatures and display a larger distribution of alignment index values at the lower temperatures (i.e., more samples are located near AI_{uT} = 0). The situation is reversed for the data at x/d = 40 where there is an increased distribution of alignment index values at higher temperature. This is likely due to the structural makeup of a reacting jet. At x/d = 20, the highest velocity values and the highest local Reynolds numbers occur at lower temperatures near centerline (see Figs. 6.18, 6.20, and 7.12), while lower velocities and local Reynolds numbers occur for high-temperature conditions. With increased local Reynolds number (and presumably turbulence levels), there will be an increased probability of misalignment between the temperature and velocity fields due to insufficient time for scalar gradient to align. The jet flame has a different structure at x/d = 40, where the highest temperatures and velocities are near centerline and both decrease as a function of radial position. In this manner, the highest turbulence levels (even with the increased kinematic viscosity) occur at elevated temperatures and lead to a broader distribution of alignment index values. These arguments also are consistent with the observed behavior of the jpdfs; that is, with increasing Reynolds number (a-c or d-e), for a given temperature (focus on low temperature at x/d

= 20 and high temperatures for x/d = 40), there is an increasing probability of alignment index values other than ±1.

The alignment index was further conditioned on various magnitudes of the thermal

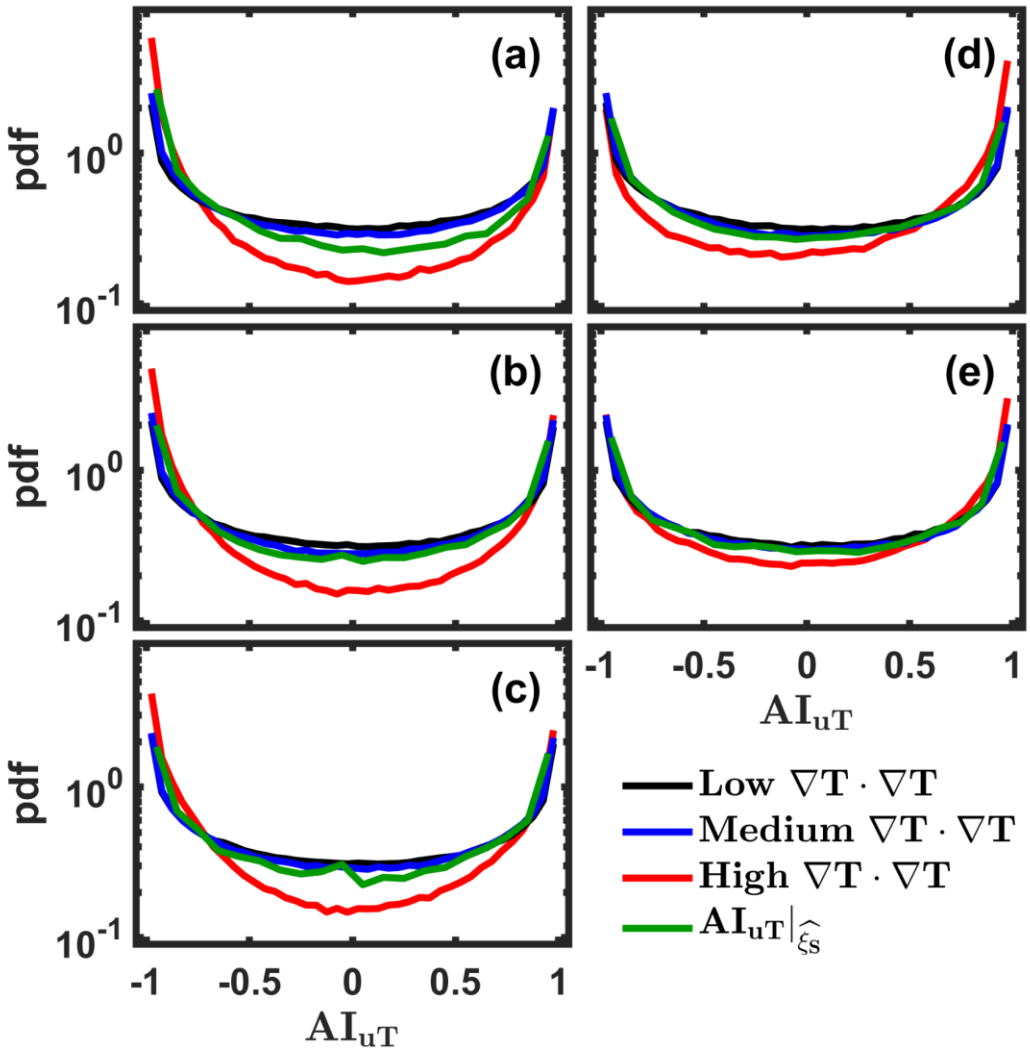

Figure 7.25: Probability density function (pdf) of alignment index between axial velocity and temperature conditioned on different magnitudes of thermal dissipation Also shown in the pdf of the alignment index conditioned on the stoiochiometric mixture fraction. (a) Re = 10,000, x/d = 20. (b) Re = 20,000, x/d = 20. (c) Re = 30,000, x/d = 20. (d) Re = 10,000, x/d = 40. (e) Re = 20,000, x/d = 40.

dissipation rate ("High", "Medium", and "Low") as established above in Fig. 7.23, as well as on the stoichiometric mixture fraction value. The results are shown in Fig. 7.25 for all flames and axial locations. Figure 7.25 shows that the alignment index for the cases of "Low" and "Medium" dissipation levels are largely the same for all flames and axial positions. The probability of $AI_{uT} = -1$ is approximately 80% higher than the lowest probable value, $AI_{uT} = -0$. With the exception of the Re = 10,000 case at x/d = 20, the pdfs of AI_{uT} conditioned on the stoichiometric mixture fraction display approximately the same behavior as the pdfs conditioned on "Low" and "Medium" values of the thermal dissipation rate with slightly lower probability of orthogonal alignment ($AI_{uT} = -0.$). However, the pdfs conditioned on large magnitudes of dissipation ("High") show distinctly different behavior compared with the other conditioned cases. For large-magnitude dissipation, there is a notable increase in the peak value of the pdf (opposed gradients at x/d = 20 and aligned gradients at x/d = 40) with a significant reduction in the probability of other alignments. This result indicates a strong correlation between velocity-temperature structural overlap and the presence of high-magnitude thermal dissipation.

7.5.3 Joint and Conditional Statistical Analysis of Gradient Quantities

A primary benefit of high-resolution velocity and temperature images is that statistical relationship amongst various gradient quantities for both the kinematic properties (i.e., vorticity, and strain rate) and the thermal properties (including the thermal dissipation rate) of the flow can be explored.

7.5.3.1 Joint Vorticity and Thermal Dissipation Statistics

Figure 7.26 shows the joint pdf (jpdf) of the thermal dissipation rate with ω_z for all Reynolds numbers and axial positions. As shown in Fig. 7.26, the distribution of vorticity

magnitudes increases with increasing Reynolds number for a given axial location and decreases with increasing axial position for a given Reynolds number. For a given thermal dissipation rate, the distribution of vorticity values is symmetric, but for a given vorticity value, the pdf of thermal

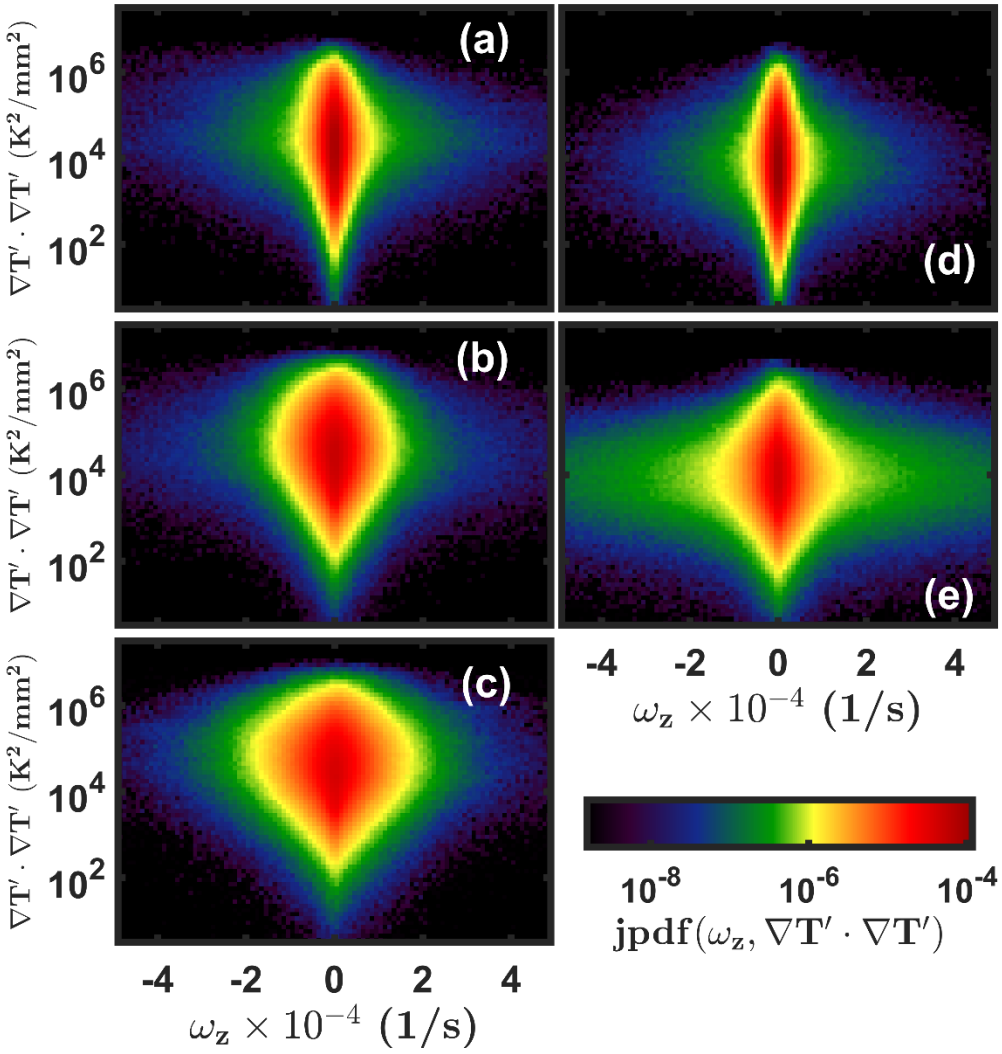

Figure 7.26: Joint pdfs (jpdfs) of vorticity ω_Z and thermal dissipation rate. (a) Re = 10,000, x/d = 20. (b) Re = 20,000, x/d = 20. (c) Re = 30,000, x/d = 20. (d) Re = 10,000, x/d = 40. (e) Re = 20,000, x/d = 40.

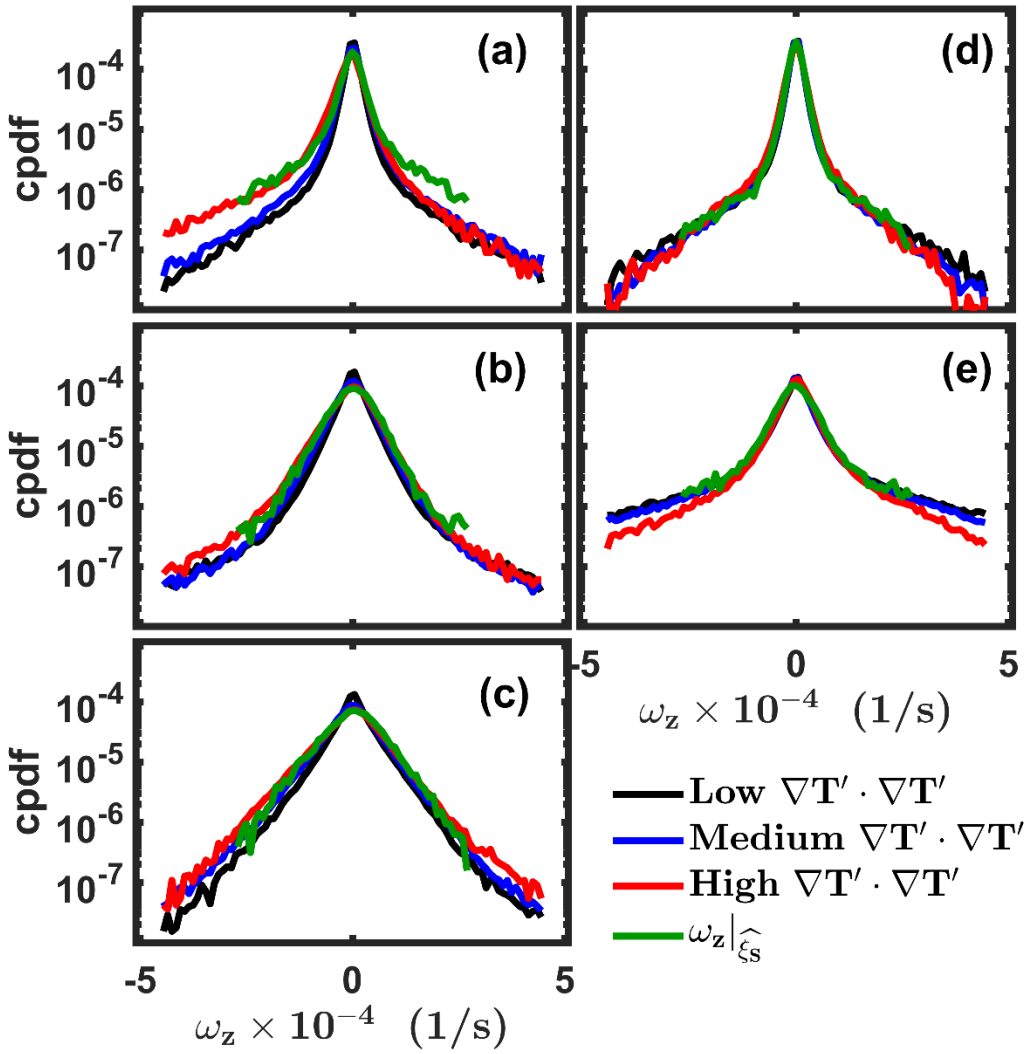

Figure 7.27: Probability density function (pdf) of ω_z conditioned on various magnitudes of thermal dissipation rate. Also shown is the pdf of vorticity conditioned on the stoichiometric contour (a) Re = 10,000, x/d = 20. (b) Re = 20,000, x/d = 20. (c) Re = 30,000, x/d = 20. (d) Re = 10,000, x/d = 40. (e) Re = 20,000, x/d = 40.

dissipation rate exhibits negative skewness. For both axial positions, the degree of skewness decreases with increasing Reynolds number.

Figure 7.27 shows the pdfs of vorticity conditioned on the various magnitudes of the thermal dissipation rate as well as conditioned on the stoichiometric mixture fraction. For all

Reynolds numbers and axial locations the distributions of ω_z exhibit strong non-Gaussian tails. The pdfs appear to be more "heavy tailed" (possibly power-low dependence) as opposed to exponential tails. There is a clear evolution with increasing Reynolds number in that an increasing fraction of the pdf deviates from Gaussian behavior. In terms of the effect of thermal dissipation rate magnitude, there is no apparent effect of the magnitudes increasing from "Low" to "Medium" as the pdfs of ω_z follow closely with one another. For the lowest Reynolds number case at x/d = 20, there is an increased probability of higher of large-magnitude (negative) ω_z for large-magnitude thermal dissipation rate. For this condition, there also is a higher probability of both negative and positive large-magnitude vorticity when conditioning on the stoichiometric mixture fraction. For all other Reynolds number and both flame cases at x/d = 40 all pdfs essentially collapse implying little inter-dependence between the vorticity and thermal dissipation rate.

To further explore any potential dependence of the thermal dissipation rate on the vorticity, the mean of the thermal dissipation rate, conditioned on ω_z, was computed and shown in Fig. 7.28. For the calculation of the conditional mean, vorticity bins of 1000 s^{-1} were used and only vorticity bins that contained at least 1000 samples were considered for analysis. For the Re = 10,000 case, there is notable asymmetry in the conditional mean of dissipation about $\omega_z = 0$, with larger magnitudes of dissipation occurring for negative values of vorticity. There also are smaller degrees of asymmetry in the conditional means of the thermal dissipation for the Re = 20,000 and 30,000 flames at x/d = 20. Within the uncertainty of the analysis, no asymmetries in the conditional means are observed at x/d = 40. An interesting feature from the conditional means is that the smallest magnitudes of thermal dissipation are associated with $\omega_z = 0$ (which is expected), but then small increases in vorticity magnitude are correlated with rather large increases in the magnitude of the thermal dissipation rate. With increasing Reynolds number, this effect diminishes. In fact at x/d =

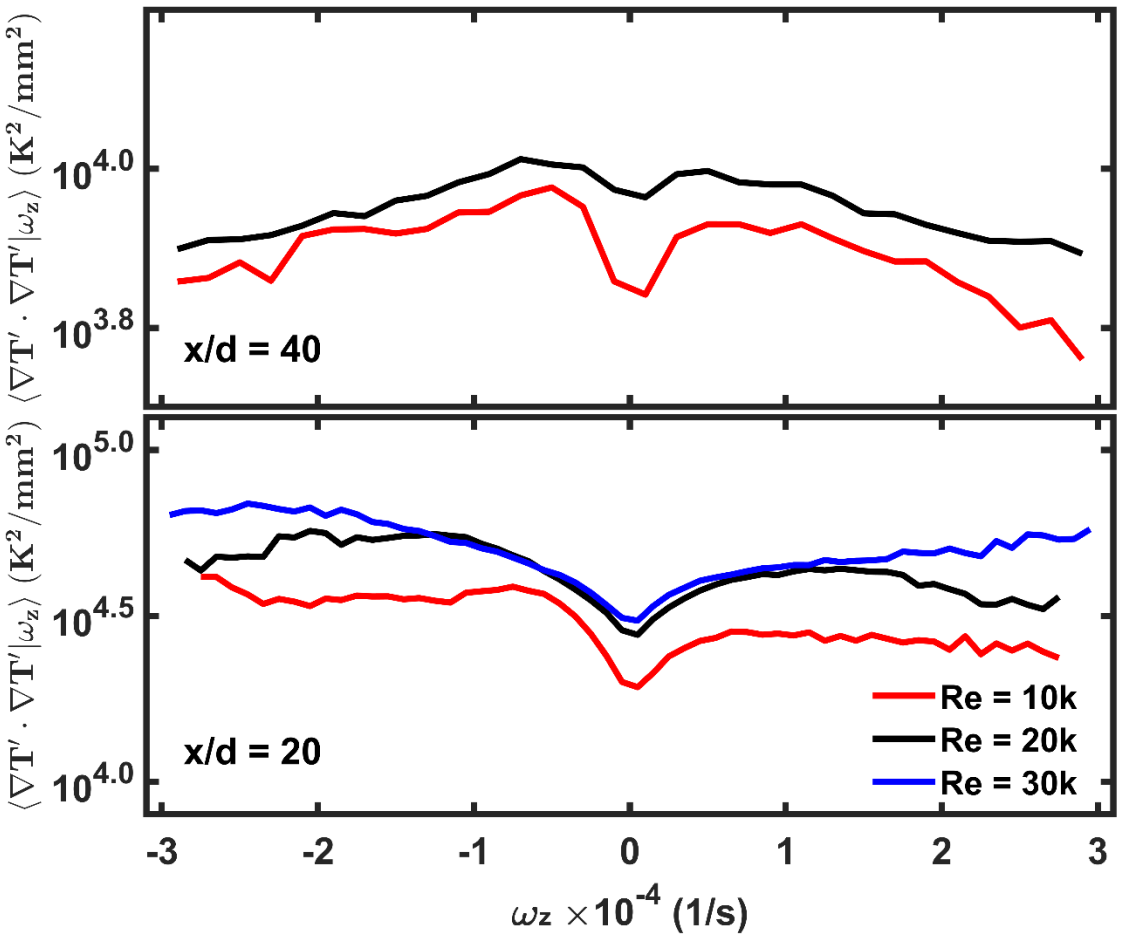

Figure 7.28: Condtional mean of the thermal dissipation rate as a function of ω_Z. (Top) x/d = 40. (Bottom) x/d = 20. Re = 10,000 shown in red, Re = 20,000 shown in black, and Re = 30,000 shown in blue.

40, any increase in ω_z leads to small reductions in the thermal dissipation rate. At x/d = 20, further increases in the magnitude of ω_z does not seem to be correlated with increases in thermal dissipation rate, except for the highest Reynolds number case, Re = 30,000. At x/d =40, large-magnitude values of vorticity are associated with decreases in thermal dissipation rate. Overall, it appears that there is little to no correlation between vorticity magnitude and thermal dissipation rate magnitude except for at the highest Reynolds number. This is consistent with DNS results that

have shown that there is not a strong correlation between regions of high scalar dissipation and vorticity [205, 220].

7.5.3.2 Joint Principal Strain Rate and Thermal Dissipation Statistics

The interaction between the strain rate field (as examined through the principal strain rate components) and the thermal dissipation rate is of particular interest for turbulent non-premixed flames. Figures 7.5-7.7 showed a single visualization displaying the interaction between the principal strain components, $\alpha, \beta,$ and γ which appeared to spatially coincide with a large-magnitude dissipation layer. In this section, it is of interest to explore the statistical relationship between the principal strain rate components and thermal dissipation to attempt to characterize primary kinematic processes governing the formation of strong scalar gradients and high magnitudes of thermal dissipation.

Figure 7.29 shows the joint pdfs of the most extensional principal strain rate component, α and the thermal dissipation rate for all flames and locations. For data at x/d = 20 it is observed for all three Reynolds number flames that there is a large positive tail of the pdf of α and the positive skewness increases with increasing magnitudes of thermal dissipation. This implies that large-magnitude extensional strain rates correlate with large-magnitude thermal dissipation. At x/d = 40, the jpdf still exhibits positive skewness, but there does not appear to be a large dependence on the magnitude of the thermal dissipation.

Figure 7.30 shows the pdfs of α conditioned on various magnitudes of the thermal dissipation rate as well as conditioned on the stochiometric mixture fraction for all Reynolds numbers and axial locations considered. At x/d = 20, there are small differences in the conditional pdfs (mainly a slight increase in positive skewness) when the thermal dissipation rate magnitude

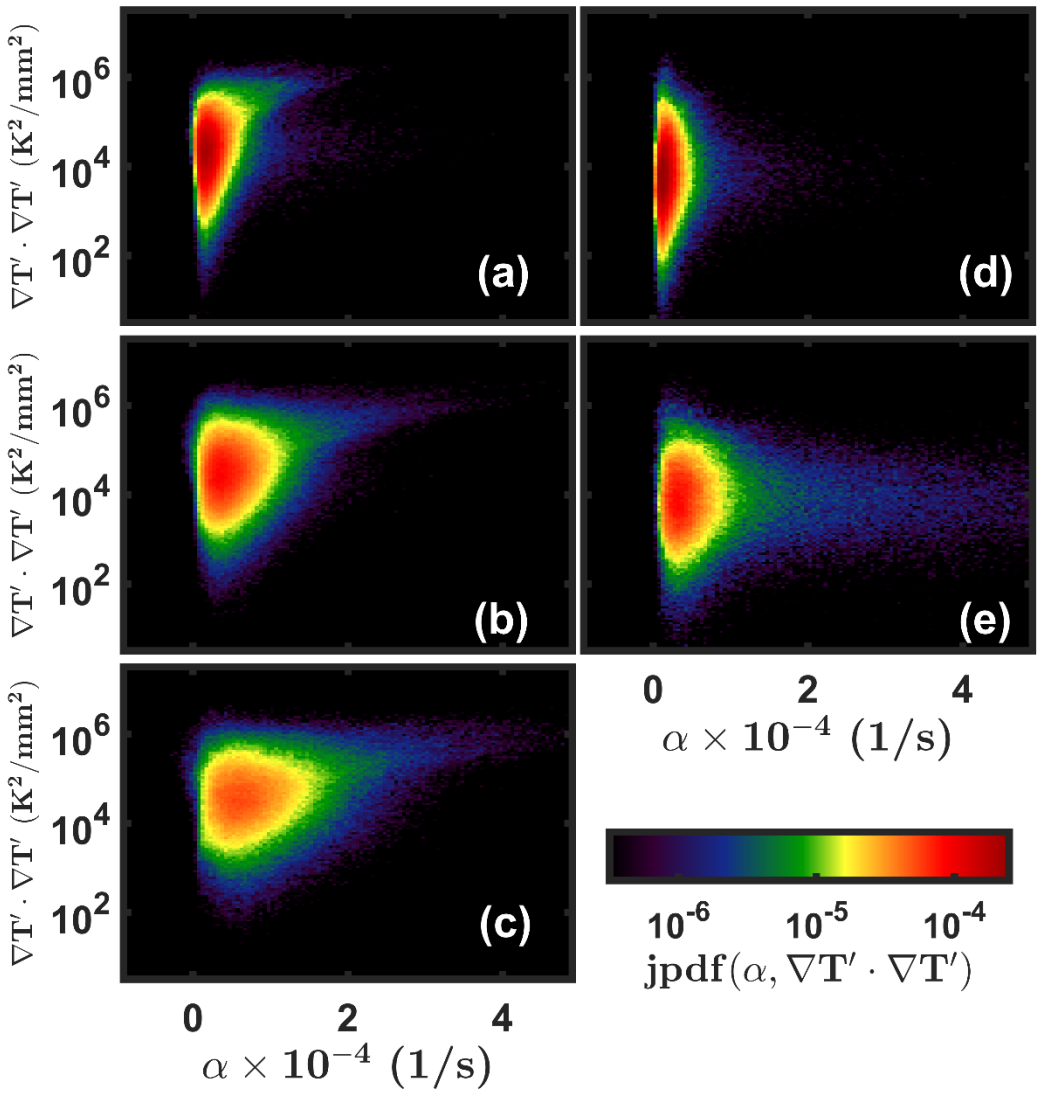

Figure 7.29: Joint pdfs (jpdfs) of extensional principal strain component α, and thermal dissipation rate. (a) Re = 10,000, x/d = 20. (b) Re = 20,000, x/d = 20. (c) Re = 30,000, x/d = 20. (d) Re = 10,000, x/d = 40. (e) Re = 20,000, x/d = 40.

is increased from "Low" to "Medium". There is a further slight increase in the positive skewness for pdfs of α conditioned on the stoichiometric mixture fraction. Based on Fig. 7.23, it is likely that the magnitudes of the thermal dissipation rate occurring at the stoichiometric contour correspond to the 50th-60th percentile of the cumulative distribution of thermal dissipation rate

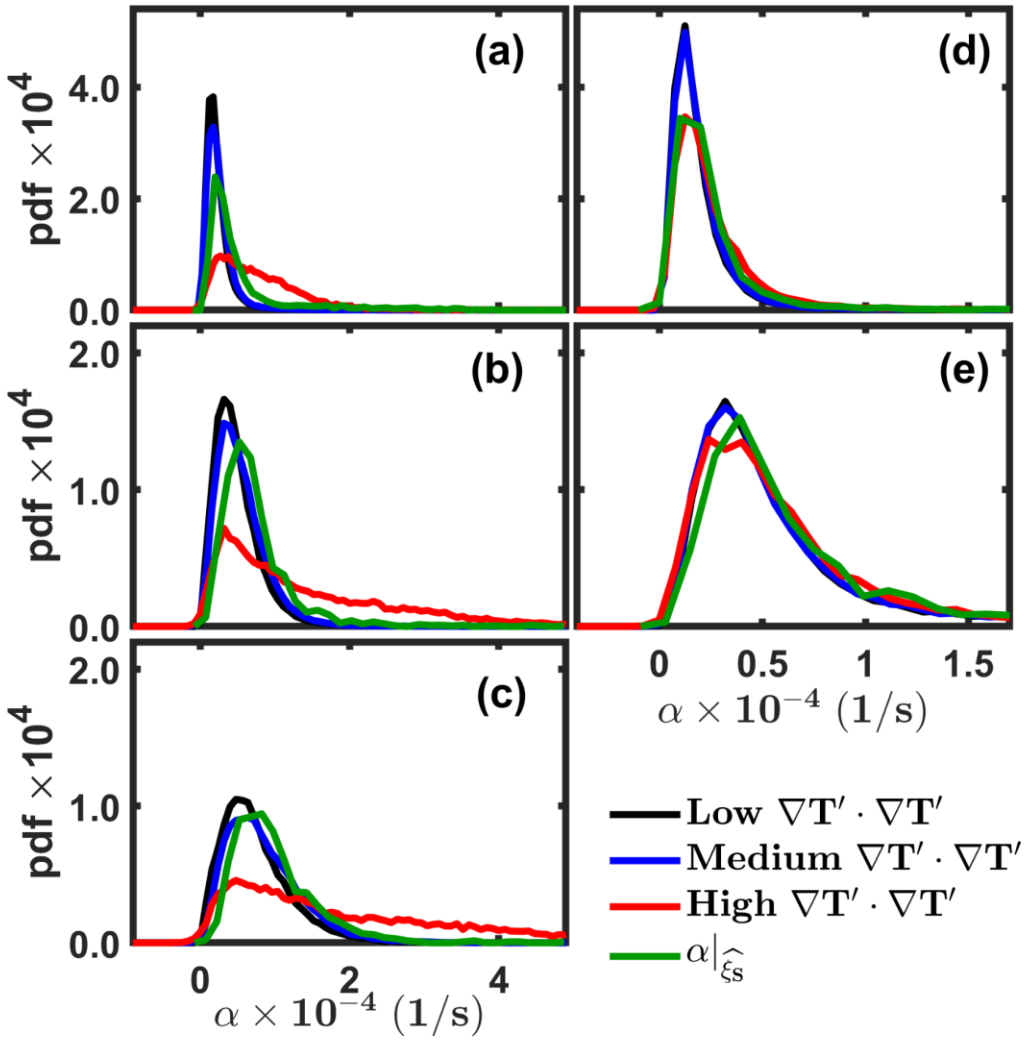

Figure 7.30: Probability density function (pdf) of α conditioned on various magnitudes of the thermal dissipation rate. Also shown is the pdf of α conditioned on stoichiometric mixture fraction value. (a) Re = 10,000, x/d = 20. (b) Re = 20,000, x/d = 20. (c) Re = 30,000, x/d = 20. (d) Re = 10,000, x/d = 40. (e) Re = 20,000, x/d = 40.

magnitudes. At x/d = 20, there are clear differences in the pdfs for α conditioned on large-magnitude dissipation. The probability of large values of α increases significantly and the positive tails of the pdf changes from exponential to near power law behavior. In addition, both the widths and the tails of the pdfs increase with increasing Reynolds number indicating a clear correlation

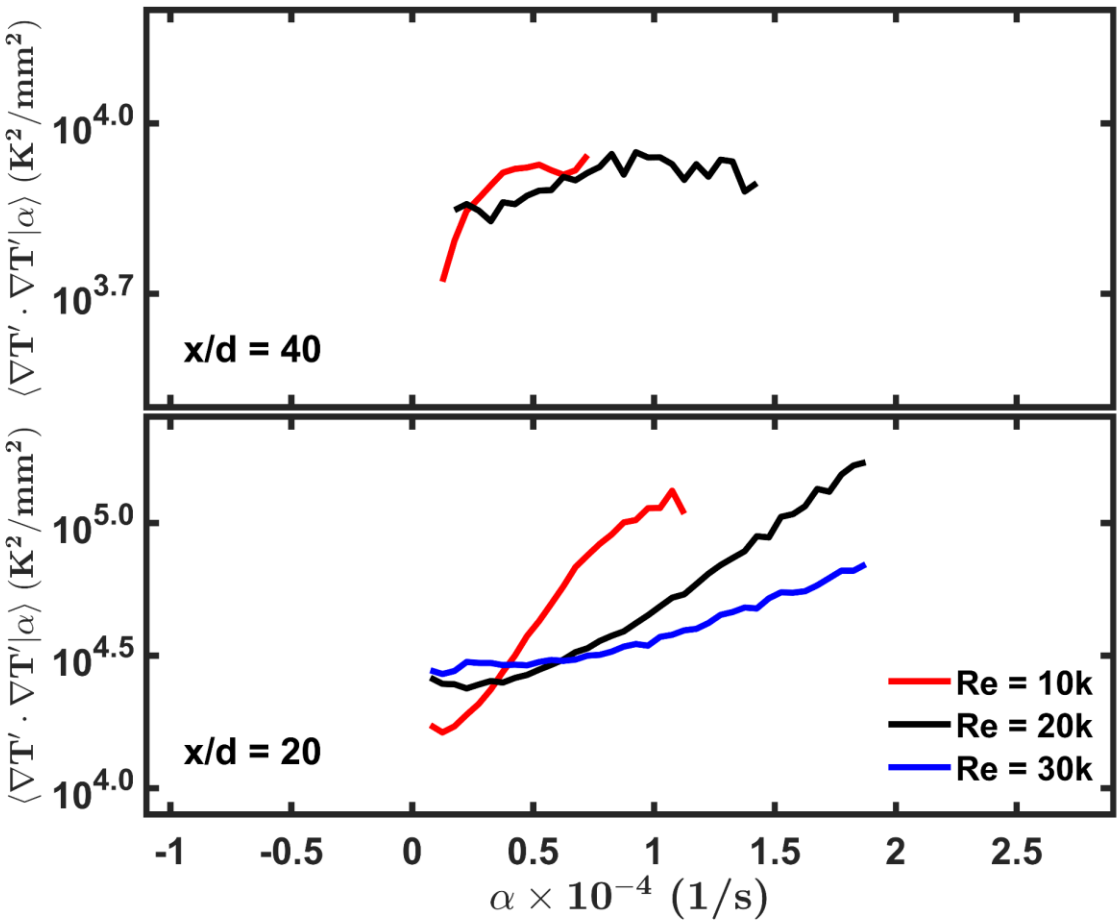

Figure 7.31: Mean thermal dissipation rate conditioned on α. (Top) x/d = 40. (Bottom) x/d = 20. Re = 10,000 shown in red, Re = 20,000 shown in black, and Re = 30,000 shown in blue.

between high values of the extensional strain and high-magnitude thermal dissipation. For x/d = 40 results, there is an increase in the width of the conditional pdfs with increasing Reynolds number as expected, but the pdfs of α all follow the same distribution regardless of conditioning constraint. This implies that at x/d = 40 (which is nearing the flame tip), there appears to be no preferential relationship between thermal dissipation rate and the most extensional principal strain rate component. Finally, it is noted that for all conditions, the most probable value of α is low regardless of the magnitude of the thermal strain rate. This shows that for the majority of the time,

the thermal dissipation rate layers experience low levels of extensional strain, which is likely due to the unsteady and intermittent nature of turbulence.

Figure 7.31 shows the mean of the thermal dissipation rate conditioned on α for all Reynolds number conditions and axial locations. For the calculation of the conditional mean, α

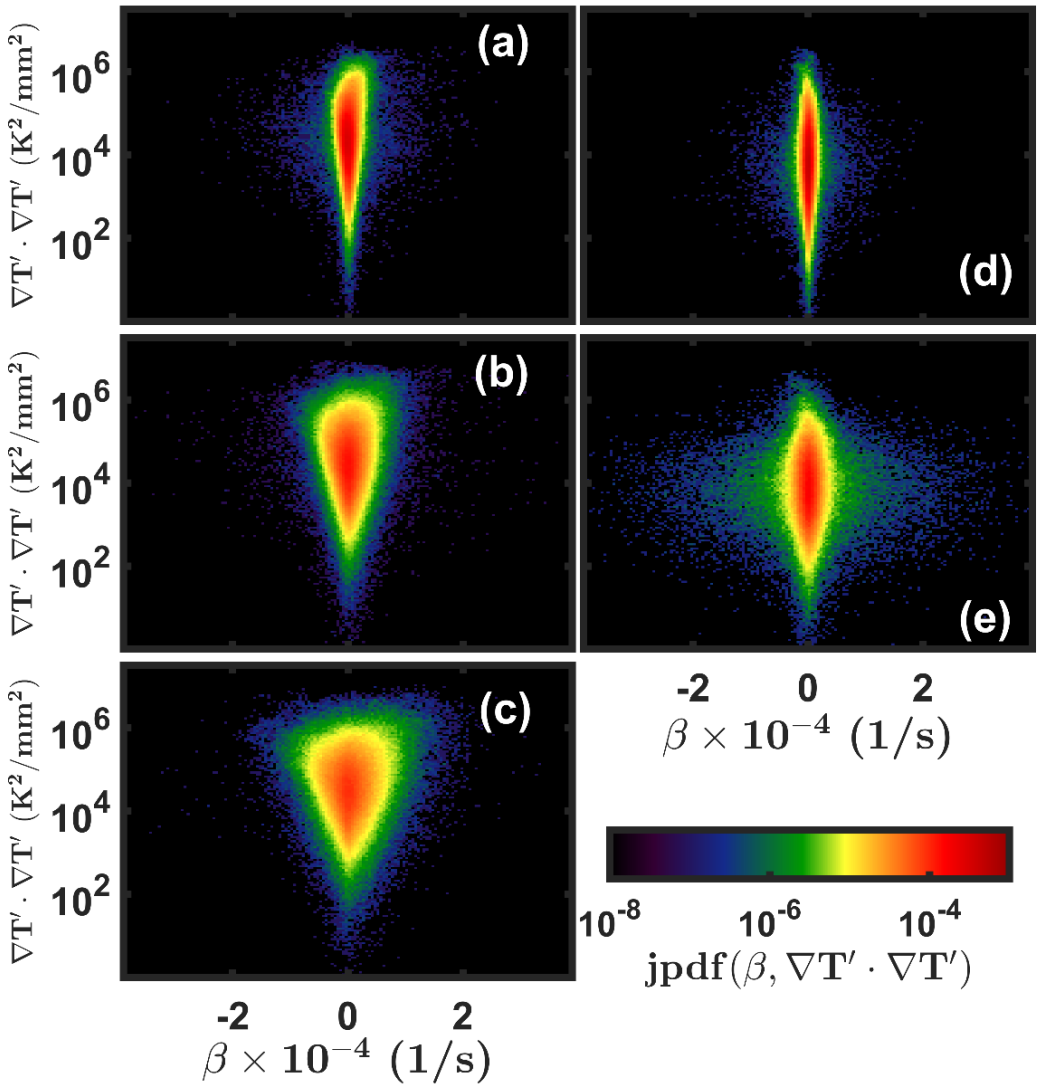

Figure 7.32: Joint pdfs (jpdfs) of intermediate principal strain rate component β and the thermal dissipation rate. (a) Re = 10,000, x/d = 20. (b) Re = 20,000, x/d = 20. (c) Re = 30,000, x/d = 20. (d) Re = 10,000, x/d = 40. (e) Re = 20,000, x/d = 40.

bins of 500 s^{-1} were used and only bins that contained at least 1000 samples were considered for analysis. At x/d = 40 the conditional mean of the thermal dissipation does not exceed 10^4 K/mm^2 and the peak value is independent of the two Reynolds numbers and value of α. This is consistent with the conditional pdf results shown in Fig. 7.30. Consistent with the pdf results shown above, at x/d = 20 there is a stronger correlation between α and the thermal dissipation rate, with an almost linear dependence of the thermal dissipation rate with α.

Figure 7.32 shows joint pdfs of intermediate principal strain rate component, β and the thermal dissipation rate for all flames and axial locations. For the data at x/d = 20, Fig. 7.32 shows that there is a negative skewness for β for dissipation rate values greater than 10^3, but the joint pdf appears symmetric about $\beta = 0$ for very small dissipation rate values. Similar to the jpdf of α, the width of the jpdf of β increases with increasing values of dissipation and with increasing Reynolds number. For the x/d = 40 measurements, jpdf appear fairly symmetric about $\beta = 0$ and the width of the pdf of β peaks at an intermediate value of dissipation (~10^3) and decreases for further increases in thermal dissipation rate.

Figure 7.33 shows the pdfs of β conditioned on various magnitudes of the thermal dissipation rate as well as conditioned on the stoichiometric mixture fraction. At x/d = 20, there only are small differences between the conditional pdfs of "Low" and "Medium" thermal dissipation rate. The difference is largely manifested in a reduction of the peak value of the pdf and a small increased probability of $\beta < 0$. Similar to the pdfs of α, there is no discernable effect of conditioning on the estimated stoichiometric mixture fraction as opposed to considering the "Medium" values of thermal dissipation rate. However, the pdfs show distinct differences for the case of "High" thermal dissipation compared to the other conditioned pdfs. There is a significant increase in the probability of $\beta > 0$. Positive values of the intermediate principal strain rate

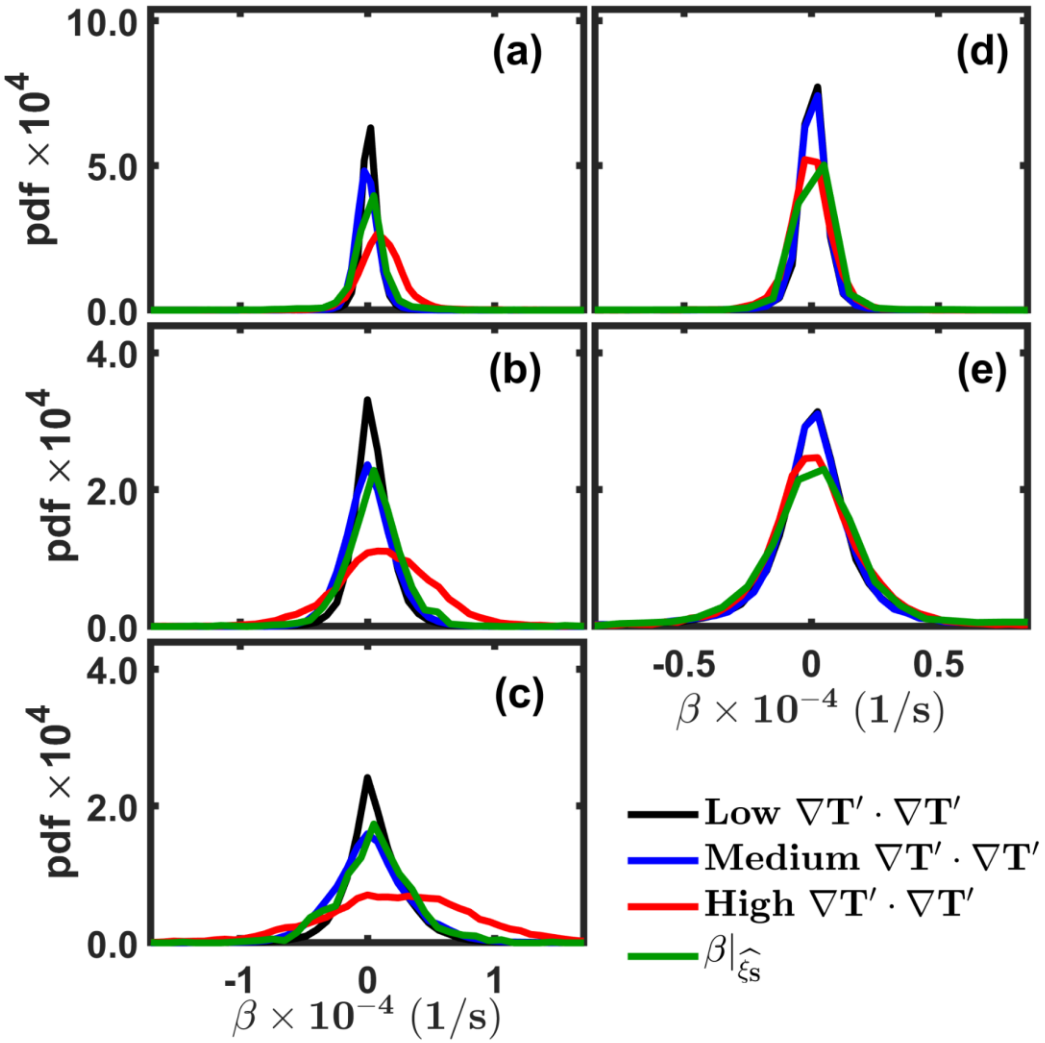

Figure 7.33: Probability density function (pdf) of β conditioned on various magnitudes of the thermal dissipation rate. Also shown is the pdf of β conditioned on the stoichiometric mixture fraction value. (a) Re = 10,000, x/d = 20. (b) Re = 20,000, x/d = 20. (c) Re = 30,000, x/d = 20. (d) Re = 10,000, x/d = 40. (e) Re = 20,000, x/d = 40.

component means that there are two extensional strain components and only one compressive strain component. This implies that the strain rate field is sheet forming and consequently, the most preferred topology of the dissipation layers will be that of layer or sheet-like structures. This is in agreement with several studies in non-reacting flows (e.g., [7, 221, 222]) and previous

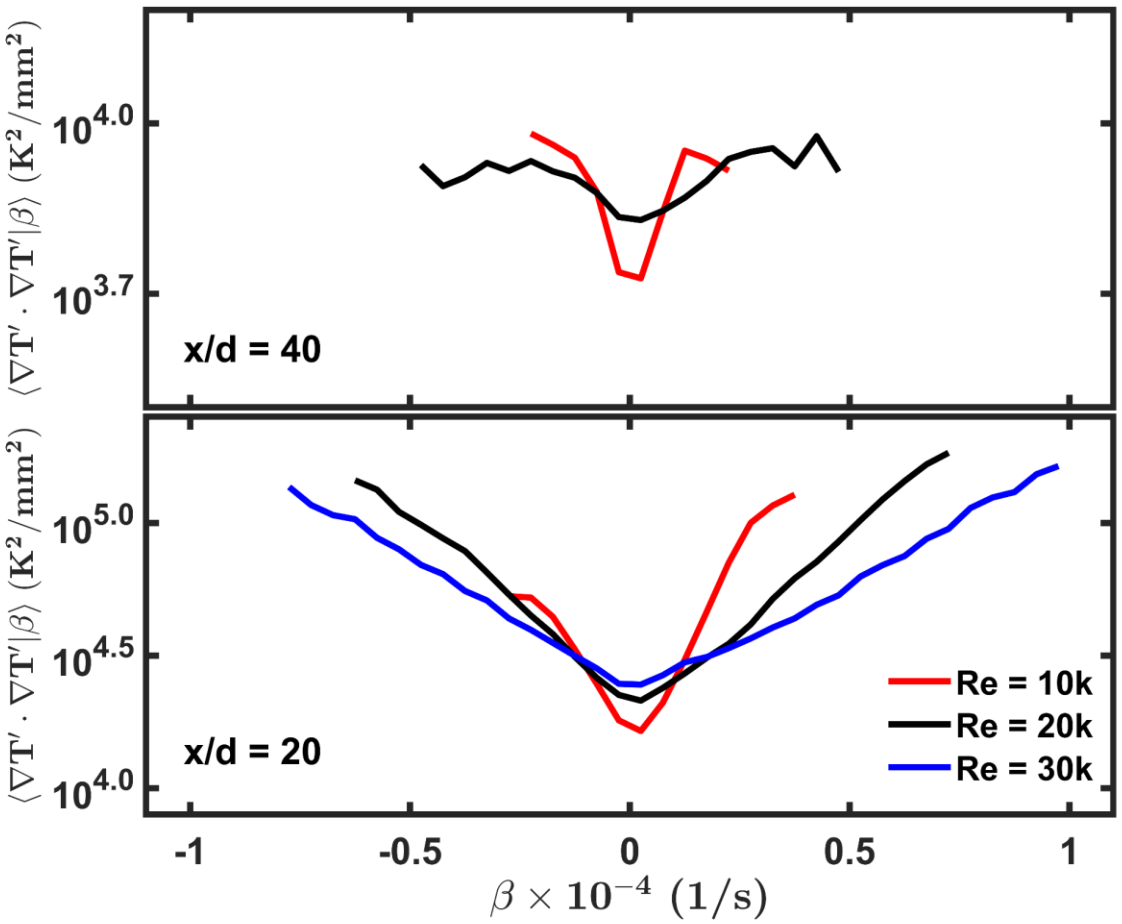

Figure 7.34: Mean thermal dissipation rate conditioned on β. (Top) x/d = 40. (Bottom) x/d = 20. Re = 10,000 shown in red, Re = 20,000 shown in black, and Re = 30,000 shown in blue.

measurements of thermal dissipation layers in reacting flows [51-54, 223]. Furthermore, Clemens et al. [7] showed that the sheet-forming strain rate fields were in fact, sheet-like themselves. The pdfs shown in Fig. 7.33 suggest that at x/d = 20, intense thermal dissipation regions are associated with a sheet-forming strain field and furthermore that high-magnitude dissipation occurs in regions of intense intermediate strain. This results is very similar to that observed in non-reacting turbulent jets when examining the pdf of the intermediate principal strain rate as a function of kinetic energy dissipation rate [7]. Their results showed that with increasing kinetic energy dissipation rate, the

peaks in the pdf of β move to more positive values and that intense kinetic energy dissipation regions occur in regions of intense positive intermediate strain. These results also agree with DNS studies of Ashurst et al. [9] and Lund and Rogers [211]. For the x/d = 40 results pdfs of β are symmetric and show no preferential correlation between β and the magnitude of the thermal dissipation rate.

Figure 7.34 shows the mean thermal dissipation rate conditioned on β for all Reynolds numbers and axial locations. For the calculation of the conditional mean, β bins of 500 s^{-1} were used and only bins that contained at least 1000 samples were considered for analysis. For all flames and axial locations the conditional mean of the thermal dissipation is at a minimum for $\beta = 0$ and increases in a nearly symmetric manner for both positive and negative values of β. At x/d = 40, the results for Re = 20,000 are a bit anomalous as compared to the remainder of the results in that the overall change in thermal dissipation magnitude is minimal with increasing values of β. For the Re = 10,000 results, there is a sharp rise in mean dissipation rate for increasing values of β, although the range of β is limited for this flame condition. At x/d = 20, all three Reynolds number cases show that there is a direct correlation between β and the thermal dissipation rate, where an increase in the magnitude of β leads to an increase in the magnitude of the thermal dissipation rate. In fact, for both positive and negative branches of β, the conditional means of dissipation appear to be approximately a linear function of β. It is interesting to note that the slope of mean dissipation rate as a function of β decreases with increasing Reynolds number. This implies that higher values of the mean dissipation rate are associated with lower values of β for the lower Reynolds number condition or equivalently, for a given value of β there is a corresponding decrease in the mean thermal dissipation rate for increasing Reynolds number. This is consistent with measurements of

Sreenivasan [224] who showed that the kinetic energy dissipation rate (relative to the rate of production) progressively decrease within increasing Reynolds number. Consistent with the pdfs shown in Fig. 7.33, there is a tendency towards $\beta > 0$ for the largest magnitudes of thermal dissipation.

Figure 7.35 shows the joint pdfs of the most compressive principal strain rate component, γ and the thermal dissipation rate for all flames and axial locations. Similar trends are observed as in the jpdfs of the most extensional strain rate α and the thermal dissipation rate. For data at x/d = 20 it is observed for all three Reynolds number flames that there is a large negative tail of the pdf of γ and the negative skewness increases with increasing magnitudes of thermal dissipation. This implies that large-magnitude compressive strain rates correlate with large-magnitude thermal dissipation. At x/d = 40, there is negative skewness in the pdf of γ for all values of the thermal dissipation rate, but the level of negative skewness peaks at an intermediate value of γ.

Figure 7.36 shows the pdfs of γ conditioned on various magnitudes of the thermal dissipation rate as well as conditioned on the stoichiometric mixture fraction. At x/d = 20, the results in Fig. 7.36 are somewhat different to those observed in Fig. 7.30 for the most extensional strain rate component α. Whereas for the conditional pdfs of α there was little change in the conditional pdfs for "Low" or "Medium" magnitudes of the thermal dissipation rate, there is a systematic increase in pdf width and negative skewness for increasing magnitude of dissipation. In addition, as the conditional magnitude of thermal dissipation is increased, the most probable value of γ increases to larger negative values. For the highest dissipation case, there is a clear indication that large-magnitude thermal dissipation is associated with intense compressive strain rate fields. At x/d = 40, all pdfs collapse to a very similar curve indicating there is no preferred relationship between increasing magnitudes of most compressive strain and thermal dissipation

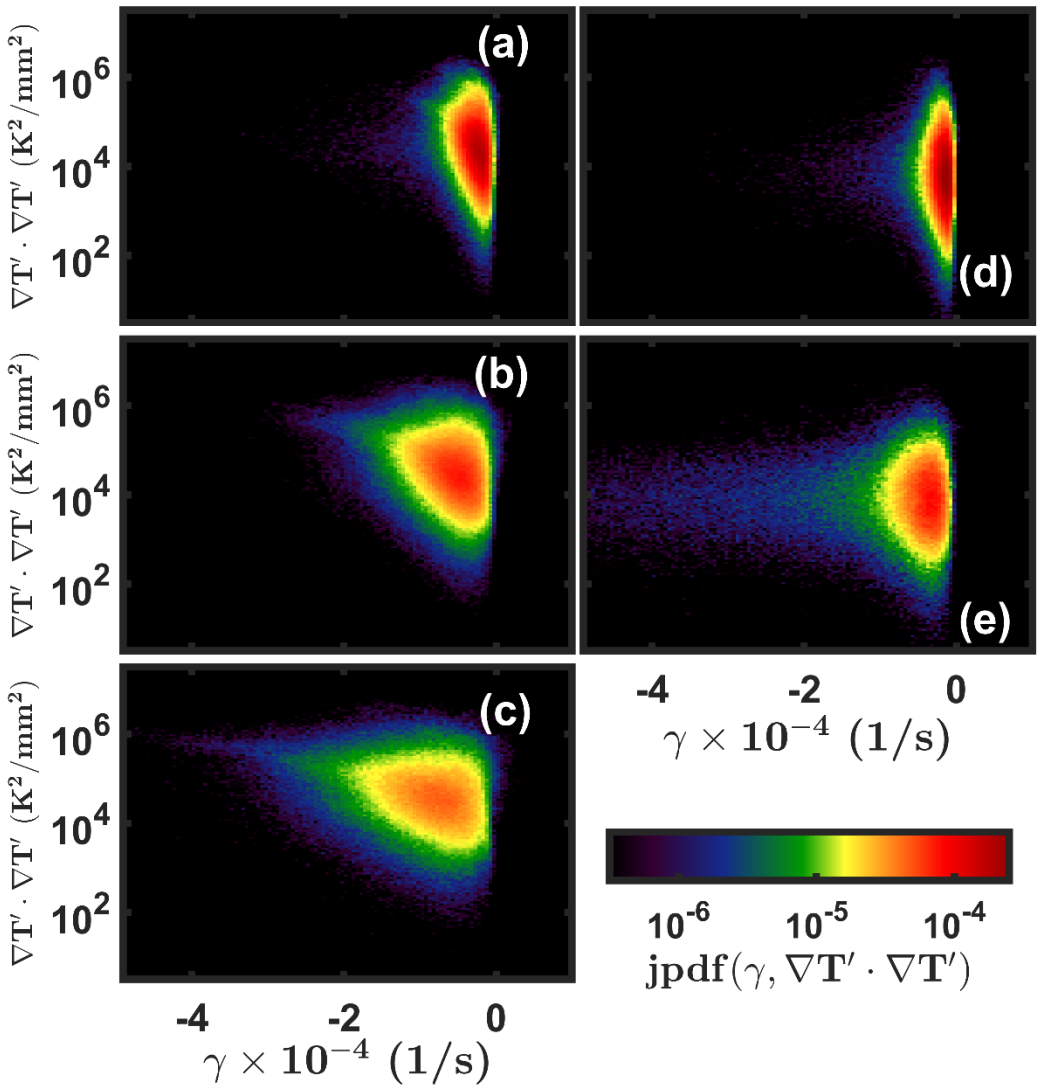

Figure 7.35: Joint pdfs (jpdfs) of compressive principal strain rate component γ and the thermal dissipation rate. (a) Re = 10,000, x/d = 20. (b) Re = 20,000, x/d = 20. (c) Re = 30,000, x/d = 20. (d) Re = 10,000, x/d = 40. (e) Re = 20,000, x/d = 40.

rate. There is an increase in the width of the pdf indicating that higher magnitudes of the compressive strain component exist for the Re = 20,000 case compared to the Re = 10,000 case.

Figure 7.37 shows the mean thermal dissipation rate conditioned on γ for all flames and axial locations. For the calculation of the conditional mean γ bins of 500 s^{-1} were used and only

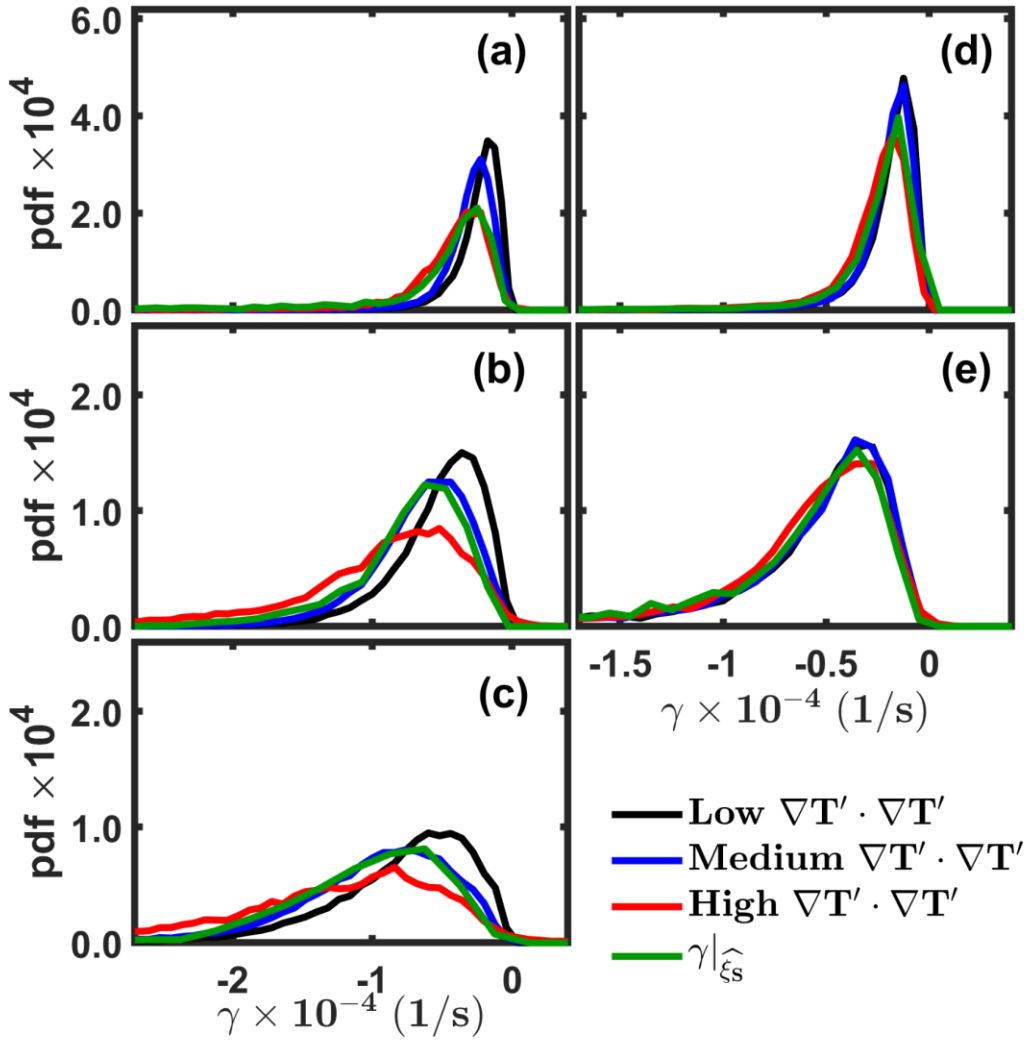

Figure 7.36: Probability density function (pdf) of γ conditioned on various magnitudes of the thermal dissipation rate. Also shown is the pdf of γ conditioned on the stoichiometric mixture fraction value for all flames and axial locations. (a) Re = 10,000, x/d = 20. (b) Re = 20,000, x/d = 20. (c) Re = 30,000, x/d = 20. (d) Re = 10,000, x/d = 40. (e) Re = 20,000, x/d = 40.

bins that contained at least 1000 samples were considered for analysis. The results at x/d = 40 are very similar to that observed for the mean thermal dissipation rate conditioned on α (Fig. 7.31) in the fact that the mean thermal dissipation rate is essentially independent of the value of γ and Reynolds number. At x/d = 20, there are some subtle differences between the mean dissipation

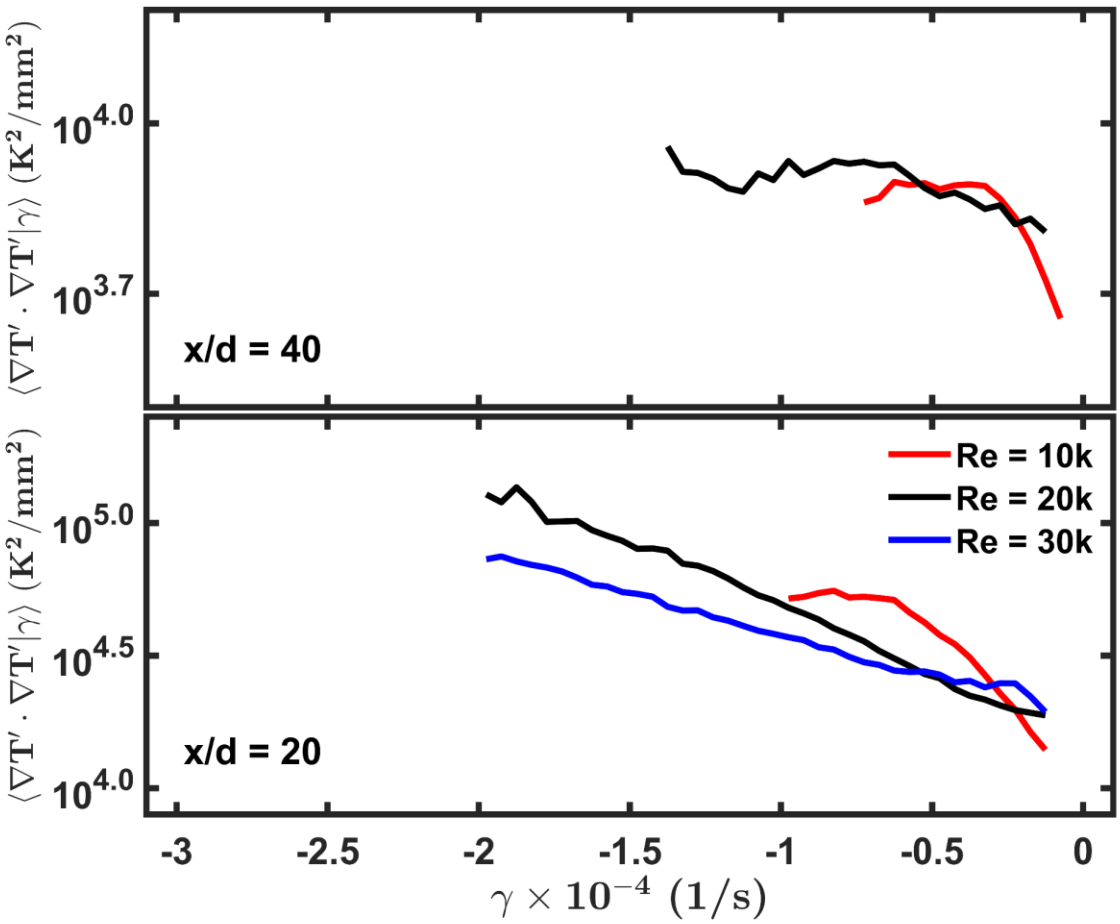

Figure 7.37: Mean of thermal dissipation rate conditioned on γ. (Top) x/d = 40. (Bottom) x/d = 20. Re = 10,000 shown in red, Re = 20,000 shown in black, and Re = 30,000 shown in blue.

Case	α^* (1/s)	β_+^* (1/s)	β_-^* (1/s)	γ^* (1/s)
Re = 20k, x/d = 20	15200	5190	-4760	-17000
Re = 30k, x/d = 20	22300	7360	-6350	-24000

Table 7.3: Comparison of principal strain values when the condtional mean of thermal dissipation reaches 10^5 K/mm^2.

mean dissipation rate, $\gamma > \alpha$. In addition, the mean thermal dissipation rate is more similar across Reynolds number for a given value γ compared to a given value of α. However, similar to the results discussed above in reference to the most extensional strain, the results shown in Fig. 7.36 conditioned on α as compared to the mean dissipation condition on γ. For example, for all Reynolds number cases the slope of the mean dissipation rate as a function of γ is less than the slope of the mean dissipation rate as a function of α. This implies that for a given value of the clearly show the strong correlation between thermal dissipation rate magnitude and the magnitude of γ, thus confirming that large magnitudes of thermal dissipation occur in regions of intense compressional strain.

To attempt to further clarify the differences between the compressive and extensional strains and to further explore the role of β on intense dissipation values, Table 7.3 shows values of α, β and γ for a conditional mean thermal dissipation rate of 10^5 K/mm^2 (denoted by ( )*) Table 7.3 shows that the compressive strain magnitude is larger than the extensional strain magnitude associated with this high value of thermal dissipation as postulated above based on the results shown in Figs. 7.31 and 7.37. In addition, the magnitude of the intermediate strain, β is double valued. The positive and negative values are denoted as $\beta_+^*$and β_-^*, respectively. At $\chi_T = 10^5$ K/mm^2, $\beta_+^* > \beta_-^*$. Both of these results suggests that (1) intense thermal dissipation regions (i.e., large-magnitude values of χ_T) are highly correlated to both the compressive and extensional principal strains, (2) the correlation is slightly stronger with the compressive strain compared to the extensional strain, and (3) intense thermal dissipation rate occurs in regions of intense intermediate strain and is strongly associated with a sheet-forming strain rate field.

Chapter 8. Summary and Future Work

8.1 Summary and Conclusions

The overarching goal of the current research is to characterize the statistical relationship and physical interactions between flow turbulence and the temperature field in turbulent non-premixed flames. This is accomplished with velocity and temperature measurements and several derived kinematic and thermal properties that are coupled in turbulent reacting flows. More specifically, the research is comprised of three main thrusts: (1) the application of high-speed (kHz acquisition rates) temperature and velocity measurements for a comparative spatio-temporal analysis of velocity and scalar fluctuations, (2) the development of a new measurement technique for simultaneous high-resolution temperature and velocity measurements in turbulent non-premixed flames, and (3) visualization and statistical analysis of the interaction between the turbulent flow and temperature fields, providing new information on the kinematic processes governing the observed flame topology.

High-repetition-rate planar temperature and velocity measurements were performed in a series of turbulent $CH_4/H_2/N_2$ non-premixed jet flames (Re = 15,200 and 22,800) that are well-known benchmark test cases within the International Workshop for Computation and Measurement of Turbulent Nonpremixed Flames ("TNF workshop"). The velocity measurements were performed using high-speed particle image velocimetry (PIV) and the temperature measurements were performed using high-speed planar Rayleigh scattering (LRS) thermometry.

The high-speed LRS-based temperature measurements, which were previously unavailable to the turbulent combustion community, were facilitated by the custom high-energy pulse burst laser system (HEPBS) developed within the Turbulence and Combustion Research Laboratory at Ohio State. The HEPBLS is a unique laser system which offers the combination of ultra-high laser pulse energies, high-repetition rates, and hundreds of sequential laser pulses per burst. During the course of this research, advances in the HEPBLS, along with the development of an optimized optical collection system led to significant advances in spatial resolution and signal-to-noise ratio compared to previous high-speed imaging measurements. A detailed assessment of the accuracy and precision of the velocity and temperature measurements was performed through a statistical comparison to previous results existing within the literature and the TNF database. Excellent agreement was observed between the statistics derived from the current high-speed imaging and previous uncorrelated, single-point measurements, giving confidence in the quantitative nature of the current results.

The spatially and temporally resolved measurements allowed the calculation of spatial, temporal, and joint spatio-temporal correlation functions as function of spatial position and Reynolds number. From the analysis of the correlation functions, integral length scales (both longitudinal and transverse) and time scales were determined for both temperature and the axial component of the velocity vector. An important part of the analysis in the current research was the direct comparison between the velocity and temperature statistics. Significant differences were observed in both the longitudinal integral length and time scales, where the integral scales for the axial velocity fluctuations were as much as three times greater than those of the temperature fluctuations. Since thermal fluctuations appear to be destroyed much more rapidly than velocity fluctuations, this indicates that the thermal dissipation is likely greater than kinetic energy

dissipation within these flames. The ratio of the longitudinal-to-transverse integral length scales were computed and used to assess isotropy within the flames. Both the temperature and velocity measurements show that the flow exhibits isotropy near centerline, but for increasing radial positions, isotropy is destroyed in the regions of high temperature and heat release.

Two-point, space-time correlations were computed and it was shown that the "elliptical model" developed by Zhao and He [161] provides improved accuracy in representing space-time correlations as compared to the commonly used Taylor's frozen flow hypothesis [156]. While the transformation appeared to more accurately represent the relationship between spatial and temporal correlations for the velocity fluctuations; its use appears satisfactory for temperature fluctuations as well. This work represents the first demonstration of the use of elliptical model in reacting flows and showed its viability for both velocity and (active) scalar fluctuations. Subsequently, the elliptical model was used to investigate the physical mechanisms governing the decorrelation of temperature and velocity fluctuations. In general the results demonstrate that the de-correlation of the axial velocity fluctuations are governed by two primary mechanisms: (i) convection by the mean flow and (ii) local turbulence-induced destruction. These observations are in agreement with those observed for velocity fluctuations in non-reacting, homogeneous shear flows [161, 165]. For the temperature fluctuations, the same two de-correlation mechanisms appear to play a significant role, but the results suggest additional effects of chemical reactivity and/or gas expansion also are important.

The second part of this research focused on directly characterizing the physical interactions and linkage between the velocity and temperature fields through simultaneous temperature and velocity measurements. This required the development of a thermometry approach that could be applied in the presence of high levels of interference originating from the scattering from PIV

tracer particles. A new variation of filtered Rayleigh scattering (FRS) was specifically developed in this work for application in turbulent non-premixed flames. FRS is a modification of traditional LRS method that uses the combination of an atomic or molecular filter placed in front of a camera and narrow linewidth laser source to reject unwanted surface/particle scattering while collecting gas-phase scattering. In this manner, gas-phase information (temperature in the current work) can be accurately deduced without interference. Proper interpretation of the measured FRS signal requires detailed knowledge of the temperature- and species-specific Rayleigh-Brillouin scattering (RBS) spectroscopy. Since this cannot be measured *in situ* during turbulent flame measurements, the RBS lineshapes are modeled and this information is incorporated into signal analysis. One of the most commonly used RBS models is the Tenti S6 kinetic model [119] which has been shown to be quite accurate, although previous assessments have been performed over a limited range of species and temperatures. As part of the current FRS-based thermometry development, a detailed assessment of the accuracy of the Tenti S6 model for combustion-relevant gas species at combustion-relevant temperatures was performed. For all individual species tested, which included N_2, O_2, Ar, CO, CO_2, H_2, CH_4, and H_2O (indirectly), the Tenti S6 model was shown to be accurate over temperatures ranging from 300 K to 1400 K. In addition, measurements in near-adiabatic hydrogen and hydrocarbon flames (1500 K < T < 2200 K) were performed that also verified the accuracy of the Tenti S6 model.

Following model assessment, a specific fuel mixture (CH_4/H_2/Ar) was designed (i.e., "fuel tailoring") such that quantitative temperature measurements could be determined from a single FRS measurement without the need for additional species information nor any assumptions about the chemistry. A comprehensive assessment of the accuracy of the approach was carried out by comparing the FRS-derived temperature results (instantaneous measurements and statistics) to

simultaneous LRS temperature measurements. The LRS measurements serve as an independent standard for assessing the experimental FRS-based results. Measurements from Re = 10,000, 20,000, and 30,000 turbulent non-premixed flames closely agree between the two measurement approaches, providing confidence in the newly developed FRS thermometry approach for quantitative temperature measurements under turbulent non-premixed flame conditions.

Simultaneous FRS and stereo PIV (sPIV) measurements were carried out in the aforementioned $CH_4/H_2/Ar$ flames, yielding the first set of joint temperature and velocity results in turbulent non-premixed flames. The accuracy of the temperature measurements in the presence of tracer particles (and associated scattering) was verified by agreement with temperature measurements from particle-free flames, demonstrating effective blocking of unwanted particle scattering. In addition to high accuracy, the FRS-based temperature measurements demonstrated high SNR and spatial resolution, where it was shown that the dissipative range was resolved. The accuracy of the three-component velocity measurements was assessed through comparisons with known scaling laws, statistical behavior, and the proper demonstration of self-similarity. Qualitative visualization showcased the interaction between temperature gradient and thermal dissipation rate fields with various kinematic properties, including the vorticity and strain rate fields. Quite frequently it was observed that large-magnitude values of strain rate appeared to be spatially coincident with regions of large thermal gradients or large-magnitude thermal dissipation, especially near the primary reaction zone. These results are consistent with previous studies in lower-Reynolds number non-premixed flames that showed the overlap between vorticity and strain rate with OH layers.

The unique set of joint velocity-temperature data also was used to generate quantitative statistics characterizing turbulent transport and flow-induced scalar topology. The axial and radial

scalar heat flux was computed as a function of radial position at axial locations of x/d = 20 and 40. In the radial direction, the calculated scalar heat flux appears to be satisfactorily described by the gradient transport (GT) hypothesis for all Reynolds numbers and at all spatial locations. However, in the axial direction, GT is observed near centerline, but for radial positions away from centerline, there appears to be evidence of counter gradient transport (CGT). The alignment index (*AI*) between the gradients of the axial component of velocity and temperature was computed. The alignment index is a statistical measure indicating the spatial alignment between the gradients of two fields and yields quantification on the degree of correlation or anti-correlation between the topological characteristics of two fields. Probability density functions (pdfs) of *AI* presented and it was observed that for all flames and spatial locations the gradients of the axial velocity and temperature were more often aligned or directly opposed versus showing a random orientation. At x/d = 20, the gradients are predominately opposed, while at x/d = 40, the gradients are mostly aligned, which is consistent with expectations based on the radial profiles of the mean axial velocity and temperature at the two spatial positions. The alignment index was further conditioned on various magnitudes of the thermal dissipation rate. For large-magnitude dissipation, there was a notable increase in the peak value of the pdf (opposed gradients at x/d = 20 and aligned gradients at x/d = 40) with a significant reduction in the probability of other alignments. This result indicated a strong correlation between velocity-temperature structural overlap and the presence of high-magnitude thermal dissipation.

Finally, the statistical relationship between the thermal dissipation rate and various kinematic properties was investigated to understand the mechanisms governing the observed topology of the temperature (scalar) field. Probability density functions and conditional statistics showed a clear relationship between large-magnitude thermal dissipation and the principal strain

rates. For high levels of dissipation, the intermediate principal strain rate was found to be preferentially positive which implies that large-magnitude thermal dissipation occurs when the strain rate field is organized into sheet-like structures (with the thermal dissipation also formed into sheet like structures). For large-magnitude dissipation, both the most extensive and compressive principal strain rates were observed to strongly correlate with the thermal dissipation. This statistical result is strongly supported by the qualitative visualization reported in this dissertation. The strong statistical correlation indicates that both play a significant role in generating the strongest dissipation structures; however, it was observed that with increasing Reynolds number, the most compressive principal strain rate plays a larger role (i.e., a stronger correlation).

8.2 Brief Comments on Future Work

The newly developed capability of simultaneous temperature and velocity measurements in turbulent non-premixed flames presents several additional research directions for understanding the interaction and coupling between flow turbulence and scalar fields in turbulent reacting flows. A key area is the topological structure of the thermal gradient and dissipation fields. Extensive work has been performed by Frank and co-workers [51-54] using high-resolution temperature measurements that includes examination of the thermal dissipation layer thicknesses, curvature, and orientation. The simultaneous temperature and velocity data from the current work allows for a critical extension to the work of Frank and co-workers by allowing for the conditioning on various kinematic parameters. This analysis will help to determine the mechanisms through which the turbulent flow forms (and destroys) the scalar topology.

In addition, an extension of the dimensionality of the velocity measurements from the current implementation of stereo PIV to tomographic PIV [135] is recommended. Tomographic PIV is an advanced PIV technique that resolves velocity vectors throughout a volume and enables the measurement of the full velocity gradient tensor. This would allow for the determination of all vorticity components as well as the direct determination of the full strain rate tensor and principal strain components. Results using measurements of the full strain rate tensor in the same turbulent flames can provide an assessment of the validity of the assumptions used to estimate the strain rate tensor and perform the principal component analysis presented in the current dissertation.

Bibliography

[1] L. L. N. Laboratory, "Energy Flow Charts," ed, 2018.

[2] A. C. Eckbreth, *Laser diagnostics for combustion temperature and species*. Amsterdam, The Netherlands: Gordon and Breach Publishers, 1996.

[3] K. Kohse-Höinghaus, R. S. Barlow, M. Aldén, and J. Wolfrum, "Combustion at the focus: laser diagnostics and control," *Proceedings of the Combustion Institute,* vol. 30, no. 1, pp. 89-123, 2005.

[4] R. S. Barlow, "Laser diagnostics and their interplay with computations to understand turbulent combustion," *Proceedings of the Combustion Institute,* vol. 31, no. 1, pp. 49-75, 2007.

[5] K. Bray, "The challenge of turbulent combustion," in *Symposium (International) on Combustion*, 1996, vol. 26, no. 1, pp. 1-26: Elsevier.

[6] R. S. Barlow. International Workshop on Measurement and Computation of Turbulent Nonpremixed Flames [Online]. Available: https://tnfworkshop.org/

[7] B. Ganapathisubramani, K. Lakshminarasimhan, and N. T. Clemens, "Investigation of three-dimensional structure of fine scales in a turbulent jet by using cinematographic stereoscopic particle image velocimetry," (in English), *Journal of Fluid Mechanics,* vol. 598, pp. 141-175, 2008 Mar 10
2015-08-15 2008.

[8] F. Lemoine, Y. Antoine, M. Wolff, and M. Lebouche, "Simultaneous temperature and 2D velocity measurements in a turbulent heated jet using combined laser-induced fluorescence and LDA," *Experiments in fluids,* vol. 26, no. 4, pp. 315-323, 1999.

[9] W. T. Ashurst, A. R. Kerstein, R. M. Kerr, and C. H. Gibson, "Alignment of vorticity and scalar gradient with strain rate in simulated Navier–Stokes turbulence," *The Physics of Fluids,* vol. 30, no. 8, pp. 2343-2353, 1987.

[10] Y. Antoine, F. Lemoine, and M. Lebouché, "Turbulent transport of a passive scalar in a round jet discharging into a co-flowing stream," *European Journal of Mechanics-B/Fluids,* vol. 20, no. 2, pp. 275-301, 2001.

[11] R. Antonia, A. Prabhu, and S. Stephenson, "Conditionally sampled measurements in a heated turbulent jet," *Journal of Fluid Mechanics,* vol. 72, no. 3, pp. 455-480, 1975.

[12] R. Chevray and N. Tutu, "Intermittency and preferential transport of heat in a round jet," *Journal of Fluid Mechanics,* vol. 88, no. 1, pp. 133-160, 1978.

[13] A. Darisse, J. Lemay, and A. Benaïssa, "Investigation of passive scalar mixing in a turbulent free jet using simultaneous LDV and cold wire measurements," *International Journal of Heat and Fluid Flow,* vol. 44, pp. 284-292, 2013.
[14] F. Lemoine, M. Wolff, and M. Lebouche, "Simultaneous concentration and velocity measurements using combined laser-induced fluorescence and laser Doppler velocimetry: Application to turbulent transport," *Experiments in Fluids,* vol. 20, no. 5, pp. 319-327, 1996.
[15] S. B. Pope, *Turbulent Flows*. Cambridge: Cambridge University Press, 2000.
[16] H. Tennekes, J. L. Lumley, and J. Lumley, *A first course in turbulence*. MIT press, 1972.
[17] N. Peters, *Turbulent combustion*. Cambridge, [England]; New York: Cambridge University Press, 2000.
[18] R. Bilger, S. Stårner, and R. Kee, "On reduced mechanisms for methane/air combustion in nonpremixed flames," *Combustion and Flame,* vol. 80, no. 2, pp. 135-149, 1990.
[19] N. Peters, "Laminar diffusion flamelet models in non-premixed turbulent combustion," *Progress in Energy and Combustion Science,* vol. 10, no. 3, pp. 319-339, 1984/01/01/ 1984.
[20] N. Peters, "Laminar flamelet concepts in turbulent combustion," *Symposium (International) on Combustion,* vol. 21, no. 1, pp. 1231-1250, 1988/01/01/ 1988.
[21] H. Pitsch and N. Peters, "A consistent flamelet formulation for non-premixed combustion considering differential diffusion effects," *Combustion and flame,* vol. 114, no. 1-2, pp. 26-40, 1998.
[22] H. Pitsch, "Large-eddy simulation of turbulent combustion," *Annu. Rev. Fluid Mech.,* vol. 38, pp. 453-482, 2006.
[23] A. Y. Klimenko, "Multicomponent diffusion of various admixtures in turbulent flow," *Fluid dynamics,* vol. 25, no. 3, pp. 327-334, 1990.
[24] R. Bilger, "Conditional moment closure for turbulent reacting flow," *Physics of Fluids A: Fluid Dynamics,* vol. 5, no. 2, pp. 436-444, 1993.
[25] A. Y. Klimenko and R. W. Bilger, "Conditional moment closure for turbulent combustion," *Progress in energy and combustion science,* vol. 25, no. 6, pp. 595-687, 1999.
[26] R. S. Barlow and J. H. Frank, "Effects of turbulence on species mass fractions in methane/air jet flames," *Symposium (International) on Combustion,* vol. 27, no. 1, pp. 1087-1095, 1998/01/01/ 1998.
[27] R. Cabra, T. Myhrvold, J. Chen, R. Dibble, A. Karpetis, and R. Barlow, "Simultaneous laser Raman-Rayleigh-LIF measurements and numerical modeling results of a lifted turbulent H2/N2 jet flame in a vitiated coflow," *Proceedings of the Combustion Institute,* vol. 29, no. 2, pp. 1881-1888, 2002.
[28] V. Bergmann, W. Meier, D. Wolff, and W. Stricker, "Application of spontaneous Raman and Rayleigh scattering and 2D LIF for the characterization of a turbulent

CH4/H2/N2 jet diffusion flame," *Applied Physics B: Lasers & Optics,* Article vol. 66, no. 4, p. 489, 1998.

[29] F. Fuest, R. S. Barlow, G. Magnotti, and J. A. Sutton, "Scalar dissipation rates in a turbulent partially-premixed dimethyl ether/air jet flame," *Combustion and Flame,* vol. 188, no. Supplement C, pp. 41-65, 2018/02/01/ 2018.

[30] D. Geyer, A. Kempf, A. Dreizler, and J. Janicka, "Scalar dissipation rates in isothermal and reactive turbulent opposed-jets: 1-D-Raman/Rayleigh experiments supported by LES," *Proceedings of the Combustion Institute,* vol. 30, no. 1, pp. 681-689, 2005/01/01/ 2005.

[31] B. Dally, A. Masri, R. Barlow, and G. Fiechtner, "Instantaneous and mean compositional structure of bluff-body stabilized nonpremixed flames," *Combustion and Flame,* vol. 114, no. 1-2, pp. 119-148, 1998.

[32] R. S. Barlow, M. J. Dunn, M. S. Sweeney, and S. Hochgreb, "Effects of preferential transport in turbulent bluff-body-stabilized lean premixed CH4/air flames," *Combustion and Flame,* vol. 159, no. 8, pp. 2563-2575, 2012.

[33] M. Gregor, F. Seffrin, F. Fuest, D. Geyer, and A. Dreizler, "Multi-scalar measurements in a premixed swirl burner using 1D Raman/Rayleigh scattering," *Proceedings of the Combustion Institute,* vol. 32, no. 2, pp. 1739-1746, 2009.

[34] R. S. Barlow, G.-H. Wang, P. Anselmo-Filho, M. Sweeney, and S. Hochgreb, "Application of Raman/Rayleigh/LIF diagnostics in turbulent stratified flames," *Proceedings of the Combustion Institute,* vol. 32, no. 1, pp. 945-953, 2009.

[35] S. Nandula, R. Pitz, R. Barlow, and G. Fiechtner, "Rayleigh/Raman/LIF measurements in a turbulent lean premixed combustor," in *34th Aerospace Sciences Meeting and Exhibit*, 1996, p. 937.

[36] S. Stårner, R. Bilger, K. Lyons, J. Frank, and M. Long, "Conserved scalar measurements in turbulent diffusion flames by a Raman and Rayleigh ribbon imaging method," *Combustion and flame,* vol. 99, no. 2, pp. 347-354, 1994.

[37] J. Kelman and A. Masri, "Reaction zone structure and scalar dissipation rates in turbulent diffusion flames," *Combustion science and technology,* vol. 133, no. 4-6, pp. 17-55, 1998.

[38] S. Starner, R. Bilger, M. Long, J. Frank, and D. Marran, "Scalar dissipation measurements in turbulent jet diffusion flames of air diluted methane and hydrogen," *Combustion science and technology,* vol. 129, no. 1-6, pp. 141-163, 1997.

[39] J. H. Frank, S. A. Kaiser, and M. B. Long, "Reaction-rate, mixture-fraction, and temperature imaging in turbulent methane/air jet flames," *Proceedings of the Combustion Institute,* vol. 29, no. 2, pp. 2687-2694, 2002.

[40] J. Frank, S. Kaiser, and M. Long, "Multiscalar imaging in partially premixed jet flames with argon dilution," *Combustion and flame,* vol. 143, no. 4, pp. 507-523, 2005.

[41] J. A. Sutton and J. F. Driscoll, "A method to simultaneously image two-dimensional mixture fraction, scalar dissipation rate, temperature and fuel consumption rate

fields in a turbulent non-premixed jet flame," *Experiments in fluids,* vol. 41, no. 4, pp. 603-627, 2006.

[42] J. A. Sutton and J. F. Driscoll, "Imaging of local flame extinction due to the interaction of scalar dissipation layers and the stoichiometric contour in turbulent non-premixed flames," *Proceedings of the Combustion Institute,* vol. 31, no. 1, pp. 1487-1495, 2007.

[43] J. A. Sutton and J. F. Driscoll, "Measurements and statistics of mixture fraction and scalar dissipation rates in turbulent non-premixed jet flames," *Combustion and Flame,* vol. 160, no. 9, pp. 1767-1778, 2013.

[44] A. Hsu, V. Narayanaswamy, N. Clemens, and J. Frank, "Mixture fraction imaging in turbulent non-premixed flames with two-photon LIF of krypton," *Proceedings of the combustion institute,* vol. 33, no. 1, pp. 759-766, 2011.

[45] M. Queiroz, "Temperature Dissipation Measurements in a Lifted Turbulent Diffusion Flame AU - BOYER, LeMOYNE," *Combustion Science and Technology,* vol. 79, no. 1-3, pp. 1-34, 1991/09/01 1991.

[46] E. Effelsberg and N. Peters, "Scalar dissipation rates in turbulent jets and jet diffusion flames," in *Symposium (International) on Combustion*, 1989, vol. 22, no. 1, pp. 693-700: Elsevier.

[47] G. Wang, N. Clemens, and P. Varghese, "Two-point, high-repetition-rate Rayleigh thermometry in flames: techniques to correct for apparent dissipation induced by noise," *Applied Optics,* vol. 44, no. 31, pp. 6741-6751, 2005.

[48] D. A. Everest, J. F. Driscoll, W. J. A. Dahm, and D. A. Feikema, "Images of the two-dimensional field and temperature gradients to quantify mixing rates within a non-premixed turbulent jet flame," *Combustion and Flame,* vol. 101, no. 1 - 2, pp. 58-60, 1995.

[49] G. H. Wang, R. S. Barlow, and N. T. Clemens, "Quantification of resolution and noise effects on thermal dissipation measurements in turbulent non-premixed jet flames," *Proceedings of the Combustion Institute,* vol. 31, no. 1, pp. 1525-1532, 2007/01/01/ 2007.

[50] G. H. Wang, N. T. Clemens, P. L. Varghese, and R. S. Barlow, "Turbulent time scales in a nonpremixed turbulent jet flame by using high-repetition rate thermometry," *Combustion and Flame,* vol. 152, no. 3, pp. 317-335, 2008/02/01/ 2008.

[51] S. A. Kaiser and J. H. Frank, "Imaging of dissipative structures in the near field of a turbulent non-premixed jet flame," *Proceedings of the Combustion Institute,* vol. 31, no. 1, pp. 1515-1523, 2007/01/01/ 2007.

[52] J. H. Frank and S. A. Kaiser, "High-resolution imaging of dissipative structures in a turbulent jet flame with laser Rayleigh scattering," *Experiments in Fluids,* vol. 44, no. 2, pp. 221-233, 2008.

[53] S. A. Kaiser and J. H. Frank, "Spatial scales of extinction and dissipation in the near field of non-premixed turbulent jet flames," *Proceedings of the Combustion Institute,* vol. 32, no. 2, pp. 1639-1646, 2009/01/01/ 2009.

[54] J. H. Frank and S. A. Kaiser, "High-resolution imaging of turbulence structures in jet flames and non-reacting jets with laser Rayleigh scattering," *Experiments in Fluids,* vol. 49, no. 4, pp. 823-837, 2010/10/01 2010.
[55] S. Burke and T. Schumann, "Diffusion flames," *Industrial & Engineering Chemistry,* vol. 20, no. 10, pp. 998-1004, 1928.
[56] M. Aldén, J. Bood, Z. Li, and M. Richter, "Visualization and understanding of combustion processes using spatially and temporally resolved laser diagnostic techniques," *Proceedings of the Combustion Institute,* vol. 33, no. 1, pp. 69-97, 2011.
[57] B. Böhm, C. Heeger, R. L. Gordon, and A. Dreizler, "New Perspectives on Turbulent Combustion: Multi-Parameter High-Speed Planar Laser Diagnostics," *Flow, Turbulence and Combustion,* journal article vol. 86, no. 3, pp. 313-341, April 01 2011.
[58] K. Kohse-Höinghaus and J. B. Jeffries, *Applied combustion diagnostics*. New York: Taylor & Francis, 2002.
[59] N. M. Laurendeau, "Temperature measurements by light-scattering methods," *Progress in Energy and Combustion Science,* vol. 14, no. 2, pp. 147-170, 1988/01/01/ 1988.
[60] F.-Q. Zhao and H. Hiroyasu, "The applications of laser Rayleigh scattering to combustion diagnostics," *Progress in Energy and Combustion Science,* vol. 19, no. 6, pp. 447-485, 1993/01/01/ 1993.
[61] D. A. Long, *Raman spectroscopy*. New York: McGraw-Hill, 1977.
[62] J. W. Daily, "Laser induced fluorescence spectroscopy in flames," *Progress in Energy and Combustion Science,* vol. 23, no. 2, pp. 133-199, 1997/01/01/ 1997.
[63] D. A. Greenhalgh, "Quantitative CARS Spectroscopy," in *Advances in Non-linear Spectroscopy*New York: Wiley, 1988, pp. 193-251.
[64] C. Abram, B. Fond, and F. Beyrau, "Temperature measurement techniques for gas and liquid flows using thermographic phosphor tracer particles," *Progress in Energy and Combustion Science,* 2018.
[65] G. H. Wang, N. T. Clemens, and P. L. Varghese, "High-repetition rate measurements of temperature and thermal dissipation in a non-premixed turbulent jet flame," *Proceedings of the Combustion Institute,* vol. 30, no. 1, pp. 691-699, 2005/01/01/ 2005.
[66] B. Bork, B. Böhm, C. Heeger, S. R. Chakravarthy, and A. Dreizler, "1D high-speed Rayleigh measurements in turbulent flames," *Applied Physics B,* journal article vol. 101, no. 3, pp. 487-491, November 01 2010.
[67] J. Westerweel, "Fundamentals of digital particle image velocimetry," *Measurement science and technology,* vol. 8, no. 12, p. 1379, 1997.
[68] A. Favre, "Review on space-time correlations in turbulent fluids," *Journal of Applied Mechanics,* vol. 32, no. 2, pp. 241-257, 1965.
[69] J. M. Wallace, "Space-time correlations in turbulent flow: A review," *Theoretical and Applied Mechanics Letters,* vol. 4, no. 2, p. 022003, 2014/01/01/ 2014.

[70] B. Thurow, N. Jiang, and W. Lempert, "Review of ultra-high repetition rate laser diagnostics for fluid dynamic measurements," *Measurement Science and Technology,* vol. 24, no. 1, p. 012002, 2012.
[71] V. Sick, "High speed imaging in fundamental and applied combustion research," *Proceedings of the Combustion Institute,* vol. 34, no. 2, pp. 3509-3530, 2013.
[72] T. M. Dyer, "Rayleigh scattering measurements of time-resolved concentration in a turbulent propane jet," *AIAA Journal,* vol. 17, no. 8, pp. 912-914, 1979.
[73] M. P. Wernet, "Temporally resolved PIV for space–time correlations in both cold and hot jet flows," *Measurement Science and Technology,* vol. 18, no. 5, p. 1387, 2007.
[74] O. Buxton and B. Ganapathisubramani, "PIV measurements of convection velocities in a turbulent mixing layer," in *Journal of Physics: Conference Series*, 2011, vol. 318, no. 5, p. 052038: IOP Publishing.
[75] W. Wang, X.-L. Guan, and N. Jiang, "TRPIV investigation of space-time correlation in turbulent flows over flat and wavy walls," *Acta Mechanica Sinica,* vol. 30, no. 4, pp. 468-479, 2014.
[76] C. Schulz and V. Sick, "Tracer-LIF diagnostics: quantitative measurement of fuel concentration, temperature and fuel/air ratio in practical combustion systems," *Progress in energy and combustion science,* vol. 31, no. 1, pp. 75-121, 2005.
[77] J. D. Smith and V. Sick, "Crank-angle resolved imaging of biacetyl laser-induced fluorescence in an optical internal combustion engine," *Applied Physics B,* vol. 81, no. 5, pp. 579-584, 2005.
[78] J. D. Smith and V. Sick, "Quantitative, dynamic fuel distribution measurements in combustion-related devices using laser-induced fluorescence imaging of biacetyl in iso-octane," *Proceedings of the Combustion Institute,* vol. 31, no. 1, pp. 747-755, 2007.
[79] B. Peterson and V. Sick, "Simultaneous flow field and fuel concentration imaging at 4.8 kHz in an operating engine," *Applied Physics B,* vol. 97, no. 4, p. 887, 2009.
[80] V. Sick, M. C. Drake, and T. D. Fansler, "High-speed imaging for direct-injection gasoline engine research and development," *Experiments in fluids,* vol. 49, no. 4, pp. 937-947, 2010.
[81] R. Gordon, C. Heeger, and A. Dreizler, "High-speed mixture fraction imaging," *Applied Physics B,* vol. 96, no. 4, pp. 745-748, 2009.
[82] M. Köhler, I. Boxx, K. Geigle, and W. Meier, "Simultaneous planar measurements of soot structure and velocity fields in a turbulent lifted jet flame at 3 kHz," *Applied Physics B,* vol. 103, no. 2, p. 271, 2011.
[83] M. Cundy, P. Trunk, A. Dreizler, and V. Sick, "Gas-phase toluene LIF temperature imaging near surfaces at 10 kHz," *Experiments in fluids,* vol. 51, no. 5, pp. 1169-1176, 2011.
[84] S. D. Hammack, C. D. Carter, J. R. Gord, and T. Lee, "Nitric-oxide planar laser-induced fluorescence at 10 kHz in a seeded flow, a plasma discharge, and a flame," *Applied optics,* vol. 51, no. 36, pp. 8817-8824, 2012.

[85] N. Fuhrmann, E. Baum, J. Brübach, and A. Dreizler, "High-speed phosphor thermometry," *Review of Scientific Instruments,* vol. 82, no. 10, p. 104903, 2011.
[86] C. D. Carter, S. Hammack, and T. Lee, "High-speed planar laser-induced fluorescence of the CH radical using the $$C^{ 2} \varSigma ^{ + } {-}X^{ 2} \varPi \left({0,0} \right)$$ C 2 Σ + - X 2 Π 0 , 0 band," *Applied Physics B,* vol. 116, no. 3, pp. 515-519, 2014// 2014.
[87] C. D. Carter, S. Hammack, and T. Lee, "High-speed flamefront imaging in premixed turbulent flames using planar laser-induced fluorescence of the CH C−X band," (in English), *Combustion & Flame,* vol. 168, 2016.
[88] J. Zhang, K. K. Venkatesan, G. B. King, N. M. Laurendeau, and M. W. Renfro, "Two-point time-series measurements of minor-species concentrations in a turbulent nonpremixed flame," *Optics letters,* vol. 30, no. 23, pp. 3144-3146, 2005.
[89] K. K. Venkatesan, J. Zhang, G. B. King, N. M. Laurendeau, and M. W. Renfro, "Hydroxyl space-time correlation measurements in partially premixed turbulent opposed-jet flames," *Applied Physics B: Lasers & Optics,* Article vol. 89, no. 1, pp. 129-140, 2007.
[90] J. Zhang, G. King, and N. Laurendeau, "Characterization of fluctuating hydroxyl concentrations in a turbulent nonpremixed hydrogen–nitrogen jet flame," *Applied Physics B,* vol. 97, no. 4, p. 897, 2009.
[91] M. W. Renfro, W. A. Guttenfelder, G. B. King, and N. M. Laurendeau, "Scalar time-series measurements in turbulent CH4/H2/N2 nonpremixed flames: OH," *Combustion and Flame,* vol. 123, no. 3, pp. 389-401, 2000/11/01/ 2000.
[92] M. W. Renfro, J. P. Gore, and N. M. Laurendeau, "Scalar time-series simulations using flamelet state relationships for turbulent non-premixed flames," *Combustion and flame,* vol. 129, no. 1-2, pp. 120-135, 2002.
[93] R. Bilger, "The Structure of Diffusion Flames," *Combustion, Science and Technology,* vol. 13, pp. 155-170, 1976.
[94] K. Nomura and S. Elghobashi, "Mixing characteristics of an inhomogeneous scalar in isotropic and homogeneous sheared turbulence," *Physics of Fluids A: Fluid Dynamics,* vol. 4, no. 3, pp. 606-625, 1992.
[95] P. Kothnur and N. Clemens, "Effects of unsteady strain rate on scalar dissipation structures in turbulent planar jets," *Physics of Fluids,* vol. 17, no. 12, p. 125104, 2005.
[96] A. M. Steinberg, J. F. Driscoll, and N. Swaminathan, "Statistics and dynamics of turbulence–flame alignment in premixed combustion," *Combustion and Flame,* vol. 159, no. 8, pp. 2576-2588, 2012.
[97] T. Sponfeldner, I. Boxx, F. Beyrau, Y. Hardalupas, W. Meier, and A. Taylor, "On the alignment of fluid-dynamic principal strain-rates with the 3D flamelet-normal in a premixed turbulent V-flame," *Proceedings of the Combustion Institute,* vol. 35, no. 2, pp. 1269-1276, 2015.

[98] B. Coriton and J. H. Frank, "Impact of heat release on strain rate field in turbulent premixed Bunsen flames," *Proceedings of the Combustion Institute,* vol. 36, no. 2, pp. 1885-1892, 2017.
[99] J. F. Driscoll, R. W. Schefer, and R. W. Dibble, "Mass fluxes <ρ′u′> and <ρ′υ′> measured in a turbulentnonpremixed flame," *Symposium (International) on Combustion,* vol. 19, no. 1, pp. 477-485, 1982/01/01/ 1982.
[100] R. W. Dibble, W. Kollmann, and R. W. Schefer, "Conserved scalar fluxes measured in a turbulent nonpremixed flame by combined laser Doppler velocimetry and laser Raman scattering," *Combustion and Flame,* vol. 55, no. 3, pp. 307-321, 1984/03/01/ 1984.
[101] J. Rehm and N. Clemens, "The relationship between vorticity/strain and reaction zone structure in turbulent non-premixed jet flames," in *Symposium (International) on Combustion*, 1998, vol. 27, no. 1, pp. 1113-1120: Elsevier.
[102] M. Gamba, N. Clemens, and O. Ezekoye, "Volumetric PIV and 2D OH PLIF imaging in the far-field of a low Reynolds number nonpremixed jet flame," *Measurement Science and Technology,* vol. 24, no. 2, p. 024003, 2012.
[103] M. Heitor, A. Taylor, and J. Whitelaw, "Simultaneous velocity and temperature measurements in a premixed flame," *Experiments in Fluids,* vol. 3, no. 6, pp. 323-339, 1985.
[104] L. P. Goss, D. D. Trump, and W. M. Roquemore, "Combined CARS/LDA instrument for simultaneous temperature and velocity measurements," *Experiments in Fluids,* vol. 6, no. 3, pp. 189-198, 1988/01/01 1988.
[105] L. P. Goss, D. D. Trump, W. F. Lynn, T. H. Chen, W. J. Schmoll, and W. M. Roquemore, "Second-generation combined CARS-LDV instrument for simultaneous temperature and velocity measurements in combusting flows," *Review of Scientific Instruments,* vol. 60, no. 4, pp. 638-645, 1989.
[106] Y. Li and R. Gupta, "Simultaneous measurement of absolute OH concentration, temperature and flow velocity in a flame by photothermal deflection spectroscopy," *Applied Physics B,* vol. 75, no. 8, pp. 903-906, 2002.
[107] S. Hu, D. Mosbacher, J. Wehrmeyer, and R. Pitz, "Simultaneous Temperature, Species and Velocity Measurements via Combined Raman Spectroscopy and HTV," in *40th AIAA/ASME/SAE/ASEE Joint Propulsion Conference and Exhibit*, 2004, p. 4167.
[108] D. Most and A. Leipertz, "Simultaneous two-dimensional flow velocity and gas temperature measurements by use of a combined particle image velocimetry and filtered Rayleigh scattering technique," *Applied Optics,* vol. 40, no. 30, pp. 5379-5387, 2001/10/20 2001.
[109] D. Most, F. Dinkelacker, and A. Leipertz, "Direct determination of the turbulent flux by simultaneous application of filtered rayleigh scattering thermometry and particle image velocimetry," *Proceedings of the Combustion Institute,* vol. 29, no. 2, pp. 2669-2677, 2002/01/01/ 2002.

[110] G. Laufer, *Introduction to optics and lasers in engineering*. Cambridge University Press, 1996.
[111] N. T. Clemens, "Flow Imaging," in *Encyclopedia of Imaging Science and Technology*: John Wiley & Sons, Inc., 2002.
[112] W. T. Silfvast, *Laser fundamentals*. Cambridge university press, 2004.
[113] M. J. Papageorge, T. A. McManus, F. Fuest, and J. A. Sutton, "Recent advances in high-speed planar Rayleigh scattering in turbulent jets and flames: increased record lengths, acquisition rates, and image quality," *Applied Physics B-Lasers and Optics,* vol. 115, no. 2, pp. 197-213, May 2014.
[114] R. K. Hanson, J. M. Seitzman, and P. H. Paul, "Planar laser-fluorescence imaging of combustion gases," *Applied Physics B,* vol. 50, no. 6, pp. 441-454, 1990.
[115] V. Weber, J. Brübach, R. Gordon, and A. Dreizler, "Pixel-based characterisation of CMOS high-speed camera systems," *Applied Physics B,* vol. 103, no. 2, pp. 421-433, 2011.
[116] R. B. Miles, W. R. Lempert, and J. N. Forkey, "Laser Rayleigh scattering," *Measurement Science and Technology,* vol. 12, no. 5, p. R33, 2001.
[117] M. Born and E. Wolf, "Principles of Optics Pergamon Press," *Chap,* vol. 3, no. 1, p. 118, 1980.
[118] T. A. McManus, I. T. Monje, and J. A. Sutton, "Experimental assessment of the Tenti S6 model for combustion-relevant gases and filtered Rayleigh scattering applications," *Applied Physics B,* vol. 125, no. 1, p. 13, 2019/01/02 2019.
[119] G. Tenti, C. D. Boley, and R. C. Desai, "On the Kinetic Model Description of Rayleigh–Brillouin Scattering from Molecular Gases," *Canadian Journal of Physics,* vol. 52, no. 4, pp. 285-290, 1974/02/15 1974.
[120] S. A., M. G. J., B. F., V. D., d. H. S., and C. C., "ADM-Aeolus Doppler wind lidar Observing System Simulation Experiment," *Quarterly Journal of the Royal Meteorological Society,* vol. 132, no. 619, pp. 1927-1947, 2006.
[121] B. Witschas, C. Lemmerz, and O. Reitebuch, "Daytime measurements of atmospheric temperature profiles (2–15 km) by lidar utilizing Rayleigh–Brillouin scatterin," *Optics Letters,* vol. 39, no. 7, pp. 1972-1975, 2014.
[122] R. Miles, J. Forkey, and W. Lempert, "Filtered Rayleigh scattering measurements in supersonic/hypersonic facilities," in *28th Joint Propulsion Conference and Exhibit*(Joint Propulsion Conferences: American Institute of Aeronautics and Astronautics, 1992.
[123] M. Boguszko and G. S. Elliott, "On the use of filtered Rayleigh scattering for measurements in compressible flows and thermal field," *Experiments in Fluids,* vol. 38, no. 1, pp. 33-49, 2005.
[124] U. Doll, G. Stockhausen, and C. Willert, "Pressure, temperature, and three-component velocity fields by filtered Rayleigh scattering velocimetr," *Optics Letters,* vol. 42, no. 19, pp. 3773-3776, 2017.

[125] U. Doll, G. Stockhausen, and C. Willert, "Endoscopic filtered Rayleigh scattering for the analysis of ducted gas flows," *Experiments in Fluids,* vol. 55, no. 3, p. 1690, 2014/02/22 2014.
[126] F. Benhassen, M. D. Polanka, and M. F. Reeder, "Trajectory Measurements of a Horizontally Oriented Buoyant Jet in a Coflow Using Filtered Rayleigh Scattering," *Journal of Aerospace Engineering,* vol. 30, no. 1, p. 04016067, 2017.
[127] J. Brübach, J. Zetterberg, A. Omrane, Z. S. Li, M. Aldén, and A. Dreizler, "Determination of surface normal temperature gradients using thermographic phosphors and filtered Rayleigh scatterin," *Applied Physics B,* vol. 84, no. 3, pp. 537-541, 2006.
[128] P. M. Allison, T. A. McManus, and J. A. Sutton, "Quantitative fuel vapor/air mixing imaging in droplet/gas regions of an evaporating spray flow using filtered Rayleigh scattering," *Optics Letters,* vol. 41, no. 6, pp. 1074-1077, Mar 2016.
[129] D. Hoffman, K. U. Münch, and A. Leipertz, "Two-dimensional temperature determination in sooting flames by filtered Rayleigh scattering," *Optics Letters,* vol. 21, no. 7, pp. 525-527, 1996/04/01 1996.
[130] G. Elliott, N. Glumac, and C. Carter, "Molecular filtered Rayleigh scattering applied to combustion," *Measurement Science and Technology,* vol. 12, no. 4, p. 452, 2001.
[131] A. P. Yalin, Y. Z. Ionikh, and R. B. Miles, "Gas temperature measurements in weakly ionized glow discharges with filtered Rayleigh scattering," *Applied Optics,* vol. 41, no. 18, pp. 3753-3762, 2002/06/20 2002.
[132] S. P. Kearney, R. W. Schefer, S. J. Beresh, and T. W. Grasser, "Temperature imaging in nonpremixed flames by joint filtered Rayleigh and Raman scattering," *Applied Optics,* vol. 44, no. 9, pp. 1548-1558, 2005.
[133] M. Raffel, C. Willert, and J. Kompenhans, *Particle Image Velocimetry: A Practical Guide*. 1998.
[134] A. K. Prasad, "Stereoscopic particle image velocimetry," *Experiments in fluids,* vol. 29, no. 2, pp. 103-116, 2000.
[135] F. Scarano, "Tomographic PIV: principles and practice," *Measurement Science and Technology,* vol. 24, no. 1, p. 012001, 2012.
[136] R. D. Keane and R. J. Adrian, "Optimization of particle image velocimeters. I. Double pulsed systems," *Measurement Science and Technology,* vol. 1, no. 11, pp. 1202-1215, 1990/11/01 1990.
[137] "FlowMaster," LaVision, Ed., ed. Germany, 2018.
[138] F. Scarano and M. L. Riethmuller, "Iterative multigrid approach in PIV image processing with discrete window offset," *Experiments in Fluids,* vol. 26, no. 6, pp. 513-523, 1999/05/01 1999.
[139] R. J. Adrian, "Dynamic ranges of velocity and spatial resolution of particle image velocimetry," *Measurement Science and Technology,* vol. 8, no. 12, p. 1393, 1997.
[140] A. Stella, G. Guj, J. Kompenhans, M. Raffel, and H. Richard, "Application of particle image velocimetry to combusting flows: design considerations and

uncertainty assessment," *Experiments in Fluids,* vol. 30, no. 2, pp. 167-180, 2001/02/01 2001.

[141] C. J. Sung, C. K. Law, and R. L Axelbaum, "Thermophoretic Effects on Seeding Particles in LDV Measurements of Flames," *Combustion Science and Technology,* vol. 99, no. 1-3, pp. 119-132, 1994/08/01 1994.

[142] B. R. Munson, D. F. Young, and T. H. Okiishi, *Fundamentals of fluid mechanics*. Seventh edition. Hoboken, NJ : John Wiley & Sons, Inc., [2013], 2013.

[143] W. Meier, R. S. Barlow, Y. L. Chen, and J. Y. Chen, "Raman/Rayleigh/LIF measurements in a turbulent CH4/H2/N2 jet diffusion flame: experimental techniques and turbulence–chemistry interaction," *Combustion and Flame,* vol. 123, no. 3, pp. 326-343, 2000/11/01/ 2000.

[144] A. Melling, "Tracer particles and seeding for particle image velocimetry," *Measurement Science and Technology,* vol. 8, no. 12, pp. 1406-1416, 1997/12/01 1997.

[145] F. Fuest, M. J. Papageorge, W. R. Lempert, and J. A. Sutton, "Ultrahigh laser pulse energy and power generation at 10kHz," *Optics Letters,* vol. 37, no. 15, pp. 3231-3233, 2012/08/01 2012.

[146] M. Papageorge and J. A. Sutton, "Statistical processing and convergence of finite-record-length time-series measurements from turbulent flows," *Experiments in Fluids,* vol. 57, no. 8, p. 126, 2016/07/23 2016.

[147] K. M. Tacina and W. J. Dahm, "Effects of heat release on turbulent shear flows. Part 1. A general equivalence principle for non-buoyant flows and its application to turbulent jet flames," *Journal of Fluid Mechanics,* vol. 415, pp. 23-44, 2000.

[148] C. Schneider, A. Dreizler, J. Janicka, and E. P. Hassel, "Flow field measurements of stable and locally extinguishing hydrocarbon-fuelled jet flames," (in English), *Combustion & Flame,* vol. 135, no. 1/2, 2003.

[149] R. Patton, K. Gabet, N. Jiang, W. Lempert, and J. Sutton, "Multi-kHz mixture fraction imaging in turbulent jets using planar Rayleigh scattering," *Applied Physics B,* vol. 106, no. 2, pp. 457-471, 2012.

[150] P. Lavoie, G. Avallone, F. De Gregorio, G. P. Romano, and R. A. Antonia, "Spatial resolution of PIV for the measurement of turbulence," *Experiments in Fluids,* journal article vol. 43, no. 1, pp. 39-51, July 01 2007.

[151] Y. Zhu and R. A. Antonia, "Effect of wire separation on X-probe measurements in a turbulent flow," *Journal of Fluid Mechanics,* vol. 287, pp. 199-223, 1995.

[152] R. A. Antonia, Y. Zhu, and J. Kim, "On the measurement of lateral velocity derivatives in turbulent flows," *Experiments in Fluids,* journal article vol. 15, no. 1, pp. 65-69, June 01 1993.

[153] P. V. Vukoslavčević, N. Beratlis, E. Balaras, J. M. Wallace, and O. Sun, "On the spatial resolution of velocity and velocity gradient-based turbulence statistics measured with multi-sensor hot-wire probes," *Experiments in Fluids,* journal article vol. 46, no. 1, p. 109, August 07 2008.

[154] G. K. Batchelor, "Small-scale variation of convected quantities like temperature in turbulent fluid Part 1. General discussion and the case of small conductivity," *Journal of Fluid Mechanics,* vol. 5, no. 1, pp. 113-133, 1959.
[155] G. Wang, A. N. Karpetis, and R. S. Barlow, "Dissipation length scales in turbulent nonpremixed jet flames," *Combustion and Flame,* vol. 148, no. 1, pp. 62-75, 2007/01/01/ 2007.
[156] G. I. Taylor, "Statistical Theory of Turbulence," *Proceedings of the Royal Society of London. Series A - Mathematical and Physical Sciences,* 10.1098/rspa.1935.0158 vol. 151, no. 873, p. 421, 1935.
[157] A. Birch, D. Brown, M. Dodson, and J. Thomas, "The turbulent concentration field of a methane jet," *Journal of Fluid Mechanics,* vol. 88, no. 3, pp. 431-449, 1978.
[158] C. W. Smith, J. W. Bieber, and W. H. Matthaeus, "Cosmic-ray pitch angle scattering in isotropic turbulence. II-Sensitive dependence on the dissipation range spectrum," *The Astrophysical Journal,* vol. 363, pp. 283-291, 1990.
[159] N. R. Bansal, "Characterization of kinematic properties of turbulent non-premixed jet flames using high-speed Particle Image Velocimetry," M.Sc. Masters, Mechanical Engineering, Ohio State University, 2017.
[160] J. A. B. Wills, "On convection velocities in turbulent shear flows," *Journal of Fluid Mechanics,* vol. 20, no. 3, pp. 417-432, 1964.
[161] X. Zhao and G.-W. He, "Space-time correlations of fluctuating velocities in turbulent shear flows," *Physical Review E,* vol. 79, no. 4, p. 046316, 04/16/ 2009.
[162] M. Papageorge, "A study of scalar mixing in gas phase turbulent jets using high repetition rate imaging," The Ohio State University, 2017.
[163] X. He *et al.*, "Reynolds numbers and the elliptic approximation near the ultimate state of turbulent Rayleigh-Bénard convection," (in English), *New J. Phys. New Journal of Physics,* vol. 17, no. 6, 2015.
[164] L. Guo, D. Li, X. Zhang, and G.-W. He, "LES prediction of space-time correlations in turbulent shear flow," *Acta Mechanica Sinica,* vol. 28, no. 4, pp. 993-998, 2012.
[165] G.-W. He and J.-B. Zhang, "Elliptic model for space-time correlations in turbulent shear flows," *Physical Review E,* vol. 73, no. 5, p. 055303, 05/24/ 2006.
[166] M. G. Allen, "Diode laser absorption sensors for gas-dynamic and combustion flows," *Measurement Science and technology,* vol. 9, no. 4, p. 545, 1998.
[167] P. Emmerman, R. Goulard, R. Santoro, and H. Semerjian, "Multiangular absorption diagnostics of a turbulent argon-methane jet," *Journal of Energy,* vol. 4, no. 2, pp. 70-77, 1980.
[168] R. W. Dibble and R. E. Hollenbach, "Laser rayleigh thermometry in turbulent flames," *Symposium (International) on Combustion,* vol. 18, no. 1, p. 1489, 01/01/Number 1/January 1981 1981.
[169] T. A. McManus, M. J. Papageorge, F. Fuest, and J. A. Sutton, "Spatio-temporal characteristics of temperature fluctuations in turbulent non-premixed jet flames," *Proceedings of the Combustion Institute,* vol. 35, pp. 1191-1198, 2015.

[170] J. N. Forkey, W. R. Lempert, and R. B. Miles, "Corrected and calibrated I2 absorption model at frequency-doubled Nd:YAG laser wavelengths," *Applied Optics,* vol. 36, no. 27, pp. 6729-6738, 1997/09/20 1997.
[171] J. Forkey, "Development and demonstration of filtered Rayleigh scattering : a laser based flow diagnostic for planar measurement of velocity, temperature, and pressure," 1996.
[172] R. Patton and J. Sutton, "Seed laser power effects on the spectral purity of Q-switched Nd:YAG lasers and the implications for filtered rayleigh scattering measurements," *Applied Physics B: Lasers & Optics,* Article vol. 111, no. 3, pp. 457-468, 2013.
[173] C. D. Boley, R. C. Desai, and G. Tenti, "Kinetic Models and Brillouin Scattering in a Molecular Gas," *Canadian Journal of Physics,* vol. 50, no. 18, pp. 2158-2173, 1972/09/15 1972.
[174] M. O. Vieitez *et al.*, "Coherent and spontaneous Rayleigh-Brillouin scattering in atomic and molecular gases and gas mixtures," *Physical Review A,* vol. 82, no. 4, p. 043836, 10/25/ 2010.
[175] Y. Ma *et al.*, "Analysis of Rayleigh-Brillouin spectral profiles and Brillouin shifts in nitrogen gas and ai," *Optics Express,* vol. 22, no. 2, pp. 2092-2104, 2014.
[176] B. Witschas, M. O. Vieitez, E.-J. van Duijn, O. Reitebuch, W. van de Water, and W. Ubachs, "Spontaneous Rayleigh–Brillouin scattering of ultraviolet light in nitrogen, dry air, and moist ai," *Applied Optics,* vol. 49, no. 22, pp. 4217-4227, 2010.
[177] Z. Y. Gu, W. Ubachs, and W. van de Water, "Rayleigh–Brillouin scattering of carbon dioxide," *Optics Letters,* vol. 39, no. 11, pp. 3301-3304, 2014.
[178] Z. Gu and W. Ubachs, "A systematic study of Rayleigh-Brillouin scattering in air, N2, and O2 gases," *The Journal of Chemical Physics,* vol. 141, no. 10, p. 104320, 2014/09/14 2014.
[179] Z. Gu, B. Witschas, W. van de Water, and W. Ubachs, "Rayleigh–Brillouin scattering profiles of air at different temperatures and pressure," *Applied Optics,* vol. 52, no. 19, pp. 4640-4651, 2013.
[180] *Planar Doppler Velocimetry Hardware*. Available: https://psp-tsp.com/pdv/pdv-hardware.html
[181] T. L. Labus and E. P. Symons, "Experimental investigation of an axisymmetric free jet with an initially uniform velocity profile," 1972.
[182] J. Gauntner, P. Hrycak, D. Lee, and J. Livingood, "Experimental flow characteristics of a single turbulent jet impinging on a flat plate," 1970.
[183] M. Thring and M. Newby, "Combustion length of enclosed turbulent jet flames," in *Symposium (International) on Combustion*, 1953, vol. 4, no. 1, pp. 789-796: Elsevier.
[184] R. D. Hancock, K. E. Bertagnolli, and R. P. Lucht, "Nitrogen and hydrogen CARS temperature measurements in a hydrogen/air flame using a near-adiabatic flat-

flame burner," *Combustion and Flame,* vol. 109, no. 3, pp. 323-331, 1997/05/01/ 1997.
[185] M. J. Papageorge, C. Arndt, F. Fuest, W. Meier, and J. A. Sutton, "High-speed mixture fraction and temperature imaging of pulsed, turbulent fuel jets auto-igniting in high-temperature, vitiated co-flows," *Experiments in Fluids,* vol. 55, no. 7, p. 1763, 2014/06/17 2014.
[186] J. A. Sutton and J. F. Driscoll, "Rayleigh scattering cross sections of combustion species at 266, 355, and 532 nm for thermometry application," *Optics Letters,* vol. 29, no. 22, pp. 2620-2622, 2004.
[187] C. Carter, "Laser-based Rayleigh and Mie scattering methods," ed: Wiley, New York, 1996, pp. 1078-1093.
[188] J. A. Sutton and R. A. Patton, "Improvements in filtered Rayleigh scattering measurements using Fabry–Perot etalons for spectral filtering of pulsed, 532-nm Nd:YAG output," *Applied Physics B,* vol. 116, no. 3, pp. 681-698, 2014// 2014.
[189] R. L. McKenzie, "Measurement capabilities of planar Doppler velocimetry using pulsed lasers," *Applied Optics,* vol. 35, no. 6, pp. 948-964, 1996/02/20 1996.
[190] T. A. McManus and J. A. Sutton, "Quantitative Planar Temperature Imaging in Turbulent Non-premixed Flames using Filtered Rayleigh Scattering," *Applied Optics (submitted),* 2019.
[191] "CHEMKIN-PRO 15112," ed. San Diego: Reactio Design, 2011.
[192] G. P. Smith *et al.* (2000). *GRI-Mech 3.0*. Available: http://www.me.berkeley.edu/gri_mech/
[193] J. Kojima, C.-M. Lee, and Q.-V. Nguyen, "Laser Pulse-Stretching Using Multiple Optical Ring-Cavities," ed. United States: NASA Center for Aerospace Information (CASI), 2002.
[194] I. Daubechies and W. Sweldens, "Factoring wavelet transforms into lifting steps," *Journal of Fourier Analysis and Applications,* journal article vol. 4, no. 3, pp. 247-269, May 01 1998.
[195] D. Garcia, "Robust smoothing of gridded data in one and higher dimensions with missing values," *Computational statistics & data analysis,* vol. 54, no. 4, pp. 1167-1178, 2010.
[196] B. Wieneke, "PIV anisotropic denoising using uncertainty quantification," *Experiments in Fluids,* vol. 58, no. 8, p. 94, 2017/07/07 2017.
[197] J. Westerweel and F. Scarano, "Universal outlier detection for PIV data," *Experiments in Fluids,* journal article vol. 39, no. 6, pp. 1096-1100, December 01 2005.
[198] T. Peng, "CircularHough_Grd," ed. Mathworks, 2006.
[199] P. Holoborodko, "Noise Robust Gradient Operators.," 2009.
[200] I. Wygnanski and H. Fiedler, "Some measurements in the self-preserving jet," *Journal of Fluid Mechanics,* vol. 38, no. 3, pp. 577-612, 1969.
[201] P. E. Dimotakis, "The mixing transition in turbulent flows," *Journal of Fluid Mechanics,* vol. 409, pp. 69-98, 2000.

[202] P. E. Dimotakis, "Turbulent mixing," *Annu. Rev. Fluid Mech.,* vol. 37, pp. 329-356, 2005.
[203] J. Zhou, R. J. Adrian, S. Balachandar, and T. Kendall, "Mechanisms for generating coherent packets of hairpin vortices in channel flow," *Journal of fluid mechanics,* vol. 387, pp. 353-396, 1999.
[204] P. Chakraborty, S. Balachandar, and R. J. Adrian, "On the relationships between local vortex identification schemes," *Journal of fluid mechanics,* vol. 535, pp. 189-214, 2005.
[205] R. M. Kerr, "Higher-order derivative correlations and the alignment of small-scale structures in isotropic numerical turbulence," *Journal of Fluid Mechanics,* vol. 153, pp. 31-58, 1985.
[206] E. D. Siggia, "Numerical study of small-scale intermittency in three-dimensional turbulence," *Journal of Fluid Mechanics,* vol. 107, pp. 375-406, 1981.
[207] J. Jiménez, A. A. Wray, P. G. Saffman, and R. S. Rogallo, "The structure of intense vorticity in isotropic turbulence," *Journal of Fluid Mechanics,* vol. 255, pp. 65-90, 1993.
[208] A. Attili and F. Bisetti, "Conditional Flow Statistics And Alignment Of Principal Strain Rates, Vorticity, And Scalar Gradients In A Turbulent Nonpremixed Jet Flame," in *Proceedings of Ninth International Symposium on Turbulence and Shear Flow Phenomena (TSFP-9)*, 2015.
[209] A. M. Steinberg, B. Coriton, and J. Frank, "Influence of combustion on principal strain-rate transport in turbulent premixed flames," *Proceedings of the Combustion Institute,* vol. 35, no. 2, pp. 1287-1294, 2015.
[210] B. Coriton and J. H. Frank, "High-speed tomographic PIV measurements of strain rate intermittency and clustering in turbulent partially-premixed jet flames," *Proceedings of the Combustion Institute,* vol. 35, no. 2, pp. 1243-1250, 2015.
[211] T. S. Lund and M. M. Rogers, "An improved measure of strain state probability in turbulent flows," *Physics of Fluids,* vol. 6, no. 5, pp. 1838-1847, 1994.
[212] A. Lipatnikov and J. Chomiak, "Effects of premixed flames on turbulence and turbulent scalar transport," *Progress in Energy and Combustion Science,* vol. 36, no. 1, pp. 1-102, 2010.
[213] D. Han and M. G. Mungal, "Simultaneous measurement of velocity and CH layer distribution in turbulent non-premixed flames," *Proceedings of the Combustion Institute,* vol. 28, no. 1, pp. 261-267, 2000/01/01/ 2000.
[214] K. K.-y. Kuo and R. Acharya, *Fundamentals of turbulent and multiphase combustion*. John Wiley & Sons, 2012.
[215] N. Heys, F. Roper, and P. Kayes, "A mathematical model of laminar axisymmetrical natural gas flames," *Computers & Fluids,* vol. 9, no. 1, pp. 85-103, 1981.
[216] G. Wang, N. Clemens, and P. Varghese, "High-repetition rate measurements of temperature and thermal dissipation in a non-premixed turbulent jet flame," *Proceedings of the combustion Institute,* vol. 30, no. 1, pp. 691-699, 2005.

[217] L. K. Su and N. T. Clemens, "The structure of fine-scale scalar mixing in gas-phase planar turbulent jets," *Journal of Fluid Mechanics,* vol. 488, pp. 1-29, 2003.
[218] V. R. Vedula *et al.*, "Residual-stress predictions in polycrystalline alumina," *Journal of the American Ceramic Society,* vol. 84, no. 12, pp. 2947-2954, 2001.
[219] S. Chaudhuri, H. Kolla, H. L. Dave, E. R. Hawkes, J. H. Chen, and C. K. Law, "Flame thickness and conditional scalar dissipation rate in a premixed temporal turbulent reacting jet," *Combustion and Flame,* vol. 184, pp. 273-285, 2017.
[220] J. Chen, J. Lienau, and W. Kollmann, "Numerical Simulation of Low Re-number Turbulence in Round Jets," in *Ninth Symposium on" Turbulent Shear Flows"*, 1993, vol. 9, pp. 1-6.
[221] K. A. Buch and W. J. A. Dahm, "Experimental study of the fine-scale structure of conserved scalar mixing in turbulent shear flows. Part 2. Sc≈1," *Journal of Fluid Mechanics,* vol. 364, pp. 1-29, 1998.
[222] K. A. Buch and W. J. A. Dahm, "Experimental study of the fine-scale structure of conserved scalar mixing in turbulent shear flows. Part 1. Sc [Gt] 1," *Journal of Fluid Mechanics,* vol. 317, pp. 21-71, 1996.
[223] D. A. Feikema, D. Everest, and J. F. Driscoll, "Images of dissipation layers to quantify mixing within a turbulent jet," *AIAA journal,* vol. 34, no. 12, pp. 2531-2538, 1996.
[224] K. R. Sreenivasan, "On the scaling of the turbulence energy dissipation rate," *The Physics of fluids,* vol. 27, no. 5, pp. 1048-1051, 1984.